



energies

Advances in Hydrogen Energy

Edited by

Samuel Simon Araya and Vincenzo Liso

Printed Edition of the Special Issue Published in *Energies*

Advances in Hydrogen Energy

Advances in Hydrogen Energy

Editors

Samuel Simon Araya

Vincenzo Liso

MDPI • Basel • Beijing • Wuhan • Barcelona • Belgrade • Manchester • Tokyo • Cluj • Tianjin



Editors

Samuel Simon Araya
AAU Energy
Aalborg University
Aalborg
Denmark

Vincenzo Liso
AAU Energy
Aalborg University
Aalborg
Denmark

Editorial Office

MDPI
St. Alban-Anlage 66
4052 Basel, Switzerland

This is a reprint of articles from the Special Issue published online in the open access journal *Energies* (ISSN 1996-1073) (available at: www.mdpi.com/journal/energies/special_issues/Advances_Hydrogen_Energy).

For citation purposes, cite each article independently as indicated on the article page online and as indicated below:

LastName, A.A.; LastName, B.B.; LastName, C.C. Article Title. <i>Journal Name</i> Year , <i>Volume Number</i> , Page Range.
--

ISBN 978-3-0365-1935-7 (Hbk)

ISBN 978-3-0365-1934-0 (PDF)

© 2021 by the authors. Articles in this book are Open Access and distributed under the Creative Commons Attribution (CC BY) license, which allows users to download, copy and build upon published articles, as long as the author and publisher are properly credited, which ensures maximum dissemination and a wider impact of our publications.

The book as a whole is distributed by MDPI under the terms and conditions of the Creative Commons license CC BY-NC-ND.

Contents

About the Editors	vii
Preface to "Advances in Hydrogen Energy"	ix
Muhammad Aziz, Agung Tri Wijayanta and Asep Bayu Dani Nandiyanto Ammonia as Effective Hydrogen Storage: A Review on Production, Storage and Utilization Reprinted from: <i>Energies</i> 2020 , <i>13</i> , 3062, doi:10.3390/en13123062	1
Linda Barelli, Gianni Bidini and Giovanni Cinti Operation of a Solid Oxide Fuel Cell Based Power System with Ammonia as a Fuel: Experimental Test and System Design Reprinted from: <i>Energies</i> 2020 , <i>13</i> , 6173, doi:10.3390/en13236173	27
Giovanni Cinti, Vincenzo Liso, Simon Lennart Sahlin and Samuel Simon Araya System Design and Modeling of a High Temperature PEM Fuel Cell Operated with Ammonia as a Fuel Reprinted from: <i>Energies</i> 2020 , <i>13</i> , 4689, doi:10.3390/en13184689	47
Meiting Guo, Xiao Ru, Zijing Lin, Guoping Xiao and Jianqiang Wang Optimization Design of Rib Width and Performance Analysis of Solid Oxide Electrolysis Cell Reprinted from: <i>Energies</i> 2020 , <i>13</i> , 5468, doi:10.3390/en13205468	65
Zeng Gao, Fei Ji, Dongfeng Cheng, Congxin Yin, Jitai Niu and Josip Brnic Hydrolysis-Based Hydrogen Generation Investigation of Aluminum System Adding Low-Melting Metals Reprinted from: <i>Energies</i> 2021 , <i>14</i> , 1433, doi:10.3390/en14051433	83
Giuseppe Sdanghi, Gaël Maranzana, Alain Celzard and Vanessa Fierro Towards Non-Mechanical Hybrid Hydrogen Compression for Decentralized Hydrogen Facilities Reprinted from: <i>Energies</i> 2020 , <i>13</i> , 3145, doi:10.3390/en13123145	95
Konstantin I. Matveev and Jacob Leachman Numerical Simulations of Cryogenic Hydrogen Cooling in Vortex Tubes with Smooth Transitions Reprinted from: <i>Energies</i> 2021 , <i>14</i> , 1429, doi:10.3390/en14051429	123
Hyemin Song, Younghyeon Kim, Dongjin Yu, Byoung Jae Kim, Hyunjin Ji and Sangseok Yu A Computational Analysis of a Methanol Steam Reformer Using Phase Change Heat Transfer Reprinted from: <i>Energies</i> 2020 , <i>13</i> , 4324, doi:10.3390/en13174324	137
Guoqiang Wang, Feng Wang and Bohong Chen Performance Study on Methanol Steam Reforming Rib Micro-Reactor with Waste Heat Recovery Reprinted from: <i>Energies</i> 2020 , <i>13</i> , 1564, doi:10.3390/en13071564	151
Samuel Simon Araya, Sobi Thomas, Andrej Lotrič, Simon Lennart Sahlin, Vincenzo Liso and Søren Juhl Andreasen Effects of Impurities on Pre-Doped and Post-Doped Membranes for High Temperature PEM Fuel Cell Stacks Reprinted from: <i>Energies</i> 2021 , <i>14</i> , 2994, doi:10.3390/en14112994	169

Chongbo Zhou, Lingyi Guo, Li Chen, Xin Tian, Tiefeng He and Qinghua Yang Pore-Scale Modeling of Air–Water Two Phase Flow and Oxygen Transport in Gas Diffusion Layer of Proton Exchange Membrane Fuel Cell Reprinted from: <i>Energies</i> 2021 , <i>14</i> , 3812, doi:10.3390/en14133812	187
Torsten Berning and Søren Knudsen Kær A Thermodynamic Analysis of an Air-Cooled Proton Exchange Membrane Fuel Cell Operated in Different Climate Regions Reprinted from: <i>Energies</i> 2020 , <i>13</i> , 2611, doi:10.3390/en13102611	205
Artem Chesalkin, Petr Kacor and Petr Moldrik Heat Transfer Optimization of NEXA Ballard Low-Temperature PEMFC Reprinted from: <i>Energies</i> 2021 , <i>14</i> , 2182, doi:10.3390/en14082182	219
Torsten Berning On the Nature of Electro-Osmotic Drag Reprinted from: <i>Energies</i> 2020 , <i>13</i> , 4726, doi:10.3390/en13184726	237

About the Editors

Samuel Simon Araya

Samuel Simon Araya is an associate professor at Aalborg University since 2015 and the leader of the Fuel Cell Systems research group since January 2018. He obtained his MSc in environmental engineering in 2008 from the University of Perugia in Italy and his PhD degree in energy technology in 2012 at Aalborg University, Denmark. He has more than 12 years of experience in research, teaching, supervision and project management in the field of fuel cells and hydrogen technologies. His research interests include the experimental characterization and modeling of electrochemical energy conversion devices, mainly reformed methanol-fed high temperature PEM fuel cells (HT-PEMFCs), low temperature PEM fuel cells and electrolyzers, at single cell, stack and system levels. He is involved in several national and international research projects on the diagnostics, characterization, development and deployment of both fuel cells and electrolyzer systems for enhanced hydrogen solutions.

Vincenzo Liso

Ass. Prof. Vincenzo Liso is currently an associate professor at the Department of Energy Technology, Denmark, where he earned his PhD in solid oxide fuel cells systems in 2012. He earned his MSc degree in environmental engineering from University of Perugia, Italy, in 2005. He teaches and works on research projects in the field of chemical and electrochemical processes, system thermal integration and fuel conversion. He has acted both as a research project leader and research project manager in cooperation with companies and other research institutions.

Preface to “Advances in Hydrogen Energy”

This book, which is a reprint of articles published in the Special Issue *Advances in Hydrogen Energy* in *Energies*, seeks to contribute to disseminating the most recent advancements in the field of hydrogen energy. It does so by presenting scientific works from around the world covering both modeling and experimental analysis. The focus is placed on research covering all aspects of the hydrogen energy, from production to storage and final use, including the development of other easy to store and transport hydrogen-based energy carriers via the power-to-x (PtX) route, such as ammonia and methanol.

Hydrogen energy research and development has attracted growing attention as one of the key solutions for clean future energy systems. In order to reduce greenhouse gas emissions, governments across the world are developing ambitious policies to support hydrogen technology, and an increasing level of funding has been allocated for projects of research, development, and demonstration of these technologies. At the same time, the private sector is capitalizing on the opportunity with larger investments in hydrogen technology solutions.

While intense research activities have been dedicated to this field, several issues require further research prior to achieving full commercialization of hydrogen technology solutions. This book addresses some of these issues by presenting detailed models to optimize design strategies and operating conditions for the entire hydrogen value chain, covering production via electrolysis, storage and use in different types of fuel cells and in different forms of energy carriers. It also includes comprehensive reviews of some aspects of the hydrogen economy and experimental results obtained from the operations of different fuel cell technologies.

The editors would like to thank all the authors for their contributions, the reviewers for their time and effort in assessing the quality of the papers and the MDPI editorial office for their assistance in managing the Special Issue and the book.

Samuel Simon Araya, Vincenzo Liso

Editors

Review

Ammonia as Effective Hydrogen Storage: A Review on Production, Storage and Utilization

Muhammad Aziz ^{1,*} , Agung Tri Wijayanta ² and Asep Bayu Dani Nandiyanto ³

¹ Institute of Industrial Science, The University of Tokyo, Tokyo 153-8505, Japan

² Mechanical Engineering Department, Engineering Faculty, Sebelas Maret University, Surakarta 57126, Indonesia; agungtw@uns.ac.id

³ Departemen Kimia, Universitas Pendidikan Indonesia, Bandung 40154, Indonesia; nandiyanto@upi.edu

* Correspondence: maziz@iis.u-tokyo.ac.jp; Tel.: +81-3-5452-6196

Received: 18 March 2020; Accepted: 10 June 2020; Published: 12 June 2020



Abstract: Ammonia is considered to be a potential medium for hydrogen storage, facilitating CO₂-free energy systems in the future. Its high volumetric hydrogen density, low storage pressure and stability for long-term storage are among the beneficial characteristics of ammonia for hydrogen storage. Furthermore, ammonia is also considered safe due to its high auto ignition temperature, low condensation pressure and lower gas density than air. Ammonia can be produced from many different types of primary energy sources, including renewables, fossil fuels and surplus energy (especially surplus electricity from the grid). In the utilization site, the energy from ammonia can be harvested directly as fuel or initially decomposed to hydrogen for many options of hydrogen utilization. This review describes several potential technologies, in current conditions and in the future, for ammonia production, storage and utilization. Ammonia production includes the currently adopted Haber–Bosch, electrochemical and thermochemical cycle processes. Furthermore, in this study, the utilization of ammonia is focused mainly on the possible direct utilization of ammonia due to its higher total energy efficiency, covering the internal combustion engine, combustion for gas turbines and the direct ammonia fuel cell. Ammonia decomposition is also described, in order to give a glance at its progress and problems. Finally, challenges and recommendations are also given toward the further development of the utilization of ammonia for hydrogen storage.

Keywords: ammonia; hydrogen; production; storage; utilization; CO₂ free

1. Introduction

The adoption of fossil fuels in conventional energy systems has led to the increase of the concentration of greenhouse gases (GHGs) in the atmosphere and the rise of ocean levels [1]. Being aware of this reality, recently, the adoption of renewable energy has increased rapidly due to its low environmental impacts. In addition, the massive deployment and the maturity of technology have made renewable energy economic and competitive against conventional fossil fuels. It is expected that a clean and CO₂-free energy system can be realized to improve the quality of human life. The Conference of Parties 21 (COP21), held in 2015, issued the world commitments to the mitigation of climate change and keeping the increase of the global average temperature below 2 °C higher than the pre-industrial level [2]. Moreover, the Marrakech Partnership for Global Climate Action has strongly promoted collective striving for the 1.5 °C temperature goal through mutual collaboration among governments, regions, businesses and investors [3].

Liberalization and decentralization in the energy sector has also opened up the opportunity to the customers to behave simultaneously as energy producer and consumer. The fluctuating demand and supply sides in the future energy system also require an effective adoption of secondary energy

sources (energy carriers) which can be effectively and economically produced, stored and utilized. The future energy system is expected to be able to facilitate the optimum utilization of local energy resources (especially renewable energy) [4], reduction of global GHG emission, improvement of urban environmental quality and creation of industrial activities focusing the energy sector toward a sustainable economy [5].

Hydrogen (H_2) is one of the secondary energy sources which produces no GHG by-products during its utilization, because the oxidation of hydrogen generates water (H_2O). It is the most abundant element in the universe (more than 90% of the total available atoms), the lightest element (molecular weight of 2.016) and non-toxic [6]. Hydrogen has significantly higher gravimetric energy density (120 MJ/kg) compared to other conventional fuels, such as gasoline (44 MJ/kg). In addition, hydrogen can be produced from various kinds of primary energy sources, including renewables and non-renewables. Many technological routes are available, including thermochemical routes (gasification, chemical looping, reforming), biochemical routes (fermentation) and electrolysis [7]. Furthermore, the utilization of hydrogen as an energy source can also be performed via various technologies, such as fuel cells, combustion and mixing with other fuels. However, hydrogen suffers a disadvantage in its volumetric energy density, which is only 3 Wh/L, leading to difficulties in its storage. Hydrogen storage is the key enabling technology which will lead to the successful deployment of hydrogen, including its economic sustainability.

There are several key parameters in the selection of hydrogen storage methods and materials, including: (a) gravimetric and volumetric hydrogen densities, (b) energy efficiency, (c) refueling time, (d) durability, (e) cost, (f) standards, (g) technology maturity and (h) life-cycle and efficiency analysis [8]. Energy efficiency deals with the energy consumed during both the storage and release of hydrogen to and from its storage states or hydrogen storage materials. Furthermore, durability is correlated to its lifetime, especially in case of reversible hydrogen storage materials. Standards for the storage systems and interface are required in order to facilitate the implementation of the storage technology, as well as safety and public acceptance. The successful development of hydrogen storage is crucial for the future of hydrogen economy [9,10].

In order to store hydrogen effectively, different hydrogen storage technologies have been studied and developed. These include compressed and liquefied hydrogen, liquid organic carriers [11], metal hydrides [12,13], methanol (CH_3OH) and ammonia (NH_3). Hydrogen storage covers both mobile and stationary systems. Compressed hydrogen is the simplest way to store hydrogen, although its hydrogen density is low ($42.2 \text{ kg-H}_2/\text{m}^3$ at 69 MPa). Compressed hydrogen requires high pressure to effectively store the gaseous hydrogen. In the case of a hydrogen vehicle, a high pressure tank of about 70 MPa is currently required in order to store the hydrogen to achieve a similar driving range to conventional vehicles. Moreover, as hydrogen is a very light and small element, leakage from high pressure can easily occur, in addition to the problem related to hydrogen embrittlement. Liquid hydrogen is also considered promising and efficient as a hydrogen storage option, because it has higher hydrogen density ($70.8 \text{ kg-H}_2/\text{m}^3$), which is about 800 times that of uncompressed hydrogen (0.08988 kg/m^3 at standard temperature and pressure (STP)), as well as high purity. However, in order to bring hydrogen into the liquid phase, refrigeration to a very low temperature ($-253 \text{ }^\circ\text{C}$) is required, leading to high energy consumption. Moreover, due to this cooling requirement, liquid hydrogen is not preferred for long term storage or long distance of transportation, because the energy input needed to keep the temperature very low is also intensive. Another problem of liquid hydrogen is the conversion of ortho-hydrogen (where the spins of both nuclei are in the same direction) to para-hydrogen (where the spins of both nuclei are in opposite directions) [14]. As this isomer conversion is exothermic, the generated heat causes the boil-off phenomenon, in which a part of liquid hydrogen is evaporated into a gaseous form.

Solid-state systems are also considered a potential hydrogen storage method. They can reversibly adsorb and release hydrogen. The storage of hydrogen occurs by two different methods: physisorption and chemisorption [15,16]. In the former, hydrogen molecules are adsorbed on the surface of

an adsorbent (storage medium) due to the intermolecular force that exists between the adsorbate (hydrogen) and adsorbent. Physisorption hydrogen storages include carbon nanotubes, activated carbon, zeolites and metal-organic frameworks (MOFs). These materials are advantageous in terms of their reversibility and relatively fast kinetics. However, they have several disadvantages, including low hydrogen storage (lower than 5 wt% at room temperature) and their requirement of low temperatures for larger hydrogen storage capacities [17,18]. On the other hand, in chemisorption hydrogen storage, hydrogen chemically reacts with solids, producing hydrides. These hydrides can be categorized into metal, complex and chemical hydrides. Recently, various complex hydrides have been developed, including NaAlH_4 , $\text{Mg}(\text{NH}_2)_2\text{-LiH}$. Although these materials show high hydrogen density (up to 10 wt%), their hydrogenation and dehydrogenation are very complex and their reversibility is relatively low [19,20]. In addition, these processes also lead to the decrease of energy efficiency, especially the dehydrogenation process, which is generally endothermic.

Methanol is also a promising candidate for hydrogen storage, as well the utilization of CO_2 via hydrogenation [21]. The adoption of methanol is strongly correlated with the idea of power-to-product (P2X), which utilizes surplus electricity to produce chemical fuels. Hydrogen can be released from methanol through thermolysis, steam reforming and partial oxidation [21]. However, the adoption of methanol to store hydrogen leads to environmental problems in the utilization site because of the release of CO_2 when methanol is directly utilized or decomposed. This leads to a non CO_2 -free energy system. In addition, the separation of CO_2 is also energy intensive. The established CO_2 separation based on absorption using amine solution consumes approximately 1.1 kWh/kg- CO_2 [22].

On the other hand, ammonia is highly valued as a potential hydrogen storage option. It has high hydrogen density (17.8 wt%), as well as high flexibility in its utilization, including mobile and stationary applications. Due to its stability for long-term storage and transportation, ammonia can fulfill the demand to store the energy in time (stationary energy storage) and in space (energy export and import) [23]. Ammonia can be utilized by extracting its stored hydrogen or directly utilized as fuel. Ammonia is currently adopted as an agricultural fertilizer, refrigerant gas and in the manufacture of explosives, pesticides and other chemicals. Therefore, the infrastructures to produce, store, transport and utilize ammonia have been globally established [24], leading to its proven economic performance. In addition, regulations and procedure for ammonia handling have been established well in the world. The ammonia economy has been investigated in numerous studies, including studies of islanded systems [25], process modeling and fertilizer production using renewable energy [23]. However, for applications in the energy sector, ammonia still faces various challenges, including its properties, conversion technologies and possible environmental problems following its utilization.

Figure 1 shows the possible routes for the production and utilization of ammonia. Ammonia can be produced from both fossil fuels and renewable energy sources. These primary energy sources are then converted to ammonia through several processes, including pre-treatment, conversion and synthesis. In addition, the surplus electricity can also be converted to hydrogen [26], which is further converted to ammonia, leading to the application of power-to-ammonia. The produced ammonia is then stored, transported and distributed to the users for its utilization. Numerous countries in the world have a strong motivation to utilize ammonia as one of key players in future energy system. Therefore, these countries have tried to set the future road map, as well as developing the technologies to realize the plan. Japan has clearly decided its plan for ammonia adoption. The ammonia supply chain in the energy sector has been targeted for realization by 2030 [27]. In the beginning, 300 kW-class gas turbines will be tested until the end of 2020. Moreover, other movements to utilize ammonia, including advanced combined cycles, direct ammonia-fueled fuel cells and the co-firing of ammonia at existing coal-fired power plants, have also been started [28]. Australia has also accelerated research and development programs for ammonia utilization in order to store the produced hydrogen by the country and then export it to other countries [29]. Similar research motivation to push the adoption of ammonia has also been shown by the UK [30] and Germany [31]. In addition, the electricity generation and industrial sectors have been targeted as the first projected market.

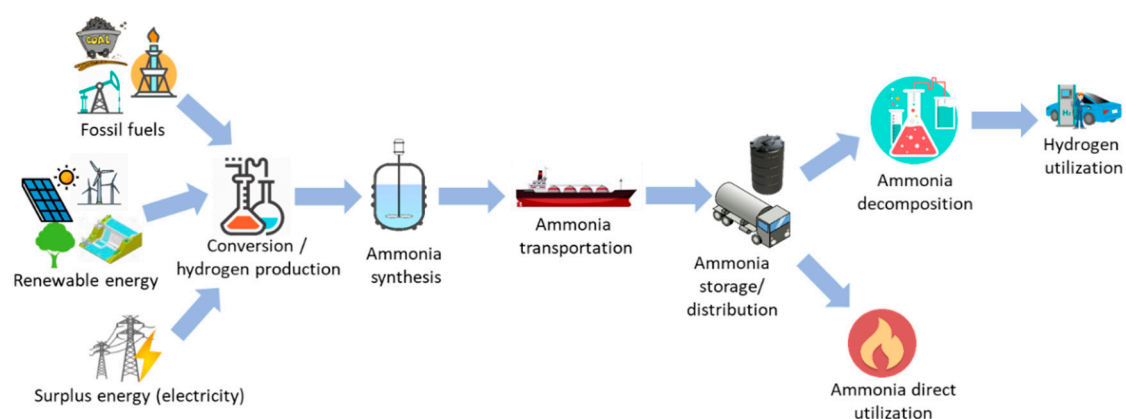


Figure 1. Production and utilization routes of ammonia in the energy sector.

This work reviews potential technologies, covering the production, storage and utilization of ammonia, as well as its important role in the energy system. Section 2 describes the characteristics of ammonia, especially in terms of its advantages and disadvantages as a hydrogen storage mechanism. Section 3 explains several possible ammonia production technologies, including conventional and advanced production systems. Section 4 describes potential ammonia storage methods, especially liquid ammonia. Furthermore, the utilization of ammonia is described in Section 5, especially direct utilization technologies. The decomposition of ammonia and separation of the hydrogen gas stream are also described in this section. Challenges and recommendations related to the adoption of ammonia are discussed in Section 6. Finally, Section 7 concludes the points reviewed in this work.

2. Characteristics of Ammonia

2.1. Physical Properties

Ammonia is alkaline, colorless and has a relatively strong odor. Table 1 shows the detailed parameters of the physical properties of ammonia. From techno-economic analysis, ammonia is considered to be the least expensive fuel compared to other conventional fuels, such as gasoline, natural gas, liquefied petroleum gas (LPG), methanol and hydrogen [32]. In addition, liquid ammonia has a relatively high volumetric energy density, 12.7 MJ/L, which is higher than liquid hydrogen (8.49 MJ/L) and compressed hydrogen (4.5 MJ/L at pressure of 69 MPa and temperature of 25 °C). The boiling temperature of ammonia is -33.4 °C at atmospheric pressure. Furthermore, ammonia has a significantly higher combustion heat, 11.2 MJ/L, compared to liquid hydrogen (8.58 MJ/L).

Gaseous ammonia can dissipate very quickly in the air under atmospheric conditions due to its lighter density than the air (0.769 kg/m³ compared to 1.225 kg/m³ at STP), minimizing explosion and fire risks in case of leakage. Furthermore, as ammonia has a higher auto ignition temperature (650 °C) than hydrogen (520 °C), ammonia has a lower risk of fire than hydrogen. The apparent toxicity (vapor pressure relative to toxicity at atmospheric temperature) of liquid ammonia is about three orders of magnitude higher than gasoline and methanol. This is due to the phenomenon that liquid ammonia has an immediately dangerous to life or health (IDLH) concentration of about 300 ppm, but its vapor pressure is relatively high; 8.58×10^2 kPa at 20 °C [33].

The challenges faced by ammonia include its narrow flammability range, which is 15.15–27.35% in dry air and 15.95–26.55% in 100% relative humidity air. Hence, it is usually considered to be non-flammable during its storage and transportation. In addition, as ammonia has nitrogen as its main component, the utilization of ammonia, especially in high temperatures, potentially leads to NO_x formation. Therefore, the combustion management of ammonia is crucial. Moreover, as ammonia is categorized as a toxic chemical, it is important to carry out appropriate hazard management in order to mitigate its danger to humanity and the environment.

Table 1. Detailed physical characteristics of ammonia [34,35].

Properties	Unit	Value
Molar mass	g/mol	17.031
Density at STP	kg/m ³	0.769
Melting point	°C	−77.73
Boiling point at 100 kPa	°C	−33.4
Vapor pressure at 20 °C	kPa	858
Heat of evaporation	MJ/kg	1.371
Auto ignition temperature	°C	650
Critical temperature	°C	132.4
Critical pressure	MPa	11.28
Viscosity at 25 °C	μPa·s	10.07
Heat capacity at constant pressure (101.325 kPa, 15 °C)	kJ/mol·°C	0.037
Heat capacity at constant volume (101.325 kPa, 15 °C)	kJ/mol·°C	0.028
Heat of combustion	MJ/L	11.2
Thermal conductivity	mW/m·°C	22.19
Critical density	g/mL	0.24
Condensation pressure at 25 °C	MPa	0.99
Flammability limit (equivalence ratio)	-	0.63–1.4
Adiabatic flame temperature	°C	1800
Max. laminar burning velocity	m/s	0.07

2.2. Hydrogen Storage Performance

Table 2 lists the characteristics comparison of hydrogen storage methods, including compressed hydrogen, liquid hydrogen, methanol and liquid ammonia. Liquid ammonia is able to store hydrogen in volumes much higher (121 kg-H₂/m³) than liquid hydrogen (70.8 kg-H₂/m³), which is about 1.7 times as high. Liquid ammonia can be stored at relatively low pressure (0.99 MPa at a temperature of 25 °C), which is significantly lower than that of compressed hydrogen. However, in terms of physical density, liquid ammonia has the higher density (600 kg/m³) than compressed and liquid hydrogen, leading to heavier storage and transportation.

Methanol is a strong competitor for the storage of hydrogen. It has higher energy density than ammonia (20.1 MJ/kg compared to 18.6 MJ/kg). However, it has both lower gravimetric and volumetric hydrogen contents than ammonia (12.5 wt% and 99 kg-H₂/m³ compared to 17.8 wt% and 121 kg-H₂/m³, respectively) [36]. As methanol involves CO₂ in its synthesis, its utilization and decomposition also release CO₂, leading to the environmental concerns. Methanol reformation also leaves the problem of the production of carbon monoxide (CO), which can poison most of the catalysts adopted in fuel cells, and hence shortens the life time of the fuel cell [37].

Table 2. Characteristics comparison of compressed hydrogen, liquid hydrogen, methanol and liquid ammonia [36,38,39].

Properties	Unit	Compressed Hydrogen	Liquid Hydrogen	Methanol	Liquid Ammonia
Storage method	-	Compression	Liquefaction	Ambient	Liquefaction
Temperature	°C	25 (room)	−252.9	25 (room)	25 (room)
Storage pressure	MPa	69	0.1	0.1	0.99
Density	kg/m ³	39	70.8	792	600
Explosive limit in air	%vol	4–75	4–75	6.7–36	15–28
Gravimetric energy density (LHV)	MJ/kg	120	120	20.1	18.6

Table 2. Cont.

Properties	Unit	Compressed Hydrogen	Liquid Hydrogen	Methanol	Liquid Ammonia
Volumetric energy density (LHV)	MJ/L	4.5	8.49	15.8	12.7
Gravimetric hydrogen content	wt%	100	100	12.5	17.8
Volumetric hydrogen content	kg-H ₂ /m ³	42.2	70.8	99	121
Hydrogen release	-	Pressure release	Evaporation	Catalytic decomposition T > 200 °C	Catalytic decomposition T > 400 °C
Energy to extract hydrogen	kJ/mol-H ₂	-	0.907	16.3	30.6

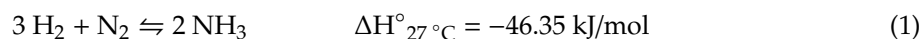
To release the hydrogen from ammonia, a relatively huge amount of energy is consumed (30.6 kJ/mol-H₂). On the other hand, the regasification of liquid hydrogen only consumes very low energy (0.907 kJ/mol-H₂). Therefore, ammonia decomposition is a challenging task, especially in terms of total energy efficiency in the utilization of ammonia. The decomposition of ammonia must be followed by hydrogen separation in the case that a high purity of hydrogen is demanded at the utilization site. On the other hand, compressed and liquid hydrogen can deliver highly pure hydrogen.

3. Ammonia Production

Currently, about 200 Mt/y of ammonia is manufactured globally [40], making it the world's second most commonly produced chemical after sulfuric acid (H₂SO₄). Similarly to hydrogen, ammonia can be produced from different primary energy sources, including biomass, coal, natural gas, solar, wind, geothermal, hydro and nuclear sources. Ammonia can be produced through different conversion technologies: thermochemical, electrochemical, photochemical and plasma [41]. However, with the consideration of technological feasibility and total energy efficiency [42,43], in this work, three main conversion technologies (Haber–Bosch, electrochemical and thermochemical cycle processes) are described. Furthermore, recent trends in the development of enhanced systems in order to improve the total energy efficiency during ammonia production are also described.

3.1. Conventional Ammonia Production (Haber–Bosch Process)

The currently adopted ammonia production process basically employs the system invented by Fritz Haber and Carl Bosch about 100 years ago [40]. Therefore, this system is well known as Haber–Bosch process. About 85% of total production of ammonia worldwide is produced by this process [44]. The ammonia synthesis occurs according to reaction (1).



Ammonia synthesis is an exothermic reaction (negative enthalpy change), and it occurs spontaneously at low temperatures (negative entropy change). Although it is favored at room temperature, the reaction rate at which the reaction occurs at room temperature is too slow to be applicable for at an industrial scale. In order to increase the kinetics of the reaction to achieve the targeted conversion rate, high pressure and temperature are required. To effectively synthesize ammonia from its main components (hydrogen and nitrogen), the reaction should be performed at a relatively high temperature and pressure of 400–500 °C and 10–30 MPa, respectively, with the assistance of an iron-based catalyst. This condition is demanded due to the high dissociation energy (941 kJ/mol) of triple-bonded nitrogen. However, to bring the reaction under this high temperature and pressure, about 30 MJ/kg-NH₃ of energy is required [45].

The production of ammonia from natural gas is conducted by reacting methane (natural gas) with steam and air, coupled with the subsequent removal of water and CO₂. The products of this process are hydrogen and nitrogen, which are the feedstock for the main ammonia synthesis. During the

process, the removal of sulfur and other impurities is important, because they can reduce and damage the performance of the catalyst during synthesis. In the ammonia synthesis process, both nitrogen and hydrogen are compressed to relatively high pressure to be fed to the synthesis reactor, where the catalyst is immersed inside. The produced ammonia, together with the unreacted hydrogen, argon and other impurities, is then cooled down for ammonia condensation in order to separate the ammonia from the other gases. The unreacted hydrogen and nitrogen are then recycled back and mixed together with the new feedstock. To avoid a build-up of impurities, such as argon, a small part of the gases is purged from the process. Ammonia synthesis produces a small amount of heat, which is released from the reactor; therefore, it can be recovered and utilized for other processes, such as steam and power generation. In general, about 88% of hydrogen's calorific value can be conserved [46].

Another challenge in the Haber–Bosch process is its low conversion rate; therefore, the process must be recycled to achieve the expected production flow rate. However, at pressure of 30 MPa, the conversion rate from the reaction is still low, no more than 25% [47]. This stream recirculation causes some problems, including the need for an additional recirculation system and a larger reactor, leading to high investment and operation costs.

When hydrogen is produced via water electrolysis, nitrogen can be supplied via air separation. Air separations for nitrogen production can be conducted via membrane, cryogenic, absorption and adsorption technologies [48]. For large scales, cryogenic separation is considered more economical than other methods. In addition, cryogenic air separation could produce a high purity of products [49].

The energy consumed during ammonia production, including conversion from primary sources, typically ranges from about 28 to 37 GJ/t [44]. An ammonia production system from any primary source, such as natural gas, is considered complex, as it includes many combined processes. Figure 2 shows the schematic diagram of conventional ammonia production from natural gas. The system consists of different processes: steam reformation, the water–gas shift reaction, CO₂ removal, syngas purification, and ammonia synthesis and separation. Therefore, efforts to reduce the total energy consumption require the improvement of the whole process involved. Due to high energy intensity of ammonia production, ammonia synthesis emits a total of 289.8 Mt-CO₂ annually [25], which is almost 0.93% of global CO₂ emissions [50].

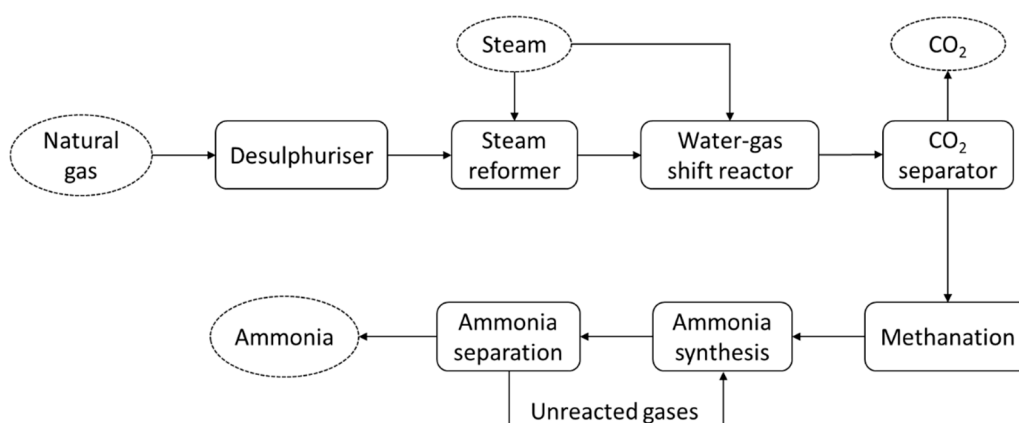


Figure 2. Schematic diagram of ammonia production from natural gas, employing the Haber–Bosch process.

Focusing on the Haber–Bosch process, many efforts to reduce its extreme conditions have been carried out. They include the introduction of an extra component in order to inhibit the catalysis and the alteration of geometry and electronic nature of the reacting components in order to optimize the energetics of catalysis [51]. Ru-based catalysts can basically facilitate ammonia synthesis under mild conditions (at a temperature of 300–450 °C and pressure of 4–15 MPa), which is significantly lower than the conditions required for iron-based catalysts. However, Ru-based catalysts are expensive and suffer from hydrogen poisoning [52,53]. Alkaline earth metal oxides and hydroxides have been identified as

promoters to improve the catalytic performance of Ru-based catalysts [54]. Several electrides (crystals in which electrons serve as anions), such as $\text{Ca}_2\text{N:e}^-$, which can be deposited in Ru nanoparticles have the potential to facilitate ammonia synthesis at 200 °C [55]. Transition metals (TM) can also improve synthesis performance, including lowering the pressure and temperature. This is due to the existence of scaling relations between the transition-state energy required for the dissociation of nitrogen and the adsorption energy of all the intermediates [56,57]. Furthermore, Kawamura and Taniguchi [58] have tested sodium melt as a catalyst for ammonia synthesis. By using this type of catalyst, the synthesis could be carried out at reaction temperatures of 500–590 °C and atmospheric pressure. However, further analysis and experimentation are required to bring this method to the level of being applicable.

3.2. Electrochemical Processing

Although electrochemical processing is significantly under-developed compared to the Haber–Bosch process, it is expected to realize higher energy performance. The energy consumed by this process is about 20% lower than the Haber–Bosch process [59]. Figure 3 shows the schematic flow diagram of electrochemical ammonia synthesis. The process is considered simple; therefore, its application is considered to potentially reduce system configuration and control complexity. In addition, the investment cost can be lower compared to currently adopted ammonia synthesis systems.

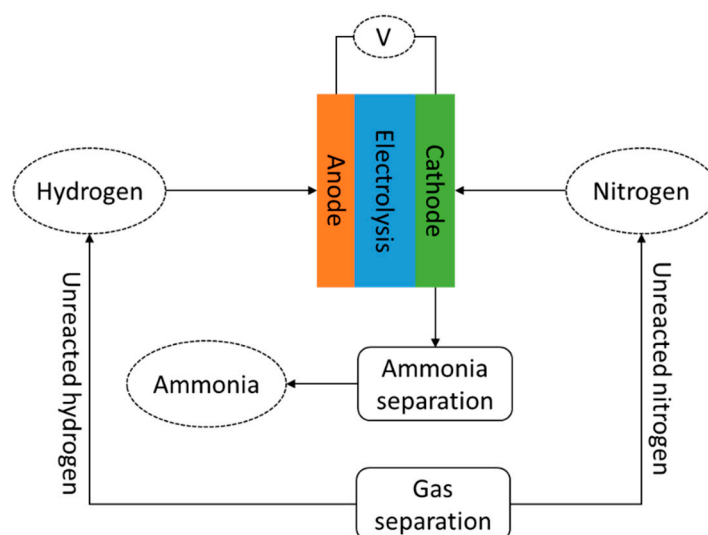


Figure 3. Schematic diagram of electrochemical ammonia synthesis.

The reactions at both cathode and anode in proton conducting cells are shown in reactions (2) and (3), respectively. The reactions at each cathode and anode are basically reversible.



Four different types of electrolytes are currently available: (a) liquid electrolytes, (b) molten salt, (c) composite membranes and (d) solid state electrolytes. Liquid electrolytes can operate under atmospheric temperature and pressure [60]. There are some potential liquid electrolytes, including LiClO_4 (0.2 M) in tetrahydrofuran [60], LiClO_4 in ionic liquid, LiClO_4 in H_2SO_4 and Li_2SO_4 in H_2SO_4 [61]. Ammonia production of 3.68×10^{-10} mol/cm²·s could be obtained, while the system efficiency can reach about 58%, indicating that about 58% of the current supplied to the system is converted into ammonia. However, the research related to this issue is still limited to lab experiments, in small dimensions of cells and limited operation times [41].

A molten salt type electrolyte is generally operated at a temperature range of 300–500 °C [62]. There are some potential chemicals for use as electrolytes, such as LiCl, KCl and CsCl, with dissolved Li_3N [63]. The reported ammonia production rate is 3.3×10^{-9} mol/cm²·s, and the efficiency is about 72%. Moreover, the system with composite electrolytes also includes solid electrolytes, which are combined with low melting salt, and have an operating temperature of 300–700 °C. The electrolytes comprise the main ionic conducting phase and an additional phase that is attached to the main phase to improve the electrical, mechanical and thermal properties [33]. As the representative of composite electrolytes, alkali metal carbonate (such as LiCO_3) and oxide (such as LiAlO_2) and CeO_2 doped with Sm_2O_3 have shown the expected properties, including oxygen ion, carbonate ion and proton conductivity [64]. In addition, Amar et al. [64] have tested mixed Na, K and Li carbonates, in addition to the LiAlO_2 , as the electrolyte. They obtained an ammonia production rate of 2.32×10^{-10} mol/cm²·s at a temperature of about 400 °C. The system with solid electrolytes generally operates in very wide operating temperatures, from room temperature to about 800 °C. There are different materials which can be included in this type of electrolyte. These include perovskites (such as cerate and zirconate) [65], fluorites (such as doped zirconia, ceria and thoria), pyrochlores (such as calcium doped lanthanum zirconate) and other materials (including brownmillerite, eulytite and monazite) [33]. The challenges of this type of electrolyte include their structural stability and the high sintering temperature (up to 1700 °C) which is required to achieve a high density. By adopting this kind of solid state electrolyte, the ammonia production rate of 3.1×10^{-9} mol/cm²·s could be achieved under the temperature of 570 °C, with an efficiency of about 75% [33,66].

3.3. Thermochemical Cycle of Ammonia Production

As an alternative process for ammonia production, a process employing the thermochemical cycle has been developed [67]. The system consists of two circulated processes: reduction (nitrogen activation) and steam-hydrolysis (ammonia formation). Both reactions are summarized as follows:



Figure 4 shows the schematic diagram of the thermochemical cycle of ammonia production. The primary energy sources are pre-treated and converted to carbon before being fed to the thermochemical cycle process. In the first reduction process (reaction (4)), the AlN is produced through the carbothermal reduction of Al_2O_3 and nitrogen. This reaction is endothermic and occurs under a reaction temperature of about 1500 °C. Moreover, in the second reaction, which is steam-hydrolysis (reaction (5)), the AlN produced in the first reduction process is reacted with steam (H_2O) producing Al_2O_3 . The produced Al_2O_3 from this second reaction is then circulated to the first reduction process. Detailed reaction kinetics have been analyzed in detail in [68].

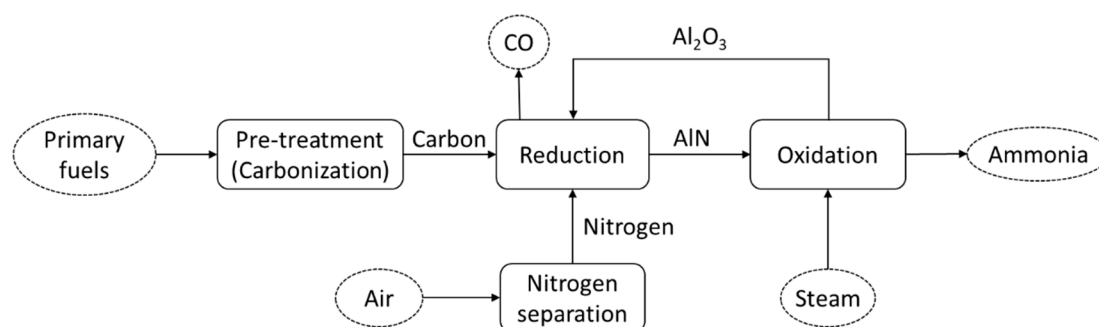


Figure 4. Schematic diagram of the thermochemical cycle of ammonia production.

Unlike the Haber–Bosch process, this thermochemical cycle can be carried out at atmospheric pressure and without a catalyst. The process allows independent reaction control for nitrogen activation (reaction (4)) and ammonia formation (reaction (5)). Furthermore, as could be observed from reaction (4), the system can produce ammonia directly from carbonized material, instead of pure hydrogen. Therefore, this system is expected to be able to reduce the energy consumption during ammonia production. However, this system has the biggest challenge related to its very high operating temperature, leading to limited heat sources and materials. Various ideas have been suggested for the heat supply, including the utilization of concentrated solar heat.

Juangsa and Aziz [69] have developed an integrated system, consisting of nitrogen production, ammonia production employing the thermochemical cycle and power generation. In their system, the heat required for reduction is basically covered by heat generated by the combustion of fuel gases produced during ammonia production. The system can achieve a high total theoretical energy efficiency of about 69%. In addition, they also stated that the oxidation temperature has a significant role in the performance of the system.

3.4. Advanced Ammonia Production Systems

Due to increasing concern related to economic and environmental impacts, efforts to propose and develop an advanced ammonia production system have been carried out intensively. These include both thermochemical and electrochemical processes.

Cinti et al. [70] have proposed a combined system which consists of solid oxide electrolyser, nitrogen production with pressure-swing adsorption and Haber–Bosch process. Moreover, the same group [25] also developed an integrated system covering methane steam reforming and Haber–Bosch process. They mainly focused on system integration and heat recovery to improve the total energy efficiency. Furthermore, Aziz et al. [71] have proposed an integrated system for hydrogen conversion to ammonia with a relatively high total energy efficiency. Their system includes cryogenic nitrogen separation with a single distillation reactor, the Haber–Bosch process and power generation. The produced heat during ammonia synthesis, as well as the purged gas (containing a little hydrogen and ammonia), is recovered and utilized for power generation. In addition, they employed both exergy recovery and process integration in order to realize high energy efficiency [72].

Other integrated systems for the production of ammonia from various kinds of primary energy sources have been developed. Nurdiawati et al. [73] have proposed algae-based ammonia production by integrating algae drying, gasification, chemical looping, ammonia synthesis (the Haber–Bosch process) and power generation. In their system, the nitrogen separation process is omitted due to the utilization of nitrogen-rich flue gas from the chemical looping. Their system is able to efficiently convert the algae to ammonia, with a total energy efficiency of about 64%, including an ammonia production efficiency of 63%. A different system has also been developed by the same group [74], with the main difference in hydrothermal gasification and nitrogen production. Another combined system to convert the agricultural waste from a palm oil mill has also been proposed and evaluated by Ajiwibowo et al. [75]. In their system, the supercritical water gasification of blended empty fruit bunch and palm oil mill effluent is combined with syngas chemical looping and Haber–Bosch-based ammonia synthesis.

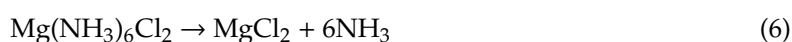
4. Ammonia Storage and Transportation

The advantages of ammonia, especially compared to other hydrogen storage methods, include its well established global distribution network, handling method and regulations covering its storage and transportation. Ammonia has a higher auto ignition temperature (650 °C) compared to hydrogen (520 °C), methane (630 °C) and propane (450 °C), leading to its excellent safety. Ammonia is a gas under atmospheric conditions. Ammonia transportation in a liquid form is generally performed due to its significantly higher density. The transportation can be performed through pipelines, tank-cars

and tanker vessels. In the case of tanker vessels, ammonia is generally cooled down to a temperature of about $-33\text{ }^{\circ}\text{C}$, allowing the utilization of unpressurized containers [46].

To store ammonia in a liquid condition, which is quite similar that of propane, two methods are basically adopted. The first method is to increase its pressure while maintaining the temperature at the ambient level, such as 0.99 MPa at $25\text{ }^{\circ}\text{C}$. The second method is to decrease the temperature while maintaining the pressure at the atmospheric level; in this case, ammonia is cooled down to $-33.4\text{ }^{\circ}\text{C}$ at atmospheric pressure [76]. This mild condition is beneficial, as a light and low-cost tank can be adopted while maintaining its volumetric density. The infrastructure being used for propane can also be adopted to store liquid ammonia. Therefore, the economic performance for ammonia storage is considered well established, as well as the regulations for operations and storage.

In order to improve the safety issues during storage and transportation, the storage of ammonia in a solid form has also been developed [77]. It is basically performed by binding the ammonia in metal amine complexes ($\text{M}(\text{NH}_3)_n\text{X}_m$), such as $\text{Mg}(\text{NH}_3)_6\text{Cl}_2$ and $\text{Ca}(\text{NH}_3)_8\text{Cl}_2$. In case of $\text{Mg}(\text{NH}_3)_6\text{Cl}_2$, the reaction occurs as follows:



These metal amines have a great gravimetric hydrogen density of about 10 wt% (9.19 and 9.78 wt% for $\text{Mg}(\text{NH}_3)_6\text{Cl}_2$ and $\text{Ca}(\text{NH}_3)_8\text{Cl}_2$, respectively) [77]. Another benefit of employing metal amines to store ammonia is that their apparent toxicity is very low, which is comparable to gasoline and methanol. For example, $\text{Mg}(\text{NH}_3)_6\text{Cl}_2$ has an IDLH concentration of about 300 ppm, but its vapor pressure is very low, at 1.4×10^{-3} bar (at $20\text{ }^{\circ}\text{C}$). The ammonia from the metal amines can be released through the desorption process [78]. The desorption of $\text{Ca}(\text{NH}_3)_8\text{Cl}_2$ can be carried out at a relatively low temperature of about $60\text{ }^{\circ}\text{C}$, leading to a high ammonia vapor pressure of 0.7 bar at room temperature.

5. Ammonia Utilization

Currently, ammonia is mainly adopted as an agricultural fertilizer (about 80%), while the remaining 20% is utilized for food production, industrial materials, refrigerants and additives [79]. For energy harvesting, the utilization of ammonia has not been widely adopted. Figure 5 shows the potential utilization of ammonia, covering both direct utilization and decomposition to hydrogen. Two main established technologies to harvest the energy from ammonia include the internal combustion engine and the fuel cell. The utilization of ammonia as a fuel is expected to realize a clean energy system, as there is neither CO_2 nor SO_x emission, nor soot formation [80]. However, further development for a broader range of energy harvesting from ammonia is demanded.

Efforts to use ammonia in the energy sector have been conducted for several decades. Ammonia was blended with coal gas as a fuel for the reciprocating engines of buses in the 1940s during World War II in Belgium [81]. Previously, the patent to utilize blended ammonia, hydrogen and nitrogen as fuel was also registered in 1938 [82]. In addition, NASA adopted liquid ammonia as the main fuel for the X-15 hypersonic rocket, blended with liquid oxygen, which was successful in achieving the fastest speed of Mach 6.7 [83].

The utilization of ammonia faces numerous challenges due to its characteristics. The heating value of ammonia is significantly lower than that of other hydrocarbons. The narrow equivalence ratio (0.63 to 1.4) and high auto ignition temperature give ammonia low flammability. Ammonia has an adiabatic flame temperature of $1800\text{ }^{\circ}\text{C}$, which is lower than hydrogen ($2110\text{ }^{\circ}\text{C}$), methane ($1950\text{ }^{\circ}\text{C}$) and propane ($2000\text{ }^{\circ}\text{C}$). This leads to lower radiation heat transfer, which is important during combustion and heat transfer. In addition, it has a low maximum laminar burning velocity (0.07 m/s), which is significantly lower than hydrogen (2.91 m/s), methane (0.37 m/s) and propane (0.43 m/s).

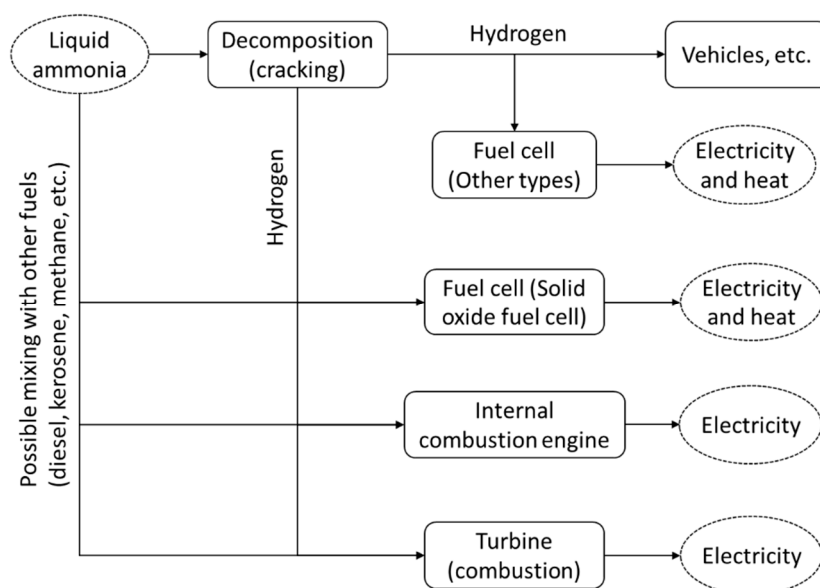


Figure 5. Potential utilization of ammonia, including direct utilization and decomposition to hydrogen.

5.1. Internal Combustion Engine

The utilization of ammonia as fuel for an internal combustion engine was intensively studied in the mid-1960s [84,85]. These works confirmed that ammonia has potential as the primary fuel for a spark ignition engine. Starkman et al. [84] found that a maximum theoretical output of about 70% of that of hydrocarbons could be achieved when gaseous ammonia was injected. In addition, engine modifications were required to control the fuel flow and spark timing in the case that a conventional spark ignition engine with existing compression ratios was adopted.

The octane number of ammonia is 111 [86]. A thermal efficiency of about 30% and power output of 85% can be achieved by utilizing ammonia in an internal combustion engine. The power output is limited due to the backfire caused by the lack of water injection and exhaust gas recirculation. Therefore, the amount of NO_x released can be pushed to be significantly lower than that of gasoline. One big challenge in ammonia combustion is that the minimum ignition energy required by ammonia is about 16 times higher than fossil fuels [87]. Ammonia combustion mainly occurs through the following reaction:



The low combustion rate of ammonia results in inconsistent combustion under low engine loads and/or high engine speeds [88]. Therefore, combustion promoters (e.g., gasoline, diesel and hydrogen) are necessary to facilitate more stable combustion. Ryu et al. [89] have conducted a study of blended gasoline and ammonia in a four-stroke spark-ignition engine. They stated that the appropriate injection timing for ammonia is in the range of 320–370 before the top dead center (BTDC). The peak cylinder pressure was slightly lower than that fueled by gasoline alone. Moreover, the use of ammonia led to the increase of NO_x emission and the engine slip phenomenon due to incomplete combustion.

A blend of ammonia and diesel was tested by Reiter and Kong [90] using a four-cylinder turbocharged diesel engine. They found that, in order to realize a favorable fuel efficiency, ammonia can be injected in the range of 40–60%, based on the total fuel energy. The increase of ammonia seemed to increase the amount of emitted NO_x , but reduce the amount of soot emission. In addition, Boretti [91] simulated the ignition performance of mixed diesel and ammonia. His results revealed that ammonia blending is also able to maintain ignition performance, including power density, power efficiency and load control. The important thing in this issue was the required injection pressure, which is relatively high for the ammonia to achieve the expected performance.

The blend of ammonia and hydrogen has been studied by Frigo and Gentili [92] using a four stroke twin cylinder spark ignition engine with a volume of 505 cm³. They stated that the additional injection of hydrogen is necessary to improve the ignition and increase the combustion velocity. The ratio of injected hydrogen depends significantly on the load, while engine speed has less influence.

5.2. Turbine-Based Power Generation

The idea to utilize ammonia for gas turbines was started in mid of 1960s [93], although its practical adoption as a single fuel for turbines is still limited and has not been widely commercialized. Since then, research related to the utilization of ammonia as fuel has not been actively performed, except in research related to NO_x formation. Research on the utilization of ammonia as gas turbine fuel was restarted in the 1990s, especially the utilization of mixed ammonia and hydrogen [94] and ammonia and natural gas [95].

According to previous research and development projects, there are some challenges when ammonia is employed as turbine fuel. In addition to slower kinetics and lower combustion temperatures, the utilization of liquid ammonia as fuel leads to unstable and low combustion efficiency [96]. The use of a swirler and flame holder can stabilize the combustion and increase its efficiency and reduce the emitted NO_x [97]. The vaporization of liquid ammonia before the combustion and utilization of additives during combustion, as well as the cracking of molecules, are methods to increase combustion performance. Moreover, another challenge in the utilization of ammonia as turbine fuel is its relatively slow chemical reaction rate, leading to a lower laminar burning velocity [98]. Furthermore, as the flow rate of air is also reduced in order to facilitate sufficient residence time for the reaction, the mixing of ammonia and air is considered inefficient due to its low Reynolds number [99]. The combustion of ammonia basically produces no CO₂, which is beneficial in terms of environmental issues. However, the lack of concentration of CO₂ in the flue gas leads to the problems in heat transfer, as CO₂ is considered an excellent heat carrier during combustion and heat transfer. Moreover, the quenching distance for the mixed ammonia–air under stoichiometric conditions is about 3.5 larger than that of propane [100].

Keller et al. [101] proposed a combined cycle with two steps of combustion. The first main combustion uses ammonia as fuel, which is reacted with air, producing nitrogen, water and hydrogen. These hot gases are then expanded in a gas turbine. In the second step of combustion, which occurs in a heat recovery steam generator, the hydrogen in the flue gas is reacted with air, adding heat for steam generation.

A research group at Fukushima Renewable Energy Institute (FREA), Fukushima, Japan, has succeeded in demonstrating the utilization of ammonia for a micro gas turbine (50 kW) [102]. They used three different types of fuels, including pure ammonia, mixed ammonia–kerosene and mixed ammonia–methane [102]. Their developed system adopted a heat regenerative cycle in order to improve combustion efficiency and flame stability. Their system mainly consists of a vaporizer, gas compressor, gas turbine and selective catalytic reduction (SCR) unit (Figure 6). SCR was adopted to reduce the NO_x concentration before the flue gas is exhausted into the atmosphere. From the demonstration test, it was revealed that pure ammonia can realize a combustion efficiency of 89–96%, while the residual ammonia can be utilized as an additive in the SCR. In addition, it was considered that the combustor inlet temperature significantly influences the combustion efficiency, as well as the emissions. Furthermore, when mixed with other fuels, the increase of the ammonia ratio leads to the increase of the NO_x concentration in the flue gas.

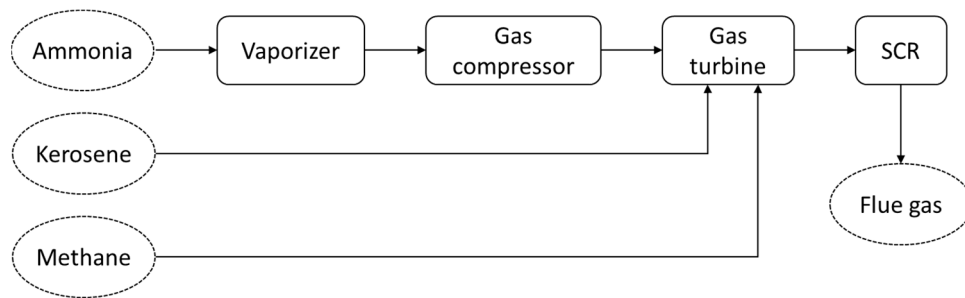
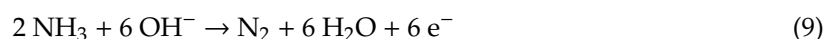


Figure 6. Main schematic diagram of an ammonia-based micro gas turbine (adapted from [102]).

5.3. Direct Ammonia Fuel Cell

In the case that hydrogen needs to be released from ammonia, the decomposition of ammonia to hydrogen can be conducted via thermochemical and electrochemical routes [103]. However, ammonia also can be utilized using a direct fuel cell, without the need of decomposition or cracking. Fuel cells are the technology which can generate electricity from chemical resources based on electrochemical reactions [104]. In general, fuel cells can be categorized to several types, depending on their electrolyte materials, application and operating conditions. These categories include alkaline fuel cells (AFC), alkaline membrane fuel cells (AMFC), phosphoric acid fuel cells (PAFC), molten carbonate fuel cells (MCFC), proton exchange membrane fuel cells (PEMFC), direct methanol fuel cells (DMFC) and solid oxide fuel cells (SOFC). Among them, SOFC is considered promising due to its high energy efficiency, high fuel flexibility and excellent environmental friendliness [105]. SOFC operates at a relatively high operating temperature; about 700 to 1000 °C.

Although hydrogen is considered to be the most optimal chemical for electricity production via SOFC, other fuels, including ammonia, have also been investigated, and they have shown relatively high efficiency [106]. Ammonia can be directly fed as fuel for AFC, AMFC and SOFC. AFC is the technology which was developed at the early stage of fuel cell technologies. AFC operates at low temperatures of 50–200 °C using an aqueous potassium hydroxide (KOH) electrolyte with a concentration of about 30%. The electrodes have a double layer structure, consisting of an active electrocatalyst layer (an organic mixture of catalyst, carbon black and polytetrafluoroethylene) and a hydrophobic layer (porous organic layer) [107]. Oxygen is fed at the cathode side, and it has a further reaction with water, forming hydroxide ions. These ions move to the anode side through the electrolyte and react with ammonia, producing nitrogen and water. During the reaction, as the produced water and heat must be removed from the system, the electrolyte is recirculated and the water is evaporated. The typical electric efficiency of AFC is about 40–45% [108]. One of the problems in conventional ammonia-fed AFC is the formation and precipitation of carbonate ions. As this formation involves the hydroxide anion, the amount of hydroxide anions which react with ammonia drops accordingly. This results in the performance drop of the cell [109]. In order to solve this problem, the anion exchange membrane-based fuel cell (AMFC) was developed, which is free from cations, such as K⁺ [110,111]. In principle, both AFC and AMFC have similar reactions at both cathode and anode, shown as reactions (8) and (9), respectively.



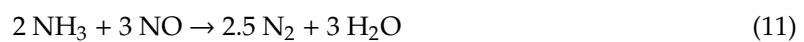
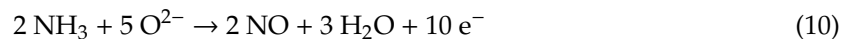
Recently, to further improve the system efficiency, the development of catalysts and new anion exchange membranes have been carried out [112]. Single metal catalysts, such as Ru, Rh, Pd, Ir and Pt, and bimetallic catalysts, including Pt-Ru, Pt-Ir/C and Pt-Ni/C, have been investigated in order to enhance ammonia oxidation activity [113–115].

Compared to both AFC and AMFC, SOFC is considered to have higher energy efficiency [116]. The high reaction temperature of SOFC results in the possibility of ammonia decomposition at the

anode; hence, the produced hydrogen can be utilized further for the electrochemical reaction. Farr and Vayenas [117,118] have studied the utilization of ammonia using a solid electrolyte reactor employing yttria stabilized zirconia (YSZ) with Pt electrodes. Their research objective was mainly to cogenerate electricity and nitric oxide (NO) as important chemical feedstock. Moreover, ammonia was first analyzed as a single fuel for SOFC by Wojcik et al. [119], also using YSZ-based SOFC with Pt electrodes. They reported that their experiment could achieve a power density of 50 mW/cm² at 800 °C.

Electrolytes for SOFC can be categorized into proton-conducting (SOFC-H) and oxygen-ion-conducting (SOFC-O) electrolytes. Oxygen-ion conducting electrolytes are currently widely adopted. This includes the widely adopted YSZ. Proton-conducting electrolytes have a lower activation energy for proton transfer, resulting in possible lower operating temperatures compared to oxygen-ion conducting electrolytes. Therefore, proton-conducting SOFC tends to have higher energy efficiency [120].

SOFC fed with ammonia as fuel operates based on oxygen ion and proton conducting electrolytes. The reactions at the anode side occur following the reactions (10) and (11), while one at the cathode follows the reaction (12).



Because the diffusion of O₂ through the electrolyte is relatively slow, reaction (10) is considered to be the limiting reaction. As a result, NO is produced and can react with ammonia, producing nitrogen and water (reaction (11)). Recently, various promising electrolytes have been developed in order to improve conductivity and increase power density. These include BaCe_{0.9}Nd_{0.1}O_{3-δ} [121] and Ce_{0.8}Sm_{0.2}O_{1.9} [122]. In addition, in order to minimize the formation of nitric oxide, the addition of doping materials, such as BaCeO₃ and BaZrO₃ have also been evaluated [123]. The typical electric efficiency of ammonia-fed SOFC is 50–55% [108].

5.4. Mixing with Other Fuels

In order to advance the combustion performance of ammonia, blending with other enhancers, such as methane, propane, hydrogen, gasoline and kerosene, is usually adopted [100]. Blending with hydrogen has been tested by many researchers, and it has a potential to enhance the combustion flame, as well as to maintain CO₂-free combustion [124–126]. As hydrogen can be produced from ammonia, from a fuel transportation point of view, this fuel blending is considered practically feasible. Hydrogen has very high reactivity; therefore, its mixing with ammonia leads to an exponential increase in its laminar burning velocity compared to pure ammonia. The ammonia and hydrogen mixture has been evaluated and applied in a spark engine, leading to a robust engine cycle [92]. In addition, the blend of ammonia and hydrogen has also been tested for gas turbines [94], resulting in an excellent flame velocity. However, the high diffusivity of hydrogen resulted in a narrow operational envelope. In addition, they also stated that the high concentration of NO_x is caused by the excessive production of radicals, including OH and O.

Mixing ammonia with other hydrocarbon fuels generally leads to a higher flame velocity, radiation intensity and rate of heat release, as well as lower CO₂ emissions [40]. This blending is also considered promising in terms of a gentle shift from hydrocarbon to non-carbon-based fuels. Henshaw et al. [127] studied the effect of ammonia blending on the laminar burning velocity of methane-based combustion. It was found that increasing the ammonia concentration resulted in a slower laminar burning velocity. The same tendency has also been stated by Xiao et al. [95], who have simulated the laminar flame speed. They also found that the increase in the ammonia fraction in the fuel blend led to a negative effect on the flame speed. It was considered that the increase in the ammonia fraction caused the flame propagation to be weakened. This slower flame speed was also considered to be due to the decrease of chemical reactivity following the increase of the ammonia fraction.

In addition, Valera-Medina et al. [100] also studied the combustion performance of mixed ammonia and methane, in terms of flame stability and emission, using a tangential swirl burner. According to their results, the full premix of fuels before the combustion cannot guarantee an optimum condition for ammonia combustion, leading to the necessity to find a better method for fuel injection. In addition, a lower swirl number is necessary to optimize the combustion performance, because a higher swirl number reduces the residence time, promoting ammonia cracking with a lower oxygen intake and an increase in radical reactions. The mixture of ammonia and propane has also been researched previously in [128,129]. Similar results to the above results of the addition of ammonia to methane were obtained.

5.5. Ammonia Decomposition

The hydrogen in ammonia can be released through the decomposition process; therefore, wider possibilities for hydrogen utilization can be realized. Unlike methanol decomposition, ammonia decomposition produces no carbon monoxide, resulting in stable hydrogen utilization for PEMFC and PAFC [130]. PEMFC and PAFC are very sensitive to ammonia due to the acidic nature of their electrolytes. A hydrogen stream with an ammonia concentration of less than 0.1 ppm is highly expected for both fuel cells [108]. Both PAFC and PEMFC have an electric efficiency of 40–45% and 40–48%, respectively. Ammonia decomposition and its subsequent separation and purification processes are energy-intensive; therefore, efforts to improve their energy efficiency, reliability and scalability are necessary. Because ammonia decomposition is endothermic and requires high temperatures (>500 °C), further developments to bring this reaction to a mild temperature region are demanded.

Similar to its synthesis, the decomposition of ammonia is basically a thermo-catalytic reaction. The decomposition is a stepwise sequence, beginning with ammonia adsorption on the metal and followed sequentially by ammonia dehydrogenation and the recombinative desorption of nitrogen and hydrogen [131]. The catalytic activity of catalysts can be observed through their turnover frequency (TOF), although the decomposition conditions also significantly influence their catalytic performance [132]. The catalytic activity is significantly influenced by the type of active metal used as the main catalyst, type of support material, particle size, surface area, dispersion of catalyst and promoting material [38]. The presence of the additives and the alteration of the support material can modify the nitrogen desorption step and the catalytic properties of the catalyst [38]. Ganley et al. [133] have observed the catalytic activity of different single-metal catalysts with Al₂O₃ as the support material and found the activity order to be Pb, Te, Se \cong Cu < Pd < Cr < Pt \cong Fe < Ir < Co < Rh < Ni < Ru. However, due to different ammonia concentrations and types of support material, other studies mentioned a different catalytic activity order for Pt, Fe, Ni, Co and Pd [134,135].

Although Ru shows the highest catalytic activity, it is expensive, resulting in a high cost of ammonia decomposition. To solve this problem, efforts to reduce Ru in the catalyst and develop non-Ru catalysts have been made, while keeping the catalytic activity high. These efforts include the modification of the primary catalyst component and utilization of promoter and support materials [132]. In addition, inactive metals can also be used as catalysts with further treatments of surface modifications, promoter additions and alloying techniques [136].

Numerous promoting materials have been adopted to increase catalytic activity, including K, Na, Li, Ce, Ba, La and Ca [137]. In addition, K-based compounds, such as KNO₃, KOH, K₂CO₃, KF, KCl, K₂SO₄ and KBr, also have potential as promoting materials [137]. These promoting materials donate their electrons to the surface of support material, leading to charge balancing during the decomposition [134]. The promoting material also facilitates intermediate step stabilization due to its low ionization energy [138]. Moreover, support materials, which are electronically conductive, cheap and have high surface area, are also expected to improve catalytic activity [132]. Potential support materials include carbon nanotubes, template SiO₂ [139], porous Al₂O₃ [140], active carbon, graphitic carbon and mesoporous carbon [141]. Among the combinations of catalyst and support material, a catalyst of Ru on carbon nanotubes shows the highest ammonia conversion [38]. This is due to the

high dispersion of Ru particles and the inhibition of particle growth of the catalyst [142], resulting in the stability of the catalyst and high catalytic activity.

Further studies to ensure the comparable results of catalytic decomposition using different catalysts and conditions are required in order to clarify the optimum decomposition performance. In real applications, as economic performance is important, catalytic activity is not the only parameter pursued. However, the stability and lifetime of the materials (including the catalyst, promoters and support materials) are also crucial factors for consideration, because they significantly influence capital and running costs, and maintenance.

The hydrogen released by ammonia decomposition needs to be separated and purified, as the ammonia potentially damages PEMFC [143]. Ammonia poisoning increases both charge-transfer and diffusion resistances, leading to the decrease of electrochemical performance [143]. Additionally, the existence of ammonia in the hydrogen gas is disadvantageous due to its toxicity, even in an ammonia-tolerant energy conversion system (such as AFC). In order to remove the residual ammonia from the hydrogen gas stream, sorbent materials have been proposed. Miyaoka et al. [144] investigated the Li exchange type X zeolite to purify the hydrogen gas stream, and obtained 0.01–0.02 ppm of ammonia at the gas stream outlet (with an inlet concentration of 1000 ppm). Van Hassel et al. [145] have also developed a metal halide sorbent system, consisting of impregnated super activated carbon with metal chlorides. They showed that the system has a good cyclic stability. The sorbents can be regenerated through heating, resulting in the release of ammonia.

Membrane-based separation and purification systems have also been developed recently. This kind of separation has the benefit of possible simultaneous nitrogen removal; hence, secondary purifications (e.g., pressure-swing adsorption) can be avoided. Dolan et al. [146] have developed Pd-coated vanadium membranes in a tubular geometry. The developed membranes showed high permeability (higher than 3.0×10^{-7} mol/m \cdot s \cdot Pa^{0.5} at temperatures higher than 320 °C) and robustness. In addition, as vanadium is a relatively cheap material, this kind of membrane results in a low cost separation compared to a single Pd-based membrane.

6. Challenges and Recommendations

The biggest challenges related to the realization of a hydrogen-based society are related to its economy and technological maturity. A hydrogen economy was initially introduced by John Bockris in 1970 [147], aiming at the massive deployment of hydrogen to substitute current fossil fuels [148]. Although it is very challenging task, the realization of a hydrogen economy is expected to strengthen three key pillars in energy sectors, which are energy security, economy [149] and the environment [150,151]. The target to realize this hydrogen economy has been issued by several countries, including the USA [5], the European Union [152] and Japan [153].

Wijayanta et al. [154] analyzed the economic performance of different hydrogen storage methods, including liquid hydrogen, methylcyclohexane and ammonia. According to their study, with the assumptions that hydrogen is transported from Australia to Japan [155] and the production cost of hydrogen is 8 JPY/Nm³-H₂ in 2050 [153], the direct utilization of ammonia (no need for decomposition) is considered to be the most economic, with a predicted final hydrogen price of 21 JPY/Nm³-H₂ in 2050. However, when a high purity of hydrogen is required, liquid hydrogen is slightly cheaper than the ammonia with decomposition (24 JPY/Nm³-H₂ compared to 26 JPY/Nm³-H₂). Based on the findings of [153], it is strongly recommended to utilize ammonia directly, whether employing combustion or a direct ammonia fuel cell. The technologies related to the direct combustion of ammonia need to be accelerated, so that an optimum combustion performance can be achieved.

Furthermore, related to production and decomposition of ammonia, various technologies are considered crucial for development. The conventional Haber–Bosch process relies heavily on natural gas [156]. The adoption of ammonia in the energy sector must be able to facilitate renewable energy sources; therefore, efficient technologies for the synthesis of ammonia (such as electrochemical and membrane-based synthesis) are urgently demanded. However, this effort faces a big challenge due

to the equilibrium conversion during ammonia decomposition, which is significantly dependent on temperature, as well being an endothermic reaction. In addition, the rate of ammonia decomposition also decreases significantly when the reaction reaches its equilibrium [157]. The application of a membrane to separate the hydrogen is effective in order to avoid this equilibrium limitation [158]. The development of catalysts in order to increase the decomposition performance, as well as its economy, is strongly suggested.

In ammonia utilization, a direct ammonia fuel cell is believed to be advantageous, especially in terms of energy efficiency. However, lowering the temperature in the fuel cell is very challenging (due to the difficulty in breaking the N–H bonds in ammonia), due to hurdles in finding suitable electro-catalysts for adoption as the electrode and minimizing the cross-over of ammonia [111]. In the case of SOFC, the integration of a stable anode, in order to increase the durability of the anode and electrolyte interface, becomes one of the key issues for the success of ammonia-fed SOFC. The goals of this include the avoidance of nitride formation and sustaining the local temperature change during its operation [159].

The integration of several processes, both in the production and utilization sites, is also considered to be an effective way to improve the total energy efficiency. In the production site, the integration of ammonia synthesis into the hydrogen production processes, such as gasification, water–gas shift and steam reformation, is promising for the realization of high total energy efficiency in hydrogen production and storage [75]. In addition, the technology to lower the temperature during ammonia decomposition should be accelerated. Integrated ammonia decomposition and power generation in the utilization site is also an excellent way to utilize ammonia with lower exergy destruction.

Finally, when projecting the adoption of ammonia as a promising secondary energy source, as well as a hydrogen storage method, the technologies and policies for its development must be in line with the realization of a CO₂-free energy system. In addition, a massive deployment of renewable energy and the tremendous variety in the patterns of energy demand lead to a highly flexible and responsive energy system. Adaptive ammonia production and utilization are considered to be key technologies in the future.

7. Conclusions

Hydrogen is considered to be a promising secondary energy source (energy carrier) in the future. However, because of its very low volumetric energy density in a gaseous form under atmospheric conditions, hydrogen needs to be stored and transported effectively in any form, with high gravimetric and volumetric hydrogen densities. Among the available technologies, ammonia shows superiorities over the others, especially in terms of storage, transportation and utilization. In this review, the production, storage and utilization of ammonia were described. Several important technologies for each section have been explained. In ammonia production, although the Haber–Bosch process is an established synthesis technology, electrochemical processes to produce ammonia seem to be promising for the future, due to their higher energy efficiency. Regarding ammonia storage, ammonia has strong advantages compared to other hydrogen storage media because it can be stored as a liquid under mild conditions, similar to propane. Therefore, the storage and transportation infrastructure and regulations are basically well established. Finally, ammonia utilization covers numerous different technologies, including internal combustion engines, combustion for turbines and fuel cells. In terms of total energy efficiency, ammonia fuel cells with direct feeding are believed to be promising. Further studies correlated to energy-efficient and cost-effective ammonia production and utilization are demanded. These technologies should be developed in the context of CO₂-free systems. Parallel efforts to accelerate the adoption of renewable energy, the mutual conversion of hydrogen and ammonia, and the adaptive management of energy systems are demanded urgently. Furthermore, issues related to the ammonia economy also become crucial, especially in terms of its adoption into the energy system. Considering the highly potential characteristics of ammonia, the conversion of renewable energy to ammonia (renewable ammonia) is considered promising in the future.

Author Contributions: Conceptualization, M.A.; resources, M.A., A.T.W., A.B.D.N.; writing—original draft preparation, M.A., A.T.W., A.B.D.N.; writing—review and editing, M.A., A.T.W., A.B.D.N. All authors have read and agreed to the published version of the manuscript.

Funding: This work was partially supported by JSPS KAKENHI, Grant Number 19K04211. A.T.W. would like to acknowledge the support of the World Class Research Program, the Ministry of Research and the Technology/National Agency for Research and Innovation of the Republic of Indonesia in the fiscal year 2020.

Conflicts of Interest: The authors declare no conflict of interest.

References

1. Ekwurzel, B.; Boneham, J.; Dalton, M.W.; Heede, R.; Mera, R.J.; Allen, M.R.; Frumhoff, P.C. The rise in global atmospheric CO₂, surface temperature, and sea level from emissions traced to major carbon producers. *Clim. Chang.* **2017**, *144*, 579–590. [CrossRef]
2. United Nations Framework Convention on Climate Change (UNFCCC). Report of the conference of the parties on COP 21. In Proceedings of the Conference of the Parties on its Twenty-First Session, Paris, France, 30 November–13 December 2015; Volume 1, p. 1192.
3. United Nations Framework Convention on Climate Change (UNFCCC). Marrakech Partnership at COP 25. Available online: <https://unfccc.int/climate-action/marrakech-partnership-at-cop-25> (accessed on 2 February 2020).
4. Abe, J.O.; Popoola, A.P.I.; Ajenifuja, E.; Popoola, O.M. Hydrogen energy, economy and storage: Review and recommendation. *Int. J. Hydrog. Energy* **2019**. [CrossRef]
5. Durbin, D.J.; Malardier-Jugroot, C. Review of hydrogen storage techniques for on board vehicle applications. *Int. J. Hydrog. Energy* **2013**, *38*, 14595–14617. [CrossRef]
6. Juangsa, F.B.; Prananto, L.A.; Mufrodi, Z.; Budiman, A.; Oda, T.; Aziz, M. Highly energy-efficient combination of dehydrogenation of methylcyclohexane and hydrogen-based power generation. *Appl. Energy* **2018**, *226*, 31–38. [CrossRef]
7. Aziz, M.; Juangsa, F.B.; Kurniawan, W.; Budiman, B.A. Clean co-production of H₂ and power from low rank coal. *Energy* **2016**, *116*, 489–497. [CrossRef]
8. US Department of Energy Hydrogen Storage Challenges. Available online: <https://www.energy.gov/eere/fuelcells/hydrogen-storage-challenges> (accessed on 9 April 2020).
9. Zhang, Y.H.; Jia, Z.C.; Yuan, Z.M.; Yang, T.; Qi, Y.; Zhao, D.L. Development and application of hydrogen storage. *J. Iron Steel Res. Int.* **2015**, *22*, 757–770. [CrossRef]
10. Chalk, S.G.; Miller, J.F. Key challenges and recent progress in batteries, fuel cells, and hydrogen storage for clean energy systems. *J. Power Sour.* **2006**, *159*, 73–80. [CrossRef]
11. Shukla, A.; Karmakar, S.; Biniwale, R.B. Hydrogen delivery through liquid organic hydrides: Considerations for a potential technology. *Int. J. Hydrog. Energy* **2012**, *37*, 3719–3726. [CrossRef]
12. Wijayanta, A.T.; Nakaso, K.; Aoki, T.; Kitazato, Y.; Fukai, J. Effect of pressure, composition and temperature characteristics on thermal response and overall reaction rates in a metal hydride tank. *Int. J. Hydrog. Energy* **2011**, *36*, 3529–3536. [CrossRef]
13. Hadjixenophontos, E.; Dematteis, E.M.; Berti, N.; Wołczyk, A.R.; Huen, P.; Brighi, M.; Le, T.T.; Santoru, A.; Payandeh, S.H.; Peru, F.; et al. A review of the MSCA ITN ECOSTORE-Novel complex metal hydrides for efficient and compact storage of renewable energy as hydrogen and electricity. *Inorganics* **2020**, *8*, 17. [CrossRef]
14. Kamiya, S.; Nishimura, M.; Harada, E. Study on introduction of CO₂ free energy to Japan with liquid hydrogen. *Phys. Procedia* **2015**, *67*, 11–19. [CrossRef]
15. Jia, Y.; Sun, C.; Shen, S.; Zou, J.; Mao, S.S.; Yao, X. Combination of nanosizing and interfacial effect: Future perspective for designing Mg-based nanomaterials for hydrogen storage. *Renew. Sustain. Energy Rev.* **2015**, *44*, 289–303. [CrossRef]
16. Eftekhari, A.; Fang, B. Electrochemical hydrogen storage: Opportunities for fuel storage, batteries, fuel cells, and supercapacitors. *Int. J. Hydrog. Energy* **2017**, *42*, 25143–25165. [CrossRef]
17. Chamoun, R.; Demirci, U.B.; Miele, P. Cyclic dehydrogenation-(Re)hydrogenation with hydrogen-storage materials: An overview. *Energy Technol.* **2015**, *3*, 100–117. [CrossRef]

18. Niaz, S.; Manzoor, T.; Pandith, A.H. Hydrogen storage: Materials, methods and perspectives. *Renew. Sustain. Energy Rev.* **2015**, *50*, 457–469. [[CrossRef](#)]
19. Babu, A.R.V.; Devunuri, N.; Prashanthi, Y.; Merugu, R.; Teja, A.J.R. Magnesium hydrides for hydrogen storage: A mini review. *Int. J. Chemtech. Res.* **2014**, *6*, 3451–3455.
20. Lai, Q.; Paskevicius, M.; Sheppard, D.A.; Buckley, C.E.; Thornton, A.W.; Hill, M.R.; Gu, Q.; Mao, J.; Huang, Z.; Liu, H.K.; et al. Hydrogen storage materials for mobile and stationary applications: Current state of the art. *Chem. Sus. Chem.* **2015**, *8*, 2789–2825. [[CrossRef](#)]
21. Goeppert, A.; Czaun, M.; Jones, J.-P.; Surya-Prakash, G.K.; Olah, G.A. Recycling of carbon dioxide to methanol and derived products-closing the loop. *Chem. Soc. Rev.* **2014**, *43*, 7995–8048. [[CrossRef](#)]
22. Bui, M.; Adjiman, C.S.; Bardow, A.; Anthony, E.J.; Boston, A.; Brown, S.; Fennell, P.S.; Fuss, S.; Galindo, A.; Hackett, L.A.; et al. Carbon capture and storage (CCS): The way forward. *Energy Environ. Sci.* **2018**, *11*, 1062–1176. [[CrossRef](#)]
23. Ikäheimo, J.; Kiviluoma, J.; Weiss, R.; Holttinen, H. Power-to-ammonia in future north European 100% renewable power and heat system. *Int. J. Hydrog. Energy* **2018**, *43*, 17295–17308. [[CrossRef](#)]
24. Fecke, M.; Garner, S.; Cox, B. Review of global regulations for anhydrous ammonia production, use, and storage. *Inst. Chem. Eng. Symp. Ser.* **2016**, *2016*, 1–11.
25. Frattini, D.; Cinti, G.; Bidini, G.; Desideri, U.; Cioffi, R.; Jannelli, E. A system approach in energy evaluation of different renewable energies sources integration in ammonia production plants. *Renew. Energy* **2016**, *99*, 472–482. [[CrossRef](#)]
26. Ajiwibowo, M.W.; Darmawan, A.; Aziz, M. A conceptual chemical looping combustion power system design in a power-to-gas energy storage scenario. *Int. J. Hydrog. Energy* **2019**, *44*, 9636–9642. [[CrossRef](#)]
27. Crolius, S.H. NH₃ Energy Implementation Conference: A Brief Report. Available online: <https://www.ammoniaenergy.org/articles/nh3-energy-implementation-conference-a-brief-report/> (accessed on 5 March 2020).
28. Muraki, S. Development of technologies to utilize green ammonia in energy market policies and actions toward a low carbon society. In Proceedings of the 2018 NH₃ Fuel Conference, Pittsburgh, PA, USA, 1 November 2018; p. 20.
29. Crolius, S.H. Great Strides in NH₃ Commitment and Progress in Australia. Available online: <https://www.ammoniaenergy.org/articles/great-strides-in-nh3-commitment-and-progress-in-australia/> (accessed on 27 February 2020).
30. Brown, T. HIALBA-IDEA: Think Tank Launches in Scotland to Deploy CSIRO Technology, Become Green Energy Exporter. Available online: <https://www.ammoniaenergy.org/articles/hialba-idea-think-tank-launches-in-scotland-to-deploy-csiro-technology-become-green-energy-exporter/> (accessed on 27 February 2020).
31. Bennani, Y.; Bennani, Y.; Perl, A.; Patil, A.; van Someren, C.E.J.; Heijne, L.J.M.; van Steenis, M.; Patil, A.; van Someren, C.E.J.; Heijne, L.J.M.; et al. *Power-to-Ammonia: Rethinking the Role of Ammonia-From a Value Product to a Flexible Energy Carrier*; Hanzehogeschool Groningen: Groningen, The Netherlands, 2016; pp. 1–110.
32. Zamfirescu, C.; Dincer, I. Ammonia as a green fuel and hydrogen source for vehicular applications. *Fuel Process. Technol.* **2009**, *90*, 729–737. [[CrossRef](#)]
33. Giddey, S.; Badwal, S.P.S.; Kulkarni, A. Review of electrochemical ammonia production technologies and materials. *Int. J. Hydrog. Energy* **2013**, *38*, 14576–14594. [[CrossRef](#)]
34. National Library of Medicine Ammonia. Available online: <https://pubchem.ncbi.nlm.nih.gov/compound/Ammonia> (accessed on 28 April 2020).
35. National Institute of Standard and Technology Ammonia. Available online: <https://webbook.nist.gov/cgi/cbook.cgi?ID=C7664417> (accessed on 28 April 2020).
36. Andersson, J.; Grönkvist, S. Large-scale storage of hydrogen. *Int. J. Hydrog. Energy* **2019**, *44*, 11901–11919. [[CrossRef](#)]
37. Metkemeijer, R.; Achard, P. Comparison of ammonia and methanol applied indirectly in a hydrogen fuel cell. *Int. J. Hydrog. Energy* **1994**, *19*, 535–542. [[CrossRef](#)]
38. Makepeace, J.W.; He, T.; Weidenthaler, C.; Jensen, T.R.; Chang, F.; Vegge, T.; Ngene, P.; Kojima, Y.; Jongh, P.E.; de Chen, P.; et al. Reversible ammonia-based and liquid organic hydrogen carriers for high-density hydrogen storage: Recent progress. *Int. J. Hydrog. Energy* **2019**, *44*, 7746–7767. [[CrossRef](#)]
39. Cross-ministerial Strategic Innovation Promotion Program (SIP) Energy Carriers 2016. Available online: https://www.jst.go.jp/sip/pdf/SIP_energycarriers2015_en.pdf (accessed on 28 April 2020).

40. Kobayashi, H.; Hayakawa, A.; Somarathne, K.D.K.A.; Okafor, E.C. Science and technology of ammonia combustion. *Proc. Combust. Inst.* **2019**, *37*, 109–133. [[CrossRef](#)]
41. Li, C.; Wang, T.; Gong, J. Alternative strategies toward sustainable ammonia synthesis. *Trans. Tianjin Univ.* **2020**, *26*, 67–91. [[CrossRef](#)]
42. Banerjee, A.; Yuhas, B.D.; Margulies, E.A.; Zhang, Y.; Shim, Y.; Wasielewski, M.R.; Kanatzidis, M.G. Photochemical nitrogen conversion to ammonia in ambient conditions with femo-chalcogels. *J. Am. Chem. Soc.* **2015**, *137*, 2030–2034. [[CrossRef](#)] [[PubMed](#)]
43. Klinsrisuk, S.; Tao, S.; Irvine, J.T.S. 18-Membrane reactors for ammonia production. In *Membrane Reactors for Energy Applications and Basic Chemical Production*; Basile, A., Paola, L., Di, L., Hai, F., Piemonte, V., Eds.; Woodhead Publishing: Cambridge, MA, USA, 2015; pp. 543–563. ISBN 978-1-78242-223-5.
44. Rafiqul, I.; Weber, C.; Lehmann, B.; Voss, A. Energy efficiency improvements in ammonia production-perspectives and uncertainties. *Energy* **2005**, *30*, 2487–2504. [[CrossRef](#)]
45. Wang, L.; Xia, M.; Wang, H.; Huang, K.; Qian, C.; Maravelias, C.T.; Ozin, G.A. Greening ammonia toward the solar ammonia refinery. *Joule* **2018**, *2*, 1055–1074. [[CrossRef](#)]
46. Avery, W.H. A role for ammonia in the hydrogen economy. *Int. J. Hydrog. Energy* **1988**, *13*, 761–773. [[CrossRef](#)]
47. Cheema, I.I.; Krewer, U. Operating envelope of Haber-Bosch process design for power-to-ammonia. *RSC Adv.* **2018**, *8*, 34926–34936. [[CrossRef](#)]
48. Smith, A.R.; Klosek, J. A review of air separation technologies and their.pdf. *Fuel Process. Technol.* **2001**, *70*, 115–134. [[CrossRef](#)]
49. Aneke, M.; Wang, M. Potential for improving the energy efficiency of cryogenic air separation unit (ASU) using binary heat recovery cycles. *Appl. Eng.* **2015**, *81*, 223–231. [[CrossRef](#)]
50. Gilbert, P.; Thornley, P. Energy and carbon balance of ammonia production from biomass gasification. In *Proceedings of the Bio-Ten Conference, Birmingham, UK, 20–22 September 2010*; pp. 1–9.
51. Wang, Q.; Guo, J.; Chen, P. Recent progress towards mild-condition ammonia synthesis. *J. Energy Chem.* **2019**, *36*, 25–36. [[CrossRef](#)]
52. Siporin, S.E.; Davis, R.J. Use of kinetic models to explore the role of base promoters on Ru/MgO ammonia synthesis catalysts. *J. Catal.* **2004**, *225*, 359–368. [[CrossRef](#)]
53. Brown, D.E.; Edmonds, T.; Joyner, R.W.; McCarroll, J.J.; Tennison, S.R. The genesis and development of the commercial BP doubly promoted catalyst for ammonia synthesis. *Catal. Lett.* **2014**, *144*, 545–552. [[CrossRef](#)]
54. Bielawa, H.; Hinrichsen, O.; Birkner, A.; Muhler, M. The ammonia-synthesis catalyst of the next generation: Barium-promoted oxide-supported ruthenium. *Angew. Chem. Int. Ed.* **2001**, *40*, 1061–1063. [[CrossRef](#)]
55. Kitano, M.; Inoue, Y.; Ishikawa, H.; Yamagata, K.; Nakao, T.; Tada, T.; Matsuishi, S.; Yokoyama, T.; Hara, M.; Hosono, H. Essential role of hydride ion in ruthenium-based ammonia synthesis catalysts. *Chem. Sci.* **2016**, *7*, 4036–4043. [[CrossRef](#)] [[PubMed](#)]
56. Medford, A.J.; Vojvodic, A.; Hummelshøj, J.S.; Voss, J.; Abild-Pedersen, F.; Studt, F.; Bligaard, T.; Nilsson, A.; Nørskov, J.K. From the Sabatier principle to a predictive theory of transition-metal heterogeneous catalysis. *J. Catal.* **2015**, *328*, 36–42. [[CrossRef](#)]
57. Vojvodic, A.; Medford, A.J.; Studt, F.; Abild-Pedersen, F.; Khan, T.S.; Bligaard, T.; Nørskov, J.K. Exploring the limits: A low-pressure, low-temperature Haber-Bosch process. *Chem. Phys. Lett.* **2014**, *598*, 108–112. [[CrossRef](#)]
58. Kawamura, F.; Taniguchi, T. Synthesis of ammonia using sodium melt. *Sci. Rep.* **2017**, *7*, 7–10. [[CrossRef](#)] [[PubMed](#)]
59. Lipman, T.; Shah, N. *Ammonia as an Alternative Energy Storage Medium for Hydrogen Fuel Cells: Scientific and Technical Review for Near-Term Stationary Power Demonstration Projects*; Final Report; University of California: Berkeley, CA, USA, 2017.
60. Tsuneto, A.; Kudo, A.; Sakata, T. Lithium-mediated electrochemical reduction of high pressure N₂ to NH₃. *J. Electroanal. Chem.* **1994**, *367*, 183–188. [[CrossRef](#)]
61. Watanabe, M.; Thomas, M.L.; Zhang, S.; Ueno, K.; Yasuda, T.; Dokko, K. Application of ionic liquids to energy storage and conversion materials and devices. *Chem. Rev.* **2017**, *117*, 7190–7239. [[CrossRef](#)]
62. Kamer, P.C.J.; Vogt, D.; Thybaut, J. *Contemporary Catalysis*; The Royal Society of Chemistry: London, UK, 2017; ISBN 978-1-84973-990-0.
63. Murakami, T.; Nishikiori, T.; Nohira, T.; Ito, Y. Electrolytic synthesis of ammonia in molten salts under atmospheric pressure. *J. Am. Chem. Soc.* **2003**, *125*, 334–335. [[CrossRef](#)]

64. Amar, I.A.; Lan, R.; Petit, C.T.G.; Arrighi, V.; Tao, S. Electrochemical synthesis of ammonia based on a carbonate-oxide composite electrolyte. *Solid State Ion.* **2011**, *182*, 133–138. [CrossRef]
65. Iwahara, H. Technological challenges in the application of proton conducting ceramics. *Solid State Ion.* **1995**, *77*, 289–298. [CrossRef]
66. Soloveichik, G. Electrochemical synthesis of ammonia as a potential alternative to the Haber–Bosch process. *Nat. Catal.* **2019**, *2*, 377–380. [CrossRef]
67. Gálvez, M.E.; Halmann, M.; Steinfeld, A. Ammonia production via a two-step Al₂O₃/AlN thermochemical cycle. 1. Thermodynamic, environmental, and economic analyses. *Ind. Eng. Chem. Res.* **2007**, *46*, 2042–2046.
68. Gálvez, M.E.; Frei, A.; Halmann, M.; Steinfeld, A. Ammonia production via a two-step Al₂O₃/AlN thermochemical cycle 2. Kinetic analysis. *Ind. Eng. Chem. Res.* **2007**, *46*, 2047–2053. [CrossRef]
69. Juangsa, F.B.; Aziz, M. Integrated system of thermochemical cycle of ammonia, nitrogen production, and power generation. *Int. J. Hydrog. Energy* **2019**, *44*, 17525–17534. [CrossRef]
70. Cinti, G.; Frattini, D.; Jannelli, E.; Desideri, U.; Bidini, G. Coupling solid oxide electrolyser (SOE) and ammonia production plant. *Appl. Energy* **2017**, *192*, 466–476. [CrossRef]
71. Aziz, M.; Putranto, A.; Biddinika, M.K.; Wijayanta, A.T. Energy-saving combination of N₂ production, NH₃ synthesis, and power generation. *Int. J. Hydrog. Energy* **2017**, *42*, 27174–27183. [CrossRef]
72. Darmawan, A.; Ajiwibowo, M.W.; Yoshikawa, K.; Aziz, M.; Tokimatsu, K. Energy-efficient recovery of black liquor through gasification and syngas chemical looping. *Appl. Energy* **2018**, *219*, 290–298. [CrossRef]
73. Nurdiawati, A.; Zaini, I.N.; Amin, M.; Sasongko, D.; Aziz, M. Microalgae-based coproduction of ammonia and power employing chemical looping process. *Chem. Eng. Res. Des.* **2019**, *146*, 311–323. [CrossRef]
74. Wijayanta, A.T.; Aziz, M. Ammonia production from algae via integrated hydrothermal gasification, chemical looping, N₂ production, and NH₃ synthesis. *Energy* **2019**, *174*, 331–338. [CrossRef]
75. Ajiwibowo, M.W.; Darmawan, A.; Aziz, M. Towards clean palm oil processing: Integrated ammonia production from empty fruit bunch and palm oil effluent. *J. Clean. Prod.* **2019**, *236*, 117680. [CrossRef]
76. National Institute of Standard and Technology Thermophysical Properties of Fluid Systems. Available online: <http://webbook.nist.gov/chemistry/fluid/> (accessed on 2 March 2020).
77. Christensen, C.H.; Sørensen, R.Z.; Johannessen, T.; Quaade, U.J.; Honkala, K.; Elmøe, T.D.; Køhler, R.; Nørskov, J.K. Metal ammine complexes for hydrogen storage. *J. Mater. Chem.* **2005**, *15*, 4106–4108. [CrossRef]
78. Jacobsen, H.S.; Hansen, H.A.; Andreasen, J.W.; Shi, Q.; Andreasen, A.; Feidenhans'l, R.; Nielsen, M.M.; Ståhl, K.; Vegge, T. Nanoscale structural characterization of Mg(NH₃)₆Cl₂ during NH₃ desorption: An in situ small angle X-ray scattering study. *Chem. Phys. Lett.* **2007**, *441*, 255–260. [CrossRef]
79. EasyChem Industrial Uses of Ammonia. Available online: <https://easychem.com.au/monitoring-and-management/maximising-production/industrial-uses-of-ammonia/> (accessed on 4 March 2020).
80. Li, J.; Huang, H.; Kobayashi, N.; He, Z.; Osaka, Y.; Zeng, T. Numerical study on effect of oxygen content in combustion air on ammonia combustion. *Energy* **2015**, *93*, 2053–2068. [CrossRef]
81. Kroch, E. Ammonia—a fuel for motor buses. *J. Inst. Pet.* **1945**, *31*, 213–223.
82. Mario, Z. Device for Operating Internal Combustion Engines with Mixtures of Ammonia, Hydrogen and Nitrogen Prepared from Ammonia. U.S. Patent US2140254A, 13 December 1938.
83. NASA. NASA Armstrong Fact Sheet: X-15 Hypersonic Research Program. Available online: <https://www.nasa.gov/centers/armstrong/news/FactSheets/FS-052-DFRC.html> (accessed on 10 March 2020).
84. Starkman, E.S.; Newhall, H.K.; Sutton, R.; Maguire, T.; Farbar, L. Ammonia as a spark ignition engine fuel: Theory and application. *SAE Trans.* **1967**, *75*, 765–784.
85. Pearsall, T.J.; Garabedian, C.G. Combustion of anhydrous ammonia in diesel engines. *SAE Trans.* **1968**, *76*, 3213–3221.
86. Cornelius, W.; Huellmantel, L.W.; Mitchell, H.R. *Ammonia as an Engine Fuel*; Society of Automotive Engineers: Warrendale, PA, USA, 1965.
87. Valera-Medina, A.; Marsh, R.; Runyon, J.; Pugh, D.; Beasley, P.; Hughes, T.; Bowen, P. Ammonia-methane combustion in tangential swirl burners for gas turbine power generation. *Appl. Energy* **2017**, *185*, 1362–1371. [CrossRef]
88. Gong, W.; Leo Willi, M. Power System having an Ammonia Fuelled Engine. U.S. Patent US20100019506A1, 28 January 2010.
89. Ryu, K.; Zacharakis-Jutz, G.E.; Kong, S.C. Effects of gaseous ammonia direct injection on performance characteristics of a spark-ignition engine. *Appl. Energy* **2014**, *116*, 206–215. [CrossRef]

90. Reiter, A.J.; Kong, S.C. Combustion and emissions characteristics of compression-ignition engine using dual ammonia-diesel fuel. *Fuel* **2011**, *90*, 87–97. [[CrossRef](#)]
91. Boretti, A. Novel dual fuel diesel-ammonia combustion system in advanced TDI engines. *Int. J. Hydrog. Energy* **2017**, *42*, 7071–7076. [[CrossRef](#)]
92. Frigo, S.; Gentili, R. Analysis of the behaviour of a 4-stroke Si engine fuelled with ammonia and hydrogen. *Int. J. Hydrog. Energy* **2013**, *38*, 1607–1615. [[CrossRef](#)]
93. Faehn, D.; Bull, M.G.; Shekleton, J.R. Experimental investigation of ammonia as a turbine engine fuel. *SAE Tech. Pap.* **1966**, 660769.
94. Valera-Medina, A.; Pugh, D.G.; Marsh, P.; Bulat, G.; Bowen, P. Preliminary study on lean premixed combustion of ammonia-hydrogen for swirling gas turbine combustors. *Int. J. Hydrog. Energy* **2017**, *42*, 24495–24503. [[CrossRef](#)]
95. Xiao, H.; Valera-Medina, A.; Bowen, P.J. Study on premixed combustion characteristics of co-firing ammonia/methane fuels. *Energy* **2017**, *140*, 125–135. [[CrossRef](#)]
96. Karabeyoglu, A.; Evans, B. Fuel conditioning system for ammonia-fired power plants. In Proceedings of the 9th Annual NH₃ Fuel Association Conference, San Antonio, TX, USA, 1 October 2012.
97. Meyer, T.; Kumar, P.; Li, M.; Redfern, K.; Diaz, D. Ammonia combustion with near-zero pollutant emissions. In Proceedings of the 7th Annual NH₃ Fuel Conference, Romulus, MI, USA, 26–28 September 2010.
98. Li, J.; Huang, H.; Kobayashi, N.; He, Z.; Nagai, Y. Study on using hydrogen and ammonia as fuels: Combustion characteristics and NO_x formation. *Int. J. Energy Res.* **2014**, *38*, 1214–1223. [[CrossRef](#)]
99. Newhall, H.K.; Starkman, E.S. Theoretical performance of ammonia as a gas turbine fuel. *SAE Tech. Pap.* **1966**, 660768.
100. Lee, D.; Song, H.H. Development of combustion strategy for the internal combustion engine fueled by ammonia and its operating characteristics. *J. Mech. Sci. Technol.* **2018**, *32*, 1905–1925. [[CrossRef](#)]
101. Keller, M.; Koshi, M.; Otomo, J.; Iwasaki, H.; Mitsumori, T.; Yamada, K. Thermodynamic evaluation of an ammonia-fueled combined-cycle gas turbine process operated under fuel-rich conditions. *Energy* **2020**, *194*, 116894. [[CrossRef](#)]
102. Kurata, O.; Iki, N.; Matsunuma, T.; Inoue, T.; Tsujimura, T.; Furutani, H.; Kobayashi, H.; Hayakawa, A. Performances and emission characteristics of NH₃-air and NH₃-CH₄-air combustion gas-turbine power generations. *Proc. Combust. Inst.* **2017**, *36*, 3351–3359. [[CrossRef](#)]
103. Goshome, K.; Yamada, T.; Miyaoka, H.; Ichikawa, T.; Kojima, Y. High compressed hydrogen production via direct electrolysis of liquid ammonia. *Int. J. Hydrog. Energy* **2016**, *41*, 14529–14534. [[CrossRef](#)]
104. Mekhilef, S.; Saidur, R.; Safari, A. Comparative study of different fuel cell technologies. *Renew. Sustain. Energy Rev.* **2012**, *16*, 981–989. [[CrossRef](#)]
105. Minh, N.Q. Ceramic fuel cells. *J. Am. Ceram. Soc.* **1993**, *76*, 563–588. [[CrossRef](#)]
106. Ni, M.; Leung, D.Y.C.; Leung, M.K.H. An improved electrochemical model for the NH₃ fed proton conducting solid oxide fuel cells at intermediate temperatures. *J. Power Sources* **2008**, *185*, 233–240. [[CrossRef](#)]
107. De Geeter, E.; Mangan, M.; Spaepen, S.; Stinissen, W.; Vennekens, G. Alkaline fuel cells for road traction. *J. Power Sour.* **1999**, *80*, 207–212. [[CrossRef](#)]
108. Giddey, S.; Badwal, S.P.S.; Munnings, C.; Dolan, M. Ammonia as a renewable energy transportation media. *ACS Sustain. Chem. Eng.* **2017**, *5*, 10231–10239. [[CrossRef](#)]
109. McLean, G.F.; Niet, T.; Prince-Richard, S.; Djilali, N. An assessment of alkaline fuel cell technology. *Int. J. Hydrog. Energy* **2002**, *27*, 507–526. [[CrossRef](#)]
110. Suzuki, S.; Muroyama, H.; Matsui, T.; Eguchi, K. Fundamental studies on direct ammonia fuel cell employing anion exchange membrane. *J. Power Sour.* **2012**, *208*, 257–262. [[CrossRef](#)]
111. Lan, R.; Tao, S. Direct ammonia alkaline anion-exchange membrane fuel cells. *Electrochem. Solid State Lett.* **2010**, *13*. [[CrossRef](#)]
112. Lee, K.R.; Song, D.; Park, S.B.; Han, J.I. A direct ammonium carbonate fuel cell with an anion exchange membrane. *RSC Adv.* **2014**, *4*, 5638–5641. [[CrossRef](#)]
113. Yao, K.; Cheng, Y.F. Electrodeposited Ni–Pt binary alloys as electrocatalysts for oxidation of ammonia. *J. Power Sour.* **2007**, *173*, 96–101. [[CrossRef](#)]
114. Lomocso, T.L.; Baranova, E.A. Electrochemical oxidation of ammonia on carbon-supported bi-metallic PtM (M = Ir, Pd, SnO_x) nanoparticles. *Electrochim. Acta* **2011**, *56*, 8551–8558. [[CrossRef](#)]

115. Endo, K.; Nakamura, K.; Katayama, Y.; Miura, T. Pt–Me (Me = Ir, Ru, Ni) binary alloys as an ammonia oxidation anode. *Electrochim. Acta* **2004**, *49*, 2503–2509. [[CrossRef](#)]
116. Afif, A.; Radenahmad, N.; Cheok, Q.; Shams, S.; Kim, J.H.; Azad, A.K. Ammonia-fed fuel cells: A comprehensive review. *Renew. Sustain. Energy Rev.* **2016**, *60*, 822–835. [[CrossRef](#)]
117. Farr, R.D.; Vayenas, C.G. Ammonia high temperature solid electrolyte fuel cell. *J. Electrochem. Soc.* **1980**, *127*, 1478–1483. [[CrossRef](#)]
118. Vayenas, C.G.; Farr, R.D. Cogeneration of electric energy and nitric oxide. *Science* **1980**, *208*, 593–594. [[CrossRef](#)]
119. Wojcik, A.; Middleton, H.; Damopoulos, I.; Van Herle, J. Ammonia as a fuel in solid oxide fuel cells. *J. Power Sour.* **2003**, *118*, 342–348. [[CrossRef](#)]
120. Ni, M.; Leung, D.Y.C.; Leung, M.K.H. Thermodynamic analysis of ammonia fed solid oxide fuel cells: Comparison between proton-conducting electrolyte and oxygen ion-conducting electrolyte. *J. Power Sour.* **2008**, *183*, 682–686. [[CrossRef](#)]
121. Li, Z.; Liu, R.; Wang, J.; Xu, Z.; Xie, Y.; Wang, B. Preparation of double-doped BaCeO₃ and its application in the synthesis of ammonia at atmospheric pressure. *Sci. Technol. Adv. Mater.* **2007**, *8*, 566–570. [[CrossRef](#)]
122. Meng, G.; Jiang, C.; Ma, J.; Ma, Q.; Liu, X. Comparative study on the performance of a SDC-based SOFC fueled by ammonia and hydrogen. *J. Power Sour.* **2007**, *173*, 189–193. [[CrossRef](#)]
123. Maffei, N.; Pelletier, L.; Charland, J.P.; McFarlan, A. An intermediate temperature direct ammonia fuel cell using a proton conducting electrolyte. *J. Power Sour.* **2005**, *140*, 264–267. [[CrossRef](#)]
124. Ichikawa, A.; Hayakawa, A.; Kitagawa, Y.; Kunkuma, A.S.K.D.; Kudo, T.; Kobayashi, H. Laminar burning velocity and markstein length of ammonia/hydrogen/air premixed flames at elevated pressures. *Int. J. Hydrog. Energy* **2015**, *40*, 9570–9578. [[CrossRef](#)]
125. Lee, J.H.; Kim, J.H.; Park, J.H.; Kwon, O.C. Studies on properties of laminar premixed hydrogen-added ammonia/air flames for hydrogen production. *Int. J. Hydrog. Energy* **2010**, *35*, 1054–1064. [[CrossRef](#)]
126. Kumar, P.; Meyer, T.R. Experimental and modeling study of chemical-kinetics mechanisms for H₂-NH₃-air mixtures in laminar premixed jet flames. *Fuel* **2013**, *108*, 166–176. [[CrossRef](#)]
127. Henshaw, P.F.; D’Andrea, T.; Mann, K.R.C.; Ting, D.S.K. Premixed ammonia-methane-air combustion. *Combust. Sci. Technol.* **2005**, *177*, 2151–2170. [[CrossRef](#)]
128. Zietz, U.; Baumgärtel, G. The laminar flame speeds of propane-ammonia-air mixtures. *Combust. Flame* **1969**, *13*, 329–330. [[CrossRef](#)]
129. Bockhorn, H.; Fetting, F.; Mende, J.C. The laminar flame velocities of propane/ammonia mixtures. *Combust. Flame* **1972**, *18*, 471–473. [[CrossRef](#)]
130. Chiuta, S.; Everson, R.C.; Neomagus, H.W.J.P.; Van Der Gryp, P.; Bessarabov, D.G. Reactor technology options for distributed hydrogen generation via ammonia decomposition: A review. *Int. J. Hydrog. Energy* **2013**, *38*, 14968–14991. [[CrossRef](#)]
131. Mukherjee, S.; Devaguptapu, S.V.; Sviripa, A.; Lund, C.R.F.; Wu, G. Low-temperature ammonia decomposition catalysts for hydrogen generation. *Appl. Catal. B Environ.* **2018**, *226*, 162–181. [[CrossRef](#)]
132. Lamb, K.E.; Dolan, M.D.; Kennedy, D.F. Ammonia for hydrogen storage; A review of catalytic ammonia decomposition and hydrogen separation and purification. *Int. J. Hydrog. Energy* **2019**, *44*, 3580–3593. [[CrossRef](#)]
133. Ganley, J.C.; Thomas, F.S.; Seebauer, E.G.; Masel, R.I. A priori catalytic activity correlations: The difficult case of hydrogen production from ammonia. *Catal. Lett.* **2004**, *96*, 117–122. [[CrossRef](#)]
134. Yin, S.F.; Xu, B.Q.; Zhou, X.P.; Au, C.T. A mini-review on ammonia decomposition catalysts for on-site generation of hydrogen for fuel cell applications. *Appl. Catal. A Gen.* **2004**, *277*, 1–9. [[CrossRef](#)]
135. Boisen, A.; Dahl, S.; Nørskov, J.K.; Christensen, C.H. Why the optimal ammonia synthesis catalyst is not the optimal ammonia decomposition catalyst. *J. Catal.* **2005**, *230*, 309–312. [[CrossRef](#)]
136. Bligaard, T.; Nørskov, J.K.; Dahl, S.; Matthiesen, J.; Christensen, C.H.; Sehested, J. The brønsted-evans-polanyi relation and the volcano curve in heterogeneous catalysis. *J. Catal.* **2004**, *224*, 206–217. [[CrossRef](#)]
137. Wang, S.J.; Yin, S.F.; Li, L.; Xu, B.Q.; Ng, C.F.; Au, C.T. Investigation on modification of Ru/CNTs catalyst for the generation of CO_x-free hydrogen from ammonia. *Appl. Catal. B Environ.* **2004**, *52*, 287–299. [[CrossRef](#)]
138. Hansgen, D.A.; Vlachos, D.G.; Chen, J.G. Using first principles to predict bimetallic catalysts for the ammonia decomposition reaction. *Nat. Chem.* **2010**, *2*, 484–489. [[CrossRef](#)] [[PubMed](#)]

139. Li, X.-K.; Ji, W.-J.; Zhao, J.; Wang, S.-J.; Au, C.-T. Ammonia decomposition over Ru and Ni catalysts supported on fumed SiO₂, MCM-41, and SBA-15. *J. Catal.* **2005**, *236*, 181–189. [[CrossRef](#)]
140. Bajus, S.; Agel, F.; Kusche, M.; Ní Bhriain, N.; Wasserscheid, P. Alkali hydroxide-modified Ru/γ-Al₂O₃ catalysts for ammonia decomposition. *Appl. Catal. A Gen.* **2016**, *510*, 189–195. [[CrossRef](#)]
141. Yin, S.-F.; Zhang, Q.-H.; Xu, B.-Q.; Zhu, W.-X.; Ng, C.-F.; Au, C.-T. Investigation on the catalysis of CO_x-free hydrogen generation from ammonia. *J. Catal.* **2004**, *224*, 384–396. [[CrossRef](#)]
142. Yin, S.-F.; Xu, B.-Q.; Ng, C.-F.; Au, C.-T. Nano Ru/CNTs: A highly active and stable catalyst for the generation of CO_x-free hydrogen in ammonia decomposition. *Appl. Catal. B Environ.* **2004**, *48*, 237–241. [[CrossRef](#)]
143. U.S. Department of Energy; Ohi, J.M.; Vanderborgh, N.; Voecks, G. Hydrogen fuel quality specifications for polymer electrolyte fuel cells in road vehicles. *Saf. Codes Stand. Progr.* **2016**, 1–72.
144. Miyaoka, H.; Miyaoka, H.; Ichikawa, T.; Ichikawa, T.; Kojima, Y. Highly purified hydrogen production from ammonia for PEM fuel cell. *Int. J. Hydrog. Energy* **2018**, *43*, 14486–14492. [[CrossRef](#)]
145. Van Hassel, B.A.; Karra, J.R.; Santana, J.; Saita, S.; Murray, A.; Goberman, D.; Chahine, R.; Cossement, D. Ammonia sorbent development for on-board H₂ purification. *Sep. Purif. Technol.* **2015**, *142*, 215–226. [[CrossRef](#)]
146. Dolan, M.D.; Viano, D.M.; Langley, M.J.; Lamb, K.E. Tubular vanadium membranes for hydrogen purification. *J. Memb. Sci.* **2018**, *549*, 306–311. [[CrossRef](#)]
147. Bockris, J.O.M. The hydrogen economy: Its history. *Int. J. Hydrog. Energy* **2013**, *38*, 2579–2588. [[CrossRef](#)]
148. Moliner, R.; Lázaro, M.J.; Suelves, I. Analysis of the strategies for bridging the gap towards the Hydrogen Economy. *Int. J. Hydrog. Energy* **2016**, *41*, 19500–19508. [[CrossRef](#)]
149. Nejat Veziroglu, T. Conversion to hydrogen economy. *Energy Procedia* **2012**, *29*, 654–656. [[CrossRef](#)]
150. Edwards, P.P.; Kuznetsov, V.L.; David, W.I.F. Hydrogen energy. *Philos. Trans. R. Soc. A Math. Phys. Eng. Sci.* **2007**, *365*, 1043–1056. [[CrossRef](#)]
151. Rosen, M.A.; Koochi-Fayegh, S. The prospects for hydrogen as an energy carrier: An overview of hydrogen energy and hydrogen energy systems. *Energy Ecol. Environ.* **2016**, *1*, 10–29. [[CrossRef](#)]
152. European Commission. *Hydrogen Energy and Fuel Cells: A Vision of Our Future*; European Commission: Luxembourg, 2003.
153. Hydrogen and Fuel Cells Strategy Office; Advanced Energy Systems and Structure Division; Energy Conservation and Renewable Energy Department. *Basic Hydrogen Strategy*; Trade and Industry: Tokyo, Japan, 2017; pp. 1–37.
154. Wijayanta, A.T.; Oda, T.; Purnomo, C.W.; Kashiwagi, T.; Aziz, M. Liquid hydrogen, methylcyclohexane, and ammonia as potential hydrogen storage: Comparison review. *Int. J. Hydrog. Energy* **2019**, *44*, 15026–15044. [[CrossRef](#)]
155. Mizuno, Y.; Ishimoto, Y.; Sakai, S.; Sakata, K. Economic analysis on international hydrogen energy career supply chains. *J. Jpn. Soc. Energy Resour.* **2017**, *38*, 11–17.
156. Worrell, E.; Price, L.; Neelis, M.; Galitsky, C.; Nan, Z. *World Best Practice Energy Intensity Values for Selected Industrial Sectors*; Lawrence Berkeley National Laboratory: Berkeley, CA, USA, 2007; p. 51.
157. Abashar, M.E.E. Ultra-clean hydrogen production by ammonia decomposition. *J. King Saud Univ. Eng. Sci.* **2018**, *30*, 2–11. [[CrossRef](#)]
158. Klerke, A.; Christensen, C.H.; Nørskov, J.K.; Vegge, T. Ammonia for hydrogen storage: Challenges and opportunities. *J. Mater. Chem.* **2008**, *18*, 2304–2310. [[CrossRef](#)]
159. Lan, R.; Tao, S. Ammonia as a suitable fuel for fuel cells. *Front. Energy Res.* **2014**, *2*, 3–6. [[CrossRef](#)]



© 2020 by the authors. Licensee MDPI, Basel, Switzerland. This article is an open access article distributed under the terms and conditions of the Creative Commons Attribution (CC BY) license (<http://creativecommons.org/licenses/by/4.0/>).

Article

Operation of a Solid Oxide Fuel Cell Based Power System with Ammonia as a Fuel: Experimental Test and System Design

Linda Barelli , Gianni Bidini and Giovanni Cinti * Department of Engineering, University of Perugia, Via G. Duranti 93, 06125 Perugia, Italy;
linda.barelli@unipg.it (L.B.); gianni.bidini@unipg.it (G.B.)

* Correspondence: giovanni.cinti@unipg.it

Received: 30 September 2020; Accepted: 19 November 2020; Published: 24 November 2020



Abstract: Ammonia has strong potentialities as sustainable fuel for energy applications. NH_3 is carbon free and can be synthesized from renewable energy sources (RES). In Solid Oxide Fuel Cells, NH_3 reacts electrochemically thereby avoiding the production of typical combustion pollutants such as NO_x . In this study, an ammonia-fueled solid oxide fuel cells (SOFC) system design is proposed and a thermodynamic model is developed to evaluate its performance. A SOFC short stack was operated with NH_3 in a wide range of conditions. Experimental results are implemented in the thermodynamic model. Electrical efficiency of 52.1% based on ammonia Lower Heating Value is calculated at a net power density of $0.36 \text{ W cm}_{\text{FC}}^{-2}$. The operating conditions of the after burner and of the ammonia decomposition reactor are studied by varying the values of specific parameters. The levelized cost of energy of $0.221 \text{ \$ kWh}^{-1}$ was evaluated, as introduced by the International Energy Agency, for a system that operates at nominal conditions and at a reference power output of 100 kW. This supports the feasibility of ammonia-fueled SOFC systems with reference to the carbon free energy market, specifically considering the potential development of green ammonia production.

Keywords: ammonia; SOFC; system; model; stack test

1. Introduction

The development of renewable energies, in particular wind and solar, requires the integration of energy storage solutions. Ammonia is a chemical used as a fertilizer but can be considered also as a fuel. Recently ammonia is presented as a potential energy storage solution [1,2]. Presently, ammonia is produced from natural gas but a pathway for the production of green ammonia can be designed based on hydrogen from electrolysis or biogas [3,4]. Table 1 compares ammonia with the most common fuels. Ammonia is characterized by a volumetric energy density significantly higher than compressed natural gas at 250 bar, with gravimetric energy density more than halved with respect to fossil fuels but greater than methanol.

Table 1. Energy densities of ammonia and other common fuels [5].

	Liquid Ammonia	Pressurized Hydrogen (@350 bar)	Methanol	Natural Gas (@250 bar)	Gasoline	Diesel
Volumetric energy density – GJ m^{-3}	11.38	11.73	19.8	9.8	30.6	37.2
Gravimetric energy density – MJ kg^{-1}	18.65	120.24	15.6	50	43.6	44.8

For the conversion of ammonia to power production, three main energy technologies are reported in the literature: internal combustion engines [6–9], gas turbines [10–12] and fuel cells [2,13,14].

Among these, solid oxide fuel cells (SOFCs) are the most interesting ones and whose development is presently reaching commercialization, especially in the power range of 1–250 kW and system electric efficiency above 60% based on natural gas low heating value (LHV). SOFCs operate at high temperature, 650–800 °C, reducing the cost of materials compared to low temperature fuel cells and producing heat that can be used for cogeneration application or recovered at system level to produce hydrogen through catalytic processes. This is the case of ammonia systems, where the heat can supply thermal energy to decompose ammonia. Moreover, the materials used as anodes in SOFCs are efficient catalyst for ammonia decomposition. Since both high temperature heat and catalytic material are already available in a SOFC system, it is possible to consider two types of system design: (i) ammonia can be decomposed in a specific reactor and the product gases, a mixture of hydrogen and nitrogen, are fed to the SOFC or (ii) ammonia can be directly fed to the SOFC stack. The latter is extremely interesting since the internal ammonia decomposition reaction absorbs the produced heat mitigating the need for the cooling of the SOFC power unit.

This study presents an innovative ammonia-fed SOFC system based on experimental results performed on a SOFC short stack. Literature reports studies relative to both experimental test and of power system designs of ammonia coupled with SOFC technology and study.

The experimental operation of SOFC with ammonia as a fuel is well assessed in the literature especially at the single cell level. While the first studies were dedicated to SOFCs with proton-conducting electrolyte [15–17], the so-called SOFC-H, recent studies are more focused on ion-conduction electrolyte, SOFC-O [18–20], due to higher level of maturity of the latter technology. Moving to the stack size, very little is reported in the literature in terms of experimental results. In [20], a stack operating with both ammonia and hydrogen was tested. A preliminary test was performed before testing the stack on two sealing materials and the SiO₂-Al₂O₃-R₂O-RO was selected as the most stable one. They found that the ammonia-fueled stack delivered 255 W at 56 A, reaching 53% efficiency based on the ammonia Lower Heating Value (LHV), which is almost the same performance as the one fueled with hydrogen. A second test was repeated on a stack consisted of 10 anode-supported planar cells each one with an active area of 95 cm² [21]. The stack was fed with pure ammonia and with two different decomposed ammonia mixtures, one produced with a cracking reactor and one with an auto-thermal reactor. Polarization curves show that decomposed ammonia has higher performance than pure ammonia at high current densities. Such behavior is explained by the steam produced by the electrochemical reaction that inhibits the decomposition of ammonia in the anode chamber. Pure NH₃ test achieved 232 W at 36 A with a total LHV efficiency of 36.3%. Low values of efficiency are mainly caused by low fuel use factor (U_f) used in the test (62% at 36 A). An endurance test of 1000 h was performed both with pure hydrogen and ammonia showing same degradation rate. No NO_x was measured in the exhaust gases. In [22] a four cells stack was tested comparing pure hydrogen, pure ammonia, and decomposed ammonia mixture at three operating temperatures: 800, 750 and 700 °C. Polarization curves show no significant difference between the compositions at all the three tested temperatures. Finally, in [23], a 10 cells SOFC stack based on Electrolyte Supported Cells (ESC) and with chromium-based interconnects (CFY), was tested under four anodic feeding mixtures to compare ammonia and hydrogen performance with and without steam flow addition. Results show the equivalence between hydrogen and ammonia for both pure and humidified compositions. In addition, a durability test of 1000 h at 80% use of fuel was performed. Results showed the same degradation of 1.1%/1000 h for both ammonia and hydrogen. Ex situ analysis showed that degradation is caused by nitridation process of both interconnect and Ni contact mesh.

The literature also reports studies relative to NH₃-SOFC system analysis. Design studies here reported refer to different types of SOFC technologies and of power plants. This short review focuses mainly on the integration solutions presented in terms of balance of plant design. In [24] two different schemes are presented, each one integrates two heat exchangers, for both air and fuel pre-heat, and the after burner. The two designs differ from what concerns the air management strategy: required air can be fed directly to the stack, first design, or separated in two streams, bringing to a two-stacks

strategy, second design. In the second design the separated amount of air is mixed to first stack cathodic off-gases and fed to the cathode of the second stack. This design allows both to reduce the temperature of the mixture and to increase oxygen concentration of the second stack cathodic inlet. As a result, the cathodic heat exchanger size is halved. In [25] a portable system is studied. The after burner supplies the heat to a single heat exchanger that increases air temperature to stack inlet and, at the same time, supplies heat for the decomposition of ammonia. Water is also evaporated in the heat exchanger and added to the anode inlet gas mix. The model calculates up to 41.1% of efficiency for a fuel use of 0.8. A similar design is presented in [22] but implementing a three heat exchangers solution. Two separate heat exchangers operating at high temperature recover heat separately for air and fuel. The two separated gas flows are mixed at lower temperature in an after burner that completes the oxidation of the fuel and provides hot exhausts to feed a single heat exchanger. Such a component is designed for low temperature pre-heating of both anodic and cathodic gas flows. The study shows the advantages in terms of air flow reduction due to internal ammonia decomposition reaction. A system efficiency of 50% is calculated. In [26] a combined heat and power (CHP) system based on a SOFC-H and fed with ammonia is considered for vehicular applications. The hot gases from SOFC exhausts are mixed and split in two different gas flows to preheat ammonia and air inlet flows. The study focuses on energy and exergy analysis when varying operating parameters such as fuel use, current density, and stack temperature. The maximum efficiency of 48% is calculated when the SOFC-H operates at low current density.

Recently, a new design was proposed for a system operating with ammonia and SOFC to produce heat, hydrogen, and power [27]. Two different concepts are presented whether the SOFC electricity production is designed only to sustain electricity consumption of the system or to supply electricity externally. In both cases, the system operates at low fuel use since hydrogen is one of the products of the system. In the first concept, inlet gases are preheated, recovering heat from the catalytic burner and from an external heat source. The second concept has a two-stacks strategy and part of the anode off-gases delivered by the first stack feeds the second SOFC unit. Heat balance is guaranteed by the external heat source and by heat recovery from the catalytic burner off-gases to preheat both cathodic inlet flows and part of anodic inlet. Trigeneration efficiency is 81% for the first concept and 71% for the second one.

In general, the design optimization of SOFC systems fed by ammonia is only partially investigated in the literature. This study presents an innovative system design based on experimental results on a short stack. First, an experimental test was performed on a SOFC short stack operating with ammonia in a wide range of parameters variation. Secondly, test results were used to define the correlation between operating parameters and performance. The correlation was implemented in the system design, modeled with a calculation sheet. Subsequently, nominal conditions are identified and main parameters are varied to study the effect on the equilibrium. Finally, a preliminary economic feasibility study was performed using the levelized cost of energy (LCOE) parameter as introduced by the International Energy Agency in [28].

2. Methods

The methodology followed includes three main phases. First, the experimental activity was performed to provide experimental data, subsequently implemented in the modeling phase; accordingly, Section 2.1 describes the experimental methodology in terms of short stack description, test rig and test campaign. Second, the ammonia-fueled SOFC system was modeled implementing the methods and system features (e.g., system lay-out, main components and model equations) detailed in Section 2.2. Finally, the simulation outcomes were implemented in the LCOE evaluation procedure, developed according to the methodology presented in Section 2.3. A schematic of the methodological workflow is reported in Figure 1.

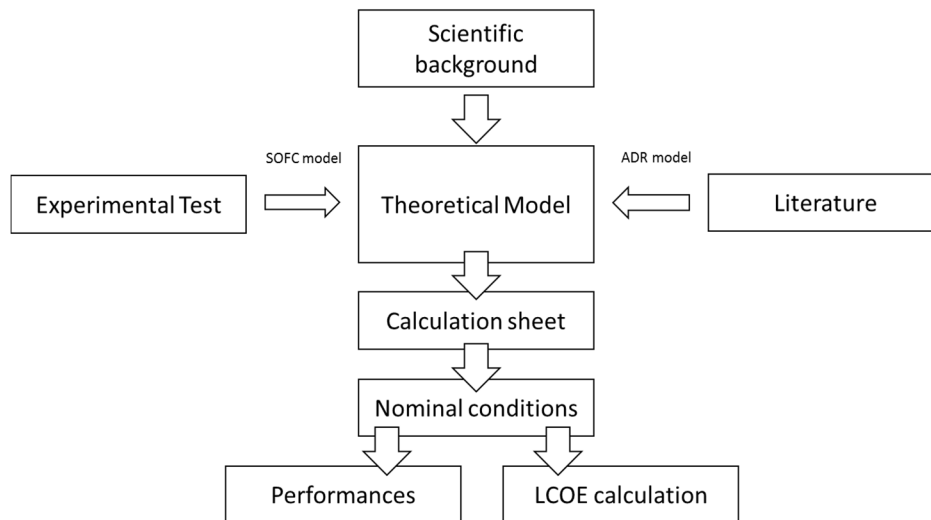


Figure 1. Schematic of the methodological workflow.

2.1. Experimental Description

To evaluate the performance of the ammonia-fed SOFC, an experimental campaign was designed and implemented on a SOFC short stack. The experimental study was performed on a six cells short stack supplied by SOLIDPower (SOLIDpower, Mezzolombardo, Italia). The stack is equipped with anode-supported planar cells. Details on stack design are reported in Table 2. Figure 2 is a picture of the test rig with the stack.

Table 2. SOFC stack design details.

Parameter	Data
Number of cells – n	6
Nominal Power	100 W
Type	Anode-Supported Cell (ASC) – Planar
Dimension	active area (A_{CELL}) 80 cm_{FC}^2
Anode	Ni/8YSZ $240 \pm 20 \mu\text{m}$
Electrolyte	8YSZ $8 \pm 2 \mu\text{m}$
Bilayer cathode	GDC + LSCF $50 \pm 10 \mu\text{m}$

The stack was operated on a laboratory test rig that allows controlling the stack operating temperature, gas flows, and operating current density. The test rig temperature and the cells voltage are measured with specific sensors placed in the stack and in the anodic and cathodic gas pipes, both inlet and outlet. Oxidant (air) and fuel (hydrogen, nitrogen, ammonia) flows are pre-heated inside the furnace, before entering the short stack. A detailed description of the test rig is reported in [29]. The aim of this study is to operate the stack at high efficiency and high power density. High efficiencies are achieved at high fuel use factor, which is the ration between the amount of hydrogen reacting electrochemically and the amount of hydrogen introduced in the stack (Equation (1)).

$$U_f = \frac{I \cdot n}{2 \cdot n_{H_2EQ} \cdot F} \quad (1)$$

where I is the operating current, n is the number of cells, F is Faraday constant and n_{H_2EQ} is the molar flow of equivalent hydrogen. In the case of pure ammonia, n_{H_2EQ} is equivalent to the amount of hydrogen obtained by the total decomposition of ammonia (reaction 2).



Same approach can be used to calculate air flow fixing the oxidant use factor (U_{ox}), as expressed by Equation (3).

$$U_{ox} = \frac{I \times x}{4 \times 0.21 \times n_{air} \times F} \quad (3)$$

were n_{air} is the molar flow of air and 0.21 is the concentration of oxygen in the air. The experimental campaign was designed to evaluate stack performance by varying the following parameters: (i) current density, (ii) fuel use, (iii) ammonia decomposition rate (X_{NH3}). X_{NH3} is useful to evaluate the performance of the stack when the decomposition of ammonia is partially or totally performed in an external decomposition reactor. Thus, it considers the amount of ammonia decomposition that occurs before entering the stack based on reaction (2), according to Equation (4) where m_{NH3in} is the total inlet ammonia molar flow rate, while m_{NH3out} is the ammonia molar flow rate at reactor outlet.

$$X_{NH3} = 1 - \frac{m_{NH3out}}{m_{NH3in}} \quad (4)$$



Figure 2. Photo of the short stack set-up.

Once the ammonia decomposition rate is defined, it is easily possible to calculate molar gas flow of ammonia, hydrogen and nitrogen entering the stack. These gas flows were fed to the short stack simulating the gas mix entering the unit when integrated with an external decomposition reactor. Table 3 reports constant and variable parameters used to define the test campaign.

Table 3. Test condition investigated in the experimental campaign.

Parameter	Symbol	Unit	Values
Current density	J	mA cm _{FC} ⁻²	200–300–500
Use of fuel	U _f	-	0.6–0.7–0.8
Ammonia decomposition	X _{NH3}	-	0–0.5–1
Temperature	TSOFC	°C	750
Use of oxygen	U _{ox}	-	0.2

During the experimental tests U_f was studied at three different values: 0.6, 0.7 and 0.8, while U_{ox} was kept at 0.2. Current density was varied at values 200, 350 and 500 mA cm_{FC}⁻². Furnace temperature was kept constant at 750 °C, selected as the state of the art for the technology. The value selected for XNH₃ are 0%, i.e., no external decomposition and pure ammonia in the stack, 50% and 100% corresponding to partial and total external decomposition, respectively. Based on the parameters in Table 2, it is possible to calculate gas flow rates for each operating point. For each test condition, the performance was evaluated in term of cell voltages after the stabilization time of 30 min.

2.2. Model Description

The system model was implemented on a Microsoft Excel[©] (Microsoft, Washington, DC, USA) calculation sheet using thermodynamic libraries taken from literature [30] and on the basis of the experimental activity outcomes, for what concerns the correlation between voltage and the main operating parameters such as current density, fuel use factor and ammonia decomposition rate. The model is zero dimensional and calculates the energy equilibrium of each component. The system scheme is reported in Figure 3. The proposed design moves from a standard state of the art solution of SOFC systems fed with natural gas. The fuel is decomposed in an external reactor and heat is recovered from the after burner off-gases (stream 10, downstream their mixing with bypassed air) to feed the reactor and to preheat air at high and low temperature.

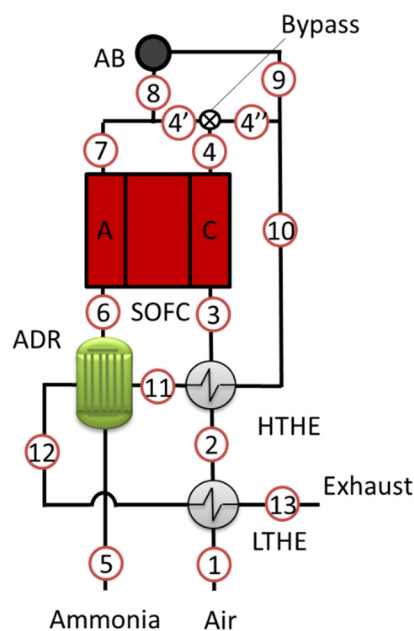


Figure 3. Scheme of the SOFC-NH₃ system.

The system is fed with pure ammonia and air and produces electrical power from the SOFC unit. The system is made of six components:

- SOFC: Solid Oxide Fuel Cell
- ADR: Ammonia Decomposition Reactor
- AB: After Burner
- HTHE: High Temperature Heat Exchanger
- LTHE: Low Temperature Heat Exchanger
- Bypass: Cathodic bypass

In addition, not reported in the scheme, the system requires an air blower and an inverter.

The SOFC unit is modeled as a reactor operating at constant temperature of 750 °C. Both anodic and cathodic gas flows enter the SOFC at 700 °C and exit at 800 °C. The gas composition is calculated

based on design parameters, i.e., current density and fuel use. The model considers the complete decomposition of ammonia in the anode according to reaction (2). This assumption is coherent with the local temperature and the presence of nickel as reaction catalyst. SOFC energy balance is calculated as follows (Equation (5)):

$$P_{\text{SOFC}} + \Delta h_{\text{anode}} + \Delta h_{\text{cathode}} - \dot{Q}_{\text{SOFC}} = 0 \quad (5)$$

where P_{SOFC} is the SOFC electric power, Δh_{anode} and $\Delta h_{\text{cathode}}$ are enthalpy flow differences between outlet and inlet of anodic and cathodic gases respectively. \dot{Q}_{SOFC} represents the heat flow losses calculated as percentage, HL_{SOFC} in Equation (6), of the total enthalpy flow differences both anodic and cathodic:

$$\dot{Q}_{\text{SOFC}} = HL_{\text{SOFC}} \times (\Delta h_{\text{anode}} + \Delta h_{\text{cathode}}) \quad (6)$$

P_{SOFC} is calculated by multiplying current density and voltage, the latter is derived from experimental activity and deeply described in the following. The stack equilibrium model allows to calculate, as main output, the inlet cathodic air flow rate and, consequently, the use of oxygen.

The Ammonia Decomposition Reactor (ADR) is modeled as an adiabatic chemical reactor integrated with a heat exchanger. The required heat of reaction is provided by system hot gases (pipe 11 in the scheme). The energy balance of the ADR is calculated as reported in Equation (7):

$$\Delta h_{\text{NH}_3} - \eta_{\text{HE}} \Delta h_{\text{hot}} = 0 \quad (7)$$

where Δh_{NH_3} is the enthalpy flow difference between outlet and inlet of the ammonia stream, Δh_{hot} is the enthalpy flow difference between outlet and inlet of the hot gases and η_{HE} is the efficiency of the heat exchanger, equal to 0.9. The same efficiency value is considered for the heat exchangers (HTHE, LTHE) implemented in the system. The decomposition rate, X_{NH_3} , is calculated as function of reactor temperature, T_{ADR} , based on the literature [21]. Values considered were taken from the Ni/Y₂O₃ case catalyst. The ADR temperature varies from 450 °C to 650 °C. The reaction does not take place below the minimum temperature and, for those values, ammonia is not decomposed. Whereas above the higher value, 650 °C, ammonia is completely decomposed. The decomposition rate, as expressed by reaction (4), is obtained with a numeric approach as regression of literature experimental data [23] as reported in Equation (8) where T_{ADR} must be expressed in °C:

$$X_{\text{NH}_3} = 12.72 - 7.46 \times 10^{-2} \times T_{\text{ADR}} + 1.4 \times 10^{-4} \times T_{\text{ADR}}^2 + 8.4 \times 10^{-8} \times T_{\text{ADR}}^3 \quad (8)$$

To distribute the heat between HTHE and LTHE, and calculate equilibrium parameters, it is necessary to set one temperature parameter that controls and optimize energy recovery in the system. The control parameter is the ADR approach, ADR_A that is the temperature difference between hot temperature inlet, pipe 11, and fuel ADR outlet temperature, pipe 6 in the scheme, corresponding to cathodic inlet temperature of 700 °C.

The after burner is modeled as an adiabatic reactor where the combustion reaction is completed. Depending on the composition of inlet flow, pipe 8 in Figure 3, the limiting reagent of the combustion can be either oxygen or hydrogen. Please note that the bypass allows controlling the amount of oxidant flow rate to the afterburner and, consequently, the O₂/H₂ ration called λ_{AB} . The control parameter is the bypass open rate, BOR, defined as the ration between the flow rate flowing to the afterburner and the total cathodic off-gases. This strategy permits to operate the after burner with different rate of O₂/H₂, including the no combustion option ($\lambda_{\text{AB}} = 0$), with the total air flow rate bypassing the after burner. The air blower is designed based on air flow rate \dot{N}_{air} and total pressure losses of cathodic pipes, ΔP_c . Blower efficiency was estimated at 0.9 and pressure losses of 0.15 bar. Ammonia is usually stored in liquid form in compressed cylinders (c.a. 10 bar) and no active system is required to pressurize the anodic line. The inverter power conversion efficiency, η_I , was set to 0.95. Table 4 reports all inlet parameters used to design the system while Table 5 reports system constant parameters.

Table 4. Inputs and outputs parameters of the model.

Inlet Parameter	Symbol	Unit
Use of fuel	Uf	-
Current density	J	A cm _{FC} ⁻²
ADR decomposition temperature	T _{ADR}	°C
Stack heat losses	HL _{SOFC}	%
Bypass Open Rate	BOR	%
ADR approach	ADR _A	°C

Table 5. Constant parameters in the model.

Constant Parameters	Symbol	Unit	Value
Blower efficiency	η _B		0.9
Heat exchangers efficiency	η _{HE}		0.9
Cathodic losses	ΔP _c	bar	0.15
SOFC temperature	T _{SOFC}	°C	750
Inverter efficiency	η _I		0.95

2.3. LCOE Model

This study aims also at assessing the economic advantages of the proposed system. This part of the study was approached by evaluating the levelized cost of energy (LCOE). The LCOE allows calculating and comparing the convenience of different typologies of power plants. Basically, the LCOE relates the total cost of a power plant, including operational costs, and the total amount of energy produced. In the calculation sheet, in which the model was studied, a section for the levelized cost of energy (LCOE) calculation was implemented. The results from the thermodynamic study, in terms of components dimensions and energy produced, were used as inputs for the LCOE study. The calculation is based on Equation (9):

$$\text{LCOE} = \frac{\sum_c \left[\left(\sum_a \frac{\text{OM}_a}{(1+r)^a} \right)_c + I_c \right]}{\sum_a \frac{E_a}{(1+r)^a}} \quad (9)$$

where OMA represents operation and maintenance costs for the component *c* and the year *a*; *r* is the discount rate; *I_c* is the investment cost of the component *c*; *E_a* is the electrical energy generated in the year *a*. The cost calculation of each component was performed based on the literature [31–35]. Equations used in the model are reported in Table 5 with their respective reference sources. The cost, *I_n*, is reported for each component previously defined and reported in the first column of the table. It is important to highlight that these equations are a literature reference that cannot completely describe technologies in a development phase; moreover, the cost of each component is extremely variable. This comment can refer to the most innovative components, such as the SOFC stack, but possibly also to technologies that are state of the art, such as heat exchangers, inverters, and blowers. The explanation is that a new application can bring innovation also in the standard components that need to be implemented and customized for the specific design. In addition, the reported equations can hardly follow the size related costs. For example, the stack equation is linear with the area, while more detailed models show a decrease of specific cost with the size increase [34]. Finally, cost prediction is extremely correlated with the development of the market and a more detailed model can be implemented considering the number of units produced per year. Nevertheless, the equations reported in Table 6 are homogenous and coherent and allow comparing different power system designs based on the same SOFC technology. Since it is not easy to evaluate the issues related to the use of ammonia, also maintenance costs are difficult to be predicted. Nonetheless, degradation of materials should improve since a carbon free fuel, ammonia, is used. Moreover, the elimination of water line and of the steam methane reformer reactor contributes to the reduction of maintenance costs. On the other hand, there is no experience about material degradation due to other causes such as nitridation of steel

materials. For the present study, the main data were taken from literature based on a 100 kW SOFC system operating with natural gas. Maintenance costs used for the calculations are reported in 1 in the equation: air_{in} : AB inlet air flow, AB_{dp} : AB pressure losses, T_{out} : AB outlet exhaust temperature.

Table 6. Capital cost function of system components.

System Component	Capital Cost Function (\$)	Ref
SOFC stack	$I_{SOFC} = n \cdot A_{cell} \cdot (2.96T_{SOFC} - 1907)$	[31,33]
Auxiliary devices	$I_{SOFC,aux} = 0.1(I_{SOFC})$	[31,33]
After Burner ¹	$I_{AB} = \left(\frac{46.08 \cdot air_{in}}{0.995 - AB_{dp}} \right) [1 + \exp(0.018 \cdot T_{out} - 26.4)]$	[31,33]
Blower	$I_B = 91.562 \left(\frac{W_B}{455} \right)^{0.67}$	[32]
Heat Exchangers	$I_{HE} = 130 \left(\frac{A_{HE}}{0.093} \right)^{0.78}$	[33,35]
Inverter	$I_I = 10^5 \left(\frac{W_{SOFC}}{500} \right)^{0.7}$	[31–33]

¹ in the equation: air_{in} : AB inlet air flow, AB_{dp} : AB pressure losses, T_{out} : AB outlet exhaust temperature.

Table 7 together with the constant parameters included in the LCOE definition as expressed by Equation (9), specifically:

- discount rate, r ;
- system availability (in percentage) defined as the amount of time, year-based, the system is on; this parameter is necessary to calculate real energy generated in the year (E_a) and the related fuel consumption;
- maintenance costs, as already commented;
- fuel cost.

Table 7. LCOE constant parameters.

Parameter	Value	Ref
Discount rate	8%	[32,36]
Lifetime of overall system	20 years	[32]
System availability	80%	[32]
Maintenance costs	36752 € y^{-1}	[32]
NH ₃ cost	272,5 € kg^{-1}	[37]

The area A_{HE} of the heat exchangers is calculated based on the definition provided by Equation (10).

$$A_{HE} = \frac{Q_{HE}}{LMTD \times U} \quad (10)$$

where A_{HE} is the heat exchanger area, Q_{HE} is the exchanged thermal power, LMTD is the logarithmic mean temperature difference and U is the exchange coefficient fixed at 30 W $m^{-2} K^{-1}$.

3. Results

The results session is divided between experimental results, model system study, and LCOE analysis. Experimental results were used to develop the stack model integrated into the overall system model. System model results were implemented in the LCOE analysis.

3.1. Experimental Results

The tests performed on the short stack, as defined in Table 3, cover 27 operating conditions. Tests scheduling was planned to reduce stack shock due to the change of operating conditions. Parameters were changed according to the hierarchy order: X_{NH_3} , fuel use and current density. Temperature was kept constant at 750 °C. X_{NH_3} was changed in the order 0%, 50% and 100%, while fuel use changed for each X_{NH_3} value in the order 0.8, 0.7 and 0.6. Finally, current density was changed, where the test starts from higher current density, 500 mA cm_{FC}⁻², and higher fuel use of 0.8, considered to be the most stressing for the stack. Subsequently, current was reduced down to minimum current density and then the gas conditions were fixed for the following U_f condition, 0.7, and then current was raised back to the higher values. Finally, the current density was raised back at 500 mA cm_{FC}⁻² and new U_f condition, 0.6, was introduced and then current was reduced stepwise down to lower values. Figure 4 reports, as example, the part of the test at 750 °C and X_{NH_3} of 50%. The graph shows the data relative to the three fuel use factors and, for each U_f , to the three current density values. The graph reports the average value of the cells voltages and the cathodic temperature measured at the outlet. Regarding stack temperature, the design temperature was set to the furnace regulating system. This means that the measured stack temperature, as reported in the graph, is not fixed but varies, in a short range, with the operating conditions. Cathodic outlet temperature is, in general, considered to be the closest to stack average temperature. In Figure 4, it is also possible to note that the voltage is quickly stabilized, while temperature has longer response time and equilibrium is not always reached.

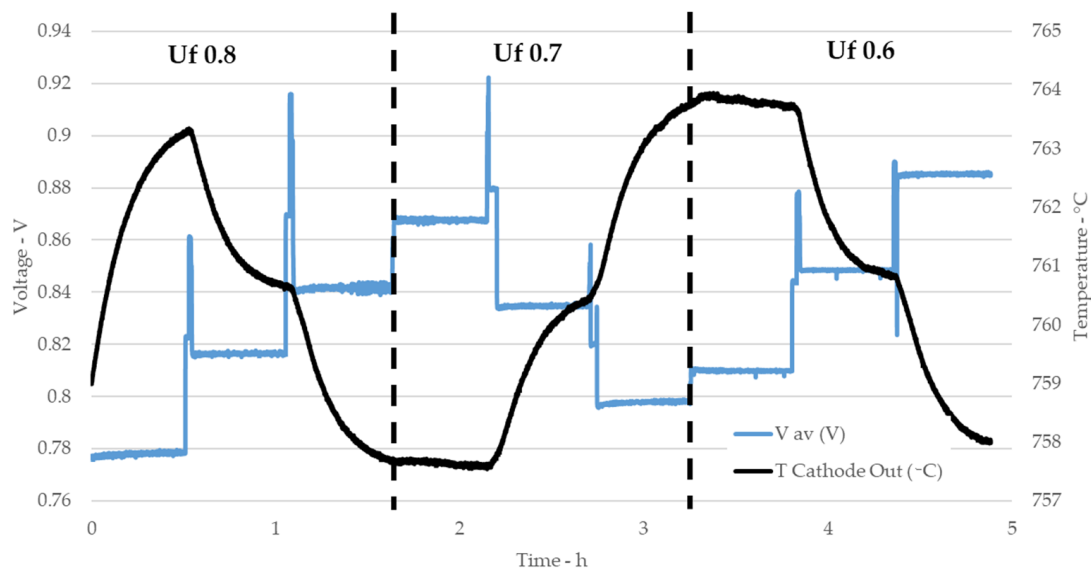


Figure 4. Example of stack test: average cell voltage and cathode temperature as function of time.

In the following analysis, the results reported refer to the average value of the six cells and calculated as average of 60 s of samples, taken at 1 Hz. To avoid the overlapping with following phase, the 60 s considered for the calculations are two minutes before the new test condition starts. Figure 5 reports the main results in terms of average cell voltage value as function of current density for fuel use of 0.8 (a), 0.7 (b) and 0.6 (c). Each graph reports three curves, one for each X_{NH_3} value. As expected, for all curves, voltages decrease with increasing current and higher U_f values corresponds to lower voltages. Regarding X_{NH_3} , there are no significant differences in terms of measured voltage between the three compositions. At higher current density, voltages values of decomposed ammonia are lower compared to ammonia containing mixtures. This trend is coherent for all U_f values and even though the difference is low, pure ammonia tests are slightly more performing than equivalent mixtures.

Stack performance in terms of efficiency and power density are reported in Figure 6a,b respectively. The curves report values for different U_f at the constant temperature of $750\text{ }^\circ\text{C}$ and constant $X_{\text{NH}_3} = 0$. Since voltages values of the other decomposition rates are extremely close each other, also power densities and efficiencies are similar and not reported. The efficiency of 56% at the higher power density of $38.6\text{ W cm}_{\text{FC}}^{-2}$ was obtained with pure NH_3 .

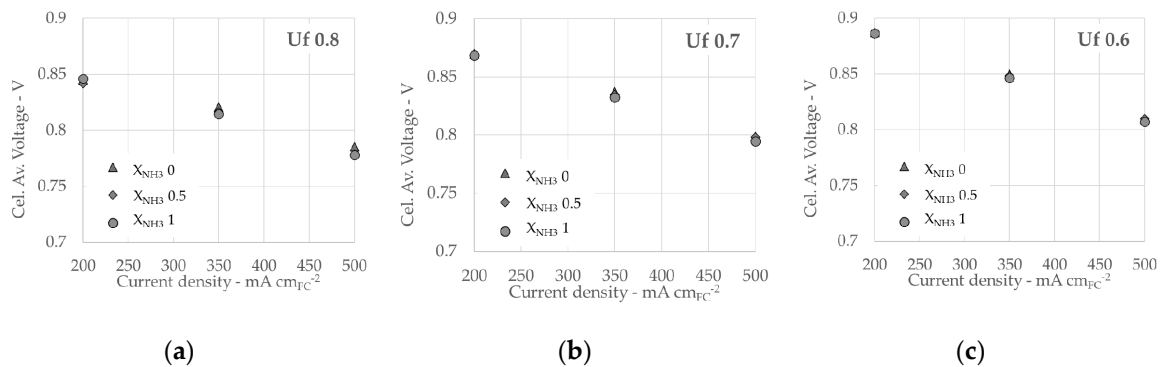


Figure 5. Stack test results at $750\text{ }^\circ\text{C}$ for U_f 0.8 (a), U_f 0.7 (b) and U_f 0.6 (c).

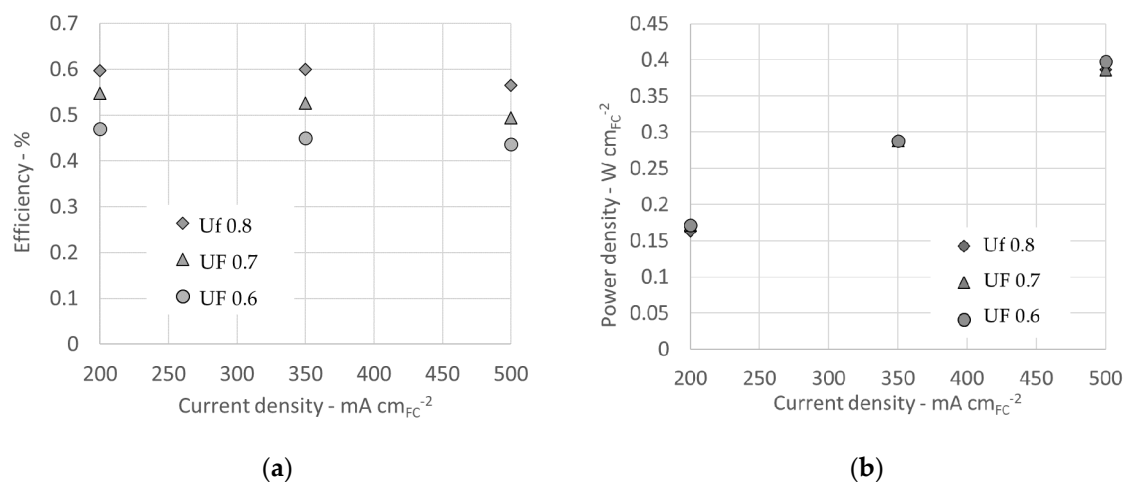


Figure 6. Stack efficiency (a) and power density (b) for pure ammonia ($X_{\text{NH}_3} = 0$) and temperature $750\text{ }^\circ\text{C}$.

Based on experimental results it was possible to define a function that relates voltage with the investigated parameters. Linear regression was always considered for each parameter. Due to the inconsistency of temperature, regression was performed separately for each temperature. At $750\text{ }^\circ\text{C}$ the regression was calculated as expressed by Equation (11).

$$V(U_f, J, X_{\text{NH}_3}) = -0.1686 U_f - 2.3638 \cdot 10^{-4} J - 3.2182 \cdot 10^{-5} X_{\text{NH}_3} + 1.0342 \quad (11)$$

Please note that J is introduced in $\text{mA cm}_{\text{FC}}^{-2}$ and X_{NH_3} assumes values in the range between 0 and 1. As expected, the correlation is negative for both U_f and J since the voltage decreases when both parameters increase. The influence of the ammonia decomposition parameter is negligible.

Emissions from the stack were sampled and analyzed. Table 8 reports the values measured at $750\text{ }^\circ\text{C}$ and pure ammonia ($X_{\text{NH}_3} = 0$), where the table reports the operating conditions and the NH_3 concentration measurements are given. Moreover, further parameters are reported to correlate the emissions to additional operating conditions. The specific emission evaluation is provided per NH_3 inlet flow rate and total current, i.e.,

- S_{NH_3} defined as the ration between NH_3 emissions concentration and ammonia inlet flow rate;
- R_{NH_3} determined as the ration between emissions and total current.

Even though it is not possible to give a complete description of the relation between emissions and operating conditions from the current measurements, a strong correlation between ammonia flows and emission emerges. Low values of ammonia inlet flow rates, such as the ones at 16 A, corresponds to much lower emissions compared to the flow rates related to the tests performed at 40 A. This tendency is described by parameter S_{NH_3} , with values close to one for small flows (i.e., at 16 A) and a coherent increase at higher values. Looking to values at 40 A it is clear, as described also by the R_{NH_3} parameter that different emission levels correspond to the same current density value. The results show that unlike what is reported in [21], the influence of ammonia inlet flow on the NH_3 emissions is greater than of U_f .

Table 8. Off-gas measurements of NH_3 emissions for pure ammonia tests.

U_f	U_{ox}	m_{NH_3} NI h^{-1}	m_{Air} NI h^{-1}	I A	J $\text{mA cm}_{\text{FC}}^{-2}$	NH_3 ppm	S_{NH_3} ppm NI h^{-1}	R_{NH_3} ppm A^{-1}
0.80	0.20	83.63	1194.71	40	500	260	3.11	6.50
0.80	0.20	33.45	477.89	16	200	40	1.20	2.50
0.60	0.20	111.51	1194.71	40	500	1000	8.97	25.00
0.60	0.20	44.60	477.89	16	200	45	1.01	2.81

3.2. Performance Analysis of the SOFC- NH_3 System

The experimental results of the stack were implemented in the theoretical model, as defined in Equation (10). The system was studied and nominal conditions, as reported in Table 9, were identified. Electrochemical operating conditions of the SOFC stack were fixed with the selection of fuel use of 0.8 and current density of $0.5 \text{ A cm}_{\text{FC}}^{-2}$. These values represent a standard trade-off between power density that requires high values of current density, and efficiency that requires small currents. ADR temperature was set to $350 \text{ }^\circ\text{C}$, meaning that no decomposition is considered in the ADR and the chemical reaction takes place totally inside the stack. The BOR was set to one, meaning that all the air coming from the cathode outlet goes into the after burner. The ADR approach was fixed to $20 \text{ }^\circ\text{C}$.

Table 9. Inputs values of system nominal conditions.

Parameter	Unit	Value
U_f		0.8
J	$\text{A cm}_{\text{FC}}^{-2}$	0.5
T_{ADR}	$^\circ\text{C}$	350
HL_{SOFC}	-	0.05
BOR	-	1
ADR_A	$^\circ\text{C}$	20

Table 10 reports main results of the system operation under nominal condition. The stack energy balance requires an oxygen use of 0.17, corresponding to a specific air flow rate of $2.93 \text{ NI h}^{-1} \text{ cm}_{\text{FC}}^{-2}$. The stack operates at cell voltage of 0.78 V producing a power density of $0.36 \text{ W cm}_{\text{FC}}^{-2}$. System gross efficiency is 54.2% while net efficiency is 52.1%. Since all ammonia decomposition takes place inside the stack, X_{NH_3} is zero. The lambda of the after burner is 9.78, as a consequence of flowing all cathodic exhausts into the after burner.

Table 10. Outputs parameters values of system nominal conditions.

Parameter	Symbol	Unit	Value
Use of oxygen	U _{ox}	-	0.17
Cell voltage	V	V	0.78
Power density	P _{SOFC}	W cm _{FC} ⁻²	0.36
Net efficiency	η _{net}	-	52.1%
Gross efficiency	η _{gross}	-	54.2%
ADR reaction rate	X _{NH3}	-	0
Off-gases temperature	T ₁₃	°C	192.60
Heat Exchangers total area	a _{THE}	cm _{HE} ² cm _{FC} ⁻²	1.67
NH ₃ flow rate	m _{NH3}	g h ⁻¹ cm _{FC} ⁻²	0.13
Air flow rate	N _{air}	Nl h ⁻¹ cm _{FC} ⁻²	2.93
Lambda After Burner	λ _{AB}	-	9.78

Table 11 reports gas compositions for all pipes. Please note that hydrogen is completely oxidized in the after burner and off-gases contain only oxygen, nitrogen, and water (steam).

Table 11. Outputs parameters values of system in nominal conditions.

	Air (1,2,3)	NH ₃ in (5)	NH ₃ Dec. (6)	Anode Out (7)	Cathode Out (4,4',4'')	AB Mix (8)	AB Out (9)	Off-Gases (9,10,11,12,13)
H ₂ O	0.0%	0.0%	0.0%	60.0%	0.0%	6.6%	8.4%	8.4%
N ₂	79.0%	0.0%	0.0%	25.0%	81.9%	75.7%	76.9%	76.9%
H ₂	0.0%	0.0%	0.0%	15.0%	0.0%	1.6%	0.0%	0.0%
NH ₃	0.0%	100.0%	100.0%	0.0%	0.0%	0.0%	0.0%	0.0%
O ₂	21.0%	0.0%	0.0%	0.0%	18.1%	16.1%	14.7%	14.7%

Table 12 reports parameters values of the heat exchangers, including ADR. For each component inlet and outlet temperature of both hot and cold gas flows are reported. The table reports also LMTD, specific heat exchanged in the heat exchanger, q_{HE}, U and specific area of the heat exchanger, a_{HE}, of each heat exchanger. Both values of q_{HE} and a_{HE} are specific per unit of fuel cell area. The total specific area of heat exchangers, as reported in Table 10, is 1.67 cm_{HE}² cm_{FC}⁻².

Table 12. Data of the heat exchangers.

Parameter	Unit	LTHE	HTHE	ADR
T _{hot in}	°C	662.30	919.87	720.00
T _{hot out}	°C	192.60	720.00	662.30
T _{cold in}	°C	20.00	496.94	20.00
T _{cold out}	°C	496.94	700.00	700.00
LMTD	°C	168.96	221.46	179.37
q _{HE}	W cm _{FC} ⁻²	0.58	0.27	0.07
U	W m ⁻² K ⁻¹	30	30	30
a _{HE}	cm _{HE} ² cm _{FC} ⁻²	1.15	0.40	0.13

The system was studied also in the neighborhood of the nominal condition. Figure 7 reports results relative to BOR variation keeping constant all other input parameters. In detail Figure 7a shows the trend of λ_{AB} and of the system off-gases temperature as function of BOR. The increase in BOR corresponds to the increase of oxidant flow into the afterburner. Off-gases temperatures show a significant initial increase and a plateau for BOR value of 0.05 corresponding to the stoichiometric λ_{AB} value of 0.5. Below this value, the combustion of hydrogen is not completed and all system temperatures decrease, including the off-gases temperature that reaches a minimum value of 57.4 °C. This specific aspect is deeper described by the graph reported in Figure 7b where a_{THE} and chemical losses are reported. Chemical losses are calculated as the ratio between energy content in the off-gases,

in terms of hydrogen lower heating value, and total inlet ammonia energy. Both curves show an initial decrease, for BOR values lower than 0.05, and a successive stabilization. If no air reaches the afterburner, hydrogen is not combusted and all heat exchangers operate at lower temperatures. Consequently, LMTD decreases for each heat exchanger component and a_{THE} increases. Regarding the chemical losses, for BOR equal to zero, hydrogen in the stack exhausts will be vented in atmosphere. Such amount corresponds to chemical losses of 22.7% of total energy input. When the after burner reaches values bigger than stoichiometric, a_{THE} remains constant and chemical losses are null, since no hydrogen is vented. This study shows that the system can operate without the afterburner. This is an interesting peculiarity of this system, derived by the use of ammonia as a fuel. Hydrogen is not a harmful gas for the environment and the emission is not limited by environmental regulations. On the one hand, it is possible to eliminate the after burner and the potential emissions typical of all combustion reactions, including the hydrogen one. On the other hand, the lower values of heat exchangers temperature brings to an increase of total surface of the components. Since the BOR variation does not modify the electrochemical performance and ammonia consumption, the net efficiency remains constant at 52.1%.

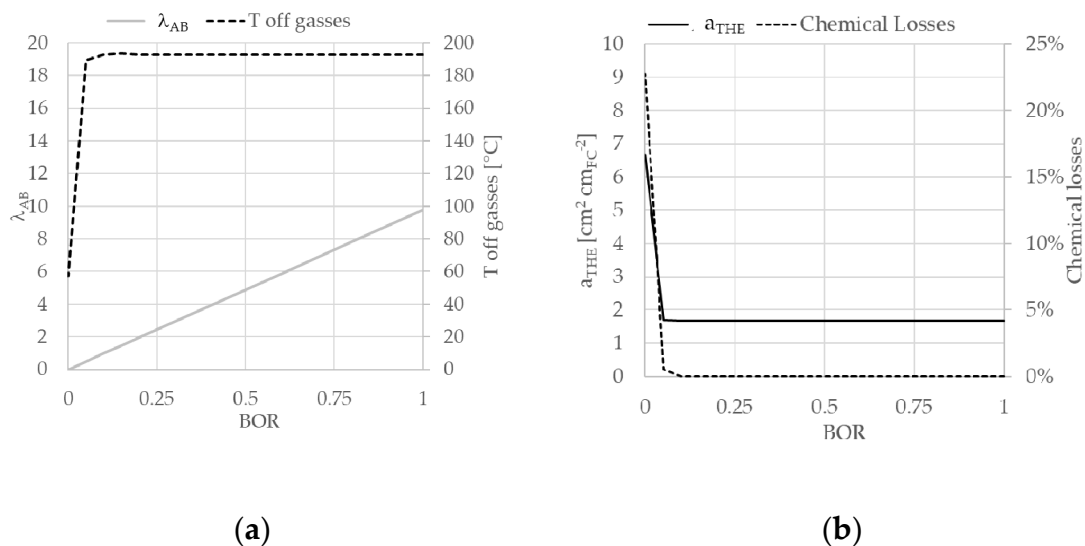


Figure 7. Graphs reporting results of BOR study results: λ_{AB} and $T_{off\ gases}$ (a) and a_{THE} and chemical losses (b).

Figure 8 shows the study of T_{ADR} variation, where Figure 8a reports the use of oxygen and net efficiency variation while Figure 8b reports off-gases temperature. The variation of T_{ADR} from 350 °C to 650 °C moves the decomposition reaction from the stack to the ADR. The result is a decrease in U_{ox} , since there is no cooling effect of the reaction inside the stack. Efficiency slightly decreases due to the effect of X_{NH_3} in Equation (10).

Based on the model results in nominal condition it was possible to calculate absolute values of the main parameters for a 100 kW system, shown in Table 13. The total area of SOFC is 28.04 m^2 , while the total area of heat exchangers is 46.67 m^2 . The table also reports absolute values of ammonia and air flow rates.

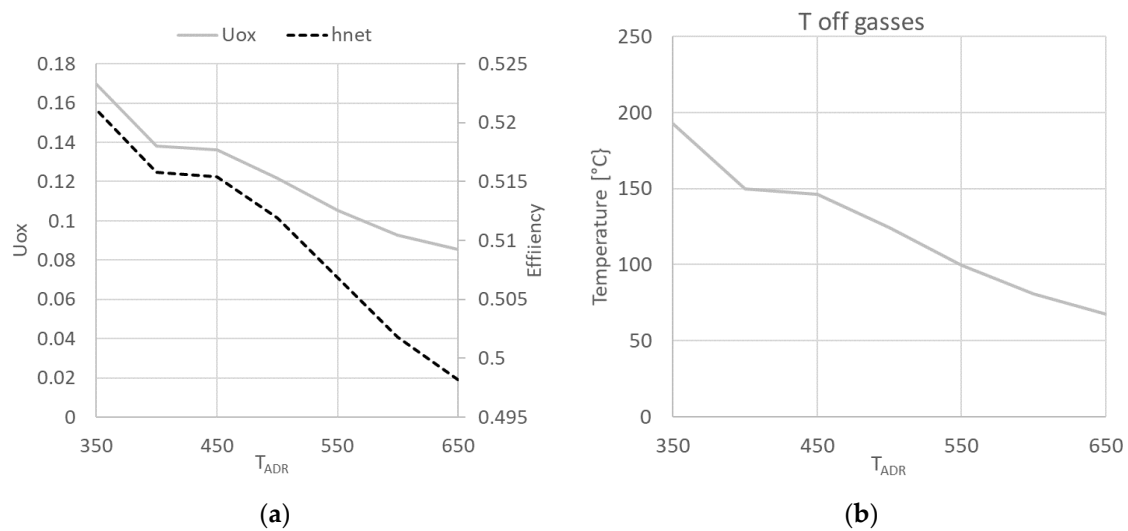


Figure 8. Variation of U_{ox} and η_{net} (a) and of off-gases temperature (b) as function of T_{ADR} .

Table 13. Absolute parameters values for a 100 kW system.

Parameter	Unit	Value
System Power	kW	100
Total A_{SOFC}	m^2	28.04
Total A_{THE}	m^2	46.67
NH_3 flow rate	$g\ s^{-1}$	10.29
Air flow rate	$NI\ s^{-1}$	228.28

3.3. LCOE Analysis of the SOFC- NH_3 System according to Different Designs

LOCE study was dedicated to nominal condition and based on the simulation results presented in the previous Section 3.2. For the calculations, constant parameters were used as reported in Table 5. In addition, the study considers the availability of ammonia and no cost for its distribution and storage was considered. The LCOE, according to the procedure detailed in Section 2.3, results in $0.221\ \$\ kWh^{-1}$ for nominal design conditions. The capital cost of each component and relative quote for a 100 kW system is reported in Table 14. The most significant share of the cost fall in the stack and in the inverter. It is notable that low temperature heat exchange has a much higher cost that the high temperature one due to the higher exchange area required to complete heat transfer at lower temperature (see a_{HE} values in Table 12).

Table 14. Component costs of a 100 kW system operating in nominal condition.

Component	Value (\$)	Quote
Stack	31,444.41	34.4%
Stack AUX	3144.44	3.4%
High Temperature Heat Exchanger	5463.60	6.0%
Ammonia Decomposition Reactor	2207.34	2.4%
Low Temperature Heat Exchanger	12,408.59	13.6%
After Burner	436.45	0.5%
Blower	3915.19	4.3%
Inverter	32,413.13	35.5%
TOT	94,790.50	-

It is possible to compare the obtained LCOE value with the literature. In particular, in [32] a 100 kW SOFC system fed by natural gas reports a LCOE of 0.264 \$ kWh⁻¹. The reference system is equivalent to the ammonia system here presented, with a slightly lower electrical efficiency of 51.7%. The value, as reported in [32], is calculated with reference to a Korean fuel cost of 16.61 \$ GJ-LHV⁻¹. It is important to comment that the fuel cost plays an important role in the LCOE calculation. The value considered in the reference is in the range of household market. If we look to the European industrial market, the cost of natural gas decreases down to 7.88 \$ GJ-LHV⁻¹ (1.11 €/€ exchange rate) [38]. In this sense the ammonia value of 16.37 \$ GJ-LHV⁻¹ [37] is closer to household natural gas market. This explains why the LCOE obtained in the current work is lower than the one in the reference. Moving to the industrial market, this could be more meaningful due to the size of the system, the LCOE of natural gas system will drop down to 0.194 \$ kWh⁻¹ since the fuel cost share is 50% out of the total. Results are coherent, considering that today ammonia in the market is produced from natural gas. As already explained in the introduction, the ammonia convenience has to be considered in the carbon free energy market and the potential development of green ammonia production.

4. Discussion and Conclusions

This study presents the design and modeling of an ammonia-fed SOFC system based on experimental campaign on a six cells SOFC short stack. An innovative design is presented, and the relative model was implemented to calculate thermodynamic parameters.

The experimental study of operating conditions of a SOFC short stack fed with ammonia was performed. The correlation with use of fuel, current density, and ammonia decomposition was studied at an operating temperature of 750 °C. The external ammonia decomposition has a minimum influence on performance, meaning that internal cracking of ammonia in the stack is a feasible solution. The stack achieves up to 60% efficiency at 750 °C. Measurements done on the ammonia emissions show NH₃ content in the range 40–250 ppm when moving to the highest current densities.

The system model allowed to calculate up to 52.1% of net efficiency in nominal condition. The parameter study showed how external decomposition of ammonia increases the size of the heat exchangers with no advantages in terms of efficiency. The most feasible strategy to variate system power is to rate the current density. Reduction of current density improves the efficiency of the system and increases oxygen use.

System LCOE of 0.221 \$ kWh⁻¹ was calculated for a 100 kW system operating in nominal conditions. It is important to underline that the LCOE study is based on literature reference but the cost of components are strongly dependent on market development and technology innovations.

The study and the model developed in this study constitutes an important support for the design of an ammonia-fed SOFC energy system and provides indication for the sizing of the power unit.

Author Contributions: Conceptualization, G.C.; methodology, G.C. and L.B.; software, G.C.; validation, G.C.; formal analysis, G.C. and L.B.; investigation, G.C.; resources, G.B. and G.C.; data curation, G.C.; writing—original draft preparation, G.C.; writing—review and editing, G.C., G.B. and L.B.; visualization, G.C. and L.B.; supervision, G.C. and L.B.; project administration, G.C. and G.B.; funding acquisition, G.C. All authors have read and agreed to the published version of the manuscript.

Funding: The study was supported by the Fuel Cell and Hydrogen 2 Joint Undertaking under grant agreement No. 736,648 (NET-Tools project). The activities were also supported by ENVIU, PROTON VENTURES BV and C-JOB & PARTNERS BV, in the frame of a scientific collaboration.

Acknowledgments: The study was supported by the Fuel Cell and Hydrogen 2 Joint Undertaking under grant agreement No. 736,648 (NET-Tools project). The activities were also supported by ENVIU, PROTON VENTURES BV and C-JOB & PARTNERS BV, in the frame of a scientific collaboration.

Conflicts of Interest: The authors declare no conflict of interest.

Abbreviations

The following abbreviations and symbols are used in this manuscript:

Abbreviation	Description	Unit
AB	After Burner	
A _{CELL}	SOFC cell active area	cm _{FC} ²
ADR	Ammonia Decomposition Reactor	
ADRA	ADR approach	°C
A _{HE-aHE}	Area of the Heat Exchanger - specific per fuel cell area	cm _{HE} ² -cm _{HE} ² cm _{FC} ⁻²
A _{SOFC}	Total SOFC active area	cm _{FC} ²
ASR	Area Specific Resistance	Ω cm _{FC} ²
BOR	Bypass Open Rate	
CHP	Combined Heat and Power	
D _{NH3}	Ammonia decomposition	
HE	Heat Exchanger	
HTHE	High Temperature Heat Exchanger	
J	Current density	mA cm _{FC} ⁻²
LCOE	Levelized Cost Of Energy	\$ kWh ⁻¹
LMTD	Logarithmic Mean Temperature Difference	°C
LTHE	Low Temperature Heat Exchanger	
OM	Operation and Management	
Q _{HE-qHE}	Heat exchanged in the Heat Exchanger - specific per fuel cell area	W-W cm _{FC} ⁻²
RES	Renewable Energy Sources	
SOFC	Solid Oxide Fuel Cell	
SOFC-H	Proton-conducting SOFC	
SOFC-O	Ion conducting SOFC	
T _{ADR}	ADR decomposition temperature	°C
T _{SOFC}	Stack Temperature	°C
U	Thermal exchange coefficient	W m ⁻² K ⁻¹
U _f	Utilization of Fuel	
U _{ox}	Utilization of oxygen	
η _{net}	Net efficiency	
η _{gross}	Gross efficiency	

References

- Lan, R.; Irvine, J.T.S.; Tao, S. Ammonia and related chemicals as potential indirect hydrogen storage materials. *Int. J. Hydrogen Energy* **2012**, *37*, 1482–1494. [CrossRef]
- Valera-Medina, A.; Xiao, H.; Owen-Jones, M.; David, W.I.F.; Bowen, P.J. Ammonia for power. *Prog. Energy Combust. Sci.* **2018**, *69*, 63–102. [CrossRef]
- Frattoni, D.; Cinti, G.; Bidini, G.; Desideri, U.; Cioffi, R.; Jannelli, E. A system approach in energy evaluation of different renewable energies sources integration in ammonia production plants. *Renew. Energy* **2016**, *99*, 472–482. [CrossRef]
- Morgan, E.; Manwell, J.; McGowan, J. Wind-powered ammonia fuel production for remote islands: A case study. *Renew. Energy* **2014**, *72*, 51–61. [CrossRef]
- National Institute of Standards and Technology. Available online: <http://webbook.nist.gov/> (accessed on 5 February 2015).
- Lee, D.; Song, H.H. Development of combustion strategy for the internal combustion engine fueled by ammonia and its operating characteristics. *J. Mech. Sci. Technol.* **2018**, *32*, 1905–1925. [CrossRef]
- Frigo, S.; Gentili, R. Analysis of the behaviour of a 4-stroke Si engine fuelled with ammonia and hydrogen. *Int. J. Hydrogen Energy* **2013**, *38*, 1607–1615. [CrossRef]
- Lee, J.H.; Lee, S.I.; Kwon, O.C. Effects of ammonia substitution on hydrogen/air flame propagation and emissions. *Int. J. Hydrogen Energy* **2010**, *35*, 11332–11341. [CrossRef]
- Duynslaegher, C.; Jeanmart, H.; Vandooren, J. Ammonia combustion at elevated pressure and temperature conditions. *Fuel* **2010**, *89*, 3540–3545. [CrossRef]
- Valera-Medina, A.; Morris, S.; Runyon, J.; Pugh, D.G.; Marsh, R.; Beasley, P.; Hughes, T. Ammonia, Methane and Hydrogen for Gas Turbines. *Energy Procedia* **2015**, *75*, 118–123. [CrossRef]

11. Keller, M.; Koshi, M.; Otomo, J.; Iwasaki, H.; Mitsumori, T.; Yamada, K. Thermodynamic evaluation of an ammonia-fueled combined-cycle gas turbine process operated under fuel-rich conditions. *Energy* **2020**, *194*, 116894. [[CrossRef](#)]
12. Ezzat, M.F.; Dincer, I. Energy and Exergy Analyses of a Novel Ammonia Combined Power Plant Operating with Gas Turbine and Solid Oxide Fuel Cell Systems. *Energy* **2019**, 116750. [[CrossRef](#)]
13. Afif, A.; Radenahmad, N.; Cheok, Q.; Shams, S.; Kim, J.H.; Azad, A.K. Ammonia-fed fuel cells: A comprehensive review. *Renew. Sustain. Energy Rev.* **2016**, *60*, 822–835. [[CrossRef](#)]
14. Hagen, A.; Langnickel, H.; Sun, X. Operation of solid oxide fuel cells with alternative hydrogen carriers. *Int. J. Hydrogen Energy* **2019**, *44*, 18382–18392. [[CrossRef](#)]
15. Maffei, N.; Pelletier, L.; McFarlan, A. A high performance direct ammonia fuel cell using a mixed ionic and electronic conducting anode. *J. Power Source* **2008**, *175*, 221–225. [[CrossRef](#)]
16. Ni, M.; Leung, D.Y.C.; Leung, M.K.H. An improved electrochemical model for the NH₃ fed proton conducting solid oxide fuel cells at intermediate temperatures. *J. Power Source* **2008**, *185*, 233–240. [[CrossRef](#)]
17. Zhang, L.; Yang, W. Direct ammonia solid oxide fuel cell based on thin proton-conducting electrolyte. *J. Power Source* **2008**, *179*, 92–95. [[CrossRef](#)]
18. Stoeckl, B.; Subotić, V.; Preininger, M.; Schwaiger, M.; Evic, N.; Schroettner, H.; Hochenauer, C. Characterization and performance evaluation of ammonia as fuel for solid oxide fuel cells with Ni/YSZ anodes. *Electrochim. Acta* **2019**, *298*, 874–883. [[CrossRef](#)]
19. Cinti, G.; Desideri, U.; PENCHINI, D.; Discepoli, G. Experimental Analysis of SOFC Fuelled by Ammonia. *Fuel Cells* **2014**, *14*, 221–230. [[CrossRef](#)]
20. Satomi, E.; Iwai, H.; Suzuki, S.; Koide, T.; Takahashi, Y.; Eguchi, K. Development of Ammonia-Fueled SOFC. *ECS Trans.* **2017**, *78*, 2537–2540. [[CrossRef](#)]
21. Okanishi, T.; Okura, K.; Srifa, A.; Muroyama, H.; Matsui, T.; Kishimoto, M.; Saito, M.; Iwai, H.; Yoshida, H.; Saito, M.; et al. Comparative Study of Ammonia-fueled Solid Oxide Fuel Cell Systems. *Fuel Cells* **2017**, *17*, 383–390. [[CrossRef](#)]
22. Cinti, G.; Discepoli, G.; Sisani, E.; Desideri, U. SOFC operating with ammonia: Stack test and system analysis. *Int. J. Hydrogen Energy* **2016**, *41*, 13583–13590. [[CrossRef](#)]
23. Stoeckl, B.; Preininger, M.; Subotić, V.; Megel, S.; Folgner, C.; Hochenauer, C. Towards a wastewater energy recovery system: The utilization of humidified ammonia by a solid oxide fuel cell stack. *J. Power Source* **2020**, *450*, 227608. [[CrossRef](#)]
24. Dekker, N.J.J.; Rietveld, G. Highly Efficient Conversion of Ammonia in Electricity by Solid Oxide Fuel Cells. *J. Fuel Cell Sci. Technol.* **2006**, *3*, 499–502. [[CrossRef](#)]
25. Farhad, S.; Hamdullahpur, F. Conceptual design of a novel ammonia-fuelled portable solid oxide fuel cell system. *J. Power Source* **2010**, *195*, 3084–3090. [[CrossRef](#)]
26. Baniasadi, E.; Dincer, I. Energy and exergy analyses of a combined ammonia-fed solid oxide fuel cell system for vehicular applications. *Int. J. Hydrogen Energy* **2011**, *36*, 11128–11136. [[CrossRef](#)]
27. Perna, A.; Minutillo, M.; Jannelli, E.; Cigolotti, V.; Nam, S.W.; Han, J. Design and performance assessment of a combined heat, hydrogen and power (CHHP) system based on ammonia-fueled SOFC. *Appl. Energy* **2018**, *231*, 1216–1229. [[CrossRef](#)]
28. International Energy Agency (IEA International Energy Agency (IEA). *World Energy Outlook 2015*; IEA Publications: Paris, France, 2015.
29. Barelli, L.; Bidini, G.; Cinti, G.; Ottaviano, A. Study of SOFC-SOE transition on a RSOFC stack. *Int. J. Hydrogen Energy* **2017**, *42*, 26037–26047. [[CrossRef](#)]
30. Malcolm, W.; Chase, J. *NIST-JANAF Thermochemical Tables*, 4th ed.; American Chemical Society: Washington, DC, USA; American Institute of Physics for the National Institute of Standards and Technology: New York, NY, USA, 1998.
31. Najafi, B.; Shirazi, A.; Aminyavari, M.; Rinaldi, F.; Taylor, R.A. Exergetic, economic and environmental analyses and multi-objective optimization of an SOFC-gas turbine hybrid cycle coupled with an MSF desalination system. *Desalination* **2014**, *334*, 46–59. [[CrossRef](#)]
32. Park, S.H.; Lee, Y.D.; Ahn, K.Y. Performance analysis of an SOFC/HCCI engine hybrid system: System simulation and thermo-economic comparison. *Int. J. Hydrogen Energy* **2014**, *39*, 1799–1810. [[CrossRef](#)]
33. Cheddie, D.F. Thermo-economic optimization of an indirectly coupled solid oxide fuel cell/gas turbine hybrid power plant. *Int. J. Hydrogen Energy* **2011**, *36*, 1702–1709. [[CrossRef](#)]

34. Scataglini, R.; Mayyas, A.; Wei, M.; Chan, S.H.; Lipman, T.; Gosselin, D.; D'Alessio, A.; Breunig, H.; Colella, W.G.; James, B.D. *A Total Cost of Ownership Model for Solid Oxide Fuel Cells in Combined Heat and Power and Power-Only Applications*; Lawrence Berkeley National Laboratory: Alameda County, CA, USA, 2015; Volume 197.
35. Park, K.; Kim, J.; Bae, J. Electrochemical analysis of $\text{Pr}_{0.3}\text{Sr}_{0.7}\text{Co}_x\text{B}_{(1-x)}\text{O}_{3-\delta}$ (B = Fe, Mn; x = 0, 0.3, 0.5, 0.7, and 1) as cathode materials for intermediate temperature SOFCs. *Solid State Ionics* **2015**, *272*, 45–52. [[CrossRef](#)]
36. Baldinelli, A.; Barelli, L.; Bidini, G. On the feasibility of on-farm biogas-to-electricity conversion: To what extent is solid oxide fuel cells durability a threat to break even the initial investment? *Int. J. Hydrogen Energy* **2018**, *43*, 16971–16985. [[CrossRef](#)]
37. Agricultural Market Information System (AMIS) 74. 2019. Available online: http://www.amis-outlook.org/fileadmin/user_upload/amis/docs/Market_monitor/AMIS_Market_Monitor_Issue_74.pdf (accessed on 19 January 2020).
38. Eurostat-Gas Prices by Type of User. Available online: <https://ec.europa.eu/eurostat/web/products-datasets/-/ten00118> (accessed on 19 January 2020).

Publisher's Note: MDPI stays neutral with regard to jurisdictional claims in published maps and institutional affiliations.



© 2020 by the authors. Licensee MDPI, Basel, Switzerland. This article is an open access article distributed under the terms and conditions of the Creative Commons Attribution (CC BY) license (<http://creativecommons.org/licenses/by/4.0/>).

Article

System Design and Modeling of a High Temperature PEM Fuel Cell Operated with Ammonia as a Fuel

Giovanni Cinti ^{1,*}, Vincenzo Liso ², Simon Lennart Sahlin ² and Samuel Simon Araya ²¹ Department of Engineering, University of Perugia, Via G. Duranti 93, 06125 Perugia, Italy² Department of Energy Technology, Aalborg University, Pontoppidanstræde 111, 9220 Aalborg, Denmark; vli@et.aau.dk (V.L.); sls@et.aau.dk (S.L.S.); ssa@et.aau.dk (S.S.A.)

* Correspondence: giovanni.cinti@unipg.it

Received: 22 July 2020; Accepted: 7 September 2020; Published: 9 September 2020



Abstract: Ammonia is a hydrogen-rich compound that can play an important role in the storage of green hydrogen and the deployment of fuel cell technologies. Nowadays used as a fertilizer, NH₃ has the right peculiarities to be a successful sustainable fuel for the future of the energy sector. This study presents, for the first time in literature, an integration study of ammonia as a hydrogen carrier and a high temperature polymer electrolyte membrane fuel cell (HT-PEMFC) as an energy conversion device. A system design is presented, that integrates a reactor for the decomposition of ammonia with an HT-PEMFC, where hydrogen produced from NH₃ is electrochemically converted into electricity and heat. The overall system based on the two technologies is designed integrating all balance of plant components. A zero-dimensional model was implemented to evaluate system efficiency and study the effects of parametric variations. Thermal equilibrium of the decomposition reactor was studied, and two different strategies were implemented in the model to guarantee thermal energy balance inside the system. The results show that the designed system can operate with an efficiency of 40.1% based on ammonia lower heating value (LHV) at the fuel cell operating point of 0.35 A/cm² and 0.60 V.

Keywords: ammonia; high temperature PEM; fuel cell

1. Introduction

Due to its versatility, hydrogen has been recently gaining traction as energy storage solution. Even though it can be produced from a variety of energy sources, its most attractive feature is the possibility of producing it from renewable energy resources and using it in various applications, either directly or after converting it into other chemical products both for energy consumption and further chemical processing.

Hydrogen is converted into electrical energy with high efficiencies in fuel cells. However, at ambient conditions (25 °C and 1 bar), hydrogen has low density of only 0.0813 g L⁻¹, which requires either a high pressure storage, e.g., 700 bar for automotive application, which increases the density to 40 g L⁻¹ and the corresponding volumetric energy density of 5.6 MJ L⁻¹, or liquid state storage, for many practical applications [1,2]. In both cases, hydrogen undergoes thermodynamic transformations, which can increase the overall storage and transportation costs significantly. Hydrogen can also be stored in carbon nanotubes, metallic hydrides, or complex hydrides under more moderate temperature and pressure conditions, but with only limited gravimetric density [2,3].

Another solution is to store and transport hydrogen indirectly in the chemical bonds of other chemicals, thereby increasing volumetric energy density and, consequently, transportability. Methanol and ethanol are some of the most common examples of such hydrogen rich alcohols, where hydrogen is chemically bonded with carbon, also known as carbon-based fuels [4–6]. An issue

that makes carbon-based fuels less appealing is the involvement of carbon dioxide, both in the synthesis process and in the power conversion. CO₂ has to be supplied to the chemical plant and released during the power production process. This means that two different cycles have to be closed: the hydrogen cycle and the carbon dioxide cycle. While hydrogen can be made entirely renewable by relying on renewable energy sources, such as wind and solar for the hydrogen production via water electrolysis, for the carbon cycle to close, the carbon dioxide should either come from carbon-capture or from biomass sources [4].

An interesting alternative to this is the carbonless molecule of ammonia. In the case of ammonia, the gas involved is nitrogen, which means that the additional loop that has to be closed is the N₂ cycle. Nitrogen can be separated from air to feed the chemical process, usually the Haber–Bosh process, and released back to the atmosphere during energy consumption, making the overall system completely carbon-free [7]. Recently, alternative green ammonia synthesis methods, including electrochemical synthesis at lower temperature and pressure conditions, are being investigated [7–9].

Therefore, one of the advantages of the ammonia over other carbon-based fuels is the absence of CO₂ emissions at the point of use. For carbon-based fuels on the other hand, even when the carbon cycle is closed, CO₂ is still emitted locally and the power generation is not carbon-free. However, concerning local emissions, if NH₃ is used in combustion engines, the productions of NO_x should be considered [7], an issue that is significantly alleviated or even eliminated when using NH₃ in fuel cell systems. Moreover, the availability of nitrogen is much higher than carbon dioxide. If, for instance, atmospheric air is considered as a source for both gases, nitrogen is available at high concentrations of around 79%, while carbon dioxide is in the range of hundreds of ppm (416 ppm as of June 2020 [10]). However, it is worth mentioning that some sites, including biogas plants, bioethanol plants, and emission-intensive industries, can be used as sources of high concentration of CO₂ to produce carbon-based fuels, such as methanol through the power-to-X scheme [4]. The concentration of N₂ and CO₂ in the feedstock is directly related not only to the separation cost, both in terms of energy and economics, but also to the availability of the quantities necessary to feed the respective fuel synthesis plants.

NH₃ has a high hydrogen concentration of 75 mol% and is liquid at a relatively low pressure of 10 bar, with high energy density of 15.6 MJ L⁻¹ compared to liquid hydrogen, which has an energy density of 9.1 MJ L⁻¹ at cryogenic temperature or compressed hydrogen, 5.6 MJ L⁻¹ at 70 MPa [11]. Moreover, ammonia as a well-known fertilizer with a mature production technology, is one of the most produced chemicals worldwide, which can count on a well-established distribution network [11]. However, its application in the energy sector is not significant and has only been investigated more recently as a fuel in several combustion-based energy systems. Experiences are reported in power systems based on gas turbine technology and on internal combustion engines [7,11]. In general, combustion of ammonia suffers from low flame speed and high resistance to auto-ignition, which calls for pre-mixing with other fuels as combustion promoters, e.g., hydrogen, that can be obtained with a partial decomposition of ammonia itself [11].

An alternative solution is the use of ammonia in fuel cells [12]. Fuel cells are electrochemical devices that directly transform the chemical energy of fuels into electricity without the typical emissions of combustion-based cycles. Ammonia can be coupled with fuel cells directly in solid oxide fuel cells (SOFC) and direct ammonia fuel cells (DAFC) or via a pre-decomposition into nitrogen and hydrogen in polymer electrolyte membrane fuel cells (PEMFC) [13,14]. Due to the peculiarity of fuel cells, the presence of nitrogen in the fuel stream only acts as a diluent of hydrogen and does neither generate any pollutant nor cause significant performance decay, allowing all fuel cells to operate with a mixture of nitrogen and hydrogen.

Even though it is possible to design a system where ammonia is decomposed and then the fuel stream is fed to any fuel cell unit, such a coupling should consider the presence of ammonia in the decomposed gas, which may poison the membrane electrode assembly (MEA) of certain fuel cell types. For instance, PEMFCs are extremely sensitive to ammonia contamination, where NH₃ poisons the

Pt/C anode catalyst and reacts with the acidic Nafion membrane [15,16]. According to ISO14687-2, the maximum level of concentration of ammonia in hydrogen used in the PEM fuel cell vehicle is 0.1 ppm [13]. To reach the ISO target, it is necessary to introduce a purification technology after ammonia decomposition [13]. A concept design of a PEMFC-based system is proposed in [17], where the decomposition reactor is heated electrically, reaching 99.5% conversion of ammonia. However, to the knowledge of the authors, only one experience that couples the ammonia decomposition reactor and PEM fuel cells has been reported, where 500–1000 ppm of ammonia impurity from the ammonia cracking chamber is eliminated in a selective ammonia oxidation (SAO) reactor before the produced hydrogen can be used in a PEMFC [18]. The introduction of an additional gas purification phase increases the cost of the system and introduces additional energy losses. In general, the lower the tolerance of the end use device to ammonia, the higher the cost of the clean-up.

Another promising fuel cell technology is the high temperature PEM fuel cell (HT-PEMFC). In an HT-PEMFC, the traditional Nafion membrane, used in the low temperature PEM fuel cell technology, is substituted with a phosphoric acid-doped polybenzimidazole (PBI) membrane that operates in the temperature range 120–200 °C [19]. The higher operating temperatures increase the tolerance to impurities, for example, CO tolerance increases up to 3% compared to only few ppm in low temperature PEM fuel cells [19]. Due to this higher tolerance to impurities, HT-PEMFCs have been extensively studied in conjunction with methanol reformer, where the effects of the different resulting impurities, namely CO, CO₂, and CH₃OH have been reported with satisfactory tolerances for single cells and stacks [20–22]. Moreover, steam methane reforming and HT-PEMFC systems are also available in the literature [23–25].

However, despite the popularity of ammonia as a chemical commodity, and its potential as a storage for renewable hydrogen, its use in HT-PEMFCs has been largely ignored. While it is expected that traces of NH₃ will react with the PA-based electrolyte, the tolerance of an HT-PEMFC to NH₃ is only reported in [26], where a general tolerance to percentage of NH₃ is reported from an internal report. The development of HT-PEMFC technology and the strong interest in the use of ammonia as a fuel opens the possibility for the development of ammonia-fed HT-PEM fuel cell systems.

Therefore, this study presents for the first time in literature, a system study of an HT-PEMFC stack coupled with the ammonia decomposition unit. An integrated system design has been developed and thermodynamic studies of the system model were performed. A complete ammonia decomposition process is assumed, and hence, the corresponding high ammonia cracking temperatures, where full ammonia conversion is expected to take place, are used in the model. Consequently, the experiments were also done only for the dilution effect of nitrogen in the feed-gas and ammonia slip was ignored.

2. Materials and Methods

In this section, the modeling approach for the ammonia-fuel cell system is described. The fuel cell electrical performance obtained by the experimental test is used as input for the novel heat integrated system concept of an ammonia-fueled HT-PEMFC. The system model was studied with zero-dimensional thermodynamic models of the reactors and heat exchangers. The model was implemented in a calculation sheet (MSExcels[®]) that calculates energy balance and gas flows. The gas thermo-physical properties were taken from a freely available database (NIST-JANAF [27]). The reaction mechanisms for the ammonia decomposition and the ammonia and hydrogen combustion process were implemented in Cantera [28] using a Python programming language script.

2.1. Experimental

Experiments for the current work were carried out in a Greenlight Innovation fuel cell test station on a 37 cell HT-PEMFC stack with an active area of 165 cm². The tests were first done with pure hydrogen for 24 h at 0.4 A cm⁻² and the stoichiometric ratios were set to 1.3 on the anode side and 2.5 on the cathode side. Successively, a test with gas mixture containing 68.3% hydrogen and 31.7% nitrogen in the anode feed was performed for the same duration at the same conditions of current

density and stoichiometric ratios. A typical HT-PEMFC operating temperature of 160 °C was chosen for the tests. Galvanostatic polarization measurements were used for characterizing the different operating conditions. For this, the current was varied from 0 to 75 A at smaller steps of 2.5 A in the range between 0–10 A to better capture the activation overpotential and a current step of 5 A was used for the remainder of the polarization measurements.

2.2. Modeling

A schematic of the system design is shown in Figure 1. The design of the new system is based on the experience obtained from reformed methanol-fed HT-PEMFC systems. In a methanol-based system, the fuel is first reformed into a hydrogen rich gas mixture that contains CO₂, traces of CO, and unconverted methanol before entering the fuel cell unit. The heat required for the reforming process is supplied by a burner, which is first fed with a separate flow of methanol dedicated to the combustion reaction during the startup phase and then successively sustained by the anode off-gas [4]. In the current work, a similar approach was considered, where ammonia is first decomposed, and the resulting hydrogen–nitrogen mixture is fed to the fuel cell. The main challenge, compared to the methanol-based system, is the higher operating temperature of the ammonia decomposition reactor, which ranges between 550–900 °C [13,29], compared to the relatively low methanol steam reforming reactor of around 200–300 °C [4]. These higher operating temperatures require an optimized and innovative energy balance strategy. Moreover, the decomposition temperature is strongly related to the ammonia tolerance level of the HT-PEMFC. The lower the tolerance, the higher the decomposition temperature. However, it is worth mentioning that more recent advances in materials have shown that near equilibrium conversion of ammonia can be achieved at temperatures below 500 °C with higher activity catalysts based on ruthenium and alkali-based catalysts such as sodium and lithium imide [29].

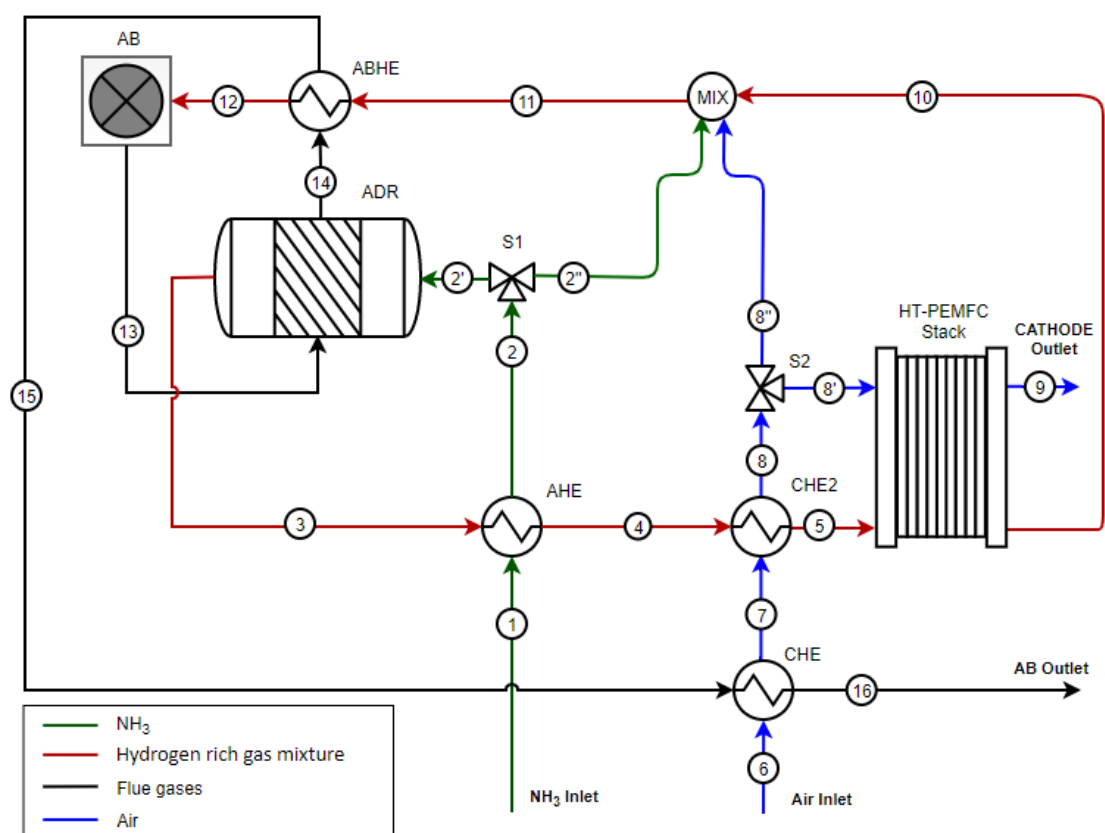


Figure 1. Conceptual schematic of the integrated ammonia decomposition reactor-HT-PEMFC system.

In the current work, a complete decomposition of ammonia is considered for the system design, even though, it has been reported that the HT-PEMFC can tolerate some ammonia in the anode feed [26], allowing for an even simpler system design. However, further studies are required to better understand the effects of ammonia on the performance and durability of HT-PEMFCs before a system can be designed around the assumption of tolerance to traces of ammonia.

Ammonia decomposition is an endothermic reaction and requires external heat to maintain the desired operating temperature. Analogous to a methanol reformer, in the proposed scheme, the heat for ammonia decomposition is supplied by an after burner (AB). In the schematic shown in Figure 1, the gas flow pipes are numbered from 1 to 16. Since ammonia enters the system at ambient temperature, it is pre-heated before entering the ammonia decomposition reactor (ADR) in the ammonia heat exchanger (AHE). Before entering the reactor, a splitter allows to separate part of the ammonia and send it via the mixer to the afterburner. However, ammonia–air mixture suffers from low flame rate and high resistance to auto-ignition, leading to longer ignition delay times, and therefore, it is normally mixed with other fuels for combustion [11,30]. In the current system, the splitter can be activated in specific operating conditions to support combustion, for example, during the start-up or when the unit operates in off design conditions. However, at nominal operating conditions, the design assumes that the entire flow of ammonia is directed to the ADR, which is modeled as an equilibrium reactor with a heat exchanger. The heat in this case is supplied by the anode off gasses of the fuel cell, which are combusted in the afterburner.

The decomposed ammonia is then cooled down to the fuel cell temperature in the AHE, where heat is recovered and used to pre-heat the inlet ammonia to 30 °C below the ADR operating temperature to guarantee the heat recovery. Before reaching the fuel cell inlet, the decomposed mixture enters a second heat exchanger, called cathodic heat exchanger 2 (CHE2), where the remaining heat is used to pre-heat the inlet cathodic air up to the fuel cell temperature.

The oxygen in the air is necessary for both the HT-PEMFC and for the afterburner. In the splitter S2, the total inlet air is separated in two different streams: the cathodic gas flow (8' in the schematic), and the afterburner air flow (8'' in the figure). The cathodic off gasses (pipe 9 in the figure) are vented into the atmosphere, while the anodic gas flow that contains the unreacted hydrogen is sent to the afterburner to complete oxidation and provide heat for the system thermal integration. The anode off gasses (pipe 10), the afterburner air flow (pipe 8''), and in some specific operating conditions that require more heat the ammonia flow (pipe 7''), are mixed in the mixer. A high temperature heat exchanger, afterburner heat exchanger (ABHE), pre-heats the gas mixture before reaching the afterburner. The level of pre-heat is defined by the outlet temperature of the gas mixture (T_{12} in the schematic). This temperature is a design parameter for the system and is discussed in the results section. The afterburner exhausts are cooled in the three components ADR, ABHE, and CHE before they are vented into the atmosphere (gas stream 16 in the figure).

The design allows to optimize the heat recovery and to guarantee the operating conditions of the base components: HT-PEMFC and ADR. All heat exchangers, including the ADR, are modeled with the following energy balance equation:

$$\Delta h_{\text{hot}} = \eta_{\text{HE}} \Delta h_{\text{cold}}, \quad (1)$$

where Δh is the difference between outlet and inlet gas enthalpy of heat exchanger of hot gasses (Δh_{hot}) and cold gasses (Δh_{cold}) and η_{HE} is the heat exchanger efficiency.

Both the afterburner and the mixer are modeled as adiabatic units with no thermal losses. In the afterburner, the oxidation of the fuel is completed, and the produced heat increases the off gases temperature. The afterburner is designed based on the excess of oxygen parameter (EO_{AB}), which is the molar ratio between the inlet oxygen and the stoichiometric value. This parameter allows to calculate the air flow for the afterburner and to design the splitter S2.

The HT-PEMFC is designed based on the experimental results for the electrochemical performances and on the gas thermos-physical properties for the energy balance. HT-PEMFC operating conditions are

defined by operating temperature (T_{Cell}), current density (J), and gas flowrates. The gas flowrates into the two electrodes of the fuel cell depend on the anode stoichiometry (λ_{anode}) and cathode stoichiometry (λ_{cathode}) set points and are used to calculate the ammonia flowrate into the ADR. The fuel cell is modeled as the isothermal unit and a specific heat flow \dot{Q}_{FC} is calculated from the energy balance and has to be subtracted by the fuel cell cooling system. The energy balance of the HT-PEMFC is calculated as follows:

$$\Delta h_{\text{anode}} + \Delta h_{\text{cathode}} + P_{\text{FC}} + \dot{Q}_{\text{FC}} = 0, \quad (2)$$

where P_{FC} is the specific power density of the HT-PEMFC, Δh_{anode} and $\Delta h_{\text{cathode}}$ are the specific enthalpy difference between outlet and inlet gasses of anode and cathode, respectively. The parameters that are necessary to calculate the system energy balance are reported in Table 1, where all the parameters (flow rates, current, power, etc.) are per unit of the fuel cell active area.

Table 1. Model input parameters.

Inlet Parameter	Symbol	Unit
Anode Stoichiometry	λ_{anode}	-
Cathode Stoichiometry	λ_{cathode}	-
Current density	J	A cm^{-2}
Cell temperature	T_{cell}	$^{\circ}\text{C}$
Excess Oxygen after burner	EO_{AB}	-
AB inlet temperature	T_{12}	$^{\circ}\text{C}$
ADR Temperature	T_{ADR}	$^{\circ}\text{C}$
Heat Exchanger efficiency	η_{HE}	-

The model allows to calculate the energy balance of all components, gas composition, temperature, and flow rate of all gas flows. At the fuel cell level, it is possible to calculate operating voltage, power density (P_{FC}), and heat flow (ΔH_{FC}). At the system level, efficiency η_s is calculated as follows:

$$\eta_s = \frac{P_{\text{FC}}}{m_{\text{NH}_3} \cdot \text{LHV}_{\text{NH}_3}}, \quad (3)$$

where m_{NH_3} is the ammonia specific flow rate and LHV_{NH_3} is the ammonia lower heating value.

3. Results

In this section, the results produced from the modeling of the ammonia decomposition process and the $\text{NH}_3/\text{H}_2/\text{air}$ combustion are presented. The experimental results on the performance of the fuel cell stack in the presence of nitrogen in the anode feed gas have also been presented. These models serve to set the temperature limits for the operation of the ADR and AB in the system model. Furthermore, the overall system performance at different operating conditions is described.

3.1. Complete Ammonia Decomposition and Its Effects on the Fuel Cell Stack Performance

Hydrogen is produced via ammonia decomposition through the following endothermic reaction ($\Delta H = 45.6 \text{ kJ/molNH}_3$) without the addition of oxygen or steam:



Ganley et al. [31] reported that the reaction must be enabled by a catalyst. The kinetics of the reaction have been investigated with several supported metals as catalysts (Ru, Ir, Ni, Rh, Pt, Pd, Fe), where the highest catalytic activity is observed over Ru-based catalysts and a comparable high catalytic activity has been obtained at higher temperatures on the less expensive Ni-based catalysts [32]. In an experimental study, Chellappa et al. [33] found that ammonia decomposition

can be considered a first order reaction, with the reaction rate depending solely on the ammonia concentration. Differently from the ammonia synthesis, the decomposition can be conducted at low pressures (1–2 atm) for thermodynamic reasons (principle of Le Chatelier). The ammonia conversion in the decomposition reactor can be calculated as:

$$X_{\text{NH}_3} = 1 - \frac{X_{\text{NH}_3,\text{out}}}{X_{\text{NH}_3,\text{in}}}, \quad (5)$$

where $X_{\text{NH}_3,\text{in}}$ and $X_{\text{NH}_3,\text{out}}$ are the ammonia molar fractions at the inlet and outlet of the reactor. The factor indicates how much ammonia is converted into hydrogen. From the experimental and numerical analysis in [34], we can see in Figure 2 that above a temperature of 600 °C, ammonia can be fully converted in the reactor over a wide range of ammonia flow rates, which in the figure, is expressed using the factor W/F i.e., Ni–Pt/Al₂O₃ catalyst loading weight to ammonia flow rate ratio. This is consistent with findings in [32] where ammonia decomposition was tested on nickel- and ruthenium-based catalysts. Besides, we can see that to achieve the same ammonia conversion values, higher ammonia flow rates will require higher temperatures of operation.

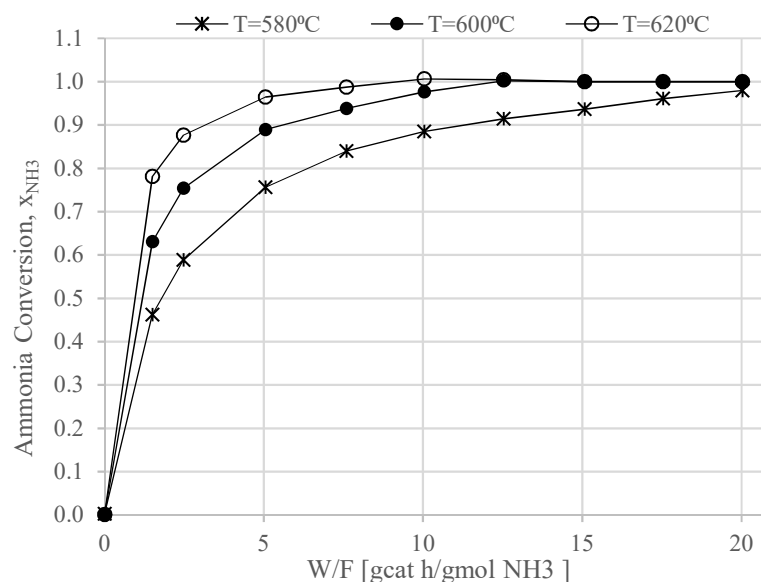


Figure 2. Effect of temperature on ammonia decomposition at different contact time i.e., catalyst weight/volume flow rates (W/F) using Ni–Pt/Al₂O₃ catalyst (Adapted from [34] with permission from Elsevier).

The theoretical limits of the ammonia conversion can be deduced from the ammonia decomposition thermodynamic equilibrium composition at atmospheric pressure at different temperatures in Figure 3. It can be seen that higher temperatures produce higher ammonia conversions.

The experimental data shown in Figure 4 show that 31.7% nitrogen in the anode stream has only slight dilution effect on the fuel cell stack performance. This value is above the maximum concentration of nitrogen that can be obtained from the complete decomposition of ammonia (Figure 3), and hence, it can be concluded that in the absence of NH₃ slip in the feed gas (via complete decomposition or gas purification), a hydrogen–nitrogen gas mixture at concentrations corresponding to the typical ammonia decomposition process does not degrade the fuel cell performance.

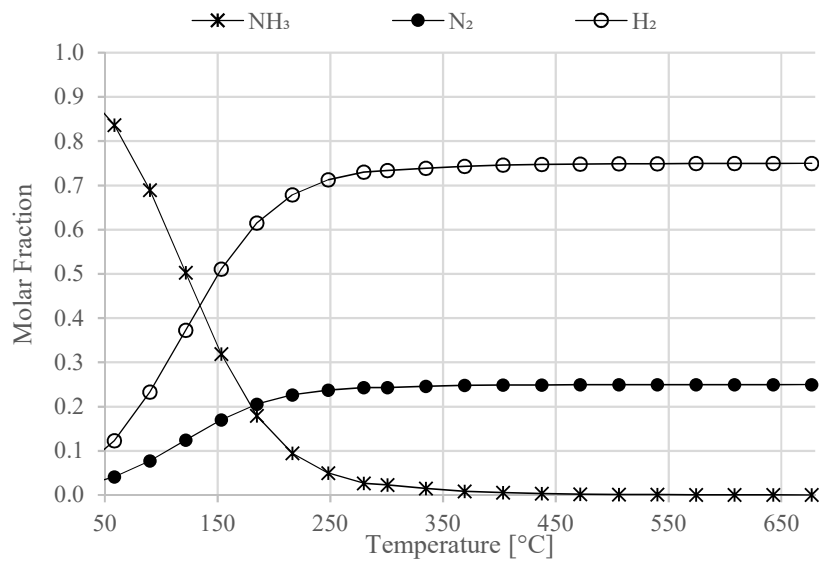


Figure 3. Molar fraction composition of ammonia decomposition at atmospheric pressure based on chemical equilibrium.

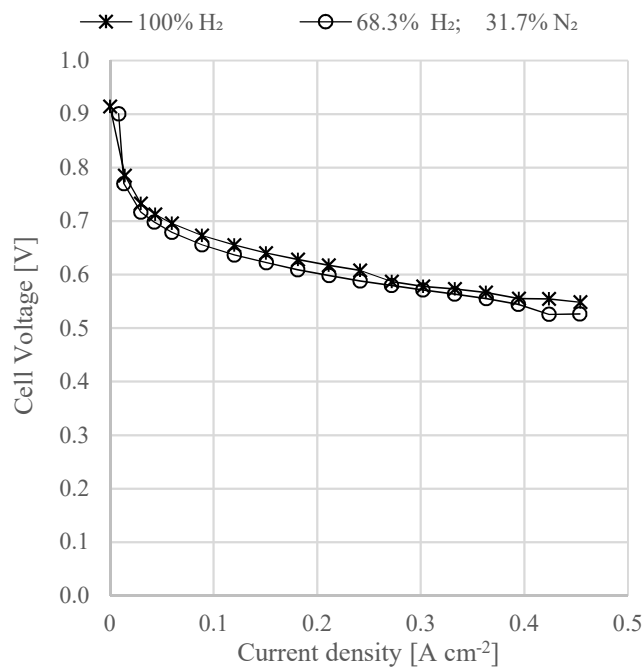


Figure 4. Experimental polarization curves of a HT-PEMFC stack fueled by hydrogen and a mixture of hydrogen and nitrogen.

3.1.1. Afterburner

In the afterburner reactor, hydrogen and ammonia are combusted to produce the heat required for the endothermic ammonia decomposition reaction. Ammonia and hydrogen combustion has previously been studied, where it has been shown that ammonia combustion in air is difficult due to the high auto ignition temperature and low laminar flame velocity [35–37]. However, it has been demonstrated that the swirling flow of the burnt mixture can facilitate the process by providing hot gases and radicals to the incoming fresh fuel and by increasing the residence time [38]. Ammonia combustion is especially necessary during the system start-up when the ammonia decomposition has not reached the operating temperature and hydrogen is not yet available in the stream at the burner inlet.

Chemical kinetics of $\text{NH}_3/\text{H}_2/\text{air}$ combustion is complex—detailed kinetics models have been studied, among others, by Otomo et al. [36] and by Nakamura et al. [39]. In this study, the reaction mechanism in [39] has been implemented to estimate the NO_x concentration in the burnt gases at different temperatures. The reaction mechanism was implemented in Cantera [28] using a Python programming language script. The afterburner is simulated as a “continuous stirred-tank reactor” (CSTR) at a pressure of 1 atm. The simulated inlet gas compositions consider the stoichiometric combustion of NH_3/air for the system start-up and the H_2/air combustion at different operating values of the anode stoichiometry and the excess air in the afterburner.

In air pollution, parts per million (ppm) by mole or by volume is used to account for the amount of pollutants. These quantities can be assumed equal in the case of an ideal gas. From Figure 5, it can be seen that the NO_x concentration in ppm is affected by combustion temperature in the afterburner. The model results show that while NO production in the case of the ammonia/air combustion starts to increase continuously already at temperatures below $1200\text{ }^\circ\text{C}$, their production from H_2/air combustion remains negligible below $1370\text{ }^\circ\text{C}$. Therefore, since the burner operates under H_2/air combustion at nominal conditions, the latter temperature has been chosen as the upper limit for the adiabatic combustion temperature in the system modeling. Furthermore, a local peak in NO concentration is visible in the temperature range of the ammonia autoignition of around $650\text{ }^\circ\text{C}$. In [40], the NO formation pathways from ammonia combustion were described and it was shown that in the ignition region, the majority of atomic nitrogen is oxidized to NO.

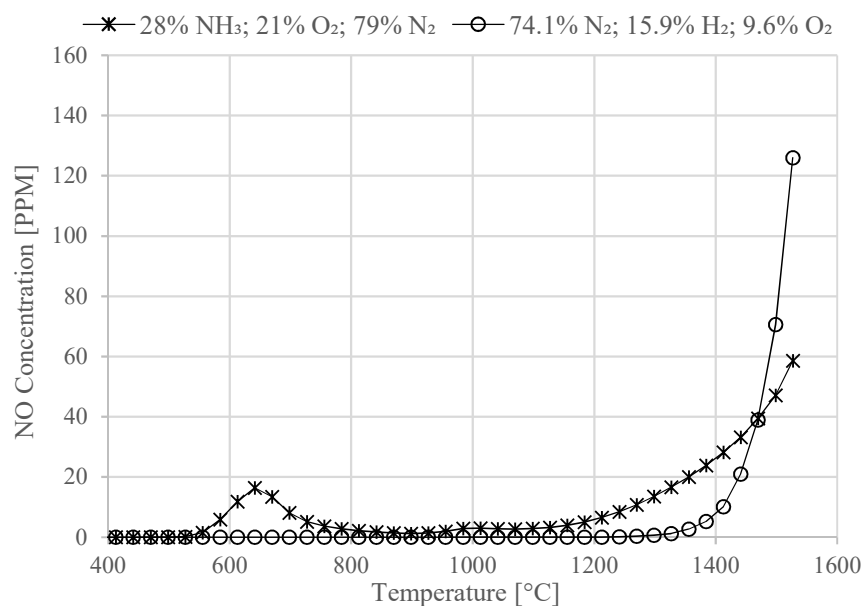


Figure 5. Concentration of NO in ppm in the afterburner outlet gases due to $\text{NH}_3/\text{H}_2/\text{air}$ combustion. One case refers to the combustion of ammonia during the system startup, while the other curve refers to the H_2/air combustion.

3.1.2. System Modeling

The model implemented in the calculation sheet was studied by varying the operating parameters. The selected nominal conditions are reported in Table 2.

Table 2. Nominal operating parameters of the system.

Parameter	Value
λ_{anode}	1.37
λ_{cathode}	2.5
J	0.35 A cm ⁻²
T _{cell}	160 °C
EO _{AB}	1.65
T _{AB,in}	330 °C
T _{ADR}	600 °C
η_{HE}	0.85

Anode stoichiometry was set to 1.37, whereby the excess amount of hydrogen that does not react in the fuel cell is oxidized in the afterburner to provide the heat necessary to balance the internal heat requirement of the system, in particular, for the ammonia decomposition reactor. Note that this value is slightly higher than the one used in the experimental test and voltage values calculated by the model may slightly underestimate real values. However, in an experimental work performed in a similar short HT-PEMFC stack, it was found that once hydrogen starvation is avoided at around an anode stoichiometric ratio of 1.3, further increase in λ_{anode} does not improve the fuel cell stack performance [41].

Cathode stoichiometry was selected from the experimental data to 2.5 and is a standard operating condition for an HT-PEMFC. Typical HT-PEMFC operating conditions were also used for current density and temperature, at 0.35 a cm⁻² and 160 °C, respectively.

The ammonia decomposition reaction temperature was set to 600 °C, which, according to the literature data in Figure 2, gives complete ammonia decomposition at satisfactory *W/F* ratio. In spite of the fact that complete ammonia conversion can be achieved at the chosen operating temperature, in reality, ammonia concentration in the ppb level may be present in the decomposed mixture. However, this limit is compatible with the HT-PEMFC tolerance available in literature [26]. To keep the afterburner temperature below the risk of NO_x formation, the afterburner inlet temperature, T₁₂, was set to 330 °C. The effect of this parameter on the system energy balance is discussed below. All heat exchangers operate with an efficiency of 0.85.

This optimization follows the afterburner excess of oxygen, which is set at 1.65. When EO_{AB} is set, the total air flow rate required by the system is calculated. The main system outputs are given in Table 3, where it can be seen that at a cell voltage of 0.60 V, the power density is 0.21 W cm⁻², which corresponds to a system efficiency of 40.1%. However, it is worth noting that this value does not consider the energy consumption of the ancillary devices such as the air blower, inverter, and HT-PEMFC cooling system.

Table 3. System output parameters under nominal operating conditions.

Parameter	Value
Cell voltage	0.60 V
P _{FC}	0.21 W cm ⁻²
\dot{Q}_{FC}	0.23 W cm ⁻²
System efficiency	0.401
Afterburner exhaust temperature	1357.62 °C
Ammonia specific flow rate	0.10 g h ⁻¹ cm ⁻²
Air specific flow rate	1.08 Nl h ⁻¹ cm ⁻²
S2 opening ratio	0.8

The afterburner off gases temperature, T₁₃, is 1357.62 °C. The specific inlet ammonia flow rate and air flow rate calculated based on the cell active area are also given in Table 3, at 0.10 g h⁻¹ cm⁻² and 1.08 Nl h⁻¹ cm⁻², respectively. Finally, the opening ratio of splitter S2, calculated as the ratio between

the air flowrate into the cathode and the total inlet air flowrate into the system is found to be 0.8 at nominal operating conditions.

In Table 4, gas compositions of all pipes are reported. The afterburner inlet flow, AB in Table 4, is a mixture of only oxygen, nitrogen, and hydrogen. The selected composition allows to reach an afterburner adiabatic temperature of 1362.26 °C.

Table 4. Gas composition of all mixtures.

	Air (6,7,8,8',8'')	NH ₃ in (1,2,2',2'')	NH ₃ Ref (3,4)	Anode Out (10)	Cathode Out (9)	AB in (11,12)	AB Out (13,14,15,16)
H ₂ O	0.0%	0.0%	0.0%	0.0%	15.5%	0.0%	14.5%
CO ₂	0.0%	0.0%	0.0%	0.0%	0.0%	0.0%	0.0%
N ₂	79.0%	0.0%	40.0%	71.2%	72.9%	75.3%	80.8%
H ₂	0.0%	0.0%	60.0%	28.8%	0.0%	13.5%	0.0%
NH ₃	0.0%	100.0%	0.0%	0.0%	0.0%	0.0%	0.0%
O ₂	21.0%	0.0%	0.0%	0.0%	11.6%	11.2%	4.7%

Table 5 reports the operating values of the heat exchangers and the ammonia decomposition reactor. The inlet and outlet temperatures of the hot (T_1) and the cold (T_2) gas flows are shown for the different components. Minimum temperature difference, pinch point, is also reported as ΔT_{\min} . Finally, logarithmic mean temperature difference (LMTD) and exchanged heat, \dot{Q} , are reported. All pinch points are higher than 30 °C, which is the design value of the AHE. The amount of heat exchanged in the ADR has a higher value compared to the other units since the heat has to cover also energy requirement for the chemical reaction. All data reported in Table 5 can be used for a detailed design of the heat exchangers and to calculate single efficiency of each component. However, the design of each component is beyond the aim of this study.

Table 5. Data of the heat exchangers.

		AHE	ADR	ABHE	CHE	CHE ₂
T ₁ in	°C	600.00	1357.62	592.99	393.00	218.20
T ₁ out	°C	218.20	592.99	393.00	87.85	160.00
T ₂ in	°C	20.00	570.00	160.36	20.00	114.02
T ₂ out	°C	570.00	600.00	330.00	114.02	160.00
ΔT_{\min}	°C	30.00	22.99	232.64	67.85	45.98
LMTD	°C	89.08	210.18	247.50	149.33	51.85
\dot{Q}	W cm ⁻²	0.04	0.11	0.03	0.04	0.02

The thermal optimization of the system is based on the three parameters λ_{anode} , T_{12} , and EO_{AB} . Anode stoichiometry defines not only the amount of hydrogen required for in the HT-PEMFC, but also the remaining amount of hydrogen that enters into the afterburner. Hydrogen reacts in the burner, providing heat to all the successive components, except the fuel cell, which produces heat. For higher values of λ_{anode} , system efficiency decreases, due to higher consumption of fuel, and the temperature of the system off gasses increases. This could be of some interest in the case of cogeneration application.

The optimization of T_{12} and EO_{AB} allows to distribute the heat of the afterburner among all the heat exchangers, while also maintaining the AB adiabatic flame temperature below 1370 °C. This limit was introduced to reduce NO_x production according to the modeling results obtained in this work (Figure 5). In detail, higher values of EO_{AB} reduce the adiabatic flame temperature but increase the consumption of air. The pre-heat temperature, T_{12} , is designed as a tradeoff between AB off gasses temperature and a complete heat recovery in the ABHE. Figure 6 shows the influence of AB inlet temperature on the temperature of AB off gasses and on system exhausts temperature.

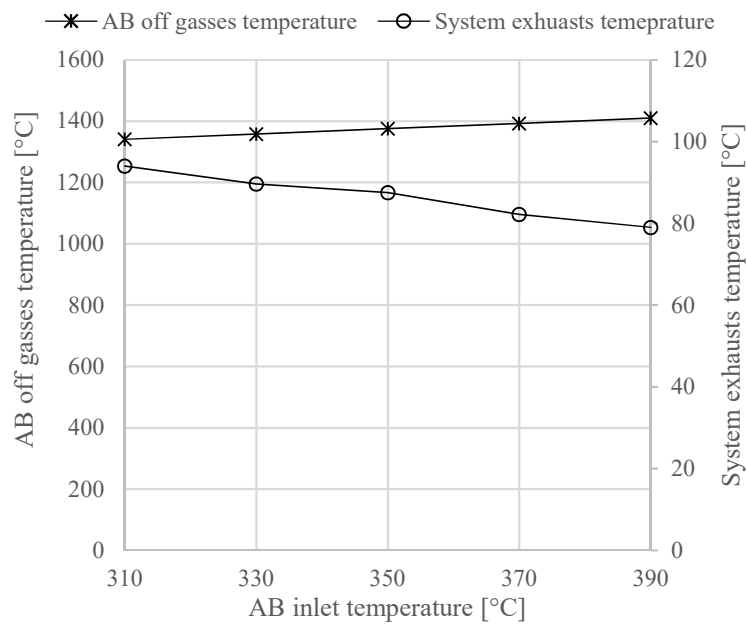


Figure 6. AB off gasses and system exhaust temperatures as function AB inlet temperature.

The model was also studied for different design values. The HT-PEMFC stack current density was varied from 0.25 to 0.45 A cm⁻², with step of 0.05 A cm⁻², keeping all other parameters constant. Figure 7 shows the results of the study, where the power density and system efficiency is given in Figure 7a,b shows air flow rate and Q_{FC}, both as function of current density. As expected, power density increases with increasing current density, while the opposite behavior characterizes the system efficiency. This is a typical tradeoff for fuel cell systems between power density and efficiency. Both Q_{FC} and air flowrate affect the energy consumption of ancillaries.

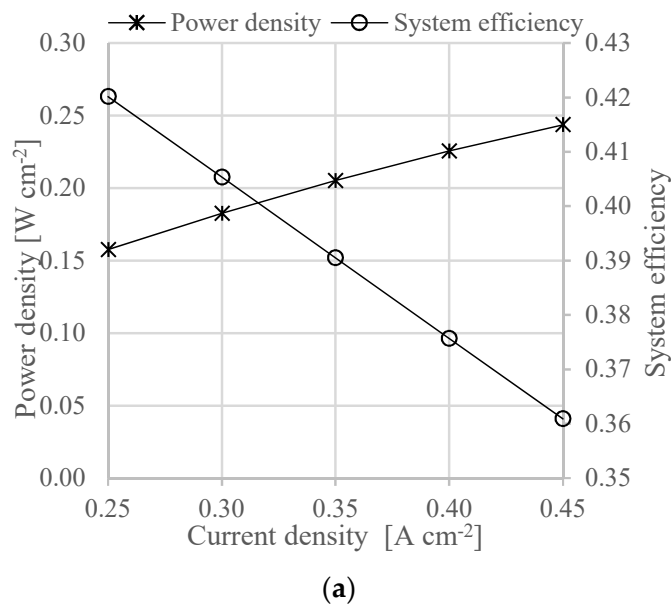
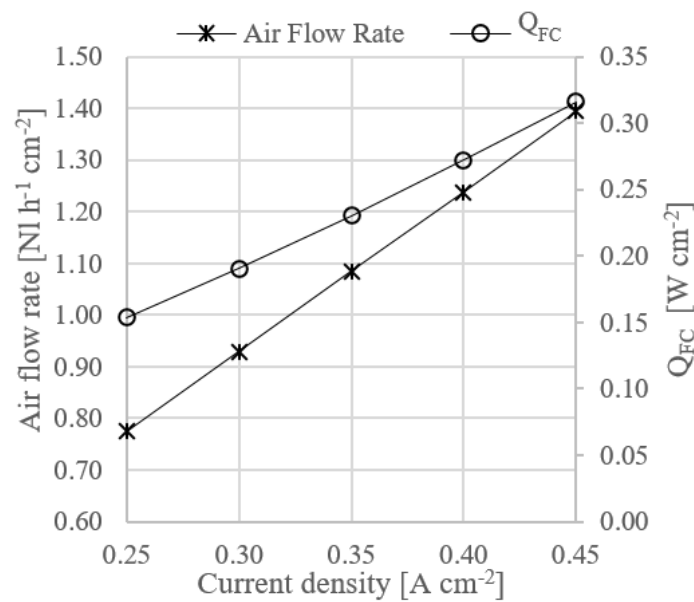


Figure 7. Cont.



(b)

Figure 7. (a) Power density and system efficiency as function of current density. (b) Air flow rate and heat generation in the fuel cell as a function of current density.

4. Discussion

4.1. Ammonia Decomposition for the HT-PEMFC System

Ammonia decomposition experiments and models have shown that above a temperature of 600 °C, ammonia can be fully converted in the reactor over a large range of ammonia flow rates [32,34]. However, in an integrated system with an HT-PEMFC, a small amount of ammonia may still slip from the reactor outlet. In [42], it was reported that small traces of ammonia can degrade the performance of PEM fuel cells. It has also been shown experimentally that ammonia in phosphoric acid fuel cells (PAFC) can react with the electrolyte to produce $(\text{NH}_4)\text{H}_2\text{PO}_4$, which results in a more sluggish oxygen reduction reaction (ORR) at the cathode [43]. Since the commonly used PBI-based membrane electrolyte in HT-PEMFCs is doped in phosphoric acid, similar degradation mechanisms are expected to take place in the presence of ammonia in HT-PEMFCs. However, the authors also reported that the effect can be reduced by increasing the cathode potential and a complete performance recovery can be achieved when the contaminant is removed. In addition, there are several ways to reduce the ammonia concentration even further, such as absorption and adsorption processes for ammonia or membranes for hydrogen separation [44].

In comparison with methanol reforming, which is characterized by a complex system of three reactions; methanol steam reforming, methanol decomposition, and water gas shift [45], ammonia decomposition is given by the single equilibrium reaction given by Equation (4). Hence, while in the case of methanol reforming, a compromise is necessary among the different contaminants of the reformat gas depending on the reforming temperature and reactants flowrates, complete ammonia decomposition has the potential to provide clean hydrogen. This is because some of the contaminants in the methanol reformat gas are byproducts of the reforming process itself, with higher methanol conversion resulting in more CO and CO₂ and lower conversion ratios leaving more unconverted methanol in the reformat gas. Even though tolerances of up to 2% of CO (in the presence of CO₂) [46] and 3% of methanol [47] are reported in the literature, CO and methanol are nonetheless detrimental to an HT-PEMFC during long-term exposure and their combined effects could significantly lower these tolerance values. Moreover, it not possible to maintain both contaminants at low levels by increasing

the reforming temperature as this would increase the methanol conversion, thereby decreasing the methanol slip but also increasing the CO concentration in the reformat gas [45]. With ammonia decomposition on the other hand, if a proper system heat integration is done, a complete ammonia decomposition at chemical equilibrium contains only H₂ and N₂, as shown in Figure 3, which does not have any degrading effects on the fuel cell stack performance as can be seen from the experimental results in Figure 4.

4.2. Ammonia Fueled HT-PEMFC System Analysis

Based on the results in nominal condition, it is possible to design a 10 kW power system based on ammonia as a fuel and HT-PEMFC. Main system parameters are reported in Table 6. For a 10 kW system, around 295 cells of 165 cm² of active area are necessary. Ammonia inlet flow rate of 1.37 g s⁻¹ is required as fuel consumption and an air flow rate of 14.68 NI s⁻¹ has to be provided by the air blower.

Table 6. Data of the 10 kW system.

System Power	10.00	kW
Number of Cells (165 cm²)	≈295	
NH₃ Flow Rate	1.37	g s ⁻¹
Air Flow Rate	14.68	NI s ⁻¹

It is important to underline that the detailed design of the heat exchanger is necessary to evaluate the efficiency of the components. The ammonia decomposition reactor has to be designed to evaluate the amount of catalyst required to reach the complete decomposition of the ammonia. The natural evolution of the study is the evaluation of HT-PEMFC tolerance to NH₃ traces. The limit of the technology could bring two different scenarios. If the tolerance is extremely low, an additional clean-up unit may be necessary, increasing the complexity of the system. If the tolerance is in the order of percentage, it is possible to reduce ADT temperature moving all the system temperature to lower values. The latter scenario is interesting as it brings the NH₃ system closer to the existing methanol-fueled HT-PEMFC power units and it will be possible to recover part of the know-how included and already developed components for the balance of the plant. In addition, the reduction of ammonia decomposition temperature reduces the dimension of the heat exchangers due to the general reduction of LMTD values. In the definition of the off-design operation and start-up, the direct use of ammonia in the afterburner has to be investigated. In particular, the operation of the afterburner with a pure ammonia mixture requires a deeper investigation.

5. Conclusions

In this work, a design concept of a heat-integrated ammonia-fueled HT-PEMFC system is presented. Zero-dimensional models of the reactors and heat exchangers were developed, including those of the afterburner and the ammonia decomposition reactor. The study can be considered as a first attempt to demonstrate the thermodynamic feasibility of such a system. According to the chemical equilibrium studies in this work, the ammonia decomposition reactor can fully convert the ammonia into hydrogen and nitrogen. However, the process is endothermic and high operating temperatures of above 600 °C need to be ensured in the decomposition reactor, which in the proposed concept, is provided by the afterburner.

Moreover, the NO_x emission of the combustion processes involved in the proposed system have been analytically investigated. The model showed that both ammonia/air combustion and H₂/air combustion results in a limited amount of NO production of around 22 ppm and 4 ppm, respectively, below 1370 °C. Therefore, the afterburner temperature should be kept below this temperature in order to limit the production of NO during the combustion process. Since the combustion of ammonia is characterized by low flame speed and long ignition time, in the proposed concept, ammonia combustion is only used during the startup phase, and during normal operating conditions, the unreacted hydrogen

at the anode outlet is used in the afterburner as it can sustain the system thermal requirements with a fuel cell anode stoichiometric ratio of 1.37.

An experimental test on an HT-PEMFC short stack was also conducted to observe the cell electrical performance using a fuel mixture with a composition of hydrogen and nitrogen gas similar to the one at the outlet of the ammonia decomposition reactor. The experimental results showed that in the absence of the NH₃ slip in the feed gas (via complete decomposition or gas purification), a hydrogen–nitrogen gas mixture at concentrations corresponding to a typical ammonia decomposition process does not degrade the fuel cell stack performance.

At system level, the proposed design allows to reach a total efficiency of 40.1% at a power density of 0.21 W cm⁻². The heat recovery strategy allows to feed the ammonia decomposition reactor and to preheat the gas before entering the HT-PEMFC.

Author Contributions: Conceptualization, G.C., V.L., S.L.S. and S.S.A.; methodology, G.C., V.L., S.L.S. and S.S.A.; software, G.C., V.L. and S.S.A.; validation, G.C., V.L. and S.S.A.; formal analysis, G.C., V.L. and S.S.A.; investigation, G.C., V.L., S.L.S. and S.S.A.; resources, G.C., V.L. and S.S.A.; data curation, G.C., V.L. and S.S.A.; writing—original draft preparation, G.C., V.L. and S.S.A.; writing—review and editing, G.C., V.L., S.L.S. and S.S.A.; visualization, G.C., V.L. and S.S.A.; project administration, G.C. and S.S.A.; funding acquisition, G.C. and S.S.A. All authors have read and agreed to the published version of the manuscript.

Funding: The activities were supported, in the frame of a scientific collaboration, by ENVIU, PROTON VENTURES BV and C-JOB & PARTNERS BV, which are acknowledged. This research has also received funding from the Danish Energy Technology Development and Demonstration Program (EUDP) through the projects COBRA Drive (grant number—64018-0118). The study was supported by the Fuel Cell and Hydrogen 2 Joint Undertaking under grant agreement No. 736648 (NET-Tools project).

Conflicts of Interest: The authors declare no conflict of interest. The funders had no role in the design of the study; in the collection, analyses, or interpretation of data; in the writing of the manuscript, or in the decision to publish the results.

Abbreviations

The following abbreviations and symbols are used in this manuscript:

AB	Afterburner
ABHE	Afterburner Heat Exchanger
ADR	Ammonia Decomposition reactor
ADT	Ammonia Decomposition temperature
AHE	Ammonia Heat Exchanger
CHE	Cathode Heat Exchanger
EO	Excess of Oxygen
LHV	Low Heating Value
LMTD	Logarithmic Mean Temperature Difference
HT-PEMFC	High Temperature Proton Exchange Membrane Fuel Cell

References

1. Møller, K.T.; Jensen, T.R.; Akiba, E.; Li, H.-W. Hydrogen—A sustainable energy carrier. *Prog. Nat. Sci. Mater. Int.* **2017**, *27*, 34–40. [[CrossRef](#)]
2. Nikolaidis, P.; Poullikkas, A. A comparative overview of hydrogen production processes. *Renew. Sustain. Energy Rev.* **2017**, *67*, 597–611. [[CrossRef](#)]
3. Sakintuna, B.; Lamari-Darkrim, F.; Hirscher, M. Metal hydride materials for solid hydrogen storage: A review. *Int. J. Hydrog. Energy* **2007**, *32*, 1121–1140. [[CrossRef](#)]
4. Simon Araya, S.; Liso, V.; Cui, X.; Li, N.; Zhu, J.; Sahlin, S.L.; Jensen, S.H.; Nielsen, M.P.; Kær, S.K. A Review of the Methanol Economy: The Fuel Cell Route. *Energies* **2020**, *13*, 596. [[CrossRef](#)]
5. Ni, M.; Leung, D.Y.C.; Leung, M.K.H. A review on reforming bio-ethanol for hydrogen production. *Int. J. Hydrog. Energy* **2007**, *32*, 3238–3247. [[CrossRef](#)]
6. Demirbaş, A. Biofuels sources, biofuel policy, biofuel economy and global biofuel projections. *Energy Convers. Manag.* **2008**, *49*, 2106–2116. [[CrossRef](#)]

7. Yapicioglu, A.; Dincer, I. A review on clean ammonia as a potential fuel for power generators. *Renew. Sustain. Energy Rev.* **2019**, *103*, 96–108. [CrossRef]
8. Garagounis, I.; Vourros, A.; Stoukides, D.; Dasopoulos, D.; Stoukides, M. Electrochemical synthesis of ammonia: Recent efforts and future outlook. *Membranes* **2019**, *9*, 112. [CrossRef]
9. Wang, L.; Xia, M.; Wang, H.; Huang, K.; Qian, C.; Maravelias, C.T.; Ozin, G.A. Greening Ammonia toward the Solar Ammonia Refinery. *Joule* **2018**, *2*, 1055–1074. [CrossRef]
10. National Oceanic & Atmospheric Administration (NOAA). Global Monitoring Laboratory—Carbon Cycle Greenhouse Gases n.d. Available online: <https://www.esrl.noaa.gov/gmd/ccgg/trends/monthly.html> (accessed on 22 June 2020).
11. Valera-Medina, A.; Xiao, H.; Owen-Jones, M.; David, W.I.F.; Bowen, P.J. Ammonia for power. *Prog. Energy Combust. Sci.* **2018**, *69*, 63–102. [CrossRef]
12. Afif, A.; Radenahmad, N.; Cheok, Q.; Shams, S.; Kim, J.H.; Azad, A.K. Ammonia-fed fuel cells: A comprehensive review. *Renew. Sustain. Energy Rev.* **2016**, *60*, 822–835. [CrossRef]
13. Miyaoka, H.; Miyaoka, H.; Ichikawa, T.; Ichikawa, T.; Kojima, Y. Highly purified hydrogen production from ammonia for PEM fuel cell. *Int. J. Hydrog. Energy* **2018**, *43*, 14486–14492. [CrossRef]
14. Macfarlane, D.R.; Cherepanov, P.V.; Choi, J.; Suryanto, B.H.R.; Hodgetts, R.Y.; Bakker, J.M.; Vallana, F.M.F.; Simonov, A.N. A Roadmap to the Ammonia Economy. *Joule* **2020**, *4*, 1186–1205. [CrossRef]
15. Zhang, X.; Preston, J.; Pasaogullari, U.; Molter, T. Influence of Ammonia on Membrane-Electrode Assemblies in Polymer Electrolyte Fuel Cells. *Int. J. Hydrog. Energy* **2009**, *34*, 9188–9194. [CrossRef]
16. Halseid, R.; Vie, P.J.S.; Tunold, R. Effect of ammonia on the performance of polymer electrolyte membrane fuel cells. *J. Power Sources* **2006**, *154*, 343–350. [CrossRef]
17. Alagharu, V.; Palanki, S.; West, K.N. Analysis of ammonia decomposition reactor to generate hydrogen for fuel cell applications. *J. Power Sources* **2010**, *195*, 829–833. [CrossRef]
18. Chakraborty, D.; Chorkendorff, I.; Olsen, J.L.; Lopes, H.J.; Nielsen, M.G. Use of Catalysts, Method and Apparatus for Selective Oxidation of Ammonia in a Gas Containing Hydrogen. U.S. Patents 10,005,067, 26 June 2018.
19. Araya, S.S.; Zhou, F.; Liso, V.; Sahlin, S.L.; Vang, J.R.; Thomas, S.; Gao, X.; Jeppesen, C.; Kær, S.K. A comprehensive review of PBI-based high temperature PEM fuel cells. *Int. J. Hydrog. Energy* **2016**, *41*, 21310–21344. [CrossRef]
20. Jeppesen, C.; Araya, S.S.; Sahlin, S.L.; Thomas, S.; Andreasen, S.J.; Kær, S.K. Fault detection and isolation of high temperature proton exchange membrane fuel cell stack under the influence of degradation. *J. Power Sources* **2017**, *359*, 37–47. [CrossRef]
21. Thomas, S.; Vang, J.R.; Araya, S.S.; Kær, S.K. Experimental study to distinguish the effects of methanol slip and water vapour on a high temperature PEM fuel cell at different operating conditions. *Appl. Energy* **2017**, *192*, 422–436. [CrossRef]
22. Jeppesen, C.; Polverino, P.; Andreasen, S.J.; Araya, S.S.; Sahlin, S.L.; Pianese, C.; Kær, S.K. Impedance characterization of high temperature proton exchange membrane fuel cell stack under the influence of carbon monoxide and methanol vapor. *Int. J. Hydrog. Energy* **2017**, *42*, 21901–21912. [CrossRef]
23. Arsalis, A.; Nielsen, M.P.; Kær, S.K. Modeling and optimization of a 1 kW_e HT-PEMFC-based micro-CHP residential system. *Int. J. Hydrog. Energy* **2012**, *37*, 2470–2481. [CrossRef]
24. Chen, C.-Y.; Lai, W.-H.; Chen, Y.-K.; Su, S.-S. Characteristic studies of a PBI/H₃PO₄ high temperature membrane PEMFC under simulated reformat gases. *Int. J. Hydrog. Energy* **2014**, *39*, 13757–13762. [CrossRef]
25. Najafi, B.; Mamaghani, A.H.; Baricci, A.; Rinaldi, F.; Casalegno, A. Mathematical modelling and parametric study on a 30 kW_e high temperature PEM fuel cell based residential micro cogeneration plant. *Int. J. Hydrog. Energy* **2015**, *40*, 1569–1583. [CrossRef]
26. Bandlamudi, G. *Systematic Characterization of Ht Pemfcs Containing Pbi/H 3po 4systems: Thermodynamic Analysis and Experimental Investigations*; Logos Verlag Berlin: Berlin, Germany, 2011.
27. Malcolm, W.; Chase, J. *NIST-JANAF Thermochemical Tables*, 4th ed.; American Chemical Society: Washington, DC, USA; American Institute of Physics for the National Institute of Standards and Technology: New York, NY, USA, 1998.
28. Goodwin, D.G.; Speth, R.L.; Moffat, H.K.; Weber, B.W. *Cantera: An Object-Oriented Software Toolkit for Chemical Kinetics, Thermodynamics, and Transport Processes*; Caltech: Pasadena, CA, USA, 2018. [CrossRef]

29. Giddey, S.; Badwal, S.P.S.; Munnings, C.; Dolan, M. Ammonia as a Renewable Energy Transportation Media. *ACS Sustain. Chem. Eng.* **2017**, *5*, 10231–10239. [[CrossRef](#)]
30. Nakamura, H.; Hasegawa, S. Combustion and ignition characteristics of ammonia/air mixtures in a micro flow reactor with a controlled temperature profile. *Proc. Combust. Inst.* **2017**, *36*, 4217–4226. [[CrossRef](#)]
31. Ganley, J.C.; Thomas, F.S.; Seebauer, E.G.; Masel, R.I. A Priori Catalytic Activity Correlations: The Difficult Case of Hydrogen Production from Ammonia. *Catal. Lett.* **2004**, *96*, 117–122. [[CrossRef](#)]
32. Takahashi, A.; Fujitani, T. Kinetic Analysis of Decomposition of Ammonia over Nickel and Ruthenium Catalysts. *J. Chem. Eng. Jpn.* **2016**, *49*, 22–28. [[CrossRef](#)]
33. Chellappa, A.S.; Fischer, C.M.; Thomson, W.J. Ammonia decomposition kinetics over Ni-Pt/Al₂O₃ for PEM fuel cell applications. *Appl. Catal. Gen.* **2002**, *227*, 231–240. [[CrossRef](#)]
34. Chein, R.-Y.; Chen, Y.-C.; Chang, C.-S.; Chung, J.N. Numerical modeling of hydrogen production from ammonia decomposition for fuel cell applications. *Int. J. Hydrog. Energy* **2010**, *35*, 589–597. [[CrossRef](#)]
35. Lindstedt, R.P.; Lockwood, F.C.; Selim, M.A. Detailed Kinetic Modelling of Chemistry and Temperature Effects on Ammonia Oxidation. *Combust. Sci. Technol.* **1994**, *99*, 253–276. [[CrossRef](#)]
36. Otomo, J.; Koshi, M.; Mitsumori, T.; Iwasaki, H.; Yamada, K. Chemical kinetic modeling of ammonia oxidation with improved reaction mechanism for ammonia/air and ammonia/hydrogen/air combustion. *Int. J. Hydrog. Energy* **2018**, *43*, 3004–3014. [[CrossRef](#)]
37. Li, J.; Huang, H.; Kobayashi, N.; He, Z.; Nagai, Y. Study on using hydrogen and ammonia as fuels: Combustion characteristics and NO_x formation. *Int. J. Energy Res.* **2014**, *38*, 1214–1223. [[CrossRef](#)]
38. Kobayashi, H.; Hayakawa, A.; Somarathne, K.D.K.A.; Okafor, E.C. Science and technology of ammonia combustion. *Proc. Combust. Inst.* **2019**, *37*, 109–133. [[CrossRef](#)]
39. Nakamura, H.; Hasegawa, S.; Tezuka, T. Kinetic modeling of ammonia/air weak flames in a micro flow reactor with a controlled temperature profile. *Combust. Flame* **2017**, *185*, 16–27. [[CrossRef](#)]
40. Sullivan, N.; Jensen, A.; Glarborg, P.; Day, M.S.; Grcar, J.F.; Bell, J.B.; Pope, C.J.; Kee, R.J. Ammonia conversion and NO_x formation in laminar coflowing nonpremixed methane-air flames. *Combust. Flame* **2002**, *131*, 285–298. [[CrossRef](#)]
41. Sahlin, S.L.; Araya, S.S.; Andreasen, S.J.; Kær, S.K. Electrochemical Impedance Spectroscopy (EIS) Characterization of Reformate-operated High Temperature PEM Fuel Cell Stack. *Int. J. Power Energy Res.* **2017**, *1*, 20–40. [[CrossRef](#)]
42. Uribe, F.A.; Gottesfeld, S.; Zawodzinski, T.A. Effect of ammonia as potential fuel impurity on proton exchange membrane fuel cell performance. *J. Electrochem. Soc.* **2002**, *149*, A293–A294. [[CrossRef](#)]
43. Szymanski, S.T.; Gruver, G.A.; Katz, M.; Kunz, H.R. The Effect of Ammonia on Hydrogen-Air Phosphoric Acid Fuel Cell Performance. *J. Electrochem. Soc.* **1980**, *127*, 1440. [[CrossRef](#)]
44. Lamb, K.E.; Dolan, M.D.; Kennedy, D.F. Ammonia for hydrogen storage; A review of catalytic ammonia decomposition and hydrogen separation and purification. *Int. J. Hydrog. Energy* **2019**, *44*, 3580–3593. [[CrossRef](#)]
45. Zhu, J.; Araya, S.S.; Cui, X.; Sahlin, S.L.; Kær, S.K. Modeling and Design of a Multi-Tubular Packed-Bed Reactor for Methanol Steam Reforming over a Cu/ZnO/Al₂O₃ Catalyst. *Energies* **2020**, *13*, 610. [[CrossRef](#)]
46. Araya, S.S.; Andreasen, S.J.; Kær, S.K. Experimental Characterization of the Poisoning Effects of Methanol-Based Reformate Impurities on a PBI-Based High Temperature PEM Fuel Cell. *Energies* **2012**, *5*, 4251–4267. [[CrossRef](#)]
47. Araya, S.S.; Andreasen, S.J.; Nielsen, H.V.; Kær, S.K. Investigating the effects of methanol-water vapor mixture on a PBI-based high temperature PEM fuel cell. *Int. J. Hydrog. Energy* **2012**, *37*, 18231–18242. [[CrossRef](#)]



© 2020 by the authors. Licensee MDPI, Basel, Switzerland. This article is an open access article distributed under the terms and conditions of the Creative Commons Attribution (CC BY) license (<http://creativecommons.org/licenses/by/4.0/>).

Article

Optimization Design of Rib Width and Performance Analysis of Solid Oxide Electrolysis Cell

Meiting Guo ^{1,*}, Xiao Ru ², Zijing Lin ^{1,2,3} , Guoping Xiao ⁴ and Jianqiang Wang ⁴

¹ Department of Physics, University of Science and Technology of China, No. 96, JinZhai Road, Hefei 230026, China; zjlin@ustc.edu.cn

² Hefei National Laboratory for Physical Sciences at Microscale, University of Science and Technology of China, No. 96, JinZhai Road, Hefei 230026, China; rxiao@ustc.edu.cn

³ CAS Key Laboratory of Strongly-Coupled Quantum Matter Physics, University of Science and Technology of China, No. 96, JinZhai Road, Hefei 230026, China

⁴ Key Laboratory of Interfacial Physics and Technology, Shanghai Institute of Applied Physics, Chinese Academy of Sciences, Shanghai 201800, China; xiaoguoping@sinap.ac.cn (G.X.); wangjianqiang@sinap.ac.cn (J.W.)

* Correspondence: gmt@mail.ustc.edu.cn; Tel.: +86-551-63606345

Received: 15 September 2020; Accepted: 13 October 2020; Published: 19 October 2020



Abstract: Structure design is of great value for the performance improvement of solid oxide electrolysis cells (SOECs) to diminish the gap between scientific research and industrial application. A comprehensive multi-physics coupled model is constructed to conduct parameter sensitivity analysis to reveal the primary and secondary factors on the SOEC performance and optimal rib width. It is found that the parameters of the O₂ electrode have almost no influence on the optimal rib width at the H₂ electrode side and vice versa. The optimized rib width is not sensitive to the electrode porosity, thickness, electrical conductivity and gas composition. The optimal rib width at the H₂ electrode side is sensitive to the contact resistance at the interface between the electrode and interconnect rib, while the extremely small concentration loss at the O₂ electrode leads to the insensitivity of optimal rib width to the parameters influencing the O₂ diffusion. In addition to the contact resistance, the applied cell voltage and pitch width also has a dramatic influence on the optimal rib width of the fuel electrode. An analytical expression considering the influence of total cell polarization loss, the pitch width and the contact resistance is further developed for the benefit of the engineering society. The maximum error in the cell performance between the numerically obtained and analytically acquired optimal rib width is only 0.14% and the predictive power of the analytical formula is fully verified.

Keywords: solid oxide electrolysis cell; multi-physics; optimal rib/pitch ratio; parameters sensitivity; analytical expression

1. Introduction

Renewable energy resources, including solar, wind, tidal, and biomass, are of great significance as the fossil energy crisis is becoming increasingly serious. However, their intermittence leads to an undesirable imbalance between demand and supply [1]. An energy storage device is required so that energy can be stored and released as needed. Among various candidates for energy storage, solid oxide electrolysis cells (SOECs) have gained popularity for higher efficiency and lower pollution and even no pollution. SOEC is an energy conversion device that can convert electrical energy and heat to chemical energy, by splitting H₂O/CO₂ to produce H₂ and CO. The products H₂ and CO can be used as fuel in a solid oxide fuel cell (SOFC) to produce electricity or be stored as raw materials for the synthesis of hydrocarbons via the Fischer–Tropsch reaction.

SOEC technology is of great superiority and prospect. Among three main electrolysis configurations, it has been reported that the efficiency of hydrogen production by high temperature SOEC is more than twice of that by an Alkaline electrolysis cell, and is 1.5 times of that by proton exchange membrane electrolyzer [2]. There are mainly three kinds of SOEC according to reaction gas species: high temperature H₂O electrolysis, CO₂ electrolysis, H₂O and CO₂ co-electrolysis cell. Steam electrolysis can produce H₂, which is a completely environmentally friendly fuel. In addition, H₂O is rich in nature. CO₂ electrolysis is advantageous in that it can consume CO₂ and relieve the greenhouse effect, and the product CO is easier to store and transport than H₂. However, it has a potential carbon deposit risk. H₂O and CO₂ co-electrolysis can produce H₂ and CO mixtures, and by adjusting the inlet H₂O/CO₂ ratio, it can produce applicable hydrocarbon synthesis. The steam electrolysis has the highest electrolysis efficiency while CO₂ electrolysis has the lowest efficiency, and the efficiency of H₂O/CO₂ co-electrolysis is between them. Due to the environmental friendliness and higher efficiency of steam electrolysis, high temperature H₂O electrolysis attracts increased attention. With the increase of temperature, the electricity needed to electrolyze H₂O decreases, while the low quality heat needed increases. Moreover, high temperature SOEC is not only thermodynamically beneficial but also kinetically favorable. Hence, high temperature SOEC has a more promising application perspective.

Materials, performance and degradation issues are still three challenges of SOEC technology to be settled. Extensive research about SOEC concentrates on the optimization of material microstructure [3–5], geometrical [6] and operating parameters [7] and the analysis to improve SOEC performance. Notice, however, the structural size choice is also of great significance. For example, the authors of [8] studied the effect of cathode thickness on CO₂/H₂O co-electrolysis performance under various operating conditions by experiment, which reveals that SOEC performance can be substantially improved by decreasing cathode thickness. For the time being, most of the SOEC researches were conducted experimentally [2,9–12]. Unfortunately, the experiment is expensive and time-consuming, so research about structure optimization by experiment is rare. Simulation is an efficient alternative to help the design of SOEC/SOFC to improve performance, especially when exploring a large combination of operating and structural parameters space. For example, Reference [1,11–13] studied the influence of pressure on SOEC. Ni et al. [14] researched electrode thickness, support type, electrode porosity and pore size and operating pressure on SOEC performance. It is concluded that anode-supported SOEC has the best output performance. Kong et al. [15] examined the impacts of different electrode-rib contact resistances, fuel compositions, electrode porosity, electrode thicknesses and electrode conductivity on the optimal anode and cathode ribs of SOFC independently.

The development of SOEC is later than that of SOFC. As the reverse process of SOFC, SOEC has basically the same materials system as SOFC. The research of SOFC is enlightening to the development of SOEC. In the last 20 years, during the simulation of SOFC, it found out that rib width design is of great significance to improve the cell performance [15–18], which has also been experimentally confirmed [19]. Actually, as early as 2003, Lin [16] had provided a phenomenological model and analytical expressions to estimate the rib effects on the concentration and ohmic polarization of anode-supported SOFC stacks. Jeon et al. [20] described a microstructure model and examined the influence of the rib and pitch widths and the electrode-interconnect contact area specific resistance (ASR) on the stack-cell performance. The authors of [17] investigated the effect of ASR between the electrode and the rib on the performance of SOFC, and conducted the rib width optimization by 2D SOFC multi-physical modes. In [18], the authors primarily compared the optimal rib width result attained by 2D and 3D multi-physical models, and revealed that the optimization result of 2D and 3D models are in good agreement. The authors of [15,21] optimized the anode and cathode rib width for anode-supported and cathode-supported SOFCs, respectively. An analytical expression of optimal rib width is deduced to help the engineering design of SOFC. In [22], the authors conducted the optimization of the cylindrical interconnect rib width of SOFC, and it found out that anode and cathode rib width should be optimized separately, which is in consistent with the conclusion in Reference [21].

Reference [23] studied the influence of rib size on the performance of a reversible solid oxide cell. It takes into account the efficiency of a solid oxide fuel cell and electrolysis cell comprehensively.

However, the polarization process of SOEC is vastly different from SOFC. During past years, to our knowledge, it is still not clear how to choose the rib width when fabricating the SOEC interconnector characterized by the rib-channel structure, i.e., the optimization of rib width has not been clearly addressed. This paper conducts a comprehensive parameter sensitivity analysis on the rib width optimization of SOEC by 2D multi-physics simulations. Analytical expressions for the optimal cathode rib width design are obtained to provide an easy-to-use guide for designing the rib-channel layout of SOEC.

2. Model Description

A typical unit of SOECs contains a dense electrolyte sandwiched by a porous anode and cathode, channels and inter-connector. To obtain better electrochemical performance, a relatively denser and thinner porous layer are generally added between the electrode and electrolyte, which is called the function layer. The working principle of SOEC is illustrated in Figure 1a. Figure 1b shows a 2D cross section of the SOEC repeating unit, displaying the rib-channel design parameters: the pitch width, d_{pitch} , and the rib width, d_{rib} . The multi-physics coupled modeling is applied to a pitch unit of SOEC and considers the mass, species, momentum transfer processes, the current conduction and the electrochemical reaction.

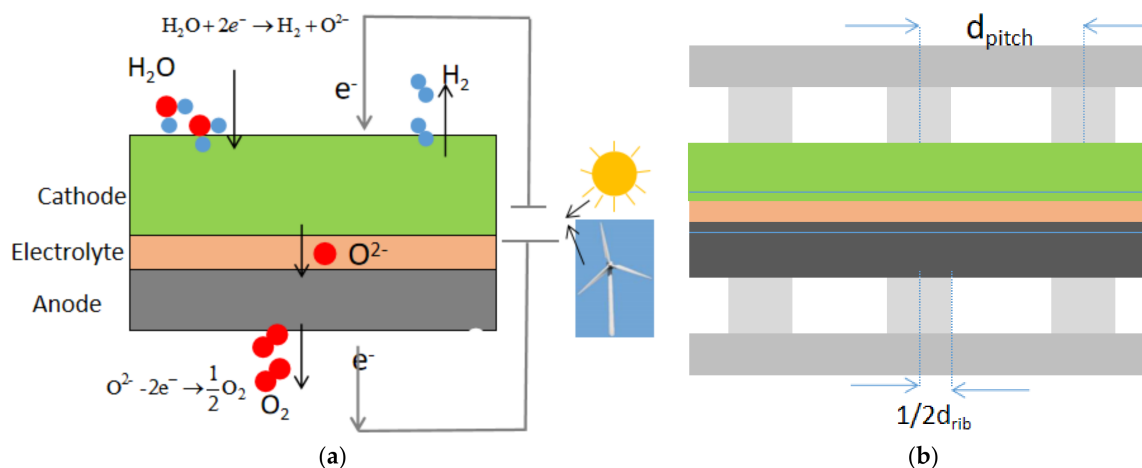


Figure 1. (a) Schematic of solid oxide electrolysis cell (SOEC) working principle; (b) a cross section of a SOEC repeating unit.

2.1. Species Transfer Process

The species conservation equation can be expressed as:

$$\nabla \cdot \vec{N}_i = \nabla \cdot (-D_i^{eff} C_i + C_i \vec{u}) = S_i \quad (1)$$

$$S_{H_2} = \frac{j}{2F} \quad (2)$$

$$S_{H_2O} = -\frac{j}{2F} \quad (3)$$

$$S_{O_2} = \frac{j}{4F} \quad (4)$$

Here, N_i is the total molar flux vector, which includes the convective flow and the diffusion flow. D_i^{eff} , C_i , and S_i are effective diffusion coefficient, molar concentration and source or sink of species

i , respectively. S_i is source or sink of species i by electrochemical consumption and production in the electrode.

The species diffusion is modeled by a multi-component Dusty–Gas model [24], which is proved to be the most accurate model to simulate gas diffusion in a porous electrode of SOFC [25]. A binary molecular diffusion coefficient is generally used directly in channels, where gas convective transfer rather than the diffusion transfer is dominant, and the binary molecular mutual diffusion coefficient is expressed as [18]:

$$D_{ij} = \frac{2.198 \times T^{1.75}}{P \left(V_i^{1/3} + V_j^{1/3} \right)} \left(\frac{1}{M_i} + \frac{1}{M_j} \right)^{0.5} \quad (5)$$

where T , v_i and M_i is the temperature, diffusion volume and mole mass of species i . P is the total gas pressure.

In the electrode, the influence of porosity and tortuosity should be considered to describe the effective binary molecular diffusion coefficient:

$$D_{ij}^{eff} = \frac{\epsilon}{\tau} D_{ij} \quad (6)$$

ϵ , τ are porosity and tortuosity of the electrode, respectively.

In the electrode, molecular mutual diffusion dominates when the electrode pore is larger than the molecular mean free path, while Knudsen diffusion becomes primary when the pore size is small and the collision between the species and pore wall increases. The effective Knudsen diffusion coefficient is expressed as:

$$D_{ik}^{eff} = \frac{2\epsilon}{3\tau} r_g \sqrt{\frac{8RT}{\pi M_i}} \quad (7)$$

Here r_g is pore radius, and r_g is expressed as:

$$r_g = \frac{2}{3} * \frac{1}{1 - \epsilon} * \frac{1}{\varphi_{el}/r_{el} + \varphi_{io}/r_{el}} \quad (8)$$

Considering both molecular diffusion and Knudsen diffusion simultaneously, the effective diffusion coefficient in the electrode is formally expressed as [18]:

$$D_i^{eff} = \frac{D_{ij}^{eff} D_{ik}^{eff}}{D_{ij}^{eff} + x_i D_{jk}^{eff} + x_j D_{ik}^{eff}} \quad (9)$$

2.2. Electrochemical Reaction Model

The electrochemical reactions include the H_2O reduction reaction at the fuel electrode and the oxidation reaction at the O_2 electrode, which are expressed as:



The electronic current and ion current are governed by charge continuity equations:

$$\nabla \cdot \vec{i}_{el} = \nabla \cdot (-\sigma_{el}^{eff} \nabla \phi_{el}) = \begin{cases} j_{TPB} \lambda_{TPB}^{eff} & \text{fuel electrode} \\ -j_{TPB} \lambda_{TPB}^{eff} & \text{air electrode} \end{cases} \quad (12)$$

$$\nabla \cdot \vec{i}_{io} = \nabla \cdot (-\sigma_{io}^{eff} \nabla \phi_{io}) = \begin{cases} -j_{TPB} \lambda_{TPB}^{eff} & \text{fuel electrode} \\ 0 & \text{electrolyte} \\ j_{TPB} \lambda_{TPB}^{eff} & \text{air electrode} \end{cases} \quad (13)$$

$$j_{TPB} = j_0 \left[\exp\left(\frac{n\alpha F\eta}{RT}\right) - \exp\left(-\frac{n\beta F\eta}{RT}\right) \right] \quad (14)$$

where n is the number of electrons transferred in the electrochemical reaction, i_{el} and i_{io} are the electronic and ionic current density vector, ϕ_{el} , ϕ_{io} are the electronic and ionic potential. $\lambda_{TPB,eff}$ is the effective three phase boundary (TPB) density per unit. j_{TPB} is the current density at TPB.

Nernst potential is the minimum cell voltage needed to drive an electrochemical reaction in SOEC:

$$E_{nerst} = \frac{-\Delta G}{2F} + \frac{RT}{2F} \ln\left(\frac{P_{H_2}}{P_{H_2O}}\right) + \frac{RT}{4F} \ln\left(\frac{P_{O_2}}{P_0}\right) \quad (15)$$

Here, ΔG is the Gibbs free energy change of electrochemical reaction. P_{H_2} , P_{O_2} , P_{H_2O} are partial pressures of H_2 , O_2 and H_2O . P_0 is the standard atmospheric pressure.

The applied voltage in an operating SOEC is:

$$V_{cell} = E_{nerst} + \eta_{ohmic} + \eta_{act} + \eta_{con} \quad (16)$$

where η_{ohmic} , η_{act} , η_{con} are ohmic, activation and concentration loss, respectively. Ohmic loss is induced by the conductivity resistance of electron and ion transfer in solid components and is calculated according to Ohm's law:

$$\eta_{ohm} = j * ASR_{ohm} \quad (17)$$

Here, ASR_{ohm} is total area specific resistance.

The occurrence of the electrochemical reaction needs to overcome the reaction activation energy barrier, leading to irreversible activation loss. The relationship between current density and the activation loss is described by the Butler–Volmer equations:

$$\begin{cases} j_{0,H_2} = j_{0,H_2}^{ref} \exp\left(-\frac{E_{H_2}}{R} \left(\frac{1}{T} - \frac{1}{T_{ref}}\right)\right) \left(\frac{P_{H_2} P_{H_2O}}{P_{H_2,ref} P_{H_2O,ref}}\right) \\ j_{0,O_2} = j_{0,O_2}^{ref} \exp\left(-\frac{E_{O_2}}{R} \left(\frac{1}{T} - \frac{1}{T_{ref}}\right)\right) \left(\frac{P_{O_2}}{P_{O_2,ref}}\right)^{0.25} \end{cases} \quad (18)$$

The concentration polarization is induced by a change of species concentration when SOEC is in operation:

$$\eta_{concen,a} = \frac{RT}{2F} \ln\left(\frac{P_{H_2} P_{H_2O,ref}}{P_{H_2,ref} P_{H_2O}}\right) \quad (19)$$

$$\eta_{concen,a} = \frac{RT}{4F} \ln\left(\frac{P_{O_2}}{P_{O_2,ref}}\right) \quad (20)$$

E_{O_2} and E_{H_2} are, respectively, the activation energies for the O_2 and H_2 electrode electrochemical reactions.

2.3. Effective Material Property Model

The intrinsic material conductivity is temperature dependent [1,6,15,26]:

$$\sigma_{Ni}^0 = 3.27 \times 10^6 - 1065.3T \quad (21)$$

$$\sigma_{YSZ}^0 = 6.25 \times 10^4 \times \exp(-10,300/T) \quad (22)$$

$$\sigma_{LSCF}^{el} = 22,591 - 1.6 \times 10^6 \times \exp(-6024/T) \quad (23)$$

$$\sigma_{LSCF}^{io} = 1.1 \times 10^9 \times \exp(-181,000/R/T) \quad (24)$$

$$\sigma_{GDC}^0 = 3.5 \times 10^3 \times 10^{(-6471/T)} \quad (25)$$

where R is the universal gas constant.

For the porous electrode, the relationship between the material macro property and microstructure can be expressed by coordination number theory and percolation theory [27]:

$$\sigma_k^{\text{eff}} = \sigma_k^0 * \left(\frac{\varphi_k - \varphi_k^t}{1 + \varepsilon / (1 - \varepsilon) - \varphi_k^t} \right)^2 \quad (26)$$

where σ_k^0 is the intrinsic electric conductivity of the k^{th} phase material in the dense solid. φ_k is the volume fraction of the k^{th} phase particles in the composite material, φ_k^t is the percolation threshold volume fraction of the k phase particles, which is determined by

$$Z \frac{\psi_{\text{el}}^t / r_{\text{el}}}{\psi_{\text{el}}^t / r_{\text{el}} + (1 - \psi_{\text{el}}^t) / r_{\text{io}}} = 1.764 \quad (27)$$

$$Z \frac{\psi_{\text{io}}^t / r_{\text{io}}}{(1 - \psi_{\text{io}}^t) / r_{\text{el}} + \psi_{\text{io}}^t / r_{\text{io}}} = 1.764 \quad (28)$$

where Z is the average coordination number for each particle and set as six for a random packing of spheres [15]. r_{el} and r_{io} are, respectively, the electronic conductivity particle radius and the ionic conductivity particle radius.

LSCF is a material that can conduct electrons and ions simultaneously. For the LSCF-GDC composite electrode, the effective electronic conductivity is expressed as:

$$\sigma_{\text{el}}^{\text{eff}} = \sigma_{\text{LSCF}}^{\text{el}} [(1 - \varepsilon) \varphi_{\text{LSCF}} P_{\text{LSCF}}^t]^\gamma \quad (29)$$

The effective ionic conductivity can be considered as the parallel current conduction of LSCF and GDC. The ionic conductivity of the composite electrode is expressed as:

$$\sigma_{\text{io}}^{\text{eff}} = \sigma_{\text{LSCF}}^{\text{io}} [(1 - \varepsilon) \varphi_{\text{LSCF}} P_{\text{LSCF}}^t]^\gamma + \sigma_{\text{GDC}}^{\text{io}} [(1 - \varepsilon) \varphi_{\text{GDC}} P_{\text{GDC}}^t]^\gamma \quad (30)$$

where γ is a Bragg factor and is usually set as 1.5. P_k is the percolation probability of phase k . Both the percolation probabilities of LSCF and GDC are assumed to be 1.

The TPB density per unit volume of a composite electrode with a binary mixture is expressed as [27]:

$$\lambda_{\text{TPB}} = 2\pi \min(r_{\text{el}}, r_{\text{io}}) \sin\left(\frac{\theta}{2}\right) n n_{\text{io}} Z_{\text{io-el}} P_{\text{el}} P_{\text{io}} \quad (31)$$

The relevant physical quantities are expressed as follows,

$$P_k = \left(1 - \left(\frac{3.764 - Z_{k,k}}{2} \right)^{2.5} \right)^{0.4} \quad (32)$$

$$Z_{k,k} = Z * \frac{\varphi_k / r_k}{\varphi_{\text{el}} / r_{\text{el}} + \varphi_{\text{io}} / r_{\text{io}}} \quad (33)$$

$$n = \frac{1 - \varepsilon}{\frac{4\pi}{3} r_{\text{el}}^3 (n_{\text{el}} + (1 - n_{\text{el}}) \gamma^3)} \quad (34)$$

$$n_{\text{el}} = \frac{\varphi_{\text{el}} \gamma^3}{1 - \varphi_{\text{el}} + \gamma^3 \varphi_{\text{el}}} \quad (35)$$

$$n_{\text{io}} = 1 - n_{\text{el}} \quad (36)$$

$$Z_{\text{io-el}} = \frac{Z}{2} \left(1 + \frac{r_{\text{io}}^2}{r_{\text{el}}^2} \right) \frac{\varphi_{\text{el}} / r_{\text{el}}}{\varphi_{\text{el}} / r_{\text{el}} + \varphi_{\text{io}} / r_{\text{io}}} \quad (37)$$

More details about the specific symbols are referred to in [27].

The multi-physics simulations are conducted with the commercial finite element software COMSOL 4.3b. Simulations were first carried out to reproduce the performance of an experimental cell that is designated as the standard cell. The parameters used to reproduce the experiment are listed in Table 1, and are referred to as the standard parameter set. Unless explicitly stated otherwise, the parametric analysis was conducted by varying one parameter as the variable while all the other parameters are kept as the standard case.

Table 1. Basic model parameters used in the standard cell modeling.

	CSL (NiO + YSZ)	CFL (NiO + YSZ)	Electrolyte (YSZ)	Diffusion Barrier Layer (GDC)	Anode (LSCF + GDC)
Thickness (um)	400	10	15	3	25
ϵ	0.4	0.3	0	0.05	0.4
Tortusity	30	30	-	3	3
E_{H_2} (Kj/mol)	-	120 [28]	-	-	-
E_{O_2} (Kj/mol)	-	-	-	-	120 [14]
σ_{el}^{eff} (S/m)	71,728	71,728	-	-	2806
σ_{io}^{eff} (S/m)	-	0.087	2.65	5.8	1.18
α, β	-	0.5,0.5	-	-	0.5,0.5
r_g (um)	0.6	0.3	-	-	0.55
Phase Volume Fraction	50%:50%	50%:50%	100%	100%	50%:50%

2.4. Model Verification

To verify the multi-physics model of SOEC, simulated I–V data are compared with our experimental results. The experimental cell contains a cathode support layer (CSL), a cathode function layer (CFL), an electrolyte, a diffusion barrier layer and the anode. CSL and CFL are mixtures of nickle oxide (NiO) and yttria stabilized zirconia (YSZ), and the electrolyte is a dense YSZ layer. The composite anode is made of $La_{0.6}Sr_{0.4}Co_{0.2}Fe_{0.8}O_{3-\delta}$ (LSCF) and $Ce_{0.9}Gd_{0.1}O_{1.95}$ (GDC). The diffusion barrier layer (GDC) is sandwiched between anode and electrolyte to avoid formation of the insulating phase. The SOEC is operating at 750 °C with the inlet gas $H_2O:H_2 = 0.9:0.1$ at the cathode side and $O_2:N_2 = 0.21:0.79$ at the anode side. Furthermore, the pitch width and rib width are 2 and 1 mm, respectively. The contact resistance is set at $0.056 \Omega cm^2$ as deduced by our impedance measurement. The other parameters used to reproduce the experiment are listed in Table 1. The micro-structure parameters are taken from the literature experiments [29–32].

As can be seen from Figure 2, the experimental and simulation results agree well, demonstrating the validity of the multi-physics model. Naturally, some discrepancies between the experimental and theoretical I–V curves are observed. Nevertheless, the theoretical and experimental difference is less than 0.02 V for any given current densities.

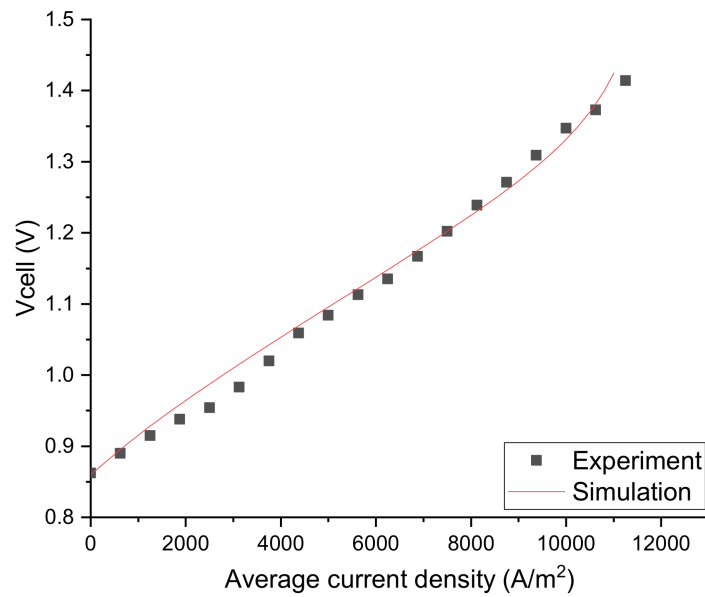


Figure 2. Comparison of experimental and simulated I–V curves.

3. Results

3.1. Parameters Sensitivity Analysis for Rib Width Optimization at the H₂ Electrode Side

As seen in Figure 3, the current density first increases to a peak value then decreases with the increase of rib width. This is quite understandable as the concentration loss increases and the ohmic loss decreases when the rib width increases. Therefore, there is an optimized rib width d_{rib-m} where the current density reaches its maximum value. When $d_{rib} < d_{rib-m}$, with the increase of rib width, the decrease of ohmic loss is higher than the increase of concentration loss, the current density tends to increase. When $d_{rib} > d_{rib-m}$, with the increase of rib width, the decrease of ohmic loss is smaller than the increase of concentration loss, and the current density decreases. The competition between the concentration polarization and the ohmic polarization determines the final optimized rib width.

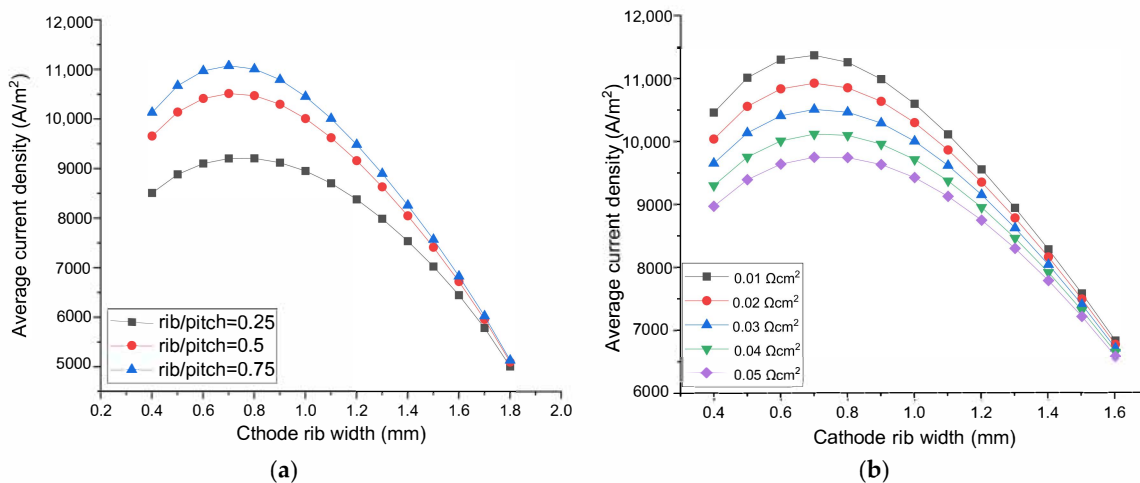


Figure 3. Cont.

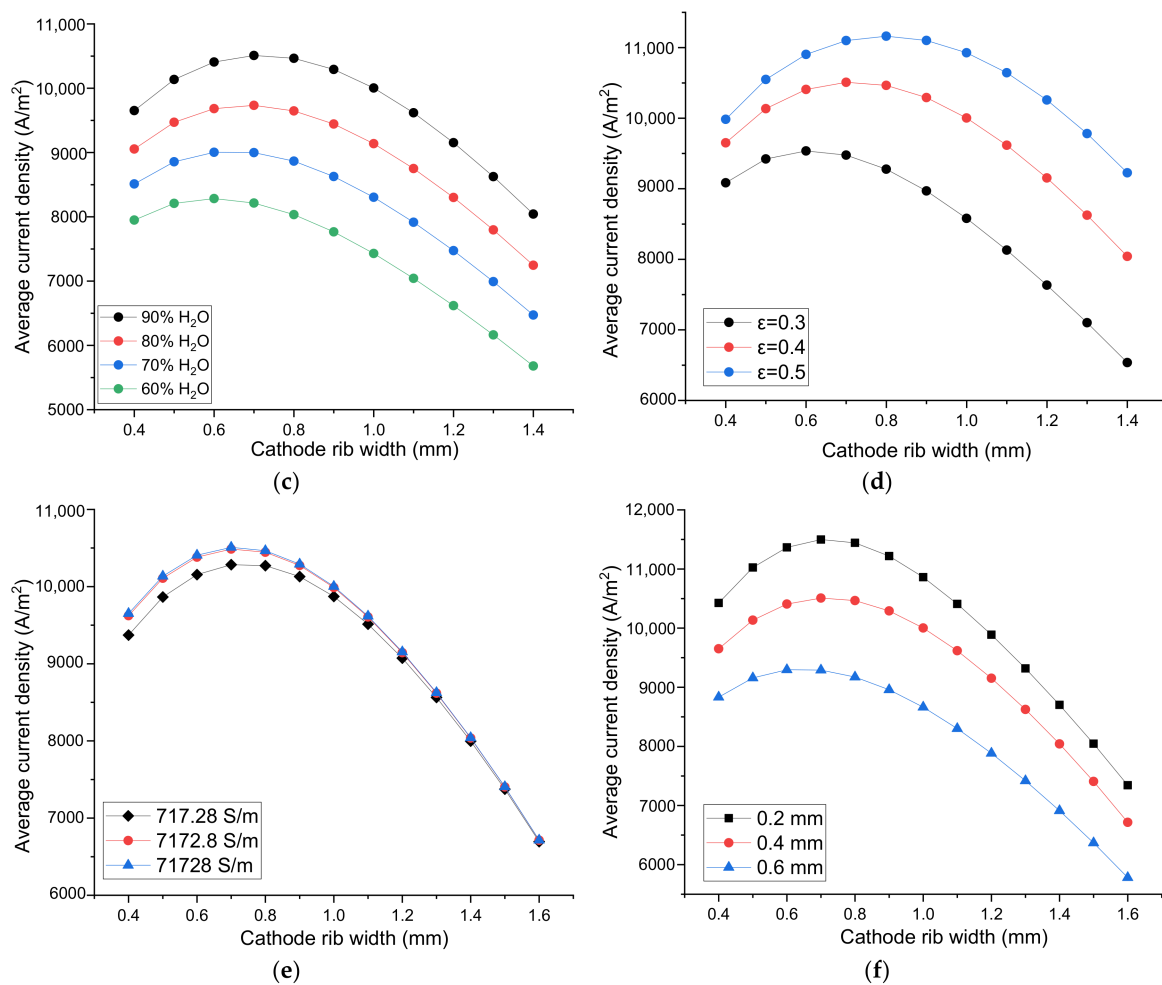


Figure 3. The effect of rib width on the SOEC performance. Parameter on the O₂ electrode side: (a) the rib/pitch ratio, (b) the rib-electrode ASR. Parameter on the H₂ electrode side: (c) Inlet H₂O content, (d) Electrode porosity, (e) Electrode conductivity, (f) Electrode thickness.

As shown in Figure 3a, when the rib/pitch width ratio at the O₂ electrode side increases from 0.25 to 0.5 then to 0.75, the optimized H₂ electrode rib width is 0.752, 0.720, 0.710 mm, respectively. Notice, however, although the optimized rib widths are different, the width of 0.72 mm is sufficiently optimal for all the O₂ electrode rib/pitch ratio conditions. The maximum current density difference between optimal rib width and 0.72 mm are only 0.05%, 0.007% for the rib/pitch ratio of 0.25 and 0.75, respectively. Therefore, it is concluded that the optimized rib width at the H₂ electrode side is not sensitive to the rib/pitch ratio at the O₂ electrode side.

The experimentally measured ASR of SOFC is in the range 0.01–0.05 Ωcm² [33]. SOEC has the same electrode and inter-connector materials. However, the oxidation atmosphere of both the electrodes of SOEC means potentially larger oxidation risk of inter-connector than SOFC, so the maximum ASR studied here is 0.08 Ωcm². ASR of both the electrodes in the range of 0.04–0.08 Ωcm² is used to conduct parameter sensitivity analysis to optimize rib width. To study the parameters' influence on the rib width optimization at one electrode side, ASR of another electrode side is set as 0.03 Ωcm². As displayed in Figure 3b, when ASR between the O₂ electrode and rib increases from 0.01 to 0.05 Ωcm², the current density decreases gradually because of the increased ohmic loss. The optimized H₂ electrode rib width is 0.689, 0.705, 0.720, 0.734, 0.746 mm when ASR at the O₂ electrode side are 0.01, 0.02, 0.03, 0.04, 0.05 Ωcm², respectively. However, when choosing 0.72 mm as the optimal rib width for the other four cases, the differences between the maximum current density at the optimal rib width and the current density with a rib width of 0.72 mm are 0.0756%, 0.0165%,

0.0128%, 0.04% for ASR 0.01, 0.02, 0.04, 0.05 Ωcm^2 , respectively. Hence, the optimized rib width on the H_2 electrode side is not sensitive to the ASR on the O_2 electrode side.

Along the fuel flow direction, H_2O is consumed gradually, the molar fraction of H_2O changes correspondingly. Furthermore, for practically operating SOEC, high H_2O conversion rate is favorable, so the research about the rib width optimization should take into account different H_2O molar fractions. Figure 3c shows, for a fixed rib width, the current density increases with the increase of H_2O molar fraction. This is because the Nernst potential decreases and the electrochemical reaction rate increases with the increased H_2O molar fraction, and the current density increases when the applied voltage is fixed. The optimal rib width is 0.720, 0.687, 0.648, 0.602 mm when H_2O molar fractions are 90%, 80%, 70%, 60%, respectively. Because with the increase of H_2O molar fraction, current density increases, concentration polarization and ohmic polarization both increase simultaneously, which leads to a slight change in the optimized rib width. This result is also in accordance with that of SOFC [15]. Nevertheless, 0.65 mm width is sufficiently optimal for SOEC with different H_2O molar fraction, because the difference between the maximum current density and the current density at the rib width of 0.65 mm is only 0.0002%, 0.0004%, 0.0001%, 0.0028% for SOEC with the inlet H_2O molar fraction of 90%, 80%, 70%, 60%, respectively. The optimized rib width can be considered independent of the H_2O fraction.

The SOEC H_2 electrode porosity is in the range of 0.3–0.5 [34]. As shown in Figure 3d, the optimal rib width increases with the increase of electrode porosity due to the reduced gas diffusion resistance. For the porosity of 0.3, 0.4, 0.5, the optimized rib width is 0.616, 0.720, 0.800 mm, respectively. Even the optimized rib width for the three porosities seems to be quite different, the maximum current densities for porosity 0.3 and 0.5 are only 0.98% and 0.35% higher than the current density with a rib width of 0.720 mm. Therefore, the optimized rib width is not sensitive to the H_2 electrode porosity.

As shown in Figure 3e, when the H_2 electrode electrical conductivity increases from 717.28 to 7172.8 S/m, the current density increases relatively drastically. However, when H_2 electrode electrical conductivity increases from 7172.8 to 71,728 S/m, the current density has almost no change. It means that the electrical conductivity of 7172.8 S/m is large enough, electrical conductivity larger than 7172.8 S/m has no evident improvement for SOEC performance. The optima rib width for the electrode electric conductivity of 717.28, 7172.8 and 71,728 S/m is 0.741, 0.722 and 0.719 mm, respectively. However, using a rib width of 0.720 mm, the current density differs from the maximum only by 0.03% for the conductivity of 717.28 S/m, and virtually zero for the conductivity of 71,728 and 7172.8 S/m. Hence, the optimal rib width is basically independent of the electrode conductivity.

As seen in Figure 3f, the performance of SOEC decreases with the increase of H_2 electrode thickness. The increase of electrode thickness means longer gas diffuse path from the channel-electrode interface to the active three phase boundary. The diffusion process becomes more difficult, and the concentration loss increases accordingly. Moreover, a thicker electrode inevitably leads to larger ohmic loss for current in the thickness direction. Hence, the overall SOEC performance decreases when electrode thickness increases. However, as the electrode thickness increases, the optimized rib width changes only slightly. The optimized rib width for the electrode thickness of 0.2, 0.4 and 0.6 are 0.719, 0.720 and 0.646 mm, respectively. However, the width of 0.720 mm is sufficiently optimal. The current density for the rib width of 0.72 mm differs only 0.006% and 0.41% from the maximum for the electrode thickness of 0.2 and 0.6 mm, respectively. Therefore, the optimal rib width is insensitive to the electrode thickness. The reason behind this is that both the concentration and ohmic polarizations increase comparatively at the same time when the electrode thickness increases.

As displayed in Figure 4a, fixing the rib width, the current density decreases significantly with the increase of rib–electrode ASR due to directly the increased ohmic polarization loss. Moreover, the optimal H_2 electrode rib width increases, because the increased ohmic loss due to the increase of ASR can be partially offset by increasing the rib width. As seen in Figure 4b, the optimized rib width increases almost linearly with the increase of ASR. When ASR increases from 0.01 to 0.05 Ωcm^2 , the optimized rib width increases from 0.511 to 0.840 mm, or an increase of 64.4%. This ASR effect

is quite dramatic. With the increase of ASR, the current density decreases, the concentration loss decreases passively. The increased ohmic loss and the decreased concentration loss collectively leads to the dramatic increase of the optimal rib width.

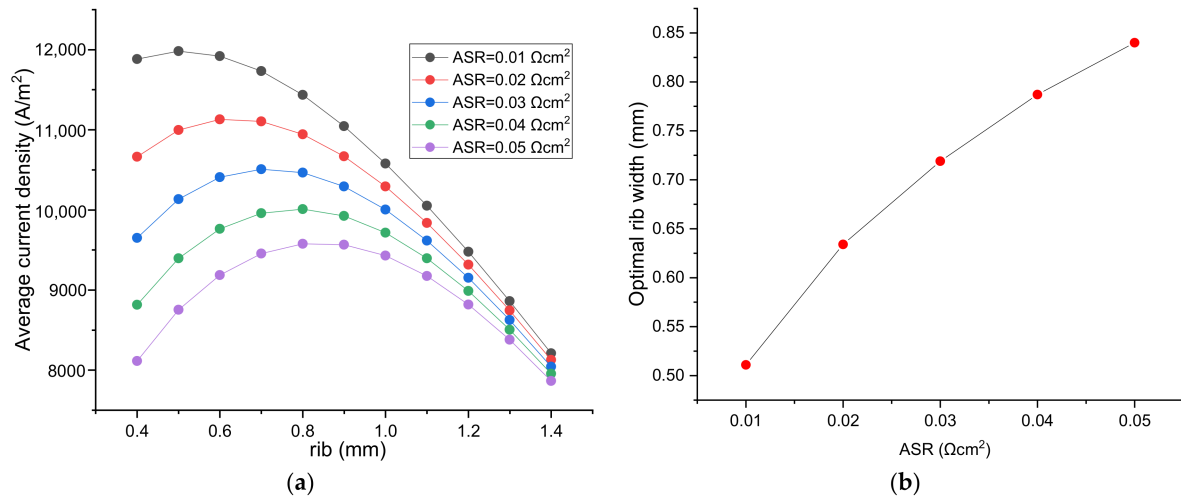


Figure 4. (a) The effect of ASR of the H₂ electrode and rib interface on SOEC performance and the optimized rib width; (b) The relationship between optimal rib width and ASR.

3.2. Parameters Sensitivity Analysis for the Rib Width Optimization on the O₂ Electrode Side

As can be seen in Figure 5a, with the increase of rib/pitch ratio on the H₂ electrode side, the current density decreases, which can be attributed to the increased concentration polarization in the cathode due to the increased rib width. When the rib/pitch ratio increases from 0.25 to 0.5, the SOEC performance decreases slightly. However, when the rib/pitch ratio increases from 0.5 to 0.75, the SOEC performance decreases drastically. It can be inferred that when the rib/pitch ratio exceeds 0.5, the negative effect of the concentration loss increase is far greater than the positive effect of the ohmic loss decrease as induced by the increase of the H₂ electrode rib width. However, when the rib width on the O₂ electrode side increases, the current density increases all the way, independent of the rib/pitch ratio on the H₂ electrode side, indicating the optimized rib width on the O₂ electrode side is not sensitive to the rib/pitch ratio on the H₂ electrode side.

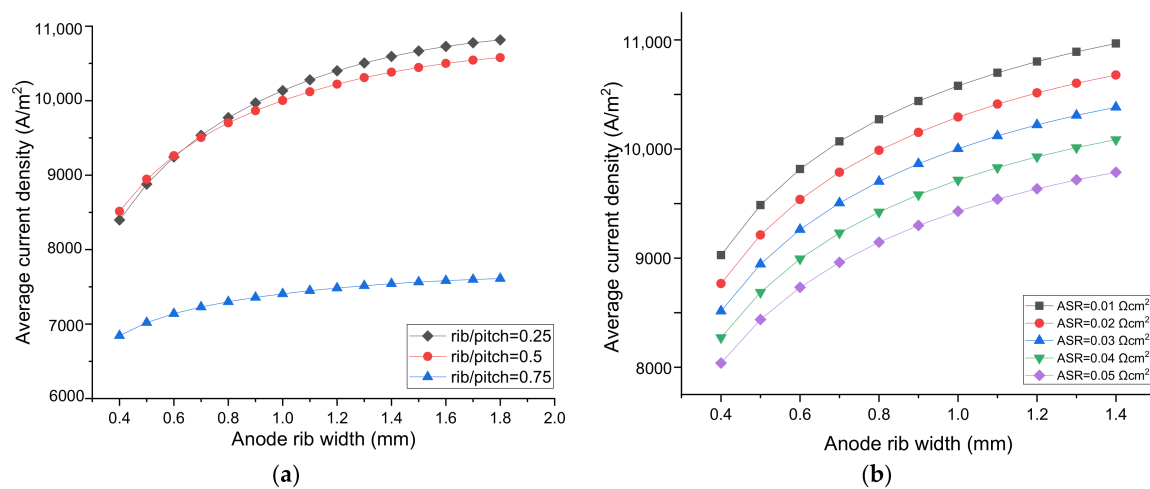


Figure 5. Cont.

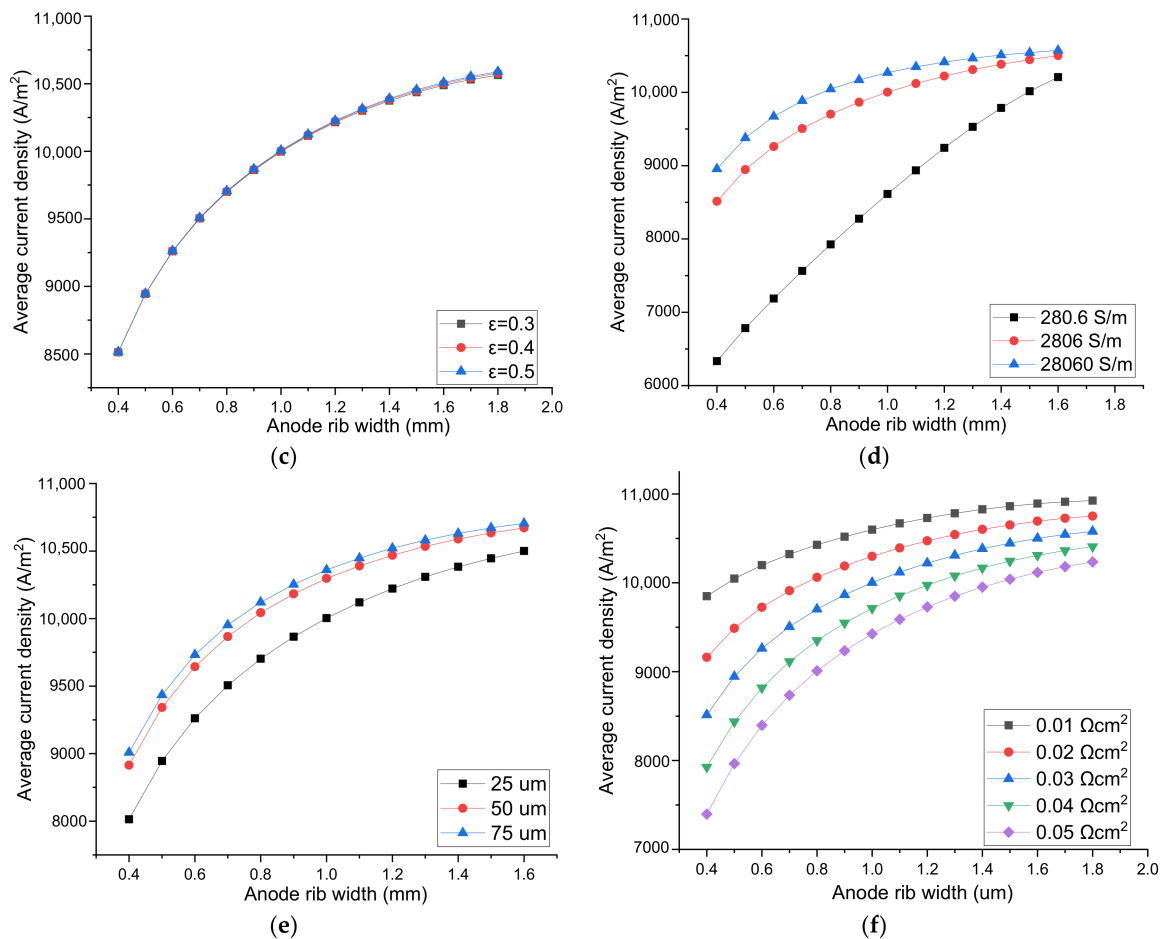


Figure 5. The effect of parameters on SOEC performance and the optimal O_2 electrode rib width. H_2 electrode parameters: (a) rib/pitch ratio on the H_2 electrode side; (b) rib- H_2 electrode area specific resistance (ASR); O_2 electrode parameters: (c) porosity; (d) electrical conductivity; (e) thickness; (f) rib- O_2 electrode ASR.

As shown in Figure 5b, when ASR on the H_2 electrode side increases from $0.01 \Omega\text{cm}^2$ to $0.05 \Omega\text{cm}^2$, the current density decreases gradually. For a fixed ASR, the current density increases with the increased rib width on the O_2 electrode side, independent of the ASR change on the H_2 electrode side. Hence, the optimized O_2 —electrode rib width is not sensitive to the ASR of the H_2 electrode.

Figure 5c shows the current density increases extremely slightly with the increase of O_2 electrode porosity from 0.3 to 0.4 then to 0.5, indicating the polarization loss induced by O_2 diffusion inside the anode is rather small. This is also ascribed to the thinness of the O_2 electrode. Furthermore, the current density increases with the increase of rib width, for all the anode porosities examined. It can be concluded that the optimal O_2 -electrode rib width is independent of the O_2 electrode porosity.

Figure 5d shows the current density increases with the increase of the O_2 electrode electrical conductivity, due to the decreased ohmic polarization. The current density increases more dramatically when the conductivity increases from 280.6 to 2806 S/m, but increases slightly when the conductivity increases from 2806 to 28,060 S/m, indicating the ohmic polarization is no longer a major factor limiting the cell performance when the anode conductivity is above 2806 S/m. For a fixed conductivity, the current density increases with the increase of rib width. The increase of current density with the rib width is quite large for the low conductivity of 280.6 S/m, but only moderate for the conductivity of 2806 and 28,060 S/m, indicating a conductivity of 2806 S/m is adequately high for the anode.

Figure 5e shows the current density increases with the increase of O_2 electrode thickness, which is opposite to the trend of the cathode shown in Figure 4f. The opposite trends imply that the major

polarization factors in the anode and cathode are different. The concentration loss is more influential than the ohmic polarization in the cathode, while the ohmic polarization is much larger than the concentration polarization in the anode. The thicker anode increases the difficulty of both the O₂ diffusion and the current conduction along the electrode thickness direction. However, the current passage through the narrow cross section of the electrode to the rib is the main ohmic polarization loss. The increase of electrode thickness can reduce the major ohmic loss and improves the SOEC performance, as observed experimentally [19]. For all the anode thicknesses considered, the current density increases with the increased O₂ electrode rib width, due to the reduced ohmic polarization by the shorter conduction path.

As shown in Figure 5f, fixing the rib width, the SOEC performance decreases with the increased anode ASR due to the increased ohmic loss. Meanwhile, the current density increases continuously with the increase of rib width, independent of the ASR value, confirming the concentration loss is far lower than the ohmic loss in the O₂ electrode. The optimal rib width can be quite close to the whole pitch size.

3.3. Analytical Expression of the Optimal Rib/Pitch Ratio on the H₂ Electrode Side

From Figure 6, it can be seen that with the increase of pitch width, the optimal rib width increases, while the optimal rib/pitch ratio (R) decreases. Furthermore, for a SOEC with pitch width 2 mm and ASR 0.01 Ωcm², the optimal rib width is 0.387 and 0.603 mm when loaded with applied voltage 1.6 and 1.2 V, increasing by 56%, so the influence of the applied voltage on optimal rib width cannot be ignored. The specific voltage is meaningless, the possible influence factor is the total polarization loss $\eta = V_{\text{cell}} - E_{\text{nerst}}$. However, here the explored total polarization change is induced only by applied voltage change. Combining the parameters sensitivity analysis above, it can be distinguished that ASR, polarization loss and pitch width from all the parameters studied as the major factors affecting optimal rib width. Here we take the rib/pitch ratio into consideration, and analytically express the relationship between optimal rib/pitch ratio with pitch width, rib-electrode ASR, total polarization loss. Finally, we get the expression for the applicable voltage range 1.2–1.6 V for SOEC. The optimal rib/pitch ratio is denoted as R_{1.2V}, R_{1.4V}, R_{1.6V}.

$$R_{1.2V} = (-0.4294 \times \text{ASR} - 0.03264) \times d_{\text{pitch}} + (5.2165 \times \text{ASR} + 0.33022) \quad (38)$$

$$R_{1.4V} = (-0.3804 \times \text{ASR} - 0.02809) \times d_{\text{pitch}} + (4.7373 \times \text{ASR} + 0.27819) \quad (39)$$

$$R_{1.6V} = (-0.2994 \times \text{ASR} - 0.01684) \times d_{\text{pitch}} + (4.3912 \times \text{ASR} + 0.19651) \quad (40)$$

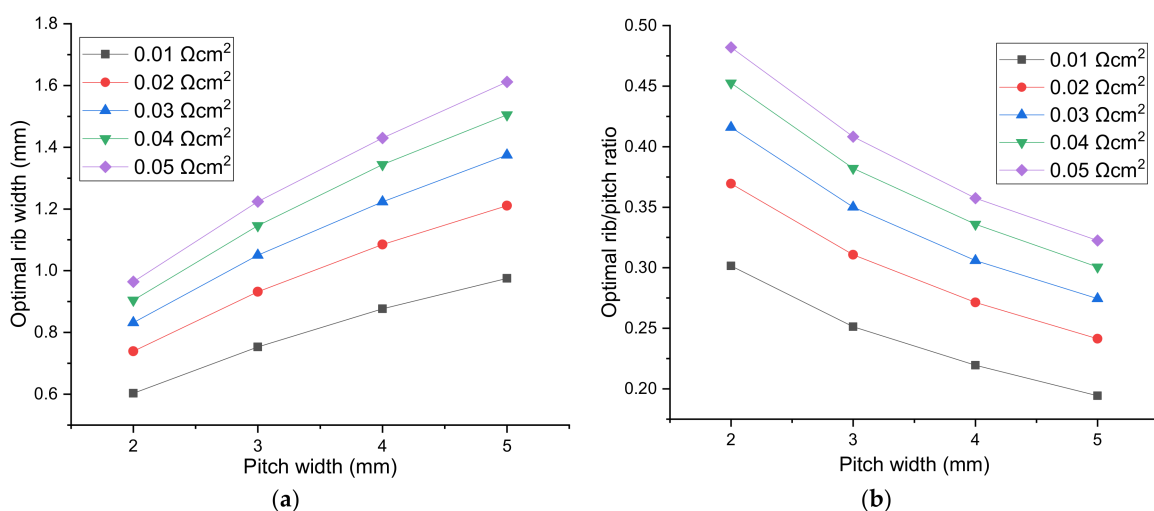


Figure 6. Cont.

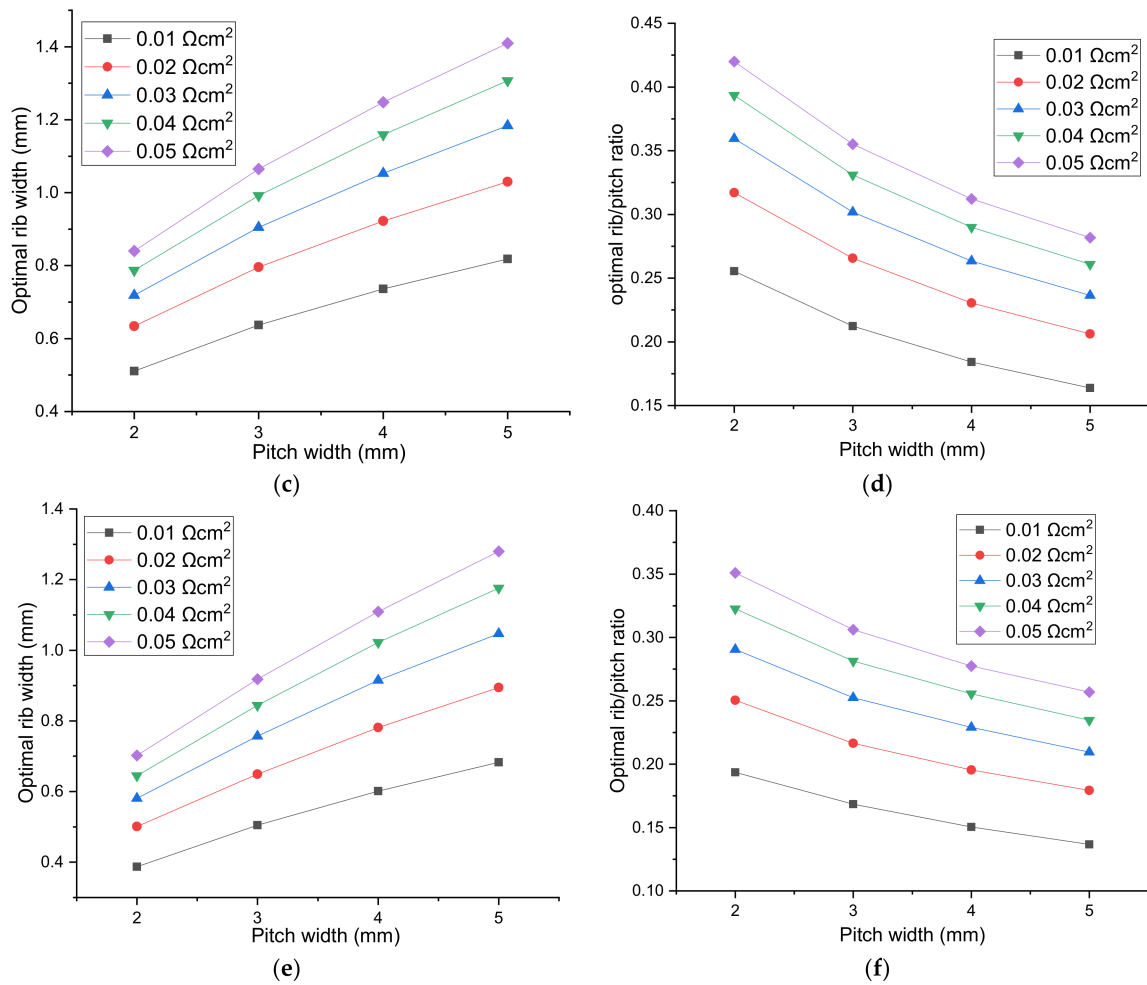


Figure 6. The optimal H₂ electrode rib width and rib/pitch ratio for different pitch width for the cell voltage of (a,b): 1.2 V; (c,d): 1.4 V; (e,f): 1.6 V.

R can be expressed generally as $R = (a_1 \cdot ASR + a_2) + (a_3 \cdot ASR + a_4)$. The total polarization for SOEC with applied voltage 1.2, 1.4, 1.6 is 0.34, 0.54, 0.74, respectively. The four sets of coefficients are listed in Table 2 and the relationship between the coefficients and η is displayed in Figure 7.

Table 2. Coefficient of R.

η	a1	a2	a3	a4
0.34	-0.4294	-0.03264	5.1265	0.33022
0.54	-0.3804	-0.02809	4.7373	0.27819
0.74	-0.2994	-0.01684	4.3912	0.19651

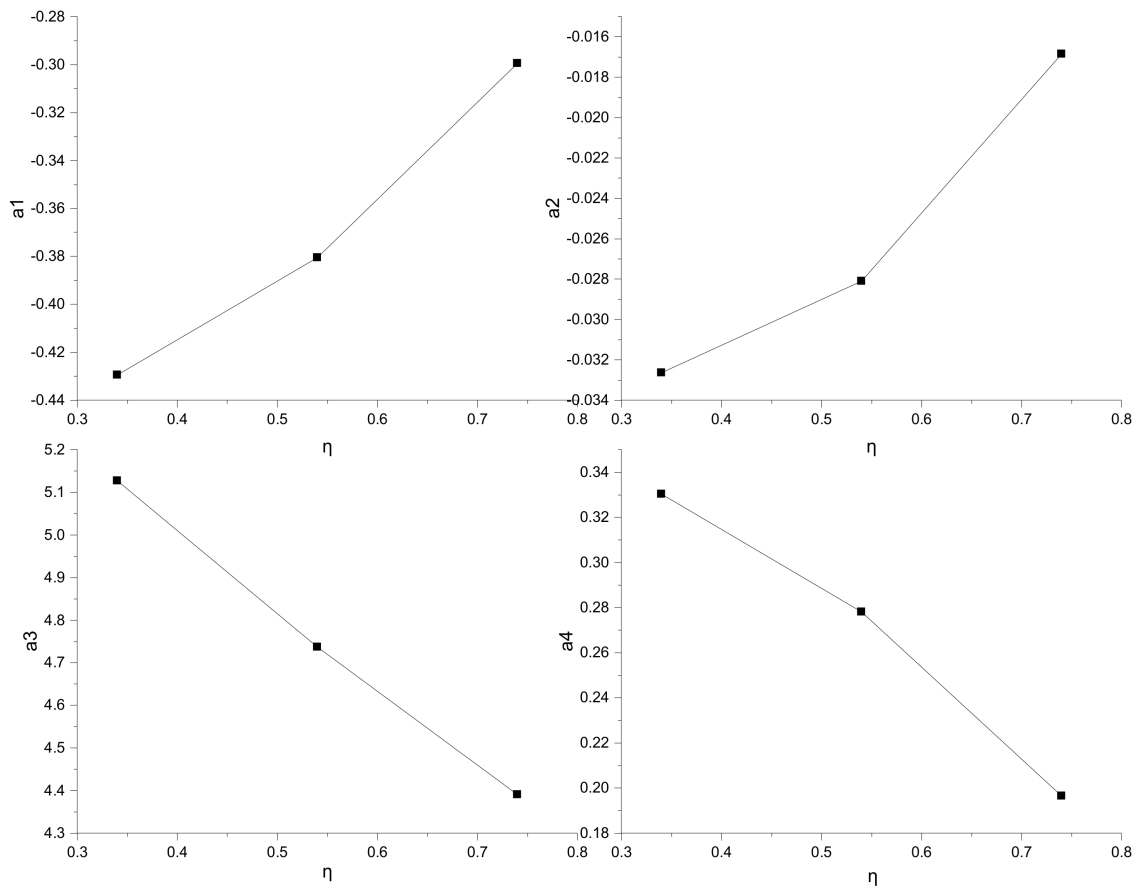


Figure 7. The relationship between coefficient a1, a2, a3, a4 and η.

By simplifying the relationship between a₁, a₂, a₃, a₄ and η, a₁ = 0.325η – 0.54523, a₂ = 0.0395η – 0.04719, a₃ = –2.06325η + 5.89582, a₄ = –0.33428η + 0.4488 are obtained to describe the relationship between η and a₁, a₂, a₃, a₄ linearly. The synthetic expression of R considering the influence of pitch width, rib—electrode ASR, and the total polarization is formulated as:

$$R = [(0.325 \times \eta - 0.54523) \times ASR + (0.0395 \times \eta - 0.04719)] \times d_{pitch} + [(-2.06325 \times \eta + 5.89582) \times ASR + (-0.33428 \times \eta + 0.44882)] \quad (41)$$

It should be pointed out that in Equation (41), the units of ASR, η, d_{pitch} are Ωcm², V, mm, respectively. Subsequently, the optimal rib can be formulated as:

$$d_{rib,a} = [(-2.06325 \times \eta + 5.89582) \times ASR + (-0.33428 \times \eta + 0.44882)] \times d_{pitch} + [(0.325 \times \eta - 0.54523) \times ASR + (0.0395 \times \eta - 0.04719)] \times d_{pitch}^2 \quad (42)$$

Here, d_{rib,a} (mm) is the optimal rib width obtained analytically. It should be noted that even the d_{rib,a} (mm) is the quadratic function of d_{pitch}, the coefficient for the first order term is an order of magnitude larger than the quadratic term. Therefore, the relationship between optimal rib width and pitch width is mainly linear.

To verify the reliability of Equation (42), two accuracy parameters are defined as

$$\lambda_1 = \frac{i_{max-n} - i_{max-a}}{i_{max-n}} \quad (43)$$

$$\lambda_2 = \frac{d_{rib-n} - d_{rib-a}}{drib - n} \quad (44)$$

where $i_{\max-n}$ is the maximum current density corresponding to the optimal rib width $d_{\text{rib-n}}$ obtained numerically. $i_{\max-a}$ is the maximum current density for the analytically predicted optimal rib width $d_{\text{rib-a}}$. λ_1, λ_2 are defined to evaluate the effectiveness of the analytical expression for predicting optimal rib width. Even the maximum margin of error for optimal rib width (λ_2) is about 8.575%, the current density for the analytically predicted optimal rib is only 0.14% different from the maximum current density for the numerically attained optimal rib width. Hence, the cathode rib width predicted by Equation (42) is sufficiently optimal.

4. Conclusions

We have developed a comprehensive mathematical model for the performance research of SOEC. The impacts of the electrode rib widths on SOEC performance are systematically examined by varying the contact resistance, fuel composition, electrode porosity, electrode thickness and electrode electric conductivity. Different from rib width at the H₂ electrode side, the optimal rib width at the O₂ electrode side is not so sensitive to ASR and other parameters. With the increase of rib width, current density almost increases all the way, because the concentration polarization at the O₂ electrode side is too small, the ohmic loss induced by ASR is overwhelmingly greater than concentration loss. Nevertheless, the current density increase rate decreases when rib width is large enough. More importantly, it finds out three main factors affecting optimal rib width at the H₂ electrode side: ASR at the rib–electrode interface, the pitch width, and the applied cell voltage. Giving the pitch width and contact resistance, the optimal rib width decreases with the increase of cell voltage. Giving the cell voltage and contact resistance, the optimal rib width increases and the optimal rib/pitch ratio decreases with the increase of pitch width. When ASR at H₂ electrode side is in the range of (0.01, 0.05) Ωcm^2 , the optimal rib width at the cell voltage of 1.4 V is in the range (0.511, 0.840), (0.637, 1.065), (0.736, 1.248) and (0.818, 1.410) mm for the corresponding pitch width of 2, 3, 4 and 5 mm, respectively. Finally, an analytical expression is proposed to formulate the relationship between the optimal rib width and total polarization loss, ASR, and pitch width. The prediction error between the maximum current density obtained by numerically and analytically optimal rib width is within 0.14%, proving the predictive ability of the analytical expression.

Author Contributions: Conceptualization, M.G.; methodology, M.G. and Z.L.; validation, M.G. and X.R.; formal analysis, M.G. and Z.L.; investigation, M.G., X.R. and G.X.; data curation, M.G. and G.X.; writing—original draft preparation, M.G.; writing—review and editing, M.G. and Z.L.; supervision, Z.L.; project administration, Z.L. and J.W.; funding acquisition, Z.L. and J.W. All authors have read and agreed to the published version of the manuscript.

Funding: This research was funded by the National Natural Science Foundation of China (11774324 & 12074362), the Strategic Priority Research Program of the Chinese Academy of Sciences (XDA 21080200) and the Youth Innovation Promotion Association of the Chinese Academy of Sciences (2018298).

Acknowledgments: The financial support of the National Natural Science Foundation of China (11774324 & 12074362), the Strategic Priority Research Program of the Chinese Academy of Sciences (XDA 21080200) and the Youth Innovation Promotion Association of the Chinese Academy of Sciences (2018298) are gratefully acknowledged.

Conflicts of Interest: The authors declare no conflict of interest.

References

1. Lee, S.J.; Jung, C.Y.; Yi, S.C. Computational analysis on the electrode geometric parameters for the reversible solid oxide cells. *Electrochim. Acta* **2017**, *242*, 86–99. [[CrossRef](#)]
2. Liu, T.L.; Wang, C.; Hao, S.J.; Fu, Z.Q.; Peppley, B.A.; Mao, Z.M.; Wang, J.L.; Mao, Z.Q. Evaluation of polarization and hydrogen production efficiency of solid oxide electrolysis stack with La_{0.6}Sr_{0.4}Co_{0.2}Fe_{0.8}O_{3- δ} -Ce_{0.9}Gd_{0.1}O_{1.95} oxygen electrode. *Int. J. Hydrogen Energy* **2016**, *41*, 15970–15978. [[CrossRef](#)]
3. Hauch, A.; Brodersen, K.; Chen, M.; Mogensen, M.B. Ni/YSZ electrodes structures optimized for increased electrolysis performance and durability. *Solid State Ion.* **2016**, *293*, 27–36. [[CrossRef](#)]

4. Wang, Y.; Yang, Z.; Han, M.; Chang, J. Optimization of Sm_{0.5}Sr_{0.5}CoO_{3-δ}-infiltrated YSZ electrodes for solid oxide fuel cell/electrolysis cell. *RSC Adv.* **2016**, *6*, 112253–112259. [[CrossRef](#)]
5. Shao, L.; Wang, S.; Qian, J.; Ye, X.; Wen, T. Optimization of the electrode-supported tubular solid oxide cells for application on fuel cell and steam electrolysis. *Int. J. Hydrogen Energy* **2013**, *38*, 4272–4280. [[CrossRef](#)]
6. Li, W.; Shi, Y.; Luo, Y.; Cai, N. Theoretical modeling of air electrode operating in SOFC mode and SOEC mode: The effects of microstructure and thickness. *Int. J. Hydrogen Energy* **2014**, *39*, 13738–13750. [[CrossRef](#)]
7. Baldinelli, A.; Barelli, L.; Bidini, G. Performance characterization and modelling of syngas-fed SOFCs (solid oxide fuel cells) varying fuel composition. *Energy* **2015**, *90*, 2070–2084. [[CrossRef](#)]
8. Mahmood, A.; Bano, S.; Yu, J.H.; Lee, K.H. Performance evaluation of SOEC for CO₂/H₂O co-electrolysis: Considering the effect of cathode thickness. *J. Co₂ Util.* **2019**, *33*, 114–120. [[CrossRef](#)]
9. Zheng, Y.; Li, Q.; Chen, T.; Wu, W.; Xu, C.; Wang, W.G. Comparison of performance and degradation of large-scale solid oxide electrolysis cells in stack with different composite air electrodes. *Int. J. Hydrogen Energy* **2015**, *40*, 2460–2472. [[CrossRef](#)]
10. Leng, Y.; Chan, S.H.; Liu, Q. Development of LSCF-GDC composite cathodes for low-temperature solid oxide fuel cells with thin film GDC electrolyte. *Int. J. Hydrogen Energy* **2008**, *33*, 3808–3817. [[CrossRef](#)]
11. Riedel, M.; Heddrich, M.P.; Friedrich, K.A. Analysis of pressurized operation of 10 layer solid oxide electrolysis stacks. *Int. J. Hydrogen Energy* **2019**, *44*, 4570–4581. [[CrossRef](#)]
12. Fan, H.; Keane, M.; Singh, P.; Han, M.J. Electrochemical performance and stability of lanthanum strontium cobalt ferrite oxygen electrode with gadolinia doped ceria barrier layer for reversible solid oxide fuel cell. *J. Power Sources* **2014**, *268*, 634–639. [[CrossRef](#)]
13. Henke, M.; Willich, C.; Kallo, J.; Friedrich, K.A. Theoretical study on pressurized operation of solid oxide electrolysis cells. *Int. J. Hydrogen Energy* **2014**, *39*, 12434–12439. [[CrossRef](#)]
14. Ni, M.; Leung, M.K.H.; Leung, D.Y.C. Parametric study of solid oxide steam electrolyzer for hydrogen production. *Int. J. Hydrogen Energy* **2007**, *32*, 2305–2313. [[CrossRef](#)]
15. Kong, W.; Li, J.; Liu, S.; Lin, Z. The influence of interconnect ribs on the performance of planar solid oxide fuel cell and formulae for optimal rib sizes. *J. Power Sources* **2012**, *204*, 106–115. [[CrossRef](#)]
16. Lin, Z.; Stevenson, J.W.; Khaleel, M.A. The effect of interconnect rib size on the fuel cell concentration polarization in planar SOFCs. *J. Power Sources* **2003**, *117*, 92–97. [[CrossRef](#)]
17. Liu, S.; Song, C.; Lin, Z. The effects of the interconnect rib contact resistance on the performance of planar solid oxide fuel cell stack and the rib design optimization. *J. Power Sources* **2008**, *183*, 214–225. [[CrossRef](#)]
18. Liu, S.; Kong, W.; Lin, Z. Three-dimensional modeling of planar solid oxide fuel cells and the rib design optimization. *J. Power Sources* **2009**, *194*, 854–863. [[CrossRef](#)]
19. Kornely, M.; Leonide, A.; Weber, A.; Ivers-Tiffée, E. Performance limiting factors in anode-supported cells originating from metallic interconnector design. *J. Power Sources* **2011**, *196*, 7209–7216. [[CrossRef](#)]
20. Jeon, D.H.; Nam, J.H.; Kim, C.-J. Microstructural Optimization of Anode-Supported Solid Oxide Fuel Cells by a Comprehensive Microscale Model. *J. Electrochem. Soc.* **2006**, *153*, A406. [[CrossRef](#)]
21. Kong, W.; Gao, X.; Liu, S.; Su, S.; Chen, D. Optimization of the interconnect ribs for a cathode-supported solid oxide fuel cell. *Energies* **2014**, *7*, 295–313. [[CrossRef](#)]
22. Gao, X.; Zhang, Q.; Zhang, W.; Chen, D. Optimization of distributed cylindrical interconnect ribs for anode- and cathode-supported solid oxide fuel cell. *Int. J. Electrochem. Sci.* **2015**, *10*, 7521–7534.
23. Nguyen, V.N.; Fang, Q.; Packbier, U.; Blum, L. Long-term tests of a Jülich planar short stack with reversible solid oxide cells in both fuel cell and electrolysis modes. *Int. J. Hydrogen Energy* **2013**, *38*, 4281–4290. [[CrossRef](#)]
24. Kong, W.; Zhu, H.; Fei, Z.; Lin, Z. A modified dusty gas model in the form of a Fick's model for the prediction of multicomponent mass transport in a solid oxide fuel cell anode. *J. Power Sources* **2012**, *206*, 171–178. [[CrossRef](#)]
25. Tseronis, K.; Kookos, I.K.; Theodoropoulos, C. Modelling mass transport in solid oxide fuel cell anodes: A case for a multidimensional dusty gas-based model. *Chem. Eng. Sci.* **2008**, *63*, 5626–5638. [[CrossRef](#)]
26. Yang, C.; Wang, J.; Zhao, J.; Wu, Y.; Shu, C.; Miao, H.; Wang, F.; Ye, W.; Yuan, J. CFD modeling and performance comparison of solid oxide fuel cell and electrolysis cell fueled with syngas. *Int. J. Energy Res.* **2019**, *43*, 2656–2677. [[CrossRef](#)]
27. Chen, D.; Lin, Z.; Zhu, H.; Kee, R.J. Percolation theory to predict effective properties of solid oxide fuel-cell composite electrodes. *J. Power Sources* **2009**, *191*, 240–252. [[CrossRef](#)]

28. Zhu, H.; Kee, R.J. Modeling distributed charge-transfer processes in SOFC membrane electrode assemblies. *J. Electrochem. Soc.* **2008**, *155*, B715. [CrossRef]
29. Kim, S.J.; Choi, G.M. Stability of LSCF electrode with GDC interlayer in YSZ-based solid oxide electrolysis cell. *Solid State Ion.* **2014**, *262*, 303–306. [CrossRef]
30. Jiang, S.P. Sintering behavior of Ni/Y2O3-ZrO2 cermet electrodes of solid oxide fuel cells. *J. Mater. Sci.* **2003**, *38*, 3775–3782. [CrossRef]
31. Çelikbilek, O.; Siebert, E.; Jauffrès, D.; Martin, C.L.; Djurado, E. Influence of sintering temperature on morphology and electrochemical performance of LSCF/GDC composite films as efficient cathode for SOFC. *Electrochim. Acta* **2017**, *246*, 1248–1258. [CrossRef]
32. Reddy, K.R.; Karan, K. Sinterability, mechanical, microstructural, and electrical properties of gadolinium-doped ceria electrolyte for low-temperature solid oxide fuel cells. *J. Electroceram.* **2005**, *15*, 45–56. [CrossRef]
33. Wei, W.; Chen, W.; Ivey, D.G. Oxidation resistance and electrical properties of anodically electrodeposited Mn-Co oxide coatings for solid oxide fuel cell interconnect applications. *J. Power Sources* **2009**, *186*, 428–434. [CrossRef]
34. Lee, T.-R.; Im, H.N.; Jeon, S.Y.; Yoo, Y.S.; Chavan, A.U.; Song, S.J. Dependence of H₂O/CO₂ Co-Electrolysis Performance of SOEC on Microstructural and Thermodynamic Parameters. *J. Electrochem. Soc.* **2016**, *163*, F728–F736. [CrossRef]

Publisher’s Note: MDPI stays neutral with regard to jurisdictional claims in published maps and institutional affiliations.



© 2020 by the authors. Licensee MDPI, Basel, Switzerland. This article is an open access article distributed under the terms and conditions of the Creative Commons Attribution (CC BY) license (<http://creativecommons.org/licenses/by/4.0/>).

Article

Hydrolysis-Based Hydrogen Generation Investigation of Aluminum System Adding Low-Melting Metals

Zeng Gao ^{1,*}, Fei Ji ¹, Dongfeng Cheng ¹, Congxin Yin ¹, Jitai Niu ² and Josip Brnic ³ 

¹ School of Materials Science and Engineering, Henan Polytechnic University, Jiaozuo 454003, China; jifei0108@163.com (F.J.); cdf_alex@hpu.edu.cn (D.C.); Ycx7469@163.com (C.Y.)

² School of Materials Science and Engineering, Harbin Institute of Technology, Harbin 150001, China; jtn@hit.edu.cn

³ Faculty of Engineering, University of Rijeka, 51000 Rijeka, Croatia; brnic@riteh.hr

* Correspondence: gaozeng@hpu.edu.cn

Abstract: In this age of human civilization, there is a need for more efficient, cleaner, and renewable energy as opposed to that provided by nonrenewable sources such as coal and oil. In this sense, hydrogen energy has been proven to be a better choice. In this paper, a portable graphite crucible metal smelting furnace was used to prepare ten multi-element aluminum alloy ingots with different components. The microstructure and phase composition of the ingots and reaction products were analyzed by X-ray diffraction (XRD), scanning electron microscopy (SEM), and differential scanning calorimetry (DSC). The reaction was carried out in a constant temperature water bath furnace at 60 °C, and the hydrogen production performance of the multi-element aluminum alloys in different proportions was compared by the drainage gas collection method. The experimental results show that the as-cast microstructure of Al–Ga–In–Sn aluminum alloy is composed of a solid solution of Al and part of Ga, and a second phase of In₃Sn. After the hydrolysis reaction, the products were dried at 150 °C and then analyzed by XRD. The products were mainly composed of AlOOH and In₃Sn. Alloys with different compositions react at the same hydrolysis temperature, and the hydrogen production performance is related to the ratio of low-melting-point metal elements. By comparing two different ratios of Ga–In–Sn (GIS), the hydrogen production capacity and production rate when the ratio is 6:3:1 are generally higher than those when the ratio is 7:2:1. The second phase content affects the hydrogen production performance.

Keywords: low melting metal; Al-based alloy; metal smelting; hydrogen production



Citation: Gao, Z.; Ji, F.; Cheng, D.; Yin, C.; Niu, J.; Brnic, J. Hydrolysis-Based Hydrogen Generation Investigation of Aluminum System Adding Low-Melting Metals. *Energies* **2021**, *14*, 1433. <https://doi.org/10.3390/en14051433>

Academic Editor: Samuel Simon Araya

Received: 7 February 2021

Accepted: 2 March 2021

Published: 5 March 2021

Publisher's Note: MDPI stays neutral with regard to jurisdictional claims in published maps and institutional affiliations.



Copyright: © 2021 by the authors. Licensee MDPI, Basel, Switzerland. This article is an open access article distributed under the terms and conditions of the Creative Commons Attribution (CC BY) license (<https://creativecommons.org/licenses/by/4.0/>).

1. Introduction

With progress in science and technology, energy comes into focus for society in terms of quality of life. As the carrier of carbon-free energy, hydrogen is not only the lightest element but also the most abundant resource in nature. Hydrogen has a very high calorific value of combustion and is a clean and efficient ideal energy source [1–9]. The hydrolysis of aluminum is an environmentally friendly reaction, and the products are pollution-free. However, it is very easy to form a compact oxide film on the surface of aluminum. Breaking the oxide film becomes a key breakthrough point for hydrogen production [10–17]. Common methods include dissolving the oxide film in an acid alkaline and neutral solution, and preparing an aluminum alloy by ball milling and by activating it [18–22]. A common chemical hydrogen production method is to store the hydrogen in a hydrogen storage tank and to then transport it. The quality of hydrogen accounts for 5–7% of the quality of the storage tank [23]. Hydrogen production from a metal ingot reaction is not only more efficient but also more convenient for transportation and storage. As one of the most common metal elements, aluminum has many advantages such as low cost, abundant reserves, and good preservation. In particular, the alumina hydroxide generated after an aluminum hydrolysis reaction not only is pollution-free but also can

be reused [24]. Therefore, metal aluminum is the preferred raw material for hydrogen production by hydrolysis.

A.V. Ilyukhina et al. [16] used a series of low-melting-point alloys based on the metal gallium, such as Ga70-In30, Ga70-In25-Zn3, and Ga62-In25-Sn13, in an aluminum powder alloying treatment. When the content of the liquid alloy in the alloy was 5–10 wt.%, the hydrogen production performance of aluminum powder in 25 °C water had a small relationship with the contents of the activator. However, the hydrogen production rate decreased significantly when its content continued to decrease. The hydrolysis rate of aluminum powder depends on the hydrolysis temperature. Fan et al. [18] prepared a type of Al-Li powder alloy by mechanical ball milling. The maximum hydrogen production rate of the alloy at room temperature was 233 mL/(min·g) and the maximum hydrogen production was 743 mL/g. After that, the Al-5.3Ga-5.4Sn-2In-7.3Zn alloy was prepared by ball milling. The hydrogen production of aluminum alloy powder reached 770 mL/(g·Al) within 7 min, and the hydrogen production rate reached 77.3%. Gai et al. [22] studied the reaction of pure aluminum with different particle sizes and water at different temperatures. For a certain reaction temperature, the smaller the particle size, the greater the possibility of reaction. M.C Roul [19] proposed an activation mechanism of Al-X alloy (X = Zn, Hg, or In) that is the well-known aluminum alloy dissolution–redeposition mechanism, which became the theoretical basis of aluminum alloy activation mechanisms.

This experiment mainly uses alloying to treat metal aluminum. This method is based on adding low-melting-point metals, such as Ga, In, Sn, Ca, Mg, Zn, Bi, etc. The main reason for choosing an alloying method is that this method can hydrolyze metal aluminum in neutral solution or aqueous solution with a pH value close to neutral, which can significantly improve the activity of aluminum. For alloying methods, common treatment methods are ball milling and the smelting method; this experiment chooses the smelting method because the smelting method has the following advantages over the ball mill method: 1. The operational method is simple. 2. It has a small material loss during the experiment. 3. The precision of alloy composition is easy to control. 4. It is easier to control the hydrolysis speed during the hydrolysis process. 5. An alloy produced after ball milling is not easy to preserve and even has safety risks [25–28]. The alloy block after smelting and casting is easier to preserve. Only aluminum itself participates in the reaction, and the low-melting-point metal can be collected and reused after the reaction. This method greatly reduces the cost of preparing hydrogen, which is of great help to the development of hydrogen production by aluminum hydrolysis and has more scientific and practical value.

This article is improved based on the above research. The experiment uses a portable graphite crucible metal melting furnace, and continuously inert gas is introduced into the melting furnace to prevent oxidation. In such experimental conditions, to achieve a high rate of hydrogen production and to obtain ideal hydrogen production, a multi-element aluminum alloy was formed by adding low-melting-point metals (Ga, In, and Sn) in different proportions. Then, the content of aluminum in the alloy is changed to compare the influence of alloy composition on hydrogen production. Then, X-ray diffraction (XRD), differential scanning calorimetry (DSC), scanning electron microscopy (SEM), and other characterization methods are used for correlation analysis and to further study the phenomena involved.

2. Materials and Methods

2.1. Alloy Preparation

This study used a portable graphite crucible metal smelting furnace to prepare multiple aluminum alloys. The raw materials were industrial pure Al plates (99.99%), Ga blocks (99.99%), In particles (99.99%), and Sn particles (99.99%). The melting points of the metals are shown in Table 1.

Table 1. The melting points of the metals.

Materials	Al	Ga	In	Sn
melting point (°C)	660.00	29.76	156.61	231.89

In the experiment, 10 types of Al-Ga-In-Sn aluminum alloy ingots with different composition ratios were prepared using the metal smelting method (sample numbers 1–10). We weighed a total of 20 g of different alloying elements and mixtures of different mass ratios into a custom-sized cylindrical quartz crucible and then put the quartz crucible into the melting furnace, continued to pass CO₂ into the furnace, and set the melting temperature of the melting furnace to 850 °C. The smelted alloy ingots were placed in sealed sample bags, and these sample bags were placed in a large amount of discolored silica gel particles to reduce oxidation. If necessary, we cut the ingot appropriately to obtain the appropriate size for later experiments. The alloy chemical compositions for experiment are shown in Table 2.

Table 2. Alloy compositions used for experiments.

Specimen No.	Element (wt.%)			
	Al	Ga	In	Sn
1#	50	35	10	5
2#	60	28	8	4
3#	70	21	6	3
4#	80	14	4	2
5#	90	7	2	1
6#	50	30	15	5
7#	60	24	12	4
8#	70	18	9	3
9#	80	12	6	2
10#	90	6	3	1

2.2. Observation of Phase Structure and Microstructure

The Merlin Compact scanning electron microscope (SEM) and the OXFORD energy spectrometer (EDS) attached to a microscope were used to analyze the microstructure and composition of the alloy ingot and the product after the hydrolysis reaction. In addition, SmartLab (9 kW) X-ray diffraction for phase analysis was used, with Cu K α as the radiation source, while other details were as follows: the scanning speed was 10–80°, the step size was 0.2°, and the acquisition and scanning speed was 10°/min. The thermodynamic monitoring and analysis of alloy ingots were analyzed by a Setaram Evolution 2400 thermal analyzer (TG-DSC). The measurement temperature range was 23–615 °C, and the scanning speed was 5 °C/min.

2.3. Test on Hydrolysis Performance of Aluminum Alloy

The test can be described as follows. We put 200 mL of tap water into a three-necked flask with a volume of 500 mL, placed it in an electronic constant temperature water bath furnace, and set the temperature of the water bath furnace to 60 °C. We cut out a 1 g sample and put it in the flask, then used the drainage method to calculate the amount of hydrogen generated, used an electronic weighing accuracy of 0.01 g to weigh the collected water, and used Equation (1) to convert the volume of hydrogen. The proportion of the sample was measured 3 times under certain conditions, and the final average value was taken. A schematic diagram of the hydrogen production reaction device is shown in Figure 1.

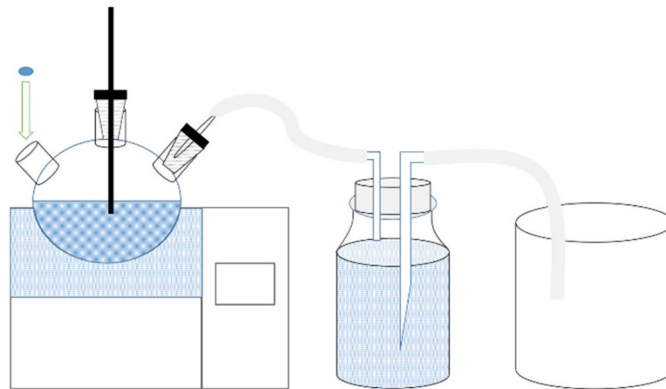


Figure 1. Schematic diagram of hydrogen production performance test device.

In reaction Equation (1), V is the volume of hydrogen generated, m is the mass of discharged water, and ρ is the density of water. We used Equation (2) to calculate the hydrogen production conversion rate of the alloy at different ratios. In the formula, $R1$ is the hydrogen production conversion rate, V is the actual hydrogen production volume, and VT is the theoretically calculated hydrogen production volume. The volume of 1 mol H_2 in standard state is 22.4 L, and the volume of H_2 produced by 1 g of aluminum is 1245 mL. The experiment was carried out at room temperature and atmospheric pressure (1 atm and 25 °C), and the volume of 1 mol H_2 under this condition was 24.45 L. The theoretical volume was 1358.4 mL of H_2 produced by 1 g of aluminum.

$$V = m/\rho, \quad (1)$$

$$R1 = V/VT \times 100\%, \quad (2)$$

The hydrogen production performance data were taken from the average of three experimental data, and the changes in hydrogen production and hydrogen production rate of multi-element aluminum alloys under different proportions were explored and rationally analyzed. After the reaction, the reactant obtained was dried in a drying oven at 150 °C before proceeding to the next step of analysis.

3. Results and Discussion

3.1. SEM Observation and Analysis

In order to study the microstructure of the alloy ingots, scanning electron microscopy and energy spectrum tests were carried out on the multi-element aluminum alloy ingots with different proportions. The sample was highly active and easily oxidized, so it needed to be quickly put into the sample table and vacuumed. It can be seen from Figure 2 that, under the microscopic conditions, when the proportion of Ga-In-Sn (GIS) is 50 wt.%, the surface structure appears granular. As the proportion of low-melting-point metals in the alloy decreases, the alloy surface becomes less grainy and the surface becomes smoother dense and slatted. As the alloy is solidified and formed after natural cooling in the molten state, a large amount of internal stress in the alloy leads to a fracture of the alloy during the nucleation process, resulting in a large number of voids and cracks in the alloy.

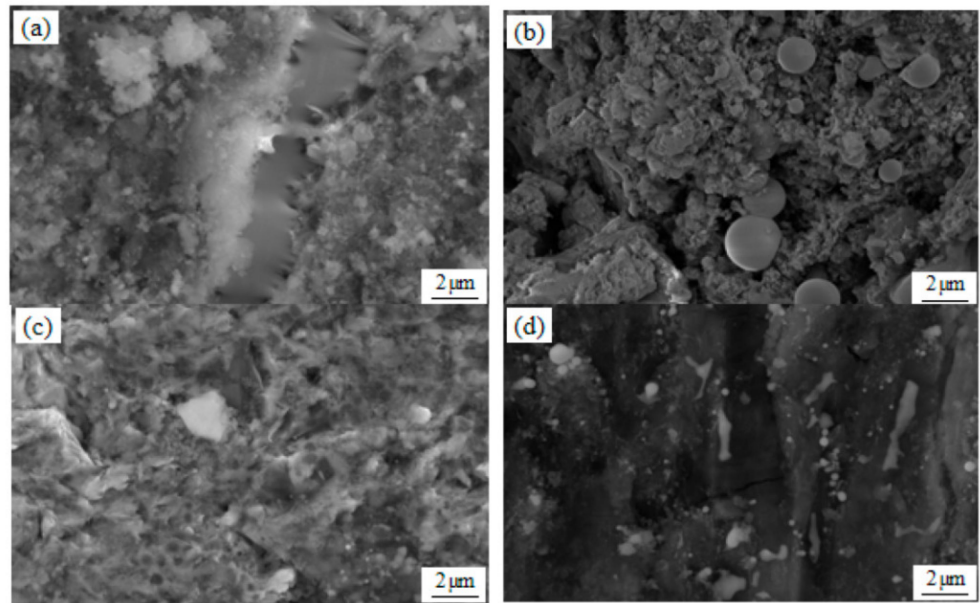


Figure 2. Scanning electron microscopy (SEM) image at 5000 \times of the aluminum alloy when the ratio of Ga-In-Sn is 7:2:1 and 6:3:1: (a) 50 wt.%Al-50 wt.%Ga-In-Sn (GIS) (7:2:1), (b) 50 wt.%Al-50 wt.%GIS (6:3:1), (c) 80 wt.%Al-20 wt.%GIS (7:2:1), and (d) 80 wt.%Al-20 wt.%GIS (6:3:1).

It can be seen from the EDS surface scan results in Figure 3 that a large amount of off-white low-melting alloy phases are scattered on the grain boundary surface of the alloy. Its main component is composed of low-melting-point metal Ga, followed by a small amount of In, Sn, and Al. Combined with the EDS surface scan, it can be observed that the distribution of elements in the alloy is relatively uniform, but there is still a certain degree of segregation. One of the main reasons for this phenomenon is that the solubility of the alloy decreases in the solid state. According to the alloy phase diagram, the degree of intermetallic compound formation is limited. Therefore, segregation occurs in a local area of the alloy. The second reason is that only a small amount of low-melting-point metal forms a solid solution with Al when the temperature drops. Large amounts of Ga, In, and Sn exist in the α -Al phase as segregation. According to Figure 2d, in addition to the spherical low-melting-point alloy phase, there are other alloy phases with different sizes. There are also a lot of low-melting metals in the gap. The main reason for the above phenomenon is that the metal aluminum solidifies in the form of dendrite during solidification. At the same time, the low-melting-point metal has limited solid solubility in aluminum, which leads to the liquid low-melting-point metal being squeezed into the cracks of aluminum grain. With the continuous decrease in temperature, the gap phases of different sizes are solidified and precipitated out. The size and shape of the gap phase are related to the proportion of low-melting-point metal in the alloy. The larger the proportion is, the more brittle the alloy, the more easily it is broken, and the larger the size of the gap phase.

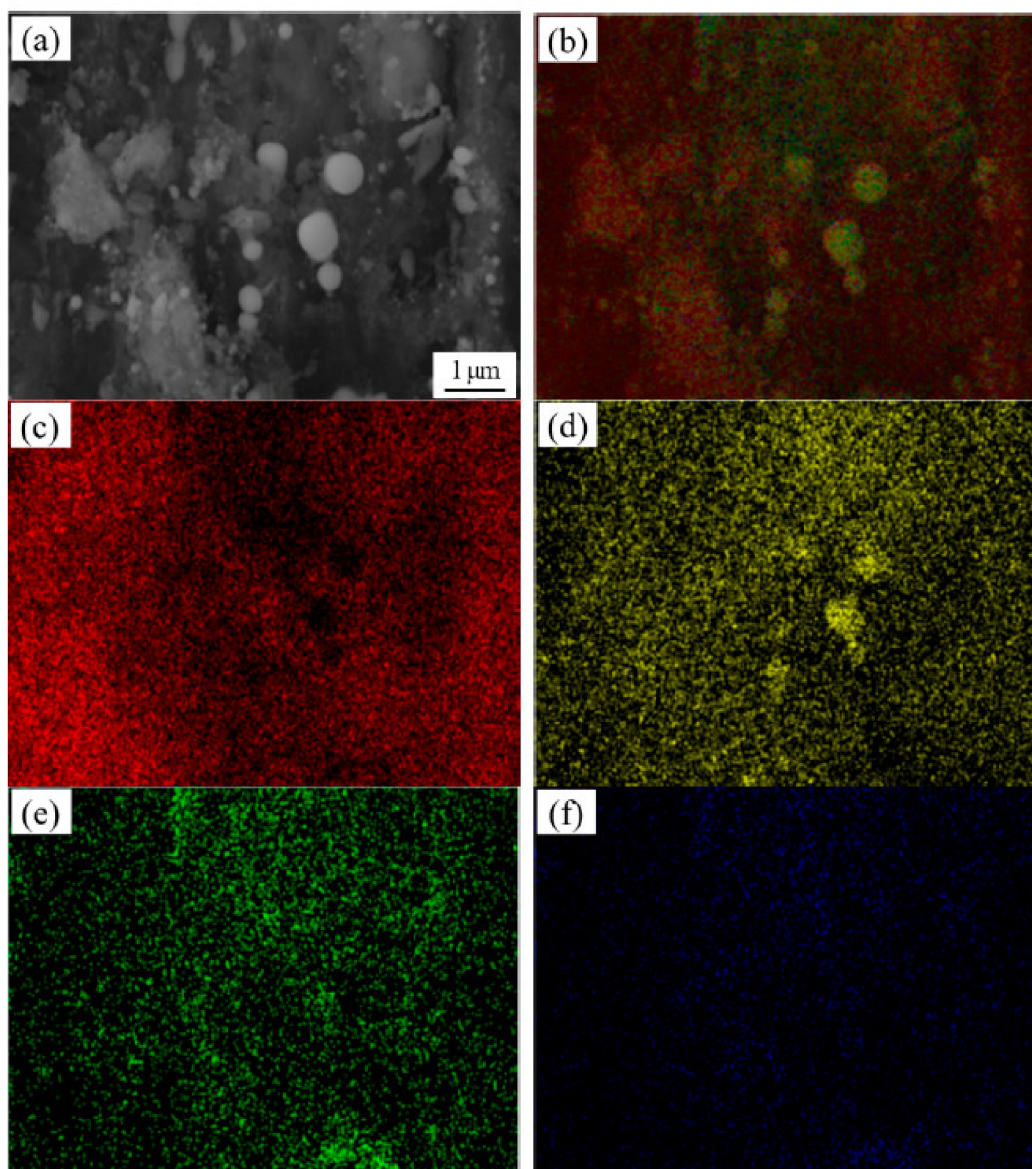


Figure 3. Scans of 80 wt.%Al-20 wt.%GIS (6:3:1) EDS surface of the alloy: (a) SEM diagram of the aluminum alloy at 10,000 \times , (b) EDS hierarchical image, (c) Al layer, (d) Ga layer, (e) In layer, and (f) Sn layer.

The microstructure of the reaction product after the hydrolysis reaction is shown in Figure 4. Observation at 1000 \times times shows that the morphology of the hydrolyzed product is lamellar, agglomerating together in a massive form. Compared with the alloy particles before the reaction, the degree of fragmentation is increased and a large amount of the internal structure of the particles is dispersed due to progress in the hydrolysis reaction, showing the shape of needles and phosphorus flakes. At a high magnification of 10,000 \times , it can be observed that the hydrolyzed product has a large number of pores, which may be due to the release of a large amount of hydrogen from the aluminum–water reaction.

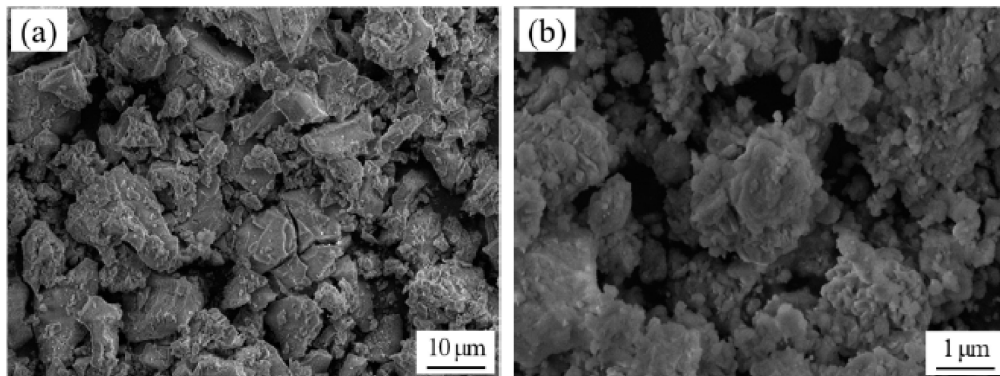


Figure 4. SEM images of the 50 wt.%Al-50 wt.%GIS (6:3:1) reaction product at (a) 1000 \times and (b)10,000 \times .

3.2. XRD Examination

Figure 5 is the XRD pattern of two groups of ingots with different GIS ratios. It can be seen from the figure that there are three characteristic peaks, and the four sharper characteristic peaks are characteristic peaks of Al, the strength of which is significantly higher than that of other phases. There is no obvious characteristic peak of Ga because Ga enters into the lattice of Al to form a solid solution. The characteristic peak is covered by the characteristic peak of Al. With the increase in Ga content, the characteristic peak of Al has an obvious phenomenon of left deviation. The peaks of In_3Sn and In are relatively weak. When the ratio degree of In-Sn is 3:1, it is concluded that there are more second phases on the alloy surface according to SEM diagram observation and EDS component analysis, and the second phase is In_3Sn combined with the XRD results. When the ratio of In-Sn is 2:1, the characteristic peak of In_3Sn cannot be detected but the characteristic peak of weak In can be detected. After hydrolysis reaction, some spherical droplets can be observed after the hydrolysate is dried. Therefore, the hydrolysate was further analyzed by X-ray diffraction, and the results are shown in Figure 6. The obvious characteristic peak of In_3Sn can be seen in the figure, which proves that the liquid alloy phase does exist in this aluminum alloy. It is because of this liquid alloy phase that aluminum can be continuously solvated in liquid phase. Finally, it can diffuse freely and be transported to the surface of the alloy to make contact with water to produce hydrogen by hydrolysis reaction.

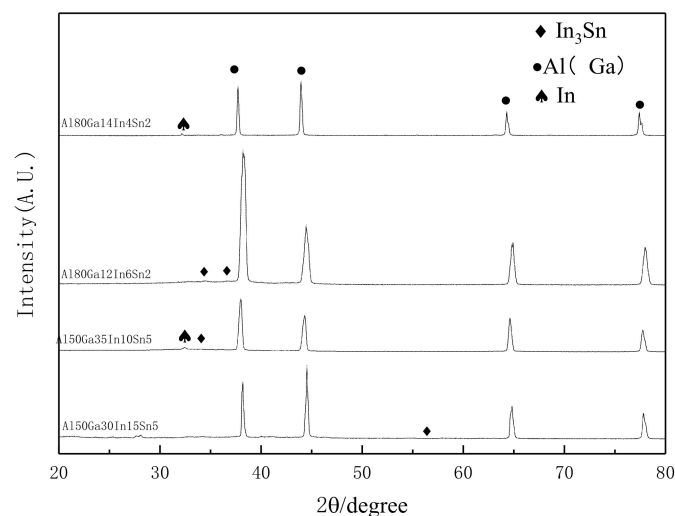


Figure 5. Alloy ingot X-ray diffraction (XRD) with different GIS contrasts.

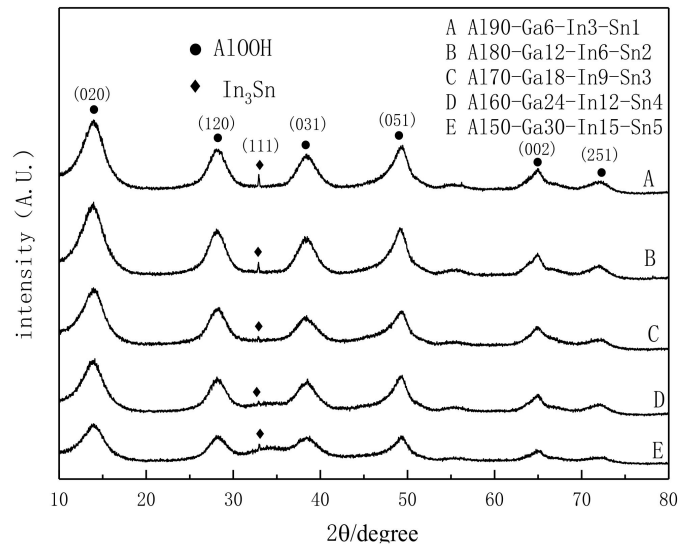


Figure 6. GIS XRD map of hydrolysate at 6:3:1.

Different drying products were generated from aluminum alloy hydrolyzed products at different drying temperatures. $\text{Al}(\text{OH})_3$ was generated when the drying temperature was lower than $72\text{ }^\circ\text{C}$. The drying product is AlOOH in the range of $72\text{--}172\text{ }^\circ\text{C}$. When the drying temperature is greater than $172\text{ }^\circ\text{C}$, the hydrolysis product is Al_2O_3 . In this experiment, the drying temperature was $150\text{ }^\circ\text{C}$, so the characteristic peak detected by X-ray diffraction was AlOOH .

3.3. DSC Analysis of Alloy Ingot

Figure 7 shows the DSC heating curve of Sn alloy samples with the ratio of 80 wt.%Al-12 wt.% Ga-6 wt.%In-2 wt.%Sn alloy. The test temperature range was $23\text{--}615\text{ }^\circ\text{C}$, and the heating rate was $20\text{ }^\circ\text{C}/\text{min}$. During the heating process, the alloy has an endothermic peak due to melting at the melting point. In the figure, a small endothermic peak can be observed around $30\text{ }^\circ\text{C}$. According to the Al-Ga binary phase diagram, the eutectic temperature of the Al-Ga binary alloy is $26.6\text{ }^\circ\text{C}$. The temperature here is close to the eutectic temperature of the Al-Ga binary alloy. The phase transition occurred in $46\text{ }^\circ\text{C}$ alloy, and it is speculated that the liquid phase is eutectic formed by gallium, indium, and tin alloy with a low melting point. After that, there is a weak characteristic peak at $142\text{ }^\circ\text{C}$. According to a In-Sn binary phase diagram, the melting point range of In_3Sn is relatively large, which is about $120\text{--}143\text{ }^\circ\text{C}$. Combined with EDS component analysis and XRD analysis, it is concluded that the characteristic peak should be caused by the formation of intermetallic compound In_3Sn . As the temperature rises, there is no obvious change from $200\text{ }^\circ\text{C}$ to $500\text{ }^\circ\text{C}$ until an obvious endothermic peak appears at $605\text{ }^\circ\text{C}$. A more sharp peak corresponds to the melting point value of the alloy, which should be the melting point of the aluminum-based solid solution.

3.4. Analysis of Alloy Hydrogen Production Performance

Woodall et al. [29] first studied the optimization of the hydrogen production performance of aluminum alloys using low-melting point metals and proposed the diffusion activation mechanism of aluminum alloy ingot hydrolyzed to produce hydrogen. The essence of the mechanism is the eutectic reaction between the low-melting-point metal, with aluminum as the driving force. The aluminum atoms at the grain boundaries are wrapped by the liquid metal, resulting in the rupture of the dense oxide film, which can contact water and undergo a hydrolysis reaction. The low-melting-point metal does not participate in this process. The hydrolysis reaction produces a concentration difference with the continuous consumption of aluminum, and the unreacted aluminum atoms continue

to diffuse from the aluminum lattice into the liquid alloy until the aluminum is basically consumed by the hydrolysis reaction. The quantity and rate of hydrogen production are two important indexes to measure the hydrogen production performance of alloys.

In order to test the effect of changing the ratio degree of low-melting alloy and increasing the content of the second-phase In_3Sn on the hydrogen production performance, the hydrolytic hydrogen production test was carried out on the multi-component aluminum alloy with different contents in a constant temperature water bath at 60°C . Figure 8 is the comparison diagram of the hydrogen production performance of aluminum alloy under different metal ratios at low melting points.

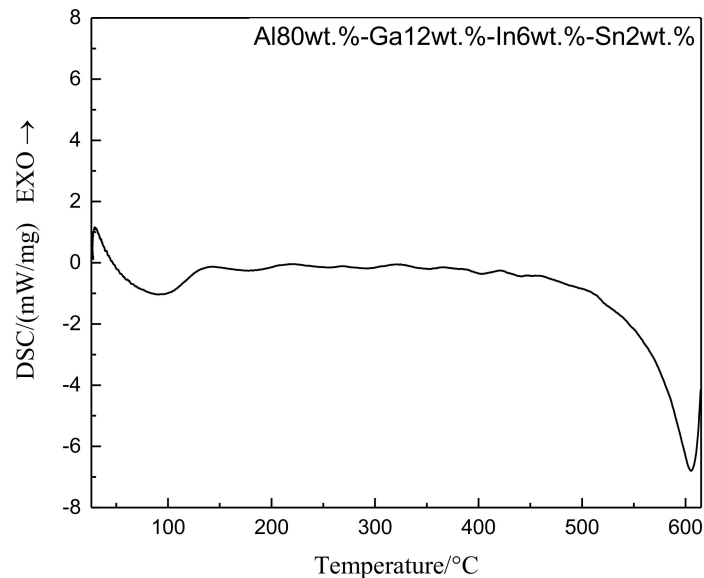


Figure 7. Temperature rise curve of differential scanning calorimetry (DSC) of alloy samples.

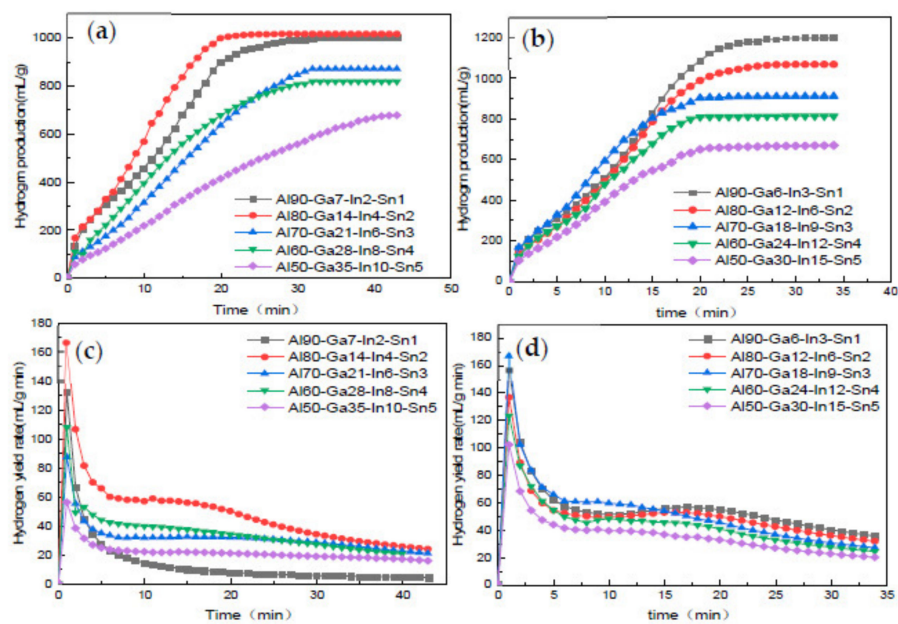


Figure 8. Comparison of the hydrogen generation performance of Al-Ga-In-Sn alloys: (a) hydrogen production comparison with GIS ratio 7:2:1, (b) hydrogen production comparison with GIS ratio 6:3:1, (c) hydrogen production rate comparison with GIS ratio 7:2:1, and (d) hydrogen production rate comparison with GIS ratio 6:3:1.

Figure 8a–d show the hydrogen yield and hydrogen production rate curves of different Al contents hydrolyzed in water at 60 °C when the ratios of GIS (Ga-In-Sn) are 7:2:1 and 6:3:1. As can be seen from Figure 8a,c, when GIS is 7:2:1, hydrogen production and hydrogen production rate are the highest when Al content is 80%, and only when Al content is 80% and 90%, the reaction is basically complete within 20 min while the reaction time of other contents is relatively long. In Figure 8b,d, the GIS is 6:3:1. According to previous detection and analysis, when In and Sn exist in the alloy at a ratio of 3:1, the possibility and content of the second-phase In_3Sn are improved. It can be clearly observed in the figure that, although the change in Al content in the alloy affects the proportion of low-melting-point alloy in the multi-alloy, the alloy basically reacts completely within about 20 min. Compared with the influence of the proportions of two different low-melting metals on Al content of 90%, the low-melting metals only accounted for 10% at this time. When the GIS was 7:2:1, the hydrogen production was reduced and the hydrogen production rate was only 80.96% due to the decrease in low-melting metal content. The maximum hydrogen production rate was up to 157 mL/g min and the hydrogen production rate was up to 97.99% when GIS was 6:3:1.

Figure 9a,b are the comparison diagrams of hydrogen production and hydrogen production rate when the Al content is 50% and the Al content is 90% under different GIS ratios. It can be seen from the figure that the hydrogen production, hydrogen production rate, and maximum hydrogen production rate when the GIS ratio is 6:3:1 are significantly higher than those when GIS ratio is 7:2:1, regardless of the proportion of low-melting point metal in the alloy being the highest (50 wt.%) or the lowest (10 wt.%). Considering the improvement in hydrogen production performance and the reduction in production cost, In and Sn can be used to share the cost of expensive Ga when the GIS ratio is 6:3:1. Under these conditions, aluminum can be hydrolyzed sufficiently even if the content of low-melting-point metal is reduced, so that the whole reaction can reach a faster reaction rate and can obtain the ideal hydrogen production rate.

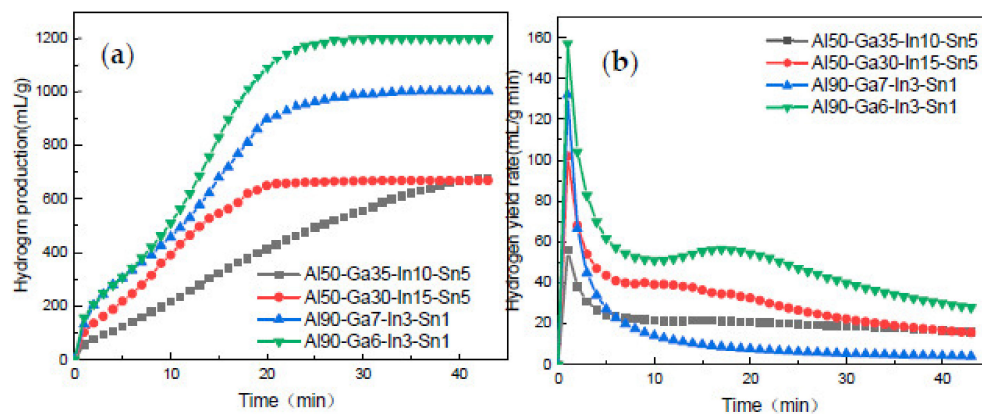


Figure 9. Comparison of hydrogen production performance of Al50 and Al90 at different GIS ratios: (a) hydrogen production comparison chart and (b) hydrogen production rate comparison chart.

4. Conclusions

It is a safer and more environmentally friendly hydrogen production technology to hydrolyze aluminum after alloying. High purity hydrogen is not only a good alternative to fossil fuels but also an ideal hydrogen source for fuel cells. It is an important research direction to produce hydrogen immediately and to supply hydrogen on demand. In this work, multi-element aluminum alloy was smelted in a portable metal smelting furnace with CO_2 continuously introduced, in which the ratios of low-melting-point metals Ga, In, and Sn were 7:2:1 and 6:3:1. The alloy ingot was hydrolyzed in a constant temperature water bath furnace at 60 °C within 24 h after melting and casting. The hydrogen production

properties of the alloys with different proportions were compared. Combined with SEM, EDS, XRD, and DSC for further analysis, the observation results are as follows:

- (1) While using low-melting-point metals Ga, In, and Sn to improve the hydrogen production performance of aluminum hydrolysis, changing the proportion degree of low-melting-point metals can effectively improve the hydrogen production amount and rate.
- (2) Combining the results of scanning electron microscopy and X-ray diffraction, the following conclusions can be drawn: when the ratio of In and Sn in the alloy is 3:1, the occurrence probability and content of the alloy phase In_3Sn can be effectively improved.
- (3) When GIS is 7:2:1, because of the decrease in metal content at low melting point, the alloy phase that can promote hydrolysis reaction cannot be formed better, resulting in a reduction in hydrogen production far below the theoretical value. However, when GIS is 6:3:1, the maximum instantaneous hydrogen production rate is up to 157 mL/(g min) and the hydrogen production efficiency is very close to the theoretical value.

Author Contributions: Conceptualization, Z.G.; methodology, F.J. and C.Y.; investigation, Z.G., F.J., and D.C.; writing—original draft preparation, F.J.; writing—review and editing, Z.G. and J.B.; supervision, J.N. and J.B. All authors have read and agreed to the published version of the manuscript.

Funding: This research was funded by the National Natural Science Foundation of China (grant No. 51245008) and by the Science and Technology Project of Henan Province, China (No. 202102210036).

Institutional Review Board Statement: Not applicable.

Informed Consent Statement: Not applicable.

Data Availability Statement: Not applicable.

Conflicts of Interest: The authors declare no conflict of interest.




References

1. Sun, H. Hydrogen energy is arousing great attention all over the world. *Int. J. Hydrogen Energy* **2020**. [[CrossRef](#)]
2. Von Jouanne, A.; Brekken, T.K.A. Ocean and Geothermal Energy Systems. *Proc. IEEE* **2017**, *105*, 2147–2165. [[CrossRef](#)]
3. Srinivasan, M.; Velu, A.; Madhubabu, B. The Potential Impact of Solar Technology on the Environment. *J. Energy Chem.* **2019**, *1*.
4. Dawood, F.; Anda, M.; Shafiullah, G.M. Hydrogen production for energy: An overview. *Int. J. Hydrogen Energy* **2020**, *45*, 3847–3869. [[CrossRef](#)]
5. Dincer, I.; Acar, C. Innovation in hydrogen production. *Int. J. Hydrogen Energy* **2017**, *42*, 14843–14864. [[CrossRef](#)]
6. Momirlan, M.; Veziroğlu, T. Recent directions of world hydrogen production. *Renew. Sust. Energ. Rev.* **1999**, *3*, 219–231. [[CrossRef](#)]
7. Mayakrishnan Gopiraman, D.D.S.G. Sustainable and Versatile CuO/GNS Nanocatalyst for Highly Efficient Base Free Coupling Reactions. *ACS Sustain. Chem. Eng.* **2015**, *3*, 150904102130008.
8. Sathiskumar, C.; Ramakrishnan, S.; Vinothkannan, M.; Kim, A.R.; Karthikeyan, S.; Yoo, D.J. Nitrogen-Doped Porous Carbon Derived from Biomass Used as Trifunctional Electrocatalyst toward Oxygen Reduction, Oxygen Evolution and Hydrogen Evolution Reactions. *Nanomaterials* **2019**, *10*, 76. [[CrossRef](#)] [[PubMed](#)]
9. Yaqiong, Z.; Jiawei, C.; Qiang, P.; Lingzhi, S.; Zhigang, W.; Zhongkai, W. Hydrogen bonding assisted toughness enhancement of poly(lactide blended with a bio-based polyamide elastomer of extremely low amounts. *Appl. Surf. Sci.* **2020**, *506*, 144684.
10. Zhiznin, S.Z.; Vassilev, S.; Gusev, A.L. Economics of secondary renewable energy sources with hydrogen generation. *Int. J. Hydrogen Energy* **2019**, *44*, 11385–11393. [[CrossRef](#)]
11. Irankhah, A.; Fattahi, S.M.S.; Salem, M. Hydrogen generation using activated aluminum/water reaction. *Int. J. Hydrogen Energy* **2018**, *43*, 15739–15748. [[CrossRef](#)]
12. Dupiano, P.; Stamatis, D.; Dreizin, E.L. Hydrogen production by reacting water with mechanically milled composite aluminum-metal oxide powders. *Int. J. Hydrogen Energy* **2011**, *36*, 4781–4791. [[CrossRef](#)]
13. Czech, E.; Troczynski, T. Hydrogen generation through massive corrosion of deformed aluminum in water. *Int. J. Hydrogen Energy* **2010**, *35*, 1029–1037. [[CrossRef](#)]
14. Choi, G.; Ziebarth, J.T.; Woodall, J.M.; Kramer, R.; Allen, C.R. Mechanism of Hydrogen Generation via Water Reaction with Aluminum Alloys. In Proceedings of the 2010 18th Biennial University/Government/Industry Micro/Nano Symposium, West Lafayette, IN, USA, 28 June–1 July 2010; pp. 1–4.

15. Saluena Berna, X.; Martinez Maezlu, R.; Borge Bravo, G.; Daga Monmany, J.M.; Martinez Lopez, J. Generating Hydrogen by Means of Reaction with Aluminium. U.S. Patent Application 14/765,062, 17 December 2015.
16. Ilyukhina, A.V.; Ilyukhin, A.S.; Shkolnikov, E.I. Hydrogen generation from water by means of activated aluminum. *Int. J. Hydrogen Energy* **2012**, *37*, 16382–16387. [[CrossRef](#)]
17. Parmuzina, A.V.; Kravchenko, O.V. Activation of aluminium metal to evolve hydrogen from water. *Int. J. Hydrogen Energy* **2008**, *33*, 3073–3076. [[CrossRef](#)]
18. Fan, M.Q.; Sun, R.X.; Xu, R. Study of the controllable reactivity of aluminum alloys and their promising application for hydrogen generation. *Energy Convers. Manag.* **2010**, *51*, 594–599. [[CrossRef](#)]
19. Reboul, M.C.; Gimenez, P.; Rameau, J.J. A Proposed Activation Mechanism for Al Anodes. *Corrosion* **2012**, *40*, 366–371. [[CrossRef](#)]
20. Huang, X.N.; Wu, Z.H.; Cao, K.; Zeng, W.; Lv, C.J.; Huang, Y.X. Hydrogen Generation by Hydrolysis of the Ball Milled Al-C-KCl Composite Powder in Distilled Water. *Key Eng. Mater.* **2012**, *519*, 87–91. [[CrossRef](#)]
21. Razali, H.; Sopian, K.; Mat, S. The Application of Aluminum and Hydrochloric Acid to Produce Hydrogen for Internal Combustion Engine Via Hydrogen Mixture with Gasoline based on Specific Fuel Consumption. In *Advanced Materials Research*; Trans Tech Publications Ltd.: Bäch, Switzerland, 2012; Volume 875, pp. 1804–1811.
22. Gai, W.Z.; Fang, C.S.; Deng, Z.Y. Hydrogen generation by the reaction of Al with water using oxides as catalysts. *Int. J. Energy Res.* **2014**, *38*, 918–925. [[CrossRef](#)]
23. Kunowsky, M.; Suárez García, F.; Linares Solano, Á. High pressure hydrogen storage. *Investigació* **2013**. [[CrossRef](#)]
24. Qiao, D.; Lu, Y.; Tang, Z.; Fan, X.; Wang, T.; Li, T.; Liaw, P.K. The superior hydrogen-generation performance of multi-component Al alloys by the hydrolysis reaction. *Int. J. Hydrogen Energy* **2019**, *44*, 3527–3537. [[CrossRef](#)]
25. Wang, C.; Yang, T.; Liu, Y.; Ruan, J.; Yang, S.; Liu, X. Hydrogen generation by the hydrolysis of magnesium-aluminum-iron material in aqueous solutions. *Int. J. Hydrogen Energy* **2014**, *39*, 10843–10852. [[CrossRef](#)]
26. Wang, D. Analyzing the Feasibility of Generating Hydrogen Al-Ga Alloy using Fly Ash as Raw Materials. *Shenhua Sci. Technol.* **2016**, *14*, 7–10.
27. Yoo, H.; Ryu, H.; Cho, S.; Han, M.; Bae, K.; Lee, J. Effect of Si content on H₂ production using Al–Si alloy powders. *Int. J. Hydrogen Energy* **2011**, *36*, 15111–15118. [[CrossRef](#)]
28. Evans, D.S.; Prince, A. Thermal analysis of Ga-In-Sn system. *Met. Sci.* **2013**, *12*, 411–414. [[CrossRef](#)]
29. Woodall, J.M.; Ziebarth, J.; Allen, C.R. The Science and Technology of Al-Ga Alloys as a Material for Energy Storage, Transport and Splitting Water. In *Proceedings of the Asme Energy Nanotechnology International Conference*, Santa Clara, CA, USA, 5–7 September 2007.

Review

Towards Non-Mechanical Hybrid Hydrogen Compression for Decentralized Hydrogen Facilities

Giuseppe Sdanghi ^{1,2}, Gaël Maranzana ², Alain Celzard ¹ and Vanessa Fierro ^{1,*}

¹ IJL, Université de Lorraine, CNRS, 88000 Epinal, France; Giuseppe.Sdanghi@icmcb.cnrs.fr (G.S.); alain.celzard@univ-lorraine.fr (A.C.)

² LEMTA, Université de Lorraine, CNRS, F-54000 Nancy, France; gael.maranzana@univ-lorraine.fr

* Correspondence: vanessa.fierro@univ-lorraine.fr; Tel.: +33-3-72-74-96-77

Received: 17 May 2020; Accepted: 15 June 2020; Published: 17 June 2020



Abstract: The cost of the hydrogen value chain needs to be reduced to allow the widespread development of hydrogen applications. Mechanical compressors, widely used for compressing hydrogen to date, account for more than 50% of the CAPEX (capital expenditure) in a hydrogen refueling station. Moreover, mechanical compressors have several disadvantages, such as the presence of many moving parts, hydrogen embrittlement, and high consumption of energy. Non-mechanical hydrogen compressors have proven to be a valid alternative to mechanical compressors. Among these, electrochemical compressors allow isothermal, and therefore highly efficient, compression of hydrogen. On the other hand, adsorption-desorption compressors allow hydrogen to be compressed through cooling/heating cycles using highly microporous materials as hydrogen adsorbents. A non-mechanical hybrid hydrogen compressor, consisting of a first electrochemical stage followed by a second stage driven by adsorption-desorption of hydrogen on activated carbons, allows hydrogen to be produced at 70 MPa, a value currently required for the development of hydrogen automotive applications. This system has several advantages over mechanical compressors, such as the absence of moving parts and high compactness. Its use in decentralized hydrogen facilities, such as hydrogen refueling stations, can be considered.

Keywords: hydrogen storage; hydrogen compression; non-mechanical compressors; electrochemical compressors; activated carbons

1. Introduction

According to the US Energy Information Administration, the breakdown of total world energy consumption by sector in 2018 was 33% for industry, 33% for transportation, 24% for the residential sector, and 10% for services [1]. In recent years, energy demand related to the transport sector has risen dramatically, from 26% in 2012 to 33% in 2018, and a further increase is expected. Globally, about 95% of vehicles currently use petroleum-based fuels, which partly explains the above-mentioned trend. Indeed, the demand for oil in industrialized countries, where the number of vehicles is growing exponentially every year, has increased from 56% to 72% during the last decade [2]. On the other hand, coal is expected to remain the predominant fuel for other energy applications, primarily power generation, for a long time to come. Nevertheless, the uncontrolled use of fossil fuels cannot continue indefinitely, due, at least, to environmental reasons and the need to fight climate change.

In addition, irreversible environmental issues will be inevitable if the global energy scenario continues to rely on fossil fuels for a long time. CO₂ emissions have increased significantly in recent years, reaching 34 Mt per year, 40% higher than in 2010 [3]. The main consequence is the intensification of the greenhouse effect on our planet, and with it the increase in its average temperature. Indeed, Earth's average temperature has increased by just over 1 K since 1880. Two thirds of global warming

has occurred since 1975, at a rate of about 0.15–0.20 K per decade [4]. At this rate, global warming will be detrimental to ecosystems and human health, as infectious diseases will emerge due to the warmer and wetter environment.

For all the aforementioned reasons, the search for energy sources that could be both environmentally friendly and limitless is currently in great demand. The use of hydrogen as an energy vector fits perfectly into this framework, especially if it is produced from renewable sources. Indeed, hydrogen is a clean energy vector, and it is advocated as a serious candidate to replace fossil fuels, especially in the transport sector. Stationary hydrogen storage can also be envisaged as a guarantee of energy supply in the event of power grid failure or fluctuations in wind and solar energy. Indeed, the intermittency of renewable energy sources implies their storage in efficient and reactive storage systems, giving rise to the concept of smart grids. In this framework, power-to-hydrogen systems use expanding and inexhaustible renewable energy resources to power electrolyzers, producing hydrogen from water [5,6], thus reducing the load on the electricity grid and the risk of power outages [7]. Thus, electricity can be used to produce hydrogen by water electrolysis, and electrical energy can be produced by using hydrogen in fuel cell systems.

Since hydrogen is widely used in industry for the production of ammonia and the hydrogenation of petroleum products, the hydrogen sector, which includes production in decentralized facilities, storage and distribution, is already mature. However, the potential benefits of hydrogen as a fuel can be realized once storage methods are optimized and an efficient and safe distribution infrastructure is in place. In this context, the storage of hydrogen requires its compression. Mechanical compressors (piston, diaphragm, linear, and ionic liquid compressors), which are universally used for the compression of all gases, are not very suitable for the specific case of hydrogen. Research on new compression technologies, such as non-mechanical hydrogen compressors (metal hydrides, electrochemical, and adsorption-desorption compressors) is thus highly demanded, particularly with regard to the development of decentralized infrastructure for the production and use of hydrogen in situ.

2. Hydrogen as a Fuel

Hydrogen could play a key role in this critical scenario, as it could promote the development of new, innovative, and environmentally friendly solutions for energy use, which could lead to a transition towards divestment from fossil fuels [8]. Hydrogen has the highest gravimetric energy density among all non-nuclear fuels, i.e., 33 kWh kg⁻¹ (based on the net calorific value). In comparison, the gravimetric energy density of gasoline is 13 kWh kg⁻¹, which is three times less than that of hydrogen. Nevertheless, the density of hydrogen is very low and equal to 0.089 g L⁻¹ at 298 K and 1 atm. This means that hydrogen exhibits the lowest volumetric energy density among the commonly used fuels, i.e., 0.003 kWh L⁻¹ (compared to around 10 kWh L⁻¹ for gasoline). Therefore, the realization of an efficient and practical hydrogen storage system is a significant challenge. Approximately 11,000 L would be required to store 1 kg of hydrogen or 33 kWh of energy. On the contrary, 1 kg of gasoline is stored in a volume of 1.3 L under the same conditions (considering a density of 775 g L⁻¹), which is four orders of magnitude less than what is expected for hydrogen. Several ways of increasing the volumetric energy density of hydrogen are currently available, and will be discussed in the next section.

The only reaction product of hydrogen combustion in air is water, which is one of the most important advantages over fossil fuels in terms of environmental impact. The hydrogen diffusion coefficient in air, 0.62 cm² s⁻¹, is four times higher than that of natural gas. As a result, hydrogen dilutes very quickly in air, which is undoubtedly a safety advantage. Similarly, hydrogen flames are extinguished faster than those of gasoline or natural gas because hydrogen has a relatively high laminar flame velocity compared to other fuels (265–325 cm s⁻¹). However, the flammable limits for the percentage by volume of hydrogen in air at atmospheric pressure are 4% and 75%. In addition, hydrogen–air mixtures can ignite with a very low energy input, of one-tenth that required to ignite a gasoline–air mixture.

Hydrogen is the most abundant element in the universe, but its exhaust velocity is so high that it is not retained in the Earth's atmosphere. However, underwater exudations of natural hydrogen have recently been discovered, as well as the existence of geological structures from which large flows of natural hydrogen are released. Despite this, hydrogen used in the industrial sector is currently produced from fossil and renewable sources by various synthesis methods (Figure 1). The most widely used methods, based on mature technologies, are steam reforming of natural gas and partial oxidation of hydrocarbons. Nevertheless, these methods also produce large amounts of greenhouse gases and are therefore not environmentally friendly [9]. For this reason, methods for producing hydrogen from renewable sources have been developed in recent years, making a significant contribution to sustainable development. Among these, water electrolysis has proven to be a valid solution, since it allows the production of hydrogen from water [10]. Whenever electricity is available at low cost, water electrolysis is already used worldwide for industrial applications of a few MW. However, the production of hydrogen by water electrolysis costs about USD 4–8 kg⁻¹ (for the specific case of polymer electrolyte membrane technology), which is around four times more expensive than the steam reforming method, i.e., USD 1.3 kg⁻¹ [11]. Hydrogen production from biomass through supercritical water gasification and fermentation processes is also considered a sustainable alternative to hydrogen synthesis from fossil fuels [12,13]. However, the hydrogen production cost, about USD 3.5 kg⁻¹ for a biomass price of USD 100 tons⁻¹, is still too high to represent a real alternative to steam reforming [14]. Solar energy is also another sustainable and environmentally friendly way to produce hydrogen [15–18]. Solar-driven high-temperature steam electrolyzers were found to produce pure hydrogen with a rate of 1.2 g s⁻¹, with an efficiency of around 25% [16]. Renewable hydrogen can also be generated by solar-driven water splitting. However, the search for stable and efficient photoelectrodes with reasonably higher photocurrent densities is required before commercialization [19].

According to statistics reported by the International Energy Agency, approximately 70 Mt of hydrogen are produced worldwide each year [20], of which 96% is produced from fossil fuels. The lowest cost of hydrogen production, USD 1.3 kg⁻¹, is obtained by steam reforming of natural gas. This value is not significantly different from the production cost of liquid fuels used today, such as gasoline (the average global price of gasoline in May 2020 was USD 0.92 L⁻¹ [21]). This low cost is due to the fact that 55% of the hydrogen is produced to synthesize ammonia in a very mature process that has been used for 100 years [22].

The biggest drawback of the hydrogen value chain is in the storage, transportation and distribution stages, which increase the price of hydrogen at the pump to USD 8–10 kg⁻¹ [23]. Indeed, the hydrogen refueling station, including storage systems, can account for more than 75% of the final hydrogen pump price [24].

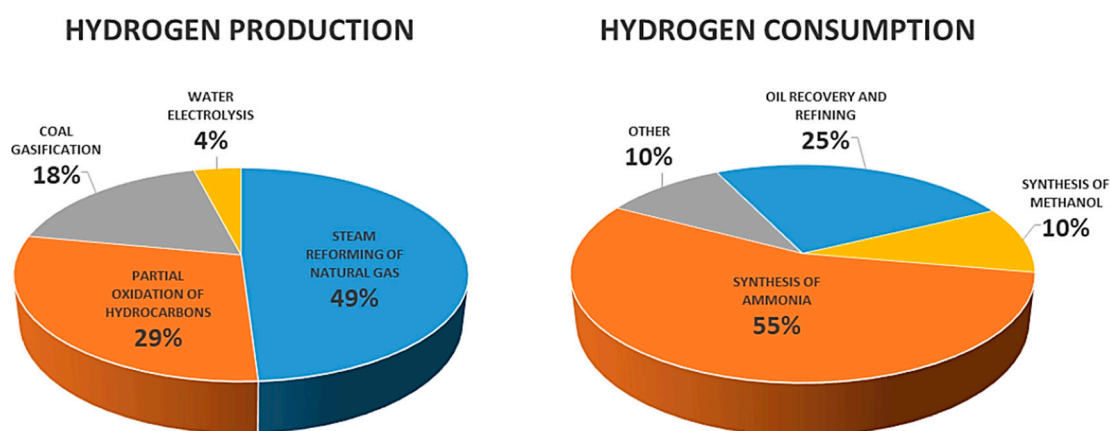


Figure 1. Global hydrogen production and consumption.

3. Hydrogen Storage for Automotive Applications

The low volumetric energy density of hydrogen is a critical feature in automotive applications. Indeed, hydrogen vehicles will have to represent a concrete alternative to conventional internal combustion engine vehicles to allow global commercialization. This means that at least 5 kg of hydrogen must be stored to cover a distance of 500 km; hence, only a tank volume of 61,000 L may allow this at 298 K and 1 atm. Nevertheless, technical solutions to reduce this huge volume exist, as discussed below.

3.1. Compressed Hydrogen Tanks

Compression is the most widely used methods to allow efficient storage of hydrogen, although it is not the cheapest approach [25]. The main effect of gas compression is to increase its density. Indeed, a density of 42.9 g L⁻¹ is obtained by compressing hydrogen to 70 MPa and 298 K, which results in an increase in density of four orders of magnitude compared to the density at ambient conditions. Hence, 1 kg of hydrogen can be stored in a volume of approximately 23 L under the above-mentioned conditions. There are already hydrogen vehicles equipped with 70 MPa pressure tanks [26], which are capable of covering a distance of 500 km with 5 kg of hydrogen on board.

High-pressure hydrogen storage requires special tanks, which can both withstand hyperbaric conditions and prevent metal embrittlement by the hydrogen molecules. To this end, four different types of high-pressure tanks are currently used. The performance of a high-pressure tank is usually expressed by the performance index [27], i.e., the product pressure × volume × mass⁻¹ (Figure 2). Type IV tanks are the most widely used to store hydrogen at very high pressure, as they ensure the best performance [28]. These tanks are made of carbon fiber, which reduces the weight of the storage system. Furthermore, a polymer inner lining prevents leakages. The cost of a type IV tank is around USD 14.75 kWh⁻¹ when considering a manufacturing rate of 500,000 tanks per year [29]. On the contrary, types I and II are metal tanks and their use on-board is therefore difficult to envisage due to their high weight. Finally, type III tanks are made of composite materials, with an inner lining of aluminum, which makes them heavier than type IV tanks.

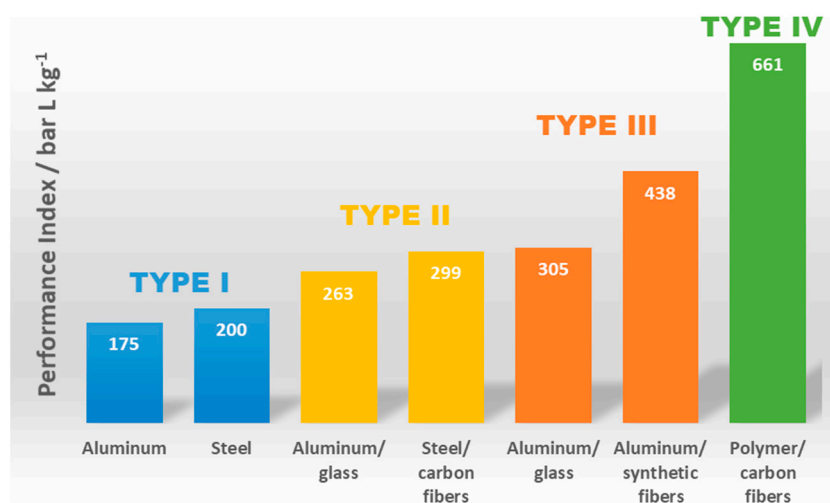


Figure 2. Different typologies of high-pressure hydrogen tanks and their performance indexes (adapted from [27]).

Although compression has proven to be an efficient solution for the storage of hydrogen, it has to be taken into account that it requires energy to take place. Therefore, 5% and 15% of the energy of hydrogen is consumed when it is compressed at 35 MPa and 70 MPa, respectively [30]. Thus, the amount of energy required increases with the pressure. This means that an energy cost equal to

5 kWh is required to compress 1 kg of hydrogen to 70 MPa, whereas the gravimetric energy density of hydrogen is 33 kWh at atmospheric pressure.

3.2. Liquid Hydrogen

The density of liquid hydrogen, i.e., 70.8 g L⁻¹ at atmospheric pressure, is 40% higher than compressed gaseous hydrogen at 70 MPa, further reducing the size of the storage system. Indeed, 1 kg of liquid hydrogen is stored in a volume of 13.6 L, whereas it takes 23 L to store the same amount of gaseous hydrogen at 70 MPa. Nevertheless, special tanks are required to store liquid hydrogen at 20 K, as they must provide efficient thermal isolation to minimize losses due to hydrogen evaporation. Such losses are estimated to be about 1–5% per day [31]. Cryogenic tanks are made of an inner and outer lining, comprising an empty layer and several aluminum sheets alternated with glass fibers to prevent heat transfer, including radiation. Heat transfer within a cryogenic tank can also be minimized by increasing the volume-to-surface ratio, as in the case of spherical tanks. Evaporation of hydrogen causes an increase in pressure inside the cryogenic tank, and thus requires depressurization procedures by periodic evacuation. Therefore, additional hydrogen losses have to be taken into account [32].

Liquid hydrogen tanks can store approximately 8 kg of hydrogen in volumes of 120 L. However, the production of liquid hydrogen is quite expensive. Around 10 kWh kg⁻¹ are required to liquefy hydrogen, i.e., 30% of the hydrogen chemical energy [33]. In addition, the capital expenditure (CAPEX) of industrial plants for hydrogen liquefaction is relatively high. A significant reduction in this cost could be achieved by increasing the production of liquid hydrogen from the current capacity of 5 tons per day to 150 tons per day [34] in the framework of centralized production.

3.3. Solid Storage in Metal Hydrides

Large hydrogen storage capacities, even higher than those generally obtained with compressed or liquefied hydrogen, can be achieved by absorption of hydrogen in metal hydrides. Indeed, up to 100 g of hydrogen per L can be stored in metal hydrides (in the specific case of MgH₂), whereas 8.3 g per L and 70.8 g per L can be stored by compression at 15 MPa and liquefaction, respectively [35].

The storage of hydrogen in metal hydrides occurs by absorption, i.e., a volume phenomenon that involves the formation of chemical bonds between the hydrogen molecules and those of the substrate (chemisorption). Hydrogen storage capacities up to 7.6 wt.% have been obtained with Mg-based hydrides, e.g., MgH₂ [36]. Furthermore, the kinetics of hydrogen absorption and desorption reactions in metal hydrides have been shown to be fully reversible [37]. Nevertheless, very high temperatures, even above 573 K, may be required to cause hydrogen desorption, which is one of the main disadvantages of hydrogen storage in metal hydrides [38]. The United States Department of Energy (DOE) has established that hydrogen storage capacities equal to or greater than 6.5 wt.% must be provided by a metal hydride system. This value takes into account both the weight of the storage material and that of the entire system, which comprises all supporting components and auxiliary systems. Hence, systems based on metal hydrides are unlikely to meet this target at present. Moreover, desorption temperatures between 333 and 393 K are demanded to consider the metal hydrides storage systems for commercialization [39]. Such a high desorption temperature is due to the high binding energy between the hydrogen and metal atoms, which can reach 60–100 kJ mol⁻¹ [40]. In addition, absorption and desorption kinetics can be slow, with desorption times that can exceed 60 min (e.g., in the case of Mg-Al₂O₃) [36].

Intermetallic hydrides of the AB₅ composition (with A = rare earth metal and B = Ni or Co) have shown excellent performance as reversible chemical storage media of hydrogen gas. Particularly attractive behaviors were found for LaNi₅H_{6.7}, as it is formed at pressures slightly above atmospheric pressure with a desorption temperature close to 293 K [41]. Nevertheless, the virtually achievable reversible hydrogen storage capacities of most intermetallic hydrides do not exceed 2 wt.% (1.5 wt.% for AB₅ hydrides, 1.8 wt.% for AB₂, and 2 wt.% for BCC alloys [41]). Since metal hydrides are relatively heavy, the weight ratio of stored hydrogen to the total storage system can be as low

as 1–3% [42]. In addition, hydrogen absorption in metal hydrides is an exothermic phenomenon, which requires efficient cooling of the entire tank. Despite these latter drawbacks, hydrogen storage in metal hydrides remains particularly advantageous in terms of safety. Indeed, the hydrogen pressure inside a metal hydride tank is generally much lower than that reached in pressurized tanks, thus minimizing the risk of leaks [43]. For this reason, hydrogen storage in metal hydrides has proven to be an appropriate solution for short-distance vehicles such as scooters, golf carts, and electric bikes. Moderate quantities of hydrogen are required in this case, thus metal hydrides with low desorption temperature, such as the Ti-based hydrides (AB₂-type) are a suitable solution [44]. Furthermore, metal hydride storage systems are very compact, making them even more suitable for short distances. For the storage of hydrogen on board fuel cell vehicles (FCV), “distributed hybrid hydrogen storage vessels” have recently been proposed, in which hydrogen is stored both in hydride materials and in pressurized tanks [45]. The hybrid concept benefits from both a higher storage capacity than its single metal hydrides counterpart and better thermal management. Moreover, it is more flexible and ensures a quick response to transient working conditions (such as acceleration or vehicle start-up).

3.4. Solid Storage in Microporous Materials

Hydrogen can interact with the surface of several microporous materials through weak Van der Waals forces, forming a monolayer. The interaction energies involved are very low, of the order of 0.01–0.1 eV [46], which means that no chemical bonds are generated between the hydrogen molecules and the surface of the microporous materials. This interaction is a completely reversible process, also known as “physisorption”. Several materials have been shown to have increased adsorption capacities, such as carbon-based materials (i.e., activated carbons, carbon nanotubes, and fullerenes), zeolites, metal organic frameworks (MOFs), and certain types of polymers [47–51]. Physisorption allows large hydrogen storage capacities to be reached. Indeed, it is generally assumed that the density of adsorbed hydrogen can be approximated to the density of liquid hydrogen, i.e., 70 g L⁻¹, when the temperature is lowered to 77 K [52]. Hence, the use of adsorption on microporous materials instead of pure compression would give a volume gain of around 22% to the hydrogen storage system [53]. This advantage can be achieved in particular in the pressure range from 5 to 20 MPa [54].

The amount of hydrogen adsorbed on microporous materials is approximately proportional to their specific surface area, i.e., their micropore volume, but also depends on the size distribution and average width of the micropores [55]. A considerable hydrogen storage capacity of 9.9 wt.% at 77 K and 5.6 MPa has been measured for a MOF called NU-100 (Northwestern University 100) with a Brunauer, Emmett, and Teller (BET) area of 6143 m² g⁻¹ and a total pore volume of 2.82 cm³ g⁻¹ [56]. This is one of the highest values ever achieved for hydrogen adsorption. It has also been shown that carbon adsorbents, especially activated carbons, have relatively high hydrogen adsorption capacities, on average 7 wt.% at 77 K and 4 MPa [57]. These values are higher than the gravimetric hydrogen storage recommended by the DOE for automotive applications, i.e., 5.5 wt.% by 2025 [39,58]. Nevertheless, not only the weight of the adsorbent but also the weight of the whole system must be taken into account. Moreover, the DOE recommends meeting such capacities in the temperature range of 233 to 358 K. This means that the DOE target remains difficult to achieve at room temperature, although hydrogen storage capacities can be improved by doping with metallic nanoparticles and heteroatoms [59–61].

4. The Hydrogen Value Chain

After being produced and before being used, hydrogen is packaged, distributed, stored, and delivered. The most complex issues requiring solutions are mainly related to these last two steps [62]. Indeed, the development of an efficient hydrogen supply chain has to take into account the energy lost between the source and the end user, in particular during transport and distribution. To date, there are two main ways to enable hydrogen distribution: centralized and decentralized (Figure 3).

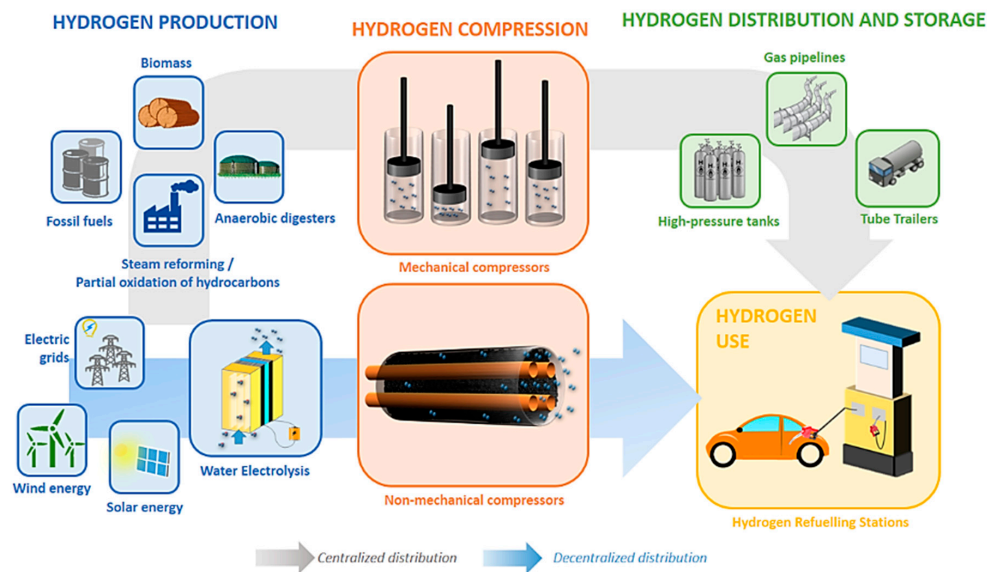


Figure 3. The hydrogen value chain for the specific case of automotive applications.

4.1. Centralised Hydrogen Distribution

When hydrogen is produced in large industrial facilities, it can be compressed in situ and then distributed to users. In this scenario, hydrogen can be distributed in two ways: (i) through pipelines or (ii) stored in high-pressure tanks delivered by trucks.

Pipeline distribution of hydrogen is adopted primarily when hydrogen is produced in large industrial facilities from fossil fuels, for example, through the steam reforming of natural gas, which is the cheapest method for hydrogen production today and the most widely used when large quantities of hydrogen are required. Approximately $200,000 \text{ Nm}^3 \text{ h}^{-1}$ are typically produced by an industrial facility for steam reforming of natural gas [63]. Recently, hydrogen has also been produced by electrolysis in industrial facilities located near power plants, resulting in a few hundreds of $\text{Nm}^3 \text{ h}^{-1}$ of hydrogen [64]. To date, approximately 4500 km of pipelines are used to distribute hydrogen worldwide, half of which are in the United States (Figure 4) [65]. The installation of hydrogen pipelines requires a very high capital cost. Therefore, this solution has been proven only suitable for small to medium distances. In addition, the distribution of hydrogen through pipelines is undoubtedly less efficient than the distribution of methane. In order to compensate for pressure losses, the gas distributed through pipelines must be compressed at regular intervals. Thus, the energy required to compress the gas depends only on its volume and the pressure to be reached. Nevertheless, the energy recovered during the subsequent use of the gas is different. Indeed, 1 m^3 of methane has an energy content of 9.89 kWh, whereas the same volume of hydrogen has 3 kWh. This means that the energy to be spent on hydrogen distribution through pipelines is three times higher than that spent on methane, for a desired amount of energy recovered [66].

Hydrogen can also be stored in high-pressure tanks delivered by trucks. In general, hydrogen is compressed to 25 MPa and then stored in tubes grouped in several packages. Normally, each group contains nine tubes, each with a volume of up to 2000 L [67]. This solution is particularly suitable when hydrogen has to be delivered to small hydrogen refueling stations, which are not served by the pipeline network. The tubes are usually made of metal; hence, they are type I high-pressure tanks (Figure 2). As mentioned earlier, very high pressures cannot be achieved using type I tanks. Therefore, the DOE's goal is to produce large type III or type IV tanks, e.g., polymer tanks, to allow hydrogen storage at higher pressures, i.e., storage of larger quantities [68]. It has been shown that the cheapest way to store and deliver hydrogen is by compression and truck delivery, particularly for small hydrogen refueling stations and low demand [69]. However, transporting hydrogen is probably a dangerous solution. Although the probability of an accident is not greater than that of any other vehicle

travelling on the same road, the risk of ignition of hydrogen-rich gas mixtures that may form near a leak remains an important issue to consider. Indeed, the minimum energy to ignite a stoichiometric hydrogen–air mixture is 0.02 mJ at 298 K and 1 atm. The presence of moving parts close to any leak can be a dangerous source of ignition. Despite this drawback, several safety measures are adopted to minimize the risk of ignition as much as possible. These include the use of a concrete liner to further reduce the risk of leakage.

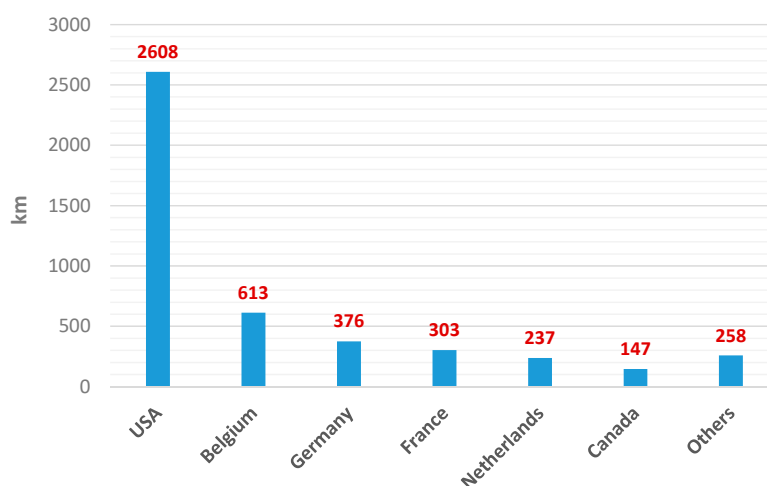


Figure 4. Global distribution of hydrogen pipelines (adapted from [57]).

4.2. Decentralized Facilities

A second scenario in the hydrogen value chain, which has attracted significant attention in recent years, is based on small and medium-sized facilities, where hydrogen is produced, stored, and distributed in situ at the same location. A good example is a hydrogen refueling station, designed to power a small number of fuel cell vehicles. Decentralized hydrogen production facilities typically supply a limited amount of hydrogen per day. Hydrogen can therefore be produced by electrolysis of water, resulting in production volumes of a few hundred $\text{Nm}^3 \text{h}^{-1}$. This is an important advantage since electricity is supplied to the hydrogen refueling stations, and water electrolysis is carried out directly on site. Indeed, electricity is much easier to transport than gas, thanks to the significant presence of high-voltage grids and distribution networks around the world. For instance, the high-voltage network in France covers a distance of more than 100,000 km, whereas the low and medium-voltage lines used for the distribution of electricity to users have a cumulative length of approximately 1.3 million kilometers [70].

For water electrolysis, three technologies are currently available: (i) alkaline water electrolysis (AEL); (ii) solid polymer electrolyte electrolysis (SPEL); and (iii) solid oxide electrolysis (SOEL). AEL uses concentrated liquid alkaline solutions of KOH or NaOH as electrolyte, and non-noble metals such as nickel as electrodes. Alternatively, SPEL relies on the use of proton or anion exchange membranes (PEMs/AEMs) as electrolyte, i.e., solid acids or lyes conducting protons or hydroxide ions, respectively. In PEM electrodes, only a catalyst based on the expensive platinum group can achieve good performance, whereas low-cost transition metal catalysts can be used for AEM electrolysis. Thus, both AEL and SPEL can operate between 323 and 353 K. On the other hand, SOEL uses ceramic materials as electrolyte and mixed ionic-electronic conductors (MIECs), such as A_2MO_4 oxides (A = rare earth, alkaline earth; M = transition metal), as electrodes. Despite several advantages, such as their flexibility and reversibility in electrolysis and fuel cell modes, this technology still faces some challenges to become economically competitive in the market. Indeed, SOEL operates at temperatures above 873 K, which promotes the degradation phenomena of the ceramic materials [71,72]. AEL has proved to be a key technology for large-scale hydrogen production powered by renewable energy [73]. The investment costs for AEL are from USD 800 to 1500 kW^{-1} , whereas a higher cost

between USD 1400 and 2100 kW^{-1} is necessary for the SPEL. Moreover, the lifetime of AEL is longer than that of SPEL (90,000 h vs. 20,000 h) [74]. Nevertheless, PEM water electrolysis is more efficient over a broader dynamic load range than AEL, especially due to the shorter start-up time and the lower footprint [74,75]. Thus, over the last five years, PEM systems with a power of several hundred kW or even MW have started to appear, corresponding to hydrogen production rates of around 10 to 20 kg h^{-1} , [11]. In addition, high-pressure hydrogen can be produced by PEM water electrolysis with a high efficiency of about 70%. In fact, such a system allows the production of hydrogen at a pressure as high as 5 MPa, whereas AEL is limited to 3 MPa [76]. In the framework of automotive hydrogen applications, where hydrogen has to be compressed to 70 MPa anyway, this is an important advantage to reduce costs further. Water electrolyzers have been tested on a large scale, with a hydrogen production rate of 1 $\text{Nm}^3 \text{h}^{-1}$ and operating pressures up to 13 MPa [77,78]. Even though hydrogen can evolve at high pressure under isothermal conditions during water electrolysis, hydrogen permeation through the electrolyte increases with operating pressure, resulting in a loss of efficiency and safety risks [79].

In this context, hydrogen can only be defined as an environmentally friendly fuel if the electricity required for the operation of water electrolysis is produced by renewable sources, such as wind or solar energy (Figure 5). However, the potential benefits of this solution can only be realized after significant improvements in photovoltaic and wind power systems. The current price of hydrogen at the pump at a refueling station equipped with a renewable energy electrolyzer is approximately USD 17 kg^{-1} in Europe and USD 12.5 kg^{-1} in the United States [80,81]. This is significantly higher than the average pump price of gasoline, which is USD 2 kg^{-1} [82]. This large difference is mainly due to the cost of producing hydrogen. In the case of wind turbines, the cost of producing hydrogen by electrolysis can range from USD 8 kg^{-1} to USD 30 kg^{-1} , depending on turbine and electrolyzer technology used [83]. Despite the high cost, several hydrogen refueling stations powered by renewable sources are already operational globally. In France, the FaHyence hydrogen refueling station produces about 40 kg of hydrogen per day, which can power 20–25 hydrogen vehicles daily [84].

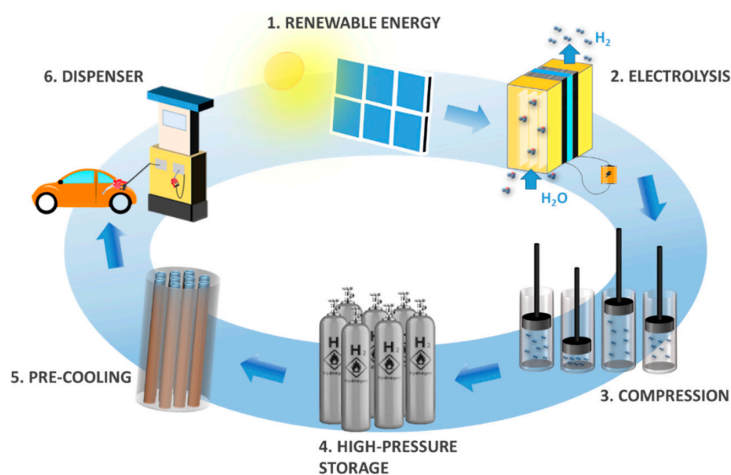


Figure 5. Scheme of hydrogen refueling stations driven by renewable sources.

In the case of decentralized facilities, the local hydrogen economy is generally penalized by higher investment costs, lower annual utilization rates, and higher electricity prices than in the case of centralized production [24], which explains why decentralized hydrogen refueling stations have not yet achieved economic profitability. Indeed, the total cost of a hydrogen refueling station can be as high as USD 3.2 million [85], which means that significant hydrogen production is required to recoup the investment. A reduction in the above cost can be achieved by increasing the efficiency of water electrolyzers, which is currently about 60% [74].

5. Hydrogen Compression

Hydrogen compression is a critical step in the hydrogen value chain. In the case of its centralized production by large industrial facilities, hydrogen is compressed close to the production site, i.e., before being distributed by pipelines or by tube trailers. On the other hand, when hydrogen is produced in situ in decentralized facilities, a compression system is placed downstream of the electrolyzer.

The use of large-scale technologies operating at high pressures allows hydrogen to be supplied at medium pressure, thus reducing both the compression work and the cost of compressing up to 70 MPa. As mentioned in Section 4.2, PEM water electrolysis has proved to be a key technology for the large-scale hydrogen production at medium pressures. Salt cavern storage is also another promising technology for high-pressure hydrogen storage due its low investment cost, high sealing potential, and low cushion gas requirement. Underground hydrogen storage is not significantly different from underground storage of natural gas. Thus, they are less susceptible to fire and have a relatively smaller surface facility than traditional storage tanks, which facilitates their integration in the landscape and existing infrastructure [86]. With a storage volume of 580,000 m³, the salt cavern of Clemens Dome (TN, USA) allows hydrogen storage up to 13.5 MPa, whereas the one in Moss Bluff (USA), with a storage volume of 566,000 m³, allows even higher pressures (15.2 MPa) [87]. In Europe, there are also suitable salt caverns that could be used for underground hydrogen storage, with a virtual storage volume of up to 750,000 m³ [88]. Despite the aforementioned advantages, geological, technological, economic, legal, and social obstacles have to be overcome before full-scale underground hydrogen storage can be implemented. Hence, the lower cost of hydrogen production through PEM water electrolysis will be the decisive factor for the implementation of this method of hydrogen storage on an industrial scale [86].

Hydrogen compression remains therefore a fundamental part of the hydrogen value chain at present. To date, mechanical compressors are the most widely used devices for compressing hydrogen. Mechanical hydrogen compressors rely on a very mature technology, and are used in particular when high flow rates of hydrogen have to be processed, in the order of thousands of Nm³ h⁻¹ [89]. Several types of mechanical hydrogen compressors are available today. However, mechanical compressors have several drawbacks, making it necessary to look for alternative compression systems, which may be advantageous from both a technical and economic point of view.

5.1. Mechanical Hydrogen Compressors

Although mechanical compressors are widely used to drive the compression of several gases, they are not appropriate in the specific case of hydrogen. In addition, they do not yet meet the safety and reliability criteria necessary for their use, either in semi-industrial applications or at the level of the general public [90]. The main reason for this is that hydrogen tends to leak through the moving seals of mechanical compressors. This sealing problem inevitably implies a significant reduction in the potentially achievable efficiency. Moreover, hydrogen is easily absorbed by metals, causing embrittlement phenomena that can affect the mechanical performance of materials [91].

Mechanical compressors, such as reciprocating compressors, have several moving parts. Indeed, hydrogen compression is driven by the movement of several pistons, linked to a crankshaft, which, by means of a connecting rod, converts the linear movement of the pistons into a continuous rotational movement. Reciprocating compressors therefore have a high degree of structural complexity, which is undoubtedly a drawback. First of all, this involves a high maintenance cost, due to the presence of a high number of gears and valves, and the piston-crankshaft-connecting rod described above. The maintenance cost of mechanical compressors is estimated at 5% of the total investment cost per year [92]. In addition, lubricating oils have to be used to reduce any friction between the different moving parts, with the risk of hydrogen contamination [93]. Noise and vibration from moving parts must also be taken into account. Additionally, the latter is a problem for the environment of the compressor, especially in terms of workers' health. Finally, reciprocating compressors are not a suitable choice when high compression ratios are demanded, e.g., to compress hydrogen from 0.1 to 10 MPa.

This is because the size of the cylinders may be too large, preventing efficient cooling of the hydrogen during compression. This leads to an increase in the heat produced and makes it more difficult to manage the heat transfer [94].

Diaphragm compressors avoid the use of lubricating oils. In these devices, the hydrogen is completely isolated from the piston. Indeed, the movement of the piston is transmitted to a hydraulic fluid, which in turn transmits the movement to a thin membrane called a “diaphragm”, which isolates the compression chamber from the hydraulic part. Diaphragm compressors are particularly suitable for applications requiring low flow rates, because too high flow rates can lead to premature diaphragm failure, and also because of the limited volume of the compression chambers commonly used [95,96]. On the other hand, ionic liquid compressors have been specifically developed to increase the compression efficiency in the case of hydrogen. Ionic liquids can replace the solid piston for compressing hydrogen because of their intrinsically low vapor pressure, excellent tribological behavior, and negligible solubility of hydrogen in these liquids [97–100]. Ionic liquid compressors have been proven to be the best solution for the mechanical compression of hydrogen. These devices are capable of compressing hydrogen from 0.5 MPa to 100 MPa in only five steps and with a specific energy consumption of about 2.7 kWh kg⁻¹, which is almost 25% of the specific energy consumption of a reciprocating compressor [101]. Moreover, ionic liquid compressors also have a very high efficiency of about 70% [102].

Although reciprocating compressors are most commonly used for hydrogen applications, centrifugal compressors are also an option. Indeed, a reciprocating compressor costs about 50% more than a centrifugal compressor [103]. The design of a centrifugal compressor is a multidimensional engineering task, since such a compressor is subject to a multitude of aerodynamic, thermodynamic, rotor dynamic, and mechanical parameters that are mutually interconnected and whose constraints largely determine the machine design [104]. Hydrogen centrifugal compressors consist of a succession of impellers that increase the hydrogen pressure. The case sections are then customarily connected in tandem to a common drive shaft [105]. Unlike reciprocating compressors, the compression ratio depends largely on the molecular weight of the gas in a centrifugal compressor. Indeed, the head of a centrifugal compressor is designed to increase the kinetic energy of the gas, which is then converted into pressure energy in the diffuser. Because of the low molecular weight of hydrogen, centrifugal compressors need tip-speeds that are around three times higher than those used for natural gas. Moreover, the aforementioned high-speed and purity requirements pose problems of seal design, contamination, vibration, and rotor dynamics [106]. Furthermore, because of its low specific gravity, hydrogen tends to return to the inlet, which reduces the efficiency of the centrifugal compressor. Thus, the impellers are easily subject to failure [107].

Although several types of mechanical devices for hydrogen compression exist and are available on the market, several of their disadvantages have to be taken into account. Beyond the drawbacks related to embrittlement phenomena mentioned above, contamination by lubricating oils, structural complexity, and maintenance difficulty, mechanical compressors normally consume between 5 and 15% of the energy stored by hydrogen. Additional problems arise when considering the installation of mechanical compressors in decentralized facilities, such as hydrogen refueling stations. This is because mechanical compressors are relatively large and can therefore take up a lot of space. Nevertheless, the major shortcoming of mechanical hydrogen compressors has to be addressed: their high cost. If hydrogen production is not taken into account, mechanical compression of hydrogen dominates the distribution of costs in a decentralized facility. Indeed, it is responsible for 54% of the CAPEX, 28% of the total energy consumption, and 18% of the operating and maintenance expenditure (OPEX) of a hydrogen refueling station [108]. Furthermore, the purchase price of a mechanical compressor is in the order of several hundred thousand dollars [109]. Therefore, the compression of a large amount of hydrogen must be carried out in order to amortize this cost.

5.2. Non-Mechanical Hydrogen Compressors

5.2.1. Metal Hydride Compressors

Non-mechanical hydrogen compressors have several advantages over mechanical compressors, including: (i) no moving components; (ii) quiet operation; (iii) high reliability and safety; and (iv) structural simplicity and greater compactness.

Of all non-mechanical hydrogen compressors, metal hydride compressors have attracted significant attention in recent years. They are thermally driven compressors because they use the properties of hydride-forming metals, alloys, or intermetallic compounds to absorb and desorb hydrogen simply by heat and mass transfer in the reaction system. Hydrogen absorption occurs at low temperature and lasts until the equilibrium pressure is equal to the feed pressure. When the metal hydride is heated, the hydrogen is desorbed and released at a higher pressure [110]. Metal hydride compressors are thoroughly described elsewhere [111]. No moving parts are present in a metal hydride compressor, which prevents the use of lubricating oils as needed in the case of mechanical compressors. However, this technology is limited both by the performance of the hydrides used and by heat management. Indeed, a multi-stage configuration is required to allow hydrogen compression up to 70 MPa [112]. This means that different types of metal hydrides have to be used in series, so that the desorption pressure of the first stage at high temperature can be slightly higher than the absorption pressure of the next stage at low temperature. In this way, the hydrogen is progressively compressed. Despite this, high desorption temperatures must be used in order to achieve high discharge pressures. To date, the average desorption temperature in metal hydride compressors is typically about 573 K, which significantly reduces efficiency by up to 10% [111]. Nevertheless, if the discharge pressure of a metal hydride compressor is sufficiently low, its cost may be lower than that of a mechanical hydrogen compressor operating at the same compression ratio [113].

5.2.2. Electrochemical Compressors

Based on the same principles as proton-exchange membrane fuel cells (PEMFCs), the electrochemical hydrogen compressor (EHC) has proven to be the most appropriate choice when hydrogen compression by a convenient, compact, cheap, and high-efficiency system is required [114]. Low-pressure hydrogen is fed to the anode of an electrochemical cell consisting of two electrodes, a polymer membrane, and gas diffusion layers. Here, the hydrogen is oxidized (Figure 6), thus splitting into protons and electrons, while electrical energy is supplied to the system. While the electrons follow the external electric circuit driven by a power supply, the protons pass through the polymer membrane to the cathode, where the hydrogen reduction reaction takes place. Hence, molecular hydrogen is produced there. The use of a backpressure regulator allows a flow of hydrogen at the desired discharge pressure. It is important to highlight that, unlike PEMFCs, the cathode of an EHC is blocked, i.e., no air is introduced. EHC requires very efficient core materials [115]. Nafion[®] is generally used as a membrane for EHCs [116]. Indeed, Nafion[®] offers high proton conductivity (0.13 S cm^{-1} at 348 K and 100% relative humidity), durability above 60,000 h, and high chemical stability [117]. Membrane-electrodes assemblies (MEA) are used to speed up the electrochemical process, in which metal nanoparticles, especially platinum, are dispersed in a solid electrolyte matrix in a similar way as PEMFCs, because of their excellent catalytic properties [118].

The compression mechanism described above is purely electrochemical, so that no moving unit is needed to drive it. This translates into a very high efficiency, up to 60% [119]. Furthermore, the EHC provides isothermal compression of hydrogen, which requires a lower energy demand compared to a polytropic or adiabatic process [120], and very high discharge pressures can be reached, even up to 100 MPa [121]. Despite all of these advantages, the efficiency of an EHC decreases considerably as the discharge pressure increases. Indeed, the permeation of molecular hydrogen through the PEM from cathode to anode increases linearly with the pressure difference over the EHC [122], reducing the amount of high-pressure hydrogen at the outlet of the EHC. This phenomenon is also known as “back-diffusion”.

For this reason, the use of EHC was found to be more appropriate for low-pressure applications, such as power-to-gas or as a pump for hydrogen recirculation in fuel cell vehicles [123], as well as in high-pressure hybrid systems where the EHC performs a first pre-compression stage [124,125]. In addition, the EHC can also function as a purifying device, which is an important advantage when hydrogen is mixed with other gases, e.g., in H₂-CH₄ hythane mixtures [126]. Compared to other conventional means of hydrogen purification and compression, the EHC combines low energy cost, high H₂ recovery and purity, low maintenance, low cost, and low operating temperature [127].

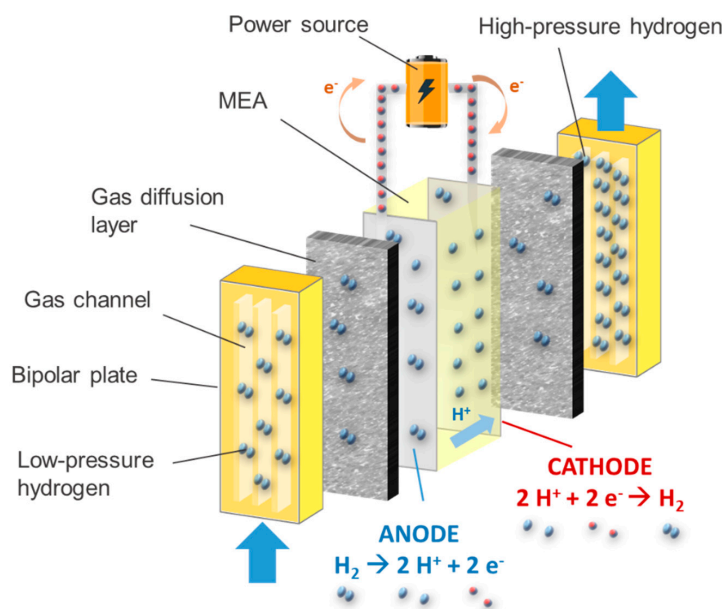


Figure 6. Scheme of the components and reactions taking place in an electrochemical hydrogen compressor.

5.2.3. Adsorption–Desorption Compressors

The adsorption of hydrogen on nanotextured materials, thus having both a high specific surface area and microporosity, has been studied in depth in the context of hydrogen storage in solids, as shown in the previous sections. In addition, hydrogen physisorption on microporous materials can be exploited to drive hydrogen compression, which represents a new and innovative way of compressing hydrogen in a non-mechanical way, and is therefore worth exploring.

An adsorption–desorption compressor is a thermally driven compressor, just like metal hydride hydrogen compressors. Therefore, hydrogen compression comes from thermal cycles consisting of progressive cooling and heating stages. Hydrogen adsorption is initially carried out at cryogenic temperatures. Indeed, the density of adsorbed hydrogen increases considerably as the temperature of the system is lowered. It is generally assumed that the density of the adsorbed hydrogen can be approximated to the density of liquid hydrogen [128,129]. Some authors have even observed a behavior similar to that of solid hydrogen in the adsorbed phase [130]. Hence, hydrogen adsorption is generally carried out at 77 K, i.e., at the temperature of liquid nitrogen, which is easy to achieve from an industrial point of view. Under these conditions, the density of the adsorbed hydrogen is thus equal to 70.8 g L⁻¹.

Hydrogen compression comes from the desorption of the pre-adsorbed amount of hydrogen. This is because hydrogen passes from the adsorbed phase, which is denser, to the bulk phase in a confined tank volume when the temperature rises. This can be done by removing the Dewar vessel filled with liquid nitrogen, where the compression tank is initially placed to drive the adsorption, thus leaving the tank at room temperature. Alternatively, a cooling system can be designed and placed inside the tank, in contact with the microporous adsorbent material, to manage better temperature gradients (Figure 7). In addition, microporous materials with high thermal conductivity should be

used in order to increase the kinetics of adsorption and desorption. For instance, activated carbons, which have been shown to be well suited for hydrogen adsorption with their many advantages [47], have an average thermal conductivity of about $0.2 \text{ W m}^{-1} \text{ K}^{-1}$ [131], which may decrease the efficiency of the adsorption–desorption compressor. Nevertheless, the use of composite adsorbents, such as mixed powders of flexible graphite and activated carbon, can increase the effective thermal conductivity of the porous bed [132].

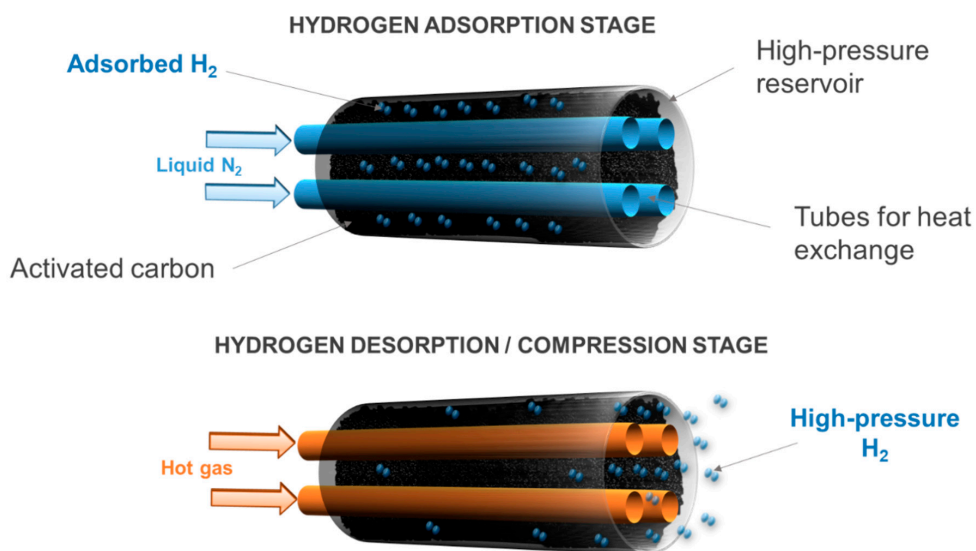


Figure 7. Operating principles of an adsorption–desorption compressor.

The adsorption–desorption compressor has all of the common advantages of non-mechanical compressors. Indeed, even if this technology is still too new to allow an accurate assessment of its performance and costs, the absence of moving parts undoubtedly contributes significantly to the reduction of installation and maintenance costs compared to mechanical compressors.

5.3. Overview of Costs and Efficiency

The US Department of Energy (DOE) has identified some targets to boost the widespread use of hydrogen compressors [133]. Specifically, referring to a device compressing hydrogen from 10 to 87.5 MPa, these targets are:

- uninstalled cost of the compressor system: USD 275,000
- specific energy consumption: 1.6 kWh kg^{-1}
- annual maintenance costs: 4% of the uninstalled costs.

The capital cost of a mechanical compressor averages USD 170,000 [134], whereas the OPEX is estimated at 5% of the capital cost per year [109]. While these costs are quite in line with DOE's targets, the efficiency of a conventional mechanical hydrogen compressor is relatively low, around 45% [135]. Higher efficiencies (around 70%) can be obtained with an ionic liquid compressor. Indeed, such devices are able to compress hydrogen from 0.5 to 100 MPa in only five steps and a specific energy consumption of around 2.7 kWh kg^{-1} —almost 25% of the specific energy consumption of conventional mechanical compressors [101].

There are several advantages of using a metal hydride compressor rather than a reciprocating compressor. According to a recent study on systems compressing hydrogen from 0.7 to 25 MPa [134], the CAPEX of a metal hydride compressor is around USD 150,000, compared to USD 170,000 for a reciprocating compressor operating under the same conditions. The OPEX value of a metal hydride compressor is estimated to be about USD 1000, compared to USD 9000 for a reciprocating compressor. In addition, the metal hydride compressor requires less electric energy to drive the compression

of hydrogen, i.e., only 0.5 kW compared to the 20 kW of the reciprocating counterpart. There is also a significant advantage in terms of volume and weight (400 L and 100 kg for the metal hydride compressor; 6000 L and 3600 kg for the reciprocating compressor). Nevertheless, the specific energy consumption of a metal hydride compressor is relatively high due to the low thermal conductivity of the absorbent materials and the high heat of absorption. Indeed, around 10 kWh kg⁻¹ may be required for a two-stage compression, lowering the compression efficiency to 10%.

The CAPEX of an electrochemical compressor can be as low as USD 170 per unit of hydrogen compression rate (kg day⁻¹), compared to USD 2300 for the mechanical counterpart [114]. The OPEX of an electrochemical compressor is also estimated to be lower than that of a reciprocating compressor (<USD 1 kg⁻¹ vs. USD 1.75–2.3 kg⁻¹). The specific energy consumption of an electrochemical hydrogen compressor is, on average, less than 4 kWh kg⁻¹, and strictly depends on the compression ratio. Indeed, electrochemical compressors have a high efficiency (>60%) and low energy consumption for low-pressure applications not exceeding 10 MPa [119].

Finally, the hydrogen adsorption–desorption compressor has been designed too recently to provide detailed information on CAPEX and OPEX, as well as on performance. The CAPEX is expected to be lower than that of a mechanical compressor, because of the significantly reduced number of moving parts and the more compact size. Nevertheless, the OPEX of an adsorption–desorption compressor can be quite high due to the wide operating temperature range and the use of liquid nitrogen, even though the heat of adsorption is 10 times lower than that of absorption in metal hydrides.

Tables 1 and 2 summarize the main characteristics of mechanical and non-mechanical hydrogen compressors, respectively. A thorough description of current hydrogen compression technologies and performance is given elsewhere [94].

Table 1. Main characteristics of mechanical hydrogen compressors.

Characteristic	Piston	Diaphragm	Ionic Liquid
Compression Rate (Nm ³ h ⁻¹)	~10,000	<1000	<1000
Efficiency	~45%	~45%	>70%
Cost	~USD 170,000 ¹	~USD 2300 kg ⁻¹ day ⁻¹	no data
Energy consumption (kWh kg ⁻¹)	<5	<5	~2.7
Advantages	<ul style="list-style-type: none"> - Mature technology - Adaptability to a large range of flow rates - High discharge pressures - Contamination by lube oils 	<ul style="list-style-type: none"> - Low power consumption - Low cooling requirement - Ideal for handling pure gases and explosives 	<ul style="list-style-type: none"> - High efficiency - High compression ratio - Low energy consumption - Reduced wear and long service - Low noise emissions - Quite isothermal compression - No gas contamination - Small number of moving units
Disadvantages	<ul style="list-style-type: none"> - Embrittlement phenomena - Several moving parts - Manufacturing and maintenance complexity - Difficulty in managing heat transfer - Presence of vibrations and noise - Not suitable for high compression ratios 	<ul style="list-style-type: none"> - Diaphragm failure - Complex design - Limited throughput 	<ul style="list-style-type: none"> - Liquid leaks - Cavitation phenomena - Corrosion

¹ Capital expenditure, compression from 0.7 to 25 MPa [134].

Table 2. Main characteristics of non-mechanical hydrogen compressors.

Characteristic	Metal Hydrides	Electrochemical	Adsorption–Desorption
Compression Rate (Nm ³ h ⁻¹)	<10	<10	no data ²
Efficiency (%)	<10	~60	no data ²
Cost (USD)	~150,000 ¹	~170 kg ⁻¹ day ⁻¹	no data ²
Energy consumption (kWh kg ⁻¹)	10	<4	no data ²
Advantages	<ul style="list-style-type: none"> - Thermally driven compressor - Absence of moving parts - Compact design - Safety - Absence of noise - High-purity hydrogen production 	<ul style="list-style-type: none"> - Low cost of operation - High-purity hydrogen production - No moving parts - Very high compression efficiency - Use as a purifier 	<ul style="list-style-type: none"> - Thermally driven compressor - No necessity for sealing - No moving parts, no vibration, no noise - Low cost of adsorbents - Low heat of adsorption
Disadvantages	<ul style="list-style-type: none"> - High desorption temperature - High heat of absorption - Limited heat transfer - Necessity of using appropriate alloys - Low efficiency - High weight - Low compression rates 	<ul style="list-style-type: none"> - Difficulty in manufacturing the cell assembly - Difficulty in realizing a perfect sealing - High cell resistance - Not suitable for very high discharge pressures - Low compression rates 	<ul style="list-style-type: none"> - Low thermal conductivity of adsorbents - Difficulty in thermal management - Low-temperature operation (77 K)

¹ Capital expenditure, compression from 0.7 to 25 MPa [134]; ² Adsorption–desorption compressor is still a novel technology, thus it is difficult to give precise assessment of its performances and cost.

6. Non-Mechanical and Hybrid Hydrogen Compression in Decentralized Facilities

For the development of fuel cell vehicles, it is necessary that the amount of hydrogen to be stored on board should be sufficient to cover a distance of up to 500 km. For example, hydrogen must be compressed to 70 MPa in order to store 5 kg in 120 L, at least [136–138]. To date, the available non-mechanical hydrogen compression technologies are not capable of achieving such a value if used alone. Nevertheless, if a hybrid configuration is adopted, consisting of a preliminary first stage compressing the hydrogen up to medium pressures and a second stage completing the compression to 70 MPa, it is possible to realize a non-mechanical compression system that could be used in hydrogen refueling stations. Therefore, we investigated the feasibility of a hybrid hydrogen compression system comprising: (i) a first EHC stage, up to 4–8 MPa and (ii) an adsorption–desorption compressor that compresses hydrogen up to 70 MPa (Figure 8).

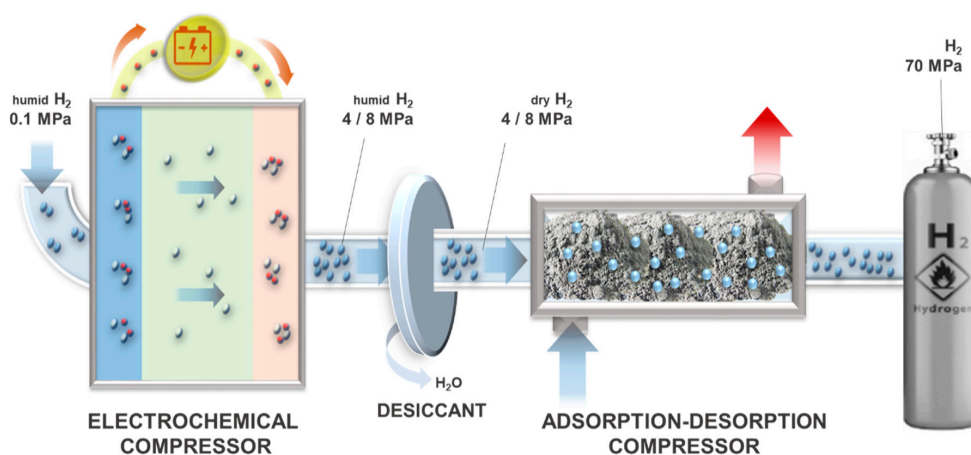


Figure 8. Scheme of a hybrid hydrogen compression: electrochemical at low pressure, adsorption–desorption at high pressure.

Figure 8 shows the proposed hybrid hydrogen-compression system without moving parts, as it is completely non-mechanical. It is also quiet in operation and has a simple structure and compact

dimensions compared to mechanical hydrogen compressors. The performance of each stage of the aforementioned system is discussed below.

6.1. Performance of the Electrochemical Compressor

As mentioned in the previous sections, the EHC is a very compact device that allows hydrogen to be compressed with high efficiency. This is due to the fact that hydrogen compression in an EHC is isothermal, which requires less energy than polytropic or adiabatic compression. Nevertheless, high efficiencies can be only achieved if the discharge pressure is not too high, in order to prevent hydrogen back-diffusion. For this reason, the EHC represents a suitable solution in a hybrid hydrogen compressor if it is used as a first pre-compression stage up to medium pressures, e.g., 4–8 MPa.

One of the most important core materials of an EHC is the membrane, whose role is to drive the protons from the anode to the cathode. The membrane thickness has been found to play a key role in the performance of an EHC. Indeed, we have found that thin membranes, such as Nafion[®] XL (30 μm thick), perform better than thicker membranes, such as Nafion[®] 117 (175 μm). Indeed, at 333 K, for an applied current density of 0.33 A cm^{-2} and a discharge pressure of 4 MPa, Nafion[®] XL achieved an overall efficiency of 53%, compared to 37% obtained using Nafion[®] 117 under the same conditions [120]. This large difference is due to the cell voltage required to drive the electrochemical reactions. Indeed, a cell voltage of 0.137 V was supplied using Nafion[®] 117 under the aforementioned conditions, whereas around 0.06 V was supplied with Nafion[®] XL (Figure 9). These data are in agreement with those obtained by Grigoriev et al. [139], who proved that it is possible to compress hydrogen from 0.1 MPa to 4.8 MPa using a single-stage EHC, applying a cell voltage of 0.14 V and at 0.2 A cm^{-2} , and using Nafion[®] 117 as the membrane. The aforementioned difference was obviously due to the higher ohmic resistance within the EHC, which resulted from the use of a thicker membrane, adding a significant overpotential contribution. It is important to underline that the detrimental contribution of the ohmic overpotential to the overall efficiency was much greater than that given by the hydrogen back-diffusion. Indeed, the hydrogen back-diffusion is inversely proportional to the membrane thickness [140]. An equivalent current density due to the back-diffusion equal to 5.22 mA cm^{-2} was obtained using Nafion[®] 117, whereas 45.31 mA cm^{-2} (i.e., nine times more) was obtained in the case of Nafion[®] XL.

Although EHC is based on the same technology and core materials as PEMFCs, some changes must be anticipated. This is the case for gas diffusion layers. While in PEMFCs carbon papers are recognized globally for the efficient transport of reagents and products into and out of the system [141], they are not able to withstand the large pressure gradients on the EHC. Therefore, porous titanium transfer layers, with a small average pore size (3–5 μm) and a high thickness (of the order of millimeters), can be used.

The rate of production of high-pressure hydrogen in an EHC, \dot{n}_{H_2} , (NL h^{-1}), only depends on the global current density supplied to the system, I (A cm^{-2}), and the amount of energy lost due to back-diffusion, I_{loss} (A cm^{-2}), according to Faraday's law:

$$\dot{n}_{\text{H}_2} = \frac{(I - I_{\text{loss}}) S}{2F} \quad (1)$$

where S (cm^{-2}) is the active area of the EHC and F (96,485 C mol^{-1}) is the Faraday constant. According to Equation (1), \dot{n}_{H_2} is about 15.6 NL h^{-1} at 1 A cm^{-2} , and increases linearly to 31.2 and 46.98 NL h^{-1} at 2 and 3 A cm^{-2} , respectively. In addition, the choice of the most appropriate I to be applied to the EHC is essential for practical applications. Indeed, the obvious advantage of supplying a high I to the EHC lies in its greater compactness and lower CAPEX, as well as in the higher rate of production of high-pressure hydrogen. Nevertheless, OPEX is relatively high under these conditions, and it can only be significantly reduced by decreasing I . Therefore, an I in the range of 0.5 to 1 A cm^{-2} is commonly used in an EHC compressor, such as in PEM water electrolyzers and PEMFCs [139].

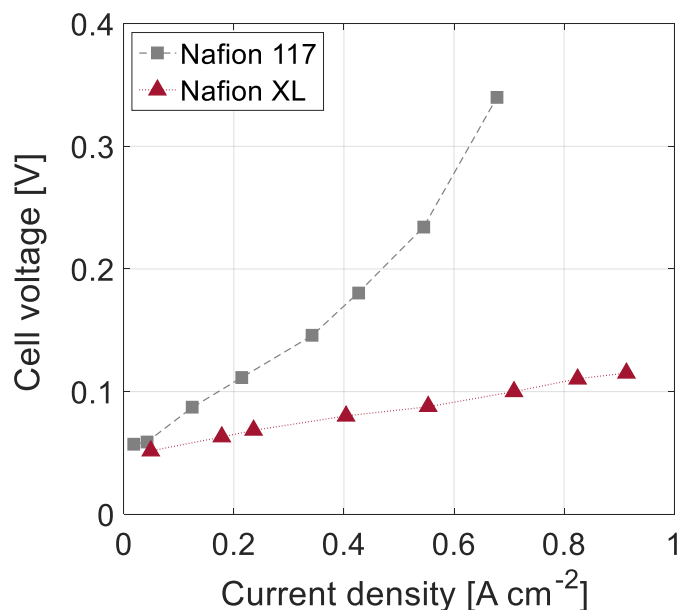


Figure 9. Polarization curves for different membranes ($T = 333$ K, stoichiometry 1.2, relative humidity of inlet hydrogen = 90%, discharge pressure = 4 MPa).

In order to improve the performance of an EHC, efficient water management inside the device must be ensured. Indeed, the transfer of protons from the anode to the cathode of the EHC, i.e., the ionic conductivity of the Nafion[®] membrane, is only enhanced if the membrane is well hydrated homogeneously. Unlike PEMFCs, water is not a reaction product in the EHC. Therefore, water is generally fed along with hydrogen into the anode compartment of the EHC. Unreacted hydrogen can also be recirculated from the anode outlet to the anode inlet to improve system efficiency, after rewetting and when high hydrogen stoichiometry is used. Liquid water can also be fed to the cathode side, which allows a better humidification of the membrane. Both of the aforementioned solutions are particularly appropriate when the anode pressure is above 0.1 MPa, i.e., when the molar fraction of water at the anode inlet is significantly lower than that of hydrogen. Nevertheless, a low-pressure pump for hydrogen recirculation and a high-pressure pump for feeding water to the high-pressure compartment shall be added to the system, resulting in an additional OPEX. It has been proved that a relative humidity of 90% in the hydrogen flow fed to the EHC allows a homogeneous humidification of the membrane, which results in a stable and enhanced performance and high efficiency. Indeed, when hydrogen at low relative humidity is fed to the EHC, i.e., <30%, unstable performance is observed. The EHC acts in such a way as to “consume” water on the cathode side, leading to a progressive dehydration of the membrane and, consequently, a significant reduction in efficiency [120]. Since water is used to humidify the EHC membrane, the high-pressure hydrogen flow produced at the cathode is wet. Thus, a desiccant must be used downstream of the EHC to dry the compressed hydrogen that will be fed into the next compression stage, i.e., the adsorption–desorption compressor (Figure 8).

6.2. Performance of the Adsorption–Desorption Compressor

Several materials can be used in the adsorption–desorption compression of hydrogen, provided they have both a high specific surface area and adequate pore size distribution. Indeed, it is essential that the adsorbent material have a high hydrogen adsorption capacity in order to produce large amounts of high-pressure hydrogen. Of all of the microporous adsorbent materials investigated in recent years for hydrogen adsorption, it has been shown that metal organic frameworks (MOFs) have outstanding BET (Brunauer, Emmett and Teller) areas, even higher than $6000 \text{ m}^2 \text{ g}^{-1}$, capable of adsorbing up to 10 wt.% of hydrogen at 77 K and 6 MPa [48]. Likewise, hyper-crosslinked polymers, silicas, aluminas, and zeolites have also shown high hydrogen adsorption capacities [49,51,142,143].

Nevertheless, most of these materials are relatively expensive, and their properties gradually degrade with ageing. Therefore, carbon materials, e.g., activated carbons, have proven to be the most suitable adsorbent materials for an adsorption–desorption compressor due to their moderate cost, high chemical stability, and textural properties suitable for hydrogen adsorption [47,144].

Beyond the absence of any moving part, one of the main advantages of an adsorption–desorption compressor is the ability to control the hydrogen discharge pressure by both the charging pressure and the desorption temperature. Indeed, numerical simulations have shown that it is possible to compress hydrogen up to 70 MPa by heating an adsorption–desorption compressor from 77 to 298 K and when hydrogen is fed at 4 MPa [145]. At a charging pressure of 0.1 MPa, a discharge pressure of 12 MPa was reached, which is not sufficient for automotive hydrogen applications [146]. This feature highlights the need for a first preliminary compression stage upstream of an adsorption–desorption compressor, as discussed above. Improvements are possible by increasing the desorption temperature. Indeed, it was shown that the amount of desorbed hydrogen can increase from 5% to 14% of the total amount of pre-adsorbed hydrogen when the system is heated further from 298 to 353 K [145], which considerably increases the amount of high-pressure hydrogen produced by the compressor. Temperatures above 298 K can be reached by using the heat recovered from the first compression stage. It is worth mentioning that a high-pressure water electrolyzer may also be used as a preliminary stage of the adsorption–desorption compressor. These devices typically operate at 353 K [10], so that the waste heat from the electrolyzer may be used to heat the adsorption–desorption compressor, thus improving the overall system efficiency.

The adsorption–desorption compressor is almost entirely controlled by heat exchange with the external environment. Figure 10a shows the time evolution of pressure and temperature that we obtained when using a 0.5 L adsorption–desorption compressor filled with 0.175 kg of commercially activated carbon (MSP20X, Kansai Coke&Chemicals, Hyogo, Japan). The increase in hydrogen pressure inside the tank was strictly related to the increase in temperature. Thus, the ambient temperature and the highest discharge pressure of 65 MPa were reached in 80 min. The time evolution shown in Figure 10 was obtained by heating the compressor by natural convection, i.e., by removing it from liquid nitrogen and keeping it at ambient temperature. It should be mentioned that we have only focused on a proof of concept in this study, so we did not evaluate the energy performance of such a thermally driven adsorption–desorption compressor. Indeed, an industrial system must have internal heat exchangers to optimize heat transfer, as shown in Figure 7. Methods to further reduce energy consumption, increase efficiency, and reduce the duration of the compression stage may include the use of cheap waste heat as previously stated, but also the cold recovery.

The data shown in Figure 10a were obtained by feeding hydrogen at 8 MPa into the adsorption–desorption compressor. Indeed, the activated carbon used has a very low bulk density (350 g L^{-1}), which limits the available specific surface area and micropore volume for hydrogen adsorption in the tank. Therefore, increasing the hydrogen charging pressure was found to be a good solution to increase the amount of hydrogen adsorbed in the compressor [125]. Nevertheless, the discharge pressure reached under these conditions was 65 MPa, slightly lower than that required by hydrogen automotive applications. For this reason, either increasing the charging pressure to 9 MPa or increasing the desorption temperature above 298 K could allow 70 MPa to be reached. By adopting the second solution, thus increasing the desorption temperature to 323 K, a high-pressure hydrogen flow was produced by the compressor, as shown in Figure 10b. Approximately 32 NL h^{-1} were quickly released by the compressor once the pressure inside the tank was 70 MPa, and a decreasing flow was then obtained for about 60 min. The high-pressure hydrogen flow vanished when the pressure inside the tank was below 70 MPa. The ratio of the total mass of high-pressure hydrogen produced to the tank volume was then equal to approximately 1 g L^{-1} for these non-optimized conditions.

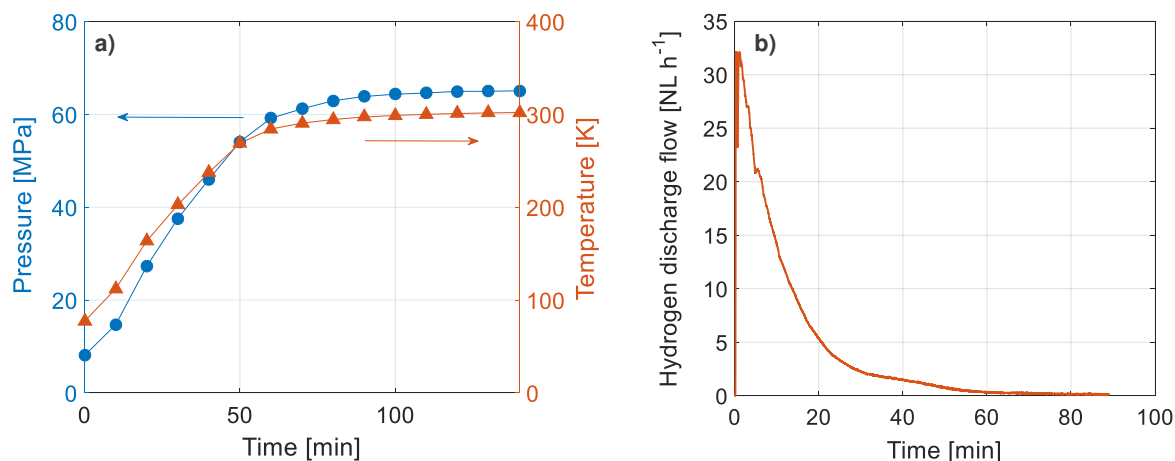


Figure 10. (a) Time evolution of pressure and temperature in an adsorption–desorption compressor and; (b) high-pressure hydrogen flow produced by the adsorption–desorption compressor (charging pressure = 8 MPa, $V = 0.5$ L, amount of adsorbent = 0.175 kg).

In order to make this system a feasible alternative to mechanical compressors or other types of non-mechanical compressors, several improvements are necessary. Mixtures of graphite-activated carbons could be used to increase the effective thermal conductivity of the porous bed, while a densification processes could be used to increase the bulk density of the adsorbent [147,148]. Such methods would increase the amount of hydrogen adsorbed within the porous bed and, with it, the mass of compressed hydrogen.

The energy optimization of the proposed adsorption–desorption compression is in progress. Thus, a system consisting of two tanks operating with a 180° phase shift is being studied. Indeed, the specific energy required by this system can be improved by using the frigories of the first tank during heating to cool the second tank. In this way, a thermally driven compressor could become a valid alternative to mechanical compressors from an industrial point of view.

7. Conclusions

Reducing the cost of hydrogen storage is crucial for the development of automotive hydrogen applications, such as fuel cell vehicles. In fact, the storage, transportation, and distribution stages cause significant increases in the price of hydrogen at the pump, which is currently at USD 8–10 kg⁻¹.

High-pressure hydrogen storage has been proven to be the most suitable method for storing hydrogen in decentralized facilities, i.e., at hydrogen refueling stations, compared to liquid-phase storage and storage in absorbed form in solid materials. Nevertheless, mechanical compressors, which are the most widely used technology for compressing hydrogen today, are responsible for more than 50% of CAPEX, 20% of OPEX, and about 30% of the total energy consumption of a hydrogen refueling station. Furthermore, mechanical compressors have several disadvantages, such as the presence of many moving parts, hydrogen embrittlement, high consumption of energy, high structural complexity, and difficult heat management.

Non-mechanical compressors, such as metal hydride, electrochemical, and adsorption–desorption compressors, may be a suitable alternative to replace mechanical compressors in decentralized facilities. Indeed, they have several advantages, such as the absence of moving parts that contributes significantly to the reduction of installation and maintenance costs compared to mechanical compressors. Metal hydride compressors ensure both safe storage and compression of hydrogen. As they require heat exchange, they are also known as thermally driven compressors. The search for appropriate alloys is essential for the development of such technology, as it requires both low desorption temperatures and high pressures.

Electrochemical compressors are based on the use of selective polymeric membranes, such as Nafion[®], to compress hydrogen gas, and have been proven to provide the highest level of compression efficiency (up to 60%) when the discharge pressure is not too high. Indeed, the efficiency of such devices is affected by the hydrogen back-diffusion. Electrochemical compressors have been found to offer good performances when equipped with a thin membrane at 1 A cm⁻².

Adsorption–desorption compressors rely on the ability of hydrogen to bind weakly to the surface of highly porous solids, such as carbon materials or metal-organic frameworks. Like metal hydride compressors, adsorption–desorption compressors are also thermally driven. Nevertheless, operation at a cryogenic temperature, down to 77 K, is required to enhance hydrogen uptakes. Such devices are able to compress hydrogen up to 70 MPa in a single step.

Hybrid configurations, consisting of: (i) a first electrochemical stage up to 4–8 MPa; and (ii) a second stage based on cyclic adsorption–desorption on carbon materials, make it possible to reach 70 MPa in a compact and quiet device. This could represent a promising alternative to mechanical hydrogen compressors in the framework of decentralized facilities, such as hydrogen refueling stations.

Author Contributions: Writing—original draft preparation, G.S.; writing—review and editing, project administration and funding acquisition, G.M.; writing—review and editing, A.C.; Conceptualization, writing—review and editing, project administration and funding acquisition, V.F. All authors have read and agreed to the published version of the manuscript.

Funding: This study was partly supported by the French PIA project “Lorraine Université d’Excellence”, reference ANR-15-IDEX-04-LUE. We gratefully acknowledge the financial support of CHEERS and TALiSMAN projects, funded by FEDER.

Conflicts of Interest: The authors declare no conflict of interest.

References

1. International Energy Agency. World Energy Balances 2019—Analysis. Available online: <https://www.iea.org/reports/world-energy-balances-2019> (accessed on 2 May 2020).
2. Dunn, S. Hydrogen futures: Toward a sustainable energy system. *Int. J. Hydrog. Energy* **2002**, *27*, 235–264. [CrossRef]
3. International Energy Agency. CO₂ Emissions Statistics—Data Services. Available online: <https://www.iea.org/subscribe-to-data-services/co2-emissions-statistics> (accessed on 2 May 2020).
4. NASA. Global Climate World of Change: Global Temperatures. Available online: <https://earthobservatory.nasa.gov/world-of-change/global-temperatures> (accessed on 2 May 2020).
5. Thema, M.; Bauer, F.; Sterner, M. Power-to-Gas: Electrolysis and methanation status review. *Renew. Sustain. Energy Rev.* **2019**, *112*, 775–787. [CrossRef]
6. Mazza, A.; Bompard, E.; Chicco, G. Applications of power to gas technologies in emerging electrical systems. *Renew. Sustain. Energy Rev.* **2018**, *92*, 794–806. [CrossRef]
7. Gondal, I.A. Hydrogen integration in power-to-gas networks. *Int. J. Hydrog. Energy* **2019**, *44*, 1803–1815. [CrossRef]
8. Hall, C.A.S.; Lambert, J.G.; Balogh, S.B. EROI of different fuels and the implications for society. *Energy Policy* **2014**, *64*, 141–152. [CrossRef]
9. Nikolaidis, P.; Poullikkas, A. A comparative overview of hydrogen production processes. *Renew. Sustain. Energy Rev.* **2017**, *67*, 597–611. [CrossRef]
10. Parra-Restrepo, J.; Blligny, R.; Dillet, J.; Didierjean, S.; Stemmelen, D.; Moyne, C.; Degiovanni, A.; Maranzana, G. Influence of the porous transport layer properties on the mass and charge transfer in a segmented PEM electrolyzer. *Int. J. Hydrog. Energy* **2020**, *45*, 8094–8106. [CrossRef]
11. Babic, U.; Suermann, M.; Büchi, F.N.; Gubler, L.; Schmidt, T.J. Critical Review—Identifying Critical Gaps for Polymer Electrolyte Water Electrolysis Development. *J. Electrochem. Soc.* **2017**, *164*, F387–F399. [CrossRef]
12. Hosseini, S.E.; Wahid, M.A. Hydrogen production from renewable and sustainable energy resources: Promising green energy carrier for clean development. *Renew. Sustain. Energy Rev.* **2016**, *57*, 850–866. [CrossRef]

13. Ausiello, A.; Micoli, L.; Turco, M.; Toscano, G.; Florio, C.; Pirozzi, D. Biohydrogen production by dark fermentation of *Arundo donax* using a new methodology for selection of H₂-producing bacteria. *Int. J. Hydrog. Energy* **2017**, *42*, 30599–30612. [CrossRef]
14. Salkuyeh, Y.K.; Saville, B.A.; MacLean, H.L. Techno-economic analysis and life cycle assessment of hydrogen production from different biomass gasification processes. *Int. J. Hydrog. Energy* **2018**, *43*, 9514–9528. [CrossRef]
15. Hosseini, S.E.; Wahid, M.A. Hydrogen from solar energy, a clean energy carrier from a sustainable source of energy. *Int. J. Energy Res.* **2020**, *44*, 4110–4131. [CrossRef]
16. He, W.; Namar, M.M.; Li, Z.; Maleki, A.; Tlili, I.; Safdari Shadloo, M. Thermodynamic analysis of a solar-driven high-temperature steam electrolyzer for clean hydrogen production. *Appl. Therm. Eng.* **2020**, *172*, 115152. [CrossRef]
17. Karapekmez, A.; Dincer, I. Thermodynamic analysis of a novel solar and geothermal based combined energy system for hydrogen production. *Int. J. Hydrog. Energy* **2020**, *45*, 5608–5628. [CrossRef]
18. Barbir, F. PEM electrolysis for production of hydrogen from renewable energy sources. *Sol. Energy* **2005**, *78*, 661–669. [CrossRef]
19. Ahmed, M.; Dincer, I. A review on photoelectrochemical hydrogen production systems: Challenges and future directions. *Int. J. Hydrog. Energy* **2019**, *44*, 2474–2507. [CrossRef]
20. International Energy Agency. Hydrogen—Tracking Energy Integration—Analysis. Available online: <https://www.iea.org/reports/tracking-energy-integration/hydrogen> (accessed on 2 June 2020).
21. GlobalPetrolPrices.com. Gasoline Prices around the World. Available online: https://www.globalpetrolprices.com/gasoline_prices/ (accessed on 2 June 2020).
22. Hydrogen Europe. Hydrogen in Industry. Available online: <https://hydrogeneurope.eu/hydrogen-industry> (accessed on 2 June 2020).
23. Harvey, L.D.D. *Energy and the New Reality 2: Carbon-free Energy Supply*; Earthscan: New York, NY, USA, 2010; ISBN 978-1-84407-913-1.
24. Commissariat de l'énergie atomique. L'hydrogène, les nouvelles technologies de l'énergie. *Clefs CEA* **2004**, *50*, 6.
25. Amos, W.A. *Costs of Storing and Transporting Hydrogen*; National Renewable Energy Lab.: Golden, CO, USA, 1999.
26. La Toyota. Mirai est la Voiture de Demain. Available online: <https://www.toyota.fr/new-cars/new-mirai/landing.json> (accessed on 15 April 2019).
27. Krawczak, P. Réservoirs Haute Pression en Composites. Available online: <https://www.techniques-ingenieur.fr/base-documentaire/materiaux-th11/applications-des-composites-42140210/reservoirs-haute-pression-en-composites-am5530/> (accessed on 17 June 2019).
28. Moradi, R.; Groth, K.M. Hydrogen storage and delivery: Review of the state of the art technologies and risk and reliability analysis. *Int. J. Hydrog. Energy* **2019**. [CrossRef]
29. James, B.D.; Houchins, C.; Huya-Kouadio, J.; DeSantis, D.A. *Final Report: Hydrogen Storage System Cost Analysis*; Strategic Analysis Inc.: Arlington, VA, USA, 2016.
30. Fraser, D. Solutions for hydrogen storage and distribution. In Proceedings of the PEI Wind-Hydrogen Symposium, Charlottetown, PE, Canada, 22–24 June 2003.
31. Michel, F.; Fieseler, H.; Allidières, L. Liquid hydrogen technologies for mobile use. In Proceedings of the World Hydrogen Energy Conference WHEC, Lyon, France, 13–16 June 2006.
32. Liu, Z.; Li, Y. Thermal physical performance in liquid hydrogen tank under constant wall temperature. *Renew. Energy* **2019**, *130*, 601–612. [CrossRef]
33. Sørensen, B.; Spazzafumo, G. 2—Hydrogen. In *Hydrogen and Fuel Cells*, 3rd ed.; Sørensen, B., Spazzafumo, G., Eds.; Academic Press: Cambridge, MA, USA, 2018; pp. 5–105. ISBN 978-0-08-100708-2.
34. Cardella, U.; Decker, L.; Klein, H. Roadmap to economically viable hydrogen liquefaction. *Int. J. Hydrog. Energy* **2017**, *42*, 13329–13338. [CrossRef]
35. Selvam, P.; Viswanathan, B.; Swamy, C.S.; Srinivasan, V. Magnesium and magnesium alloy hydrides. *Int. J. Hydrog. Energy* **1986**, *11*, 169–192. [CrossRef]
36. Sakintuna, B.; Lamari-Darkrim, F.; Hirscher, M. Metal hydride materials for solid hydrogen storage: A review. *Int. J. Hydrog. Energy* **2007**, *32*, 1121–1140. [CrossRef]

37. Alapati, S.V.; Johnson, J.K.; Sholl, D.S. Using first principles calculations to identify new destabilized metal hydride reactions for reversible hydrogen storage. *Phys. Chem. Chem. Phys.* **2007**, *9*, 1438–1452. [[CrossRef](#)] [[PubMed](#)]
38. Jain, I.P.; Lal, C.; Jain, A. Hydrogen storage in Mg: A most promising material. *Int. J. Hydrog. Energy* **2010**, *35*, 5133–5144. [[CrossRef](#)]
39. Department of Energy. Technical Targets for Onboard Hydrogen Storage for Light-Duty Vehicles. Available online: <https://energy.gov/eere/fuelcells/doe-technical-targets-onboard-hydrogen-storage-light-duty-vehicles> (accessed on 28 February 2017).
40. Satyapal, S.; Petrovic, J.; Read, C.; Thomas, G.; Ordaz, G. The U.S. Department of Energy’s National Hydrogen Storage Project: Progress towards meeting hydrogen-powered vehicle requirements. *Catal. Today* **2007**, *120*, 246–256. [[CrossRef](#)]
41. Hirscher, M.; Yartys, V.A.; Baricco, M.; Bellosta von Colbe, J.; Blanchard, D.; Bowman, R.C.; Broom, D.P.; Buckley, C.E.; Chang, F.; Chen, P.; et al. Materials for hydrogen-based energy storage—Past, recent progress and future outlook. *J. Alloys Compd.* **2020**, *827*, 153548. [[CrossRef](#)]
42. Sheffield, J.W.; Martin, K.B.; Folkson, R. 5—Electricity and hydrogen as energy vectors for transportation vehicles. In *Alternative Fuels and Advanced Vehicle Technologies for Improved Environmental Performance*; Folkson, R., Ed.; Woodhead Publishing: Sawston, UK, 2014; pp. 117–137. ISBN 978-0-85709-522-0.
43. Schlapbach, L.; Züttel, A. Hydrogen-storage materials for mobile applications. *Nature* **2001**, *414*, 353. [[CrossRef](#)]
44. Davids, M.W.; Lototskyy, M.; Malinowski, M.; van Schalkwyk, D.; Parsons, A.; Pasupathi, S.; Swanepoel, D.; van Niekerk, T. Metal hydride hydrogen storage tank for light fuel cell vehicle. *Int. J. Hydrog. Energy* **2019**. [[CrossRef](#)]
45. Bellosta von Colbe, J.; Ares, J.-R.; Barale, J.; Baricco, M.; Buckley, C.; Capurso, G.; Gallandat, N.; Grant, D.M.; Guzik, M.N.; Jacob, I.; et al. Application of hydrides in hydrogen storage and compression: Achievements, outlook and perspectives. *Int. J. Hydrog. Energy* **2019**, *44*, 7780–7808. [[CrossRef](#)]
46. Züttel, A. Materials for hydrogen storage. *Mater. Today* **2003**, *6*, 24–33. [[CrossRef](#)]
47. Sdanghi, G.; Maranzana, G.; Celzard, A.; Fierro, V. Hydrogen Adsorption on Nanotextured Carbon Materials. In *Hydrogen Storage Technologies*; Wiley-Blackwell: Hoboken, NJ, USA, 2018; pp. 263–320. ISBN 978-1-119-46057-2.
48. Suh, M.P.; Park, H.J.; Prasad, T.K.; Lim, D.-W. Hydrogen storage in metal-organic frameworks. *Chem. Rev.* **2012**, *112*, 782–835. [[CrossRef](#)] [[PubMed](#)]
49. Ghanem, B.S.; Msayib, K.J.; McKeown, N.B.; M. Harris, K.D.; Pan, Z.; Budd, P.M.; Butler, A.; Selbie, J.; Book, D.; Walton, A. A triptycene-based polymer of intrinsic microporosity that displays enhanced surface area and hydrogen adsorption. *Chem. Commun.* **2007**, *0*, 67–69. [[CrossRef](#)] [[PubMed](#)]
50. Thomas, K.M. Hydrogen adsorption and storage on porous materials. *Catal. Today* **2007**, *120*, 389–398. [[CrossRef](#)]
51. Makhseed, S.; Samuel, J. Hydrogen adsorption in microporous organic framework polymer. *Chem. Commun.* **2008**, 4342–4344. [[CrossRef](#)] [[PubMed](#)]
52. Durette, D.; Bénard, P.; Zacharia, R.; Chahine, R. Investigation of the hydrogen adsorbed density inside the pores of MOF-5 from path integral grand canonical Monte Carlo at supercritical and subcritical temperature. *Sci. Bull.* **2016**, *61*, 594–600. [[CrossRef](#)]
53. de la Casa-Lillo, M.A.; Lamari-Darkrim, F.; Cazorla-Amorós, D.; Linares-Solano, A. Hydrogen Storage in Activated Carbons and Activated Carbon Fibers. *J. Phys. Chem. B* **2002**, *106*, 10930–10934. [[CrossRef](#)]
54. Fierro, V.; Zhao, W.; Izquierdo, M.T.; Aylon, E.; Celzard, A. Adsorption and compression contributions to hydrogen storage in activated anthracites. *Int. J. Hydrog. Energy* **2010**, *35*, 9038–9045. [[CrossRef](#)]
55. Rzepka, M.; Lamp, P.; de la Casa-Lillo, M.A. Physisorption of Hydrogen on Microporous Carbon and Carbon Nanotubes. *J. Phys. Chem. B* **1998**, *102*, 10894–10898. [[CrossRef](#)]
56. Farha, O.K.; Özgür Yazaydın, A.; Eryazici, I.; Malliakas, C.D.; Hauser, B.G.; Kanatzidis, M.G.; Nguyen, S.T.; Snurr, R.Q.; Hupp, J.T. De novo synthesis of a metal-organic framework material featuring ultrahigh surface area and gas storage capacities. *Nat. Chem.* **2010**, *2*, 944–948. [[CrossRef](#)]
57. Cheng, H.-M.; Yang, Q.-H.; Liu, C. Hydrogen storage in carbon nanotubes. *Carbon* **2001**, *39*, 1447–1454. [[CrossRef](#)]

58. Klebanoff, L.E.; Keller, J.O. 5 Years of hydrogen storage research in the U.S. DOE Metal Hydride Center of Excellence (MHCoE). *Int. J. Hydrog. Energy* **2013**, *38*, 4533–4576. [CrossRef]
59. Schaefer, S.; Fierro, V.; Szczurek, A.; Izquierdo, M.T.; Celzard, A. Physisorption, chemisorption and spill-over contributions to hydrogen storage. *Int. J. Hydrog. Energy* **2016**, *41*, 17442–17452. [CrossRef]
60. Zhao, W.; Fierro, V.; Fernández-Huerta, N.; Izquierdo, M.T.; Celzard, A. Hydrogen uptake of high surface area-activated carbons doped with nitrogen. *Int. J. Hydrog. Energy* **2013**, *38*, 10453–10460. [CrossRef]
61. Zhao, W.; Fierro, V.; Zlotea, C.; Izquierdo, M.T.; Chevalier-César, C.; Latroche, M.; Celzard, A. Activated carbons doped with Pd nanoparticles for hydrogen storage. *Int. J. Hydrog. Energy* **2012**, *37*, 5072–5080. [CrossRef]
62. Bossel, U.; Eliasson, B.; Taylor, G. The Future of the Hydrogen Economy: Bright or Bleak? *Cogener. Compet. Power J.* **2003**, *18*, 29–70. [CrossRef]
63. Linde. Hydrogen. Available online: [//www.linde-engineering.com/en/process_plants/hydrogen_and_synthesis_gas_plants/gas_products/hydrogen/index.html](http://www.linde-engineering.com/en/process_plants/hydrogen_and_synthesis_gas_plants/gas_products/hydrogen/index.html) (accessed on 26 April 2019).
64. McPhy. Electrolyseurs pour la Production Continue et Automatisée, et/ou en grande Quantité D'hydrogène. Available online: <https://mcphy.com/fr/nos-produits-et-solutions/electrolyseurs/grande-capacite/> (accessed on 27 April 2019).
65. Hydrogen Europe. Hydrogen Transport & Distribution. Available online: <https://hydrogeneurope.eu/hydrogen-transport-distribution> (accessed on 26 April 2019).
66. Jancovici, J.-M. Que Peut-on Espérer des Piles à Combustible et de L'hydrogène? Available online: <https://jancovici.com/transition-energetique/transports/que-peut-on-esperer-des-piles-a-combustible-et-de-l-hydrogene/> (accessed on 13 May 2019).
67. Gerboni, R. 11—Introduction to hydrogen transportation. In *Compendium of Hydrogen Energy*; Woodhead Publishing Series in Energy; Gupta, R.B., Basile, A., Veziroğlu, T.N., Eds.; Woodhead Publishing: Sawston, UK, 2016; pp. 283–299. ISBN 978-1-78242-362-1.
68. US Department of Energy. 3.2 Hydrogen Delivery. In *Fuel Cells Technologies Office Multi-Year Research, Development and Demonstration (MYRD&D) Plan*; US Department of Energy: Washington, DC, USA, 2013.
69. Yang, C.; Ogden, J. Determining the lowest-cost hydrogen delivery mode. *Int. J. Hydrog. Energy* **2007**, *32*, 268–286. [CrossRef]
70. Engie. Comment est Transportée L'électricité? Available online: <https://particuliers.engie.fr/electricite/conseils-electricite/comprendre-electricite/etapes-transport-electricite.html> (accessed on 16 May 2019).
71. Effori, E.; Moussaoui, H.; Monaco, F.; Sharma, R.K.; Debayle, J.; Gavet, Y.; Delette, G.; Larbi, G.S.; Siebert, E.; Vulliet, J.; et al. Reaction Mechanism and Impact of Microstructure on Performances for the LSCF-CGO Composite Electrode in Solid Oxide Cells. *Fuel Cells* **2019**, *19*, 429–444. [CrossRef]
72. Vibhu, V.; Flura, A.; Rougier, A.; Nicollet, C.; Fourcade, S.; Hungria, T.; Grenier, J.-C.; Bassat, J.-M. Electrochemical ageing study of mixed lanthanum/praseodymium nickelates La_{2-x}Pr_xNiO_{4+δ} as oxygen electrodes for solid oxide fuel or electrolysis cells. *J. Energy Chem.* **2020**, *46*, 62–70. [CrossRef]
73. Brauns, J.; Turek, T. Alkaline Water Electrolysis Powered by Renewable Energy: A Review. *Processes* **2020**, *8*, 248. [CrossRef]
74. Carmo, M.; Fritz, D.L.; Mergel, J.; Stolten, D. A comprehensive review on PEM water electrolysis. *Int. J. Hydrog. Energy* **2013**, *38*, 4901–4934. [CrossRef]
75. Mergel, J.; Carmo, M.; Fritz, D. Status on Technologies for Hydrogen Production by Water Electrolysis. In *Transition to Renewable Energy Systems*; John Wiley & Sons, Ltd.: Hoboken, NJ, USA, 2013; pp. 423–450. ISBN 978-3-527-67387-2.
76. Buttler, A.; Spliethoff, H. Current status of water electrolysis for energy storage, grid balancing and sector coupling via power-to-gas and power-to-liquids: A review. *Renew. Sustain. Energy Rev.* **2018**, *82*, 2440–2454. [CrossRef]
77. Grigoriev, S.A.; Porembskiy, V.I.; Korobtsev, S.V.; Fateev, V.N.; Auprêtre, F.; Millet, P. High-pressure PEM water electrolysis and corresponding safety issues. *Int. J. Hydrog. Energy* **2011**, *36*, 2721–2728. [CrossRef]
78. Suermann, M.; Pătru, A.; Schmidt, T.J.; Büchi, F.N. High pressure polymer electrolyte water electrolysis: Test bench development and electrochemical analysis. *Int. J. Hydrog. Energy* **2017**, *42*, 12076–12086. [CrossRef]
79. Schalenbach, M.; Stolten, D. High-pressure water electrolysis: Electrochemical mitigation of product gas crossover. *Electrochim. Acta* **2015**, *156*, 321–327. [CrossRef]

80. Torregrossa, M. Hydrogène: Air Liquide Inaugure une Nouvelle Station à Orly. Available online: <https://www.automobile-propre.com/hydrogene-air-liquide-inaugure-nouvelle-station-orly/> (accessed on 27 April 2019).
81. California Fuel Cell Partnership. Cost to Refill. Available online: <https://cafcp.org/content/cost-refill> (accessed on 3 June 2019).
82. Prix des Carburants en France. Available online: <https://www.prix-carburants.gouv.fr/> (accessed on 27 April 2019).
83. Apostolou, D.; Enevoldsen, P.; Xydis, G. Supporting green Urban mobility—The case of a small-scale autonomous hydrogen refuelling station. *Int. J. Hydrog. Energy* **2019**, *44*, 9675–9689. [CrossRef]
84. Mainka, J.; Vivian, R. Faire Rouler les Voitures Hydrogène à Base D'énergie Renouvelable. Available online: <http://theconversation.com/faire-rouler-les-voitures-hydrogene-a-base-denergie-renouvelable-108536> (accessed on 17 May 2019).
85. H2 Station Maps. Costs and Financing. Available online: <https://h2stationmaps.com/costs-and-financing> (accessed on 17 May 2019).
86. Tarkowski, R. Underground hydrogen storage: Characteristics and prospects. *Renew. Sustain. Energy Rev.* **2019**, *105*, 86–94. [CrossRef]
87. HyUnder. *Assessment of the Potential, the Actors and Relevant Business Cases for Large Scale and Seasonal Storage of Renewable Electricity by Hydrogen Underground Storage in Europe*; European Commission: Brussels, Belgium, 2014.
88. Caglayan, D.G.; Weber, N.; Heinrichs, H.U.; Linßen, J.; Robinius, M.; Kukla, P.A.; Stolten, D. Technical potential of salt caverns for hydrogen storage in Europe. *Int. J. Hydrog. Energy* **2020**, *45*, 6793–6805. [CrossRef]
89. Hydro-Pac. High Pressure Gas Compressors, Pumps and Related Products. Available online: <http://www.hydropac.com/hydrogen-compression.html> (accessed on 27 April 2019).
90. Laurencelle, F. Développement d'un Compresseur D'Hydrogène Basé sur le Cyclage Thermique des Hydrures Métalliques. Ph.D. Thesis, Université du Québec à Trois-Rivières, Trois-Rivières, QC, Canada, 2007.
91. Dwivedi, S.N. Design Considerations for High-Pressure Reciprocating Compressors for Refinery Services. In Proceedings of the International Compressor Engineering Conference, West Lafayette, IN, USA, 17–20 July 1990.
92. Griffith, W.A.; Flanagan, E.B. Online, Continuous Monitoring Of Mechanical Condition And Performance For Critical Reciprocating Compressors. *Tex. AM Univ. Turbomach. Lab.* **2001**. [CrossRef]
93. Almasi, A. Latest practical notes and recent lessons learned on reciprocating compressors. *Aust. J. Mech. Eng.* **2016**, *14*, 138–150. [CrossRef]
94. Sdanghi, G.; Maranzana, G.; Celzard, A.; Fierro, V. Review of the current technologies and performances of hydrogen compression for stationary and automotive applications. *Renew. Sustain. Energy Rev.* **2019**, *102*, 150–170. [CrossRef]
95. Jia, X.; Zhao, Y.; Chen, J.; Peng, X. Research on the flowrate and diaphragm movement in a diaphragm compressor for a hydrogen refueling station. *Int. J. Hydrog. Energy* **2016**, *41*, 14842–14851. [CrossRef]
96. Jia, X.; Chen, J.; Wu, H.; Peng, X. Study on the diaphragm fracture in a diaphragm compressor for a hydrogen refueling station. *Int. J. Hydrog. Energy* **2016**, *41*, 6412–6421. [CrossRef]
97. MacFarlane, D.R.; Tachikawa, N.; Forsyth, M.; Pringle, J.M.; Howlett, P.C.; Elliott, G.D.; Davis, J.H.; Watanabe, M.; Simon, P.; Angell, C.A. Energy applications of ionic liquids. *Energy Env. Sci.* **2014**, *7*, 232–250. [CrossRef]
98. Plechkova, N.V.; Seddon, K.R. *Ionic Liquids Completely UnCOILed: Critical Expert Overviews*; John Wiley & Sons: Hoboken, NJ, USA, 2015; ISBN 978-1-118-83998-0.
99. Lei, Z.; Dai, C.; Chen, B. Gas Solubility in Ionic Liquids. *Chem. Rev.* **2014**, *114*, 1289–1326. [CrossRef] [PubMed]
100. Schluecker, E.; Szarvas, L.; Uerdingen, E. New developments in pumps and compressors using ionic liquids. *ACHEMA Worldw. News* **2008**, *1*, 5–7.
101. Mayer, M. From Prototype to Serial Production. Manufacturing Hydrogen Fuelling Stations. In Proceedings of the A3PS Conference 2014, Vienna, Austria, 20–21 October 2014; Available online: http://www.a3ps.at/sites/default/files/conferences/2014/papers/01_linde_mayer.pdf (accessed on 10 March 2020).
102. The Linde Group. *The Hydrogen Technologies. The Ionic Compressor 90 MPa—IC90*; Linde Group: Pullach, Germany, 2014.

103. Pahwa, P.K.; Pahwa, G.K. *Hydrogen Economy*; The Energy and Resources Institute (TERI): New Delhi, India, 2014; ISBN 978-81-7993-504-0.
104. Lüdtke, K.H. *Process. Centrifugal Compressors: Basics, Function, Operation, Design, Application*; Springer Science & Business Media: Berlin/Heidelberg, Germany, 2013; ISBN 978-3-662-09449-5.
105. Jackson, S.B. Hydrogen Compression by Centrifugal Compressors. U.S. Patent 3,401,111, 10 September 1968.
106. Witkowski, A.; Rusin, A.; Majkut, M.; Stolecka, K. Comprehensive analysis of hydrogen compression and pipeline transportation from thermodynamics and safety aspects. *Energy* **2017**, *141*, 2508–2518. [CrossRef]
107. Nie, D.; Chen, X.; Fan, Z.; Wu, Q. Failure analysis of a slot-welded impeller of recycle hydrogen centrifugal compressor. *Eng. Fail. Anal.* **2014**, *42*, 1–9. [CrossRef]
108. Parks, G.; Boyd, R.; Cornish, J.; Remick, R. *Hydrogen Station Compression, Storage, and Dispensing Technical Status and Costs*; National Renewable Energy Lab. (NREL): Golden, CO, USA, 2014.
109. Cox, K.E.; Williamson, K.D. *Hydrogen: Its Technology and Implication: Implication of Hydrogen Energy*; CRC Press: London, UK, 2018; Volume 5, ISBN 978-1-351-08175-7.
110. Laurencelle, F.; Dehouche, Z.; Goyette, J.; Bose, T. Integrated electrolyser—Metal hydride compression system. *Int. J. Hydrog. Energy* **2006**, *31*, 762–768. [CrossRef]
111. Lototskyy, M.V.; Yartys, V.A.; Pollet, B.G.; Bowman, R.C. Metal hydride hydrogen compressors: A review. *Int. J. Hydrog. Energy* **2014**, *39*, 5818–5851. [CrossRef]
112. Wang, X.; Liu, H.; Li, H. A 70 MPa hydrogen-compression system using metal hydrides. *Int. J. Hydrog. Energy* **2011**, *36*, 9079–9085. [CrossRef]
113. Stamatakis, E.; Zoulias, E.; Tzamalidis, G.; Massina, Z.; Analytis, V.; Christodoulou, C.; Stubos, A. Metal hydride hydrogen compressors: Current developments & early markets. *Renew. Energy* **2018**, *127*, 850–862. [CrossRef]
114. Moton, J.M.; James, B.D.; Colella, W.G. Advances in Electrochemical Compression of Hydrogen. In Proceedings of the ASME 2014 12th International Conference on Fuel Cell Science, Engineering and Technology, Boston, MA, USA, 30 June–2 July 2014.
115. Trégaro, M.; Rhandi, M.; Druart, F.; Deseure, J.; Chatenet, M. Electrochemical hydrogen compression and purification versus competing technologies: Part II. Challenges in electrocatalysis. *Chin. J. Catal.* **2020**, *41*, 770–782. [CrossRef]
116. Ströbel, R.; Oszcipok, M.; Fasil, M.; Rohland, B.; Jörissen, L.; Garche, J. The compression of hydrogen in an electrochemical cell based on a PE fuel cell design. *J. Power Sources* **2002**, *105*, 208–215. [CrossRef]
117. Wang, Y.; Ruiz Diaz, D.F.; Chen, K.S.; Wang, Z.; Adroher, X.C. Materials, technological status, and fundamentals of PEM fuel cells—A review. *Mater. Today* **2020**, *32*, 178–203. [CrossRef]
118. Pasierb, P.; Rekas, M. High-Temperature Electrochemical Hydrogen Pumps and Separators. *Int. J. Electrochem.* **2011**, *2011*, 1–10. [CrossRef]
119. Suermann, M.; Kiupel, T.; Schmidt, T.J.; Büchi, F.N. Electrochemical Hydrogen Compression: Efficient Pressurization Concept Derived from an Energetic Evaluation. *J. Electrochem. Soc.* **2017**, *164*, F1187–F1195. [CrossRef]
120. Sdanghi, G.; Dillet, J.; Didierjean, S.; Fierro, V.; Maranzana, G. Feasibility of Hydrogen Compression in an Electrochemical System: Focus on Water Transport Mechanisms. *Fuel Cells* **2019**, *20*, 370–380. [CrossRef]
121. HyET. Hydrogen Efficiency Technologies. Available online: <http://www.hyet.nl/newsite/technology/working-principle> (accessed on 15 March 2017).
122. Rohland, B.; Eberle, K.; Ströbel, R.; Scholta, J.; Garche, J. Electrochemical hydrogen compressor. *Electrochim. Acta* **1998**, *43*, 3841–3846. [CrossRef]
123. Wiebe, W.; Unwerth, T.V.; Schmitz, S. Hydrogen pump for hydrogen recirculation in fuel cell vehicles. *E3S Web Conf.* **2020**, *155*, 01001. [CrossRef]
124. Tao, Y.; Lee, H.; Hwang, Y.; Radermacher, R.; Wang, C. Electrochemical compressor driven metal hydride heat pump. *Int. J. Refrig.* **2015**, *60*, 278–288. [CrossRef]
125. Sdanghi, G.; Nicolas, V.; Mozet, K.; Schaefer, S.; Maranzana, G.; Celzard, A.; Fierro, V. A 70 MPa hydrogen thermally driven compressor based on cyclic adsorption-desorption on activated carbon. *Carbon* **2020**, *161*, 466–478. [CrossRef]
126. Pierre, M.; Tapan, B. *L'hydrogène*; John Libbey Eurotext: Arcueil, France, 2006; ISBN 978-2-7420-1318-0.
127. Rhandi, M.; Trégaro, M.; Druart, F.; Deseure, J.; Chatenet, M. Electrochemical hydrogen compression and purification versus competing technologies: Part I. Pros and cons. *Chin. J. Catal.* **2020**, *41*, 756–769. [CrossRef]

128. Kadono, K.; Kajjura, H.; Shiraishi, M. Dense hydrogen adsorption on carbon subnanopores at 77 K. *Appl. Phys. Lett.* **2003**, *83*, 3392–3394. [[CrossRef](#)]
129. Poirier, E.; Dailly, A. On the Nature of the Adsorbed Hydrogen Phase in Microporous Metal–Organic Frameworks at Supercritical Temperatures. *Langmuir* **2009**, *25*, 12169–12176. [[CrossRef](#)] [[PubMed](#)]
130. Ting, V.P.; Ramirez-Cuesta, A.J.; Bimbo, N.; Sharpe, J.E.; Noguera-Diaz, A.; Presser, V.; Rudic, S.; Mays, T.J. Direct Evidence for Solid-like Hydrogen in a Nanoporous Carbon Hydrogen Storage Material at Supercritical Temperatures. *ACS Nano* **2015**, *9*, 8249–8254. [[CrossRef](#)] [[PubMed](#)]
131. Xiao, J.; Yang, H.; Bénard, P.; Chahine, R. Numerical study of thermal effects in cryo-adsorptive hydrogen storage tank. *J. Renew. Sustain. Energy* **2013**, *5*, 021414. [[CrossRef](#)]
132. Wang, L.W.; Tamainot-Telto, Z.; Thorpe, R.; Critoph, R.E.; Metcalf, S.J.; Wang, R.Z. Study of thermal conductivity, permeability, and adsorption performance of consolidated composite activated carbon adsorbent for refrigeration. *Renew. Energy* **2011**, *36*, 2062–2066. [[CrossRef](#)]
133. Corgnale, C.; Sulic, M. Techno-Economic Analysis of High-Pressure Metal Hydride Compression Systems. *Metals* **2018**, *8*, 469. [[CrossRef](#)]
134. Stamatakis, E. Benchmark Analysis & Pre-feasibility study for the market penetration of Metal Hydride Hydrogen Compressor. In Proceedings of the Integrated, Innovative Renewable Energy—Hydrogen Systems and Applications Workshop, Athens, Greece, 5–7 July 2017.
135. Cornish, A.J. Hydrogen Fueling Station Cost Reduction Study. In *Survey Results and Analysis of the Cost and Efficiency of Various In-Operation Hydrogen Fueling Stations*; Engineering, Procurement & Construction, LLC: Lakewood, CO, USA, 2011. Available online: <https://www.osti.gov/servlets/purl/1120569> (accessed on 28 August 2019).
136. Rand, D.A.J.; Dell, R.M.; Dell, R. *Hydrogen Energy: Challenges and Prospects*; RSC Publishing, Royal Society of Chemistry: Cambridge, UK, 2008; ISBN 978-0-85404-597-6.
137. Hwang, H.T.; Varma, A. Hydrogen storage for fuel cell vehicles. *Curr. Opin. Chem. Eng.* **2014**, *5*, 42–48. [[CrossRef](#)]
138. Toyota Europe. Hydrogen-Powered Toyota Mirai. Pioneering the Future of Mobility. Available online: <https://www.toyota-europe.com/new-cars/mirai/> (accessed on 22 May 2019).
139. Grigoriev, S.A.; Shtatniy, I.G.; Millet, P.; Porembsky, V.I.; Fateev, V.N. Description and characterization of an electrochemical hydrogen compressor/concentrator based on solid polymer electrolyte technology. *Int. J. Hydrog. Energy* **2011**, *36*, 4148–4155. [[CrossRef](#)]
140. Schalenbach, M.; Hoefner, T.; Paciok, P.; Carmo, M.; Lueke, W.; Stolten, D. Gas Permeation through Nafion. Part 1: Measurements. *J. Phys. Chem. C* **2015**, *119*, 25145–25155. [[CrossRef](#)]
141. Ramousse, J.; Deseure, J.; Lottin, O.; Didierjean, S.; Maillet, D. Modelling of heat, mass and charge transfer in a PEMFC single cell. *J. Power Sources* **2005**, *145*, 416–427. [[CrossRef](#)]
142. Lee, J.-Y.; Wood, C.D.; Bradshaw, D.; Rosseinsky, M.J.; Cooper, A.I. Hydrogen adsorption in microporous hypercrosslinked polymers. *Chem. Commun.* **2006**, 2670–2672. [[CrossRef](#)] [[PubMed](#)]
143. Yang, S.J.; Kim, T.; Im, J.H.; Kim, Y.S.; Lee, K.; Jung, H.; Park, C.R. MOF-Derived Hierarchically Porous Carbon with Exceptional Porosity and Hydrogen Storage Capacity. *Chem. Mater.* **2012**, *24*, 464–470. [[CrossRef](#)]
144. Cabria, I.; López, M.J.; Alonso, J.A. The optimum average nanopore size for hydrogen storage in carbon nanoporous materials. *Carbon* **2007**, *45*, 2649–2658. [[CrossRef](#)]
145. Sdanghi, G.; Nicolas, V.; Mozet, K.; Maranzana, G.; Celzard, A.; Fierro, V. Modelling of a hydrogen thermally driven compressor based on cyclic adsorption-desorption on activated carbon. *Int. J. Hydrog. Energy* **2019**, *44*, 16811–16823. [[CrossRef](#)]
146. Hosseini, S.E.; Butler, B. An overview of development and challenges in hydrogen powered vehicles. *Int. J. Green Energy* **2020**, *17*, 13–37. [[CrossRef](#)]
147. Celzard, A.; Fierro, V. Preparing a Suitable Material Designed for Methane Storage: A Comprehensive Report. *Energy Fuels* **2005**, *19*, 573–583. [[CrossRef](#)]
148. Celzard, A.; Albinak, A.; Jasienko-Halat, M.; Maréché, J.F.; Furdin, G. Methane storage capacities and pore textures of active carbons undergoing mechanical densification. *Carbon* **2005**, *43*, 1990–1999. [[CrossRef](#)]



Article

Numerical Simulations of Cryogenic Hydrogen Cooling in Vortex Tubes with Smooth Transitions †

Konstantin I. Matveev *  and Jacob Leachman 

School of Mechanical and Materials Engineering, Washington State University, Pullman, WA 99164-2920, USA; jacob.leachman@wsu.edu

* Correspondence: matveev@wsu.edu

† This article is an extended version of our short paper published in Proceedings of the 2nd Pacific Rim Thermal Engineering Conference, Maui, HI, USA, 13–17 December 2019.

Abstract: Improving efficiency of hydrogen cooling in cryogenic conditions is important for the wider applications of hydrogen energy systems. The approach investigated in this study is based on a Ranque-Hilsch vortex tube (RHVT) that generates temperature separation in a working fluid. The simplicity of RHVT is also a valuable characteristic for cryogenic systems. In the present work, novel shapes of RHVT are computationally investigated with the goal to raise efficiency of the cooling process. Specifically, a smooth transition is arranged between a vortex chamber, where compressed gas is injected, and the main tube with two exit ports at the tube ends. Flow simulations have been carried out using STAR-CCM+ software with the real-gas Redlich-Kwong model for hydrogen at temperatures near 70 K. It is determined that a vortex tube with a smooth transition of moderate size manifests about 7% improvement of the cooling efficiency when compared vortex tubes that use traditional vortex chambers with stepped transitions and a no-chamber setup with direct gas injection.

Keywords: hydrogen systems; cryogenics; vortex tubes; computational fluid dynamics



Citation: Matveev, K.I.; Leachman, J. Numerical Simulations of Cryogenic Hydrogen Cooling in Vortex Tubes with Smooth Transitions. *Energies* **2021**, *14*, 1429. <https://doi.org/10.3390/en14051429>

Academic Editors: Samuel Simon Araya, Vincenzo Liso and Attilio Converti

Received: 21 January 2021
Accepted: 2 March 2021
Published: 5 March 2021

Publisher's Note: MDPI stays neutral with regard to jurisdictional claims in published maps and institutional affiliations.



Copyright: © 2021 by the authors. Licensee MDPI, Basel, Switzerland. This article is an open access article distributed under the terms and conditions of the Creative Commons Attribution (CC BY) license (<https://creativecommons.org/licenses/by/4.0/>).

1. Introduction

Hydrogen is often considered as the most promising candidate for the “green” fuel of the future. However, there are still hurdles that need to be overcome to make hydrogen sufficiently easy and economical to handle. In the liquid form, hydrogen becomes one of the most energy dense substances. However, in order to liquefy hydrogen, very low temperatures are needed, and this process is complicated by the fact that hydrogen undergoes exothermic transformation between ortho and para isomeric states during the cooling process. Therefore, improvement of the current and development of novel liquefaction systems for hydrogen is of high priority to the green energy community.

One of the promising mechanical components that can boost efficiency of cryogenic refrigeration systems is the so-called vortex tube. This device is known to produce two streams with significant temperature separation at two opposite outlets while taking a compressed fluid at the inlet (Figure 1a). Ranque [1] discovered this effect by injecting gas tangentially into a tube and producing a cold stream near the centerline while the hot gas was concentrated in the peripheral flow. Hilsch [2] investigated this phenomenon further, which led to the name Ranque-Hilsch vortex tube commonly used nowadays for this device.

Being a mechanically simple system (no moving solid parts), vortex tubes have been extensively studied since the 1950s, and several reviews can be found in [3–5]. A number of studies addressed physical mechanisms for temperature separation, characterization of the system performance and some optimization. Among various explanations for the vortex-tube thermal effect, the most common include shear work done by shear work of the inner vortex on the outer flow exposed to wall friction [6], gas expansion near the tube centerline due to rotation [7] and turbulent fluctuations in the radial direction in

compressible flow [3]. Parametric experiments with variable length-diameter ratios of the tube, number of nozzles, inlet pressure and orifice sizes were reported in [8]. Several studies considered complex systems with vortex tubes as components, such as cascading setups [9] and drying-cooling devices [10].

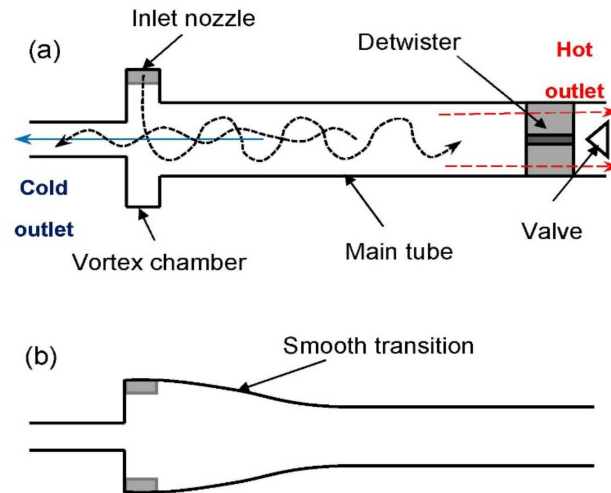


Figure 1. (a) General vortex tube schematic. Dotted curves show possible trajectories of fluid particles. Dashed lines indicate axial flow toward the hot exit (red) and cold outlet (blue). (b) Vortex tube configuration with smooth transition studied in this work.

However, there is still room for improvement of the vortex tube configurations. For hydrogen liquefaction processes, even small increases in efficiency may contribute to significant benefit, when such systems are implemented on a mass scale. An initial effort toward the development of vortex tubes for cryogenic hydrogen systems was discussed in [11].

The present study focuses on one novel shape modification of the vortex tube associated with the smooth transition between the vortex chamber and the main straight tube (Figure 1b). It was discovered that rounding of corners at this transition [12,13], making the entire tube convergent [14,15] and using conical shapes [16] can lead to the improvement of air-based vortex tubes. Experimental optimization of structural parameters of a control valve and a hot tube in a vortex-tube air separator and numerical studies of internal flow features were conducted in [17]. Performance of a novel convergent vortex tube was parametrically investigated in a test series [18], where it was found that much shorter tube lengths are possible in convergent setups in comparison with straight tubes and that valves can be eliminated as well. In the present work, the effect of a smooth transition between the vortex chamber and the main tube in a system using gaseous hydrogen as the working fluid is investigated with help of computational fluid dynamics (CFD) simulations.

In one of the initial CFD studies with vortex tubes [19], a simplistic axisymmetric flow with swirl was modeled, and some adjustment of geometrical parameters in CFD was needed to achieve agreement with test data. Computational studies using economical Reynolds-averaged Navier-Stokes (RANS) models generally suggested that the standard $k - \epsilon$ turbulence model gives better prediction [16,20]. More expensive LES-based simulations provided more insight on flow patterns [21,22].

Applications of CFD programs for modeling fluid phenomena in hydrogen and cryogenic systems have steadily increased in the last two decades. Several papers on numerical simulations relevant to cryogenic vortex tubes have been published. For example, energy and species separation in air at cryogenic conditions were investigated in [23]. Hydrogen-filled vortex tubes with traditional geometry were modeled in [24] for a wide range of inlet temperatures, including cryogenic states; and it was found that the vortex tube performance generally decreases at low temperatures. In the current work, high-fidelity numerical simulations are employed to simulate cooling of cryogenic gaseous

hydrogen in a vortex tube with novel geometrical modifications. A short version of the present paper has been previously reported at the conference [25].

2. Computational Aspects

Modeling of vortex tubes in this study was carried out with the CFD program STAR-CCM+ (Siemens, Munich, Germany), version 13.04.011. It employs a finite-volume coupled flow solver with the second order discretization. For computational economy, only steady solutions were sought, and simplified turbulence models based on the RANS formulation were utilized. The governing Reynolds-averaged equations include the mass, momentum and energy equations,

$$\frac{\partial(\rho\bar{u}_j)}{\partial x_j} = 0 \quad (1)$$

$$\frac{\partial(\rho\bar{u}_i\bar{u}_j)}{\partial x_j} = -\frac{\partial p}{\partial x_i} + \frac{\partial}{\partial x_j} \left[\mu \left(\frac{\partial\bar{u}_i}{\partial x_j} + \frac{\partial\bar{u}_j}{\partial x_i} - \frac{2}{3}\delta_{ij}\frac{\partial\bar{u}_k}{\partial x_k} \right) - \rho\overline{u'_i u'_j} \right] \quad (2)$$

$$\frac{\partial(\rho E\bar{u}_j)}{\partial x_j} = \frac{\partial}{\partial x_j} \left[-p\bar{u}_i\delta_{ij} + u_i \left\{ \mu \left(\frac{\partial\bar{u}_i}{\partial x_j} + \frac{\partial\bar{u}_j}{\partial x_i} - \frac{2}{3}\delta_{ij}\frac{\partial\bar{u}_k}{\partial x_k} \right) - \rho\overline{u'_i u'_j} \right\} \right] - \frac{\partial q_j}{\partial x_j} \quad (3)$$

where \bar{u}_i are the time-averaged velocity components, p is the pressure, ρ is the fluid density, μ is the fluid viscosity, $-\rho\overline{u'_i u'_j}$ is the turbulent stress tensor, E is the total energy per unit mass and q_j are the heat fluxes.

To model the turbulent stress, several RANS turbulent models were investigated, and the standard $k - \varepsilon$ model was found to perform best in the present study, as discussed in the next section. Moreover, the two-layer, all Y^+ option of this model was employed due to significant flow variability in the vortex tube. The specific implementation details of the numerical methods in the applied software can be found in STAR-CCM+ Manual [26].

Since the current study analyzes flow of gaseous hydrogen at cryogenic conditions, a real-gas equation of state was employed to describe the gas properties. Among several approaches available in the literature for real-gas modeling, the Redlich-Kwong model was found to treat equilibrium hydrogen gas quite accurately in the range of properties of interest to this study [27,28]. Hence, the Redlich-Kwong model was adopted for all simulations shown in this paper.

3. Model Verification and Validation

The verification study has been conducted with the most promising configuration among considered in this paper. The tube geometry with inlets and outlets is illustrated in Figure 2, while its dimensions are given in the next section. There are four inlets where stagnation properties are specified (3 atm and 77 K), the cold outlet has the stagnation pressure of 1 atm, and the hot-outlet flow rate is selected to make the cold-flow fraction equal to $\zeta = 0.46$. This fraction is defined as the ratio of the mass flow rates at the cold outlet, \dot{m}_C , and at the inlet, \dot{m}_{in} ,

$$\zeta = \frac{\dot{m}_C}{\dot{m}_{in}} \quad (4)$$

The other domain boundaries are solid walls which are treated as adiabatic no-slip surfaces.

The unstructured numerical grid was built inside the domain containing polyhedral cells that work well in situations with complex flows. Near the solid walls, five prismatic cell layers were constructed to cover the boundary layer. Because of high variations of the flow velocity inside vortex tubes and associated difficulty of ensuring the same cell thickness in terms of Y^+ values, the two-layer, all- Y^+ option was activated in all turbulent models. This approach allows for resolving a viscous sub-layer when the cell thickness corresponds to Y^+ below 5, while relying on wall functions for large Y^+ values and using a combined model for intermediate Y^+ values.

Three numerical grids (fine, intermediate, coarse) were constructed by scaling the cell linear dimension with a factor of 2 between neighboring grids. An illustration of the fine-grid slices in several tube sections is given in Figure 3. The cell count on the fine grid was about 1.6 million.

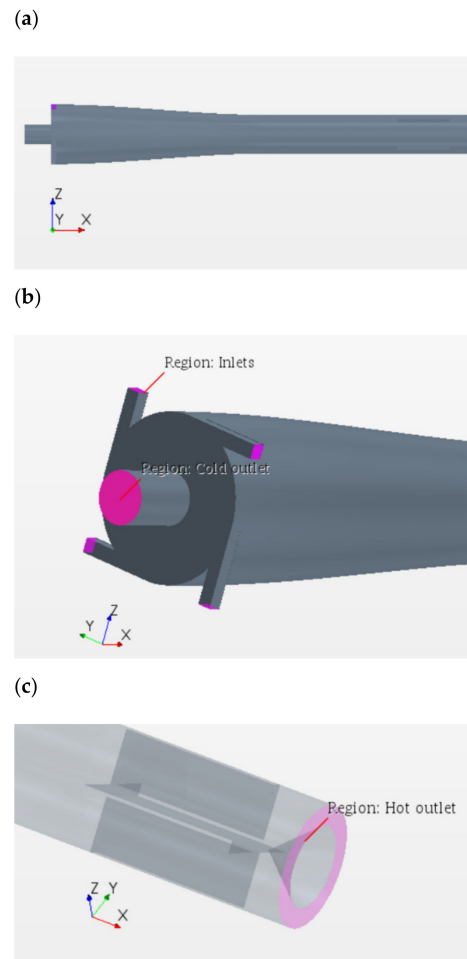


Figure 2. Geometry of the novel vortex tube: (a) side view; (b) region near inlets and cold outlet; (c), transparent view around hot outlet and de-twister.

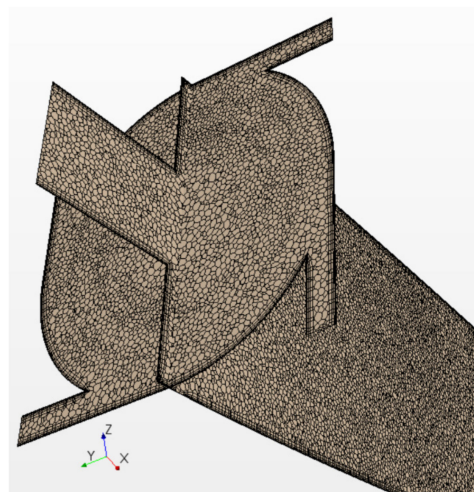


Figure 3. Numerical grid in longitudinal and transverse (through the nozzles) cross-sections of the vortex tube.

In the grid independence study, the difference between total temperatures at the inlet and cold outlet was used as the metric of convergence. The obtained results for $T_{in,tot} - T_{C,tot}$ at three grids are given in Figure 4. One can see that this parameter approaches a constant value as the number of cells increases. The numerical uncertainty, evaluated with help of Richardson extrapolation [29] and factors of safety [30], produced an estimated error of about 10% relative to results obtained with the fine grid. In all following simulations carried out in this study, the same fine-mesh settings were employed when constructing numerical grids.

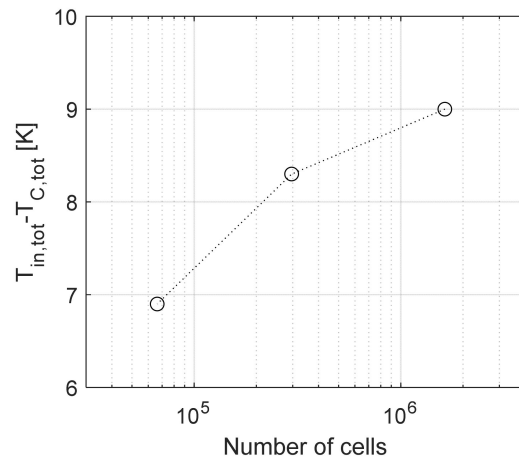


Figure 4. Total temperature drop at the cold outlet obtained on three grids.

In this work, a validation study was run against test data available for vortex tubes with air at normal conditions [31]. They reported the temperature differences between the hot and cold outlets for a common vortex tube configuration of relatively low performance. The comparison between the present numerical results and previous experimental data are shown in Figure 5. As once can see, simulation results obtained with the standard $k - \epsilon$ turbulence model are in satisfactory agreement with experimental data, while the realizable $k - \epsilon$ model predicts much lower temperature differentials. Other turbulence models were also tried, including the standard and (shear stress transport) SST $k - \omega$ models and Reynolds stress transport (RST) model. They produced results in between the two numerical models shown in Figure 5. As the standard $k - \epsilon$ turbulence model performed best with other numerical settings in the present study, it was adopted for all other simulations.

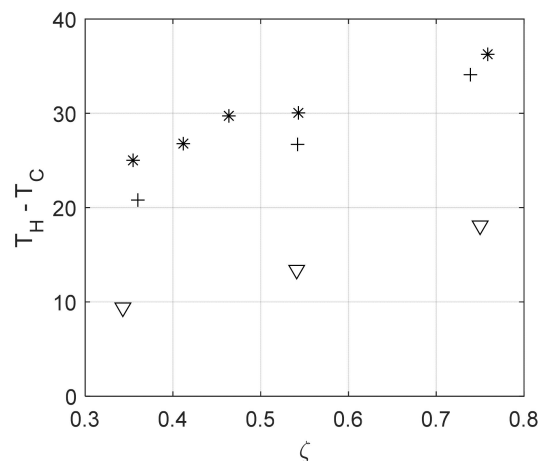


Figure 5. Comparison of experimental and numerical temperature differences between the hot and cold outlets. Stars, experimental data; crosses, standard $k - \epsilon$ model; triangles, realizable $k - \epsilon$ model.

4. Simulation Results

To come up with a reasonably efficient initial design of a vortex tube, the semi-empirical procedure of Merkulov [3] was followed. This method involves experimental charts and correlations that were obtained from tests of various air-filled vortex tubes. Here, the gas properties for hydrogen at 77 K were used instead. The temperature of 77 K corresponds to the boiling point of liquid nitrogen, which allows for relatively inexpensive cooling of hydrogen down to this temperature. Further cooling would require expensive refrigerants, such as helium-neon mixtures, and that is where the vortex tube application becomes attractive.

The external input parameters were selected as follows: (i) the inlet stagnation pressure and temperature are 3 atm and 77 K, (ii) the cold outlet pressure is 1 atm, (iii) the desirable cold-outlet stagnation temperature is about 70 K (since the expected temperature drop in vortex tubes with pressure ratio of 3 is about 10%) and (iv) the desired input mass flow rate is around 5 g/s. The applied design method produced the following recommendations for the device geometry: the main tube length of 133 mm and diameter of 14.9 mm, the cold-outlet diameter of 7.3 mm, and the total inlet area of 16 mm². To ensure adequate performance at this relatively low length-to-diameter ratio, vortex stopper (de-twister) is needed near the hot outlet, which was shown in Figure 2. Since the vortex-tube performance usually benefits from several distributed inlets, four square nozzles of side 2 mm have been chosen here. The optimal cold-flow fraction suggested by this method for the selected geometry is about 0.46.

The initial tube configuration was selected to have a constant-diameter vortex tube with direct tangential nozzle integration at one end of the main tube. This setup is illustrated as case A in Figure 6. Since a stepped vortex chamber is commonly used in practice, such a system was created by displacing nozzles outward from the tube centerline by two nozzle side lengths (case B in Figure 6). The next configuration with a smooth transition between the vortex chamber and the main tube was considered, as shown by case C in Figure 6. (It was also used for the verification study discussed above.) Since this geometry demonstrated performance improvement, even wider vortex chamber was also tried with diameter greater than the main tube diameter by 8 mm (four nozzle sides), as shown by case D in Figure 6.

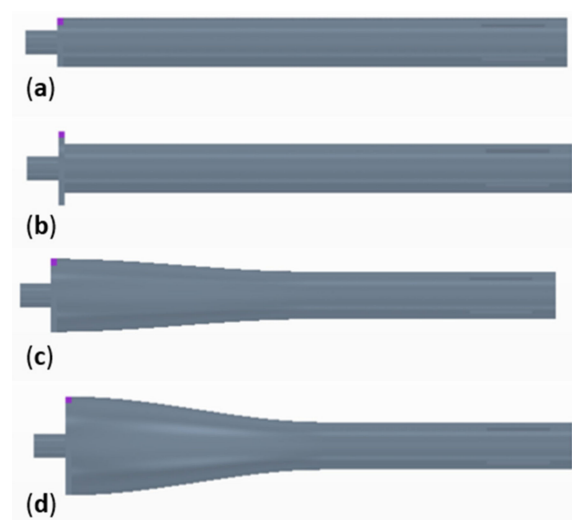


Figure 6. Investigated shapes of vortex tubes (a) case A, (b) case B, (c) case C, (d) case D. Purple square dot in the top left corner of each configuration indicates one of four inlet nozzles.

These four configurations were meshed with a fine mesh following the same approach as in the above validation study. Simulations were then carried out for these cases at the same total pressure at the inlet and cold outlet and the same inlet total temperature. The hot-outlet pressure was adjusted to keep the cold-flow fraction at the same value (0.46).

The main dimensional characteristics of the vortex tubes include the stagnation temperature separations at the outlets in comparison with the inlet stagnation temperature, $T_{in,tot} - T_{C,tot}$ and $T_{H,tot} - T_{in,tot}$. Another common metric for the vortex-tube performance is the isentropic temperature efficiency that compares actual temperature drop at the cold end to that in the isentropic processes at the same pressure ratio $p_r = P_{in,tot}/P_{C,tot}$.

$$\eta_T = \frac{T_{in,tot} - T_{C,tot}}{T_{in,tot} \left[1 - p_r^{\frac{\gamma-1}{\gamma}} \right]} \quad (5)$$

These characteristics obtained from simulations with four tube configurations are given in Figure 7. It is apparent that introducing a stepped vortex chamber (case B) reduces the system efficiency in comparison with a straight tube (case A). However, employing a smooth transition between the shifted nozzles and the main tube (case C) helps boost the temperature separation (up to 9 K at the cold side) and efficiency ($\eta_T \approx 0.44$). Case C seems to have expansion of the tube near the inlets closest to the optimum (among the studied cases), since case D with even larger cross-sectional area exhibits performance degradation.

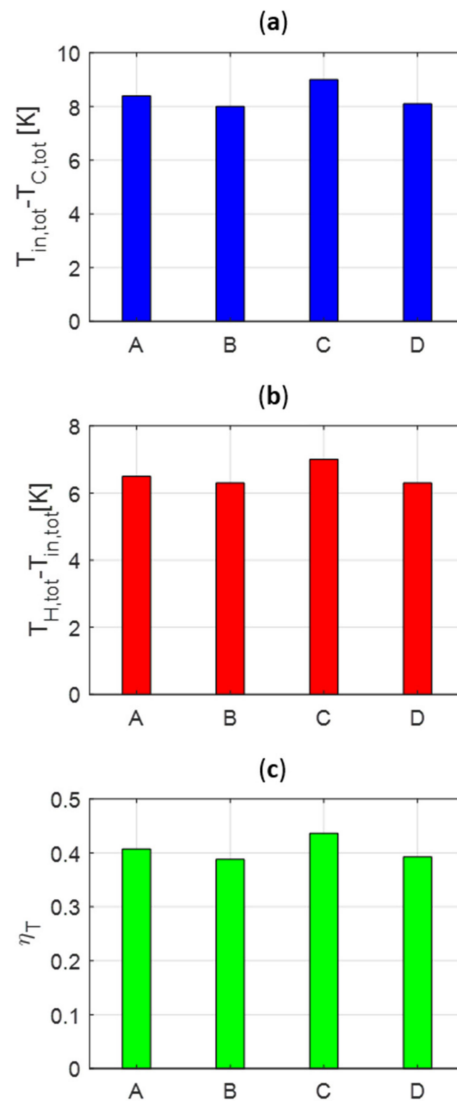


Figure 7. Predicted temperature separations at (a) cold outlet and (b) hot outlet. (c) Isentropic temperature efficiency.

Some flow characteristics of the four studied cases are presented in Figures 8–10. The flow patterns shown with help of line convolution integrals, as well as velocity magnitudes, are given in Figure 8 at longitudinal tube sections. The maximum velocity in the predominantly tangential direction is observed near the inlets. The incoming flow forms a swirl that propagates downstream keeping highest velocities closer to the walls (although velocity at the wall surface drops to zero due to no-slip condition). The flow regions near the centerline are relatively slow. The lowest velocities are shown near the hot outlet where the vortex stopper significantly decelerates the flow. It can be noticed that the vortex chamber expansions alter the size of the high-velocity swirl. It appears that case C with smooth transition and moderate widening keeps the fast near-wall flow the longest distance along the tube, which eventually leads to greater temperature separation.

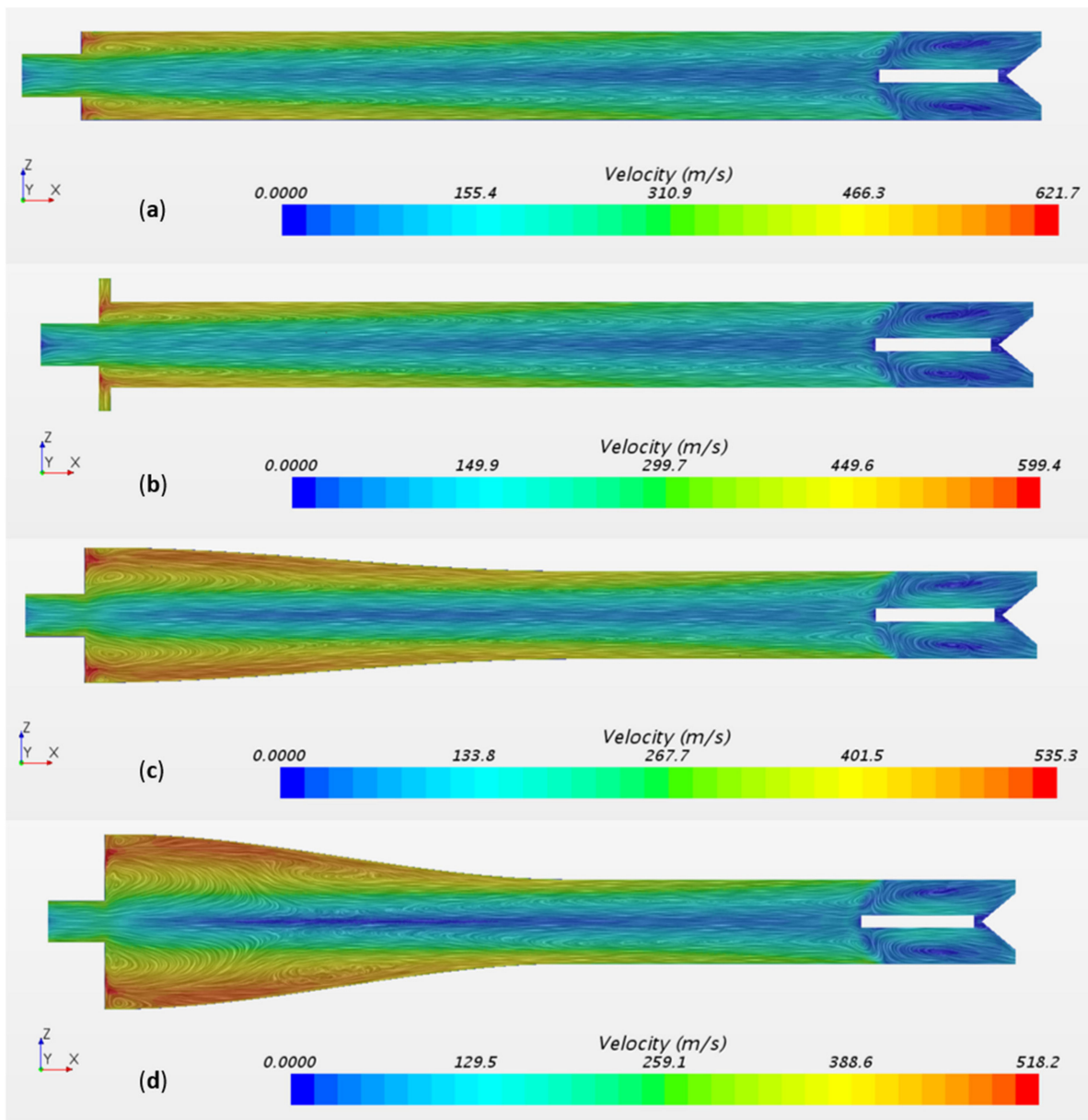


Figure 8. Flow patterns and total velocity magnitudes in the longitudinal planes: (a) case A, (b) case B, (c) case C, (d) case D.

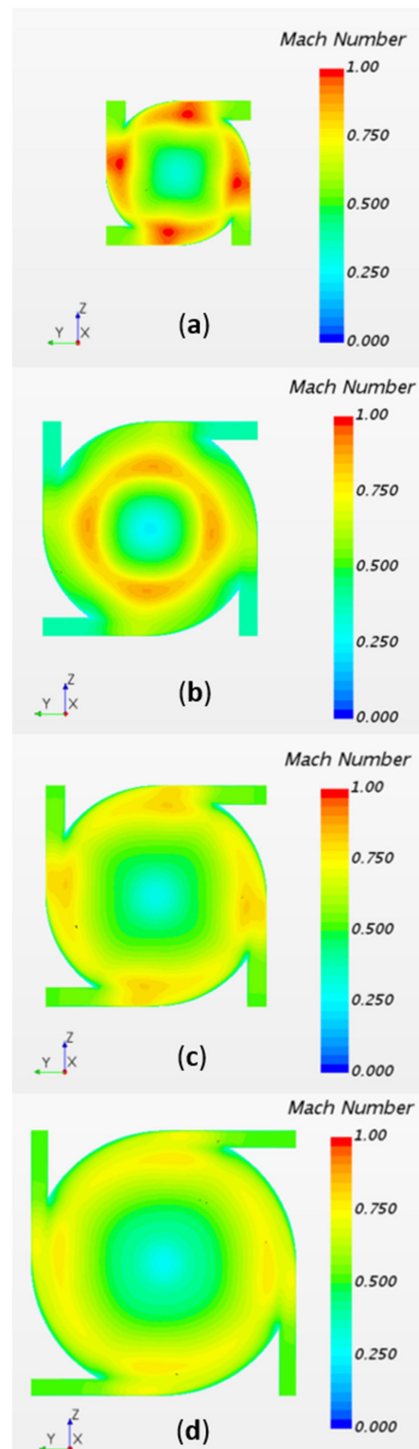


Figure 9. Mach number distribution in transverse vortex-chamber planes (a) case A, (b) case B, (c) case C, (d) case D.

In Figure 8, one can also notice slices of quasi-toroidal vortices between the outer flow with axial direction toward the hot end and the inner flow with axial motion to the cold outlet. In cases A and B these vortices are rather thin and elongated. With wider tube enlargements, these vortices grow in the radial direction, which may help to keep the faster outer flow in case C. In Case D, several vortex systems are present, which likely leads to excessive dissipation and reduction in the system efficiency.

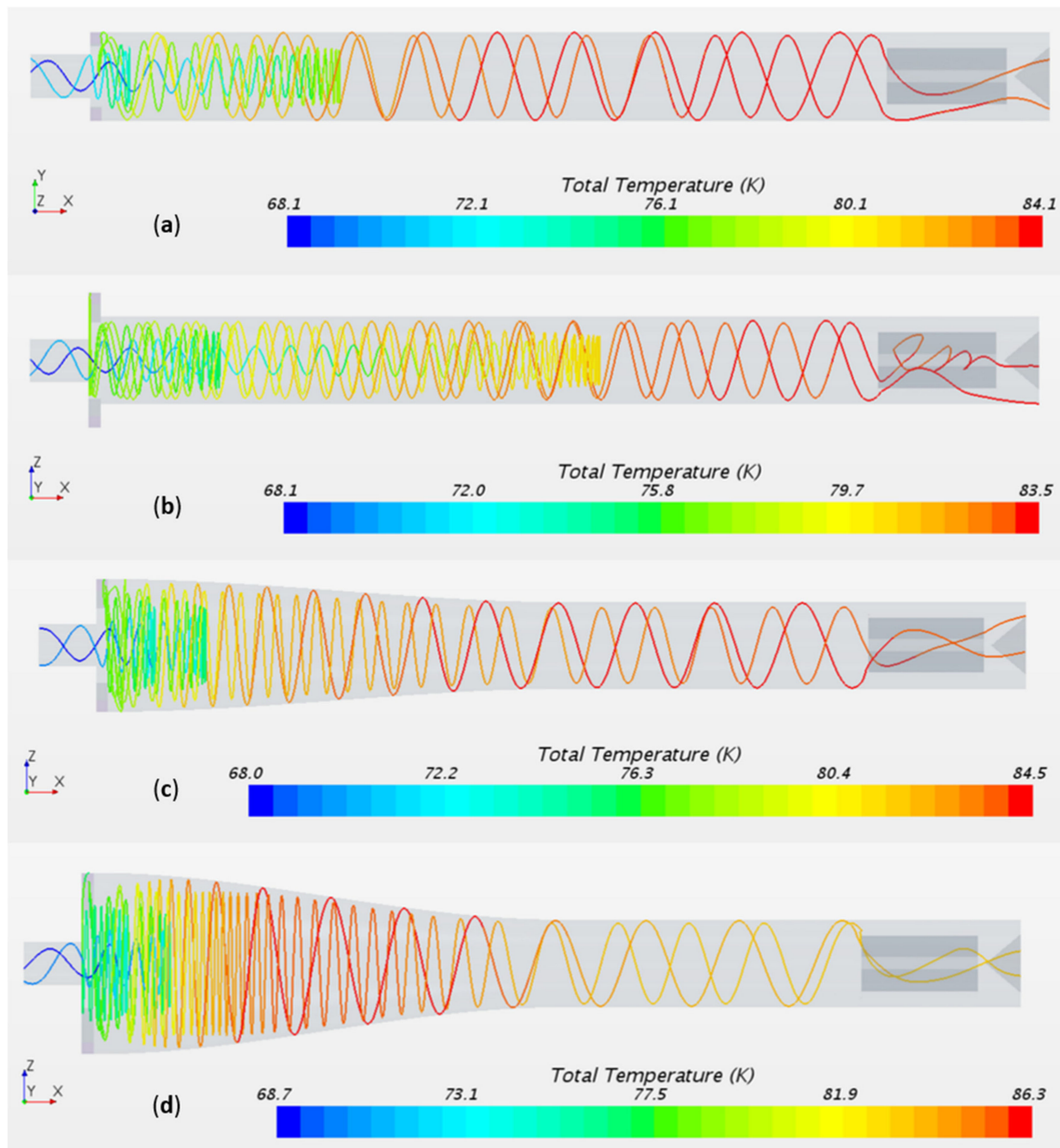


Figure 10. Vortex-tube streamlines with indicated variations of the total temperature (a) case A, (b) case B, (c) case C, (d) case D.

The flow Mach numbers in the tube transverse sections passing through the middle of nozzles are depicted in Figure 9. The highest Mach numbers (around one) are observed in the original tube (case A) without a vortex chamber. These near-sonic zones are formed at short distances from the entrances where the incoming flow from the nearest nozzle is merging with the flow supplied through other nozzles. Near the tube centerlines, the flow velocity drops substantially. In case B with a stepped vortex chamber, the high-Mach number regions are shifted toward the tube center, where the flow from the inlets enters the main tube. More uniform distribution of Mach numbers is observed in case C, while their magnitudes still reach high values. Even more uniform, but also substantially lower Mach numbers, appear in the widest case D.

The selected streamlines with superimposed total temperature magnitudes are illustrated for four studied cases in Figure 10. All streamlines have swirl shapes due to high tangential velocities. The spatial period in the axial directions increase away from the nozzles indicating reduction of the tangential speeds, while the axial velocity changes

little. The streamlines in the outer region generally demonstrate an increase in T_{tot} as they approach the hot outlet, with the exception of case D where the total temperature peaks at the end of the smooth transition between the inlets and the main tube. The streamlines originated at the nozzle closer to the tube centerline initially propagate toward the hot end, but then they change direction and proceed toward the cold outlet while reducing their radii.

Additional simulations have been conducted for cases A (original) and C (highest performing among studied setups) at low and high cold-flow fractions. The results for the cold temperature separation and isentropic efficiency are shown in Figure 11. Besides these parameters, another metric important in practical applications is introduced by multiplying the cold-flow fraction ζ and the isentropic efficiency η_T . This product characterizes the cooling capacity of the vortex tube rather than just the cold temperature. As one can see in Figure 11, case C slightly outperforms the original setup A in the entire range studied. The isentropic efficiency is the highest at the low ζ , while the capacity metric peaks at the high cold-flow fraction.

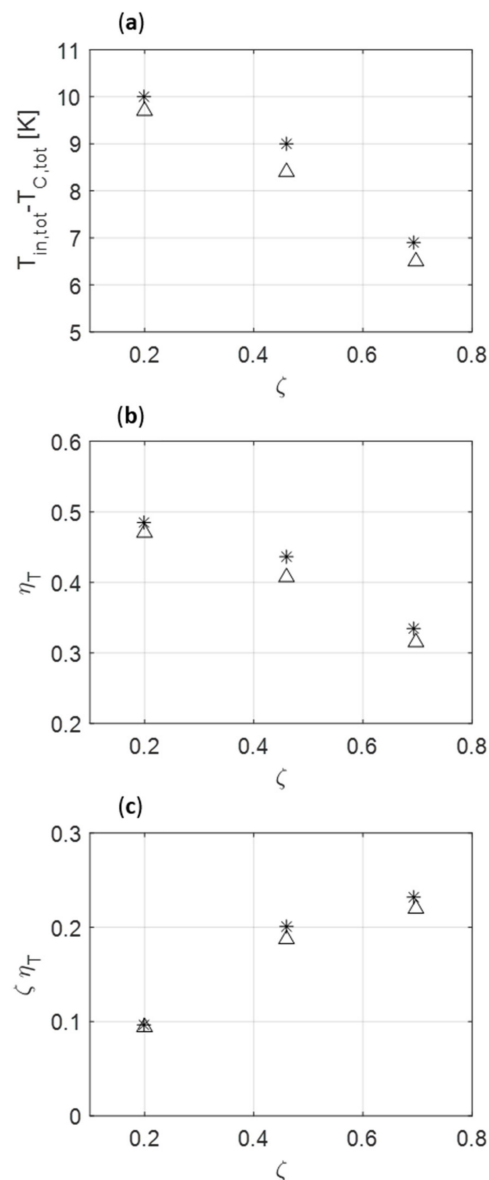


Figure 11. Metrics of performance of vortex tubes: (a) temperature separation at the cold outlet, (b) isentropic temperature efficiency, (c) non-dimensional cooling capacity. Stars, highest performing (among studied setups) case C; triangles, original case A.

5. Concluding Remarks

In the present study, flow of cryogenic hydrogen gas inside vortex tubes was numerically simulated. Verification and validation indicate reasonably good accuracy of this modeling. The innovative geometry of the vortex tube, involving a smooth transition between the vortex chamber and the main tube, resulted in increased by about 7% performance of such a tube relative to a standard straight tube. This improvement can be associated with slower degradation of the vortex strength along the tube away from the inlets, which enhances the energy transfer from the core to peripheral fluid regions. However, if the tube widening near the entrance becomes excessive, the efficiency drops since the inlet flow becomes insufficient to maintain high-velocity swirl in a wide tube.

Further optimization of the vortex tube may involve variations of other geometrical parameters of the system. A next step in modeling vortex tubes intended specifically for hydrogen liquefaction can include even lower temperatures and possibly involve hydrogen condensation and transition between ortho/para phases of hydrogen. Hence, actual properties of hydrogen beyond the simplified equations of state will need to be used. Modeling of condensation may require finer numerical grids and multi-phase approaches.

Author Contributions: Conceptualization, K.I.M. and J.L.; Formal analysis, K.I.M.; Funding acquisition, J.L.; Investigation, K.I.M.; Methodology, K.I.M. and J.L.; Project administration, J.L.; Software, K.I.M.; Validation, K.I.M.; Visualization, K.I.M.; Writing—original draft, K.I.M.; Writing—review & editing, J.L. All authors have read and agreed to the published version of the manuscript.

Funding: This research was funded by the US Department of Energy, grant number DE-EE0008429. The APC was funded by the US Department of Energy.

Data Availability Statement: The data presented in this study are available on request from the corresponding author.

Conflicts of Interest: The authors declare no conflict of interest.

References

1. Ranque, G.J. Experiences sur la detente avec production simultanees d'un echappement d'air chaud et echappement d'air froid. *J. Phys. Rad.* **1933**, *4*, 112–114.
2. Hilsch, R. The use of the expansion of gases in a centrifugal field as cooling process. *Rev. Sci. Instr.* **1947**, *18*, 108–113. [[CrossRef](#)]
3. Merkulov, A.P. *Vortex Effect and Its Application in Technology*; Mashinostroenie: Moscow, Russia, 1969.
4. Eiamsa-ard, S.; Promvong, P. Review of Ranque-Hilsch effects in vortex tubes. *Renew. Sustain. Energy Rev.* **2008**, *12*, 1822–1842. [[CrossRef](#)]
5. Thakare, H.R.; Monde, A.; Parekh, A.D. Experimental, computational and optimization studies of temperature separation and flow physics of vortex tube: A review. *Renew. Sustain. Energy Rev.* **2015**, *52*, 1043–1071. [[CrossRef](#)]
6. Aljuwayhel, N.F.; Nellis, G.F.; Klein, S.A. Parametric and internal study of the vortex tube using a CFD model. *Int. J. Refrig.* **2005**, *28*, 442–450. [[CrossRef](#)]
7. Polihronov, J.G.; Straatman, A. Thermodynamics of angular propulsion in fluids. *Phys. Rev. Lett.* **2012**, *109*, 054504. [[CrossRef](#)] [[PubMed](#)]
8. Nouri-Borujerdi, A.; Bovand, M.; Rashidi, S.; Dincer, K. Geometric parameters and response surface methodology on cooling performance of vortex tubes. *Int. J. Sustain. Energy* **2017**, *36*, 872–886. [[CrossRef](#)]
9. Bej, N.; Sinhamahapatra, K.P. Numerical analysis on the heat and work transfer due to shear in a hot cascade Ranque-Hilsch vortex tube. *Int. J. Refrig.* **2016**, *68*, 161–176. [[CrossRef](#)]
10. Acar, M.S.; Erbas, O.; Arslan, O. The performance of vapor compression cooling system aided Ranque-Hilsch vortex tube. *Therm. Sci.* **2019**, *23*, 1189–1201. [[CrossRef](#)]
11. Bunge, C.D.; Cavender, K.A.; Matveev, K.I.; Leachman, J.W. Analytical and numerical performance models of a Heisenberg Vortex Tube. *IOP Conf. Ser. Mater. Sci. Eng.* **2017**, *278*, 012132. [[CrossRef](#)]
12. Gao, C.M.; Bosschaart, K.J.; Zeegers, J.C.H.; de Waele, A.T.A.M. Experimental study on a simple Ranque-Hilsch vortex tube. *Cryogenics* **2005**, *45*, 173–183. [[CrossRef](#)]
13. Rafiee, S.E.; Sadeghiyazad, M.M. Three-dimensional CFD simulation of fluid flow inside a vortex tube on basis of an experimental model—the optimization of vortex chamber radius. *Int. J. Heat Technol.* **2016**, *34*, 236–244. [[CrossRef](#)]
14. Bej, N. Numerical Studies of the Performance Enhancement of a Ranque-Hilsch Vortex Tube. Ph.D. Thesis, Indian Institute of Technology, Kharagpur, India, 2015.
15. Rafiee, S.E.; Sadeghiyazad, M.M.; Mostafavinia, N. Experimental and numerical investigation on effect of convergent angle and cold orifice diameter on thermal performance of convergent vortex tube. *J. Therm. Sci. Eng. Appl.* **2015**, *7*, 041006. [[CrossRef](#)]

16. Matveev, K.I.; Leachman, J. Numerical investigation of vortex tubes with extended vortex chambers. *Int. J. Refrig.* **2019**, *108*, 145–153. [[CrossRef](#)]
17. Rafiee, S.E.; Sadeghiazad, M.M. Experimental and 3D-CFD investigation on optimization of the air separator structural parameters for maximum separation efficiency. *Sep. Sci. Technol.* **2017**, *52*, 903–929. [[CrossRef](#)]
18. Hong, Y.; Xu, Q.; Zhao, Y.; Xue, Y. The thermal performance of a novel convergent valveless vortex tube. *Int. J. Refrig.* **2020**, *119*, 92–101.
19. Skye, H.M.; Nellis, G.F.; Klein, S.A. Comparison of CFD analysis to empirical data in a commercial vortex tube. *Int. J. Refrig.* **2006**, *29*, 71–80. [[CrossRef](#)]
20. Dutta, T.; Sinhamahapatra, K.P.; Bandyopdhyay, S.S. Comparison of different turbulence models in predicting the temperature separation in a Ranque-Hilsch vortex tube. *Int. J. Refrig.* **2010**, *33*, 783–792. [[CrossRef](#)]
21. Farouk, T.; Farouk, B.; Gutsol, A. Simulation of gas species and temperature separation in the counter-flow Ranque-Hilsch vortex tube using the large eddy simulation technique. *Int. J. Heat Mass Transf.* **2009**, *52*, 3320–3333. [[CrossRef](#)]
22. Bianco, V.; Khait, A.; Noskov, A.; Alekhin, V. A comparison of the application of RSM and LES turbulence models in the numerical simulation of thermal and flow patterns in a double-circuit Ranque-Hilsch vortex tube. *Appl. Therm. Eng.* **2016**, *106*, 1244–1256. [[CrossRef](#)]
23. Dutta, T.; Sinhamahapatra, K.P.; Bandyopdhyay, S.S. CFD analysis of energy separation in Ranque-Hilsch vortex tube at cryogenic temperature. *J. Fluids* **2013**, *2013*, 562027. [[CrossRef](#)]
24. Chen, J.; Zeng, R.; Zhang, W.; Qiu, L.; Zhang, X. Numerical analysis of energy separation in Ranque-Hilsch vortex tube with gaseous hydrogen using real gas model. *Appl. Therm. Eng.* **2018**, *140*, 287–294. [[CrossRef](#)]
25. Matveev, K.I.; Leachman, J. Numerical study of hydrogen cooling in cryogenic vortex tubes with smooth transitions between vortex chamber and main tube. In Proceedings of the 2nd Pacific Rim Thermal Engineering Conference, Maui, HI, USA, 13–17 December 2019.
26. STAR-CCM+ Manual. 2019. Available online: <https://mdx.plm.automation.siemens.com/star-ccm-plus> (accessed on 15 December 2019).
27. Poschner, M.; Zimmermann, I.; Pfitzner, M. CFD-simulation of the combustion process in the Mascotte facility under supercritical conditions. In Proceedings of the 21st International Colloquium on the Dynamics of Explosions and Reactive Systems, Poitiers, France, 23–27 July 2007.
28. Nasrifar, K. Comparative study of eleven equations of state in predicting the thermodynamic properties of hydrogen. *Int. J. Hydrog. Energy* **2010**, *35*, 3802–3811. [[CrossRef](#)]
29. Ferziger, J.H.; Peric, M. *Computational Methods for Fluid Dynamics*; Springer: Berlin/Heidelberg, Germany, 1999.
30. Roache, P.J. *Verification and Validation in Computational Science and Engineering*; Hermosa Publishers: Albuquerque, NM, USA, 1998.
31. Dincer, K.; Baskaya, S.; Uysal, B.Z.; Uçgul, I. Experimental investigation of the performance of a Ranque-Hilsch vortex tube with regard to a plug located at the hot outlet. *Int. J. Refrig.* **2009**, *32*, 87–94. [[CrossRef](#)]

Article

A Computational Analysis of a Methanol Steam Reformer Using Phase Change Heat Transfer

Hyemin Song ¹, Younghyeon Kim ¹, Dongjin Yu ¹ , Byoung Jae Kim ² , Hyunjin Ji ³ and Sangseok Yu ^{2,*}

¹ Mechanical Engineering, Graduate School, Chungnam National University, 99 Daehangno, Yuseong-gu, Daejeon 34134, Korea; melody_05@naver.com (H.S.); viny9198@naver.com (Y.K.); real-east@hanmail.net (D.Y.)

² School of Mechanical Engineering, Chungnam National University, 99 Daehangno, Yuseong-gu, Daejeon 34134, Korea; bjkim@cnu.ac.kr

³ Agency for Defense Development, Yuseong P.O.Box 35-44, Daejeon 305-600, Korea; grgnmachine@gmail.com

* Correspondence: sangseok@cnu.ac.kr; Tel.: +82-42-821-5646; Fax: +82-42-822-5642

Received: 18 May 2020; Accepted: 17 August 2020; Published: 21 August 2020



Abstract: A methanol steam reformer converts methanol and steam into a hydrogen-rich mixture through an endothermic reaction. The methanol reformer is divided into a reaction section and a heat supply section that transfers thermal energy from 200 to 300 °C. This study presents the behavior of the methanol steam reforming reaction using the latent heat of the steam. A numerical analysis was separately conducted for two different regimes assuming constant heat flux conditions. A methanol steam reformer is an annulus structure that has a phase change heat transfer from an outer tube to an inner tube. Different from the steam zone temperature in the tube, the latent heat of steam condensation decreases, and there is a gradual between-wall temperature decrease along the longitudinal direction. Since the latent heat of steam condensation is very sensitive to the requested heat from the reformer, it is necessary to consider a refined design of a methanol reformer to obtain a large enough amount of heat by steam condensation.

Keywords: computational analysis; high-pressure methanol steam reformer; phase change heat transfer; high pressure steam condensation; hydrogen production

1. Introduction

The exhaust gases from hydrocarbon fuel exacerbate global warming, which has triggered an economy based on hydrogen. Since global warming can be reduced with highly efficient power plants, new types of power plants have also been introduced in the world. Hydrogen energy has the advantage of having a high energy density, low pollutants emission, and fuel flexibility via various sources.

As of yet, the mass production of hydrogen is done by a chemical reaction requiring hydrocarbons. Hydrocarbon-based fuel-producing methods are the steam reforming process, partial oxidation process, and autothermal reforming process. Among them, the steam reforming process is not only economical but also relatively high efficient. The methanol reformer is known for its high energy density per volume, safety, and long-term durability through proper maintenance [1,2]. Various applications are examined such that the methanol reformer is applied to the fuel cell vehicle in the Nekar 3 (1997) and Nekar 5 (2000). Another application of methanol reformers is a portable fuel cell as a micro-reformer that is used for laptop computers and military robots. Different from the above, the methanol reformer is also used for a high-temperature stationary PEMFC (Proton Exchange Membrane Fuel Cell), which is known to be more tolerable to CO poisoning [3].

The methanol reformer is also applied to an air independent power propulsion system for submarines [4]. Since methanol is safer than hydrogen, it is very attractive to satisfy the requirements of military operations. Prior to methanol reformers, metal hydride was used to store hydrogen for fuel cells. Compared with metal hydride, methanol reformers have longer durability and a larger capacity of energy storage. Since the methanol is reformed for submarines, the operating pressures are very high. Even though the high pressure prevents a highly efficient conversion operation, it is necessary to work the reformer at that pressure to conceal the submarine from an external signature.

Several studies have been done in the field of the methanol steam reforming reaction. Amphlett et al. performed experiments on methanol conversion and reported that methanol conversion increased as the molar number of water vapor increased [5]. Reiyu Chein et al. conducted a numerical study on the steam reforming reaction and identified the mole fractions of methanol, hydrogen, and carbon monoxide in the reforming process [6]. This confirms the validity of numerical analysis for the methanol steam reforming reaction. Additionally, Ataallah et al. developed a three-dimensional model using CFD to study some parameters and features that affect the performance of a methanol steam reformer in a linear reactor with a straight channel [7]. They reported that the performance of the methanol steam reforming reaction at constant inlet mass flow rates and velocities varies with the channel dimensions and operating conditions. Shuji et al. investigated the behavior of catalyst materials, sheet paper containing SiC fibers, catalyst powders, and catalyst pellets, under different space velocities (SV) in the methanol steam reforming reaction [8].

On the other hand, Ji et al. reported on the steam reforming of methanol using phase change heat transfer [9,10]. Since the methanol steam reforming temperature ranges from 200 to 300 °C, they had to select an appropriate phase change medium for the temperature range. The phase change medium of their methanol steam reformer was deionized water, and the temperature and pressure of the phase change process were determined by the operating condition of the methanol steam reforming process. This idea is novel, and they experimentally evaluated the performance of the methanol reformer; however, the operating mechanism still needs to be examined. They also show that the high-pressure operation of the methanol steam reforming reaction produces a high concentration of carbon monoxide. They also pointed out that the concentration of carbon monoxide can be significantly reduced with the increasing SM (Steam to Methanol) ratio [11].

In particular, since the reaction mechanism comprises important parameters, the reaction kinetics are widely studied and reported [1–8]. However, most of the methanol steam reforming processes in literature are heated by the combustion of fuel or hot gases. There are scarce reports about the methanol reforming process with phase change heat transfer. Additionally, since the phase change of water around 200 to 300 °C requires very high vapor pressure, it is very difficult to find an experimental or numerical study of the methanol steam reforming process with phase change heat transfer.

In this study, a computational analysis was performed to investigate the behavior of a high-pressure methanol steam reforming process with phase change heat transfer. The water vapor condensation and the methanol steam reforming reaction take place in a hollow tube. Since the temperature of the phase change medium in the radial direction is varied and in the longitudinal direction as well, the methanol steam reforming reaction is closely linked to those temperature distributions. The computational sections are divided into two different regimes: one for phase change heat transfer and the other for the methanol steam reforming process.

2. Simulation Model

The methanol steam reforming process with phase change heat transfer is conducted in annulus tubes that layer two different sizes of tubes in the same center. The methanol and the steam flow into the inner tube, and superheated steam flows into the outer tube. The flow arrangement is a parallel flow. The methanol steam reformer has two compartments, which require two different analysis schemes. One is dominated by a two-phase flow, and the other is dominated by the methanol steam reforming process in porous media. Figure 1 shows the geometric information of the computational

analysis. There is a methanol steam reforming zone inside of the hollow tube, and heat is supplied from the outer tube to the reaction zone by the phase change of the steam. The flow direction of the reformer zone and phase change zone is parallel. The total height of the tube is 700 mm, and the thickness between the inner shell and outer shell is 2.1 mm. Since heat is transferred from the outer shell to the inner shell, it is observed that the outer surface of the inner shell has condensed vapors on it. The other conditions are summarized in Table 1.

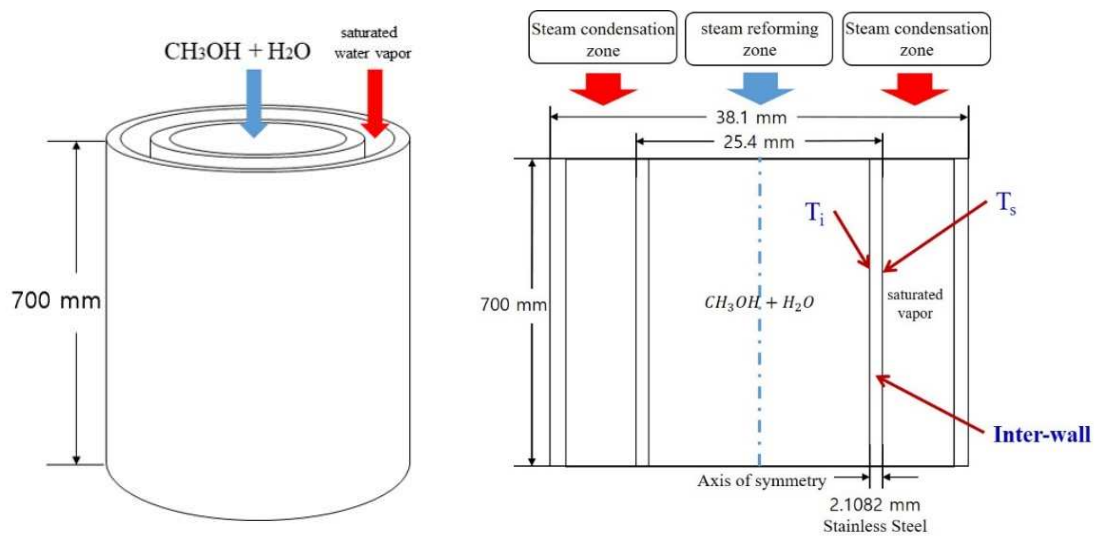


Figure 1. Geometry of methanol steam reformer for numerical computation.

Table 1. Geometric and operating parameters of numerical computation.

Parameters	Dimension	Unit	Expression
T1	280	°C	Inlet temperature
Ts	279.9616	°C	Saturation temperature
P1	64.1646	bar	Inlet pressure of steam condensation zone
P2	30	bar	Inlet pressure of reaction zone
L	70	mm	Total length
Lt	2.1082	mm	Tube thickness
r1	2.9464	mm	Inlet radius of heat source zone
r2	10.5918	mm	Inlet radius of reaction zone
R	15.6459	mm	Total radius
ρ	8055	kg/m ³	Density of solid tube
C_p	480	J/kgK	Specific heat of solid tube
k	15.1	W/mK	Thermal conductivity of solid tube

Since the vapor flow goes down by gravity, water vapor condenses on the inner surface of the outer tube. When the temperature of the water vapor meets a vapor saturation state, water droplets cover the outer tube, which act as heat transfer resistance.

2.1. Reaction Kinetics

The reaction kinetics of the methanol steam reforming process have been widely investigated. The following three processes are known to be the main reactions of the methanol steam reforming reaction [10–16]. The methanol steam reforming reaction is described by three elementary reactions:

methanol steam reforming reaction (SR), methanol decomposition (MD), and water gas shift (WGS) reaction.

Methanol steam reforming reaction (SR)



Water gas-shift reaction (WGS)



Methanol decomposition reaction (MD)



The Arrhenius equation is applied to calculate the chemical reaction rate. The basic form of the Arrhenius equation is as follows:

$$k = A \times \exp\left(-\frac{E_a}{RT}\right) \quad (4)$$

where E_a is the activation energy, A is the pre-exponential factor, and k is the reaction rate constant. The kinetics constants of the methanol steam reforming reaction at 200 to 300 °C are shown in Table 2 [14–17].

Table 2. Constants of the Arrhenius equation for methanol steam reforming reaction.

Reaction Step	A [kmol/m ³ s]	E_a [kJ/mol]	Reaction Name
$\text{CH}_3\text{OH} \rightarrow \text{CO} + 2\text{H}_2$	1.43×10^9	1.22×10^8	Methanol decomposition reaction
$\text{CO} + \text{H}_2\text{O} \rightarrow \text{CO}_2 + \text{H}_2$	5.115×10^7	8.77×10^7	Water–gas shift reaction
$\text{CH}_3\text{OH} + \text{H}_2\text{O} \rightarrow \text{CO}_2 + 3\text{H}_2$	2.002×10^9	9.27×10^7	Steam reforming reaction

2.2. Governing Equations

The gas mixture of the methanol and steam flows through the inner tube, and the steam reforming reaction is progressed. The governing equations are as follows:

Continuity equation

$$\nabla \cdot (\rho v) = 0 \quad (5)$$

Momentum equation

$$\nabla \cdot (\rho v v) = -\nabla p + \nabla \cdot (\bar{\tau}) + \rho g \quad (6)$$

Energy balance equation

$$\nabla \cdot (v(\rho E + p)) = \nabla \cdot K_{eff} \nabla T - \sum h_i J_i + S_h \quad (7)$$

$$E = h - \frac{p}{\rho} + \frac{v^2}{2}, \quad h = \sum_i Y_i h_i \quad (8)$$

$$h_j = \int_{T_{ref}}^T C_p dT, \quad \bar{J}_j = -\left(rD_{j,m} + \frac{\mu_t}{Sc_t}\right) \nabla Y_j, \quad k_{eff} = k + \frac{c_p \mu_t}{Pr_t}, \quad S_h = -\sigma_j \frac{h_j^0}{M_i} R_j. \quad (9)$$

The reforming zone is filled with a catalyst. The reaction zone is set up to be porous media, and the catalytic reaction on the surface of the pellet is simulated by chemical kinetics. It is assumed that the porous media is charged homogeneously, and the flow is laminar. Darcy's law is used to determine the internal velocity.

$$\Delta p = C_2 \frac{1}{2} \rho \Delta n v^2 + \frac{1}{\alpha} \Delta n v \mu \quad (10)$$

Darcy’s law is represented by the sum of the inertial resistance and the viscous resistance. In addition, the porosity should be set and expressed as r in the following equation.

$$k_{eff} = \gamma k_f + (1 - \gamma)k_s \tag{11}$$

The porosity (r) is the ratio of the fluid volume to the total volume. The effective heat transfer coefficient (k_{eff}) is determined by the sum of k_f , the heat transfer coefficient in the fluid zone, and k_s , the heat transfer coefficient in the solid zone. On the other hand, saturated steam flows into the empty space in the outer tube, and the condensation condition is determined by the steam pressure and temperature. When the steam is induced, the pressure is set as 64.16 bar and the saturation temperature is set to 279.96 °C (553.11 K). When the endothermic reaction takes place in the reaction zone, the heat absorption results in the condensation of the steam. The vapor condensation is calculated by the Eulerian Lee model [14]. The liquid–vapor mass transfer (evaporation and condensation) is governed by the vapor transport equation.

$$\frac{\partial}{\partial t}(\alpha_v \rho_v) + \nabla \cdot (\alpha_v \rho_v \vec{v}_v) = \dot{m}_{lv} - \dot{m}_{vl} \tag{12}$$

Here, \dot{m}_{lv} and \dot{m}_{vl} are the rates of mass transfer due to evaporation and condensation, respectively. In the evaporation–condensation problem, mass transfer from the liquid to vapor is a positive mass transfer, and the units of Equation (11) are in kg/s/m³. The mass transfer rate on the right hand side of Equation (11) is defined as follows:

$$\text{If } T_l > T_{sat}(\text{evaporation}), \dot{m}_{lv} = coeff \times \alpha_l \rho_l \frac{(T_l - T_{sat})}{T_{sat}} \tag{13}$$

$$\text{If } T_v < T_{sat}(\text{condensation}), \dot{m}_{vl} = coeff \times \alpha_v \rho_v \frac{(T_{sat} - T_v)}{T_{sat}}. \tag{14}$$

Here, α and ρ are the phase volume fraction and density, respectively. *coeff* is a coefficient that must be tuned finely and can be interpreted as a relaxation time. The volume fractions represent the space occupied by each phase. The volume V_c of phase q is defined as follows.

$$V_q = \int \alpha_q dV \tag{15}$$

$$\sum_{q=1}^n \alpha_q = 1. \tag{16}$$

The effective density of q is expressed as follows.

$$\hat{\rho}_q = \alpha_q \rho_q. \tag{17}$$

In the above expression, ρ_q is the physical density of phase q . In addition, the governing equation on q is as follows.

Continuity equation

$$\frac{\partial}{\partial t}(\alpha_q \rho_q) + \nabla \cdot (\alpha_q \rho_q \vec{v}_q) = \sum_{p=1}^n (\dot{m}_{pq} - \dot{m}_{qp}) + S_q \tag{18}$$

Here, v_q is the velocity of phase q , \dot{m}_{pq} characterizes the mass transfer from the p th to q th phase, and \dot{m}_{qp} characterizes the mass transfer from phase q to phase p .

The momentum balance equation for phase q yields

$$\frac{\partial}{\partial t}(\alpha_q \rho_q \vec{v}_q) + \nabla \cdot (\alpha_q \rho_q \vec{v}_q \vec{v}_q) = -\alpha_q \nabla p + \nabla \cdot \tau_q + \alpha_q \rho_q \vec{g} + \sum_{p=1}^n (\vec{R}_{pq} + \dot{m}_{pq} \vec{v}_{pq} - \dot{m}_{qp} \vec{v}_{qp}) + \vec{F}_q + \vec{F}_{lift,q} + \vec{F}_{vm,q}. \tag{19}$$

This is the momentum balance equation for phase q where τ_q is the q th phase stress–strain tensor.

$$\tau_q = \alpha_q \mu_q \left(\nabla \vec{v}_q + \nabla \vec{v}_q^T \right) + \alpha_q \left(\lambda_q - \frac{2}{3} \mu_q \right) \nabla \cdot \vec{v}_q I \tag{20}$$

Here, τ_q and μ_q are the shear and bulk viscosity of phase q ; \vec{F}_q is an external body force; $\vec{F}_{lift,q}$ is a lift force; $\vec{F}_{vm,q}$ is a virtual mass force; \vec{R}_{pq} is an interaction force between the phases, and p is the pressure shared by all the phases.

Lift forces act on a particle mainly due to velocity gradients in the primary phase flow field. The lift force will be more significant for larger particles, but the ANSYS Fluent® model assumes that the particle diameter is much smaller than the inter-particle spacing [14]. Thus, the inclusion of lift forces is not appropriate for closely packed particles or for very small particles. The lift force acting on a secondary phase p in a primary phase q can be calculated by the formula below.

$$\vec{F}_{lift} = -C_l \rho_q \alpha_p (\vec{v}_q - \vec{v}_p) \times (\nabla \times \vec{v}_q) \tag{21}$$

The inertia of the primary-phase mass encountered by the accelerating particles (or droplets or bubbles) exerts a “virtual mass force” on the particles. The virtual mass force is as follows.

$$\vec{F}_{vm} = C_{vm} \alpha_p \rho_q \left(\frac{d_q \vec{v}_q}{dt} - \frac{d_p \vec{v}_p}{dt} \right) \tag{22}$$

\vec{R}_{pq} depends on the fiction, pressure, cohesion, and other effects. \vec{v}_{pq} is the interphase velocity, which is defined as follow. If $\dot{m}_{pq} > 0$, then $\vec{v}_{pq} = \vec{v}_p$, If $\dot{m}_{pq} < 0$, then $\vec{v}_{pq} = \vec{v}_q$. Likewise, If $\dot{m}_{qp} > 0$ then $\vec{v}_{pq} = \vec{v}_q$, If $\dot{m}_{qp} < 0$ then $\vec{v}_{pq} = \vec{v}_p$.

2.3. Computational Methods and Boundary Conditions

Meshes are shown in Figure 2. The solver is a pressure-based solver, and a transient analysis was conducted. Additionally, axisymmetric computation was used to facilitate the analysis. The condensation/evaporation model is a Eulerian Lee Model which is provided by ANSYS Fluent®. At the wall of the outer tube, the adiabatic condition was applied for the heat transfer, and wall conditions were also selected for the momentum. Another adiabatic condition was set up along the symmetric axis. At the inter-wall between the inner tube and outer tube, a boundary condition was set up.

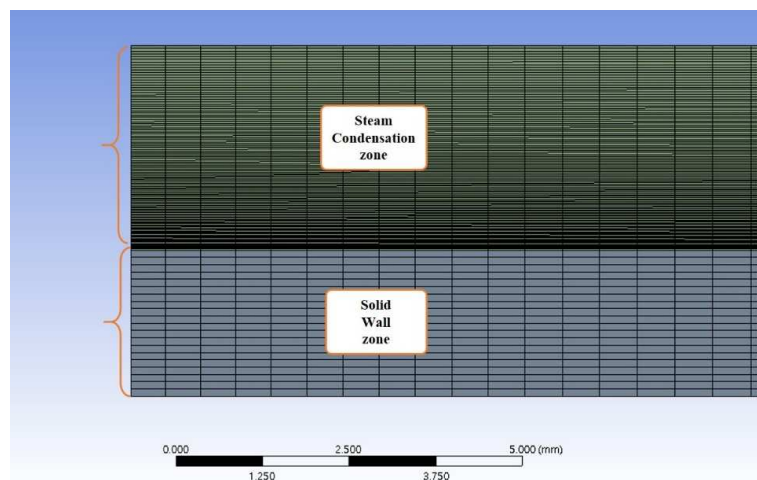


Figure 2. Meshes and domains for computational analysis.

Generally, the inner tube and outer tubes were set up to be two computational domains. However, because it is very difficult to solve the computation of two different physics simultaneously

in the commercial software ANSYS fluent[®], this study separated the computation of those physics one by one by selecting coupling boundary conditions.

The Eulerian Lee model requires fine tuning of the parameters, which is known as a frequency factor [18]. The frequency factor affects the condensation or evaporation mass transfer rate that is empirically determined. Accordingly, it is necessary to tune the frequency factor so that the phase change mass transfer rate is reasonably determined. This is a clue to tune the model so that the proper heat flux determines the heat transfer coefficients and surface temperature.

At first, the constant heat flux conditions were the boundary condition of the inner tube side of the inter-wall. The first domain was the steam reforming zone, and the second domain was the solid tube. When the methanol steam reforming reaction progresses through the inner tube, it is assumed that a constant heat flux is absorbed from the steam condensation zone.

When the constant heat flux is acting on the surface of the inner wall, the inter-wall temperatures is T_s which is the surface temperature of the phase change zone, and the inner wall temperature is T_i which is the surface temperature of the steam reforming zone. Those notations are also found in Figure 1. The constant heat flux boundary conditions were set up to be 1, 2.5, and 5 kW. Equation (22) explains the heat transfer correlation with the induction of the constant heat flux from the wall. T_s , T_i , and h are unknowns, and h is a function of T_s . The methanol and steam mixture temperature through the inner tube and steam temperature through the outer tube were varied in the longitudinal direction. The heat transfer rate should be calculated by the log mean temperature difference (LMTD). It is assumed that the steam is not fully condensed throughout the outer tube. Then, the steam temperature of the outer tube should be maintained. Then, the heat transfer rate is explained as follows:

$$q_w = \frac{2\pi Lk(T_s - T_i)}{\ln\left(\frac{r_o}{r_i}\right)} = \bar{h}A_s \Delta T_{lm} \quad (T_\infty = \text{constant}) \quad (23)$$

$$\Delta T_{lm} = \frac{\Delta T_o - \Delta T_i}{\ln\left(\frac{\Delta T_o}{\Delta T_i}\right)} \quad (24)$$

$$\frac{\Delta T_o}{\Delta T_i} = \frac{T_{steam} - T_{s,o}}{T_{steam} - T_{s,i}} = \exp\left(-\frac{PL}{\dot{m}c_p} \bar{h}\right) \quad (T_{steam} = \text{constant}). \quad (25)$$

The convection heat transfer coefficient on the wall of a circular tube is calculated by the following Equation [19].

$$\bar{h} = \frac{Re_\delta \mu_l h_{fg}}{4L(T_{sat} - T_s)} \quad (26)$$

where,

$$Re_\delta = \left[\frac{3.70k_l L (T_{sat} - T_s)}{\mu_l h_{fg} \left(\frac{v_l^2}{g}\right)^{\frac{1}{3}}} + 4.8 \right]^{0.82} \quad (30 \leq Re_\delta \leq 1800).$$

All liquid property should be obtained from the film temperature $T_f = (T_{sat} + T_s)/2$, and h_{fg} should be obtained from T_{sat} . T_s in Equation (25) is calculated by the arithmetic average of T_s in between the inlet and outlet. Since the average heat transfer coefficient \bar{h}_L is calculated by Equations (22) and (25), a new temperature T_s is updated by iteration.

The temperatures in Table 3 were used to determine the frequency factors of each heat flux case. Then, the frequency factor was fixed, and the phase change phenomena were analyzed.

Table 3. Inner wall temperature and inter-wall temperature in terms of constant heat flux conditions.

Heat Rate [kW]	T_s [K]	T_i [K]
1	545.17	542.54
2.5	534.79	527.96
5	514.39	500.73

3. Simulation Results and Discussion

3.1. Phase Change Trends with Surface Heat Absorption

As the heat fluxes were increased, the steam temperature decreased in the radial direction. Condensation was also observed on the surface. Figure 3 shows the steam temperature profile and liquid volume fraction profile in the outer tube. As expected, the near-wall temperature is about 7 K lower for the 1 kW heat absorption. Then, the wall temperature further decreased with a higher heat absorption rate. Near the inter-wall, the steam temperature slope was dramatically decreased due to heat absorption. Then, the steam temperature in the phase change zone rose rapidly to 280 °C, which is the inlet temperature of the steam. Another aspect was the temperature profile in the radial direction. As shown in Figure 3, the near-wall temperature gradient was quite large, and a very thin boundary layer was observed regardless of the absorbed heat. This is because the condensed liquid increases the thermal resistance of the heat transfer. Accordingly, the outer zone from the temperature boundary layer maintained its temperature at the phase change condition.

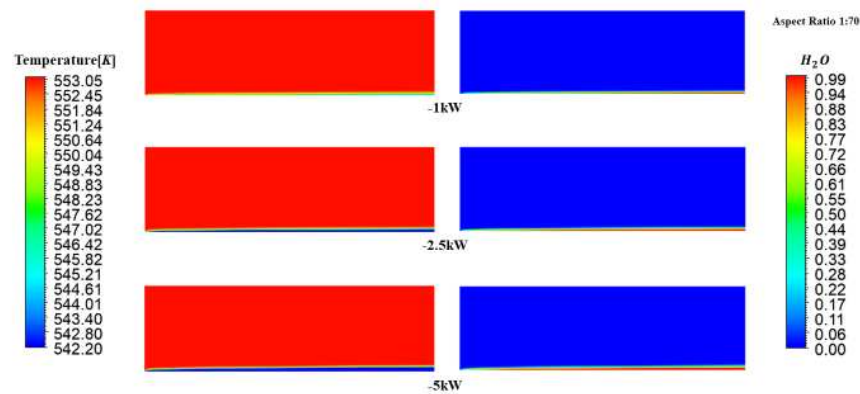


Figure 3. Vapor temperature and water volume fraction along flow direction (three different heat fluxes as well boundary conditions).

As the heat absorption increased, the liquid volume fraction near the wall is almost 1.0, which implies that the surface is covered with a thin liquid film. The gravity force made the liquid volume fraction boundary layer become thicker along the channel. As steam flows into the outer tube, the liquid volume fraction steeply increased. The more heat is absorbed, the earlier the saturated water is observed through the tube. Then, the liquid volume fraction grew near the inter-wall along the longitudinal direction. It was also shown that most of the area in the outer tube was occupied by saturated steam.

The thermal boundary layer thickness was defined as 0.999 of the free stream temperature, and the liquid volume fraction was defined as 0.999 of the saturated vapor. The results are shown in Figure 4. The thickness of the temperature boundary layer was thinner than the thickness of the liquid volume fraction boundary layer. It shows that the mixture of steam and liquid water stayed on the liquid boundary layer. As observed, the concentration boundary layer is thicker for all the heat absorption rates, and the thickness increased linearly. The thickness difference between the boundary layer is large for the 1 kW heat absorption condition. As the heat absorption rate was increased, the thickness difference between the two boundary layers changed little.

The radial temperature profile is shown in Figure 5. The linear increase zone is the solid inter-wall, and a steep temperature increase was observed from the surface of the inter-wall to the steam zone. The overall steam temperature in the radial direction was mainly constant at the saturated condition. Another observation was the gradual temperature down along the longitudinal direction. Even though the temperature of the steam was maintained, the wall temperature decreased with a higher heat flux. One interesting feature is the steam temperature. The steam temperature was maintained over

the various heat flux conditions, while the wall temperature dramatically changed with the higher heat flux.

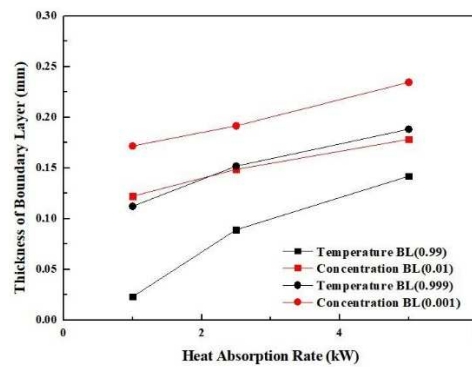


Figure 4. Temperature and liquid volume fraction boundary layer thickness at the exit of the outer tube for the three different heat absorption rates.

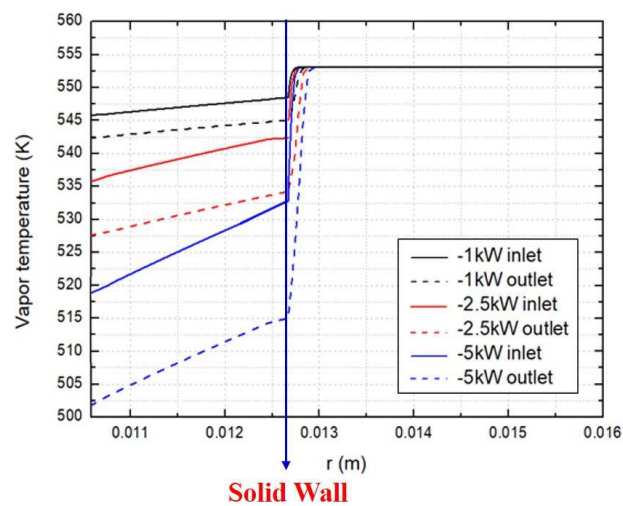


Figure 5. Evolution of radial temperature profile in terms of the heat fluxes.

The water volume fraction of the outer tube rapidly increased right after inducing the steam, and the water volume fraction was then 1 at the exit. Figure 6 shows the water volume fraction at the inlet and exit. As observed, the water volume fraction at the inlet is steeper with a higher heat absorption rate, and the water volume fraction at the exit is thicker with a higher amount of heat flux.

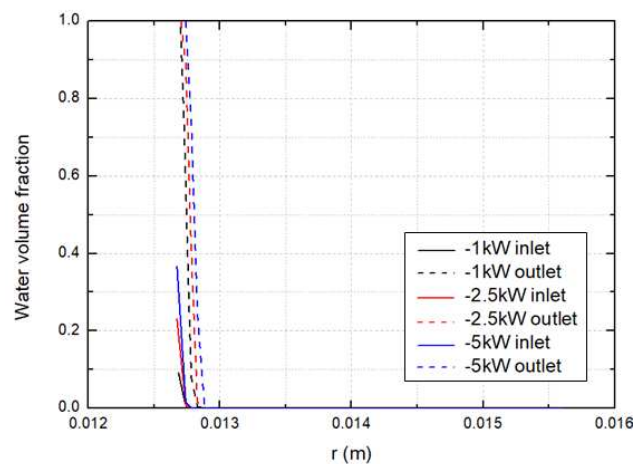


Figure 6. Water volume fraction near the wall in terms of the heat flux.

The overall liquid fraction of the saturated steam along the outer tube is determined by the integration of the liquid mass over the space. Thermodynamically, the quality is the ratio of the steam mass to the total mass and is calculated as follows.

$$x = \frac{m_g}{m_g + m_f} \quad (27)$$

$$x_w = 1 - x = \frac{m_f}{m_g + m_f} \quad (28)$$

Here, x is the quality; x_f is the water mass ratio; m_g is the mass of them steam, and m_f is the mass of the water. Figure 7 shows the total mass ratio of condensed water in the outer tube. As shown, the ratio of condensed water is proportional to the heat flux to the steam reforming process. The ratios of the water mass to the total mass for each heat flux condition were 26.38%, 33.95%, and 40.10%. Accordingly, the volume of the liquid is relatively small, and the mass of the steam is not negligible.

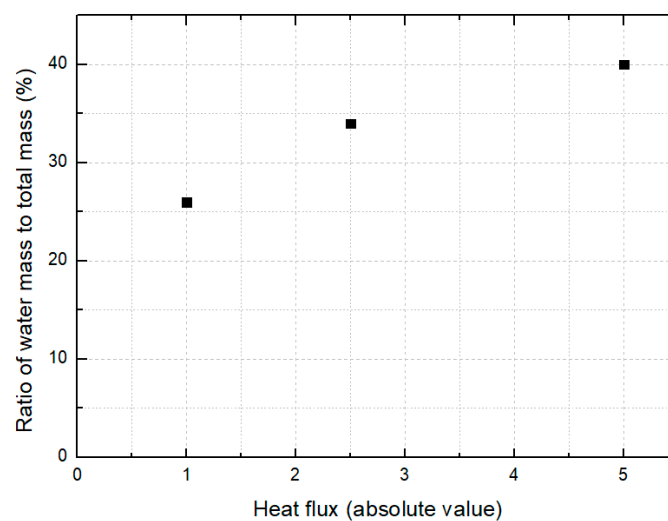


Figure 7. Ratio of water mass to total mass over three different heat fluxes.

The heat absorption from the phase changing steam results in a temperature change on the inter-wall surface. The surface temperature of the inner tube (T_i) is captured in Figure 8. As shown, the surface temperature non-linearly decreased, and the initial temperature was lower than the steam methanol inlet temperature. One reason is from heat transfer through the solid wall. The solid wall is acting as thermal resistance to the heat transfer. Another reason is the condensation of the steam from the inlet. As shown in Figure 4, a significant temperature drop is observed at the near inlet of the phase change zone. The temperature drop results in a lower temperature of the solid surface (T_i) at the inlet of the methanol steam reforming zone.

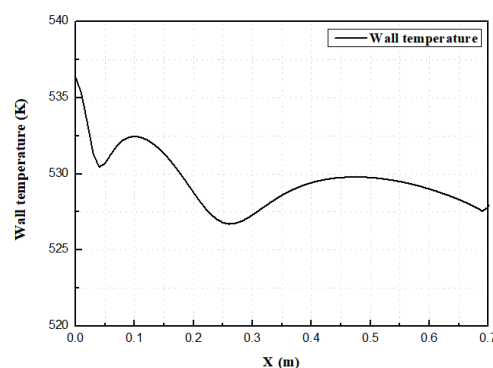


Figure 8. Inner wall temperature profile along the channel with 2.5 kW heat flux.

3.2. Physical Behavior in the Methanol Steam Reforming Reaction

The temperature profile through the inner tube was determined by the boundary conditions and reaction characteristics. The temperature trends were observed at the 2.5 kW heat flux boundary conditions. Due to the presence of the porous methanol steam reforming catalyst, the temperature profile in the radial direction is almost flat. The longitudinal temperature profile is determined by the temperature profile in Figure 8 and the symmetry condition. Figure 9 shows the temperature profile of the chemical reaction zone. The gas inlet temperature was 553 K, which was a higher temperature than the wall temperature. As observed, the initial gas temperature rapidly dropped due to the temperature difference between the gas temperature and the wall temperature. After the first hill from the higher temperature to the lower temperature, the temperature profiles can be seen in Figure 8. Then, the methanol steam mixture temperature is similar to the wall temperature. The mixture temperature was 553 K at maximum and 527 K at minimum.



Figure 9. Temperature of chemical reaction zone (2.5 kW heat flux).

Methanol steam reforming reaction consists of three reaction mechanisms: steam reforming reaction, water gas shift reaction, and methanol decomposition reaction. Those three reactions are traced in Figure 10. As observed, the order of the steam reforming reaction is almost 10^3 times greater than the other two reactions. Accordingly, the products of the reforming reaction will be mainly H_2 , CO_2 , and H_2O . Another aspect is that the reaction rates decay along the channel. Initially, the reaction rate of the steam reforming reaction was quite high and steeply decreased along the channel. It was observed that the wall temperature profile affects the decay of the methanol decomposition rate. However, the methanol steam reforming reaction rate looks less affected by the wall temperature profile. Instead, the concentration of methanol has a more significant effect on the methanol steam reforming reaction.

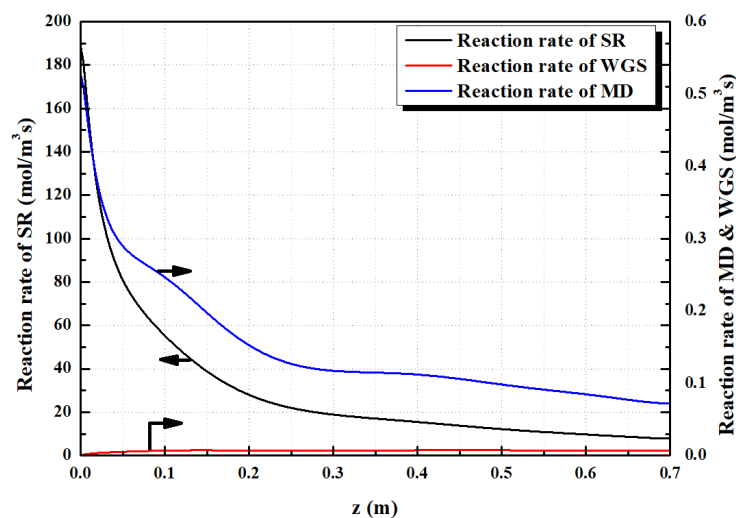


Figure 10. Contribution of elementary reaction kinetics along the tube. MD: methanol decomposition, SR: methanol steam reforming reaction, WGS: water gas shift.

Because the steam reforming reaction mechanism dominates the overall reaction, the products are mostly H_2 , CO_2 , and H_2O . Figure 11 shows the mole fraction evolution of the product gases and the decay of methanol. As observed, the concentrations of H_2 and CO_2 gradually increase along the pipe. The maximum mole fraction of H_2 is 0.58, and CH_3OH gradually decreases at the rear end of the reaction zone, resulting in a mole fraction of 0.09. The mole fraction of the reactants CH_3OH and H_2O decreases as the reaction proceeds in the Z direction. Another aspect is the consumption rate of H_2O . As observed, the H_2O concentration decreased over a short time in the frontal regime, and the concentration gradually decreased. Because the hydrogen production is dominated by steam reforming, it was observed that the consumption of water corresponded to the hydrogen concentration.



(a)



(b)



(c)



(d)

Figure 11. Cont.



(e)

Figure 11. Species concentration of the methanol steam reforming reaction zone. (a) Mole fraction of CH_3OH , (b) Mole fraction of CO , (c) Mole fraction of CO_2 , (d) Mole fraction of H_2 , (e) Mole fraction of H_2O .

4. Conclusions

In this study, computational analysis of high pressure methanol steam reforming reaction with the phase change of steam at saturation pressure are conducted.

- (1) High-pressure methanol reforming reaction and high-pressure steam condensation phenomena are connected by constant heat flux conditions. Therefore, two different physical phenomena is explained by transferred heat flux.
- (2) As the heat absorption of methanol steam reforming process results in vapor condensation, the inter-wall temperature between reforming zone and phase change zone is decreased.
- (3) Since the temperature boundary layer is thinner than the liquid volume fraction boundary layer, the steam liquid mixture stays on the liquid water layer.
- (4) The non-linear solid temperature of the inner wall affects the kinetics of the methanol decomposition reaction, but the kinetics of the steam reforming reaction and water gas shift reaction are rarely affected by the non-linear temperature profile of the inner wall.
- (5) Since the overall reaction takes place within narrow radius porous media, the negligible concentration difference is observed through the steam reforming zone.

Author Contributions: Conceptualization, Y.K. and B.J.K.; Data curation, D.Y.; Formal analysis, H.J.; Writing—original draft, H.S.; Writing—review & editing, S.Y. All authors have read and agreed to the published version of the manuscript.

Funding: This research was supported by a grant from the Agency for Defense Development (ADD) (grant number: UD180051GD).

Conflicts of Interest: The authors declare no conflict of interest.

References

1. Kim, S.; Yun, S.-W.; Lee, B.; Heo, J.; Kim, K.; Kim, Y.-T.; Lim, H. Steam reforming of methanol for ultra-pure H_2 production in a membrane reactor: Techno-economic analysis. *Int. J. Hydrogen Energy* **2019**, *44*, 2330–2339. [[CrossRef](#)]
2. Iulianelli, A.; Ribeirinha, P.; Mendes, A.; Basile, A. Methanol Steam Reforming for hydrogen generation via conventional and membrane reactor: A review. *Renew. Sustain. Energy Rev.* **2014**, *29*, 355–368. [[CrossRef](#)]
3. Sahlin, S.L.; Andreasen, S.J.; Kær, S.K. System model development for a methanol reformed 5 kW high temperature PEM fuel cell system. *Int. J. Hydrogen Energy* **2015**, *40*, 13080–13089. [[CrossRef](#)]
4. Krummrich, S.; Labrés, J. Methanol reformer—The next milestone for fuel cell powered submarines. *Int. J. Hydrogen Energy* **2015**, *40*, 5482–5486. [[CrossRef](#)]
5. Amphlett, J.C.; Evans, M.J.; Mann, R.F.; Weir, R.D. Hydrogen production by the catalytic steam reforming of methanol Part 2: Kinetics of methanol decomposition using girdler G66B catalyst. *Can. J. Chem. Eng.* **1985**, *63*, 605–611. [[CrossRef](#)]

6. Chein, R.; Chen, Y.; Chung, J.N. Numerical study of methanol-steam reforming and methanol-air catalytic combustion in annulus reactors for hydrogen production. *Appl. Energy* **2013**, *102*, 1022–1034. [[CrossRef](#)]
7. Ataallah, S.; Javad, S. Modeling and 3D-simulation of hydrogen production via methanol steam reforming in copper-coated channels of a mini reformer. *J. Power Sources* **2017**, *352*, 64–76.
8. Shuji, F.; Hirotsuka, K.; Takuya, K.; Mitsuyoshi, N.; Hiroyuki, W. Steam reforming behavior of methanol using paper-structured catalysts: Experimental and computational fluid dynamic analysis. *Int. J. Hydrogen Energy* **2008**, *33*, 1661–1670.
9. Ji, H.; Lee, J.; Choi, E.; Seo, I. Hydrogen Production from steam reforming using an indirect heating method. *Int. J. Hydrogen Energy* **2018**, *43*, 3655–3663. [[CrossRef](#)]
10. Ji, H.; Lee, J.; Choi, E.; Yang, S. Methanol Steam Reforming Using Multilayer Cup Structure for Catalyst Support. *Trans. Korean Hydrog. New Energy Soc.* **2020**, *31*, 202–209.
11. Ji, H.; Choi, E.; Lee, J. Optimal Operating Condition of Pressurized Methanol Fuel Processor for Underwater Environment. *Trans. Korean Hydrog. New Energy Soc.* **2016**, *27*, 485–493. [[CrossRef](#)]
12. Park, J.-E.; Park, J.-H.; Yim, S.-D.; Kim, C.-S.; Park, E.D. A comparative study of commercial catalysts for methanol steam reforming. *Korean Chem. Eng. Res.* **2005**, *43*, 344–351.
13. Seo, B.C.; Kim, M.C.; Kim, G.R. Methanol steam reforming reaction, 192. *Korean Chem. Eng. Res* **2017**, *10*, 438–445.
14. Purnama, H.; Ressler, T.; Jentoft, R.; Soerijanto, H.; Schlögl, R.; Schomäcker, R. CO formation/selectivity for steam reforming of methanol with a commercial CuO/ZnO/Al₂O₃ catalyst. *Appl. Catal.* **2004**, *259*, 83–94. [[CrossRef](#)]
15. Chiu, Y.-J.; Chiu, H.-C.; Hsieh, R.-H.; Jang, J.-H.; Jiang, B.-Y. Simulation of Hydrogen Production by Methanol Steam Reforming. *Energy Proc.* **2019**, *156*, 38–42. [[CrossRef](#)]
16. Choi, Y.; Stenger, H.G. Kinetics, simulation and optimization of methanol steam reformer for fuel cell applications. *J. Power Sources* **2005**, *142*, 81–91. [[CrossRef](#)]
17. Ribeirinha, P.; Boaventura, M.; Lopes, J.C.B.; Sousa, J.; Mendes, A. Study of Different Designs of Methanol Steam Reformers: Experiment and Modeling. *Int. J. Hydrogen Energy* **2014**, *39*, 19970–19981. [[CrossRef](#)]
18. Lee, W.H. ANSYS Fluent® Theory Guide 2019R1. Available online: www.ansys.com (accessed on 18 May 2020).
19. Incropera, F.P.; Lavine, A.S.; Bergman, T.L.; DeWitt, D.P. *Principles of Heat and Mass Transfer*, 7th ed.; John Wiley & Sons, Inc.: Hoboken, NJ, USA, 2013.



© 2020 by the authors. Licensee MDPI, Basel, Switzerland. This article is an open access article distributed under the terms and conditions of the Creative Commons Attribution (CC BY) license (<http://creativecommons.org/licenses/by/4.0/>).

Article

Performance Study on Methanol Steam Reforming Rib Micro-Reactor with Waste Heat Recovery

Guoqiang Wang ^{1,2}, Feng Wang ^{1,2,*} and Bohong Chen ²

¹ Key Laboratory of Low-grade Energy Utilization Technologies and Systems, Chongqing University, Ministry of Education, Chongqing 400044, China; ggglxk@cqu.edu.cn

² School of Energy and Power Engineering, Chongqing University, Chongqing 400030, China; 20161013058@cqu.edu.cn

* Correspondence: wangfeng@cqu.edu.cn; Tel.: +86-1361-8203-569

Received: 11 March 2020; Accepted: 26 March 2020; Published: 27 March 2020



Abstract: Automobile exhaust heat recovery is considered to be an effective means to enhance fuel utilization. The catalytic production of hydrogen by methanol steam reforming is an attractive option for onboard mobile applications, due to its many advantages. However, the reformers of conventional packed bed type suffer from axial temperature gradients and cold spots resulting from severe limitations of mass and heat transfer. These disadvantages limit reformers to a low efficiency of catalyst utilization. A novel rib microreactor was designed for the hydrogen production from methanol steam reforming heated by automobile exhaust, and the effect of inlet exhaust and methanol steam on reactor performance was numerically analyzed in detail, with computational fluid dynamics. The results showed that the best operating parameters were the counter flow, water-to-alcohol (W/A) of 1.3, exhaust inlet velocity of 1.1 m/s, and exhaust inlet temperature of 773 K, when the inlet velocity and inlet temperature of the reactant were 0.1 m/s and 493 K, respectively. At this condition, a methanol conversion of 99.4% and thermal efficiency of 28% were achieved, together with a hydrogen content of 69.6%.

Keywords: methanol steam reforming; hydrogen production; exhaust waste heat; rib microreactor

1. Introduction

Motor vehicles are increasing dramatically with the rapid economic development [1,2]. However, the power used by the internal combustion engine for power output generally accounts for only 30%–45% (diesel) or 20%–30% (gasoline) of the total fuel combustion heat. A car effectively uses only a small part of the fuel's chemical energy, and most is lost through the engine's cooling water and high-temperature exhaust heat [3,4]. Therefore, the exhaust heat recovery, which is very important to improve the fuel efficiency, attracts more and more attention [5,6]. Pashchenko [7] studied thermochemical recovery of heat contained in flue gases with steam methane reforming. It was found that the enthalpy increased with increasing mole fraction of combustion products in the reaction mixture. At the same time, the greenhouse effect resulting from the burning of fossil energy has seriously affected the earth. In this regard, many countries are actively investing in the development of pollution-free clean energy and alternative energy [8–10]. Hydrogen is one of the prominent alternative energy because of its many excellent properties, especially its combustion product of water [11,12]. However, difficulties in storage and ecological environment transportation of hydrogen persist [13,14]. Liquid fuel reformation is becoming an increasingly important process of hydrogen production for on-board mobile applications [15,16]. The use of bioethanol in the schemes of thermochemical recovery of heat contained in exit flue gases is also an option that was considered [17]. It was found that the degree of ethanol conversion is near unity above the temperature of 600 K. Pashchenko [18] compared

thermochemical waste-heat recuperation through steam reforming of liquid biofuels. The maximum transformation coefficient 1.187 was observed for ethanol steam reforming, and a minimum effective temperature of about 600 K was observed for methanol. Methanol, which can be converted to hydrogen at lower temperature as it contains no carbon–carbon bonds, is an excellent hydrogen carrier and is free of storage and transportation issues [19,20]. In addition, methanol can be reformed to produce hydrogen at low temperatures, with very small amount of CO in the products [21]. Hydrogen production processes are numerous, and decisions on the choice of fuel are made based on which parameter is deemed most important for the system. Among various hydrogen production technologies, hydrogen production from methanol steam reforming (MSR) has attracted attention in the industry, due to its mild reaction and high hydrogen content of products.

Hydrogen production from endothermic MSR heated by exhaust can recover waste heat of the exhaust, increasing the fuel utilization. At the same time, the hydrogen from MSR can be sent to the internal combustion engine, which improves fuel combustion efficiency [22]. Thus, MSR heated by exhaust is considered to be an effective form of waste heat recovery [23,24]. Mishra [25] designed an experimental system for hydrogen production from MSR heated by automobile exhaust, and mainly studied the effects of hydrogen flow rate and exhaust heat exchange rate, on exhaust composition and reaction performance, under different conditions. The results showed that when the throttle opening is within 20%, the exhaust temperature and heat flow can meet the needs of hydrogen production from MSR. Methanol conversion increases with the heat exchange efficiency of reformers, and heat recovery increases with increasing engine speed. However, too high an engine speed will cause the heat exchange efficiency to decrease. Kumar [26] used flow-through tubular heat exchanger and porous ceramic reactors to enhance the heat transfer, and studied hydrogen production from MSR heated by exhausts. The results showed that the methanol conversion increased with the increasing temperature of the exhaust. At exhaust temperatures of 350 °C, the hydrogen volume fraction was approximately 42%. This method can provide hydrogen for on-board applications in an internal combustion engine, greatly improving the thermal efficiency of the system. Wang [27] studied the characteristics of the MSR-coupled with thermoelectric generator system heated by automobile exhausts. The results showed that when the temperature difference between the cold and hot ends of the thermoelectric module was 22 K, the output voltage of the power chip was 55 mV, the methanol conversion was 72.6%, and the molar fraction of hydrogen was 62.6%.

The packed bed is widely used for the conventional MSR method. However, the packed bed was reported to suffer from axial temperature gradients and cold spots [28,29]. These problems, which lead to thermal stresses in the channels, result from the severe limitations of mass and heat transfer. The stability and durability of the catalyst are significantly affected by the thermal stresses. Furthermore, the severe transfer resistance led to an effectiveness factor of the catalyst that is typically less than 5% in conventional steam reformers [30]. Micro-reactors can offer a higher heat transfer rate than the traditional chemical reactors, benefit from the high surface-to-volume ratio and short conduction paths [31]. Since the small diameters of the reactor channels can shorten the radial diffusion time, a high heat transfer coefficient is acquired. Moreover, the heat transfer coefficient is known to be beneficial for the homogeneously catalyzed reaction [32]. Thus, microreactors have been increasingly seen as new tools for chemistry and chemical processes in recent years. Zhou [33] improved hydrogen production efficiency through sintered copper microreactors. Liang [34] studied the effect of the novel high-pressure propulsion on hydrogen production from MSR. The result showed that the methanol conversion increased by 11% in the microreactor. This behavior was attributed to the superior heat transfer in the microreactors. Pressure drop has been demonstrated to play a significant role in packed bed reformers in terms of the efficiency of the thermochemical heat recuperation systems [35]. However, the difficulty of introducing catalyst particles into the micro-channel persists when using micro-reactors in heterogeneously catalyzed gasphase reactions. Therefore, each channel must be packed identically to avoid misdistribution, because random packing would result in a high-pressure drop. The catalyst coating of regular geometry is convenient to be integrated into microreactors, compared to the packed

bed of catalyst particles. And the catalyst coating is found to be combined closely with the microreactor. This can intensify thermal conductivity from microreactor to the coating due to the decreased thermal contact resistance. The pressure drop is lower in a coated catalyst bed, because the coating catalyst provides the advantage of superior geometry. The activity of the coated catalyst was also found to be superior to that of the same catalyst in a packed bed for MSR [36]. Therefore, for this study, a microreactor coupled with catalyst coating is proposed to intensify the process due to its advantages of heat transfer.

Previous research work has focused on the study of systems with conventional reactors, and studies on the influence of specific operating parameters on MSR is insufficient. While the vehicles are in motion, the temperature and flow of the exhaust would change at different motor conditions. In this paper, a novel rib microreactor coupled with a catalyst coating is designed for the hydrogen production from MSR heated by automobile exhausts. The exhaust provides heat to the MSR in the same rib microreactor without outside heat source, and the effect of inlet exhaust and methanol steam on reactor performance is numerically analyzed in detail. This research can create a reference significance for the comprehensive utilization of exhaust heat and hydrogen production heated by engine exhaust reforming.

2. Materials and Methods

2.1. Physical Model

The physical model is shown in Figure 1. The exhaust heats the reactant while flowing through the rib microreactor. The mixture of methanol and water enters the reaction side from the reactant inlet, and the products flow out of the outlet. The microreactor chamber is 100 mm long, with a radius of 35 mm, and the heating side radius is 26 mm; the single reaction side angle is 10 degrees and the intermediate baffle thickness is 1 mm. As the structure, the volume, and the reaction performance of the single reaction unit of the reactor are completely same and it is a symmetric model. In order to facilitate the calculation, a half of the single reaction unit is calculated in this paper.

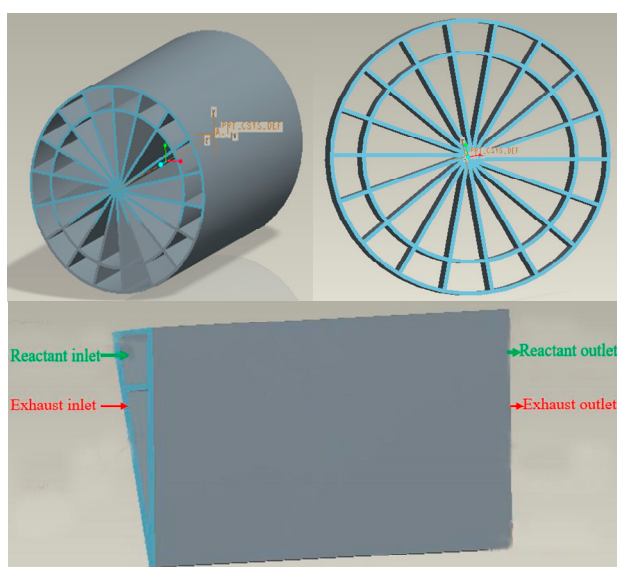


Figure 1. Schematic diagram of rib reactor.

2.2. Mathematical Model

In order to simplify the analysis, the following simplified assumptions are made for this reaction, combining the following characteristics:

- (1) All gases are considered ideal incompressible fluid;
- (2) Ignoring radiation heat transfer and body force;

- (3) The system is in a stable state, and the laminar flow model is adopted;
- (4) Ignoring the influence of gravity;
- (5) All external walls are considered thermal insulation;
- (6) Ignoring the temperature and concentration differences between catalyst and fluid; and
- (7) The catalyst area is considered as a homogeneous medium.

A universal finite rate model and the homogeneous model for the reactor in fluent software is used. The model's control equations are as follows:

Continuity equation:

$$\frac{\partial(\rho V_j)}{\partial x_j} = 0 \quad (1)$$

Component equation:

$$\rho V_j \frac{\partial Y_s}{\partial x_j} = \frac{\partial}{\partial x_j} (\rho D \frac{\partial Y_s}{\partial x_j}) + R_s \quad (2)$$

Momentum equation:

$$\frac{\partial(\rho V_j V_i)}{\partial x_j} = -\frac{\partial p}{\partial x_i} + \frac{\partial}{\partial x_j} \left(\mu \frac{\partial V_i}{\partial x_j} - \mu \frac{\partial V_j}{\partial x_i} \right) \quad (3)$$

Energy equation:

$$V_j \frac{\partial(\rho h)}{\partial x_j} = \frac{\partial}{\partial x_j} \left(k \frac{\partial T}{\partial x_j} \right) + \frac{\partial}{\partial x_j} \left(\sum_s \rho D_s \frac{\partial Y_s}{\partial x_j} h_s \right) + q \quad (4)$$

$$h_s = h_0 + \int C_{ps} dT \quad (5)$$

The ideal gas state equation:

$$p = \rho RT \sum \frac{Y_s}{M_s} \quad (6)$$

where p , T , ρ are the pressure, the temperature, and the density of the mixed gas, respectively, X_j is the direction, and V_j is the mixed gas velocity. D , λ , μ are the diffusion coefficient, thermal conductivity, and viscosity coefficient of the mixed gas, respectively, and the ideal gas mixing law is used for the calculations. Y_s is the mass fraction of component s , $s = 1-5$, respectively, for CH_3OH , H_2O , H_2 , CO_2 , CO . C_{ps} is the constant pressure specific heat, M_s is the molar mass of component s , and h_s is the enthalpy of component s .

2.3. Solving Method

The fluent software is used for simulation calculation. Three-dimensional symmetry and laminar flow model are adopted, The speed inlet is used for the inlet of reactants and exhaust use, and the pressure outlet is used for the outlets. Fluid-structure coupled heat transfer is adopted for the interface between the reactor and the heater, a symmetrical model is adopted for the symmetrical surface adopts. All the outer wall surfaces are set as adiabatic, and the copper-based catalyst is uniformly loaded inside the reactor.

2.4. Model Validation

In this paper, an experimental platform is built, and the MSR heated by the waste heat of exhaust is studied in a plate-type. After a comprehensive comparison, the reaction mechanism and kinetic model in the literature [24] are selected for calculation. The same boundary conditions and parameters as the experiment are adopted. The results are shown in Figure 2.

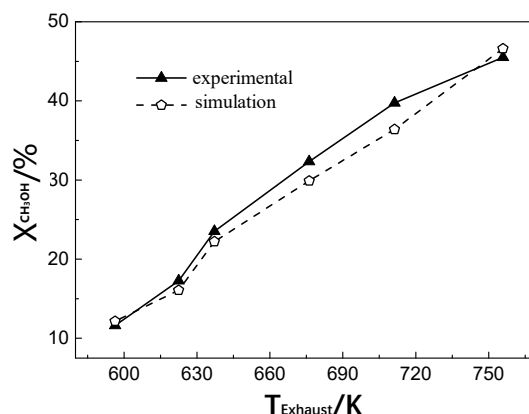


Figure 2. Comparison of the experimental and simulation results.

From the figure, it can be seen that methanol conversion changes of the simulation and the experiment are the same. The methanol conversion increases gradually with the increase of the exhaust temperature, and the maximum difference is only 0.8%. After the verification, it can be confirmed that the reaction mechanism and kinetics adopted in this paper are feasible.

3. Results and Discussions

3.1. Effects of Inlet Exhaust Velocity on MSR

At inlet reactant temperature of 453 K, inlet reactant velocity of 0.1 m/s and inlet exhaust temperature of 673 K, the characteristics of the MSR are shown as figures when the inlet exhaust velocity increases from 0.3 m/s to 1.9 m/s. Figure 3a–d shows the temperature distribution, methanol conversion, and hydrogen and carbon monoxide in the direction of the central axis on the reaction side, when the inlet velocity of the exhaust increases from 0.3 m/s to 1.7 m/s. As can be seen from the figure, the temperature, methanol conversion, the hydrogen mole fraction along the axis all increase gradually with inlet exhaust velocity. The results agree with the literatures [27,37], and suitable for heterogeneous catalytic hydrogen production from MSR in microreactor. This is because the total amount of heat supplied to MSR increases as the inlet exhaust velocity increases, so the temperature of MSR increases. Since the MSR is endothermic, the methanol conversion increases. The temperature is lower at the front section on the reaction side due to the lower inlet temperature of the reactants. With the increase of the temperature in the axial direction, the MSR is favored, and the reaction intensity increases initially and decreases afterwards, along the axis. The axial temperature does not change much before 30 mm from the inlet, and then increases gradually. The hydrogen molar fraction increases slightly before 30 mm, is comparatively larger from 30 mm to 85 mm, and tends to be gentle after 85 mm. Before 80 mm, the molar fraction of carbon monoxide increases slowly with the inlet exhaust velocity and increases at a higher rate, from 80 mm to 100 mm. The same is the trend of the hydrogen mole fraction, as the methanol conversion increases at 30 mm from the inlet and then flattens.

Figure 4a shows the outlet temperature change with the inlet exhaust velocity. With an increase in the inlet exhaust velocity, the outlet temperature of the MSR and the exhaust, and the temperature difference between the MSR and the exhaust increases. The outlet exhaust temperature is always higher than that of MSR. This is because the increase of the inlet exhaust velocity leads to a direct export of some heat, without participating in the MSR. Therefore, the outlet exhaust temperature becomes higher. As shown in Figure 4b, there is an increase in methanol conversion and thermal efficiency as the inlet exhaust velocity increases. This is because the heat absorption from the exhaust increases with an increase in the inlet exhaust velocity, and the methanol conversion. The increase of the outlet exhaust velocity leads to an increase in the output heat and a decrease in the thermal efficiency. As shown in Figure 4c, an increase in the methanol conversion causes an increase of the product, so the mole fraction of hydrogen, carbon monoxide, and carbon dioxide also increases with the increase of the

inlet exhaust velocity. When the inlet exhaust velocity is lower than 1.1 m/s, the product increases with the increasing of inlet exhaust velocity, and then tends to be stable. This is consistent with the change trend of the methanol conversion and thermal efficiency. The highest efficiency is achieved when the inlet exhaust is 1.1 m/s, and a methanol conversion and waste heat utilization ratio of 88.07% and 21.93% is obtained, respectively.

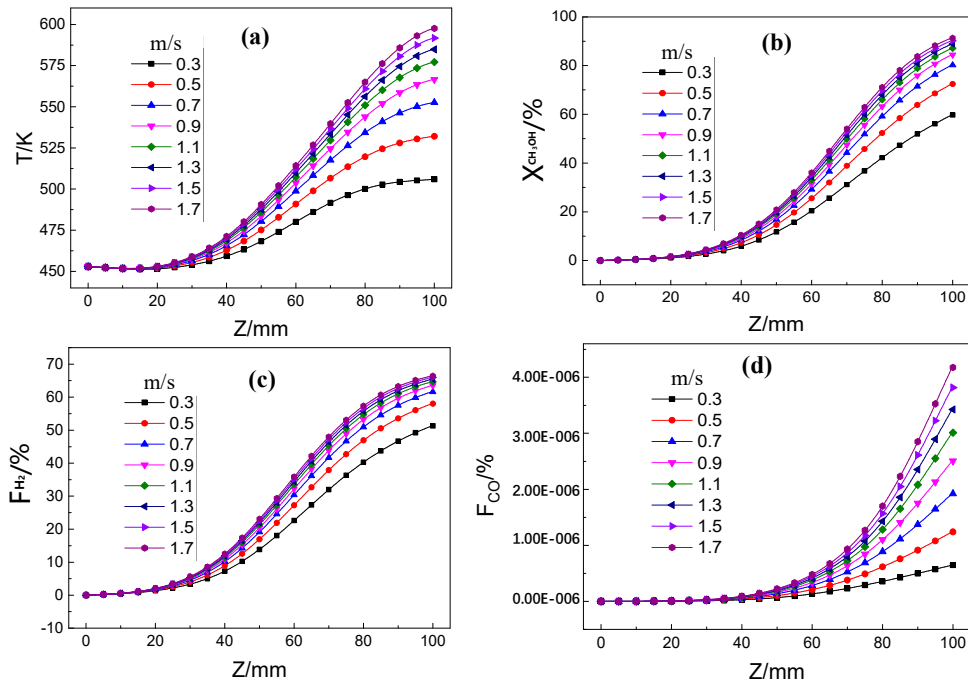


Figure 3. Temperature in the axial direction (a), methanol conversion (b), hydrogen mole fraction (c), and carbon monoxide mole fraction (d), as a function of inlet exhaust velocity.

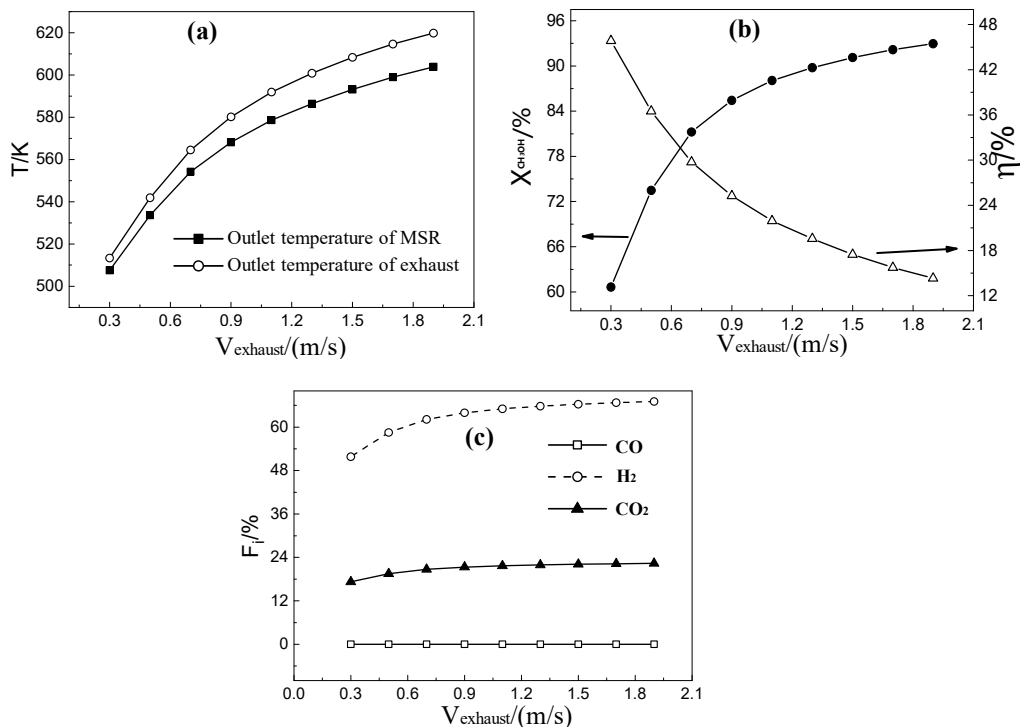


Figure 4. Outlet temperature on the reaction and exhaust side (a), methanol conversion and thermal efficiency (b), and reaction product mole fraction (c) as a function of inlet exhaust velocity.

3.2. Effects of Inlet Exhaust Temperature on MSR

At inlet reactant temperature of 453 K, inlet reactant velocity of 0.1 m/s and inlet exhaust velocity of 0.1 m/s, the characteristics of the MSR are studied when the inlet exhaust temperature increases from 573 K to 873 K. Figure 5a shows the axial temperature distribution at different inlet exhaust temperatures. As the inlet exhaust temperature increases, the heat from the exhaust to MSR increases, so the axial temperature increases. The results also agree with the literatures [37]. The temperature of the reactants increases slowly before 20 mm, and then increases rapidly from 20 mm to 80 mm, and tends to be stable after 80 mm. Due to the low inlet temperature of the reactants, it needs to absorb the heat before reaching the reaction temperature, so the temperature at the front section of the entrance side is lower. As the reactant temperature increases, the MSR deepens, causing the amount of unreacted reactants to decrease. Consequently, the amount of heat absorption along the axial direction decreases, and the axial temperature increases gradually and tends to be stable. Figure 5b–d shows the axial distribution of methanol conversion, and hydrogen and carbon monoxide mole fraction, with different inlet exhaust temperature. All of these increase with an increase of the inlet exhaust temperature and increases gradually along the axis. It can be seen that the hydrogen mole fraction changes little before 18 mm and then increases gradually. When the inlet exhaust temperature is greater than 773 K, it stabilizes at about 80 mm from the entrance. This is because the reaction is almost completed at the position of about 80 mm when the exhaust temperature is 773 K, so the amount of the product changes little. Since hydrogen is the main product of the MSR, the change trends of the hydrogen and methanol conversion are similar. The molar fraction of carbon monoxide is almost 0 before 30 mm, and increases gradually after 30 mm. This is because the temperature is lower than that of methanol decomposition, 30 mm before the entrance.

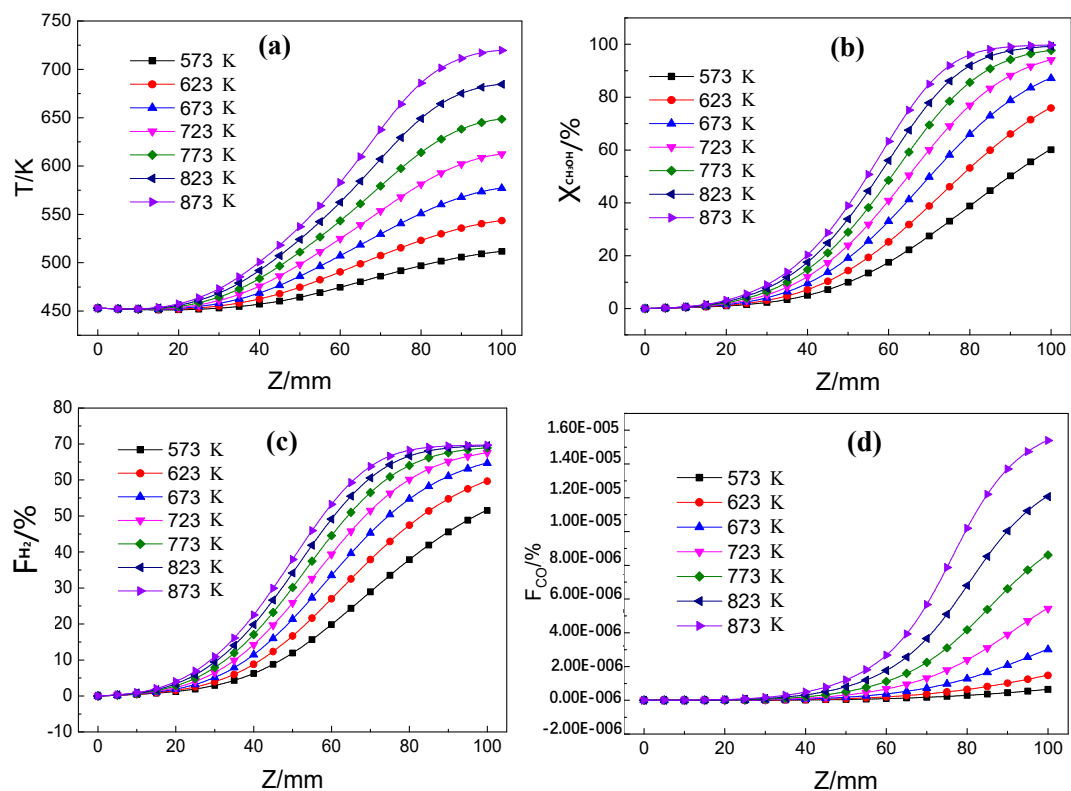


Figure 5. Axial temperature (a), methanol conversion (b), hydrogen mole fraction (c), carbon monoxide mole fraction (d), as a function of the exhaust temperature.

As shown in Figure 6a, the outlet temperature of the reactant and the exhaust increases with the inlet exhaust temperature. The higher the inlet exhaust temperature, the smaller the outlet temperature difference between the reactant and the exhaust, which decreases from 14.2 K to 6.88 K. The main reason is that the inlet exhaust temperature increase causes the heat absorbed to increase, and the main reaction section of the MSR moves parallel. In the latter part of the reaction side, the heat absorbed by the reactant is mainly used to raise the temperature of the reactant rather than supplying to the reaction. This leads to the outlet temperature rise. Figure 6b shows the change of thermal efficiency and methanol conversion with the inlet exhaust temperature. The methanol conversion increases from 61% to 99.9% and the thermal efficiency increases from 16% to 26%, with the inlet exhaust temperature. This is because the heat absorbed by the reactant increases with the increase of the inlet exhaust temperature, causing the methanol conversion to increase, as a result, more heat is utilized and the resulting thermal efficiency is higher. When the exhaust temperature is higher than 773 K, the increase of methanol conversion and thermal efficiency increases slowly. Since the heat increase caused by the inlet exhaust temperature is not supplied to MSR, the impact of the increase of the exhaust temperature on the MSR reaction becomes weak. Figure 6c shows the change of the mole fraction of the reaction product with the exhaust temperature. The products have the same change tendency, as the methanol conversion increases with the exhaust temperature. Therefore, when the inlet exhaust is 773 K, the best performance is achieved. At this time, the methanol conversion is 98%, the thermal utilization is 24.6%, and the mole fraction of hydrogen is 69%.

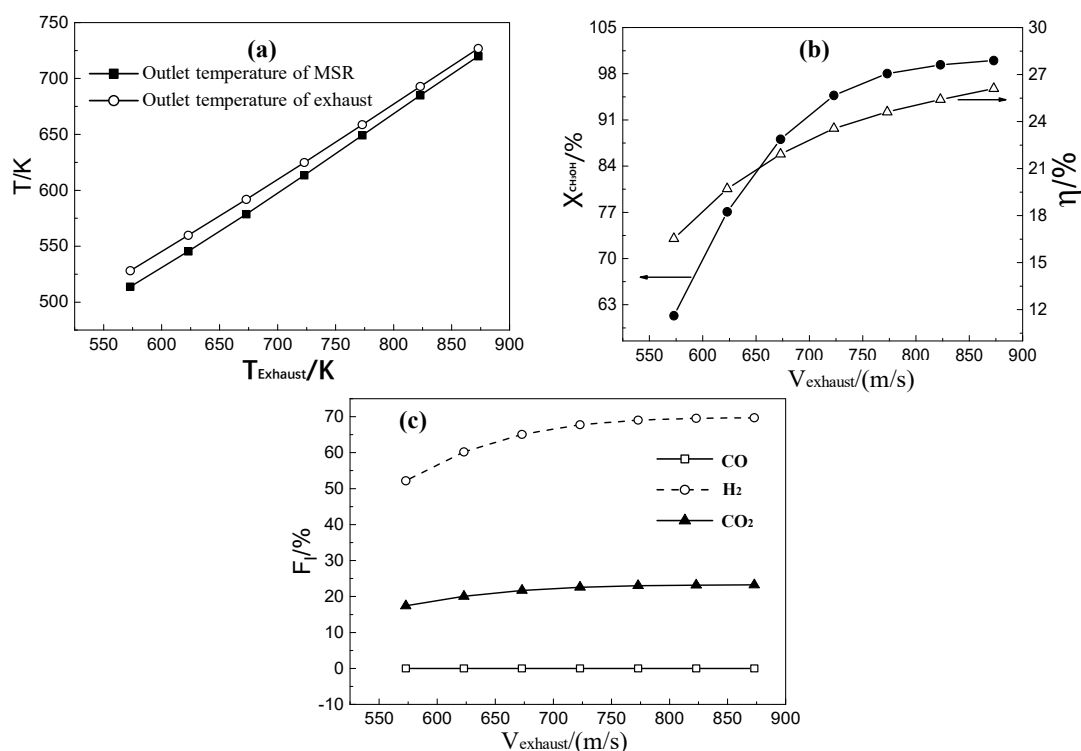


Figure 6. Outlet temperature of reactant and exhaust (a), methanol conversion and thermal efficiency (b), and mole fraction of the reaction product (c), as a function of inlet exhaust temperature.

3.3. Effects of Reactant Inlet Velocity on MSR

The characteristics of the MSR are studied when the inlet reactant velocity increases from 0.01 m/s to 0.3 m/s, at inlet exhaust velocity of 1.1 m/s, inlet exhaust temperature of 673 K, inlet reactant temperature of 453 K. As the inlet reactant velocity increases, the heat absorption by the reactant increases, resulting in a decrease of the temperature. The change laws agree with the literatures [37,38], but the increasing range is larger, because the temperature is higher than literature one. As shown in

Figure 7a, the axial temperature increases gradually along the axis and decreases with the reactant inlet velocity. When the inlet reactant velocity is 0.01 m/s, the axial temperature increases rapidly and tends to stabilize at about 55 mm from the entrance. When the inlet reactants velocity is 0.05 m/s, the axial temperature tends to be stable at about 80 mm. When the inlet reactant velocity is more than 0.05 m/s, the axial temperature increases slowly, without being stable before the outlet. The heat supplied by the exhaust can meet the needs of the MSR with the inlet reactant velocity being less than 0.05 m/s, and the reaction starts at the entrance, with the temperature rising rapidly. When the heat supplied by the exhaust cannot satisfy the reaction with the inlet reactant velocity by more than 0.05 m/s, the reaction moves in the opposite direction and the reactant temperature side increases slowly. Figure 7b–d indicate the axial distribution of methanol conversion, hydrogen, and carbon monoxide, with the inlet reactant velocity. The methanol conversion, and the mole fractions of hydrogen and carbon monoxide decrease with the increase of inlet exhaust velocity and gradually increases along the axis. As can be seen from the figure, when the inlet velocity of the reactants are 0.01 m/s and 0.05 m/s, respectively, the methanol conversion and the mole fraction of hydrogen increases rapidly and become stable near the outlet. When the inlet velocity is greater than 0.05 m/s, the methanol conversion and the hydrogen mole fraction keep increasing along the axis. When the reactant inlet velocity is small, the heat supplied is sufficient for the MSR on the reaction side. Therefore, the methanol conversion and the products are already stable before the outlet. When the inlet reactant velocity increases, the heat absorption increases, resulting in the MSR moving in the opposite direction.

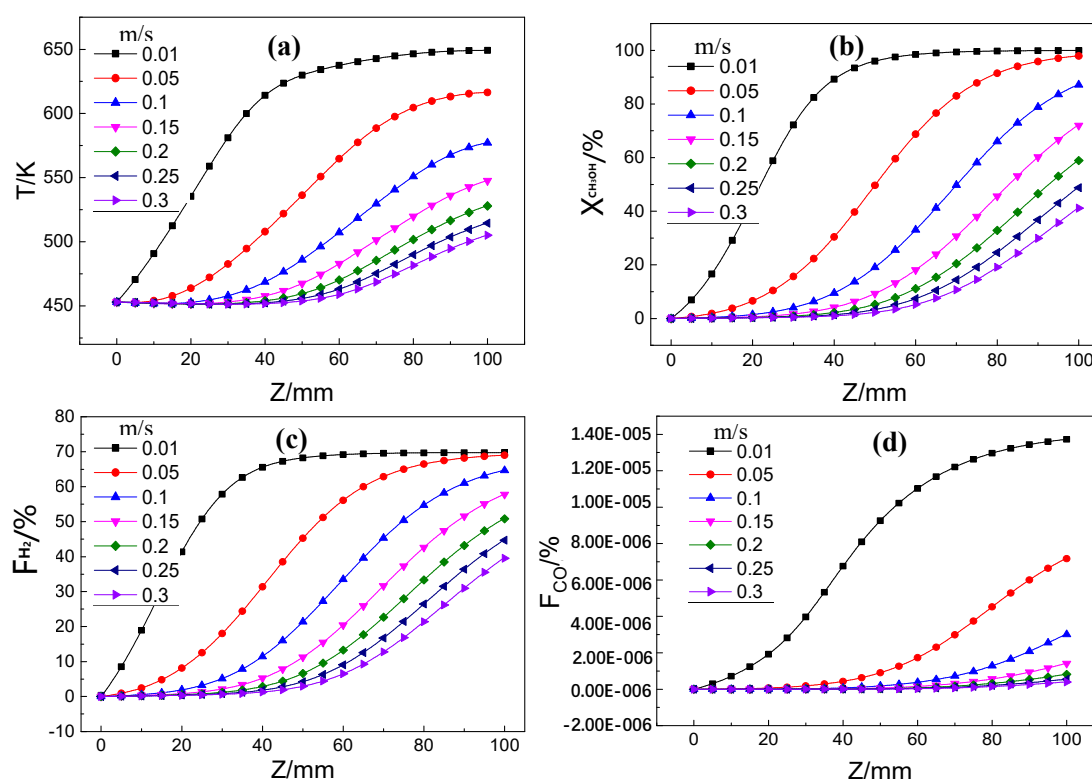


Figure 7. Temperature in the axial direction (a), methanol conversion (b), hydrogen mole fraction (c), and carbon monoxide mole fraction (d), as a function of reactant inlet velocity.

As shown in Figure 8a, when the reactant inlet velocity increases, the outlet temperature on the reactant and the exhaust decreases and the temperature difference between each other increases from 1 K to 41 K. At the constant amount of heat supplied from the exhaust, the heat required by the reactants increases when the reactant inlet velocity increases, so the outlet temperature decreases greatly. At this time, the heat is mainly used to supply the endothermic reaction. Moreover, the reactant temperature decreases with the increasing inlet reactant velocity. Figure 8b shows the change of the

thermal efficiency and methanol conversion with the inlet reactant velocity. With the increase of the inlet reactant velocity, the thermal efficiency increases from 6% to 31.7%, and the methanol conversion decreases from 99.6% to 45.7%. This is because with the increase of the inlet velocity of the reactants, the contact time becomes shorter and the total heat cannot satisfy the heat absorbed, so the methanol conversion decreases. The thermal efficiency increase is caused by the increase of the temperature difference between the reactant and the exhaust. When the exhaust inlet velocity is 1.1 m/s, and the thermal efficiency is also considered, the reactant inlet velocity of 0.1 m/s is found to be optimal. Although methanol conversion is enhanced, the actual mass of hydrogen produced is indeed small at this condition, and the throughput can be increased by integrating a certain amount of rib microreactors. As shown in Figure 8c, the mole fractions of hydrogen, carbon monoxide, and carbon dioxide vary with the inlet velocity of the reactant. It indicates that the hydrogen mole fractions decreases with the increase of the inlet reactant velocity.

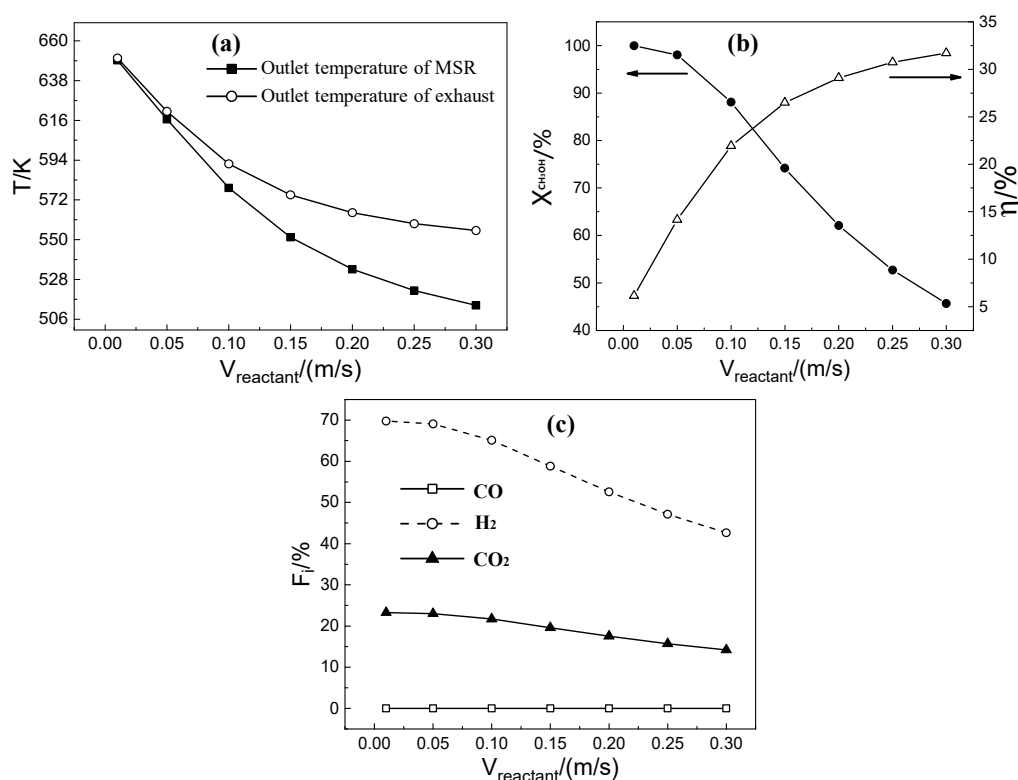


Figure 8. Outlet temperature of product and exhaust (a), methanol conversion and thermal efficiency (b), and mole fraction (c), as a function of reactant inlet velocity.

3.4. Effects of Reactant Inlet Temperature on MSR

At inlet exhaust velocity of 1.1 m/s, temperature of 673 K and inlet reactant velocity of 0.1 m/s, the characteristics of the MSR are illustrated in figures when the inlet reactant temperature increases from 359 K to 573 K. Figure 9a shows the axial temperature change with the inlet reactant temperature. The wall temperature on the reactant side increases as the inlet reactant temperature increases. When the inlet reactant temperature is higher than 493 K, the axial temperature begins to decrease, and then increases with the observed minimum temperature, at about 25 mm. When the inlet reactant temperature is below 493 K, the axial temperature increases along the axis, and increases slower after about 70 mm. At lower inlet reactant temperatures, the MSR reaction is relatively moderate without the temperature dropping significantly, and the “cold spot” appears at about 25 mm. At the lower inlet reactant temperature, the MSR reacts relatively gently without the temperature dropping significantly, so the “cold spot” is not observed. The “cold spot” temperature difference is smaller than that of the literature [28,29] because a microreactor coupled with catalyst coating which has advantages

of efficient heat transfer is adopted in this study. Most of the reaction is completed at about 70 mm, after which the temperature increases rapidly. Figure 9b–d shows the axial distribution of methanol conversion and the mole fractions of hydrogen and carbon monoxide at different inlet temperatures. It can be seen from the figure that the methanol conversion rate and the molar fraction of hydrogen and carbon monoxide gradually increase in the axial direction, and increase with the increase of the inlet reactant temperature. When the inlet reactant temperature is 533 K, the MSR reaction starts at the entrance. The main reason is that the heat carried by the reactants can reach MSR at a relatively high inlet reactant temperature, and absorbs a large amount of heat, which results in a “cold spot” at the entrance. In contrast, the MSR reaction is relatively gentle at lower inlet temperature. At this time, the methanol conversion and the mole fractions of hydrogen and carbon monoxide steadily increase along the axis. The temperature of 359 K is the vaporization temperature of the reactants, and the reactants need to absorb heat.

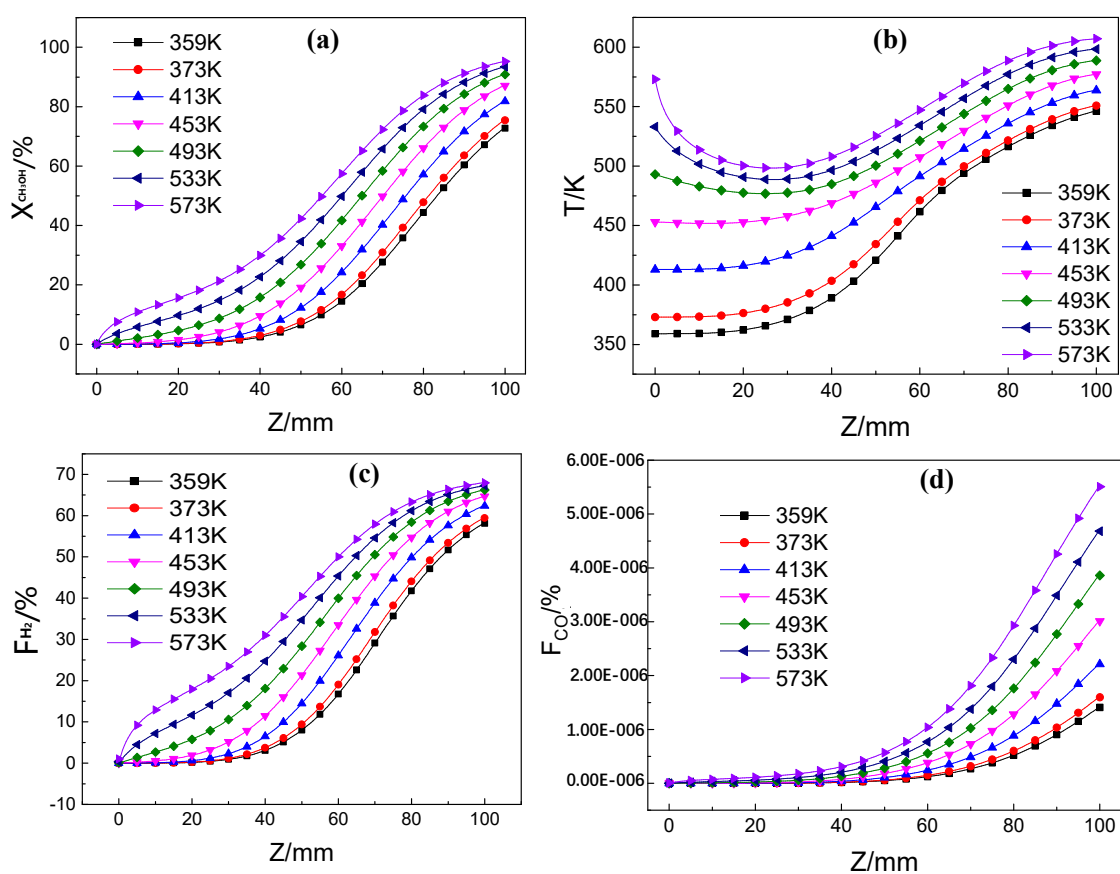


Figure 9. Temperature along the axial direction(a), methanol conversion (b), hydrogen mole fraction (c), and carbon monoxide mole fraction (d), as a function of reactant inlet temperature.

As the inlet temperature of the reactants increases, most of the reactions are completed before the outlet. At this time, the heat absorption from the exhaust reduces. Since the total amount of the exhaust is constant, the outlet temperature of the exhaust and the reaction side increases, and the temperature difference between the two sides decreases gradually. As shown in Figure 10a, the outlet temperature increases from 549 K to 607.5 K at the reaction side and the outlet temperature difference between the exhaust and the reaction side decreases from 21.9 K to 6.8 K.

Figure 10b is the change of the methanol conversion and the thermal efficiency with the reactant inlet temperature. As the reactant inlet temperature increases, the methanol conversion increases and the thermal efficiency decreases. When the inlet temperature is 359 K and 453 K, the methanol conversion is 74.5% and 88%, respectively. There is a big difference between the two conversions. The main reason is that the reaction temperature of the MSR based on the copper catalysts is higher

than 359 K. The reactant is in a state of vaporization at a temperature of 359 K, and the temperature needs to be increased before the reaction. When the reactant inlet temperature is 453 K, the reactants react as soon as it contacts the catalyst, the methanol conversion increases and the thermal efficiency decreases. As shown in Figure 10c, the mole fraction of the product increases with the increasing inlet reactant temperature, and the hydrogen mole fraction increases from 59% to 68%.

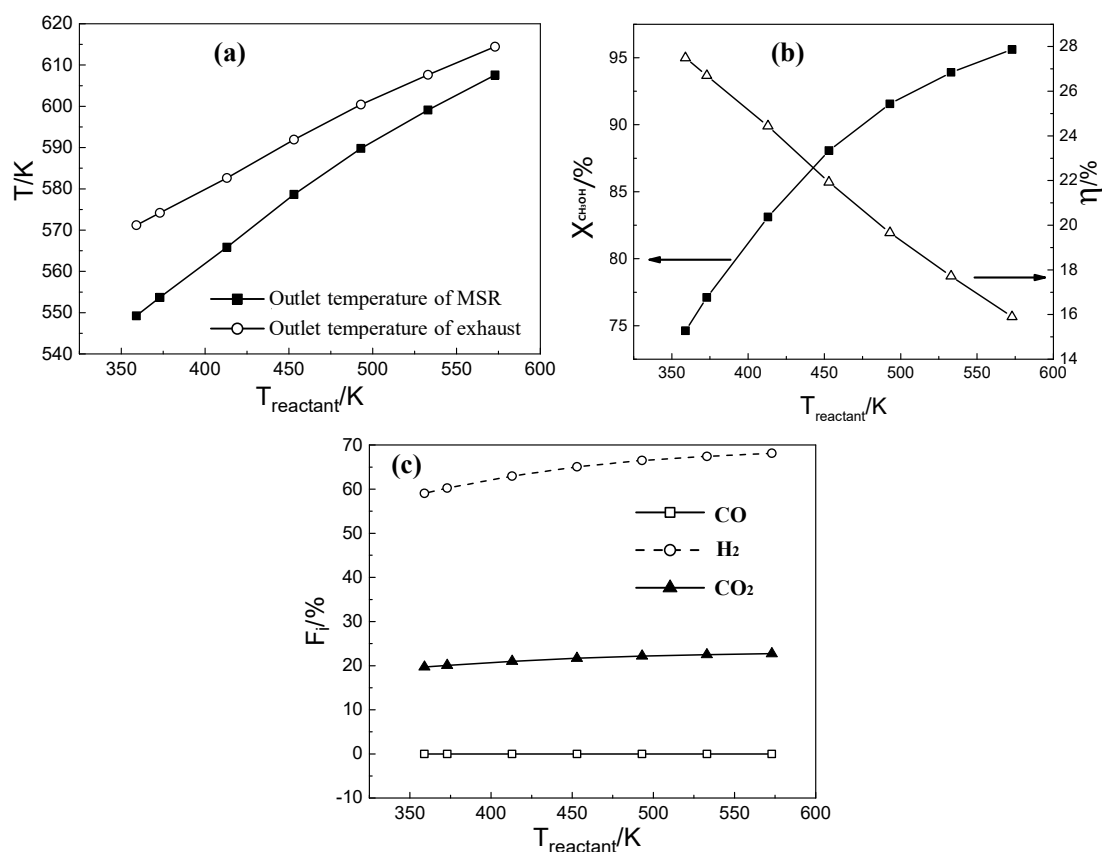


Figure 10. Outlet temperatures of the reaction side and the exhaust side (a), methanol conversion and thermal efficiency (b), and product mole fraction (c), as a function of reactant inlet temperature.

3.5. Effects of W/A on MSR

The characteristics of the MSR are shown as figures when the W/A increases from 1.1 to 1.6, at inlet reactant velocity of 0.1 m/s, temperature of 453 K and inlet exhaust velocity of 1.1 m/s. W/A (water-to-alcohol) indicates the molar ratio of water/methanol. Figure 11a shows the change of the axial temperature with the W/A. As can be seen from the figure, the axial temperature increases gradually with the increasing of W/A along the axis. When the W/A is 1.1 and 1.6, the outlet temperatures are 575 K and 582 K, respectively, with a little temperature difference observed. This indicates that W/A is not the most important factor for the MSR under the flow reaction conditions. The result agrees with the literature [33]. This is also confirmed by the change of the methanol conversion and the mole fractions of carbon monoxide and hydrogen with the W/A. As shown in Figure 11b–d, MSR does not start before about 25 mm, in all cases. This indicates that the heat is the main factor of influencing MSR. With the increase of W/A, the methanol conversion increases, as the methanol content in the unit mass of the reactant decreases at a constant heat. At the same time, as the total amount of reactant decreases, the products decrease and the mole fraction of hydrogen and carbon monoxide decreases as the W/A increases.

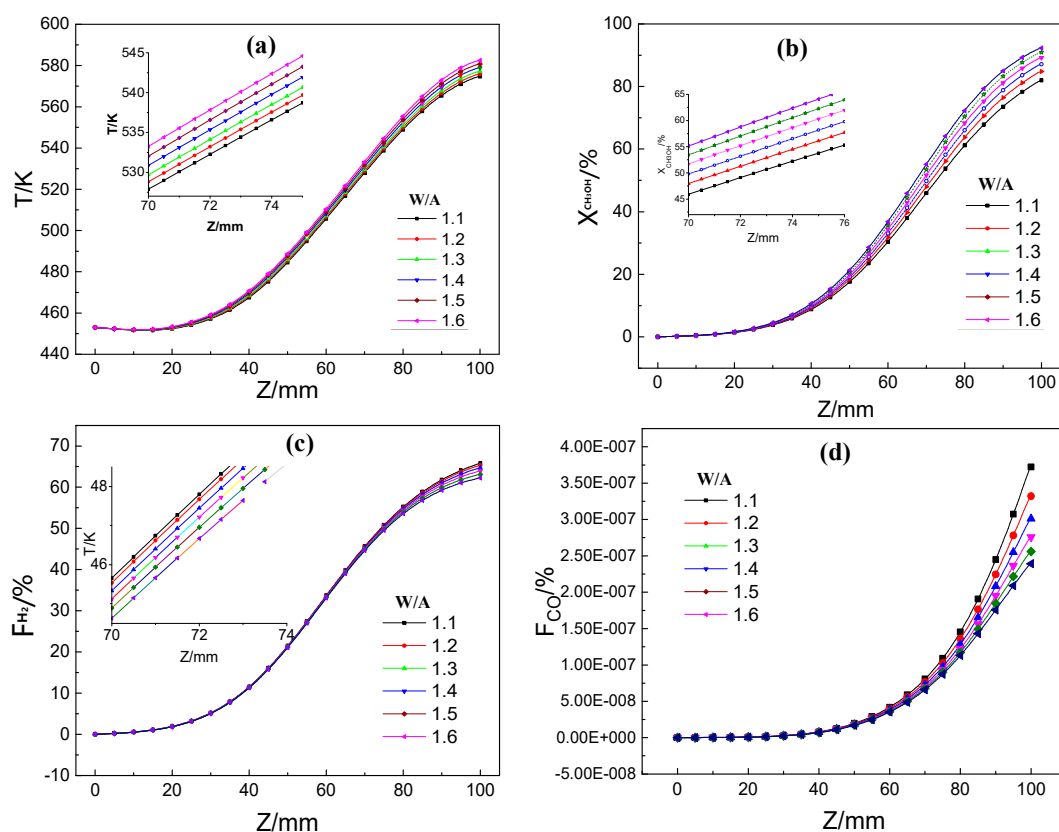


Figure 11. Axial temperature (a), methanol conversion (b), hydrogen mole fraction (c), and carbon monoxide mole fraction (d) as a function of water-to-alcohol (W/A).

As shown in Figure 12a, the outlet temperature of the reaction and exhaust side increases with the increase of W/A. The temperature difference between the reaction and exhaust side does not change significantly while the maximum and the minimum temperature difference are 14.1 K and 11.4 K, respectively. This indicates that the change of the W/A has a slight effect on the MSR reaction. Simultaneously, it is verified that the heat is the main influencing factor at this time. Figure 12b shows the methanol conversion and thermal efficiency as a function of the W/A. The methanol conversion increases from 81.7% to 93.6% with the increase of W/A, and the thermal efficiency decreases from 22.3% to 21%. With the increase of the W/A, the MSR is conducive to hydrogen production, and the methanol conversion and hydrogen production rate increase. Since water has a greater latent heat of vaporization and heat capacity, the increase of water content in the reactant leads to more heat consumption, which causes a drop in thermal efficiency. As shown in Figure 12c, the molar concentrations of carbon monoxide, hydrogen, and carbon dioxide decrease with increasing W/A, and the optimal W/A in this work is 1.3.

3.6. Effects of Parallel and Counter Flow on MSR

Figure 13 shows the temperature distribution of the parallel flow and counter flows when the inlet exhaust temperature is 773 K. Compared with the parallel flow, the temperature difference in the adjacent area of the reactor is smaller than that of the counter flow. The internal temperature increases on the reaction side, and the heat transferred from the exhaust to the MSR, increases.

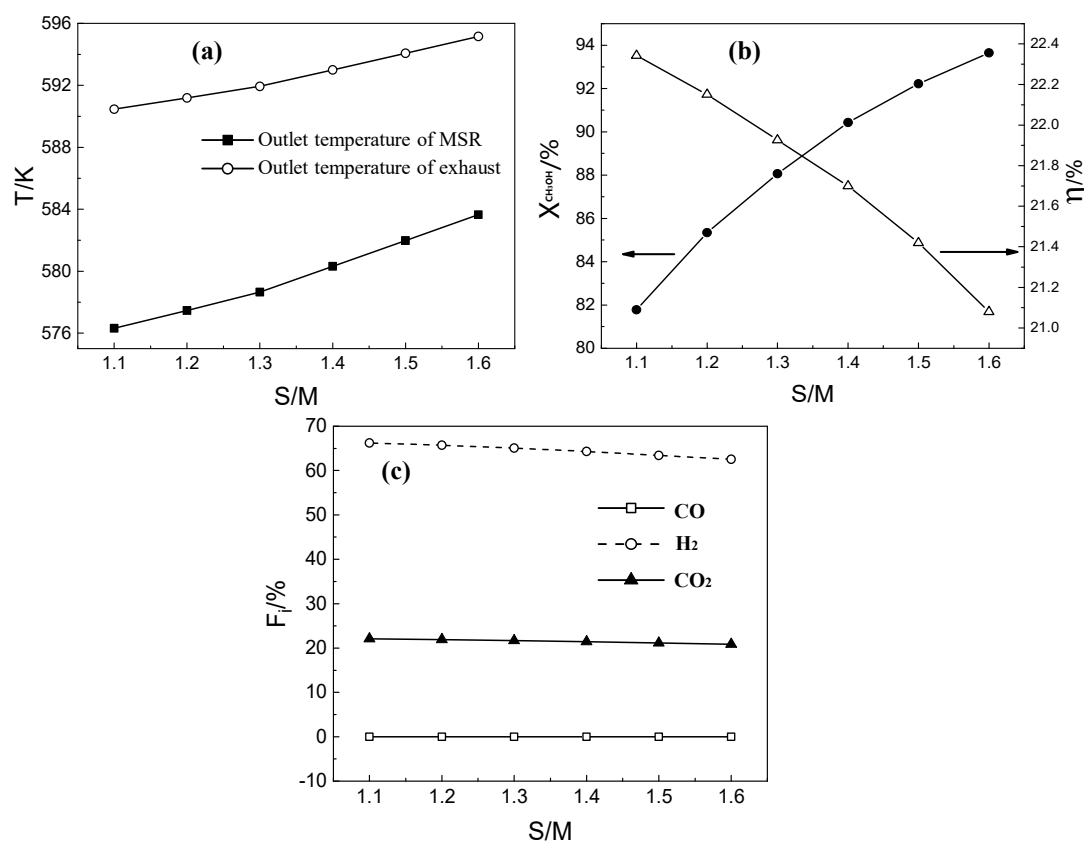


Figure 12. Outlet temperature on the reaction and exhaust side (a), methanol conversion and thermal efficiency (b), and mole fraction of reaction product (c), as a function of the W/A.

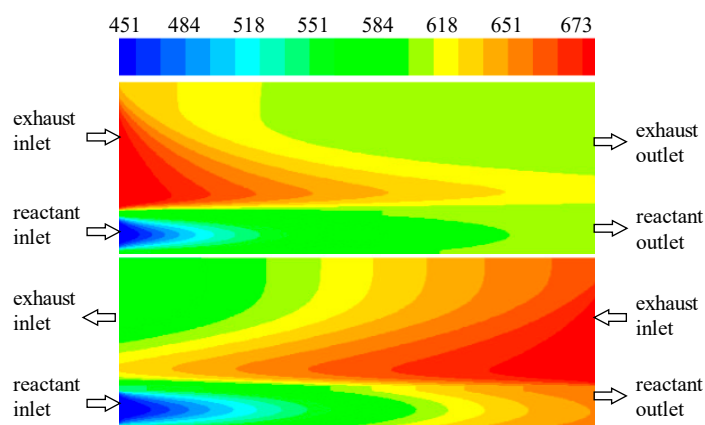


Figure 13. Temperature map of parallel and counter flow.

As shown in Figure 14a, the outlet temperatures on the reaction and the exhaust side increase along with increase of the inlet exhaust temperature, under the parallel and counter flow. At the parallel flow, the outlet temperature on the exhaust side is higher than that of the reaction side, and the outlet temperature difference decreases as the inlet exhaust temperature increases. At the parallel flow, the outlet temperature on the reaction side is higher than that of the exhaust side, and the temperature difference increases as the inlet exhaust temperature increases. At the parallel flow, the outlet of the exhaust is adjacent to the inlet of the lower temperature reactant, and the outlet of the reactants is adjacent to the inlet of high temperature exhaust, so the outlet temperature of reactants is higher than that of the exhaust. The heat supply of the exhaust is not enough for vigorous MSR in the front section, but the heat is sufficient in the rear section on the reaction side. However, for the parallel flow,

the temperature of the reaction and the exhaust side both decrease as the reaction proceeds, so the outlet temperature on the reaction side is higher.

When the inlet temperature of the exhaust increases, the heat supplied to the reactant in the rear section increases. Meanwhile, the outlet reactant temperature and the temperature difference both increase. As shown in Figure 14b, the methanol conversion increases from 61% to 98% at parallel flow, and increases from 64.8% to 99% at counter flow. The methanol conversion of the counter flow was slightly higher than that of the parallel flow. This is possibly because the MSR is relatively gentle during the counter flow. There is some difference between this result and the literature [39]. The methanol conversion of the counter flow was higher than that of the parallel flow, often higher by 5%. This is probably because the model size of literature is larger than that of this study. The temperature difference between the exhaust and the reaction side is slightly larger in this study, causing a little more heat transfer amount. Therefore, methanol conversion and the thermal efficiency both increase slightly. As shown in Figure 14c, the thermal efficiency increases with an increase of the inlet exhaust temperature in the parallel and the counter flow. The thermal efficiency of the parallel flow increases from 16% to 24% and that of the counter flow increases from 18% to 28%. It can be known that the reactor performance is a little better at the counter flow.

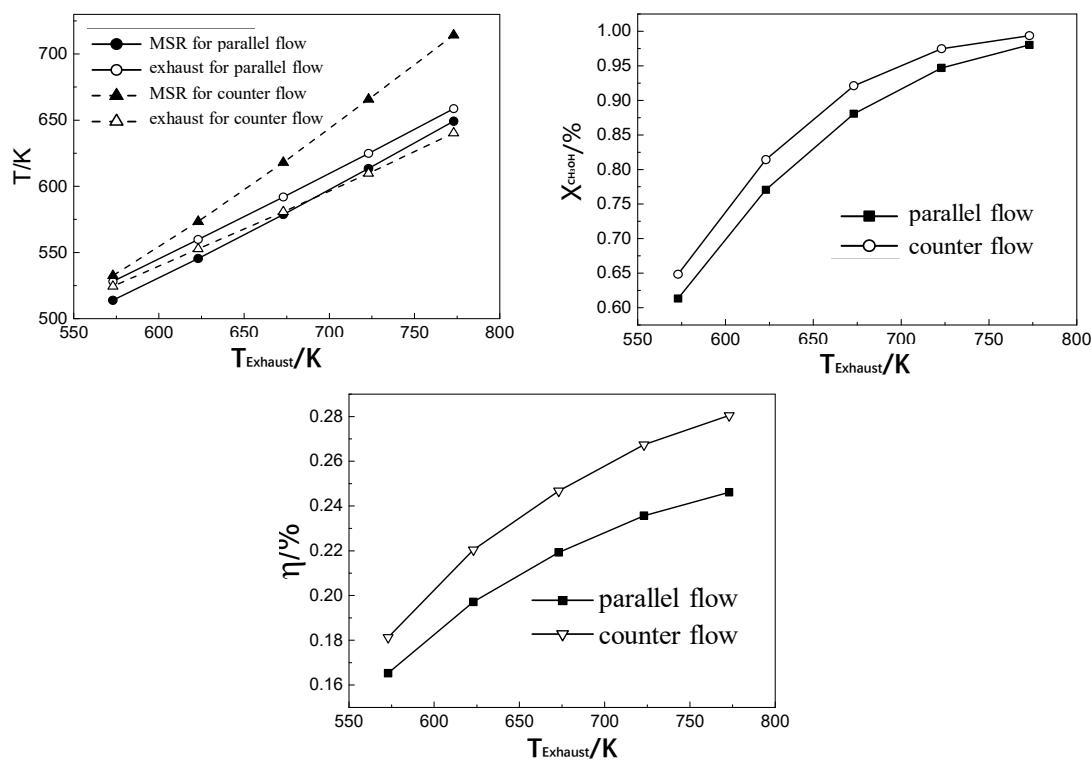


Figure 14. Outlet temperature of the methanol steam reforming (MSR) and the exhaust (a), methanol conversion (b), and the thermal efficiency (c), with inlet exhaust temperature under different inlet exhaust temperatures.

4. Conclusions

A rib microreactor for MSR heated by automobile exhaust was designed to study the effects of inlet exhaust and methanol steam on the reactor performance. The results showed that the inlet temperature of the reactants is the most influential factor for MSR. The total amount of heat supplied to MSR increased as the inlet exhaust velocity increased. The methanol conversion and hydrogen mole along the axis all increased with the inlet exhaust velocity. Since the heat absorbed by the reactant increased with increasing inlet exhaust temperature, methanol conversion increased with increasing inlet exhaust temperature. The axial temperature increased gradually along the axis and decreased

with the reactant inlet velocity. The methanol conversion, the mole fractions of hydrogen and carbon monoxide decreased with the increase of inlet exhaust velocity. The W/A slightly influenced the reactor performance of MSR. The best parameter performance of MSR was observed with inlet exhaust velocity at 1.1 m/s, inlet exhaust temperature at 773 K, inlet reactant velocity at 0.1 m/s, inlet reactant temperature at 493 K, and W/A at 1.3, under counter flow. In addition, the methanol conversion of 99.4% was achieved with a thermal efficiency of 28%. Research results are beneficial for the developments of microreactor in comprehensive utilization of waste heat from heterogeneous catalytic reaction, and provides theoretical support for designing microreactor for waste heat utilization.

Author Contributions: Funding acquisition, F.W.; Investigation, G.W.; Methodology, F.W.; Project administration, F.W.; Visualization, G.W.; Writing—original draft, G.W.; Writing—review & editing, B.C. All authors have read and agreed to the published version of the manuscript.

Funding: This research was funded by the National Natural Science Foundation of China (50906104).

Acknowledgments: The authors acknowledge data sources supported by Yanyun Li.

Conflicts of Interest: The authors declare no conflict of interest.

References

1. Han, J.; Liao, Y.; Zhang, J.; Wang, S.; Li, S. Target Fusion Detection of LiDAR and Camera Based on the Improved YOLO Algorithm. *Mathematics* **2018**, *6*, 213. [[CrossRef](#)]
2. Driely, C.; Andrew, G. An Analysis of Children Left Unattended in Parked Motor Vehicles in Brazil. *Int. J. Environ. Res. Public Health* **2016**, *13*, 649.
3. Feng-Hua, L.I.; Zhang, Y.J.; Zhang, J.; Yuan, Y.; Lin, W.U.; Mao, H.J. Characteristics of Particulate and Inorganic Elements of Motor Vehicles Based on a Tunnel Environment. *Environ. Sci.* **2018**, *39*, 1014–1022.
4. Chen, T.Z.; Yan-Li, G.E.; Liu, Y.C.; Hong, H.E. VOCs Emission from Motor Vehicles in China and Its Impact on the Atmospheric Environment. *Environ. Sci.* **2018**, *39*, 478–492.
5. Popescu, M.; Goss, J.; Staton, D.A.; Hawkins, D.; Chong, Y.C. Electrical Vehicles—Practical Solutions for Power Traction Motor Systems. *IEEE Trans. Ind. Appl.* **2018**, *54*, 2751–2762. [[CrossRef](#)]
6. Llorca, C.; Angel-Domenech, A.; Agustin-Gomez, F.; Garcia, A. Motor vehicles overtaking cyclists on two-lane rural roads. *Anal. Speed Lateral Clear.* **2017**, *92*, 302–310.
7. Pashchenko, D. Thermochemical waste-heat recuperation by steam methane reforming with flue gas addition. *Int. J. Energy Res.* **2019**, *43*, 2216–2226. [[CrossRef](#)]
8. Deb, P.; Debnath, P.; Denis, A.F.; Lepcha, O.T. Variability of soil physicochemical properties at different agroecological zones of Himalayan region: Sikkim, India. *Environ. Dev. Sustain.* **2019**, *21*, 2321–2339. [[CrossRef](#)]
9. Liu, Z.; Wang, J.; Zhang, T.; Zhou, S.; Yan, K. The effects of microbial fuel cells coupled with solar cells under intermittent illumination on sediment remediation. *Environ. Sci. Process. Impacts* **2019**, *21*, 2141–2149. [[CrossRef](#)] [[PubMed](#)]
10. Wu, Y.; Jing, X.; Gao, C.; Huang, Q.; Cai, P. Recent advances in microbial electrochemical system for soil bioremediation. *Chemosphere* **2018**, *211*, 156–163. [[CrossRef](#)]
11. Jung, G.; Chan, S.; Lai, C. Innovative membrane electrode assembly (MEA) fabrication for proton exchange membrane water electrolysis. *Energies* **2019**, *12*, 4218. [[CrossRef](#)]
12. Prapinagsorn, W.; Sittijunda, S.; Reungsang, A. Co-digestion of napier grass and its silage with cow dung for bio-Hydrogen and methane production by two-stage anaerobic digestion process. *Energies* **2017**, *11*, 47. [[CrossRef](#)]
13. Fang, L.; Li, Y.; Chen, S. Chemical looping hydrogen production using activated carbon and carbon black as multi-function carriers. *Int. J. Hydrog. Energy* **2018**, *43*, 5501–5511.
14. Wang, R.; Ni, S.; Liu, G.; Xu, X. Hollow CaTiO₃ cubes modified by La/Cr co-doping for efficient photocatalytic hydrogen production. *Appl. Catal. B Environ.* **2018**, *225*, 139–147. [[CrossRef](#)]
15. Andrade, T.S.; Papagiannis, I.; Dracopoulos, V. Visible-light activated titania and its application to photoelectrocatalytic hydrogen peroxide. *Materials* **2019**, *12*, 4238. [[CrossRef](#)]

16. Zhao, J.; Xuan, M.; Guan, X.; Qiang, W.; Wang, T. Investigation of hydrogen bubbles behavior in tungsten by high-flux hydrogen implantation. *J. Nucl. Mater.* **2018**, *503*, 198–204. [[CrossRef](#)]
17. Pashchenko, D.I. Thermochemical recovery of heat contained in flue gases by means of bioethanol conversion. *Therm. Eng.* **2013**, *60*, 438–443. [[CrossRef](#)]
18. Pashchenko, D.; Gnutikova, M.; Karpilov, I. Comparison study of thermochemical waste-heat recuperation by steam reforming of liquid biofuels. *Int. J. Hydrog. Energy* **2020**, *45*, 4174–4181. [[CrossRef](#)]
19. Zhou, Y.; Tang, J.; Zhang, C. Thermodynamic analysis of the air-cooled transcritical Rankine cycle using CO₂/R161 mixture based on natural draft dry cooling towers Thermodynamic analysis of the air-cooled transcritical Rankine cycle using CO₂/R161 mixture based on natural draft dry cooling towers. *Energies* **2019**, *12*, 3342.
20. Zhou, Y.; Li, Q.; Wang, Q. Energy Storage Analysis of UIO-66 and Water Mixed anofluids: An Experimental and Theoretical Study. *Energies* **2019**, *12*, 2521. [[CrossRef](#)]
21. Feng, S.; Ping, W.; Yi, Z.; Wark, M.; Yang, J.; Wang, X. Construction of strontium tantalate homo-semiconductor composite photocatalysts with a tunable type II junction structure for overall water splitting. *Catal. Sci. Technol.* **2018**, *8*, 3025–3033.
22. Su, S.; Zhang, L.; Zhang, Y.; Lei, J.; Pan, L. Thermodynamic simulation for hydrogen production in the methanol steam reforming system of kilowatt PEMFC. *J. Petrochem. Univ.* **2015**, *28*, 19–25.
23. Zhang, Y.; Li, H.; Han, W.; Bai, W.; Yang, Y.; Yao, M.; Wang, Y. Improved design of supercritical CO₂ Brayton cycle for coal-fired power plant. *Energy* **2018**, *155*, 1–14. [[CrossRef](#)]
24. Goldmann, A.; Sauter, W.; Oettinger, M. A Study on Electrofuels in Aviation. *Energies* **2018**, *11*, 392. [[CrossRef](#)]
25. Mishra, P.C.; Kar, S.K.; Mishra, H. Effect of perforation on exhaust performance of a turbo pipe type muffler using methanol and gasoline blended fuel: A step to NO_x control. *J. Clean. Prod.* **2018**, *183*, 869–879. [[CrossRef](#)]
26. Kumar, C.; Rana, K.B.; Tripathi, B. Effect of diesel-methanol-nitromethane blends combustion on VCR stationary CI engine performance and exhaust emissions. *Environ. Sci. Pollut. Res.* **2019**, *26*, 6517–6531. [[CrossRef](#)]
27. Feng, W.; Cao, Y.; Wang, G. Thermoelectric generation coupling methanol steam reforming characteristic in microreactor. *Energy* **2014**, *80*, 642–653.
28. Abdullah, N.; Bahruji, H.; Rogers, S.M.; Wells, P.P.; Catlow, C.R.A.; Bowker, M. Pd local structure and size correlations to the activity of Pd/TiO₂ for photocatalytic reforming of methanol. *Phys. Chem. Chem. Phys.* **2019**, *21*, 16154–16160. [[CrossRef](#)]
29. Nowicka, E.; Althahban, S.M.; Luo, Y.; Kriegel, R.; Hutchings, G.J. Highly selective PdZn/ZnO catalysts for the methanol steam reforming reaction. *Catal. Sci. Technol.* **2018**, *8*, 5848–5857. [[CrossRef](#)]
30. Qing, S.; Hou, X.; Liu, Y.; Li, L.; Fan, W. Strategic use of CuAlO₂ as a sustained release catalyst for production of hydrogen from methanol steam reforming. *Chem. Commun.* **2018**, *54*, 12242–12245. [[CrossRef](#)]
31. Chen, B.; Wang, L.; Wang, F. Study on methane steam reforming coupling high-temperature exhaust heat utilization for hydrogen production. *Int. J. Green Energy* **2019**, *16*, 1–11. [[CrossRef](#)]
32. Ngoenthong, N.; Hartley, M.; Sornchamni, T. Comparison of packed-bed and micro-channel reactors for hydrogen production via thermochemical cycles of water splitting in the presence of ceria-based catalysts. *Processes* **2019**, *7*, 767. [[CrossRef](#)]
33. Zhou, W.; Ke, Y.; Pei, P.; Yu, W.; Chu, X.; Li, S.; Yang, K. Hydrogen production from cylindrical methanol steam reforming microreactor with porous Cu-Al fiber sintered felt. *Int. J. Hydrog. Energy* **2018**, *43*, 3643–3654. [[CrossRef](#)]
34. Liang, Z.; Peng, G.; Tang, Z.; Min, L.; Sun, Y. Three dimensional porous Cu-Zn/Al foam monolithic catalyst for CO₂ hydrogenation to methanol in microreactor. *J. CO₂ Util.* **2017**, *21*, 191–199. [[CrossRef](#)]
35. Pashchenko, D. Pressure drop in the thermochemical recuperators filled with the catalysts of various shapes_ A combined experimental and numerical investigation. *Energies* **2019**, *166*, 462–470. [[CrossRef](#)]
36. Mardle, P.; Fernihough, O.; Du, S. Evaluation of the Scaffolding Effect of Pt Nanowires Supported on Reduced Graphene Oxide in PEMFC Electrodes. *Coating* **2018**, *8*, 48. [[CrossRef](#)]
37. Liao, C.H.; Horng, R.F. Investigation on the hydrogen production by methanol steam reforming with engine exhaust heat recovery strategy. *Int. J. Hydrogen Energy* **2016**, *41*, 4957–4968. [[CrossRef](#)]






38. Tripodi, A.; Compagnoni, M.; Martinazzo, R. Process simulation for the design and scale up of heterogeneous catalytic process: Kinetic modelling issues. *Catalysts* **2017**, *7*, 159. [[CrossRef](#)]
39. Pickard, W.F.; Abraham-Shrauner, B. Simplified models of the symmetric single-pass parallel-plate counterflow heat exchanger: A tutorial. *Roy Soc Open Sci* **2018**, *5*, 171617. [[CrossRef](#)]



© 2020 by the authors. Licensee MDPI, Basel, Switzerland. This article is an open access article distributed under the terms and conditions of the Creative Commons Attribution (CC BY) license (<http://creativecommons.org/licenses/by/4.0/>).

Article

Effects of Impurities on Pre-Doped and Post-Doped Membranes for High Temperature PEM Fuel Cell Stacks

Samuel Simon Araya ^{1,*}, Sobi Thomas ², Andrej Lotrič ^{3,4}, Simon Lennart Sahlin ¹, Vincenzo Liso ¹
and Søren Juhl Andreasen ⁴

¹ Department of Energy Technology, Aalborg University, 9220 Aalborg Øst, Denmark; sls@et.aau.dk (S.L.S.); vli@et.aau.dk (V.L.)

² Blue World Technologies ApS, Lavavej 16, 9220 Aalborg Øst, Denmark; sbt@blue.world

³ Faculty of Mechanical Engineering, University of Ljubljana, Aškerčeva 6, 1000 Ljubljana, Slovenia; andrej.lotric@fs.uni-lj.si

⁴ SerEnergy A/S, Lyngvej 8, 9000 Aalborg, Denmark; sja@serenergy.com

* Correspondence: ssa@et.aau.dk

Abstract: In this paper, we experimentally investigated two high temperature polymer electrolyte membrane fuel cell (HT-PEMFC) stacks for their response to the presence of reformat impurities in an anode gas stream. The investigation was aimed at characterizing the effects of reformat impurities at the stack level, including in humidified conditions and identifying fault features for diagnosis purposes. Two HT-PEMFC stacks of 37 cells each with active areas of 165 cm² were used with one stack containing a pre-doped membrane with a woven gas diffusion layer (GDL) and the other containing a post-doped membrane with non-woven GDL. Polarization curves and galvanostatic electrochemical impedance spectroscopy (EIS) were used for characterization. We found that both N₂ dilution and impurities in the anode feed affected mainly the charge transfer losses, especially on the anode side. We also found that humidification alleviated the poisoning effects of the impurities in the stack with pre-doped membrane electrode assemblies (MEA) and woven GDL but had detrimental effects on the stack with post-doped MEAs and non-woven GDL. We demonstrated that pure and dry hydrogen operation at the end of the tests resulted in significant recovery of the performance losses due to impurities for both stacks even after the humidified reformat operation. This implies that there was only limited acid loss during the test period of around 150 h for each stack.

Keywords: PEM; fuel cell; fault; diagnosis; electrochemical impedance spectroscopy; distribution of relaxation times; reformat



Citation: Simon Araya, S.; Thomas, S.; Lotrič, A.; Sahlin, S.L.; Liso, V.; Andreasen, S.J. Characterization of Humidified Reformat Impurities on Pre-Doped and Post-Doped Membranes for High Temperature PEM Fuel Cell Stacks. *Energies* **2021**, *14*, 2994.

<https://doi.org/10.3390/en14112994>

Academic Editor: Francesco Lufrano

Received: 21 April 2021

Accepted: 18 May 2021

Published: 21 May 2021

Publisher's Note: MDPI stays neutral with regard to jurisdictional claims in published maps and institutional affiliations.



Copyright: © 2021 by the authors. Licensee MDPI, Basel, Switzerland. This article is an open access article distributed under the terms and conditions of the Creative Commons Attribution (CC BY) license (<https://creativecommons.org/licenses/by/4.0/>).

1. Introduction

In recent years, proton exchange membrane fuel cells (PEMFC) have become one of the most researched and most mature fuel cell technologies [1]. However, despite the tremendous research efforts and the technological advancements thus far achieved, further optimization and improvements are still needed to reduce their cost, enhance their durability, and accelerate their commercialization [2,3].

PEMFC technology has evolved into two sub-types; one operating at low-temperature (LT-PEMFC) and the other at high-temperature (HT-PEMFC). In general, the two types consist of the same core components; bipolar plates with flow-field channels, a gas diffusion layer made of carbon fiber, a catalyst layer based on Pt particles and a carbon support, and a proton exchange membrane. The main difference between the two is the material used for the proton exchange membrane. In an LT-PEMFC the Perfluorosulfonic acid (PFSA) membranes, such as Nafion[®], are used [4], which require liquid water to achieve good proton conductivity. Hence, their operation is limited to temperatures of up to 100 °C if no over-pressure is used. Therefore, liquid water is crucial for the proper operation of a

Nafion[®]-based LT-PEMFC stack, and different techniques are being explored to enhance the humidification process [5,6].

On the other hand, an HT-PEMFC uses a polybenzimidazole (PBI) membrane impregnated with phosphoric acid (H_3PO_4) to facilitate the transfer of protons, which eliminates the need for liquid water, thereby, allowing for higher temperature operation—typically around 160 °C. This higher operating temperature comes with advantages, including easier cooling, more efficient utilization of excess heat, reduced or no water management issues, and a higher tolerance to impurities [7].

The latter also means that the HT-PEMFC systems can use (in addition to pure hydrogen) a variety of fuels, which can be converted into hydrogen-rich gas, without the need for purification. HT-PEMFC systems are commonly integrated with a reformer and use liquid methanol as a fuel, which is easier to transport and has a higher volumetric energy density compared to compressed hydrogen at 700 bar [8,9].

The advantage of using fuels that are more manageable than pure hydrogen when compared with LT-PEMFCs, especially liquid fuels, such as methanol, makes HT-PEMFCs ideal candidates to replace diesel generators for various applications, including as backups for telecom applications and auxiliary power units (APU). In addition, they are considered for combined heat and power (CHP) applications due to the efficient utilization of excess heat, while the infrastructure advantage of liquid fuels provides an edge over LT-PEMFCs for applications in heavy duty transportation both as a main power source and as range extenders [9].

However, there are still challenges that need to be addressed in order to optimize HT-PEMFCs. Durability and stability issues are some of the factors that hinder their wide spread commercialization and that are being studied to optimise fuel cell components and operating conditions [10,11]. For instance, in the steam reforming of hydrocarbons to hydrogen-rich syngas, the steam is supplied with over the stoichiometric ratios. Thus, in addition to hydrogen, CO_2 , and CO, there is always some water vapor present in the reformed gas. The presence of water can enhance the fuel cell performance by alleviating the CO poisoning effect [12].

On the other hand, Zhou et al. [13] proposed that the water content in the anode gas should be minimized to avoid the performance loss when the HT-PEMFC is operated at lower operating temperatures (i.e., 140–160 °C), and researchers reported that this may also cause faster degradation due to increased acid loss [11]. According to Park et al. [14], the performance loss due to a humidified atmosphere can be reversed by precise acid-dosing of the degraded membrane electrode assemblies (MEA).

When the doping level of a PBI membrane exceeds two H_3PO_4 molecules per PBI repeat unit, free and mobile acid molecules are present in the membrane, as only two phosphoric acid molecules can bond with each PBI repeat unit [7]. This acid can leach out of the membrane by various mechanisms, such as diffusion, capillary transport, membrane compression, evaporation, and especially, can be washed out by condensed water during shutdowns and/or cold starts [15].

The phosphoric acid anions can adsorb on the Pt particles on the cathode side and occupy the electrochemical surface area (ECSA) of the catalyst for the already slow oxygen reduction reaction (ORR) [16,17]. The low permeability of oxygen in the phosphoric acid and phosphate anion adsorption on the Pt catalyst are considered as the main causes for the lower performance of HT-PEMFC compared to LT-PEMFC under pure hydrogen operation [7,18]. As the acid tends to leach out of the membrane, it can also block some of the pores for reactant gases in the catalyst and gas-diffusion layer (GDL) and, thus, may cause significant mass transport resistance [18].

To alleviate these issues several approaches are taken to optimise the MEA core components, such as improving the design of the PBI membrane by tweaking its structure, acid doping levels, and thickness [19]. There are typically two acid doping methods for PBI membranes. The first method is called pre-doped, in which PBI is dissolved in polyphosphoric acid and the solution is then cast into a membrane. Moisture from the surrounding

environment is sufficient to induce a sol-gel transition by the hydrolysis of polyphosphoric acid to phosphoric acid resulting in phosphoric acid-doped PBI membranes.

The second method is called a post-doped membrane, where the PBI is first dissolved in an organic solvent and cast into a membrane, where the acid doping is then achieved by immersing the PBI membrane into highly concentrated phosphoric acid. The doping levels are usually higher for pre-doped membranes at up to 70 molecules of H_3PO_4 per PBI repeat unit [20], while the post-doped membranes have a doping level of around 9–12 molecules of H_3PO_4 per PBI repeat unit [21]. Due to swelling, higher doping levels in pre-doped membranes lead to these membranes being thicker compared to post-doped ones. To increase the membrane durability or acid uptake, various fillers (e.g., SiO_2 , TiO_2 , aluminium silicate, and graphene oxide) or different synthesis techniques (e.g., sulfonation, cross-linking, or the electrospinning of nanofibers) are used [19,22].

The preparation of the catalyst layer along with the pore sizes and tortuosity of the GDL are important factors when it comes to supplying reactants to the triple phase boundary (TPB) [23], which is the crucial contact point among the Pt catalyst, the PA/PBI electrolyte, and the reactants for the electrochemical reactions to take place. The amount of electrolyte (phosphoric acid) around the Pt particles is of paramount importance, where too little electrolyte will not create sufficient paths for proton transfer and will cause charge transfer issues, while too much electrolyte might cover the active sites for the reactants.

To optimize the catalyst layer, various binders (e.g., polytetrafluoroethylene (PTFE), and polyethylene oxide) can be added to make the layer more hydrophobic and/or better adhere to the membrane and the GDL [24]. Often a sub-layer, called a mesoporous layer (MPL), is used to create better contact between the catalyst layer and the GDL, which also improves the redistribution of acid in the catalyst layer, thus, also enhancing the electrochemical surface area and preventing the substantial intrusion of acid into the GDL [25,26].

Traditionally, the catalyst loading in HT-PEMFCs is higher compared to LT-PEMFCs, and current state-of-the-art electrodes have loadings of around $1\text{ mgPt}/\text{cm}^2$ [27]. Some recent studies have investigated MEAs with low platinum loading [28,29], where it was observed that the traditional MPL or catalyst layer compositions may have to be changed to allow increased Pt utilization. Martin et al. [28] showed that electrodes without any binder or ionomer in the catalyst layer and catalyst loading of only $0.1\text{ mgPt}/\text{cm}^2$ yielded a maximum performance of $0.42\text{ W}/\text{cm}^2$. Yao et al. [29] also investigated an HT-PEMFC without the MPL and with Pt loading of $0.2\text{ mgPt}/\text{cm}^2$ and achieved a power density of $0.32\text{ W}/\text{cm}^2$.

The GDL is a porous material that is traditionally made of carbon fibers and serves multiple purposes. It provides an electrically conductive pathway for current collection, passage for transport of reactants and removal of the produced heat and water, mechanical support to the MEA, and protection of the catalyst layer from corrosion or erosion caused by flows or other factors. Carbon fibers can either be woven in a so-called carbon cloth or non-woven in a form of carbon paper. The main difference between the two types is that non-woven carbon tend to be thinner, more brittle, and less compressible, compared to the woven forms.

Kannan et al. [30] compared four types of commercially available non-woven GDLs from Freudenberg that were assembled with the same type of a post-doped membrane into the MEAs. The main difference between the investigated GDLs is the composition of the MPL and surface treatment of the GDL. The lowest degradation rate was demonstrated with the GDL that most efficiently retained the phosphoric acid. Therefore, each type of GDL can be tailored to have different porosity, hydrophobicity, and conductivity characteristics.

As with all fuel cell types, the initial activation phase or break-in is crucial to allow the HT-PEMFC to reach its optimal performance and to avoid fast degradation [11]. The break-in period depends on the structure of the components comprising the MEA and on the acid doping method. In a study [21], researchers demonstrated that pre-doped MEAs required at least 30 h to achieve peak performance while post-doped MEAs underwent

minor changes in the break-in period, which may indicate that this type of MEA can be used directly without the need for a break-in period. The changes in performance during the break-in can be ascribed to redistribution of the phosphoric acid within the membrane, catalyst layer, and the GDL [25].

In this work, we study two HT-PEMFC stacks assembled with the same components but with different types of MEAs. The first MEA type consists of a post-doped membrane and a non-woven GDL, while the second consists of a pre-doped membrane and a woven GDL. These two types of stacks were exposed to various operating conditions, namely, N₂ dilution and CO and CO₂ poisoning both with and without humidification. For the experimental characterization of the effect of the different operating conditions on the stacks, polarization curves and electrochemical impedance spectroscopy (EIS) were used. The data obtained by EIS were then analyzed by using two approaches: an equivalent circuit model (ECM) and distribution of relaxation times (DRT).

2. Methodology

2.1. Experimental Setup

A schematic of the test setup used for the experiments in the current work as well as a photo of one of the fuel cell stacks are shown in Figure 1. The experimental characterization was carried out using a GreenLight Innovation fuel cell test station. Two oil-cooled HT-PEMFC stacks of 37 cells, each with active area of 165 cm², were used. The first stack employed a post-doped Dapozol membrane by Danish Power systems (DPS), which utilized meta-PBI as polymer materials and a typical acid doping level of 8–10 phosphoric acid molecules per repeat unit of PBI. The second stack used pre-doped MEAs by Serenergy A/S that utilized a direct cast membrane of the para-polybenzimidazole type with an acid doping level of 30–40 phosphoric acid molecules per polymer repeat unit.

While both membranes utilized phosphoric acid for proton conduction, the high acid content leads to less mechanical stability of the membranes resulting in differences in the chosen thicknesses of the membranes used, with the post-doped membranes being thinner than the pre-doped membranes. This thinner format of the post-doped membranes partially compensates for the lower acid doping level when it comes to the proton conductivity. Finally, the DPS MEAs employ a non-woven gas diffusion layer (GDL), whereas the Serenergy MEAs use a woven type GDL, and both MEAs have a Pt loading of the electrodes of ~1 mgPt/cm².

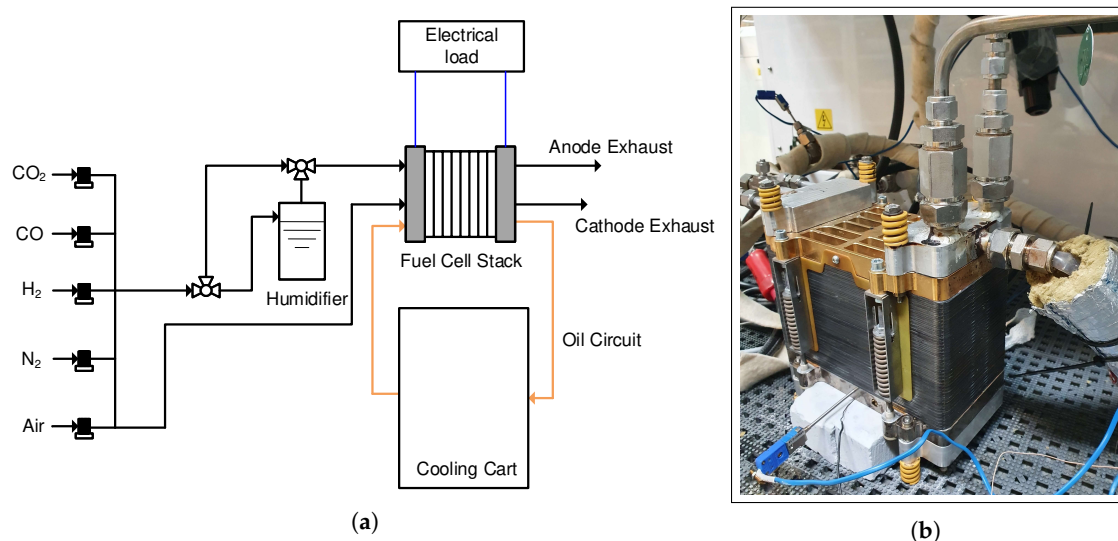


Figure 1. Test setup (a) A schematic of the test setup. (b) One of the short stacks used in the current work.

2.2. Test Procedures

The tests in the current work consisted of different gas compositions in the anode feed stream of two fuel cell stacks. At the beginning of each test (BOT), the stacks were operated under a pure and dry hydrogen feed on the anode side as a reference for the study. This was then followed by the main tests of the current work—namely, nitrogen dilution, simulated dry reformat and simulated wet reformat. Finally, pure and dry hydrogen in the anode feed was used at the end of the tests (EOT) to check the reversibility of the effects of the impurities on the fuel cell stacks. The test procedures along with the compositions of the anode feed stream for each test step are given in Table 1.

Table 1. The test procedures.

Test Step	Anode Gas Composition	Duration
Break-in	100% H ₂	50 h
Nitrogen dilution	100% H ₂ , 31.7% N ₂	24 h
Dry reformat	68.3% H ₂ , 0.9% CO, 21.8% CO ₂ , 9% N ₂	24 h
Air-bleed	2% air, 98% H ₂	5 min
Wet reformat	68.3% H ₂ , 0.9% CO, 21.8% CO ₂ , 9% H ₂ O	24 h
Air-bleed	2% air, 98% H ₂	5 min
End of test recovery	100% H ₂	24 h

Both stacks underwent a 50-h break-in procedure in the beginning of the test at 0.2 A/cm² under pure hydrogen operation. Successively, the different fuel compositions were tested on the anode side of the stack, and each fuel composition was operated for 24 h. Polarization curves and EIS spectra were recorded 1 h after the start and at the end of each 24 h test period. Galvanostatic EIS sweeps were recorded between 4 kHz and 0.1 Hz at 20 points per decade using an in-house-built frequency analyzer.

For the EIS measurements, an AC amplitude of 2.5 A was used for all set points, which corresponds to 7.5% of the operating current of 65 A. To minimize measurement errors, three impedance spectra were recorded at each test condition with 15 min of relaxation time before each measurement. The repeatability of the EIS measurements is shown in Figure 2, where it can be seen that the three EIS measurements on pure hydrogen lay on top of each other.

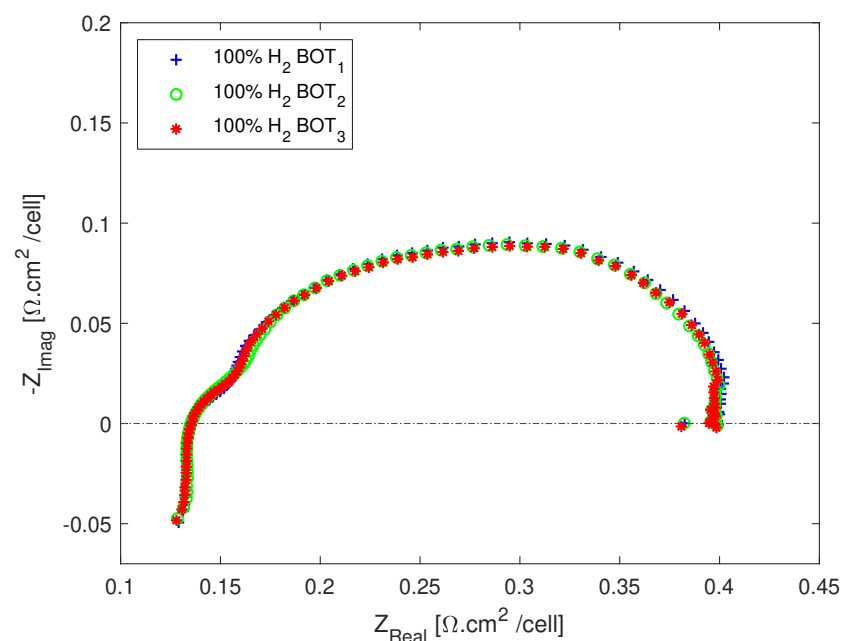


Figure 2. Repeatability of the EIS measurements.

For the polarization curve measurements, the current was increased from 0 to 75 A, with a step increase of 2.5 to 10 A to capture the activation losses better and a wider step of 5 A for the remainder of the curve. A dwell time of 3 min was used at each current during the polarization measurements. An anode stoichiometric ratio of 1.3 and cathode stoichiometric ratio of 2.5 were used for all the tests.

An air-bleed step was used in order to recover the effects of CO before proceeding to the next step whenever a test step contained CO in the anode gas composition. The air-bleed step consisted of running the fuel cell at the anode fuel composition of 2% air and 98% H₂ for five minutes at 65 A. The same test matrix was followed for both stacks to carry out the characterization study.

2.3. Data Analysis

In this work, a combination of polarization curves and EIS measurements were used to monitor the performance and investigate the effects of the different reformat compositions on two stacks. The EIS data was analyzed by means of equivalent circuit model (ECM) fits and DRT peaks in order to characterize both the post-doped and pre-doped stacks.

While ECM fits can provide a quick physical interpretation of the impedance measurements, there are still ambiguities surrounding their interpretation, and different ECMs can fit the same EIS data. Therefore, in the current work, the shapes of the impedance spectra in the Nyquist plots, the DRT peaks, and the understanding of the fuel cell stacks was used as a basis for the choice of ECM and analysis of the results. A typical ECM for a PBI-based HT-PEMFC [31,32], composed of a series connection of an inductor (L), a resistor (R_{ohm}), and three parallel resistors and constant phase elements (R||CPE), was used to analyze the different losses of the fuel cell stacks.

A constant phase element is pseudo-capacitive element used to mimic the depressed EIS data of real systems for a better fit by accounting for interface inhomogeneities [33]. In the literature, CPE has been attributed to the DC conductivity and the capacity of an ion conductor [34] as well as to the surface roughness and electrode porosity [33]. However, there are still uncertainties regarding its physical meaning [33].

Therefore, in the current work, CPE was only used for better fits by keeping the exponential coefficient α constant in the expression for the impedance of a CPE ($Z = \frac{1}{Q \times j\omega^\alpha}$, where Q is the pre-factor of the CPE and α is the exponent). Only changes in the resistances due to the different operating conditions were monitored and analyzed. A more detailed discussion on the advantages and disadvantages of analyzing impedance measurements via ECM fitting along with the typical models for HT-PEMFCs and their physical interpretations is summarized in our previous work [7].

The ECM used in this work is shown in Figure 3. In the interpretation of fitted resistances, it is generally accepted that the ohmic resistance (R_{ohm}) represents all the contact resistances, including the proton conduction across the electrolyte and its changes reflect the changes in proton conductivity [35,36]. High frequency resistance (R_{HF}) and intermediate frequency resistance (R_{IF}) are associated to charge transfer losses, with the former dominated by the anode charge transfer losses and the latter by those in the cathode [37]. Finally, the low frequency resistance (R_{LF}) is ascribed to the mass transport losses [38].

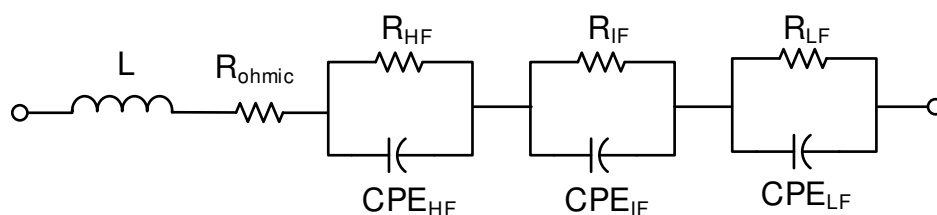


Figure 3. The equivalent circuit model used in this work.

Distribution of relaxation times (DRT) analysis is another method of analyzing impedance data, in which the impedance spectra are represented by an infinite number of infinitesimal parallel R||C-elements in series [39]. The impedance data is then resolved on the basis of the time constants and presented as a distribution of these time constants that represent the electrochemical processes in the fuel cell [40]. Further description of DRT analysis and its use in fuel cells can be found in the literature [39,41–44].

The DRT deconvolution of the impedance spectra was performed with a freely available MATLAB application (DRTtools). The deconvolution takes place by discretizing the complex impedance response given by Equation (1) into a finite number of time constants, which gives Equation (2) [39,41–43]:

$$Z(\omega) = R_0 + R_{pol} \int_0^{\infty} \frac{g(\tau)}{1 + j\omega\tau} d\tau \quad (1)$$

$$Z(\omega) = R_0 + R_{pol} \sum_{k=1}^N \frac{g_k}{1 + j\omega\tau_k} \quad (2)$$

where R_0 represents the ohmic resistance, R_{pol} represents the overall polarization resistance of the fuel cell, j is the imaginary number, ω is the frequency, $\tau = RC$ is the time constant of the single R||C—element, and $g(\tau)$ represents the distribution function. The term $\frac{g(\tau)}{1+j\omega\tau} d\tau$ in Equation (1) represents the fraction of the overall polarization with relaxation times between τ and $\tau + d\tau$ and the term g_k in Equation (2) represents the relative share of each τ_k on the overall polarization resistance. Therefore, in order to account for the absolute resistance distribution and compare the DRT analysis more easily with the information in the Nyquist plot, g_k was scaled by multiplying it with the overall polarization resistance ($h_k = R_{pol} \times g_k$) [39].

Since Equation (2) cannot be solved numerically, a Tikhonov regularization can be used to stabilize the solution numerically, which, in this work, was set to 10^{-5} , based on recommendations from the literature on fuel cells [39,43]. Even though the attribution of the different DRT peaks to the losses in the fuel cells is not straightforward, based on the literature and experience, in this work, peaks below 1 Hz were associated with mass transport losses, peaks between 10 and 50 Hz were attributed to oxygen reduction reaction (ORR) losses, and peaks above 100 Hz were considered to be due to hydrogen oxidation reaction (HOR) losses and proton conduction losses [44]. In a DRT plot, taller peaks indicate higher losses.

3. Results

3.1. Nitrogen Dilution

Nitrogen can be present in the anode feed stream of an HT-PEMFC in cases where the fuel cell is fed with reformed natural gas or decomposed ammonia. Nitrogen is known to have a dilution effect when fed into the anode of an HT-PEMFC along with hydrogen [45]. Therefore, nitrogen dilution in the current work was studied for two purposes.

First, given its presence in some reformat mixtures, it is important to investigate its effects at the stack level for the two types of MEAs. Secondly, as an easily available inert gas, nitrogen was used as a buffer gas to complete the anode gas mixtures to 100% when comparing the effects of dry and wet reformat gases on the two stacks. Therefore, nitrogen dilution analysis also has the purpose of distinguishing the effects of dilution from those of humidification. The gas recipes used for the different stages of the tests are shown in Table 1.

The results of the current work show that the performance decreased for both stacks with nitrogen dilution, Figure 4. The initial dilution effects remained unaltered for the 24 h of tests for the pre-doped stack; however, they continued to exacerbate for the post-doped stack. The initial performance of the post-doped stack was higher than that of the pre-doped stack under the same operating conditions, Figure 4a, while the polarization losses

were higher for the post-doped stack as can be seen from the slopes of the polarization curves in Figure 4a and the impedance spectra in Figure 4b.

The two types of MEAs used in the two stacks had different properties as described in the Section 2, and therefore their performances cannot be compared directly with each other. Other than the MEA properties, the stack assembly can also influence the overall performance. Hence, the current analysis will focus on how the different operating condition affected each stack and what fault features can be identified.

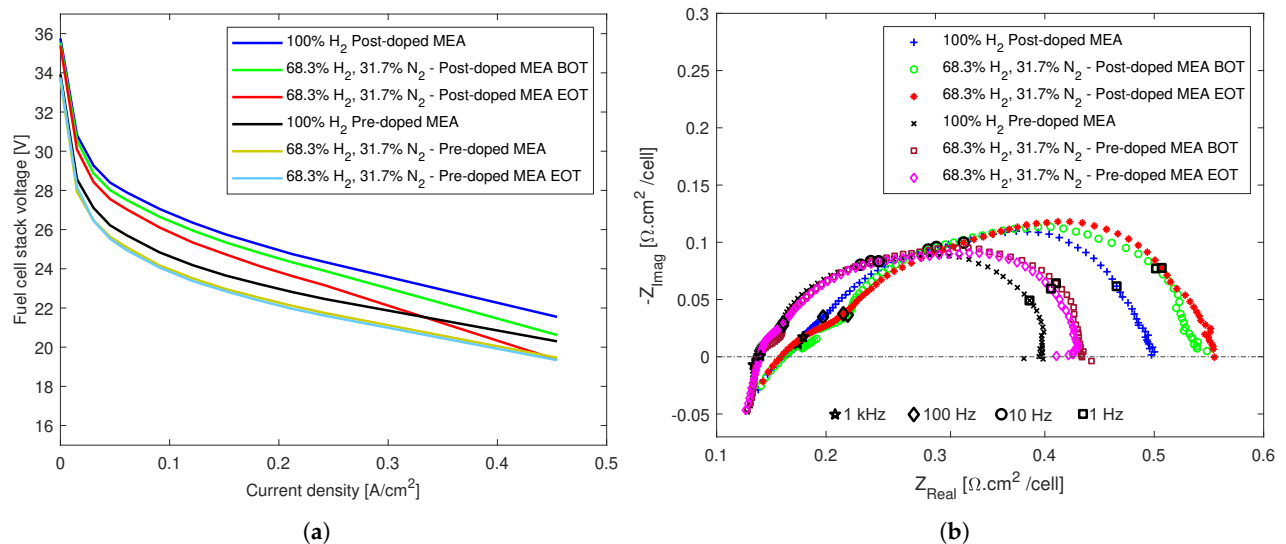


Figure 4. The effects of N₂ dilution on both stacks. (a) Polarization curves. (b) EIS spectra.

All the high frequency real axis intercepts in the Nyquist plot lay on top of each other, implying that the ohmic resistance was not affected by dilution. However, there is a size increase of the impedance spectra in all frequency regions, which implies performance losses, perhaps due to reduced triple phase boundaries as a result of the acid redistribution and eventual loss of excess acid.

In Figure 5, the fitted equivalent circuit resistances and the DRT analyses of the two stacks are shown. The ohmic resistances remain almost unaltered in both cases, with a slight decrease for the pre-doped stack, whereas R_{HF} is the resistance that is the most impacted by dilution in both cases, increasing both in the beginning and the end of the dilution tests for both stacks, Figure 5a,b.

This can be ascribed to the fact that the dilution was done by reducing the hydrogen concentration of the anode feed and substituting it with nitrogen, which significantly reduced the amount of hydrogen available for the electrochemical reaction in the active sites. The cathode charge transfer loss that dominated R_{IF} also increases for both stacks in the beginning of the dilution tests; however, while it continued to increase for the post-doped stack, it recovered for the pre-doped stack. The mass transport losses appeared unaffected for the post-doped stack, and an overall slight increase was observed for the pre-doped stack.

Figure 5c,d show the DRT analyses for the two stacks, where up to five peaks for the post-doped stack and three distinct peaks for the pre-doped stack can be seen. The additional peaks of the post-doped stack are a small one at low frequency right below 10 Hz and another at high frequency, between 1 and 10 kHz. However, none of the peaks are below 1 Hz, which highlights that the mass transport losses as result of nitrogen dilution were not significant in either stack. All the peaks were affected negatively in the beginning of the dilution tests with successive recovery for most of the peaks for both stacks, with an exception at the high frequency region for the post-doped stack, where the DRT peak size continue to increase.

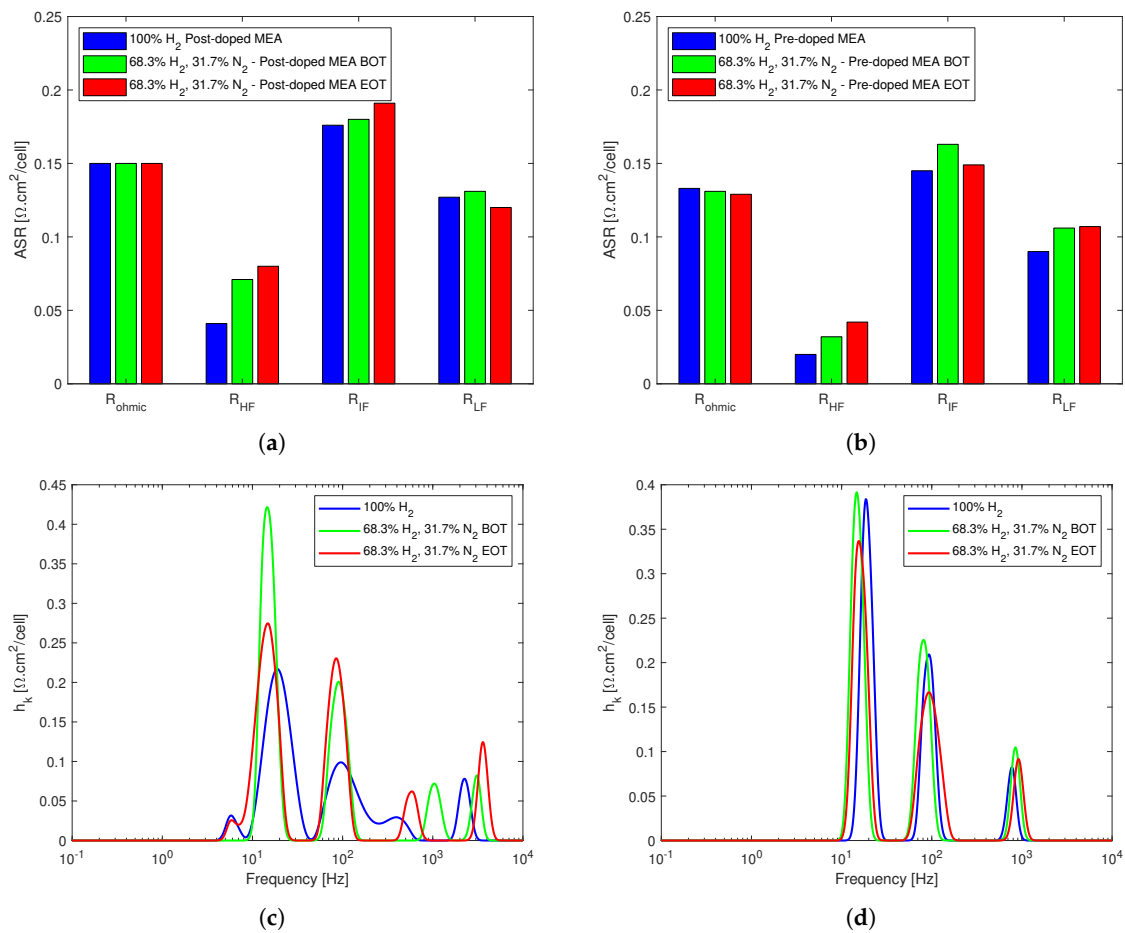


Figure 5. EIS data analysis for the effects of N₂ dilution on both stacks. (a) EC model fitted resistances for the post-doped MEA-based stack. (b) EC model fitted resistances for the pre-doped MEA-based stack. (c) DRT analysis of the post-doped MEA-based stack. (d) DRT analysis of the pre-doped MEA-based stack.

3.2. Poisoning Effects of Dry and Wet Reformate Impurities

The effects of CO and CO₂ on the performance and durability of an HT-PEMFC are fairly well investigated in the literature [7,27,46]. However, most of these studies were performed at the single cell level and often investigated only simulated dry reformate composition. In the current work, both dry and wet reformate impurities in the anode feed were studied at the stack level for two types of MEAs in order to understand not only the effect of impurities but also the effects of water vapor in the anode feed, which is an inevitable by-product of the methanol steam reforming process. Water has positive effects in low temperature PEM fuel cells, where it is used as a proton transport medium. Nonetheless, its effects on an HT-PEMFC are not fully understood, with some reporting advantages [47] and others recommending that it is avoided under certain operating conditions [13].

3.2.1. Poisoning Effects on an HT-PEMFC Stack with Post-Doped MEAs

The poisoning effects of both dry and wet reformate impurities on the fuel cell stack with a post-doped membrane and non-woven GDL-based MEAs are reported in Figure 6. From the polarization curves in Figure 6a, it can be seen that the performance decreased with the introduction of reformate impurities. The effects of both dry and wet reformate impurities are similar.

The effects for both cases are the highest in the beginning of test and there is a slight recovery, especially at higher current densities at the end of the 24 h tests. This is inline with certain reports that, even though the net effect of N₂ dilution on the thermodynamic,

kinetic, and mass-transport driving forces is approximately independent of the relative humidity, both the relative humidity and N_2 dilution affect the anode potential in the same way that water vapor also causes dilution effects [13,48,49].

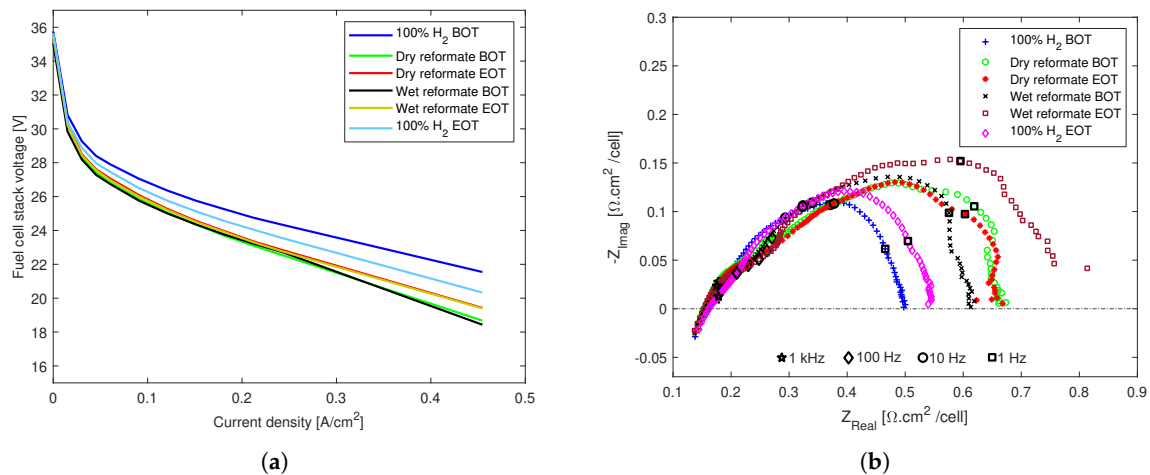


Figure 6. The effects of dry and wet reformate impurities on an HT-PEMFC stack with an MEA composed of a post-doped PBI membrane and non-woven GDL. (a) Polarization curves. (b) EIS spectra.

Similar effects can be seen from the Nyquist polts in Figure 6b, which were recorded at the higher current density end of the polarization curves at 0.4 A/cm^2 . The overall increase in the polarization resistance was clear for both dry and wet reformate impurities. While the dry reformate operation appeared to stabilize after the 24-h tests, the wet reformate operation resulted in a significant increase in polarization losses at the end of the tests, despite a slight recovery at the beginning of the tests.

The impedance data was fitted to an equivalent circuit model, and DRT analysis was performed to further analyze the effects of the impurities, Figure 7. As can already be noticed from the high frequency intercept of the Nyquist plots, the ohmic resistance remained almost unaltered throughout the test, with a slight decrease with the introduction of wet reformate, which, however, then increased to the initial values, R_{ohm} in Figure 7a. R_{HF} and R_{IF} , which are mainly associated with the charge transfer losses in the two electrodes increased significantly with the introduction of the dry reformate mixture and continued to increase slightly until the end of the tests.

Wet reformate partly recovered both of the above mentioned resistances; however, they increased back again at the end of tests. In particular, a striking increase in R_{IF} is seen at the end of the wet reformate operation, which also corresponds to what is seen in the Nyquist plots. This means that humidification exacerbated the charge transfer losses, especially those at the lower frequency region dominated by ORR. However, both R_{HF} and R_{IF} returned almost to the initial values under pure dry hydrogen operation at the end of test, which implies that the effects are reversible.

This performance recovery also means that the reason for the losses during the wet reformate operation was not related to acid loss but rather to the interaction between water vapor, CO, CO_2 , and phosphoric acid. Daletou et al. [47] studied the interaction of water vapor and phosphoric acid and found that water reacted with pyrophosphoric acid in order to maintain the equilibrium concentration of phosphoric acid at a high level, thereby, improving the proton conductivity and fuel cell performance. However, their work assessed only performances with pure hydrogen operation. The conductivity and performance improvement in this work was only observed in the initial period of operation after the introduction of water vapor into the stack.

Finally, the mass transport losses increased slightly for the dry reformate operation in the beginning of test but returned to the initial values at the end of the test. The increase in

mass transport losses was more visible for the wet reformate operation; however, this too recovered slightly with time, and the overall losses can be considered mild.

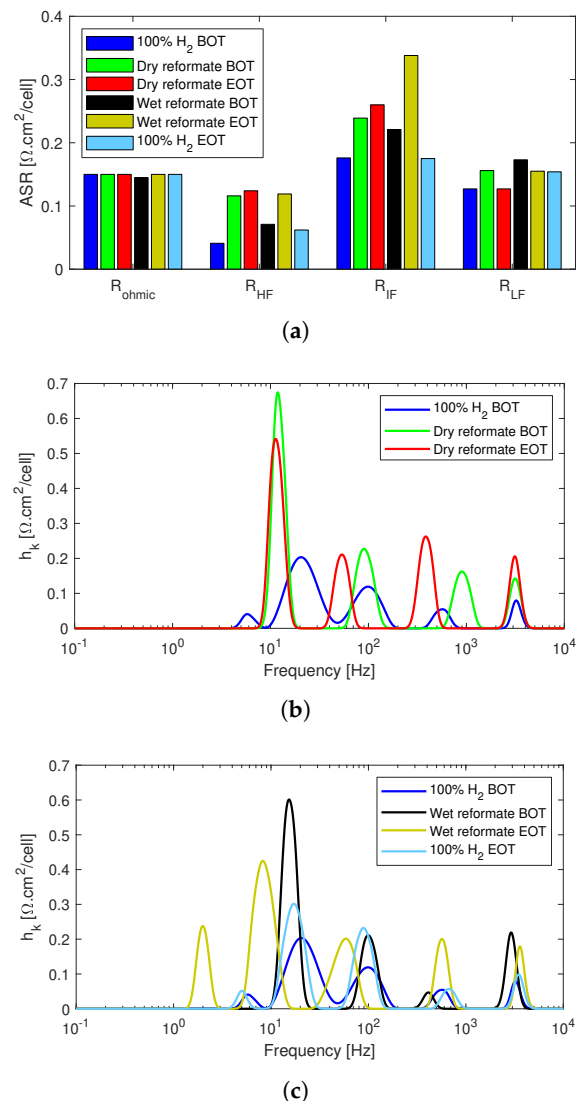


Figure 7. EIS data analysis of the poisoning effects of reformate impurities in the anode feed of the post-doped MEA-based HT-PEMFC stack. (a) Equivalent circuit model fitted resistance data. (b) DRT analysis of dry reformate. (c) DRT analysis of wet reformate.

The DRT analysis in Figure 7 shows that all the spectra had at least four distinct peaks at around 10 Hz, 100 Hz, 1 kHz, and 4 kHz. All the peaks increased in size with the introduction of dry CO and CO₂ into the anode stream, Figure 7b. While the peaks below 10 Hz decreased slightly after 24 h, the peak above 100 Hz continued to increase. The peaks remained similar in size with the introduction of humidification instead of N₂ in the anode stream along with CO and CO₂, Figure 7c.

However, after the 24 h of testing under the wet reformate conditions, a fifth peak appeared around 2 Hz. This region is on the border between the ORR processes and mass transport; however, it is more likely due to cathode charge transfer losses as it is reflected in the increase in R_{IF} in the fitted resistances in Figure 7a. Pure and dry hydrogen operation at the end of the test resulted in significant recovery as already shown from the polarization curves and Nyquist plots. While some residual losses are seen on the peak sizes between 10 Hz and 100 Hz, the high frequency peaks above 100 Hz recovered almost fully.

3.2.2. Poisoning Effects on an HT-PEMFC Stack with Pre-Doped MEAs

Similarly to the previous stack based on post-doped MEAs, the effects of CO and CO₂ were clearly visible on the stack with the pre-doped MEAs, as can be seen from the polarization curves and Nyquist plots in Figure 8ab, respectively. The performance of the stack was slightly higher for the wet reformat operation, especially above 0.25 A/cm², Figure 8a.

Considering that the reformat conditions were tested after the dry reformat conditions, this shows that the humidification alleviated the poisoning effects of CO and CO₂ on the pre-doped MEAs, and it did so until the end of the tests. This is in clear contrast with what was observed for the post-doped MEAs, where humidification did not have performance enhancing effects, and the observed recovery was mainly due to stabilization with time in both the dry and wet reformat conditions. As with the post-doped stack, the recovery with pure hydrogen at the end of tests was significant in the case of the pre-doped stack as well.

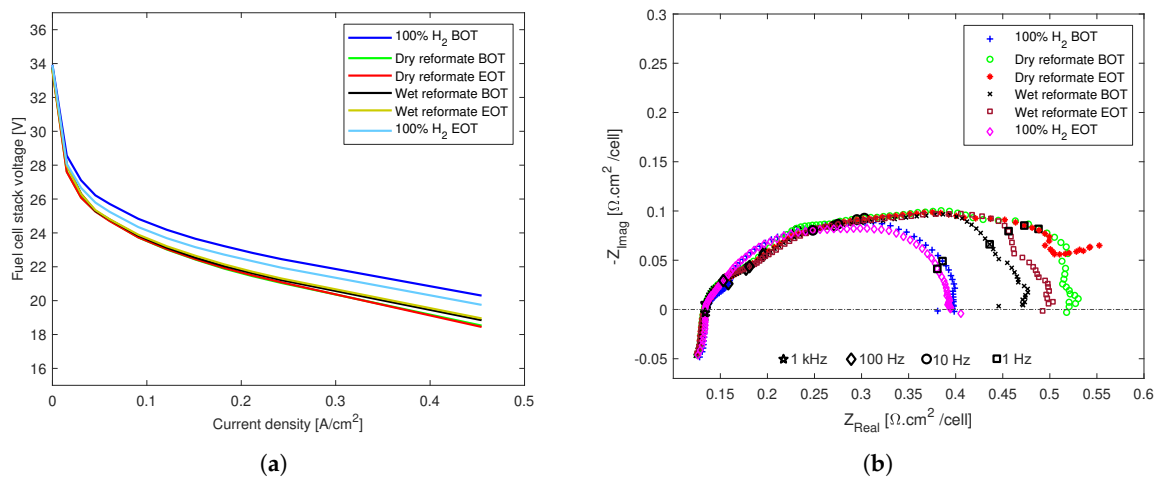


Figure 8. The effects of dry and wet reformat impurities on an HT-PEMFC stack with an MEA composed of a pre-doped PBI membrane and woven GDL. (a) Polarization curves. (b) EIS spectra.

The equivalent circuit model fitted resistances are shown in Figure 9a. It can be seen that, similarly to the post-doped stack, the ohmic resistances remain unaltered throughout the tests for the pre-doped stack as well. However, both R_{HF} and R_{IF} increase with the introduction of dry reformat and continue to increase until the end of tests. Therefore, in the case of the pre-doped stack, the recovery and stabilization seen during the dry reformat tests in the post-doped stack are not observed. The recovery happens during the wet reformat tests, where both R_{HF} and R_{IF} decrease and remain almost unaltered until the end of the wet reformat operation. The R_{HF} for the wet reformat operation was lower than that of the pure hydrogen operation, and, for R_{IF} , the values are similar to the resistance of the pure hydrogen operation. This implies that the water in this case limits the poisoning effects of CO on the stack.

Nonetheless, the effects of the dry reformat impurities on the mass transport losses were more significant in the case of pre-doped stack compared to the post-doped stack. An increase in mass transport losses was seen in the beginning of the test with dry reformat. At the end of dry reformat test, it appears, from Figure 9a, that the mass transport recovered slightly. However, this is due to the shape of the Nyquist plot of the “Dry reformat EOT” in Figure 8b, which is different from the other impedance spectra at the low frequency end and could not be fitted properly using the EC model used for the other spectra. Since changing the EC model for just one spectrum would not allow for proper comparison of the other circuit elements, it was preferred to underestimate R_{LF} .

Nonetheless, when adding the information obtained from the DRT analysis in Figure 9b, one can see that the mass transport losses indeed increased at the end of the dry reformat operation. In fact, the dry reformat operation at the end of the 24 h of test was the only

spectra in the current work that resulted in a peak below 1 Hz, which, as mentioned, is associated with mass transport losses.

Both the Nyquist plots in Figure 8b and the ECM fitted resistances in Figure 9a show that all the losses were recoverable when operating with pure hydrogen again. In fact, Nyquist plots under pure hydrogen operations before and after the tests almost overlapped each other, and, overall, the fitted resistances were similar. However, as shown in the polarization curves in Figure 8a, there was slight performance degradation at the end of the tests compared to the beginning of life. This is perhaps due to the fact that, unlike EIS, polarization curves are recorded over a range of current densities at conditions that are not completely steady state.

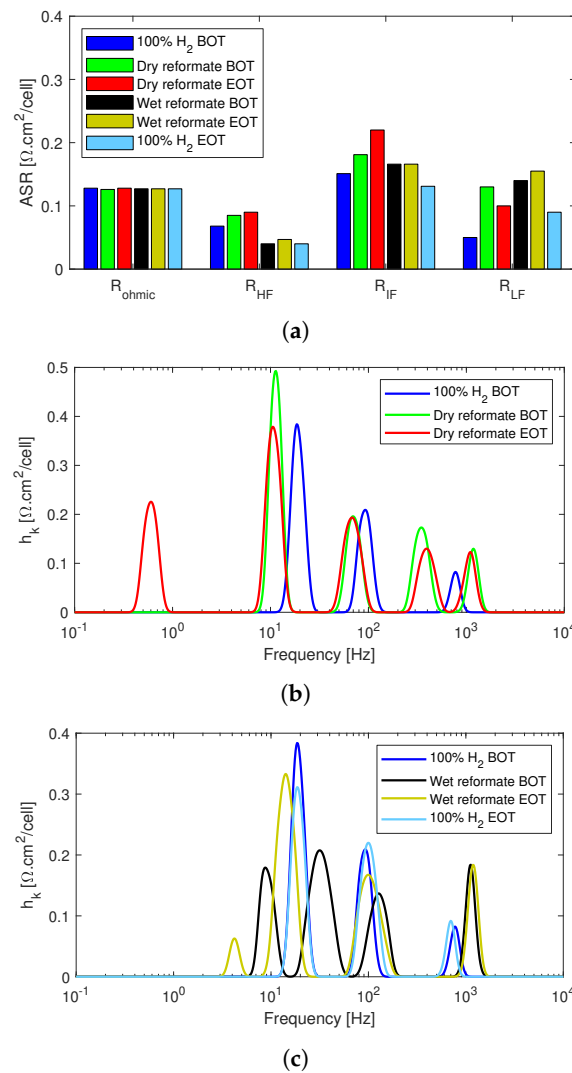


Figure 9. EIS data analysis of the poisoning effects of reformate impurities in the anode feed of the pre-doped MEA-based HT-PEMFC stack. (a) Equivalent circuit model fitted resistance data. (b) DRT analysis of dry reformate. (c) DRT analysis of wet reformate.

Unlike the post-doped stack, which had up to five DRT peaks, the pre-doped stack exhibited only three distinct peaks for pure hydrogen operation. An additional peak was then observed between 100 Hz and 1 kHz when CO and CO_2 were added to the mix. Since the nitrogen dilution tests in Figure 5d also exhibited only three peak, this additional peak in the charge transfer loss region was attributable to the presence of poisoning agents in the anode feed. It is well documented that CO covers active electrode sites, while CO_2 has dilution effects similar to those seen for N_2 with possible small poisoning effects due to CO production via the reverse-water-gas-shift reaction of CO_2 with H_2 [7,45].

With the introduction of the dry reformate mixture into the anode feed, all the DRT peaks increased in size with the exception of the peak at around 100 Hz. Continued operation under dry reformate conditions then stabilized the stack, and it regained some of the losses. However, at the end of the 24 h of dry reformate tests, a fifth peak was observed below 1 Hz. As already mentioned, even though this was not captured in the EC model fit, it can be attributed to mass transport losses, considering the shape of the EIS spectrum and the DRT peak below 1 Hz.

This shows the advantage of adding DRT analysis and not relying solely on ECM fits for the EIS analysis. In Figure 9c, it can be seen that, in the presence of water, the DRT peak sizes decreased throughout the spectrum except at the highest frequency point. However, after the end of the 24 h, the peaks around 10 Hz increased back close to the initial values.

4. Discussion

Characterization of the effects of reformate impurities in an HT-PEMFC stack is crucial not only for understanding the poisoning and degradation mechanisms to optimize the fuel cell components but also to identify the fault features for diagnostics and fault mitigation purposes. The effects of the tested operating conditions on the different EIS parameters are summarized in Table 2.

Table 2. The characteristic features of dry and wet reformate in HT-PEMFC stacks. The arrows indicate the overall trends of the parameters, where \uparrow represents an increase and \rightarrow represents no significant change.

Test	Stack with Post-Doped MEAs		Stack with Pre-Doped MEAs	
	ECM	DRT	ECM	DRT
N ₂ dilution	$R_{HF} \uparrow, R_{IF} \uparrow,$ $R_{ohm} \rightarrow, R_{LF} \rightarrow$	4 peaks \uparrow	$R_{HF} \uparrow, R_{LF} \uparrow$ $R_{ohm} \rightarrow, R_{IF} \rightarrow$	3 peaks peaks < 100 Hz \downarrow peak at 1 kHz \uparrow
Dry reformate	$R_{HF} \uparrow, R_{IF} \uparrow, R_{LF} \uparrow$ $R_{ohm} \rightarrow$	4–5 peaks \uparrow	$R_{HF} \uparrow, R_{IF} \uparrow, R_{LF} \uparrow$ $R_{ohm} \rightarrow$	3–5 peaks \uparrow peak below 1 Hz
Wet reformate	$R_{HF} \uparrow, R_{IF} \uparrow, R_{LF} \uparrow$ $R_{ohm} \rightarrow$	4–5 peaks \uparrow	$R_{HF} \downarrow, R_{LF} \uparrow$ $R_{ohm} \rightarrow, R_{IF} \rightarrow$	4 peaks peaks < 100 Hz \downarrow peak at 1 kHz \uparrow

N₂ dilution negatively affected only the charge transfer losses for both stacks, especially R_{HF} , which is mainly associated with the anode charge transfer losses. The proton conductivity and mass transport remained mostly unaltered by N₂ dilution for the stack with post-doped MEAs, while an overall slight increase in the mass transport loss was seen for the pre-doped stack. It is reported in the literature that, with the addition of an inert gas, such as nitrogen, the diffusion resistance becomes more substantial because the effective diffusion coefficient of hydrogen in the gas mixture is reduced by the Maxwell–Stefan effect [48].

However, in the current work, the effects of N₂ dilution were manifested predominantly on the reaction kinetics-dominated high and intermediate frequency resistances rather than the diffusion-dominated mass transport resistance. This could be because dilution reduces the amount of hydrogen on the reaction sites, and this effect appears to be more severe than the mass transport issue caused by N₂ dilution. This is in contrast with what some researchers have observed in half-cell and single cell tests, where the nitrogen dilution effects were limited to mass transport losses [48,50].

Similarly, the effects of CO and CO₂ poisoning on the charge transfer losses were more dominant for both stacks, particularly on the anode-dominated high frequency resistance losses, while the ohmic resistance remained unaltered during the poisoning with or without humidification. While the poisoning effects on the high frequency resistances were to be expected due to the adsorption of CO on the anode Pt particles and the consequent loss of ECSA, the effects on the intermediate frequency resistance were peculiar.

Bevilacqua et al. [50] reported similar effects on the cathode due to CO on the anode feed, which they attributed solely to the drop in voltage that caused an exponential drop in the exchange current density according to the Butler–Volmer equation and led to higher impedance. They excluded any CO cross-over from the anode to the cathode. This could explain the increase in the intermediate frequency resistances of both stacks during the poisoning tests.

The presence of water during CO poisoning, which is reported to alleviate the degrading effects of CO [12], was only observed for the stack with pre-doped MEAs. In fact, upon the introduction of humidification, both R_{HF} and R_{IF} recovered for the stack with post-doped MEAs, but then continued to increase significantly. This could be because the phosphate anions from the more mobile phosphoric acid in post-doped stacks adsorbed on the cathode [16,17] and could also impede mass transport by blocking some of the pores of the GDL while leaching out [18]. The latter could also be the reason for the mass transport loss observed during dry reformate tests on the stack with pre-doped MEAs, which has significantly higher doping levels compared with the post-doped MEAs.

Performance losses in the presence of water are usually associated with acid loss. However, the fact that there was a significant performance recovery with the pure H₂ operation at the end of the tests indicates that the reason for the losses during the wet reformate operation were not related to acid loss. Acid loss is reported to mainly happen at lower operating temperatures and during shutdown/startup cycles due to the condensation of water that can wash out the acid [13,15]. This is not the case in the current work, as there were only a limited number of shutdown/startup procedures, and the operating temperature was kept constant at 160 °C.

Studies suggest both positive and negative effects of humidification in HT-PEMFCs, where some propose that the interaction of water with phosphoric acid improves the proton conductivity and fuel cell performance and others reported negative effects of water vapor, including dilution and acid loss, especially at lower temperatures [11,13,47]. Therefore, it can be said that water vapor in an HT-PEMFC has the dual opposite effects of dilution and that of maintaining the equilibrium concentration of phosphoric acid.

The positive effects of humidification compared to dry poisoning in this work were observed in the initial period of operation after the introduction of water vapor into the stack with post-doped MEAs. However, successively, the negative effects of humidification prevailed for this type of MEAs. On the other hand, humidification alleviated the effects of CO poisoning throughout almost the entire test period and across the frequency spectrum for the stack with pre-doped MEAs. Therefore, we conclude that humidification has a beneficial effect on a reformate operated stack with pre-doped MEAs but has detrimental effects on a stack with post-doped MEAs.

Finally, some of the characteristic features shown in Table 2 can be regarded as fault features, where sudden and continuous increases in the fitted resistances and DRT peaks can be a sign of the presence of impurities. For instance, the size and number of DRT peaks increase when dry CO and CO₂ are introduced to either stack. The stack with pre-doped MEAs exhibited only three DRT peaks under pure H₂ operation and under N₂ dilution. However, when the impurities were introduced, an additional peak appeared in the charge transfer region, which can be used to identify the presence of poisoning agents in the anode feed for a stack with pre-doped MEAs.

5. Conclusions

In this paper, experimental characterization was performed for two 37-cell HT-PEMFC stacks with active areas of 165 cm². The effects of nitrogen dilution and reformate impurities were studied using polarization curves and EIS measurements. CO and CO₂ were chosen as the reformate impurities, and their effect on the stacks were investigated both with and without humidification. The two stacks used in this work employed two different types of MEAs, one with a post-doped PBI membrane and non-woven GDL and the other with a pre-doped PBI membrane and woven GDL type.

We found that N₂ had a reversible dilution effect, which was mainly manifested by the increase in the anode charge transfer losses for both stacks. This could be because dilution reduces the amount of hydrogen on the reaction sites, and this effect appeared to be more severe than the mass transport issue caused by N₂ dilution. N₂ dilution did not affect the ohmic resistance negatively in either stack. Generally, from the Nyquist plot and the DRT peaks analysis, the stack with pre-doped MEAs was less susceptible to dilution effects and had more stable operation over the dilution test period.

The effects of CO and CO₂ poisoning were also mainly seen on the charge transfer losses for both stacks, while the ohmic resistance remained unaltered even during the poisoning tests irrespective of the presence of water vapor. We also found that humidification had a beneficial effect on a reformat-operated stack with pre-doped MEAs but had detrimental effects on the stack with post-doped MEAs. Nonetheless, there was significant performance recovery for both stacks with the pure hydrogen operation at the end of the tests, implying that the poisoning effects are reversible even in the presence of humidification.

A combination of the magnitude and trend of the changes in the various parameters (equivalent circuit elements and DRT peaks) due to the different operating conditions in the current work can be used for fault matrix creation and for diagnostics purposes. The increase in the size and number of DRT peaks when dry CO and CO₂ were introduced to either stack can be considered as a CO poisoning fault feature. In particular, the stack with pre-doped MEAs exhibited only three DRT peaks under pure H₂ operation and under N₂ dilution. Therefore, the additional DRT peak in the charge transfer region during impurities operation can be used to identify the presence of poisoning agents in the anode feed for a stack with pre-doped MEAs.

Author Contributions: Conceptualization, S.S.A. and S.T.; methodology, S.S.A. and S.T.; software, S.S.A., S.T. and S.L.S.; validation, S.S.A. and S.T.; formal analysis, S.S.A.; investigation, S.S.A. and A.L.; resources, S.S.A.; data curation, S.S.A.; writing—original draft preparation, S.S.A. and A.L.; writing—review and editing, S.S.A., S.T., A.L., S.L.S., V.L. and S.J.A.; visualization, S.S.A.; supervision, S.S.A.; project administration, S.S.A. and S.J.A.; funding acquisition, S.S.A. All authors have read and agreed to the published version of the manuscript.

Funding: This research was funded by the Danish Energy Technology Development and Demonstration Program (EUDP) through the project COBRA Drive (grant number—64018-0118). Part of the research conducted for this article received funding from the European Union’s Horizon 2020 research and innovation programme under the Marie Skłodowska-Curie grant agreement No 893919.

Institutional Review Board Statement: Not applicable.

Informed Consent Statement: Not applicable.

Data Availability Statement: The data are contained within the article.

Conflicts of Interest: The authors declare no conflict of interest. The funders had no role in the design of the study; in the collection, analyses, or interpretation of data; in the writing of the manuscript, or in the decision to publish the results.

Abbreviation

The following abbreviations are used in this manuscript:

BOT	Beginning of test
CPE	Constant phase element
DRT	Distribution of relaxation time
ECM	Equivalent circuit model
EIS	Electrochemical impedance spectroscopy
EOT	End of test
GDL	Gas diffusion layer
HOR	Hydrogen oxidation reaction
HT-PEMFC	High temperature polymer electrolyte membrane fuel cell

LT-PEMFC	Low temperature polymer electrolyte membrane fuel cell
MEA	Membrane electrode assembly
MPL	Mesoporous layer
ORR	Oxygen reduction reaction
PBI	Polybenzimidazole
PFSA	Perfluorosulfonic acid
PTFE	Polytetrafluoroethylene

References

- Ho, J.C.; Saw, E.C.; Lu, L.Y.; Liu, J.S. Technological barriers and research trends in fuel cell technologies: A citation network analysis. *Technol. Forecast. Soc. Chang.* **2014**, *82*, 66–79. [\[CrossRef\]](#)
- Sharaf, O.Z.; Orhan, M.F. An overview of fuel cell technology: Fundamentals and applications. *Renew. Sustain. Energy Rev.* **2014**, *32*, 810–853. [\[CrossRef\]](#)
- Wang, Y.; Ruiz Diaz, D.F.; Chen, K.S.; Wang, Z.; Adroher, X.C. Materials, technological status, and fundamentals of PEM fuel cells—A review. *Mater. Today* **2020**, *32*, 178–203. [\[CrossRef\]](#)
- Feng, C.; Li, Y.; Qu, K.; Zhang, Z.; He, P. Mechanical behavior of a hydrated perfluorosulfonic acid membrane at meso and nano scales. *RSC Adv.* **2019**, *9*, 9594–9603. [\[CrossRef\]](#)
- Ferraris, A.; Messana, A.; Airale, A.G.; Sisca, L.; de Carvalho Pinheiro, H.; Zevola, F.; Carello, M. Nafionr tubing humidification system for polymer electrolyte membrane fuel cells. *Energies* **2019**, *12*, 1773. [\[CrossRef\]](#)
- Carello, M.; De Vita, A.; Ferraris, A. Method for Increasing the Humidity in Polymer Electrolyte Membrane Fuel Cell. *Fuel Cells* **2016**, *16*, 157–164. [\[CrossRef\]](#)
- Araya, S.S.; Zhou, F.; Liso, V.; Sahlin, S.L.; Vang, J.R.; Thomas, S.; Gao, X.; Jeppesen, C.; Kær, S.K. A comprehensive review of PBI-based high temperature PEM fuel cells. *Int. J. Hydrog. Energy* **2016**, *41*, 21310–21344. [\[CrossRef\]](#)
- Zhang, J.; Xiang, Y.; Lu, S.; Jiang, S.P. High Temperature Polymer Electrolyte Membrane Fuel Cells for Integrated Fuel Cell—Methanol Reformer Power Systems: A Critical Review. *Adv. Sustain. Syst.* **2018**, *2*, 1700184. [\[CrossRef\]](#)
- Simon Araya, S.; Liso, V.; Cui, X.; Li, N.; Zhu, J.; Sahlin, S.L.; Jensen, S.H.; Nielsen, M.P.; Kær, S.K. A Review of The Methanol Economy: The Fuel Cell Route. *Energies* **2020**, *13*, 596. [\[CrossRef\]](#)
- Büsselmann, J.; Rastedt, M.; Klicpera, T.; Reinwald, K.; Schmies, H.; Dyck, A.; Wagner, P. Analysis of HT-PEM MEAs' Long-Term Stabilities. *Energies* **2020**, *13*, 567. [\[CrossRef\]](#)
- Søndergaard, T.; Cleemann, L.N.; Becker, H.; Steenberg, T.; Hjuler, H.A.; Seerup, L.; Li, Q.; Jensen, J.O. Long-Term Durability of PBI-Based HT-PEM Fuel Cells: Effect of Operating Parameters. *J. Electrochem. Soc.* **2018**, *165*, F3053–F3062. [\[CrossRef\]](#)
- Zhou, F.; Andreasen, S.J.; Kær, S.K.; Park, J.O. Experimental investigation of carbon monoxide poisoning effect on a PBI/H₃PO₄ high temperature polymer electrolyte membrane fuel cell: Influence of anode humidification and carbon dioxide. *Int. J. Hydrog. Energy* **2015**, *40*, 14932–14941. [\[CrossRef\]](#)
- Zhou, F.; Singdeo, D.; Kær, S.K. Investigation of the Effect of Humidity Level of H₂ on Cell Performance of a HT-PEM Fuel Cell. *Fuel Cells* **2019**, *19*, 2–9. [\[CrossRef\]](#)
- Park, H.; Kim, H.; Kim, D.K.; Lee, W.J.; Choi, I.; Kim, H.J.; Kim, S.K. Performance deterioration and recovery in high-temperature polymer electrolyte membrane fuel cells: Effects of deliquescence of phosphoric acid. *Int. J. Hydrog. Energy* **2020**, *45*, 32844–32855. [\[CrossRef\]](#)
- Li, Q.; Jensen, J.O.; Savinell, R.F.; Bjerrum, N.J.; Oluf, J.; Savinell, R.F.; Bjerrum, N.J.; Jensen, J.O.; Savinell, R.F.; Bjerrum, N.J. High temperature proton exchange membranes based on polybenzimidazoles for fuel cells. *Prog. Polym. Sci.* **2009**, *34*, 449–477. [\[CrossRef\]](#)
- Liu, Z.; Wainright, J.S.; Litt, M.H.; Savinell, R.F. Study of the oxygen reduction reaction (ORR) at Pt interfaced with phosphoric acid doped polybenzimidazole at elevated temperature and low relative humidity. *Electrochim. Acta* **2006**, *51*, 3914–3923. [\[CrossRef\]](#)
- Strmcnik, D.; Escudero-Escribano, M.; Kodama, K.; Stamenkovic, V.R.; Cuesta, A.; Marković, N.M. Enhanced electrocatalysis of the oxygen reduction reaction based on patterning of platinum surfaces with cyanide. *Nat. Chem.* **2010**, *2*, 880–885. [\[CrossRef\]](#)
- Myles, T.; Bonville, L.; Maric, R. Catalyst, Membrane, Free Electrolyte Challenges, and Pathways to Resolutions in High Temperature Polymer Electrolyte Membrane Fuel Cells. *Catalysts* **2017**, *7*, 16. [\[CrossRef\]](#)
- Tahrim, A.A.; Amin, I.N.H.M. Advancement in Phosphoric Acid Doped Polybenzimidazole Membrane for High Temperature PEM Fuel Cells: A Review. *J. Appl. Membr. Sci. Technol.* **2018**, *23*, 37–62. [\[CrossRef\]](#)
- Schmidt, T.J.; Baurmeister, J. Properties of high-temperature PEFC Celtec®-P 1000 MEAs in start/stop operation mode. *J. Power Sources* **2008**, *176*, 428–434. [\[CrossRef\]](#)
- Vang, J.R.; Andreasen, S.J.; Araya, S.S.; Kær, S.K. Comparative study of the break in process of post doped and sol-gel high temperature proton exchange membrane fuel cells. *Int. J. Hydrog. Energy* **2014**, *39*, 14959–14968. [\[CrossRef\]](#)
- Zhou, Z.; Zholobko, O.; Wu, X.F.; Aulich, T.; Thakare, J.; Hurley, J. Polybenzimidazole-Based Polymer Electrolyte Membranes for High-Temperature Fuel Cells: Current Status and Prospects. *Energies* **2020**, *14*, 135. [\[CrossRef\]](#)
- Bevilacqua, N.; Asset, T.; Schmid, M.; Markötter, H.; Manke, I.; Atanassov, P.; Zeis, R. Impact of catalyst layer morphology on the operation of high temperature PEM fuel cells. *J. Power Sources Adv.* **2021**, *7*, 100042. [\[CrossRef\]](#)

24. Kim, S.; Myles, T.D.; Kunz, H.; Kwak, D.; Wang, Y.; Maric, R. The effect of binder content on the performance of a high temperature polymer electrolyte membrane fuel cell produced with reactive spray deposition technology. *Electrochim. Acta* **2015**, *177*, 190–200. [[CrossRef](#)]
25. Bevilacqua, N.; George, M.G.; Galbiati, S.; Bazylak, A.; Zeis, R. Phosphoric Acid Invasion in High Temperature PEM Fuel Cell Gas Diffusion Layers. *Electrochim. Acta* **2017**, *257*, 89–98. [[CrossRef](#)]
26. Chevalier, S.; Fazeli, M.; Mack, F.; Galbiati, S.; Manke, I.; Bazylak, A.; Zeis, R. Role of the microporous layer in the redistribution of phosphoric acid in high temperature PEM fuel cell gas diffusion electrodes. *Electrochim. Acta* **2016**, *212*, 187–194. [[CrossRef](#)]
27. Rosli, R.; Sulong, A.; Daud, W.; Zulkifley, M.; Husaini, T.; Rosli, M.; Majlan, E.; Haque, M. A review of high-temperature proton exchange membrane fuel cell (HT-PEMFC) system. *Int. J. Hydrog. Energy* **2017**, *42*, 9293–9314. [[CrossRef](#)]
28. Martin, S.; Garcia-Ybarra, P.L.; Castillo, J.L. Ten-fold reduction from the state-of-the-art platinum loading of electrodes prepared by electrospraying for high temperature proton exchange membrane fuel cells. *Electrochem. Commun.* **2018**, *93*, 57–61. [[CrossRef](#)]
29. Yao, D.; Zhang, W.; Ma, Q.; Xu, Q.; Pasupathi, S.; Su, H. Achieving high Pt utilization and superior performance of high temperature polymer electrolyte membrane fuel cell by employing low-Pt-content catalyst and microporous layer free electrode design. *J. Power Sources* **2019**, *426*, 124–133. [[CrossRef](#)]
30. Kannan, A.; Li, Q.; Cleemann, L.N.; Jensen, J.O. Acid Distribution and Durability of HT-PEM Fuel Cells with Different Electrode Supports. *Fuel Cells* **2018**, *18*, 103–112. [[CrossRef](#)]
31. de Beer, C.; Barendse, P.S.; Pillay, P.; Bullocks, B.; Rengaswamy, R. Electrical Circuit Analysis of CO Poisoning in High-Temperature PEM Fuel Cells for Fault Diagnostics and Mitigation. *IEEE Trans. Ind. Appl.* **2015**, *51*, 619–630. [[CrossRef](#)]
32. Malinowski, M.; Iwan, A.; Pasciak, G.; Parafiniuk, K.; Gorecki, L.; Pa ciak, G.; Parafiniuk, K.; Gorecki, L. Synthesis and characterization of para- and meta-polybenzimidazoles for high-temperature proton exchange membrane fuel cells. *High Perform. Polym.* **2014**, *26*, 436–444. [[CrossRef](#)]
33. Córdoba-Torres, P.; Mesquita, T.J.; Devos, O.; Tribollet, B.; Roche, V.; Nogueira, R.P. On the intrinsic coupling between constant-phase element parameters α and Q in electrochemical impedance spectroscopy. *Electrochim. Acta* **2012**, *72*, 172–178. [[CrossRef](#)]
34. Shoar Abouzari, M.R.; Berkemeier, F.; Schmitz, G.; Wilmer, D. On the physical interpretation of constant phase elements. *Solid State Ion.* **2009**, *180*, 922–927. [[CrossRef](#)]
35. Gomadam, P.M.; Weidner, J.W. Analysis of electrochemical impedance spectroscopy in proton exchange membrane fuel cells. *Int. J. Energy Res.* **2005**, *29*, 1133–1151. [[CrossRef](#)]
36. Cooper, K.; Smith, M. Electrical test methods for on-line fuel cell ohmic resistance measurement. *J. Power Sources* **2006**, *160*, 1088–1095. [[CrossRef](#)]
37. Jeppesen, C.; Araya, S.S.; Sahlin, S.L.; Thomas, S.; Andreasen, S.J.; Kær, S.K. Fault detection and isolation of high temperature proton exchange membrane fuel cell stack under the influence of degradation. *J. Power Sources* **2017**, *359*, 37–47. [[CrossRef](#)]
38. Thomas, S.; Araya, S.S.; Frensch, S.H.; Steenberg, T.; Kær, S.K. Hydrogen mass transport resistance changes in a high temperature polymer membrane fuel cell as a function of current density and acid doping. *Electrochim. Acta* **2019**, *317*, 521–527. [[CrossRef](#)]
39. Weiß, A.; Schindler, S.; Galbiati, S.; Danzer, M.A.; Zeis, R. Distribution of Relaxation Times Analysis of High-Temperature PEM Fuel Cell Impedance Spectra. *Electrochim. Acta* **2017**, *230*, 391–398. [[CrossRef](#)]
40. Schenk, A.; Grimmer, C.; Perchthaler, M.; Weinberger, S.; Pichler, B.; Heinzl, C.; Scheu, C.; Mautner, F.A.; Bitschnau, B.; Hacker, V. Platinum-cobalt catalysts for the oxygen reduction reaction in high temperature proton exchange membrane fuel cells—Long term behavior under ex-situ and in-situ conditions. *J. Power Sources* **2014**, *266*, 313–322. [[CrossRef](#)]
41. Schindler, S.; Weiss, A.; Galbiati, S.; Mack, F.; Danzer, M.A.; Zeis, R. Identification of Polarization Losses in High-Temperature PEM Fuel Cells by Distribution of Relaxation Times Analysis. *ECS Trans.* **2016**, *75*, 45–53. [[CrossRef](#)]
42. Wan, T.H.; Saccoccio, M.; Chen, C.; Ciucci, F. Influence of the Discretization Methods on the Distribution of Relaxation Times Deconvolution: Implementing Radial Basis Functions with DRTtools. *Electrochim. Acta* **2015**, *184*, 483–499. [[CrossRef](#)]
43. Heinzmann, M.; Weber, A.; Ivers-Tiffée, E. Advanced impedance study of polymer electrolyte membrane single cells by means of distribution of relaxation times. *J. Power Sources* **2018**, *402*, 24–33. [[CrossRef](#)]
44. Simon Araya, S.; Zhou, F.; Lennart Sahlin, S.; Thomas, S.; Jeppesen, C.; Knudsen Kær, S. Fault Characterization of a Proton Exchange Membrane Fuel Cell Stack. *Energies* **2019**, *12*, 152. [[CrossRef](#)]
45. Chen, C.Y.; Lai, W.H.; Chen, Y.K.; Su, S.S. Characteristic studies of a PBI/H₃PO₄ high temperature membrane PEMFC under simulated reformat gases. *Int. J. Hydrog. Energy* **2014**, *39*, 13757–13762. [[CrossRef](#)]
46. Andreasen, S.J.; Vang, J.R.; Kær, S.K. High temperature PEM fuel cell performance characterisation with CO and CO₂ using electrochemical impedance spectroscopy. *Int. J. Hydrog. Energy* **2011**, *36*, 9815–9830. [[CrossRef](#)]
47. Daletou, M.K.; Kallitsis, J.K.; Voyiatzis, G.; Neophytides, S.G. The interaction of water vapors with H₃PO₄ imbedded electrolyte based on PBI/polysulfone copolymer blends. *J. Membr. Sci.* **2009**, *326*, 76–83. [[CrossRef](#)]
48. Du, B.; Pollard, R.; Elter, J.F.; Ramani, M. Performance and Durability of a Polymer Electrolyte Fuel Cell Operating with Reformat: Effects of CO, CO₂, and Other Trace Impurities. In *Polymer Electrolyte Fuel Cell Durability*; Springer: New York, NY, USA, 2009; pp. 341–366.
49. Reimer, U.; Ehlert, J.; Janßen, H.; Lehnert, W. Water distribution in high temperature polymer electrolyte fuel cells. *Int. J. Hydrog. Energy* **2016**, *41*, 1837–1845. [[CrossRef](#)]
50. Bevilacqua, N.; Schmid, M.; Zeis, R. Understanding the role of the anode on the polarization losses in high-temperature polymer electrolyte membrane fuel cells using the distribution of relaxation times analysis. *J. Power Sources* **2020**, *471*, 228469. [[CrossRef](#)]

Article

Pore-Scale Modeling of Air–Water Two Phase Flow and Oxygen Transport in Gas Diffusion Layer of Proton Exchange Membrane Fuel Cell

Chongbo Zhou ^{1,2}, Lingyi Guo ³, Li Chen ³, Xin Tian ², Tiefeng He ¹  and Qinghua Yang ^{1,4,*}

¹ College of Mechanical Engineering, Zhejiang University of Technology, Hangzhou 310023, China; chongbo-zhou@chder.com (C.Z.); hetiefeng@sztu.edu.cn (T.H.)

² Huadian Electric Power Research Institute Co., Ltd., Hangzhou 310030, China; xin-tian@chder.com

³ Key Laboratory of Thermo-Fluid Science and Engineering of MOE, School of Energy and Power Engineering, Xi'an Jiaotong University, Xi'an 710049, China; deaster456@stu.xjtu.edu.cn (L.G.); lichennht08@mail.xjtu.cn (L.C.)

⁴ Key Laboratory of Special Purpose Equipment and Advanced Processing Technology, Ministry of Education and Zhejiang Province, Zhejiang University of Technology, Hangzhou 310023, China

* Correspondence: robot@zjut.edu.cn

Abstract: Understanding multiphase flow and gas transport occurring in electrodes is crucial for improving the performance of proton exchange membrane fuel cells. In the present study, a pore-scale model using the lattice Boltzmann method (LBM) was proposed to study the coupled processes of air–water two-phase flow and oxygen reactive transport processes in porous structures of the gas diffusion layer (GDL) and in fractures of the microscopic porous layer (MPL). Three-dimensional pore-scale numerical results show that the liquid water generation rate is gradually reduced as the oxygen consumption reaction proceeds, and the liquid water saturation in the GDL increases, thus the constant velocity inlet or pressure inlet condition cannot be maintained while the results showed that at $t = 1,200,000$ iterations after 2900 h running time, the local saturation at the GDL/MPL was about 0.7, and the maximum value was about 0.83, while the total saturation was 0.35. The current density reduced from 2.39 to 0.46 A cm⁻². Effects of fracture number were also investigated, and the results showed that for the fracture numbers of 8, 12, 16, and 24, the breakthrough point number was 4, 3, 3, and 2, respectively. As the fracture number increased, the number of the water breakthrough points at the GDL/GC interface decreased, the liquid water saturation inside the GDL increased, the GDL/MPL interface was more seriously covered, and the current density decreased. The pore-scale model for the coupled multiphase reactive transport processes is helpful for understanding the mechanisms inside the porous electrodes of PEMFC.

Keywords: proton exchange membrane fuel cell; gas diffusion layer; microscopic porous layer; fracture; two phase flow



Citation: Zhou, C.; Guo, L.; Chen, L.; Tian, X.; He, T.; Yang, Q. Pore-Scale Modeling of Air–Water Two Phase Flow and Oxygen Transport in Gas Diffusion Layer of Proton Exchange Membrane Fuel Cell. *Energies* **2021**, *14*, 3812. <https://doi.org/10.3390/en14133812>

Academic Editor: Samuel Simon Araya

Received: 30 April 2021

Accepted: 18 June 2021

Published: 24 June 2021

Publisher's Note: MDPI stays neutral with regard to jurisdictional claims in published maps and institutional affiliations.



Copyright: © 2021 by the authors. Licensee MDPI, Basel, Switzerland. This article is an open access article distributed under the terms and conditions of the Creative Commons Attribution (CC BY) license (<https://creativecommons.org/licenses/by/4.0/>).

1. Introduction

During the past few decades, the proton exchange membrane fuel cell (PEMFC) has received much attention due to several advantages including high energy efficiency, room-temperature operation and low pollution. Improving fuel cell performance highly depends on effective thermal and water management of PEMFC, which are based on a comprehensive understanding of water transport mechanisms inside the PEMFC [1]. The water transport process in GDL plays an important role in the mass transport and fuel cell performance [2]. Too much liquid water will cause flooding and hinder the oxygen transport. Therefore, it is desirable to accelerate the liquid water migration from the GDL and to reduce the liquid water saturation in GDL. In practice, the GDL is usually treated with hydrophobic polytetrafluoroethylene (PTFE) to facilitate the liquid water transport [3].

An microporous layer (MPL) is added to the GDL to help improve the transport of liquid water through the GDL [4].

Advanced visualization techniques have been adopted to conduct in situ measurement of multiphase flow inside GDL such as x-ray computed tomography (XCT), nuclear magnetic resonance, and neutron imaging. With great improvement in spatial and temporal resolution, XCT has been adopted to reconstruct the porous structures of GDL and to investigate liquid water dynamic behaviors [5–8]. Supplementary to the experiments, numerical simulation also plays important roles in investigating the effects of structural and operating parameters on liquid water transport in GDL. Models for the multiphase flow in GDL can be divided into continuum-scale models and pore-scale models [9]. At the continuum-scale, models based on the concept of representative elementary volume (REV) have been proposed for transport processes in porous media, in which the extension of the Darcy law involving relative permeability has been adopted for multiphase flow. A typical example of such continuum-scale model is the multiphase mixture model proposed by Wang et al. [10,11]. Such a model is computationally more efficient and can be used for modeling the entire cells. In this model, the capillary pressure-saturation relationship such as the Leverett–Udell function is adopted for closing the governing equations [12,13]. It has been recognized the Leverett–Udell function obtained from porous media in geology or petrology is not suitable for describing multiphase flow in GDLs. A more accurate pressure–saturation relationship has also been proposed in the literature [14–17].

The mesh size in the continuum-scale cell model is too large to consider the microscopic details of the GDL structures. To gain a deep understanding of the interactions between porous structures, multiphase flow processes, and GDL performance, pore-scale modeling has been developed and conducted. Among the many numerical methods for pore-scale modeling of multiphase flow, the lattice Boltzmann method (LBM) is preferred due to its power capacity of handling the complicated structures and of capturing the dynamic evolution of the phase interface. Using the LBM, the realistic porous structures of the GDL can be easily taken into account. This method has been most widely adopted for simulating multiphase flow in GDL [18,19]. Hao and Cheng [20] found that by adding a hydrophilic columnar through the GDL, liquid water will migrate through the GDL by the hydrophilic columnar, leaving the remaining hydrophobic part available for the reactant gas. Yu et al. [21] performed three-dimensional (3D) pore-scale simulations to study effects of distributions of PTFE on the liquid water transport inside and breakthrough the GDL. With PTFE distributed heterogeneously along the through-plane direction, the liquid water saturation curves show different shapes. The pore-scale results suggest that placing PTFE near the GDL/MPL interface facilitates the liquid water transport in GDL [21]. Effects of the PTFE distribution on the removal of one single droplet were also studied by Kakaee et al. [22]. Jinuntuya et al. [23] numerically studied at the pore-scale the liquid water transport in three types of GDL structures obtained from XCT and the effects of the GDL structure, the wettability, and the pressure difference applied on the liquid water flow pattern, breakthrough time and saturation inside the GDLs were investigated. Pore-scale two-phase flow in compressed GDL was also studied [24]. It was found that as compression ratio increases, the location of water breaking through the GDL moves from the channel to the channel/rib interface. Under a relatively high compression ratio, liquid water tends to form a water film inside GDL, which greatly hinders the reactant mass transport [24]. Deng et al. [25] adopted the LBM to simulate liquid water transport inside and at the interface of GDL and MPL. It was found that with the addition of MPL, liquid water flooding in GDL is greatly reduced.

In PEMFCs, oxygen transport through the GDL and MPL arrives at the CL and participates in the electrochemical reaction that generates water. The water is then transported in the opposite direction from the CL to the GDL, and finally removed out of the fuel cell through the GC. However, only Zhang et al. conducted a pore-scale study of such coupled processes between multiphase flow and reactive transport [26]. As the liquid water saturation increases in the GDL, the oxygen transport is gradually hindered, leading to a

lower generation rate of liquid water. Therefore, uniform liquid inlet velocity or constant pressure applied at the bottom surface of GDL, which are widely adopted in the current pore-scale simulations, is not sustainable.

From the above review, it can be found that pore-scale modeling considering the coupling processes of air–water two-phase flow and oxygen reactive transport is really rare in the literature. Understanding such coupling mechanisms is of great importance for enhancing mass transport, improving water management, and increasing the cell performance. Therefore in this study, a 3D multiphase reactive transport model was developed to study the coupled multiphase flow and oxygen transport in the GDL and MPL fractures. Furthermore, a 1D model is proposed at the GDL bottom surface to consider the transport resistance in MPL and CL. Effects of the number of the fractures on the multiphase flow are investigated in detail.

2. The Computational Domain and the Physicochemical Processes

In the present study, first, a three-dimensional domain composed of GDL and a fracture in the MPL was constructed to simulate oxygen transport as well as liquid water dynamic behaviors. The computational domain was rectangular with dimensions of $100\ \mu\text{m} \times 100\ \mu\text{m} \times 100\ \mu\text{m}$. Here, the resolution of one lattice was $1\ \mu\text{m}$. As can be seen from Figure 1a, the GDL showed layered structure characteristics. Therefore, the GDL was reconstructed by inserting the straight carbon fibers layer by layer in the through-plane direction, with the constraining parameters as the GDL porosity and the diameter of the carbon fiber. Details of the reconstruction method can be found in [27]. From the SEM image of MPL, as shown in Figure 1b, there were many fractures inside the MPL. There, fractures can provide preferred pathways for liquid water from the CL and can reduce the water flooding [5]. Therefore, at the bottom of the reconstructed GDL, an elongated rectangle was added to represent one fracture in the MPL. The final computational domain is shown in Figure 2.

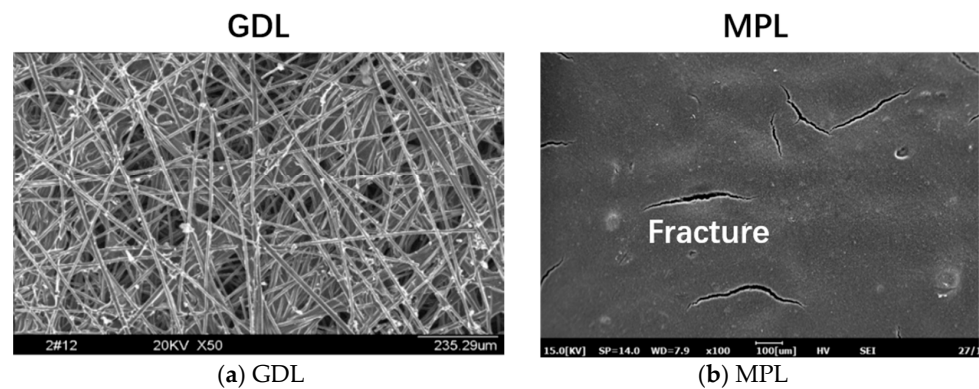


Figure 1. SEM image of GDL and MPL.

The physicochemical processes taking place inside the GDL can be described as follows. Oxygen from the top boundary diffuses into the GDL and arrives at the GDL bottom surface for the electrochemical reaction. In practice, the electrochemical reaction of oxygen actually takes place inside the CL. After diffusing through the GDL, the oxygen transports through the MPL, and arrives at the CL. Inside the CL, the oxygen first diffuses in the macropores between the carbon particles within the CL, and then into the local structures around a carbon particle, before finally being consumed at the triple-phase boundary (TPB). During the above processes, the oxygen flux is the same and can be expressed as follows:

$$D_{\text{GDL}} \frac{\partial C_{\text{oxygen}}}{\partial n} = D_{\text{MPL}} \frac{\partial C_{\text{oxygen}}}{\partial n} = D_{\text{CL, macropore}} \frac{\partial C_{\text{oxygen}}}{\partial n} = D_{\text{CL, local}} \frac{\partial C_{\text{oxygen}}}{\partial n} = k_{\text{elec}} C_{\text{oxygen}} \quad (1)$$

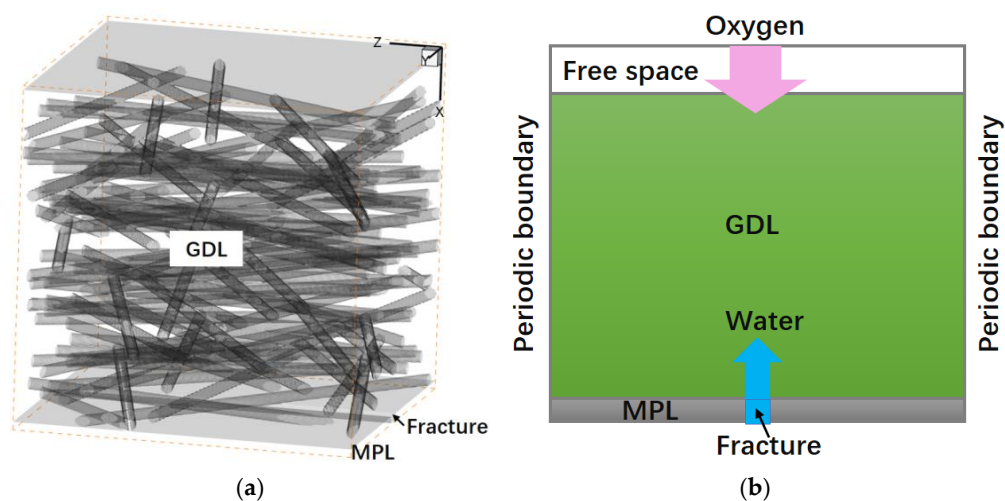


Figure 2. Computational domain (a) 3D structure and (b) schematic of the oxygen and water transport processes in the domain.

In Equation (1), D is the diffusivity and C is the oxygen concentration. The five terms refer to the flux at the GDL/MPL interface, through the MPL, the macropores in CL, the local structures in CL, and that at the TPB due to oxygen consumption, respectively. Equation (1) can be rearranged as follows:

$$J_{\text{oxygen}} = 2J_{\text{water}} = D_{\text{GDL}} \frac{\partial C_{\text{oxygen}}}{\partial n} = \frac{1}{\left(\frac{1}{k_{\text{MPL}}} + \frac{1}{k_{\text{CL, macropore}}} + \frac{1}{k_{\text{CL, local}}} + \frac{1}{k_{\text{elec}}} \right)} C_{\text{oxygen}} \quad (2)$$

where the four terms at the denominator represent the resistance through MPL and CL. J refers to the flux.

The typical pore size GDL is about 10 μm , that of MPL is about 50 nm, while that inside the CL is from 1~10 nm. Simultaneously resolving the pores in the GDL as well as that in the MPL and CL requires an enormous number of grids, which cannot be affordable by current computational resources. Therefore, in the present study, only GDL and fractures in MPL were taken into account, while the solid matrix with nanoscale pores of MPL as well as CL structures were not resolved. Thus during the simulation, Equation (1) was adopted as the boundary condition at the GDL bottom surface. This boundary condition takes into account the transport resistance during the pathway from the GDL/MPL interface to the TPB. In short, the transport processes numerically resolved in the 3D structures of GDL were combined with the 1D boundary condition described by Equation (1), and such a model was called the 3D + 1D model in the present study.

The electrochemical reaction generates water, which is assumed to be in liquid phase. The liquid water generated in the CL migrates from the fracture in MPL into the GDL [5]. Therefore, in the present study during each simulation step, the liquid water generated by Equation (2) is summarized and then averaged into every node in the fracture. Liquid water then grows from the fracture, and enters the GDL. For the air–liquid two phase flow in GDL, capillary number Ca is about $10^{-5} \sim 10^{-8}$ [19,28]. With such low Ca and the dynamic viscosity ratio between water and air at about 18, the two-phase flow in the GDL is dominated by the capillary force and effects of other forces such as gravitational force, viscous force, and inertial force can be neglected. Correspondingly, the flow is located in the capillary fingering region [29]. Therefore, neglecting the density ratio between air and liquid and setting the density ratio as unity is acceptable for simulating two-phase flow in GDL [30].

As shown in Figure 2., periodic boundary conditions were employed for the x – y plane and x – z plane. For the top and bottom boundaries at the y – z plane, no slip boundary condition was imposed. The electrochemical reaction takes place at the surface of GDL/MPL, as

described above. As liquid water migrates, it will cover the GDL/MPL interface, and under such a circumstance, the local interface is not available to the electrochemical reaction. Besides, the pores occupied by the liquid water are also not allowed for oxygen diffusion. For the inner solid fiber surface, no-slip and non-flux boundary conditions were adopted for fluid flow and mass transport, respectively. The contact angle was set as 140° for the multiphase flow simulation.

3. The Lattice Boltzmann Method

The multiphase flow and oxygen reactive transport processes in the porous structures described in Section 2 was solved using the lattice Boltzmann method (LBM). Details of the LB model are introduced as follows.

3.1. Multiphase Flow Model

In the present study, the pseudopotential multiphase LB model was employed to study air–water two-phase flow. A source term is added to consider the water generation due to electrochemical reaction. For the k th component, the evolution equation for the density distribution function with multiple-relaxation-time (MRT) collision term is defined as [31]:

$$f_i^k(\mathbf{x} + c\mathbf{e}_i\Delta t, t + \Delta t) - f_i^k(\mathbf{x}, t) = -\left(\mathbf{T}^{-1} \cdot \bar{\mathbf{D}}^k \cdot \mathbf{T}\right) \left[f_i^k(\mathbf{x}, t) - f_i^{\text{eq},k}(\mathbf{x}, t) \right] + \left(\mathbf{T}^{-1} \cdot (\mathbf{I} - \frac{\bar{\mathbf{D}}^k}{2}) \cdot \mathbf{T} \right) (F_i^k + S_i^k) \quad (3)$$

where f_i^k is the k th density distribution function at the lattice site \mathbf{x} and time t . $c = \Delta x / \Delta t$ is the lattice speed with Δx and Δt as the lattice length and time step, respectively. k equals 1 for gas and equals 2 for liquid water. The equilibrium distribution functions f^{eq} is as follows

$$f_i^{\text{eq},k} = \omega_i \rho^k \left[1 + \frac{3}{c^2} (\mathbf{e}_i \cdot \mathbf{u}^{\text{eq}}) + \frac{9}{2c^4} (\mathbf{e}_i \cdot \mathbf{u}^{\text{eq}})^2 - \frac{3}{2c^2} (\mathbf{u}^{\text{eq}})^2 \right] \quad (4)$$

For the D3Q18 lattice model used in this study, the values of the weight coefficient w_i were $w_i = 1/3, i = 0$; $w_i = 1/18, i = 1, 2, \dots, 6$; $w_i = 1/36, i = 7, 8, \dots, 18$. The transformation matrix \mathbf{T} in Equation (3) is a $(N + 1) \times (N + 1)$ matrix, with \mathbf{T}^{-1} as the inverse matrix of \mathbf{T} [31]. \mathbf{I} is the unit matrix. The diagonal relaxation matrix $\bar{\mathbf{D}}^k$ is defined as [32].

$$\bar{\mathbf{D}}^k = \text{diag}(s_0, s_1, \dots, s_{17}, s_{18}) \quad (5a)$$

$$s_{0 \sim 8, 10, 12, 16 \sim 18} = 1, s_9 = s_{11} = s_{13-15} = \frac{1}{\tau^k} \quad (5b)$$

More details of \mathbf{T} and $\bar{\mathbf{D}}^k$ can be found in Ref. [31]. The density, velocity, and viscosity are calculated by [30]

$$\rho^k = \sum f_i^k, \rho^k \mathbf{u}^k = \sum f_i^k \mathbf{e}_i + \frac{\delta t}{2} \mathbf{F}^k, \nu^k = \frac{1}{3} (\tau^k - 0.5) \frac{\Delta x^2}{\Delta t} \quad (6)$$

The effective velocity \mathbf{u}^{eq} in Equation (4) is as follows

$$\mathbf{u}^{\text{eq}} = \sum s_0^k \rho^k \mathbf{u}^k / \sum s_0^k \rho^k \quad (7)$$

In Equation (3), F_i^k is the force term and S_i^k is the source term in the LB framework. F_i^k is calculated by

$$F_i^k = \frac{\mathbf{F}^k \cdot (\mathbf{e}_i - \mathbf{u}^{\text{eq}})}{\rho^k c_s^2} f_i^{\text{eq},k} \Delta t \quad (8)$$

where F^k (also in Equation (6)) includes fluid–solid interaction force, fluid–fluid interaction force, and external body force

$$\mathbf{F}^k = \mathbf{F}_f^k + \mathbf{F}_s^k + \mathbf{F}_e^k \quad (9)$$

For the particles of the k th component at lattice site \mathbf{x} , the total fluid–fluid surface tension force is expressed as

$$\mathbf{F}_f^k = -\psi^k(\rho^k(\mathbf{x}))g_{kk'}\sum_{\mathbf{x}'}\sum_{k'}^s w(\mathbf{x}')\psi^k(\rho^{k'}(\mathbf{x}'))(\mathbf{x}' - \mathbf{x}) \quad (10)$$

where ψ is the effective mass or interparticle potential and is defined as $\psi_k(\rho_k) = 1 - \exp(-\rho_k)$. $g_{kk'}$ is the interaction strength and it effectively controls the immiscibility of the binary mixture and the surface tension force. The value of $g_{kk'}$ was taken as 1.95 in this study. If the interaction force of four nearest neighbors is considered, the weight factor $w(\mathbf{x}')$ is 1/3 and 1/12 for $|\mathbf{x}' - \mathbf{x}|_2 = 1$ and $|\mathbf{x}' - \mathbf{x}|_2 = 2$, respectively. \mathbf{F}_s^k is the fluid–solid interaction force

$$\mathbf{F}_s^k = -\psi^k(\rho^k(\mathbf{x}))g_s\sum_{\mathbf{x}'} w(\mathbf{x}')s(\mathbf{x}')(\mathbf{x}' - \mathbf{x}) \quad (11)$$

where s is an indicator function, with 0 and 1 for pore and solid, respectively. g_s controls the fluid–solid strength. By adjusting g_s , different wettability (contact angle) can be obtained.

The LB source term in Equation (3) is calculated by [33]

$$S_i^k = \omega_i S^k \left[1 + \frac{3}{c^2}(\mathbf{e}_i \cdot \mathbf{u}^{\text{eq}}) + \frac{9}{2c^4}(\mathbf{e}_i \cdot \mathbf{u}^{\text{eq}})^2 - \frac{3}{2c^2}(\mathbf{u}^{\text{eq}})^2 \right] \Delta t \quad (12)$$

where S^k is the actual source term considering the electrochemical reaction at the Pt–ionomer interface. This source term will be discussed in Section 3.3. Incorporating S^k into the evolution equation (Equation (3)) through the form of Equation (12), the Galilean invariance can be guaranteed according to previous study [33].

3.2. Mass Transport Model

Oxygen transports from the GC into the GDL and arrives at the bottom surface of GDL for the electrochemical reaction. The mass transport is solved using the LB mass transport model as follows

$$g_i(\mathbf{x} + c\mathbf{e}_i\Delta t, t + \Delta t) - g_i(\mathbf{x}, t) = \mathbf{Q}^{-1}\Lambda\mathbf{Q}(g_i(\mathbf{x}, t) - g_i^{\text{eq}}(\mathbf{x}, t)) \quad (13)$$

where g_i is the concentration distribution function at the lattice site \mathbf{x} and time t in the i th direction. g_i^{eq} is the equilibrium distribution function. The D3Q7 lattice model is adopted in this study, and g_i^{eq} was calculated by $g_i^{\text{eq}} = w_i C$, with $w_0 = 1/4$ and $w_{1-6} = 1/8$. The transformation matrix \mathbf{Q} in Equation (13) transfers the distribution function in velocity space into momentum space. \mathbf{Q}^{-1} is the inverse matrix of \mathbf{Q} , and for more details of \mathbf{Q} and \mathbf{Q}^{-1} , one can find in Ref. [34]. Λ is the relaxation coefficient matrix.

$$\Lambda = \begin{bmatrix} \tau_0 & 0 & 0 & 0 & 0 & 0 & 0 \\ 0 & \tau_{xx} & \tau_{xy} & \tau_{xz} & 0 & 0 & 0 \\ 0 & \tau_{yx} & \tau_{yy} & \tau_{yz} & 0 & 0 & 0 \\ 0 & \tau_{zx} & \tau_{zy} & \tau_{zz} & 0 & 0 & 0 \\ 0 & 0 & 0 & 0 & \tau_4 & 0 & 0 \\ 0 & 0 & 0 & 0 & 0 & \tau_5 & 0 \\ 0 & 0 & 0 & 0 & 0 & 0 & \tau_6 \end{bmatrix} \quad (14)$$

where the relaxation coefficients $\tau_{\alpha\beta}$ is related to the diffusivity

$$D_{\alpha\beta} = \zeta(\tau_{\alpha\beta} - \frac{1}{2}\delta_{\alpha\beta})\frac{\Delta x^2}{\Delta t} \quad (15)$$

where $\delta_{\alpha\beta}$ is the kronecker symbol. For isotropic mass transport, $\tau_{xx} = \tau_{yy} = \tau_{zz}$ and $\tau_{\alpha\beta}(\alpha \neq \beta) = 0$. In the present study, the values of τ_0 , τ_4 , τ_5 , and τ_6 in Equation (16) were set as unity. ζ in Equation (16) was 1/4.

3.3. Source/Sink Term for Multiphase Flow

Now, our attention turned to determining the source/sink term in Equation (12) for multiphase flow. As discussed above, liquid water enters the GDL from the fractures inside the MPL. During each time step, the total amount of liquid water generated can be determined by the summation of all the flux described by Equation (2). Then, all water generated is relocated into the fractures.

$$S^1 = -\frac{1}{V_{\text{fracture}}} \sum M_{\text{water}} J_{\text{water}} A \quad (16)$$

$$S^2 = \frac{1}{V_{\text{fracture}}} \sum M_{\text{water}} J_{\text{water}} A \quad (17)$$

where M_{water} is the molar mass; A is the surface area of each computational node; and V_{fracture} is the total volume of the fracture.

The general modeling procedure of each time step during the pore-scale modeling are as follows: (1) The pore-scale two-phase flow modeling is conducted, by which the liquid water distribution is determined; (2) The pore-scale oxygen mass transport modeling is conducted, and such modeling is not allowed in the liquid phase and only conducted in the gas phase; and (3) Based on the results in Step 2, the liquid water generation rate is determined, which is then adopted in the two-phase flow modeling in Step 1. Steps 1–3 are repeated during the simulation until the liquid water touches the top wall of the GC or the liquid water generation rate is extremely low due to the coverage of the bottom surface by liquid water or the oxygen transport is seriously hindered by the liquid water. It is worth mentioning that the pore-scale two-phase model and the oxygen reactive transport model have been well validated in our previous work, and thus the validation is not repeated here for brevity [35,36].

4. Results and Discussion

4.1. Multiphase Reactive Transport in the 3D Domain

The 3D simulation of oxygen reactive transport and air–liquid water two-phase flow was performed by a self-developed LBM code parallelized based on domain decomposition scheme using message passing interface (MPI). The domain was cut into 72 sub-domains and 72 CPU cores were adopted.

Figure 3 shows the air–liquid water interface distribution in the GDL at different times. As can be seen in Figure 3, as the oxygen reduction reaction proceeds, liquid water gradually accumulates inside the MPL fracture and enters the GDL as tiny droplets. As time goes on, these tiny droplets merge to big droplets. Affected by the complex porous structures, some droplets advance deep into the GDL, while the growth of other droplets is suppressed. The liquid water front moves in both in-plane and through-plane direction, although irregularly, but following the capillary fingering mechanism, which means that the liquid water front always advances into the pores with the largest pore size. Finally at $t = 1,200,000$ iterations, there was excessive liquid water in the GDL, and the GDL was severely flooded at the bottom half. Figure 4 further shows the bottom view of the computational domain, which provides information of coverage by the liquid water. It can be found that during the migration of the liquid water inside the GDL, the bottom surface was gradually covered by the liquid water, leading to a reduced reactive surface area. For the liquid water distribution at $t = 1,200,000$ iterations, it can be found that the transport pathway for the oxygen was seriously blocked and the reactive surface area was greatly reduced.

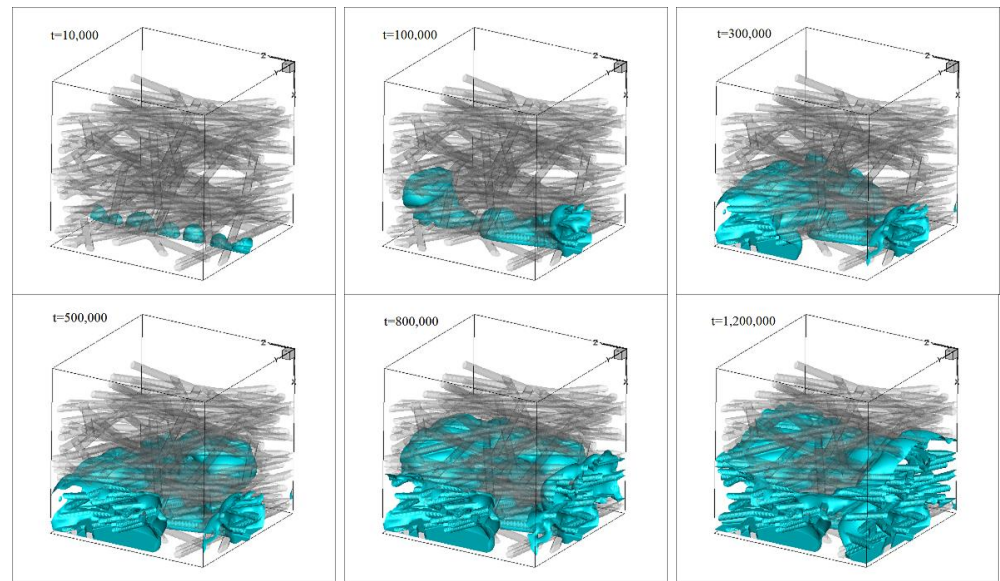


Figure 3. Time evolutions of liquid water in the computational domain.

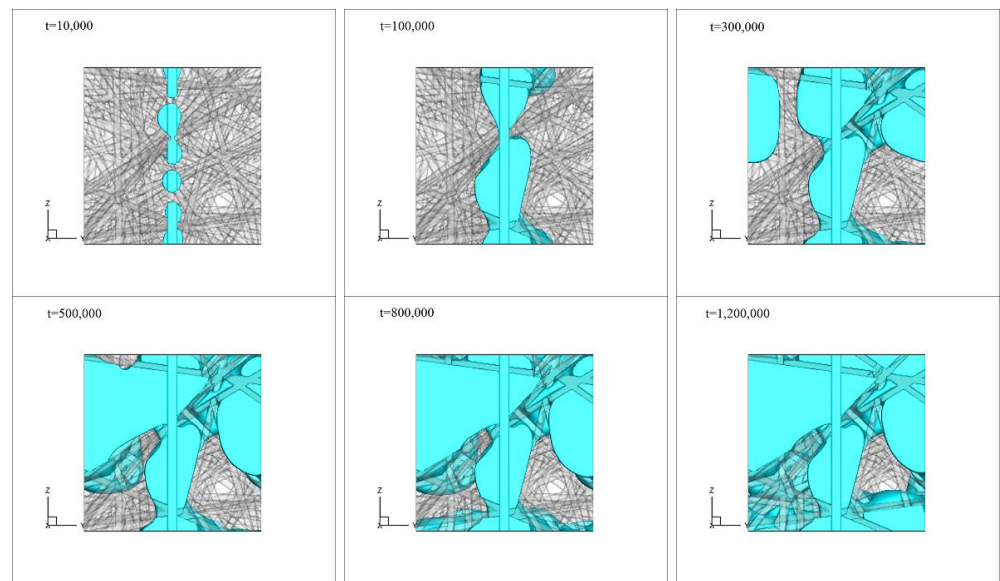


Figure 4. Bottom view of the liquid water distribution in the computational domain.

Note that in the present simulation, the multiphase flow and the oxygen reactive transport were coupled. Therefore, the more the oxygen consumed, the more liquid water generated. As the liquid water saturation increases in the GDL, the pores inside the GDL are gradually blocked, and thus less oxygen is available to the reaction at the bottom surface. Therefore, the generation rate of the liquid water gradually decreases as time proceeds. In the literature, the majority of the pore-scale study of liquid water transport in the GDL adopts either a velocity inlet or constant pressure boundary condition for the liquid water entering GDL. Such a boundary condition leads to a continuous and steady supply of liquid water into the GDL even when the GDL is seriously flooded, which in fact neglects the coupling mechanisms between air–water two-phase flow and the oxygen reactive transport. In fact, in the present study, due to the extremely slow generation rate of the liquid water in the latter stage due to the inhibition of the oxygen reactive transport process, the running time for the results shown in Figure 3 is as long as four months, leading to a total of about 2900 h for each CPU core, which is really time consuming. Even with such a long time simulation, the liquid water did not break through the GDL at $t = 1,200,000$ with

liquid saturation in the entire GDL at about 0.35. In the pore-scale study of the coupled multiphase flow and oxygen transport by Zhang et al., the liquid water mainly transports in the through-plane direction, and breakthrough of the liquid water was observed with a saturation of about 0.23 [26]. The pore-scale results in the present study as well as that of Zhang et al. suggest that liquid water transport and distribution should be controlled effectively and that the liquid water transports in the through-plane direction should be facilitated while that in the in-plane direction should be suppressed. Perforated GDL is one such scheme in which liquid water penetrates the GDL by the perforated pores [37].

The through-plane distributions of the liquid water saturation at different times are shown in Figure 5. The saturation is defined as the ratio of volume occupied by the liquid water to the entire pore volume in a given cross-section. It can be found that liquid water saturation generally decreases from the GDL/MPL interface to the GDL/GC interface. Behind the liquid water front, the liquid water saturation is below unity, indicating that the void space is partially filled by the liquid water, confirming the capillary fingering mechanism. In the literature, for pore-scale modeling adopting the uniform velocity inlet as the boundary condition, usually the local water saturation at the GDL/MPL approaches unity. The results in Figure 5 show that the local saturation when $t = 1,200,000$ was only about 0.7. The maximum value of local saturation located around $x^* = 0.25$ was about 0.83. However, liquid water saturation in the remaining parts, especially $x^* > 0.6$, was very low. Such high local high saturation leads to a small space for oxygen transport, greatly reducing the effective diffusivity of oxygen through the entire GDL, even though the averaged saturation in the entire GDL was only about 0.35 at $t = 1,200,000$. Figure 6 displays the time evolution of the current density obtained, which reduced from the initial value of 2.39 to 0.46 A cm^{-2} at $t = 1,200,000$, indicating the negative effects of liquid water on the reactive transport processes.

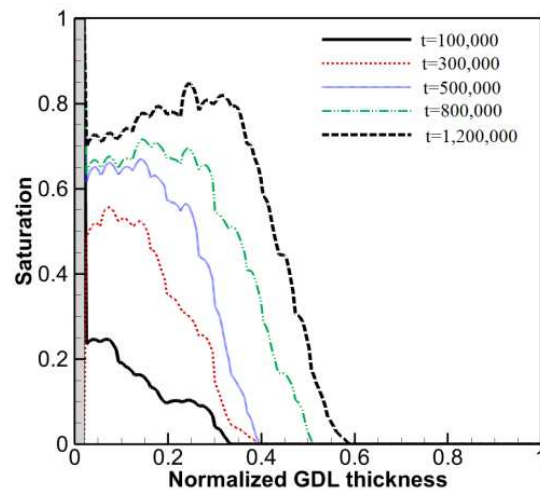


Figure 5. Through-plane liquid water saturation distribution.

4.2. Effects of the Fracture Number

The above pore-scale 3D simulation clearly show the coupling mechanisms of multiphase flow and oxygen transport processes inside the GDL. Since a 3D simulation is really time consuming, in this section, 2D simulations were conducted to investigate the effects of fracture number on the coupled processes. The computational domain is shown in Figure 7 with a size of 2048×456 lattices with the resolution of one lattice as $1 \mu\text{m}$. The domain contained a GDL, a MPL with different numbers of fractures, and a free region on the top of the GDL representing the GC. The height of the MPL, the GDL, and the free region was 7, 156, and 290, respectively. The porosity of the GDL was 0.8004. The contact angle of the solid particles in GDL, the GDL/MPL interface as well as the top wall of the GC was the same as 140° . Different number of fractures in the MPL was investigated including 8, 12, 16, and 24 fractures. The width and depth of each fracture was 10 and 4, respectively.

The gap between two neighboring fractures was 227, 157, 120, and 81 for the four different number of fractures studied. The dynamic behaviors of the liquid water, the evolution of the saturation, the saturation distribution along the y direction, the coverage area of the GDL/MPL interface, and the current density will be discussed in detail.

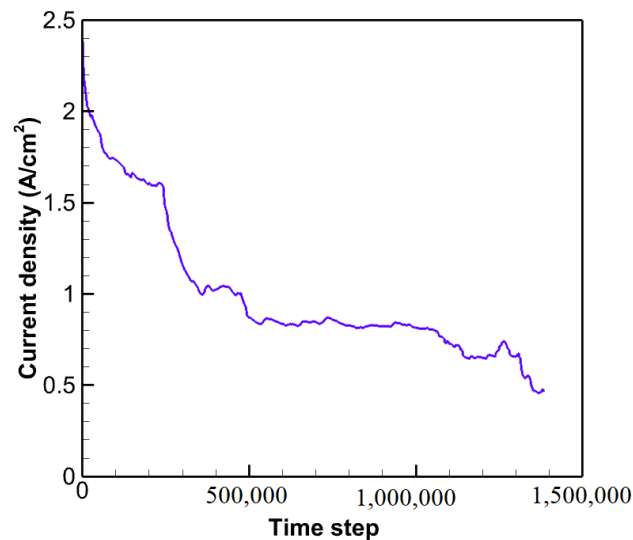


Figure 6. Time evolution of the current density.

Figure 7 shows the dynamic behaviors of liquid water in the domain with the fracture number of 8. As the reaction proceeded, liquid water is gradually generated and eight liquid clusters were observed connected to the eight fractures ($t = 40,000$). Each cluster advances inside the GDL following the mechanism of capillary fingering, namely always searching for the pore with the largest pore size. Affected by the local complicated porous structures, some clusters move mainly in the through-plane direction, while others were mainly in the in-plane direction. At $t = 200,000$, clusters A1–A3 merged into one cluster; cluster A4 found its pathway along the in-plane direction; clusters A5, A6, and A8 were trapped by local structures with relative low pore size, and cluster A7 advanced the most along the through-plane direction. At $t = 550,000$, cluster A1–A4 merged into one cluster, A5–A6 merged into one cluster, cluster A8 still advanced separately, while cluster A7 broke through the GDL and formed a tiny droplet in the GC. At $t = 750,000$, clusters A1–A4 merged and supported the growth of two droplets. At $t = 1,500,000$, clusters A5 and A6 merged and supported the growth of one droplet. Clusters A7 and A8 also merged and supported the growth of the first droplet forming in the GC. After the breakthrough, continuous pathways were created for the liquid water inside the GDL, while the dynamic change of the local liquid water distribution inside the GDL still could be observed. Finally, at $t = 3,500,000$, there were four droplets in the GC connected to different clusters. The growth rate of the four droplets in the GC were different, and it was found that the earliest breakthrough did not necessarily mean the highest growth rate. The growth rate of the droplet in the GC highly depends on the flow rate of the water cluster connected to it. Finally, it can be seen that liquid water distribution was not uniform inside the GDL. Locally, the liquid water amount at the top of GDL was low while the bottom of the GDL was seriously flooded. The GC was also severely blocked by the four droplets.

Figure 8 shows the corresponding oxygen concentration field at two $t = 45,000$ and $t = 350,000$. It was found that due to the consumption at the GDL bottom, the oxygen concentration gradually decreased from the top to the bottom of the domain. The liquid water hinders the transport of oxygen, and causes the reduction of the reactive surface area.

Figures 9–11 further show the dynamic behaviors of liquid water in the domain with fracture numbers of 12, 16, and 24. The dynamic behaviors of growth, coalescence, and breakthrough discussed in Figure 7 can also be observed and are not repeated here. It can

be found that the fractures inside the MPL significantly affects the liquid water dynamic behaviors in the GDL and GC. In particular, the breakthrough location, breakthrough time, and breakthrough point number (or droplet number in the GC) are closely related to the fracture numbers. For the breakthrough time, it is expected that the breakthrough time for the case with the most fractures is the longest. For the breakthrough point number, the results are interesting. Intuitively, more fractures in the MPL will lead to more clusters in the GDL, and thus finally more droplets appearing in the GC. However, it can be found in Figures 7 and 9–11 that the number of the breakthrough points and the thus the corresponding droplets in the GC decreased as the fracture number in the MPL increased. For the fracture numbers of 8, 12, 16, and 24, the breakthrough point number was 4, 3, 3, and 2, respectively. Note that although there were two droplets in the GC for the case with fracture numbers of 12, the left droplet was actually nourished by two breakthrough points, as can be seen at $t = 1,200,000$ and $2,100,000$. This is because as more fractures were added in the MPL, the gap between the neighboring fractures decreased, and the neighboring clusters were more easily to merge, thus resulting in fewer clusters in the GDL and finally few breakthrough points at the GDL/GC interface.

Figure 12 shows the evolution of the liquid water saturation along the y direction for the four cases with different fracture numbers. It can be found that the liquid water saturation in the GDL increases as time proceeds. After the breakthrough, the saturation distribution inside the GDL still varies. These results are in consistent with the dynamic behaviors of liquid water in Figures 7 and 9–11. For all the four images in Figure 12, it can be found that the saturation decreased and then increased across the GDL/GC interface, with a local minimum value obtained. The minimum value was usually less than 0.1. However, at the GDL/MPL interface, the local flooding was serious, and the local saturation value was higher than 0.8. Comparing the four images, it can be found that as the fracture number increases, the local liquid water saturation at the GDL/MPL increases.

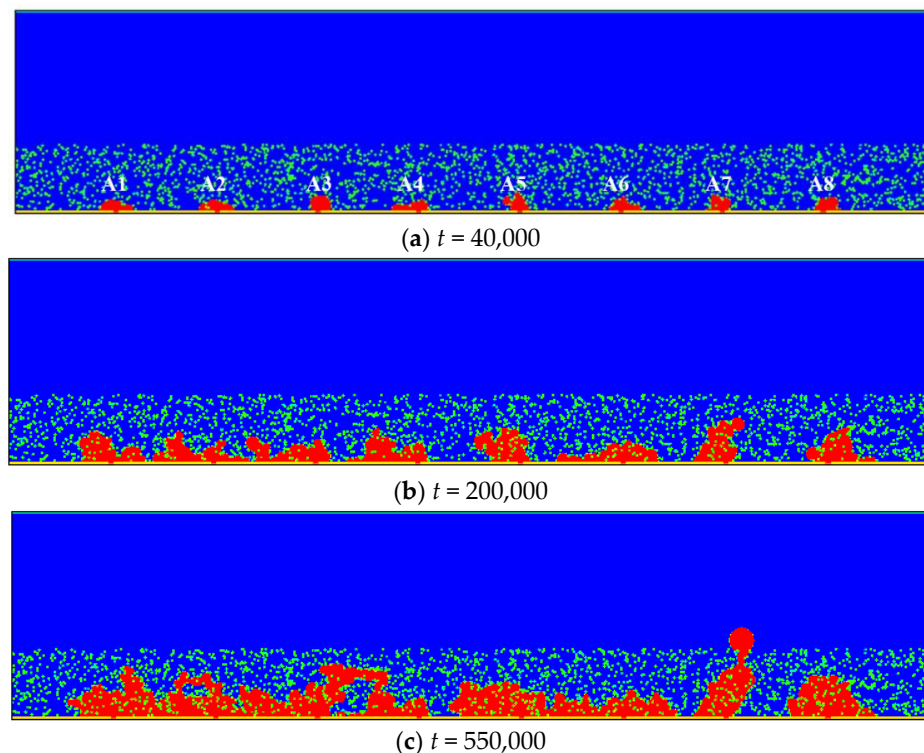


Figure 7. Cont.

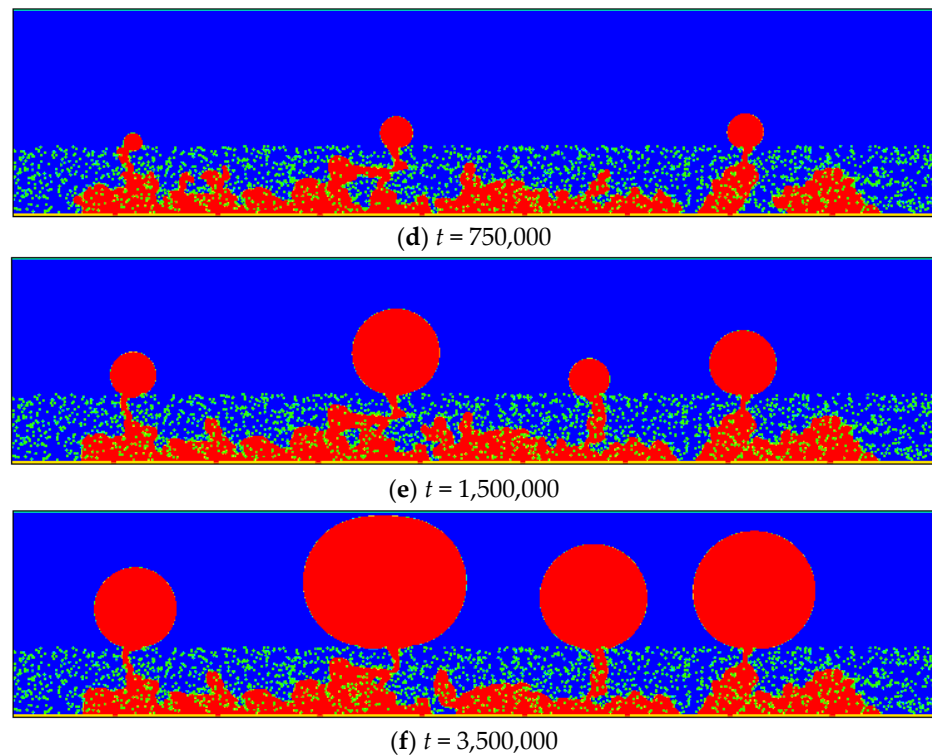


Figure 7. Time evolutions of liquid water distribution in the domain with eight fractures.

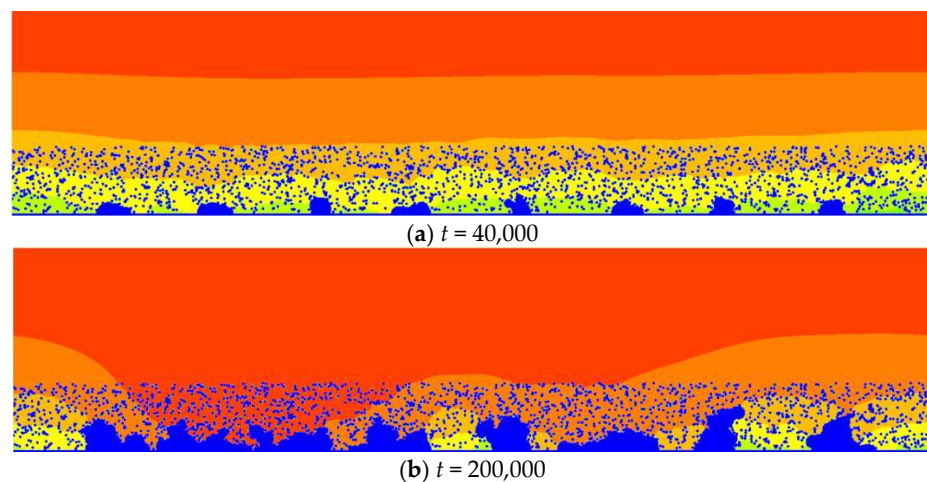


Figure 8. Distributions of oxygen concentration.

Figure 13a shows variation of the total liquid water saturation inside the GDL and the coverage of the GDL/MPL interface. Here, the total saturation is defined as the ratio between the total liquid water volume in the GDL and total volume of the void space in GDL. It can be found that the coverage ratio increases as more fractures are considered, in consistent with the local saturation at the GDL/MPL interface as discussed in Figure 12. For the total saturation, in all cases, the total saturation in the GDL gradually increased and reached a constant value. As the fracture number increased, the final value of the total saturation generally decreased. In particular, the saturation of the case with 24 fractures was much higher than the others. As discussed previously in Figures 7 and 9–11, more fractures led to fewer droplets in the GC. Therefore, it seems that for the range of fracture numbers studied in the present study, as the fracture number increased, the flooding in GDL was more severe while that in the GC was alleviated, with the former one reducing the cell performance while the latter was desirable. Finally, Figure 13b shows the time

evolutions of the current density. Corresponding to the above discussion, the current density decreases as the time proceeded due to the increased liquid water saturation. As the fracture number increased, the final value of the current density decreased.

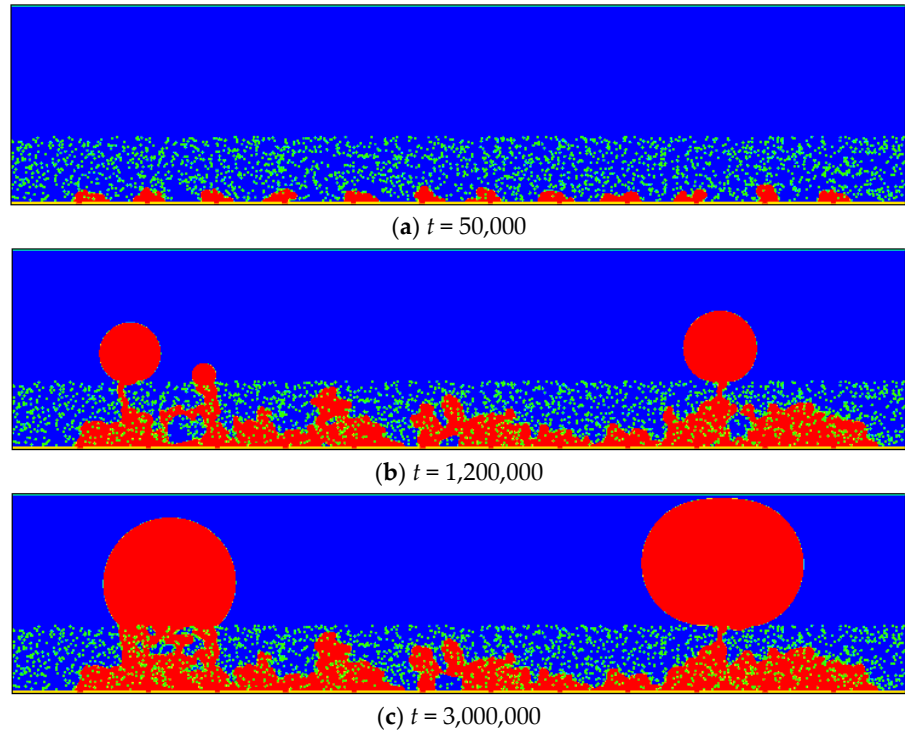


Figure 9. Time evolutions of liquid water distribution in the domain with 12 fractures.

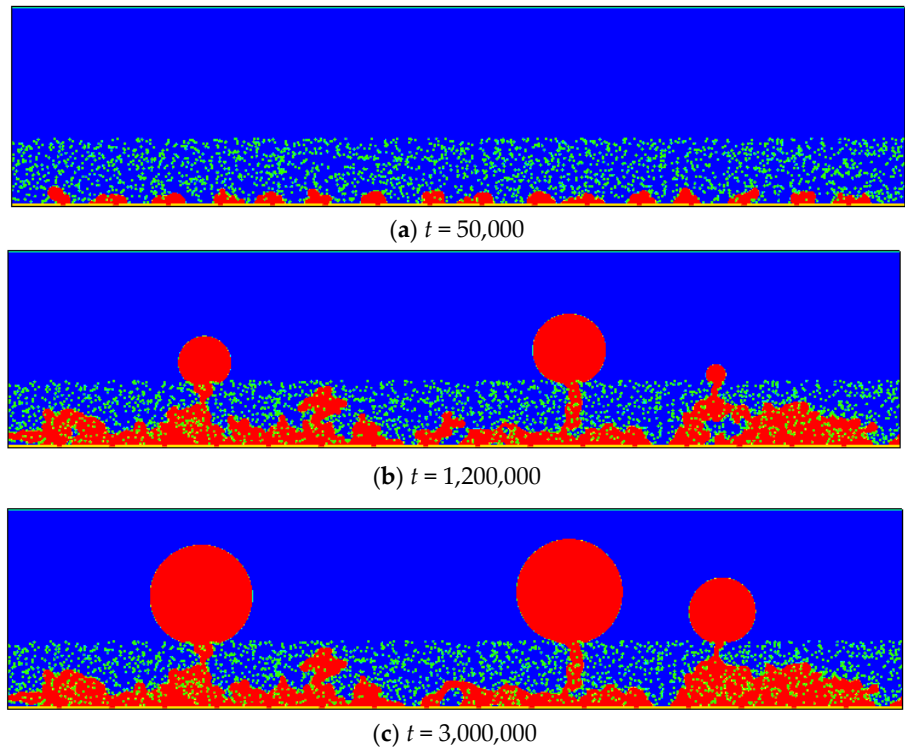


Figure 10. Time evolutions of liquid water distribution in the domain with 16 fractures.

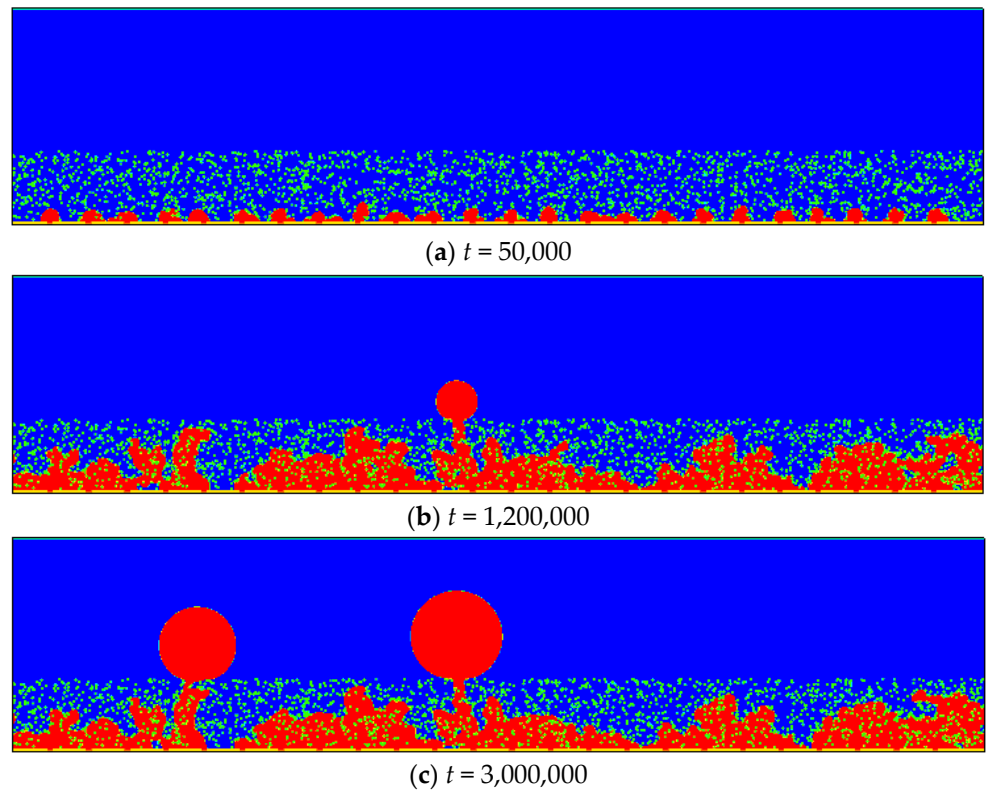


Figure 11. Time evolutions of liquid water distribution in the domain with 24 fractures.

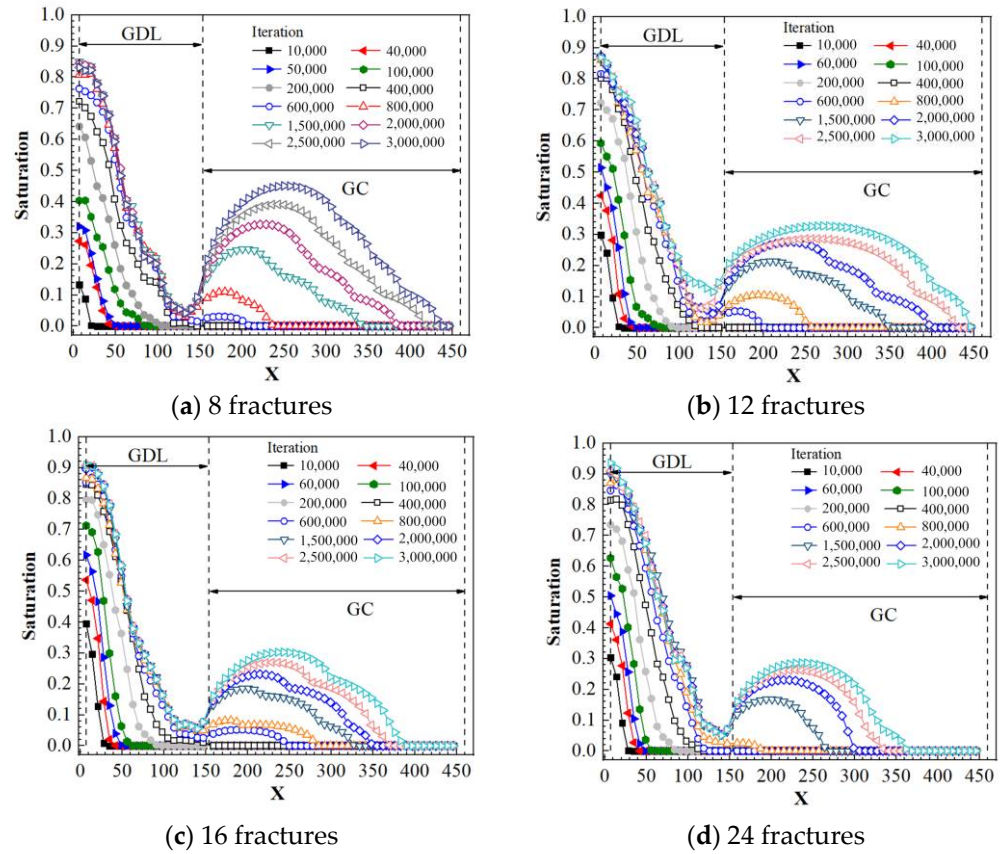
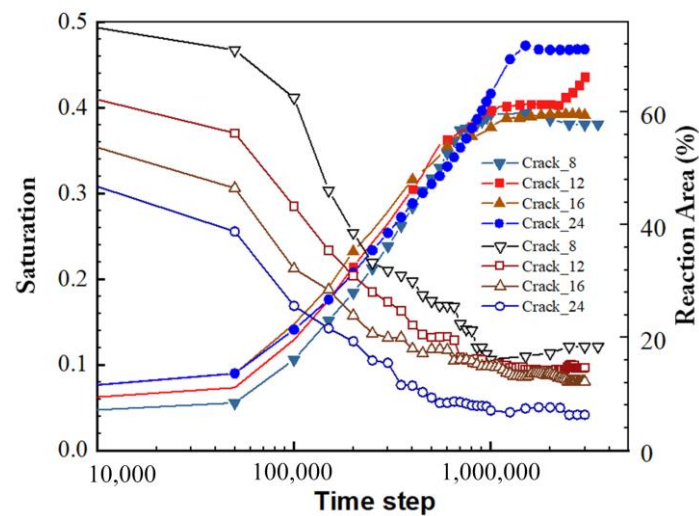
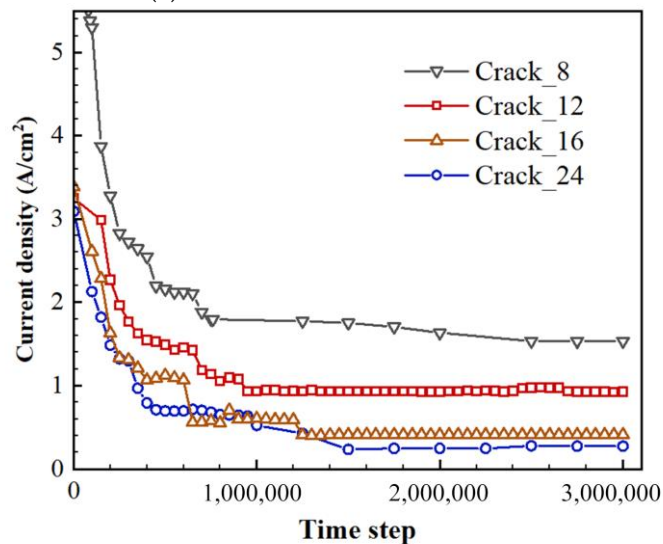


Figure 12. Through-plane liquid water saturation distribution in the domain with different fractures.



(a) Saturation and reaction area



(b) Current density

Figure 13. Time evolution of different variables: (a) saturation and reaction area and (b) current density.

5. Conclusions

Understanding multiphase reactive transport processes inside porous electrodes of PEMFC is of great importance for improving performance of PEMFC. In this study, a pore-scale model adopting the LBM was proposed for the coupled air–water two-phase flow and the oxygen transport processes in GDL and fractures of MPL. In the model, liquid water generated by the electrochemical reactions enters the GDL from the MPL fractures. The coupled mechanisms between multiphase and oxygen reactive transport are discussed in both 3D and 2D simulations. The simulation results show that as the liquid water saturation in the GDL increases, the oxygen transport is hindered, and thus the generation rate of liquid water decreases. The liquid water cannot maintain constant velocity inlet or pressure inlet boundary conditions that are widely adopted in the literature. For the 3D domain studied in the present study, the migration of the liquid water in the in-plane direction caused serious flooding, leading to breakthrough failure of the liquid water from the GDL. Through-plane migration of liquid water is highly desirable. Furthermore, the effects of fracture number on the coupled processes and some important variables such as reactive surface coverage, saturation, and current density were discussed. It was found that liquid water from the different fractures of MPL shows complex growth, coalescence,

and breakthrough behaviors in the GDL. Generally, as the fracture number in the GDL increased, the number of liquid water breakthrough points decreased, the total saturation in the GDL as well as the local saturation at the GDL/MPL interface increased, and the current density decreased. The optimization of the GDL structure and wettability based on the pore-scale modeling results is undergoing in our group.

Author Contributions: Conceptualization, C.Z. and Q.Y.; Data curation, C.Z. and L.C.; Formal analysis, X.T. and T.H.; Funding acquisition, X.T.; Investigation, C.Z. and L.G.; Methodology, C.Z. and L.C.; Project administration, Q.Y.; Resources, X.T. and Q.Y.; Software, L.G. and L.C.; Supervision, X.T. and Q.Y.; Validation, C.Z., L.C. and Q.Y.; Visualization, L.C.; Writing—original draft, C.Z.; Writing—review & editing, L.G. and Q.Y. All authors have read and agreed to the published version of the manuscript.

Funding: This research was funded by Huadian in part, grant number CHDKJ 19-01-87. The APC was funded by Zhejiang University of Technology.

Acknowledgments: This research work was supported, in part, by the project of hydrogen production from renewable energy, large-scale energy storage and comprehensive utilization of hydrogen energy (No.: CHDKJ 19-01-87).

Conflicts of Interest: The authors declare no conflict of interest.

Abbreviations

The following abbreviations and symbols are used in this manuscript:

CL	Catalyst Layer
GC	Gas Channel
GDL	Gas Diffusion Layer
LBM	Lattice Boltzmann Method
MPL	Microscopic Porous Layer
MRT	Multiple Relaxation Time
PEMFC	Proton Exchange Membrane Fuel Cell
REV	Representative Elementary Volume
TPB	Triple-Phase Boundary
XCT	X-ray Computed Tomography



References

- Li, H.; Tang, Y.; Wang, Z.; Shi, Z.; Wu, S.; Song, D.; Zhang, J.; Fatih, K.; Zhang, J.; Wang, H.; et al. A review of water flooding issues in the proton exchange membrane fuel cell. *J. Power Sources* **2008**, *178*, 103–117. [\[CrossRef\]](#)
- Nam, J.H.; Kaviani, M. Effective diffusivity and water-saturation distribution in single- and two-layer PEMFC diffusion medium. *Int. J. Heat Mass Transf.* **2003**, *46*, 4595–4611. [\[CrossRef\]](#)
- Mortazavi, M.; Tajiri, K. Effect of the PTFE content in the gas diffusion layer on water transport in polymer electrolyte fuel cells (PEFCs). *J. Power Sources* **2014**, *245*, 236–244. [\[CrossRef\]](#)
- Sadeghifar, H.; Djilali, N.; Bahrami, M. Effect of Polytetrafluoroethylene (PTFE) and micro porous layer (MPL) on thermal conductivity of fuel cell gas diffusion layers: Modeling and experiments. *J. Power Sources* **2014**, *248*, 632–641. [\[CrossRef\]](#)
- Deevanhxay, P.; Sasabe, T.; Tsushima, S.; Hirai, S. Observation of dynamic liquid water transport in the microporous layer and gas diffusion layer of an operating PEM fuel cell by high-resolution soft X-ray radiography. *J. Power Sources* **2013**, *230*, 38–43. [\[CrossRef\]](#)
- Markötter, H.; Manke, I.; Krüger, P.; Arlt, T.; Haussmann, J.; Klages, M.; Riesemeier, H.; Hartnig, C.; Scholta, J.; Banhart, J. Investigation of 3D water transport paths in gas diffusion layers by combined in-situ synchrotron X-ray radiography and tomography. *Electrochem. Commun.* **2011**, *13*, 1001–1004. [\[CrossRef\]](#)
- Ince, U.U.; Markötter, H.; George, M.G.; Liu, H.; Ge, N.; Lee, J.; Alrwashdeh, S.S.; Zeis, R.; Messerschmidt, M.; Scholta, J.; et al. Effects of compression on water distribution in gas diffusion layer materials of PEMFC in a point injection device by means of synchrotron X-ray imaging. *Int. J. Hydrogen Energy* **2018**, *43*, 391–406. [\[CrossRef\]](#)
- Flückiger, R.; Marone, F.; Stampanoni, M.; Wokaun, A.; Büchi, F.N. Investigation of liquid water in gas diffusion layers of polymer electrolyte fuel cells using X-ray tomographic microscopy. *Electrochim. Acta* **2011**, *56*, 2254–2262. [\[CrossRef\]](#)
- Sabzpushan, S.; Jafari Mosleh, H.; Kavian, S.; Saffari Pour, M.; Mohammadi, O.; Aghanajafi, C.; Hossein Ahmadi, M. Nonisothermal two-phase modeling of the effect of linear nonuniform catalyst layer on polymer electrolyte membrane fuel cell performance. *Energy Sci. Eng.* **2020**, *8*, 3575–3587. [\[CrossRef\]](#)

10. Wang, C.Y.; Cheng, P. Multiphase Flow and Heat Transfer in Porous Media. In *Advances in Heat Transfer*; Hartnett, J.P., Irvine, T.F., Jr., Cho, Y.I., Greene, G.A., Eds.; Elsevier: Amsterdam, The Netherlands, 1997; Volume 30, pp. 93–196.
11. Pasaogullari, U.; Wang, C.-Y. Two-phase transport and the role of micro-porous layer in polymer electrolyte fuel cells. *Electrochim. Acta* **2004**, *49*, 4359–4369. [[CrossRef](#)]
12. Udell, K.S. Heat transfer in porous media considering phase change and capillarity—the heat pipe effect. *Int. J. Heat Mass Transf.* **1985**, *28*, 485–495. [[CrossRef](#)]
13. Leverett, M. Capillary Behavior in Porous Solids. *Pet. Dev. Technol.* **1941**, *142*, 152–169. [[CrossRef](#)]
14. Wang, X.-D.; Wang, Y.-L.; Chen, Y.; Si, C.; Su, A.; Lee, D.-J. Proton exchange membrane fuel cell modeling with diffusion layer-based and sands-based capillary pressure correlations: Comparative study. *J. Taiwan Inst. Chem. Eng.* **2014**, *45*, 1532–1541. [[CrossRef](#)]
15. Gostick, J.T.; Fowler, M.W.; Ioannidis, M.; Pritzker, M.D.; Volkovich, Y.; Sakars, A. Capillary pressure and hydrophilic porosity in gas diffusion layers for polymer electrolyte fuel cells. *J. Power Sources* **2006**, *156*, 375–387. [[CrossRef](#)]
16. Kumbur, E.C.; Sharp, K.V.; Mench, M.M. Validated leverett approach for multiphase flow in PEFC diffusion media: I. hydrophobicity effect. *J. Electrochem. Soc.* **2007**, *154*, B1295–B1304. [[CrossRef](#)]
17. Nguyen, T.V.; Lin, G.; Ohn, H.; Wang, X. Measurement of Capillary Pressure Property of Gas Diffusion Media Used in Proton Exchange Membrane Fuel Cells. *Electrochem. Solid-State Lett.* **2008**, *11*, B127–B131. [[CrossRef](#)]
18. Molaieimesh, G.R.; Saeidi Googarchin, H.; Qasemian Moqaddam, A. Lattice Boltzmann simulation of proton exchange membrane fuel cells—A review on opportunities and challenges. *Int. J. Hydrogen Energy* **2016**, *41*, 22221–22245. [[CrossRef](#)]
19. Chen, L.; Kang, Q.; Mu, Y.; He, Y.; Tao, W. A critical review of the pseudopotential multiphase lattice Boltzmann model: Methods and applications. *Int. J. Heat Mass Transf.* **2014**, *76*, 210–236. [[CrossRef](#)]
20. Hao, L.; Cheng, P. Lattice Boltzmann simulations of water transport in gas diffusion layer of a polymer electrolyte membrane fuel cell. *J. Power Sources* **2010**, *195*, 3870–3881. [[CrossRef](#)]
21. Yu, J.; Froning, D.; Reimer, U.; Lehnert, W. Polytetrafluorethylene effects on liquid water flowing through the gas diffusion layer of polymer electrolyte membrane fuel cells. *J. Power Sources* **2019**, *438*, 226975. [[CrossRef](#)]
22. Kakaee, A.H.; Molaieimesh, G.R.; Elyasi Garmaroudi, M.H. Impact of PTFE distribution across the GDL on the water droplet removal from a PEM fuel cell electrode containing binder. *Int. J. Hydrogen Energy* **2018**, *43*, 15481–15491. [[CrossRef](#)]
23. Jinuntuya, F.; Whiteley, M.; Chen, R.; Fly, A. The effects of gas diffusion layers structure on water transportation using X-ray computed tomography based Lattice Boltzmann method. *J. Power Sources* **2018**, *378*, 53–65. [[CrossRef](#)]
24. Jeon, D.H.; Kim, H. Effect of compression on water transport in gas diffusion layer of polymer electrolyte membrane fuel cell using lattice Boltzmann method. *J. Power Sources* **2015**, *294*, 393–405. [[CrossRef](#)]
25. Deng, H.; Hou, Y.; Jiao, K. Lattice Boltzmann simulation of liquid water transport inside and at interface of gas diffusion and micro-porous layers of PEM fuel cells. *Int. J. Heat Mass Transf.* **2019**, *140*, 1074–1090. [[CrossRef](#)]
26. Zhang, D.; Cai, Q.; Gu, S. Three-dimensional lattice-Boltzmann model for liquid water transport and oxygen diffusion in cathode of polymer electrolyte membrane fuel cell with electrochemical reaction. *Electrochim. Acta* **2018**, *262*, 282–296. [[CrossRef](#)]
27. Chen, L.; Luan, H.; He, Y.; Tao, W. Pore-scale flow and mass transport in gas diffusion layer of proton exchange membrane fuel cell with interdigitated flow fields. *Int. J. Therm. Sci.* **2012**, *51*, 132–144. [[CrossRef](#)]
28. Mukherjee, P.P.; Wang, C.; Kang, Q. Mesoscopic modeling of two-phase behavior and flooding phenomena in polymer electrolyte fuel cells. *Electrochim. Acta* **2009**, *54*, 6861–6875. [[CrossRef](#)]
29. Lenormand, R.; Touboul, E.; Zarcone, C. Numerical models and experiments on immiscible displacements in porous media. *J. Fluid Mech.* **1988**, *189*, 165–187. [[CrossRef](#)]
30. Sakaida, S.; Tabe, Y.; Chikahisa, T. Large scale simulation of liquid water transport in a gas diffusion layer of polymer electrolyte membrane fuel cells using the lattice Boltzmann method. *J. Power Sources* **2017**, *361*, 133–143. [[CrossRef](#)]
31. Porter, M.L.; Coon, E.T.; Kang, Q.; Moulton, J.D.; Carey, J.W. Multicomponent interparticle-potential lattice Boltzmann model for fluids with large viscosity ratios. *Phys. Rev. E* **2012**, *86*, 036701. [[CrossRef](#)] [[PubMed](#)]
32. d’Humières, D. Multiple-relaxation-time lattice Boltzmann models in three dimensions. *Philos. Trans. R. Soc. Lond. A Math. Phys. Eng. Sci.* **2002**, *360*, 437451. [[CrossRef](#)] [[PubMed](#)]
33. Aursjø, O.; Jettestuen, E.; Vinningland, J.L.; Hiorth, A. On the inclusion of mass source terms in a single-relaxation-time lattice Boltzmann method. *Phys. Fluids* **2018**, *30*, 057104. [[CrossRef](#)]
34. Chen, L.; Zhang, R.; Kang, Q.; Tao, W. Pore-scale study of pore-ionomer interfacial reactive transport processes in proton exchange membrane fuel cell catalyst layer. *Chem. Eng. J.* **2020**, *391*, 123590. [[CrossRef](#)]
35. Chen, L.; Kang, Q.; Tao, W. Pore-scale numerical study of multiphase reactive transport processes in cathode catalyst layers of proton exchange membrane fuel cells. *Int. J. Hydrogen Energy* **2021**, *46*, 13283–13297. [[CrossRef](#)]
36. Chen, L.; Zhang, R.; He, P.; Kang, Q.; He, Y.-L.; Tao, W.-Q. Nanoscale simulation of local gas transport in catalyst layers of proton exchange membrane fuel cells. *J. Power Sources* **2018**, *400*, 114–125. [[CrossRef](#)]
37. Fang, W.; Tang, Y.; Chen, L.; Kang, Q.; Tao, W. Influences of the perforation on effective transport properties of gas diffusion layers. *Int. J. Heat Mass Transf.* **2018**, *126*, 243–255. [[CrossRef](#)]

Article

A Thermodynamic Analysis of an Air-Cooled Proton Exchange Membrane Fuel Cell Operated in Different Climate Regions

Torsten Berning  and Søren Knudsen Kær 

Department of Energy Technology, Aalborg University, 9100 Aalborg, Denmark; skk@et.aau.dk

* Correspondence: tbe@et.aau.dk

Received: 23 April 2020; Accepted: 18 May 2020; Published: 20 May 2020



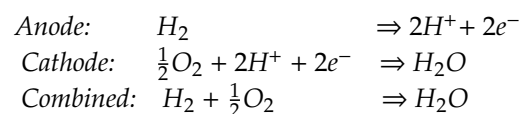
Abstract: A fundamental thermodynamic analysis of an air-cooled fuel cell, where the reactant air stream is also the coolant stream, is presented. The adiabatic cell temperature of such a fuel cell is calculated in a similar way as the adiabatic flame temperature in a combustion process. Diagrams that show the dependency of the cathode outlet temperature, the stoichiometric flow ratio and the operating cell voltage are developed. These diagrams can help fuel cell manufacturers to identify a suitable blower and a suitable operating regime for their fuel cell stacks. It is found that for standard conditions, reasonable cell temperatures are obtained for cathode stoichiometric flow ratios of $\xi = 50$ and higher, which is in very good agreement with manufacturer's recommendations. Under very cold ambient conditions, the suggested stoichiometric flow ratio is only in the range of $\xi = 20$ in order to obtain a useful fuel cell operating temperature. The outside relative humidity only plays a role at ambient temperatures above 40 °C, and the predicted stoichiometric flow ratios should be above $\xi = 70$ in this region. From a thermodynamic perspective, it is suggested that the adiabatic outlet temperature is a suitable definition of the fuel cell operating temperature.

Keywords: air-cooled proton exchange membrane fuel cells; adiabatic fuel cell temperature; thermodynamic analysis of proton exchange membrane fuel cells

1. Introduction

Air-cooled, low-temperature proton exchange membrane fuel cells (PEMFCs) are attractive for applications in the range of up to a few kW. Among the salient features is their simplicity of operation because they do not need a secondary coolant loop. The major disadvantage is the relatively low observed maximum current density of around 0.3–0.4 A/cm², which severely limits the power density [1]. Moreover, it is often difficult to operate these fuel cells in extreme climate conditions.

The principle of air-cooled fuel cells is the same as of liquid-cooled fuel cells: oxygen from air is combined with hydrogen to produce water and electricity. A certain amount of waste heat is produced due to overpotentials that predominantly occur at the fuel cell catalysts and inside the proton conductive membrane. The half-cell reactions are:



The electrons produced by the anode half-cell reaction are driven through an external circuit to the cathode by the electro-motive force, and the protons migrate through the polymer electrolyte membrane, which is proton conductive and electron repellent. In order to have the reactions occurring at an appreciable rate, overpotentials have to be applied, and these are the sources of waste heat.

While the theoretical cell potential between anode and cathode based on thermodynamics should be 1.23 V, practical operating voltages are 0.5–0.8 V. In order to obtain an appreciable voltage, numerous single fuel cells are combined in a fuel cell stack, where the stack voltage is the sum of the individual cell voltages and the current that is drawn through all cells in series. A simple schematic of a fuel cell is shown in Figure 1.

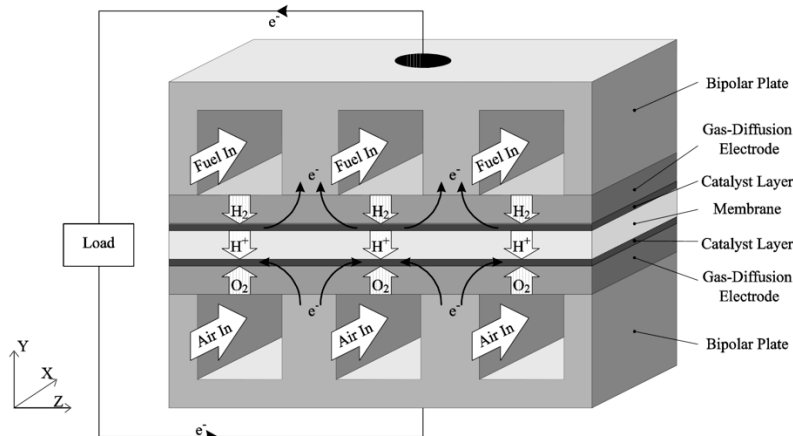


Figure 1. Proton exchange membrane fuel cell (PEMFC) schematic [2].

The thermo-neutral potential of the fuel cell reaction is 1.482 V, assuming that the product water is in the liquid phase [3]. The corresponding potential based on the lower heating values is 1.254 V [3]. The difference between the thermo-neutral potential and the fuel cell operating voltage multiplied with the fuel cell current density is the amount of waste heat that is produced inside the fuel cell, and the fuel cell efficiency is directly proportional to the fuel cell voltage.

In air-cooled, low-temperature PEMFCs, the waste heat is removed by excessive air that is being fed to the fuel cell. Therefore, the reactant air is, at the same time, the coolant air, and the stoichiometric flow ratio, ξ , must be high. Such units are already widely commercially available, a leading manufacturer being Ballard Power Systems [4].

One of the disadvantages of air-cooled PEMFCs is their low maximum current density of only around 0.4 A/cm² (e.g., References [5,6]), which severely limits the power density. By comparison, liquid-cooled PEMFCs that are being developed for automotive applications have a maximum current density of up to 2.0 A/cm², which lead to power densities in the range of 1.0 W/cm². It should be a goal to increase the maximum current density that can be drawn from an air-cooled fuel cell because this will lead to a substantial increase in their power density. It is clear that such an increase in power density also leads to a cost reduction.

Since the reactant air is directly taken from the environment, the performance and thermal management of these fuel cells is very sensitive to the ambient conditions. While it is no problem to operate such a fuel cell stack at an ambient temperature of 25 °C and typical relative humidity levels for temperate climate regions, the air-cooled fuel cell operation becomes less stable in regions with extreme temperatures. These systems are also placed in remote regions with extreme climates, and stable operation must be ensured. Thus, there is a need to fundamentally understand the impact of the ambient temperature on the expected performance or even the possibility to operate such a stack at extreme conditions.

Figure 2 summarizes suitable operating ranges as identified experimentally by Ballard Power Systems [4]. The nominal power density at standard conditions is around 0.225 W/cm² and the maximum current density is around 0.4 A/cm² [4]. Depending on the outside conditions, the cathode stoichiometric flow ratio is typically in the region $\xi_{ca} = 50$ –120, and the stack performance was observed to become unstable below a cathode side stoichiometric flow ratio of $\xi_{ca} = 20$. The ambient relative humidity has a stronger effect at temperatures higher than 40 °C, and the effect on the performance

is stronger in very dry regions. On the anode side, the stoichiometric flow ratio must be as low as possible in order to preserve the hydrogen, and in practice, stacks are operated below an anode side stoichiometry of $\xi_{an} = 1.1$ [4].

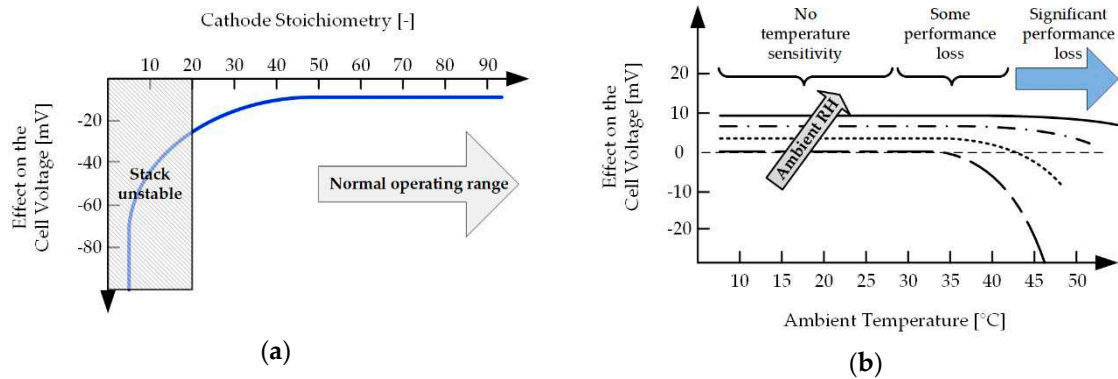


Figure 2. Effect of (a) the stoichiometric flow ratio and (b) of the ambient relative humidity and temperature on the performance of an air-cooled fuel cell stack. Adapted from Reference [4] with permission from Ballard Power Systems, January 2019.

Over the past decade, air-cooled fuel cells have been studied by several research groups. An important distinction to make is between (i) air-breathing fuel cells that rely on natural convection to provide the reactant air and which can be used for power ranges up to 100 W, and (ii) air-cooled fuel cells, where the reactant air is provided by a fan or compressor which necessitates work and increases the system complexity [7]. The latter are being considered for remote power supply, such as telecom back-up, and they operate in power ranges of up to a few kW. Because the reactant air is directly taken from and removed to the environment, this type of fuel cell is also termed an open cathode fuel cell.

Jeong et al. [8] conducted experiments on air-breathing fuel cells in a climate chamber where the operating conditions were varied. The recorded maximum current density was 0.4 A/cm^2 , and the power density was below 0.2 W/cm^2 . The anode was operated on dry hydrogen, and the water balance of the cell was measured by placing a water-absorbing material in the anode outlet and weighing the amount of water that has accumulated over a certain amount of time. The recorded water balance results were in very good agreement with our own experiments [9].

Publications of experimental studies on an existing commercial stack included Zhu et al. [5], Del Real et al. [6] and Adzakpa et al. [10]. All these groups reported current densities below 0.4 A/cm^2 .

The publication by Wu et al. [11] included a detailed literature study, and this group conducted experiments on a single cell and a stack that consisted of 5 cells. The cells were operated on humidified hydrogen at 55 °C at the anode and dry, ambient air at the cathode. The observed maximum current density for the single fuel cell experiments was around 0.3 A/cm^2 , and in case of the stack, it was below 0.25 A/cm^2 . There was no additional heating or cooling in the end plates and the results showed that the center temperature was 8 °C higher than the outer cells near the end plates.

Beside these experimental research efforts, several groups have conducted modeling studies to better understand heat and mass transfer in air-cooled PEMFCs. Sasmito et al. [12–15] published several computational fluid dynamics studies that included the predicted cell performance using the commercial software ANSYS Fluent. In Reference [12], this group investigated the placement of the fan and the effect of the channel height on the predicted performance and pressure drop. One finding was that the height of the cathode channels had a strong impact on the maximum current density, which was slightly above 0.3 A/cm^2 . In Reference [13], this group compared the performance of the cell for a natural convection stack and a forced convection stack, where the fan was placed before the stack and the fan power was varied. For forced convection, the maximum current density was 0.35 A/cm^2 before the stack was overheated, while it was below 0.2 A/cm^2 for natural convection. A novel flow reversal concept was then proposed by the same group in Reference [14], where a fan was placed before

and behind the stack and flow shifting was introduced with the goal of preventing stack overheating. While the model predicted a temperature reversal according to the periodicity of the flow shifting, no performance improvement was indicated. However, this concept helped to reduce the temperature gradients and better understand the frequency of the flow reversal. Finally, the selection of the fan based on different fan types with different performance curves was studied in Reference [15].

Shahsavari et al. [16] and Akbari et al. [17] developed a single-phase computational model of an air-cooled fuel cell using COMSOL Multiphysics®. The focus was put on a better understanding of the thermal management and the prediction of the maximum stack temperature as well as the main temperature gradient, which occurs in the flow direction. They simulated a commercial fuel cell stack by Ballard Power Systems and obtained very good agreement between their modeling predictions and the measured maximum temperature. Unfortunately, performance data or maximum current densities obtainable from that fuel cell stack were not released.

Other, very interesting work on air-cooled fuel cells was published by Meyer et al. [18,19]. Their studies focused on a commercial fuel cell design by Intelligent Energy, and the fuel cells differ from the above-listed stacks in that air is used as a coolant in separate cooling channels. The reactant air is fed in flow channels at a low stoichiometry. These air-cooled fuel cells are consequently more similar to liquid-cooled fuel cells, which was also pointed out by Sasmito et al. [13].

More work on air-cooled fuel cell stacks that have separate cooling channels include the study by Chen et al. [20], who developed a high-power air-cooled fuel cell stack with a current density above 0.8 A/cm^2 . The resulting power density was an impressive 0.6 W/cm^2 , and the stoichiometric flow ratio of the reactant air was only 1.5–2.0 and below. However, the cooling channels accounted for 55% of the bipolar plates' frontal area, which also means that the membrane-electrode-assembly had to be larger compared to, e.g., a Ballard stack. The active area of that stack was roughly 113 cm^2 and the maximum current was 100 A. The resulting power output was 2.55 kW.

Finally, a very good overview of the different cooling strategies in PEMFC stacks was given by Zhang and Kandlikar [21], while Flückiger et al. [22] conducted a thermal modeling analysis of an air-cooled fuel cell stack with edge cooling.

Air-cooled fuel cells are often used as telecom back-up applications in regions with extreme climates. In order to understand, under which conditions such fuel cells may operate, a thermodynamic analysis based on the first law of thermodynamics is conducted in this work. The calculations presented here are inspired by the calculation of the adiabatic flame temperature in a combustion process, and it will be shown that the outlet temperature of the reactant gases depend only on the ambient conditions, the stoichiometric flow ratio of the cathode air (the anode side stoichiometry is fixed to a low value) and the operating cell voltage. The latter determines the amount of waste heat that has to be removed predominantly by the excess air. In doing so, feasible operating regimes for these air-cooled fuel cells are identified and compared to the empirically determined regimes by Ballard Power Systems.

The main motivation for the current study is therefore:

- A lack of fundamental understanding concerning the required amount of air to control the fuel cell temperature, i.e., the stoichiometric flow ratio.
- A lack of fundamental understanding of how the ambient conditions affect the required air flow rates, and under what conditions it is feasible to operate such a fuel cell stack without a preheater.
- A lack of fundamental understanding of which blower has to be paired with such an air-cooled fuel cell stack under various ambient conditions.

2. Formulation of the Molar Flow Rates and the Energy Balance

2.1. Assumptions

The analysis carried out below is conducted in a similar way as the calculation of the adiabatic flame temperature in a combustion process by applying the first law of thermodynamics. It is based on

assuming ideal gas behavior, and changes in potential and kinetic energy are neglected. Moreover, the calculations assume steady-state operation.

2.2. Thermodynamic System Considered

The system under consideration is shown in Figure 3. It is the goal to determine the adiabatic outlet temperature of the reactant gases, so all the waste heat is carried out of the cell in the form of internal heat and the temperature of the product gases is increased. In contrast to the calculation of the adiabatic flame temperature in a combustion process, the electrical work performed by the fuel cell has to be accounted for because it is clear that the adiabatic outlet temperature of a fuel cell depends strongly on the cell performance. For simplicity, it is assumed that anode and cathode gas streams enter and leave the cell at the same temperature. Under such conditions, the exact water balance of the fuel cell plays no role, i.e., it does not matter whether the product water leaves from the cathode side or anode side because the water vapor leaves the cell at the same temperature.

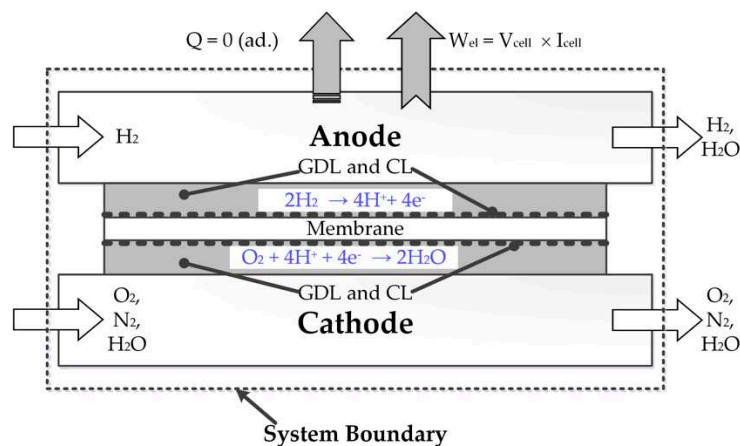


Figure 3. System boundary for the first-law analysis.

2.3. Molar Inlet Streams

In order to conduct a first-law analysis of an air-cooled system, the molar flow rates have to be formulated before the enthalpy streams are calculated. This has already been done in numerous previous articles in PEMFC (e.g., Reference [23]). The incoming molar stream of oxygen depends on the cathode stoichiometric flow ratio, ξ_{ca} , and the total current that is drawn from the fuel cell stack, I :

$$\dot{n}_{O_2,in} = \xi_{ca} \frac{I}{4F} \quad (1)$$

where F is Faraday's constant (96,485 C/mole). Note that the total current is not the physical current drawn from the fuel cell stack in experiments, but the physical current drawn from each cell multiplied with the number of cells in the stack.

On a molar basis, the incoming amount of nitrogen is:

$$\dot{n}_{N_2,in} = \frac{79}{21} \dot{n}_{O_2,in} = \frac{79}{21} \times \xi_{ca} \times \frac{I}{4F} \quad (2)$$

There is a certain amount of water vapor entering the cell that depends on the relative humidity of the ambient air, RH_{in} , which is introduced as a free parameter:

$$RH_{in} = \frac{p_{H_2O}}{p_{sat}(T)} = x_{H_2O} \frac{p_{amb}}{p_{sat}(T)} = \frac{\dot{n}_{H_2O,in}}{\dot{n}_{tot,in}} \frac{p_{amb}}{p_{sat}(T)} \quad (3)$$

From this, it follows that:

$$\dot{n}_{H_2O,in} = RH_{in} \times \frac{p_{sat}(T)}{p_{amb}} \times \dot{n}_{tot,in} = RH_{in} \times \frac{p_{sat}(T)}{p_{amb}} \times (\dot{n}_{H_2O,in} + \dot{n}_{O_2,in} + \dot{n}_{N_2,in}) \quad (4)$$

which results in:

$$\dot{n}_{H_2O,in} = RH_{in} \times \left(\frac{p_{amb}}{p_{sat}(T)} - RH_{in} \right)^{-1} \times (\dot{n}_{O_2,in} + \dot{n}_{N_2,in}) \quad (5)$$

It is desirable to express the amount of water entering the cell as a function of the current and the stoichiometry, similar to the oxygen and nitrogen stream. Inserting Equations (1) and (2) and reformulation yields:

$$\dot{n}_{H_2O,in} = RH_{in} \times \left(\frac{p_{amb}}{p_{sat}(T)} - RH_{in} \right)^{-1} \times \frac{1}{0.21} \times \xi_{ca} \frac{I}{4F} \quad (6)$$

The ratio between the water vapor flux and the incoming amount of oxygen is thus:

$$\frac{\dot{n}_{H_2O,in}}{\dot{n}_{O_2,in}} = \frac{1}{0.21} \times RH_{in} \times \left(\frac{p_{amb}}{p_{sat}(T)} - RH_{in} \right)^{-1} \quad (7)$$

The saturation pressure is only a function of the temperature and it can be conveniently expressed by Antoine's equation:

$$p_{sat}(T) = D \times \exp\left(A - \frac{B}{C + T}\right) \quad (8)$$

where $A = 8.07131$, $B = 1730.63$, $C = 233.426$ and D is introduced to convert from the unit (mmHg) into (Pa), and it is 133.233. T is the temperature given in °C. For an ambient temperature of 25 °C, the saturation pressure is thus 3158 Pa. Assuming an atmospheric total pressure, the molar flow rate of water vapor is, at a maximum ($RH_{in} = 1$), 15.3% that of oxygen.

At the anode side, dry hydrogen is assumed to enter the cell at a specified stoichiometric flow ratio:

$$\dot{n}_{H_2,in} = \xi_{an} \frac{I}{2F} \quad (9)$$

2.4. Molar Outlet Streams

For the molar stream of oxygen leaving the cell, it holds that:

$$\dot{n}_{O_2,out} = (\xi_{ca} - 1) \frac{I}{4F} \quad (10)$$

and the stream of the inert nitrogen is:

$$\dot{n}_{N_2,out} = \dot{n}_{N_2,in} = \frac{79}{21} \times \xi_{ca} \times \frac{I}{4F} \quad (11)$$

The water at the outlet is the amount that has entered the cell plus the product water. In this case, the overall water balance of the fuel cell does not matter as both the anode and outlet stream are assumed to leave the cell at the same temperature. In case of doubt, it may be assumed that all of the product water leaves at the cathode side owing to the very low anode side stoichiometric flow ratio.

$$\dot{n}_{H_2O,out} = \dot{n}_{H_2O,in} + \frac{I}{2F} = RH \times \left(\frac{p_{amb}}{p_{sat}(T)} - RH \right)^{-1} \times \frac{1}{0.21} \times \xi_{ca} \frac{I}{4F} + \frac{I}{2F} \quad (12)$$

2.5. Formulation of the Energy Balance

Applying the first law of thermodynamics to an air-cooled PEMFC according to Figure 3, it holds that:

$$Q - W_{el} = H_{prod} - H_{react} \quad (13)$$

here, Q is the heat loss of the cell and W_{el} is the work that is extracted from the cell. In the current case, the system is considered adiabatic, $Q = 0$, and W_{el} is expressed as:

$$W_{el} = V_{cell} \times I_{cell} \quad (14)$$

Because the system is assumed to be adiabatic, the calculated temperature of the outlet gases is at a maximum. If the amount of heat loss from the stack to the surroundings is known, it may be entered here. The current analysis reveals no information about the temperature distribution inside the fuel cell stack, where the local temperature can be higher than the adiabatic outlet temperature of the reactant gases. Such a temperature distribution may be obtained by a detailed analysis, as carried out by Shahsavari et al. [16].

Assuming ideal gas behavior, the enthalpy streams can be calculated as follows:

$$H = \sum \dot{n}_i h_i = \sum \dot{n}_i [h_f^0 + (h - h^0)] = \sum \dot{n}_i [h_f^0 + c_p(T - T^0)] \quad (15)$$

where h indicates molar enthalpies in (J/mol). The molar enthalpy of any species consists of two terms: the enthalpy of formation, h_f^0 , at 25 °C and 1 atm and the sensible enthalpy due to a temperature increase. The enthalpy of formation for stable elements like oxygen, nitrogen and hydrogen is zero, whereas the enthalpy of formation, h_f^0 , of liquid water vapor is $-285,830$ J/mol and of water vapor is $-241,820$ J/mol [24].

For the calculation of the adiabatic gas outlet temperatures, the first law of thermodynamics thus reduces to:

$$W_{el} = \sum \dot{n}_{prod} h_{prod} - \sum \dot{n}_{react} h_{react} \quad (16)$$

The required properties are listed in Table 1.

Table 1. Gas properties at 298 K [24].

Species	M (kg/mol)	c_p (J/mol-K)	h^0 (J/mol)
Oxygen	0.032	30.000	8682
Nitrogen	0.028	29.484	8669
Hydrogen	0.002	28.614	8468
Water Vapor	0.018	33.462	9904

For demonstration purposes only, we assume the incoming gas stream of the air-cooled system to be at the standard conditions of 25 °C and 1 atm, so that the incoming enthalpy streams of oxygen, nitrogen and hydrogen are zero compared to the standard condition. Moreover, it is assumed for simplicity that the incoming air is completely dry so that there is no water vapor entering. Therefore, according to Equation (15), the incoming enthalpy stream is zero relative to the standard conditions. The outlet pressure of the fuel cell shall also be assumed to be 1 atm.

Inserting the above expressions into the energy balance then results in:

$$V_{cell} \times I_{cell} = \dot{n}_{O_2, out} (h - h^0)_{O_2} + \dot{n}_{N_2, out} (h - h^0) + \dot{n}_{H_2, out} (h - h^0) + \dot{n}_{H_2O, out} (h_f^0 + h - h^0) \quad (17)$$

The unit on both sides is in Watts, and it is observed that the enthalpy of formation is only considered for the water. So far, we have not decided whether the product water will be in gas or liquid phase. Obviously, the maximum cell temperature will be lower when the product water is in the gas phase, but it depends on the outlet temperature when the outlet gas phase will become saturated. Given the fact that these fuel cells operate on ambient air which is typically heated up inside the cell by 20–30 °C at a high stoichiometric flow ratio, it may be assumed that the product water leaves the cell in the vapor phase.

It is observed that, according to Equations (1), (2) and (5), the molar flow rates depend directly on the cell current, I_{cell} , which means that it can be canceled out in Equation (17). Inserting the molar flow rate and canceling yields:

$$\begin{aligned}
 V_{cell} = & \frac{1}{4F} \times (\xi_{ca} - 1) \times \left(h_{O_2}(T_{out}) - 8682 \frac{\text{kJ}}{\text{kmole}} \right) \\
 & + \frac{1}{4F} \times 3.762 \times \xi_{ca} \times \left(h_{N_2}(T_{out}) - 8669 \frac{\text{kJ}}{\text{kmole}} \right) \\
 & + \frac{1}{2F} \times (\xi_{an} - 1) \times \left(h_{H_2}(T_{out}) - 8468 \frac{\text{kJ}}{\text{kmole}} \right) \\
 & + \left[RH \times \left(\frac{p_{amb}}{p_{sat}(T)} - RH \right)^{-1} \times \frac{1}{0.21} \times \frac{\xi_{ca}}{4F} + \frac{1}{2F} \right] \\
 & \times \left(-241,820 \frac{\text{kJ}}{\text{kmole}} + h_{H_2O}(T_{out}) - 8468 \frac{\text{kJ}}{\text{kmole}} \right)
 \end{aligned} \tag{18}$$

From Equation (18), it follows that there are only four independent parameters in this analysis: the cell voltage, V , the stoichiometric flow ratio of the cathode side, ξ_{Ca} , the outside relative humidity, RH , and the temperature of the outlet gases, T_{out} . This leaves aside the anode stoichiometric flow ratio, which should always be as close to unity as possible, which leads to the fact that the anode enthalpy stream is negligible. In combustion analysis, it is common to apply an iterative method to determine the temperature of the outlet gases. On the other hand, it is just as convenient to construct diagrams where the cell voltage is the y -axis and the adiabatic outlet temperature of the gases is the x -axis. With the anode stoichiometric flow ratio fixed at a low value of $\xi_{an} = 1.1$, and for a given ambient pressure and relative humidity, the cathode stoichiometric flow ratio is then the only free parameter left and a different value for ξ_{ca} will give a different curve in the V - T_{ad} -Diagram. Such diagrams can be constructed for different ambient conditions in which the fuel cell is placed, and these are shown and analyzed in the next section.

3. A Thermodynamic Analysis of Air-Cooled PEM Fuel Cells Using V - T_{ad} -Diagrams

The above equations can now be applied to study the adiabatic cell temperature, i.e., the temperature of the product gases assuming all the waste heat is carried out by the flew gases. To this end, the above equations can be entered into spreadsheet calculation software where the outlet temperature is the adjustable parameter. As can be seen from Equation (18), the relative difference between the inlet and outlet molar enthalpy streams can be given in terms of a voltage. This voltage depends only on the temperature of the outlet gases and the outside conditions. Besides the cell voltage, the cathode stoichiometric flow ratio is the most important parameter. Clearly, the ambient air temperature and the relative humidity have an impact on the adiabatic outlet temperature. In the following, four different cases will be examined in detail. In all cases, the ambient pressure was assumed to be 1 bar, but according to Equation (18), that property only plays a role in the calculation of the amount of water vapor that enters the cell.

3.1. Case 1: Standard Conditions

Standard operating conditions are that the inlet gas streams enter at 25 °C. It is assumed that the relative humidity of the ambient air was 30%. Figure 4 shows the resulting dependency between the gas outlet temperature, the stoichiometric flow ratio and the cell voltage. All the lines have a

negative slope because if the cell voltage decreases for a given stoichiometric flow ratio, more waste heat is produced and therefore, the cathode outlet temperature increases. The right-hand side of Figure 4 zooms in on the region of interest. The supplier of our fuel cell stack states that the stack outlet temperature should not exceed 60 °C and the stack voltage should be below 0.9 V to avoid irreversible degradation [4]. On the other hand, the voltage should be above 0.6 V, if possible, to ensure satisfactory cell performance. From this diagram, a working point under the given operating conditions may be read, e.g., a stoichiometry of 50 and a cell voltage of 0.7 V. Under these conditions, the adiabatic outlet temperature of the reactants will be 50 °C. Thus, the thermodynamic analysis yields a fundamental explanation of the preferred operating conditions, as specified by the manufacturer.

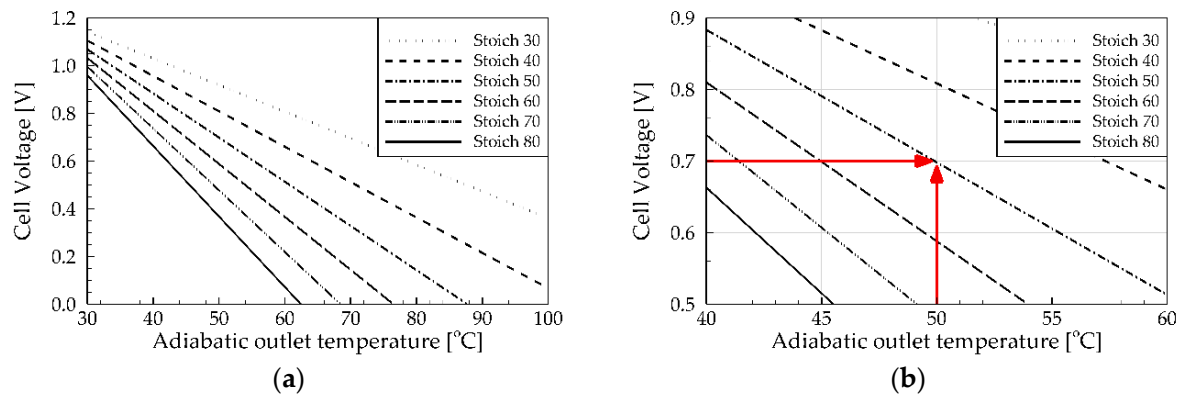


Figure 4. Dependency of the adiabatic outlet temperatures of the product stream on the operating cell voltage. The incoming conditions were a temperature of 25 °C and a relative humidity of 30%. (a) Entire voltage range, (b) close-up on the region of interest.

Varying the RH of the inlet air has only a very small impact on the results (not shown), and this is also in good agreement with Figure 2. It is interesting to note that when the cell potential drops from 0.7 V to 0.6 V, the adiabatic outlet temperature increases by only 5 °C and it would even stay the same if the stoichiometric flow ratio would be increased from 50 to around 57. In practice, the fuel cell temperature is monitored in a position inside the cathode flow channel and adjusted by the fan drawing the air through the stack [4]. Overall, these diagrams suggest that there is no inherent reason why an air-cooled fuel cell should not be operational at high current densities.

3.2. Case 2: Cold and Dry Conditions

It is a requirement that fuel cell systems for telecom back-up applications also operate in an environment with a temperature as low as −40 °C. For the sake of demonstration, it is assumed that cold air at −20 °C is indeed fed to the fuel cell. Obviously, such air cannot contain any water vapor, and the RH is set to zero (even if it would be set to 100%, there would be no water vapor entrained). Figure 5 indicates that the stoichiometric flow ratio is now a much more sensitive parameter compared to the previous case.

Reasonable cell outlet temperatures can be achieved by using a relatively low stoichiometric flow ratio between $\xi = 20$ and $\xi = 30$. An obvious problem is that the stoichiometry has to be very accurately controlled, otherwise it is nearly impossible to control the adiabatic outlet temperature. It can be seen from Figure 5 that a change of the stoichiometric flow ratio, from, e.g., $\xi = 22$ to $\xi = 24$, leads to a change in the adiabatic outlet temperature by around 5 °C. Therefore, it may be required to pre-heat the incoming air in such extreme climates.

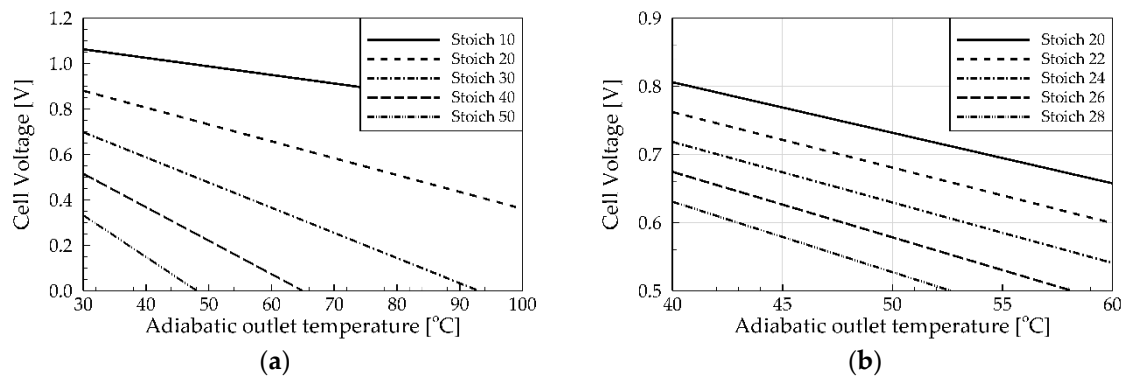


Figure 5. Dependency of the adiabatic outlet temperatures of the product stream on the operating cell voltage. The incoming conditions are a temperature of $-20\text{ }^{\circ}\text{C}$ and a relative humidity of 0%. (a) Entire voltage range, (b) close-up on the region of interest.

3.3. Case 3: Hot and Humid Conditions

A second extreme climate case is an ambient temperature of $40\text{ }^{\circ}\text{C}$ and an RH of 100%. As shown in Figure 6, in such a case, the stoichiometric flow ratio has to be chosen very high. Assuming a cell voltage of 0.7 V, the stoichiometric flow ratio would need to be in the range of $\xi = 75$ and higher to attain a reasonable adiabatic outlet temperature of $60\text{ }^{\circ}\text{C}$. Especially at elevated current densities, this would require a stronger blower. Thus, the blower specification is very tightly coupled to the fuel cell operating region. These diagrams clearly show that in every different climate zone, there is a different operating regime for the same hardware, which has to be carefully adjusted.

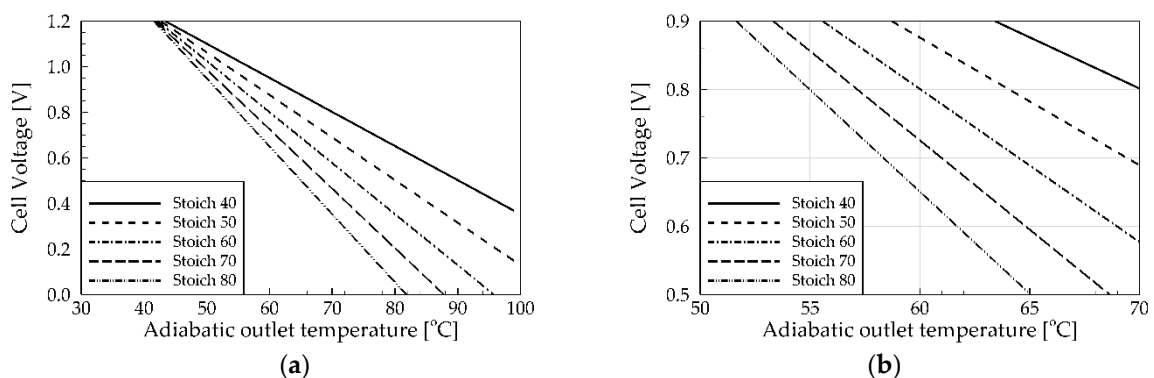


Figure 6. Dependency of the adiabatic outlet temperatures of the product stream on the operating cell voltage. The incoming conditions were a temperature of $40\text{ }^{\circ}\text{C}$ and a relative humidity of 100%. (a) Entire voltage range, (b) close-up on the region of interest.

3.4. Case 4: Hot and Dry Conditions

Finally, hot and dry outside conditions shall be investigated. Figure 7 shows the diagrams for an inlet temperature of $40\text{ }^{\circ}\text{C}$ and an outside relative humidity of 30%. While the inlet RH at lower temperatures has a weak effect on the ability to operate the cell, at elevated temperatures, this effect becomes larger. This is in very good accord with the operating conditions suggested by Ballard Power Systems [4]. From Figure 7, it is suggested to maybe choose a target cell voltage to 0.75 V in order to obtain the same adiabatic outlet temperature of $60\text{ }^{\circ}\text{C}$ for the same stoichiometric flow ratio of $\xi = 60$.

The question of how well the membrane is hydrated under such conditions is being addressed in a computational fluid dynamics study of the same fuel cell, with surprising results that have been published separately [25]. The current work focuses on thermodynamic aspects, and it can be seen that the adiabatic outlet temperature of the reactant gases can be calculated out of knowledge of the cell voltage and the stoichiometric flow ratio. The operating temperature of these air-cooled fuel cells is

usually adjusted by trial-and-error, and it may be concluded from the current analysis that the adiabatic outlet temperature is a suitable definition for the operating temperature of these fuel cells.

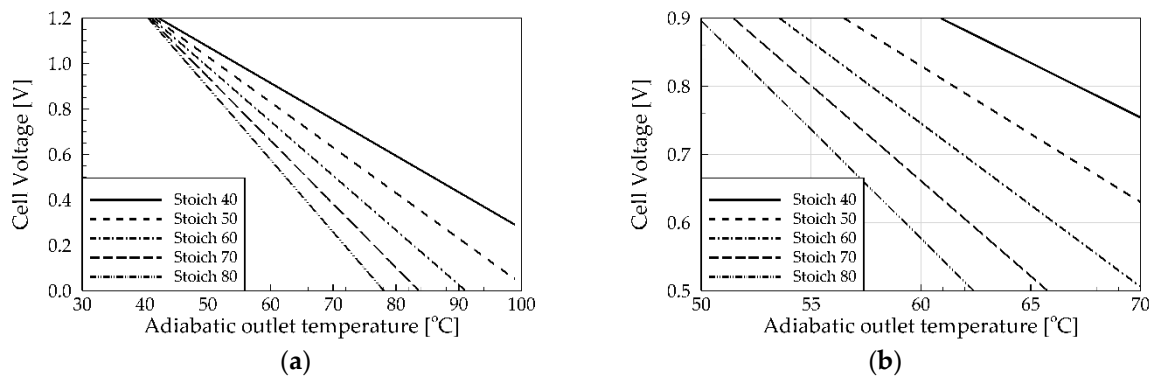


Figure 7. Dependency of the adiabatic outlet temperatures of the product stream on the operating cell voltage. The incoming conditions were a temperature of 40 °C and a relative humidity of 30%. (a) Entire voltage range, (b) close-up on the region of interest.

4. Conclusions

In this work, the first law of thermodynamics has been applied to an air-cooled fuel cell stack to calculate the adiabatic outlet temperature of the reactant gases in a similar way as is routinely done in combustion analysis. V - T_{ad} -Diagrams of the fuel cell voltage versus the adiabatic outlet temperature have been constructed that show the feasibility to operate the fuel cell in extreme climate conditions. For very cold inlet gases, the cathode stoichiometry has to be below $\xi = 30$ to attain reasonable cell operating temperatures. The diagrams have also shown that it is very important to supply all fuel cell channels with the same amount of air under cold conditions. Even a mal-distribution of less than 10% can lead to a cell-to-cell variation in the adiabatic outlet temperature of 5 °C, when generally, the cell-to-cell variation in temperature should be kept below 6 °C [4].

The second and third extreme climate cases were an outside temperature of 40 °C and either fully humidified or very low outside relative humidity. While the relative humidity generally plays a minor role in the construction of the diagrams, the inlet RH becomes more important at high outside temperatures, and this is in good agreement with the stack manufacturer's observations [4]. Stoichiometric flow ratios should be between $\xi = 60$ and $\xi = 80$ to keep the gas outlet temperatures within a reasonable region. Overall, the diagrams have shown that there is no inherent reason why air-cooled fuel cells cannot be operated at elevated current densities.

It is also important to realize that in the current study, it is assumed that all the waste heat is carried out by the reactant gases, i.e., that the stack is perfectly insulated. This was done for simplicity and to examine the extreme case. In real stacks, there is a certain amount of waste heat leaving the stack at the top and bottom, and the maximum temperature is often observed in the center of the stack [4].

While such a thermodynamic analysis gives valuable insight into the general feasibility to operate a fuel cell in extreme climate conditions, it does not allow a glimpse in the interior of the cell, and it did not give an answer to the question of why the limiting current density is only around 0.4 A/cm². From a thermodynamic perspective, a higher current might be attainable just by placing a larger fan behind the stack. Therefore, a computational fluid dynamics study has been conducted in order to shed light into the underlying heat and mass transfer that occurs inside such an air-cooled fuel cell [25].

5. Patent

Berning, T. Fuel cell assembly with a turbulence-inducing device for reduction of a temperature gradient. Patent No. WO/2019/120415, International Filing Date (17/12/2018).

Author Contributions: Conceptualization, T.B. and S.K.K.; methodology, T.B.; formal analysis, T.B.; resources, S.K.K.; writing—original draft preparation, T.B.; writing—review and editing, T.B. and S.K.K.; project administration, T.B. and S.K.K.; funding acquisition, S.K.K. All authors have read and agreed to the published version of the manuscript.

Funding: This research was funded by EUDP, Journal number 64012-0117, and carried out in collaboration with Dantherm Power A/S and Ballard Power Systems.

Conflicts of Interest: The authors declare no conflict of interest. The funders had no role in the design of the study; in the collection, analyses, or interpretation of data; in the writing of the manuscript, or in the decision to publish the results.

Nomenclature

A	constant in Antoine's equation ($A = 8.07131$)
B	constant in Antoine's equation ($B = 1730.63$)
C	constant in Antoine's equation ($C = 233.426$)
CL	Catalyst layer
c_p	specific heat and constant pressure (J/kg-K)
D	constant in Antoine's equation ($D = 133.233$)
GDL	Gas diffusion layer
h	specific enthalpy (J/mol)
H	enthalpy stream (W)
I	Fuel cell current (A)
i	Current density (A/cm ²)
F	Faraday's constant (96,487 C/mol)
M	Molecular Weight (kg/mol)
\dot{n}	Molar flow rate (mol/s)
PEMFC	Proton exchange membrane fuel cell
p	Pressure (Pa)
Q	Heat Loss (W)
RH	Relative humidity (-)
T	Temperature (°C)
V	Voltage (V)
W	Fuel cell work (W)

Subscripts

amb	ambient value
ad	adiabatic value
an	anode
ca	cathode
el	electric
f	formation value
i	denotes a species i
in	inlet value
out	outlet value
prod	product
react	reactant
sat	saturation value
tot	total value

Superscripts

0	standard value
---	----------------

Greek Symbols

ξ	Stoichiometric flow ratio (Stoich) (-)
-------	--

References

1. Sevjidsuren, G.; Uyanga, E.; Bumaa, B.; Temujin, E.; Altantsog, P.; Sangaa, D. Exergy analysis of 1.2 kW nexa fuel cell module. In *Clean Energy for Better Environment*; Aydinalp, C., Ed.; IntechOpen: London, UK, 2012.
2. Berning, T. Three-Dimensional Computational Analysis of Transport Phenomena in a PEM Fuel Cell. Ph.D. Thesis, University of Victoria, Victoria, BC, Canada, 2002.
3. Barbir, F. *PEM Fuel Cells—Theory and Practice*, 2nd ed.; Academic Press: Cambridge, MA, USA, 2012.
4. Ballard-Power-Systems-Inc. *Mark1020 ACS™ Fuel Cell Stack—Product Manual and Integration Guide*; MAN5100192-0F; Ballard-Power-Systems-Inc.: Burnaby, BC, Canada, 2008.
5. Zhu, W.H.; Payne, R.U.; Cahela, D.R.; Tatarchuk, B.J. Uniformity analysis at MEA and stack Levels for a Nexa PEM fuel cell system. *J. Power Sources* **2004**, *128*, 231–238. [[CrossRef](#)]
6. Del Real, A.J.; Arce, A.; Bordons, C. Development and experimental validation of a PEM fuel cell dynamic model. *J. Power Sources* **2007**, *173*, 310–324. [[CrossRef](#)]
7. Larminie, L.; Dicks, A. *Fuel Cell Systems Explained*, 2nd ed.; Wiley: Hoboken, NJ, USA, 2003.
8. Jeong, S.U.; Cho, E.A.; Kim, H.-J.; Lim, T.-H.; Oh, I.-H.; Kim, S.H. A study on cathode structure and water transport in air-breathing PEM fuel cells. *J. Power Sources* **2006**, *159*, 1089–1094. [[CrossRef](#)]
9. Al Shakhshir, S.; Berning, T. Employing hot wire anemometry to directly measure the water balance of a commercial proton exchange membrane fuel cell stack. *Int. J. Hydrog. Energy* **2016**, *5*, 183–188. [[CrossRef](#)]
10. Adzakpa, K.P.; Ramousse, J.; Dube, Y.; Akremi, H.; Agbossou, K.; Dostie, M.; Poulin, A.; Fournier, M. Transient air cooling thermal modeling of a PEM fuel cell. *J. Power Sources* **2008**, *179*, 164–176. [[CrossRef](#)]
11. Wu, J.; Galli, S.; Lagana, I.; Pozio, A.; Monteleone, G.; Yuan, X.Z.; Martin, J.; Wang, H. An air-cooled proton exchange membrane fuel cell with combined oxidant and coolant flow. *J. Power Sources* **2009**, *188*, 199–204. [[CrossRef](#)]
12. Sasmito, A.P.; Lum, K.W.; Birgersson, E.; Mujumdar, A.S. Computational study of forced air-convection in open-cathode polymer electrolyte fuel cell stacks. *J. Power Sources* **2010**, *195*, 5550–5563. [[CrossRef](#)]
13. Sasmito, A.P.; Birgersson, E.; Mujumdar, A.S. Numerical evaluation of various thermal management strategies for polymer electrolyte fuel cell stacks. *Int. J. Hydrog. Energy* **2011**, *36*, 12991–13007. [[CrossRef](#)]
14. Sasmito, A.P.; Birgersson, E.; Mujumdar, A.S. A novel flow reversal concept for improved thermal management in polymer electrolyte fuel cell stacks. *Int. J. Therm. Sci.* **2012**, *54*, 242–252. [[CrossRef](#)]
15. Sasmito, A.P.; Birgersson, E.; Lum, K.W.; Mujumdar, A.S. Fan selection and stack design for open-cathode polymer electrolyte fuel cell stacks. *Renew. Energy* **2012**, *37*, 325–332. [[CrossRef](#)]
16. Shahsavari, S.; Desouza, A.; Bahrami, M.; Kjeang, E. Thermal analysis of air-cooled PEM fuel cells. *Int. J. Hydrog. Energy* **2012**, *37*, 18261–18271. [[CrossRef](#)]
17. Akbari, M.; Tamayol, A.; Bahrami, M. Thermal assessment of convective heat transfer in air-cooled PEMFC stacks: An experimental study. *Energy Procedia* **2012**, *29*, 1–11. [[CrossRef](#)]
18. Meyer, Q.; Ashton, S.; Boillat, P.; Cochet, M.; Engebretsen, E.; Finegan, D.P.; Lu, X.; Bailey, J.J.; Mansro, N.; Abdulaziz, R.; et al. Effect of gas diffusion layer properties on water distribution across air-cooled, open-cathode polymer electrolyte fuel cells: A combined exsitu X-ray tomography and in-operando neutron imaging study. *Electrochim. Acta* **2016**, *211*, 478–487. [[CrossRef](#)]
19. Meyer, Q.; Ashton, S.; Jervis, R.; Finegan, D.P.; Boillat, P.; Cochet, M.; Curnick, O.; Reisch, T.; Adcock, P.; Shearing, P.R.; et al. The hydro-electro-thermal performance of air-cooled, open-cathode polymer electrolyte fuel cells: Combined localised current density, temperature and water mapping. *Electrochim. Acta* **2015**, *180*, 307–315. [[CrossRef](#)]
20. Chen, C.-Y.; Huang, K.-P.; Yan, W.-M.; Lai, M.-P.; Yang, C.-C. Development and performance diagnosis of a high power air-cooled PEMFC stack. *Int. J. Hydrog. Energy* **2016**, *41*, 11784–11793. [[CrossRef](#)]
21. Zhang, G.; Kandlikar, S.G. A critical review of cooling techniques in proton exchange membrane fuel cells. *Int. J. Hydrog. Energy* **2012**, *37*, 2412–2429. [[CrossRef](#)]
22. Flückiger, R.; Tiefenauer, A.; Ruge, M.; Aebi, C.; Wokaun, A.; Büchi, F.N. Thermal analysis and optimization of a portable, edge-air-cooled PEFC stack. *J. Power Sources* **2007**, *172*, 324–333. [[CrossRef](#)]
23. Berning, T. The dew point temperature as a criterion for optimizing operating conditions of proton exchange membrane fuel cells. *Int. J. Hydrog. Energy* **2012**, *37*, 10265–10275. [[CrossRef](#)]

24. Cengel, Y.; Boles, M.A. *Thermodynamics—An Engineering Approach*, 6th ed.; McGraw Hill: New York, NY, USA, 2007.
25. Berning, T. A Numerical investigation of heat and mass transfer in air-cooled proton exchange membrane fuel cells. In Proceedings of the ASME—JSME—KSME Joint Fluids Engineering Conference 2019, AJKFluids2019, San Francisco, CA, USA, 28 July–1 August 2019; Volume 2.



© 2020 by the authors. Licensee MDPI, Basel, Switzerland. This article is an open access article distributed under the terms and conditions of the Creative Commons Attribution (CC BY) license (<http://creativecommons.org/licenses/by/4.0/>).

Article

Heat Transfer Optimization of NEXA Ballard Low-Temperature PEMFC

Artem Chesalkin ^{1,*}, Petr Kacor ² and Petr Moldrik ²

¹ ENET Centre—Research Centre of Energy Units for Utilization of Non Traditional Energy Sources, VŠB-TUO, 17. Listopadu 2172/15, 708 00 Ostrava-Poruba, Czech Republic

² Department of Electrical Power Engineering, VŠB-TUO, 17. Listopadu 2172/15, 708 00 Ostrava-Poruba, Czech Republic; petr.kacor@vsb.cz (P.K.); petr.moldrik@vsb.cz (P.M.)

* Correspondence: artem.chesalkin@vsb.cz

Abstract: Hydrogen is one of the modern energy carriers, but its storage and practical use of the newest hydrogen technologies in real operation conditions still is a task of future investigations. This work describes the experimental hydrogen hybrid energy system (HHS). HHS is part of a laboratory off-grid system that stores electricity gained from photovoltaic panels (PVs). This system includes hydrogen production and storage units and NEXA Ballard low-temperature proton-exchange membrane fuel cell (PEMFC). Fuel cell (FC) loses a significant part of heat during converting chemical energy into electricity. The main purpose of the study was to explore the heat distribution phenomena across the FC NEXA Ballard stack during load with the next heat transfer optimization. The operation of the FC with insufficient cooling can lead to its overheating or even cell destruction. The cause of this undesirable state is studied with the help of infrared thermography and computational fluid dynamics (CFD) modeling with heat transfer simulation across the stack. The distribution of heat in the stack under various loads was studied, and local points of overheating were determined. Based on the obtained data of the cooling air streamlines and velocity profiles, few ways of the heat distribution optimization along the stack were proposed. This optimization was achieved by changing the original shape of the FC cooling duct. The stable condition of the FC stack at constant load was determined.

Keywords: hydrogen; fuel cells; hydrogen hybrid energy system; thermography; CFD modeling; heat transfer; optimization



Citation: Chesalkin, A.; Kacor, P.; Moldrik, P. Heat Transfer Optimization of NEXA Ballard Low-Temperature PEMFC. *Energies* **2021**, *14*, 2182. <https://doi.org/10.3390/en14082182>

Academic Editors: Samuel Simon Araya and Jinliang Yuan

Received: 11 February 2021

Accepted: 12 April 2021

Published: 14 April 2021

Publisher's Note: MDPI stays neutral with regard to jurisdictional claims in published maps and institutional affiliations.



Copyright: © 2021 by the authors. Licensee MDPI, Basel, Switzerland. This article is an open access article distributed under the terms and conditions of the Creative Commons Attribution (CC BY) license (<https://creativecommons.org/licenses/by/4.0/>).

1. Introduction

Hydrogen technologies find their use in a wide range of mobile and stationary applications. One of the most developing and applied ways for renewable energy storage is a way of electrochemical energy storage [1]. Hydrogen hybrid systems (HHSs) can utilize renewable energy sources (RESs) and eliminate the fluctuations of their power output by energy storage in form of hydrogen. These types of hybrid systems were examined and tested by the authors in different studies [2–4]. Typically, HHSs consist of energy production units from RESs, combined with hydrogen production and storage unit for power-to-gas conversion (PtG), fuel cell (FC) unit, and classical backup energy storage in a battery bank [5].

The proton-exchange membrane fuel cell (PEMFC) is a promising, widely developed type of the FC that could be operated at the relatively wide temperature range and uses “green” hydrogen as an alternative energy carrier for the grid-connected and off-grid installations [6]. Cells are often combined in series—FC stack [7–9]. Figure 1 shows a simplified diagram of the hydrogen PEMFC in terms of its design and principle of operation, where FP—flow plates, GDL—gas diffusion layers, and CL—catalyst layers.

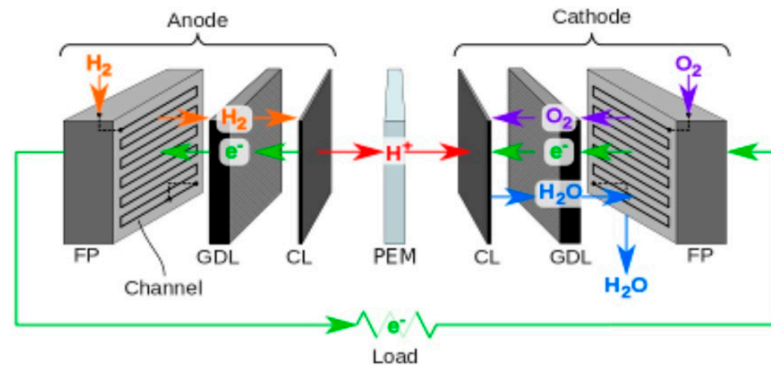


Figure 1. Construction and principle of hydrogen proton-exchange membrane fuel cell (PEMFC) [10,11].

Fuel cells use direct conversion of chemical energy into electric power, and that is the reason for their high efficiency and almost no emissions. The main type of FC emission is a thermal emission that occurs during FCs operation, especially at high loads. The FC voltage as a function of current density can be seen in Figure 2 below, where OCV is the open-circuit voltage. The value of 1.2 V represents a theoretically loss-free voltage. The actual cell voltage, including the off-load voltage, is always lower than this value.

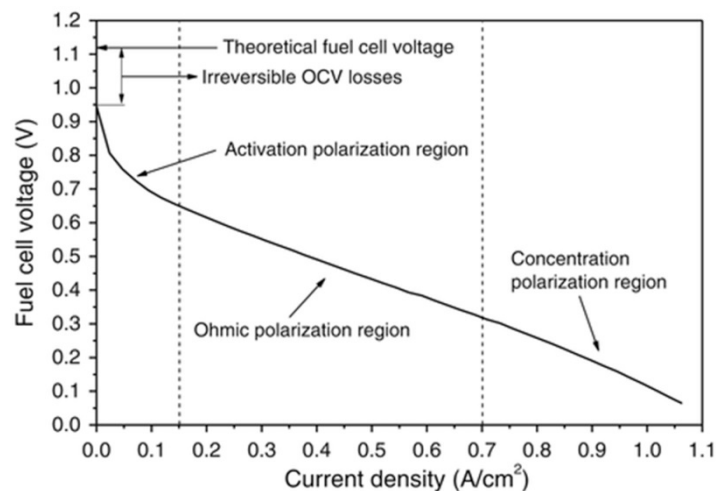


Figure 2. Fuel Cell (FC) polarization curve with voltage losses during FC load [12].

Each FC can produce the maximum theoretical voltage of 1.187 V (for 25 °C and 101.325 kPa). The FC efficiency is calculated as the ratio of the actually produced and the theoretically achievable cell voltage

$$\eta = \frac{V_{real}}{E_{cell}} = \frac{V_{real}}{1.187} \quad (1)$$

where E_{cell} refers to the voltage in every cell related to the Gibbs free energy. The real voltage in an actual cell is measured at the power load per cell as $V_{real} = 0.5\text{--}0.6$ V. The off-load voltage reaches the value of 1.1 V [13]. The typical service electrochemical efficiency per cell is approximately between 40% and 50% [14].

Studied NEXA Ballard PEMFC uses the air-based heat exchange system for stack cooling. High-temperature PEMFC provides easier heat regulation, in comparison with studied low-temperature PEMFC, due to higher working temperatures and using liquid refrigerants for stack cooling [15–17].

Several studies were focused on hydrogen storage methods development. In some cases, due to space limitation and pressure-based safety restrictions, it is possible to use hydrogen storage in a solid-state way in metal hydrides (MHs) [18–20]. Joint use of fuel cell

(FC) technologies with hydrogen storage systems based on metal hydrides (MHs) allows the utilization of FC excess heat energy for the MH hydrogen desorption process and thereby increases the HHS energy efficiency. MHs application for solar energy accumulation is one of the possible ways described by the authors in various papers [21,22]. In addition, using FCs and MHs in one system gives the possibility to provide the required pure hydrogen to the PEMFCs. LaNi—based alloys allow storing hydrogen at ambient temperatures of 25–40 °C and low pressures of 1.0–1.5 MPa, which makes the application of these alloys quite attractive in mentioned above specific conditions [23–28].

The complete experimental setup described in the work is an integral hydrogen hybrid system, which serves for the possibility of optimal energy storage from solar panels in various forms—in the form of electrical energy for direct use or storage in storage batteries, or in the form of gaseous hydrogen in classical gas cylinders and/or in a compact “solid” form in the form of metal hydrides.

One of the main components of this system is fuel cells and the associated fuel source, hydrogen, which, as mentioned above, can be stored in various forms. During the operation of the hybrid plant, overheating of the fuel cells was detected at loads close to maximum and automatic shutdown of fuel cells was observed at high loads when the ambient temperature rose above 25 degrees, while the maximum operating ambient temperature for this fuel cell declared in the documentation was 30 degrees. In this regard, the analysis of the fuel cell and the identification of local overheating zones were started, followed by the simulation of heat transfer along the entire stack of the fuel cell and modification of the elements of the cooling channel.

The main motivation of the work is the improvement in the FC cooling and heat transfer along the FC stack, which is an important issue of safe and efficient operation of the FC and hydrogen hybrid system (HHS) [29–31]. Experimental HHS was developed for joint MH and FC testing. This system, shown in Figure 3, basically consists of photovoltaic panels (PVs), a few power inverters batteries bank, hydrogen production, and storage units. Hydrogen could be stored in three different ways—in pressure vessels in a gaseous state, in metal hydrides in solid state, or converted to electricity via FC and directly used or stored in the battery bank. The lead batteries accumulation enables the storage of 550 kWh of power, and an additional 80 kWh can be stored in the lithium iron phosphate (LiFePO) batteries bank, which provides energy accumulation from the PV plant and avoid energy fluctuation for the stable H₂ production via water electrolysis process.

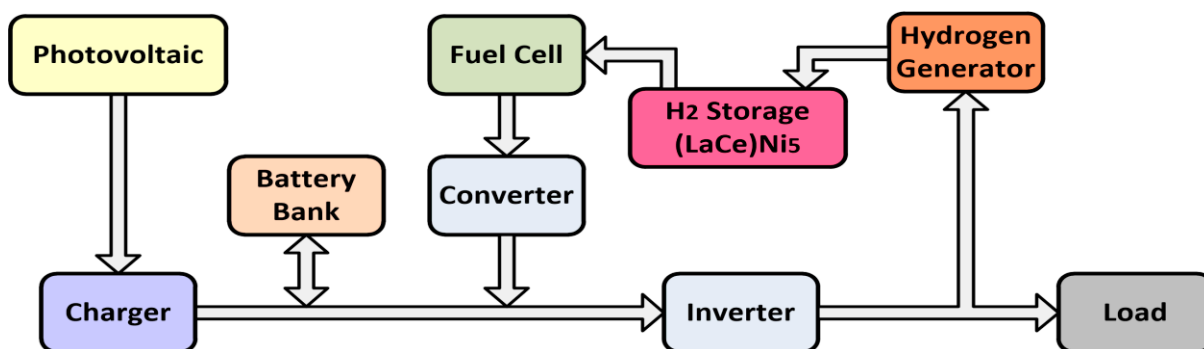


Figure 3. The basic scheme of the experimental hybrid energy system (HHS) energetic system.

According to the nameplate, the ambient operating temperature of the cell must be in the range of 3–30 °C. At a temperature around 22–25 °C, the maximum operating state cannot be reached due to local overheating of the PEMFC in its front part. This was the main reason to make an FC heat transfer optimization for more uniform stack cooling. The FC heat transfer could be studied using infrared (IR) thermography and appropriate PEMFC computational fluid dynamics (CFD) modeling [32]. IR thermography has been widely used in different industrial and research fields including analysis and cracks determine

in membrane materials and characterizing of PEMFC parameters [33–36]. Increasing the efficiency of FC cooling is indeed a popular topic in scientific studies and can be found in a number of literature sources [37,38]. Unfortunately, many authors focus their studies on the single cell and rarely assess the behavior of the PEMFC stack as a whole; therefore, the study of more uniform stack cooling was the main goal on the way of the FC heat transfer optimization.

2. Testing and Measurement Methods

The thermal field distribution over the low-temperature PEMFC was measured by the FLIR E45 thermal camera. The hydrogen produced via the anion-exchange membrane (AEM) electrolyzer with an output pressure of 3.0 MPa before entering the MH storage system or PEMFC passes through the pressure reducer. Heat field distribution across the surface of the PEMFC body was controlled by IR thermo-vision camera. Laboratory measurements of the heating curves of the NEXA module were conducted according to the block diagram shown in Figure 4.

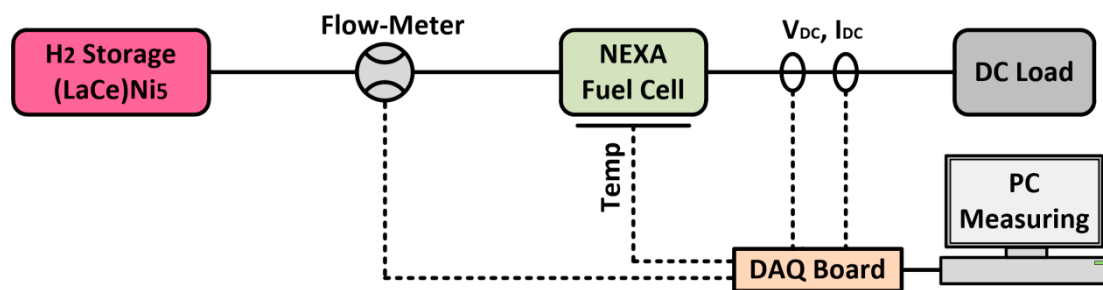


Figure 4. Diagram of the PEMFC heating distribution measurement.

The following measurements were conducted on the NEXA power module of PEMFC: Rated DC power output of this system is 1200 W; operating voltage range of the system is from 26 V (at rated power) to 42 V (no-load voltage); the total numbers of 47 cells are connected in series into the stack. The system further comprises ancillary equipment necessary for its operation, i.e., control unit, hydrogen delivery system, oxidant air supply, and cooling air supply (by cooling fan and compressor). The working parameters of the studied NEXA Ballard PEMFC are shown in Table 1.

Table 1. The main working parameters of fuel cells and hydrogen storage system [39].

NEXA Ballard LT PEMFC	
Characteristic	Value
Operation Temperature	65 °C
Rated Power	1200 W
Maximum Current I	230 A
Operating Voltage U	22–50 V
Active Area	120 cm ²
Max. H ₂ Consumption	18.5 L min ⁻¹
H ₂ Pressure	70–120 kPa

3. Experimental and Simulation Results

The measuring procedure consisted of measurements of the load characteristics of the NEXA module, its hydrogen and oxidant air consumption, water production, and the self-power consumption, which shows the relation of the power output drawn by the NEXA module from its own stack to ensure the operation of its own auxiliary devices at the certain power output. Figure 5 shows the load characteristics of the NEXA module. This module has soft source properties; the voltage of 42 V (at no load) drops to 26 V (at a rated power of 1200 W).

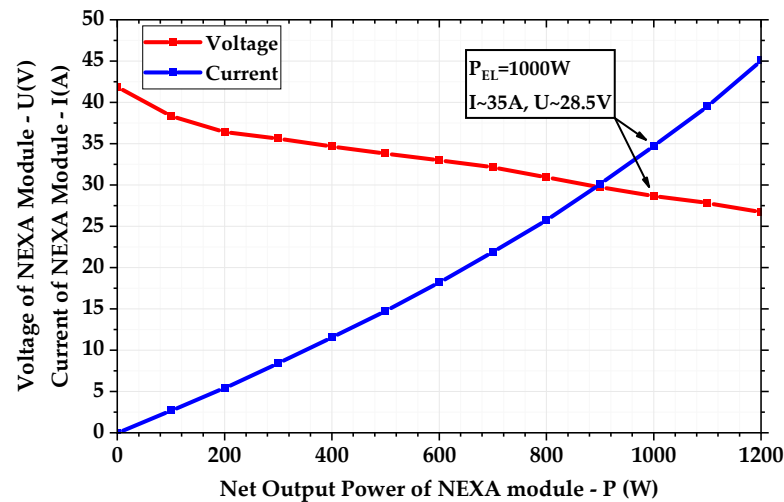


Figure 5. Load characteristics of NEXA FC stack.

The fuel consumption shown in Figure 6 has been determined from the mass flow meter with an integration member after the so-called cells purging. FC was purged with H_2 once the voltage has dropped below a certain level to restore the higher voltage in cells again. The above-mentioned purge deprives cells of impurities and water on a regular basis since those are accumulated on electrode surfaces to intercept the electrochemical reaction. The frequency of purges rises with the increase of FC power output. The fuel used for this cleaning is drained out of the system. This amount of H_2 is included in the overall fuel consumption. The maximum H_2 consumption rate of the NEXA module is 18.5 L min^{-1} . This consumption rate is proportional to the net output power of the NEXA module. The maximum air consumption rate is 90 L min^{-1} at rated power. The FC consumes O_2 from the ambient air.

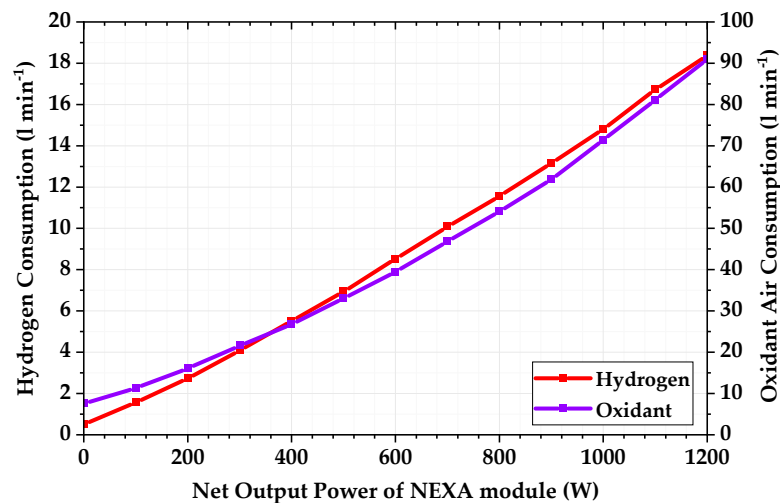


Figure 6. Fuel (hydrogen) and oxidant air consumption of NEXA FC stack.

NEXA FC stack provides power for its own support system, which consists of an oxidant air pump, cooling fan, sensors, and controllers. The required auxiliary power is 39 W (at no load). This self-power consumption increases with increasing load and is shown in Figure 7. The required auxiliary power is 290 W at rated power. The main electrical appliances include an air pump and cooling fan. The gross power of the NEXA module is given by the sum of the net output power at the module terminals and the power consumption of the module itself.

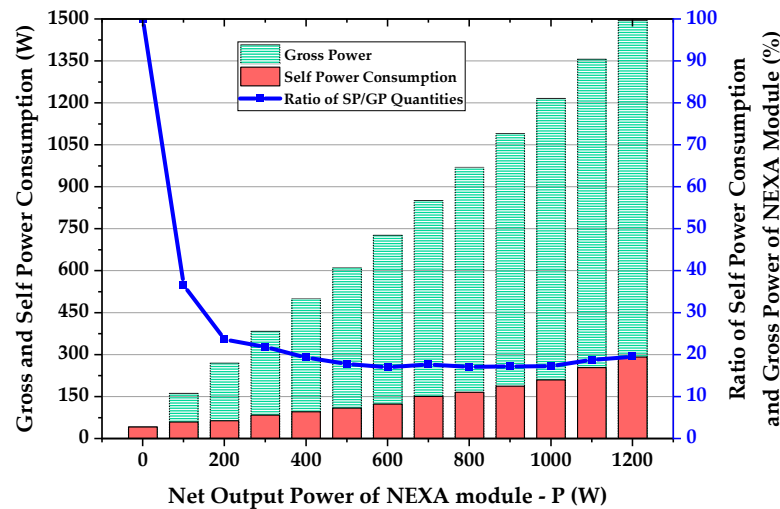


Figure 7. Gross power and self-consumption of NEXA FC stack.

In addition, the NEXA power module efficiency is presented in Figure 8. This efficiency is defined by the ratio of the net output power of the NEXA module to the lower heating value (LHV) of H_2 consumed in the reaction. In the production of electricity from H_2 , the NEXA module achieves the maximum efficiency at partial load (approx. 300 W). The efficiency decreases at higher—but also lower—loads than the stated 300 W. In the second case, in which the decrease is more dramatic, this is due to a larger ratio of the NEXA module's self-consumption to the amount of H_2 consumed. At maximum load (i.e., at rated power of 1200 W), the NEXA module has an efficiency of approx. 38%.

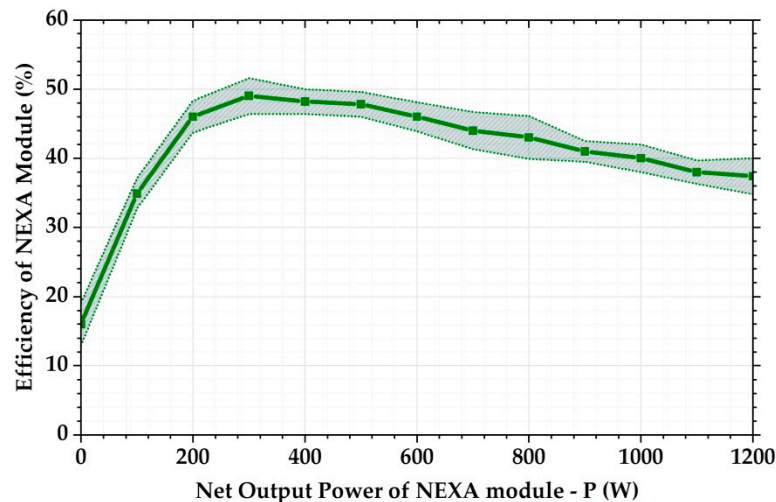


Figure 8. The output efficiency of the NEXA FC stack.

NEXA low-temperature (LT) PEMFC thermography measurements were taken at different loads set on the linked electronic DC load of 100 W, 300 W, 500 W, and 1000 W. FC temperature was measured at the cathode air exhaust of the stack.

There is no local overheating at low or middle PEMFC loads (in the range of 100–500 W), and the presented cooling system seems to be sufficient. The obtained IR thermograms show significant temperature differences between parts of the stack at higher loads; see Figure 9. The left side of the stack, located closer to the entry of the cooling air supply channel, heats up significantly more. At maximum PEMFC loads (in range of 1000–1200 W), the operation temperature of the FC reaches its limit, and FC work stops due to the thermal protection of the system. On the front side of the cooling fins, shown in Figure 9b, local

overheating is visible (marked as a rectangle). The maximum value of temperature is approximately $T = 338$ K.

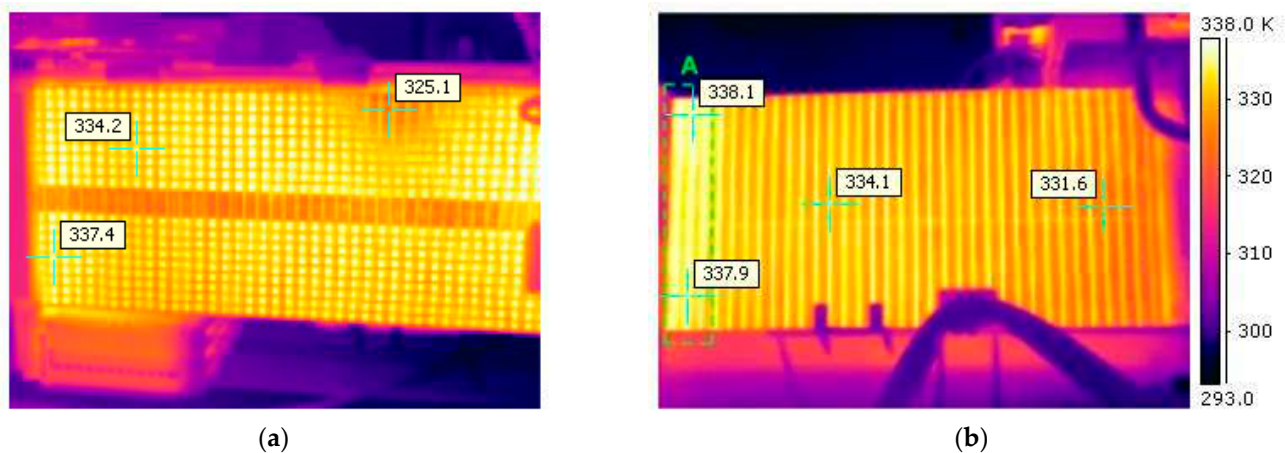


Figure 9. NEXA PEMFC stack infrared (IR)-thermography at $P = 1000$ W: (a) top view and (b) side view.

FC CFD Heat Transfer Simulation and Cooling Duct Optimization

Unequal heating of the FC stack module, detected by IR-thermography measurement, was studied by computed fluid dynamics (CFD) modeling and analyzed using the ANSYS software. The simulation determined the temperature distribution within the NEXA Ballard LT PEMFC stack. The cooling airflow velocity inside the cooling channel and cooling fins was studied. The simulation was performed at the higher problematic $P_{el} = 1000$ W load. The 47 cells connected in series form a system of channels for cooling air circulation and heat dissipation from the stack. The cooling duct for airflow circulation made from a plastic shell is located below the FC module. This plastic frame acts as well as an FC module mounting system. The inlet of the cooling channel has a shape of a rectangle hole with a dimension of $W \times H = 120 \times 80$ mm. A radial fan is mounted near the inlet of the cooling duct. All walls of the cooling duct are smooth and only the bottom side has a glued roughness surface.

Two small plastic attachments are molded on the inlet of the cooling duct and shown in Figure 10. These attachments make high distortion of the cooling streamlines, which lead to a decrease in the cooling efficiency of the system. The low cooling efficiency at the front side of the FC stack increases the temperature of cooling fins. This phenomenon was previously detected by the infrared (IR) measurements and shown in Figure 9b.

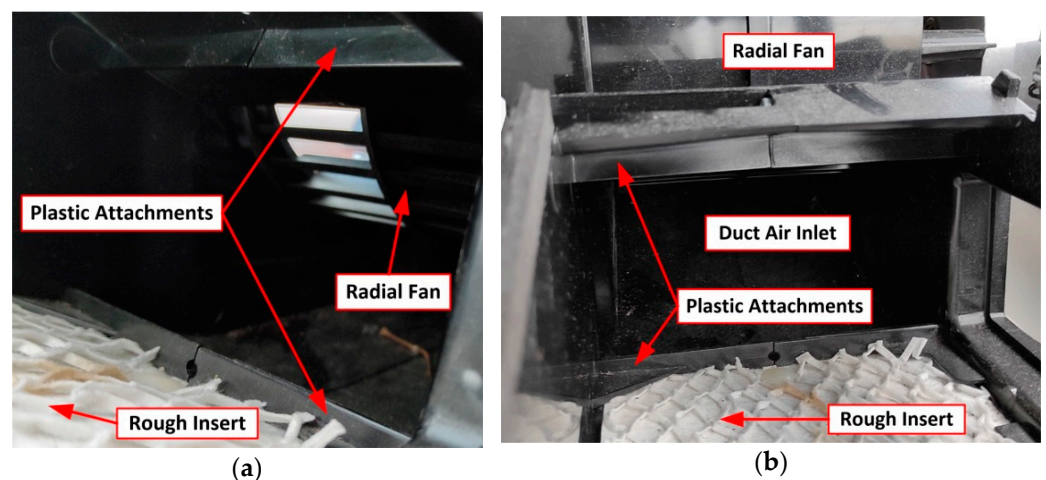


Figure 10. Interior of the cooling duct close to the fan outlet. (a) side view and (b) front view.

It is obvious that the presented cooling system needs to be improved to minimize the stack overheating during operation and at higher loads. One way to improve the FC cooling and heat transfer along the stack is to optimize the shape of the cooling duct. Another condition that should be met is using the original design of a radial fan without its replacement.

The model of the FC stack was designed via SolidWorks software. To simulate the performance of the NEXA PEMFC cooling system, fluid dynamics and thermal analysis were performed using the numerical model on the ANSYS CFX software. This model solves discrete Reynolds averaged Navier–Stokes equations to simulate the flow of the air coolant (heat transfer) along the stack. The governing equations are solved with a standard $k-\epsilon$ model for turbulence modeling. Simultaneously, the energy equation is also solved to determine the heat transfer in both solid and fluid regions [40,41]. The basic 3D model of the cooling duct including PEM and cooling fins is depicted in several view sections in Figure 11.

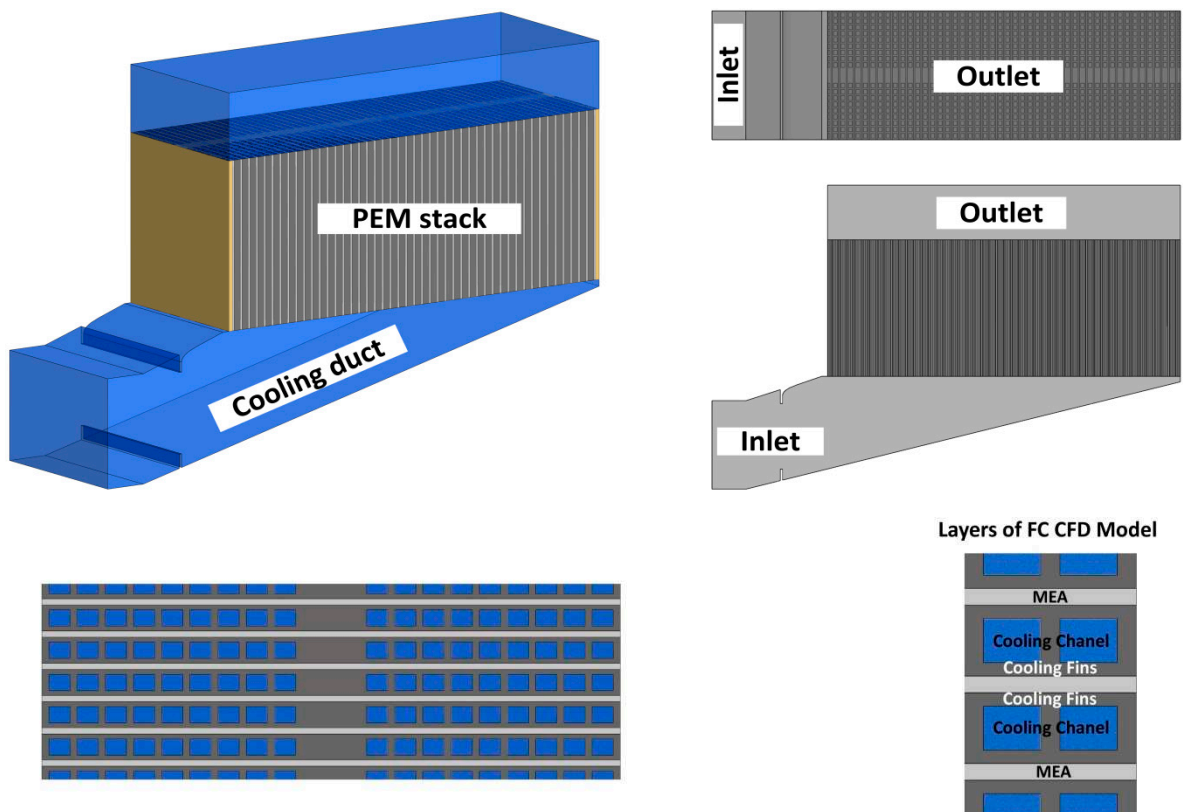


Figure 11. Geometric model of NEXA PEMFC stack used for computational fluid (CFD) simulation and optimization.

Internal power losses caused by chemical reactions in PEMFC and Joule's losses produced by electric current inside the cooling fins were modeled by heat sources in mentioned solid components. Internal heat generation is set according to the selected load $P_{el} = 1000$ W. The PEMFC current and output voltage at that load point can be found in Figure 5 ($P_{el} = 1000$ W; $V_1 = 28.5$ V; $I_1 = 35$ A; $V_{CELL} = 0.606$ V). The generated heat is calculated by the following equation [42,43]:

$$Q_{GEN} = (1.254 - V_{CELL})I_1 = P_{EL} \left(\frac{1.254}{V_{CELL}} - 1 \right) \quad (2)$$

$$Q_{GEN} = 1000 \left(\frac{1.254}{0.606} - 1 \right) = 1063 \text{ W} \quad (3)$$

All considered values of power losses and material properties that have been used for modeling are listed in Table 2.

Table 2. Material properties and power loss values used for CFD modeling [11,16].

FC Construction Parts	External Plates (Golden Coated)	Cooling Fins (Graphite/Composite)	MEA (Polymer)
Thermal Conductivity, [W (m K) ⁻¹]	318	95	0.185
Power Losses, [W]	-	410	650
Volume of the Component, [m ³]	-	1.08 × 10 ⁻³	0.43 × 10 ⁻³
Unit Loss, [W m ⁻³]	-	0.37 × 10 ⁶	1.50 × 10 ⁺⁶

The fluid domain was modeled with air as a coolant at atmospheric conditions. Part of the heat is dissipated via external areas (walls) of PEMFC by natural convection. This fact is taken into account and included in the heat transfer coefficient applied to all vertical walls of the PEMFC CFD model. For vertically oriented surfaces with natural convection conditions, the heat transfer coefficient depends on the Nusselt number, that is, properties of the coolant, geometry of the passages, and flow characteristics. The temperature dependence of the heat transfer coefficient can be evaluated by a combination of the Nusselt, Prandtl, and Rayleigh numbers [36] as follows:

$$h = \frac{k}{L} \cdot Nu_L \quad (4)$$

$$Ra_L = \frac{g\beta(T_S - T_0)L^3}{\nu\alpha} \quad (5)$$

$$Pr = \frac{\nu}{\alpha} \quad (6)$$

$$Nu_L = \left\{ 0.825 + \frac{0.387Ra_L^{1/6}}{\left[1 + \left(\frac{0.5}{Pr}\right)^{9/16}\right]^{8/27}} \right\}^2 \quad (7)$$

where h —heat transfer coefficient (W m⁻² K⁻¹); g —gravity (m s⁻²); β —thermal expansion coefficient (K⁻¹); L —characteristic length (m); ν —kinematic viscosity (m² s⁻¹), α —thermal diffusivity (m² s⁻¹); T_S —surface temperature (K); and T_0 —surroundings temperature (K). Figure 12a shows the application of heat transfer coefficient on external areas of the proton-exchange membrane (PEM) and Figure 12b shows its temperature dependence derived from Equations (4)–(7).

The CFD analysis requires high-density mesh, especially inside of all fluid parts. The velocity gradient reaches high values in the solid–fluid layers, and any coarse mesh may cause serious inaccuracy of the calculation and complicate the convergence. In this regard, the inflations of mesh cells at each transition between fluid–solid parts were applied.

Figure 13a shows the distribution of air velocity at the cross section of the front part of the original FC stack cooling duct. The mentioned figure shows a phenomenon of the swirling streamlines behind the plastic attachments. The airflow is interrupted in the front part of the cooling fins. The situation is similar in the top and bottom sides of the cooling duct. A number of the performed simulations showed the reverse airflow from cooling fins because of the low pressure behind the plastic attachments. Both CFD in Figure 13b and IR in Figure 9b temperature analysis of the NEXA PEMFC stack show the local overheating at the front part of cooling fins due to the intensive swirling of the airflow.

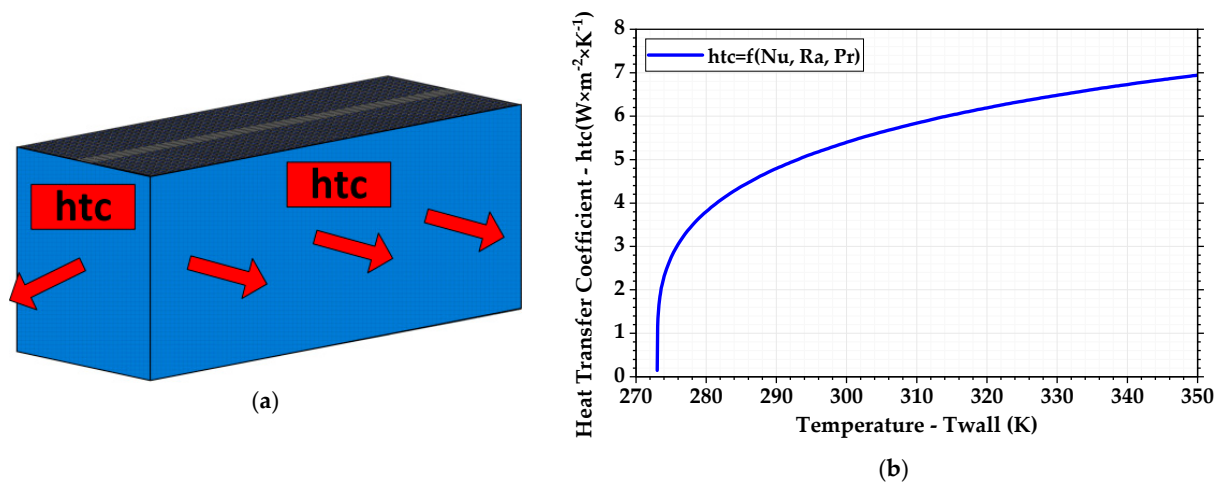


Figure 12. Applying heat transfer coefficient for external surfaces of the stack (a) application on external areas, (b) temperature dependence of heat transfer coefficient.

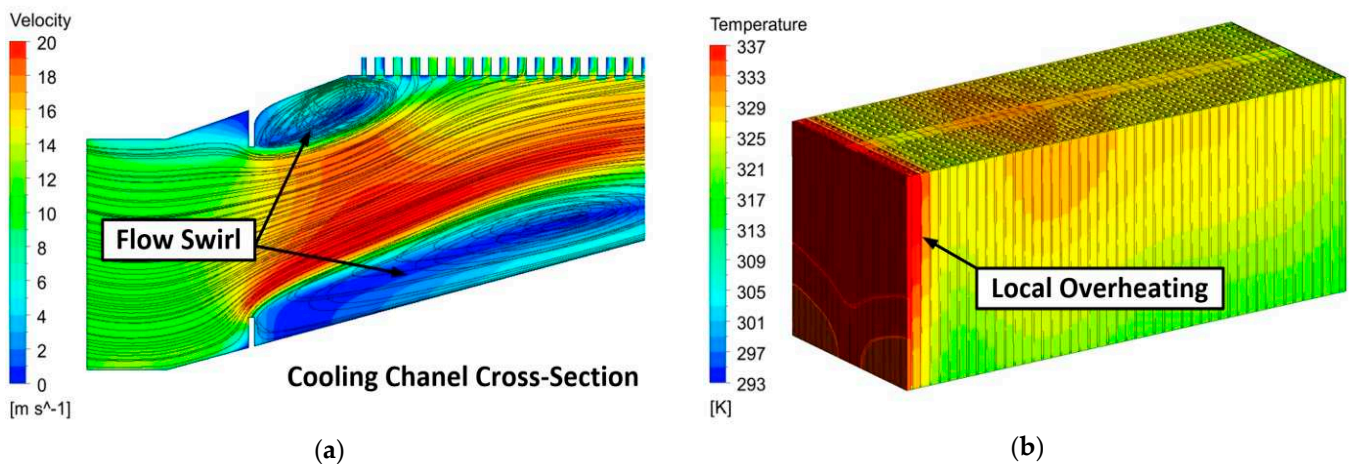


Figure 13. (a) Streamlines of the air coolant and (b) temperature distribution at $P_{el} = 1000$ W of load.

In the simulated model, the temperature differences are somewhat slightly higher. This is mainly due to the applied simplification of the CFD model, which does not take into account the complex construction of a real PEMFC. Additional devices (humidifier, control card, sensors, etc.) are placed on the sidewalls of the PEMFC structure, which generally decrease the heat dissipation to the surroundings and thus increase its overall temperature.







In the CFD model, temperature-dependent heat transfer coefficients have been applied to the entire walls of the PEMFC stack, and the CFD model is generally better cooled. Thus, the simulated temperature distribution and values on our model differ. In the CFD model, we emphasized a precise computing network (mesh) in the air duct and the boundary layer between fluid and solid objects. The model contains more than 15 million elements, and its solution is very time consuming. We believe that even with this simplification in the construction of the model, there can be found a fairly good match with real PEMFC.

The internal plastic attachments are the integrated part of the radial fan assembly and cannot be simply removed. It is possible to slightly modify its height. To increase the airflow rate to the front part of the stack, the shape modification of the airflow streamlines has to be made. The airflow adjustment can be realized without any significant disruption of the original duct design by using appropriately formed inserts (wings) and blades placed into the cooling duct.

Several modifications of the adjustments in the inlet part of the cooling duct and in its interior have been simulated. The basis of all analyzed modifications was the insertion

of variously shaped blades, which direct the flow of cooling air. Each of the mentioned options was also dimensionally modified (length of the blades, their inclination angle, and position in the cooling channel, etc.). Table 3 shows the list of the analyzed modification of the FC cooling duct.

Table 3. Analyzed modification of the cooling duct of PEMFC.

Cooling Duct Modification						
Applied Change	Original	Skewed Airfoil	Skewed Airfoil and Blades	Round and Straight Blades	Round Cover and Straight Blades	Round Cover and 3 Short Blades
Decreasing of Temperature	-	0	1	1	1	1
Simple Design Overall	-	1	0	0	1	1
Improvement	-	0	1	1	0	1
Final Decision	-	No	No	Yes	No	Yes
Type of Modification	-			A		B

The two most appropriate solutions of the cooling duct adjustment (Type A and Type B) are depicted in Figure 14.

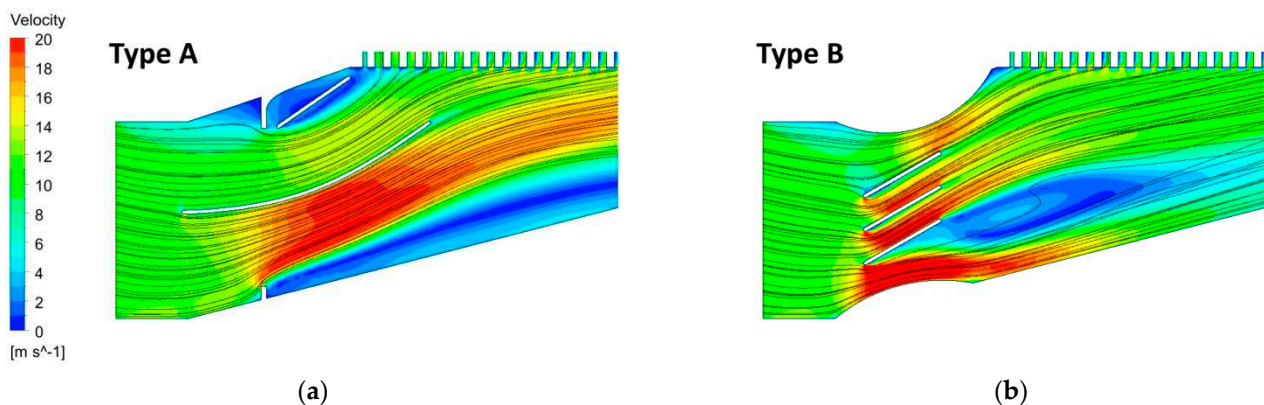


Figure 14. Streamlines and velocity profile of the modified cooling duct in (a) Type A and (b) Type B.

Figure 14 shows streamlines and velocity profiles at the input side of the cooling duct cross section. Type A modification, shown in Figure 14a, contains two additional blades. One of the blades is slightly curved and located in the center of the cooling duct. The second one has a straight shape and creates the covering of the top plastic attachment. The bottom plastic attachment is also lowered by cutting. The used system of blades in Type A modification serves especially for suitable airflow direction to the front part of the PEM stack cooling fins. Type B modification, shown in Figure 14b, is created by covering the top and bottom plastic attachment with a round surface. The rounded surface is simply made from the appropriate cut thin PVC tube. These tube pieces are glued to the internal surface of the cooling duct and easily create an effective shape for airflow. To intensify the direction of the streamline, three additional blades in the center of the cooling duct were used. The swirl occurs behind of bottom blade, but it also gradually disappears with increasing the length of the channel.

Figure 15 shows how cooling duct modification changes the temperature distribution. The local overheating at the front side of PEM, shown in Figure 15b, that corresponded to the original design of the cooling duct has been removed. The area with a higher temperature is now closer to the middle of the PEM assembly. The maximal value of temperature is also decreased in the range of 7 K, from $T_1 = 338$ K in the original design to

$T_2 = 331$ K in Type A and Type B modifications. Type B modification also shows the better temperature distribution along the stack, without any significant local temperature rise. Moreover, the round surfaces and straight blades in Type B modification can be simply manufactured in comparison to the complicated shaping of a curved blade used in Type A.

Figure 16 shows the temperature distribution and velocity profile on the section area located near the coolant outlet (approx. $H = 5$ mm). Both Type A and Type B duct modifications improve the airflow in the front part of PEMFC, which is visible mainly on the velocity profile. The temperature here also reaches lower values in comparison to the rest part of the section area. Important values of performed simulations are collected in Table 4.

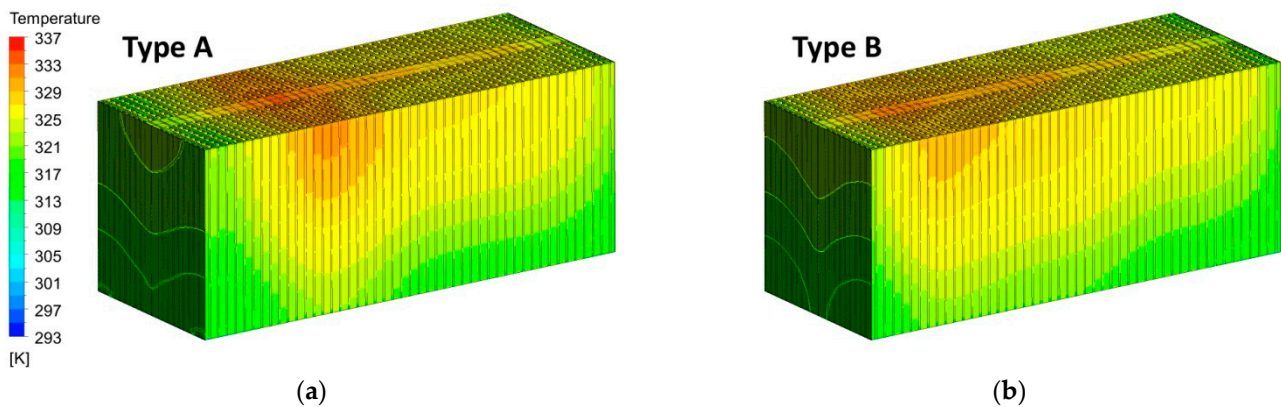


Figure 15. Temperature distribution on the proton-exchange membrane (PEM) stack across (a) Type A and (b) Type B.

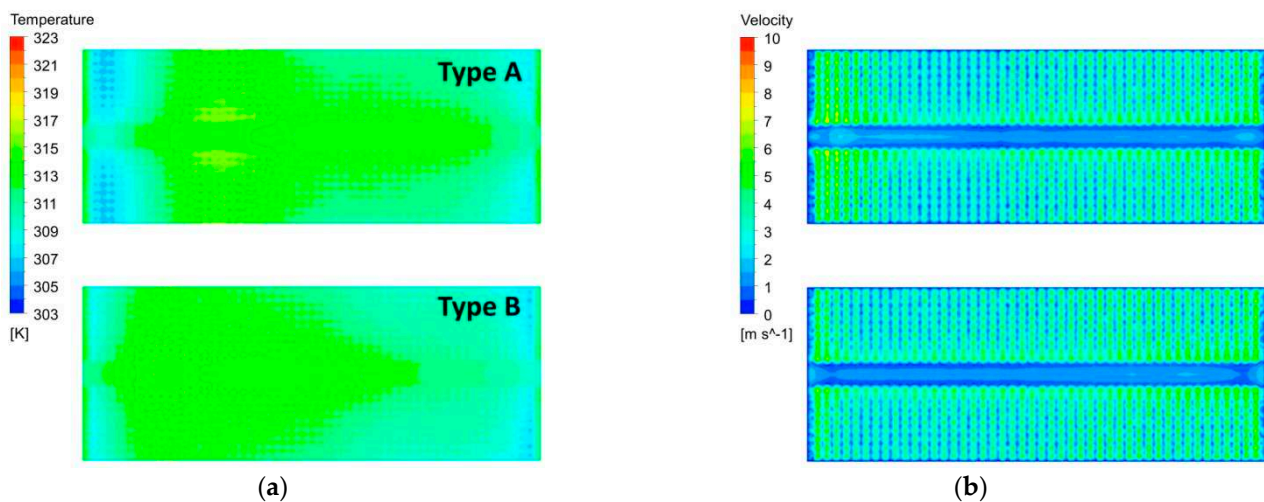


Figure 16. Temperature distribution and velocity profile on section area of PEMFC outlet in (a) Type A and (b) Type B.

The uniformity of the temperature distribution can be assessed using the homogeneity factor (temperature uniformity coefficient). The coefficient can be determined as the ratio of the temperature value to its maximum. Temperature uniformity coefficient represents the balanced distribution of temperature on the outlet surface of the PEMFC as follows:

$$\varepsilon = \frac{T_{AVG}}{T_{MAX}} \cdot 100 \quad (8)$$

Based on the performed simulations, the Type B modification (rounded covers and blades) was chosen for the final adjustment of the PEMFC cooling channel. The rounded covers were made of a plastic tube with a diameter of $D = 25$ mm and were fixed to the sides of the cooling channel by gluing. The straight blades were made of thin steel sheets

and were also glued to the sides of the channel. The blades were adjusted to have a slight inclination with respect to the cooling air inlet from the fan; see Figure 17.

After adjusting the cooling channel, the PEMFC stack was reassembled, and its parameters were measured. To validate the results of the cooling duct optimization, a load of $P = 1000\text{ W}$ was applied, in which the PEMFC showed a local overheating of the plates in the vicinity of the fan inlet.

Figure 18 shows the measurement of the PEMFC temperature using an infrared camera on the surface of the cooling air outlet. Figure 18a shows the original state of PEMFC without performed optimization, and Figure 18b shows the temperature distribution with an optimized cooling channel according to Type B.

Measurement of the PEMFC surface temperature shows that the modification leads to a temperature reduction and a more accurate heat distribution across the stack. The measurements also show that the temperature difference between the original and optimized variant of the cooling duct design is approximately 7 K, which was also shown by the performed CFD simulations; see Figures 13 and 15.

Table 4. Output values from analysis of CFD model.

FC Construction Parts	Original	Type A	Type B
Mass Flow, [kg s^{-1}]	0.0565	0.0565	0.0565
Enthalpy Difference— Δh , [J kg^{-1}]	18,036	18,525	18,644
Unit Heat in Coolant— Q_u , [J s^{-1}]	1020	1045	1053
Outlet Average Temperature— T_{avg} , [K]	312.0	311.8	311.7
Outlet Max Temperature— T_{max} , [K]	325.4	315.8	314.8
Outlet Min Temperature— T_{min} , [K]	301.8	305.9	306.3
Temperature Uniformity, [%]	95.8	98.7	98.9

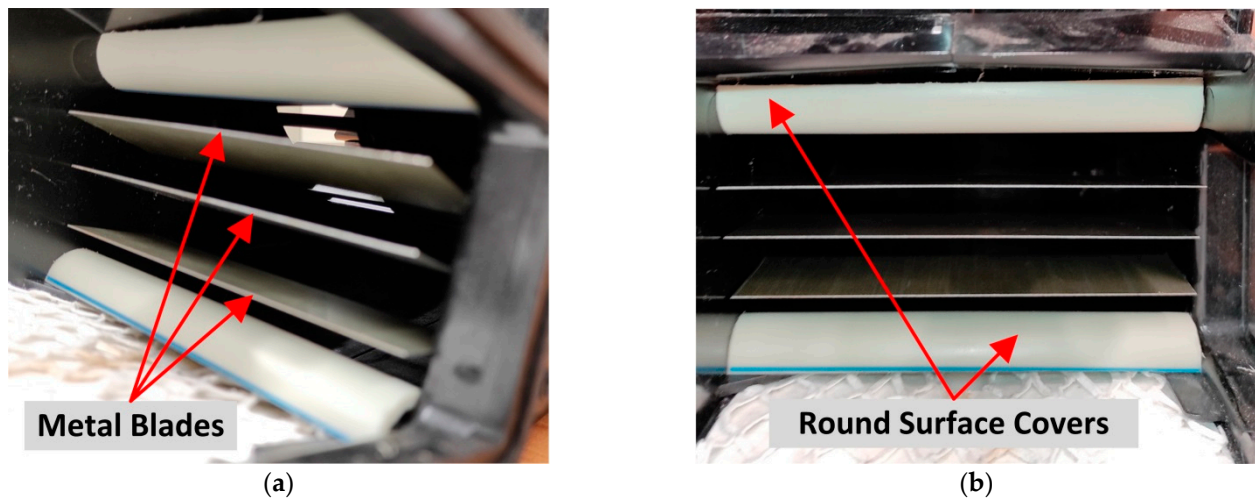


Figure 17. Adjustment of cooling duct close to the fan outlet seen in (a) side view and (b) front view.

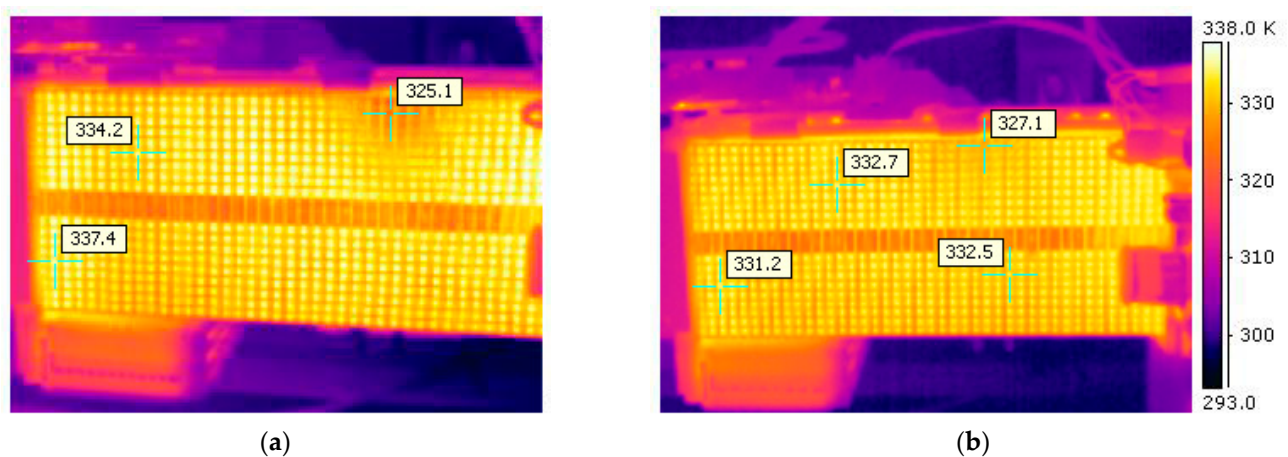


Figure 18. NEXA PEMFC stack IR-thermography at loads $P = 1000$ W in (a) original design and (b) modified cooling duct (Type B).

4. Conclusions

In this work, a concept of the HHS based on low-temperature NEXA Ballard PEMFC is presented. IR measurements and CFD analysis of the FC stack determined problematic overheated zones of the NEXA FC due to unequal heat distribution (air-cooling distribution) across the stack during high loads. Ways of the FC heat transfer optimization were studied. To avoid local overheating of the stack at the air-cooling inlet side, the modification of the original cooling duct was provided. The heat transfer computer simulation of the PEMFC with different cooling duct designs allowed us to determine the optimal conditions for the NEXA stable working and sufficient cooling at high loads around $P_{el} = 1\text{--}1.2$ kW.

In search of a more advantageous shape of the inlet shape of the PEMFC cooling duct, we have performed a number of analyses and simulations of the flow in the cooling duct. We have selected the most interesting results for our publication.

The basic entry condition for these analyses was to preserve the original FC cooling duct design/structure as much as possible. Our solution is therefore a compromise between preserving the original construction and the necessary modification of the inlet shape of the duct, which leads to an improvement in the PEMFC cooling. From this point of view, our solution is also optimal because we have achieved by simple means (glued covers and blades) the improvement of the FC cooling and temperature distribution of the PEMFC stack. The internal protrusions cannot be easily removed due to the stability of the inlet fan mount. The inner protrusions form stabilizing elements that ensure resistance to the deformation of the channel structure. The inlet part of the duct, which is attached to the fan bases of these protrusions, increases the overall stiffness of the plastic structure.

Of course, it is possible to create a new shape of the cooling channel, in which the protrusions in the inlet of the channel will be on its outer part. Such a construction can be realized, for example, by means of 3D printing. However, in the upper part of the duct, this method is impossible for application due to the overlap (dimensions) of the fan. By removing the protrusions in the lower part, the rigidity of the system will be significantly reduced.

Our main goal was the stability of the operation of PEMFC, especially at operating conditions close to the maximum values. Original FC showed instability of operation even before reaching the declared maximum output power ($P = 1200$ W), and the PEMFC was automatically switched off due to an over-temperature state.

The CFD model of the FC was built with significant simplification. The model has been based on the complicated sandwich structure with mutually coupled chemical, electrical, and thermal processes that were assessed rather from a macroscopic point of view of heat dissipation and its effective removal from the FC body.

However, even this applied simplified model shows an unsuitable construction of the cooling channel. Using the CFD model, the influence of several modifications of the inlet part of the duct to achieve higher cooling efficiency was evaluated. On a real PEMFC, this channel modification was performed and a validation measurement of the operating condition and a measurement of the surface temperature of the PEMFC stack were performed. Although the reduction in temperature may not appear significant, the channel treatment performed resulted in more even temperature distribution and generally stabilized the operation of the PEMFC.

The PEMFC is currently operated in our laboratory tends to work with higher currents ($I > 30$ A); thus, we achieve lower efficiency values ($\eta < 40\%$). The main benefit of the performed analysis and modification of the FC cooling channel is therefore the stability of FC operation at its marginal power ($P > 1000$ W). By modifying the cooling duct, we were able to reduce the operating temperature of the PEMFC and minimize local overheating points. Due to more efficient cooling, the permissible ambient temperature can be slightly exceeded while maintaining the stability of PEMFC operation. We have also measured the operation parameters of the FC with an optimized cooling duct. The FC efficiency has occurred in the range shown in Figure 8.

The next possible waste heat utilizing from the stack could be applied for the LT MH H_2 endothermic desorption process. The next steps of the research would correspond to the design of the optimal solution for sufficient heat exchange between NEXA FC and MH storage tank. Most likely, this solution will be based on the direct use of hot exhaust air from the top part of the stack for MH storage heating, without additional heating the liquid heat carrier and using a gas–liquid heat exchanger.

Author Contributions: Conceptualization, A.C. and P.K.; methodology, A.C.; software, P.K.; validation, A.C., P.K., and P.M.; formal analysis, A.C. and P.K.; investigation, A.C., P.K., and P.M.; data curation, P.K.; writing—original draft preparation, A.C.; writing—review and editing, A.C. and P.K.; visualization, P.K. and P.M.; supervision, A.C. All authors have read and agreed to the published version of the manuscript.

Funding: This research was funded by the internal funding program of the VSB—Technical University of Ostrava, identification no: SP2021/20, and by the project TK03020027: Center of Energy and Environmental Technologies.

Data Availability Statement: Not applicable.

Conflicts of Interest: The authors declare no conflict of interest.

Abbreviations

The following abbreviations and symbols are used in this manuscript:

AEM	Anion-Exchange Membrane
CFD	Computational Fluid Dynamics
CL	Catalyst Layers
FC	Fuel Cell
FP	Flow Plates
GDL	Gas Diffusion Layers
HHS	Hydrogen Hybrid Energy System
HT	High-Temperature
IR	Infrared
LHV	Lower-Heating Value
LT	Low-Temperature
MH	Metal Hydride
PEM	Proton-Exchange Membrane
PtG	Power-to-Gas
PV	Photovoltaic
PVC	Polyvinyl Chloride
RES	Renewable Sources

References

- Hirscher, M. *Handbook of Hydrogen Storage: New Materials for Future Energy Storage*; Wiley-VCH: Weinheim, Germany, 2009; ISBN 9783527322732.
- Ursúa, A.; San Martín, I.; Barrios, E.L.; Sanchis, P. Stand-alone operation of an alkaline water electrolyser fed by wind and photovoltaic systems. *Int. J. Hydrog. Energy* **2013**, *38*, 14952–14967. [[CrossRef](#)]
- Barbir, F. PEM electrolysis for production of hydrogen from renewable energy sources. *Sol. Energy* **2005**, *78*, 661–669. [[CrossRef](#)]
- Yilanci, A.; Dincer, I.; Ozturk, H.K. A review on solar-hydrogen/fuel cell hybrid energy systems for stationary applications. *Prog. Energy Combust. Sci.* **2009**, *35*, 231–244. [[CrossRef](#)]
- Yunez-Cano, A.; de González-Huerta, R.G.; Tufiño-Velázquez, M.; Barbosa, R.; Escobar, B. Solar-hydrogen hybrid system integrated to a sustainable house in Mexico. *Int. J. Hydrog. Energy* **2016**, *41*, 19539–19545. [[CrossRef](#)]
- Thomas, C.; James, B.D.; Lomax, F.D.; Kuhn, I.F. Fuel options for the fuel cell vehicle: Hydrogen, methanol or gasoline? *Int. J. Hydrog. Energy* **2000**, *25*, 551–567. [[CrossRef](#)]
- Hwang, J.; Chang, W.; Weng, F.; Su, A.; Chen, C. Development of a small vehicular PEM fuel cell system. *Int. J. Hydrog. Energy* **2008**, *33*, 3801–3807. [[CrossRef](#)]
- Mehta, V.; Cooper, J.S. Review and analysis of PEM fuel cell design and manufacturing. *J. Power Sources* **2003**, *114*, 32–53. [[CrossRef](#)]
- Yamada, Y.; Ueda, A.; Shioyama, H.; Kobayashi, T. High-throughput screening of PEMFC anode catalysts by IR thermography. *Appl. Surf. Sci.* **2004**, *223*, 220–223. [[CrossRef](#)]
- Moldrik, P.; Chesalkin, A.; Minarik, D. Infrared thermography and computer simulation in research of PEM fuel cells. In Proceedings of the 2019 20th International Scientific Conference on Electric Power Engineering (EPE), Kouty nad Desnou, Czech Republic, 15–17 May 2019. [[CrossRef](#)]
- Burheim, O.S.; Su, H.; Hauge, H.H.; Pasupathi, S.; Pollet, B.G. Study of thermal conductivity of PEM fuel cell catalyst layers. *Int. J. Hydrog. Energy* **2014**, *39*, 9397–9408. [[CrossRef](#)]
- Pinar, F.J.; Rastedt, M.; Pilinski, N.; Wagner, P. Characterization of HT-PEM membrane-electrode-assemblies. In *High Temperature Polymer Electrolyte Membrane Fuel Cells*; Springer International Publishing: Cham, Switzerland, 2016; pp. 353–386. ISBN 9783319170817. [[CrossRef](#)]
- Kopriva, M.; Minarik, D.; Sokansky, K. Setting up and Possibilities of increasing of Operation Voltage of the PEM FC. In Proceedings of the 2007 8th International Scientific Conference Electric Power Engineering (EPE), Kouty nad Desnou, Czech Republic, 6–8 June 2007; pp. 186–198, ISBN 978-80-248-1391-2.
- Srinivasan, S. *Fuel Cells*; Springer: Boston, MA, USA, 2006; ISBN 9780387251165. [[CrossRef](#)]
- EG&G Technical Services, Inc. *Seventh Edition Fuel Cell Handbook*; Office of Scientific and Technical Information (OSTI): Pittsburgh, PA, USA, 2004. [[CrossRef](#)]
- Barbir, F. *PEM Fuel Cells: Theory and Practice*, 2nd ed.; Academic Press: San Diego, CA, USA, 2012; ISBN 9780123877109.
- Badwal, S.P.S.; Giddey, S.S.; Munnings, C.; Bhatt, A.I.; Hollenkamp, A.F. Emerging electrochemical energy conversion and storage technologies. *Front. Chem.* **2014**, *2*, 79. [[CrossRef](#)]
- Züttel, A. Materials for hydrogen storage. *Mater. Today* **2003**, *6*, 24–33. [[CrossRef](#)]
- Godula-Jopek, A. *Hydrogen Production: By Electrolysis*; Wiley-VCH: Weinheim, Germany, 2015; ISBN 9783527333424.
- Basile, A.; Iulianelli, A. (Eds.) *Advances in Hydrogen Production, Storage and Distribution*; Woodhead Publishing: Cambridge, UK, 2014; ISBN 9780857097682. [[CrossRef](#)]
- Shcherbakova, L.G.; Dan'ko, D.B.; Muratov, V.B.; Kossko, I.A.; Solonin, Y.M.; Kolbasov, G.Y.; Rusetskii, I.A. Metal hydride use for solar energy accumulation. In *NATO Security through Science Series A: Chemistry and Biology*; Springer: Dordrecht, The Netherlands, 2007; pp. 699–706. ISBN 9781402055126. [[CrossRef](#)]
- Corgnale, C.; Hardy, B.; Motyka, T.; Zidan, R. Metal hydride based thermal energy storage system requirements for high performance concentrating solar power plants. *Int. J. Hydrog. Energy* **2016**, *41*, 20217–20230. [[CrossRef](#)]
- Flanagan, T.B.; Oates, W.A. Thermodynamics of intermetallic compound-hydrogen systems. In *Topics in Applied Physics*; Springer: Berlin/Heidelberg, Germany, 1988; pp. 49–85. ISBN 9783540183334. [[CrossRef](#)]
- Griessen, R.; Riesterer, T. Heat of formation models. In *Topics in Applied Physics*; Springer: Berlin/Heidelberg, Germany, 1988; pp. 219–284. ISBN 9783540183334. [[CrossRef](#)]
- Fukai, Y.; Okuma, N. Formation of superabundant vacancies in Pd hydride under high hydrogen pressures. *Phys. Rev. Lett.* **1994**, *73*, 1640–1643. [[CrossRef](#)]
- Chesalkin, A.; Martaus, A.; Averina, J.M.; Men'shikov, V.V. La–Ni based alloy modification by Ce and Fe for the next hydrogen storage in low-temperature metal hydrides. *Russ. J. Non-Ferr. Met.* **2019**, *60*, 492–498. [[CrossRef](#)]
- Jepsen, J.; Milanese, C.; Puszkiel, J.; Girella, A.; Schiavo, B.; Lozano, G.; Capurso, G.; von Colbe, J.M.B.; Marini, A.; Kabelac, S.; et al. Fundamental material properties of the 2LiBH₄-MgH₂ reactive hydride composite for hydrogen storage: (I) thermodynamic and heat transfer properties. *Energies* **2018**, *11*, 1081. [[CrossRef](#)]
- Jepsen, J.; Milanese, C.; Puszkiel, J.; Girella, A.; Schiavo, B.; Lozano, G.A.; Capurso, G.; Von Colbe, J.M.B.; Marini, A.; Kabelac, S.; et al. Fundamental Material Properties of the 2LiBH₄-MgH₂ Reactive Hydride Composite for Hydrogen Storage: (II) Kinetic Properties. *Energies* **2018**, *11*, 1170. [[CrossRef](#)]
- Li, Q.; Liu, Z.; Sun, Y.; Yang, S.; Deng, C. A review on temperature control of proton exchange membrane fuel cells. *Processes* **2021**, *9*, 235. [[CrossRef](#)]

30. Shahsavari, S.; Desouza, A.; Bahrami, M.; Kjeang, E. Thermal analysis of air-cooled PEM fuel cells. *Int. J. Hydrog. Energy* **2012**, *37*, 18261–18271. [[CrossRef](#)]
31. Andisheh Tadbir, M.; Shahsavari, S.; Bahrami, M.; Kjeang, E. Thermal management of an air-cooled PEM fuel cell: Cell level simulation. In Proceedings of the ASME 2012 10th International Conference on Fuel Cell Science, Engineering and Technology; American Society of Mechanical Engineers, San Diego, CA, USA, 23–26 July 2012. [[CrossRef](#)]
32. Al-Baghdadi, M.A.S.; Al-Janabi, H.A.S. Modeling optimizes PEM fuel cell performance using three-dimensional multi-phase computational fluid dynamics model. *Energy Convers. Manag.* **2007**, *48*, 3102–3119. [[CrossRef](#)]
33. An, Q.; Hortig, D.; Merklein, M. Infrared thermography as a new method for quality control of sheet metal parts in the press shop. *Arch. Civ. Mech. Eng.* **2012**, *12*, 148–155. [[CrossRef](#)]
34. Cerdeira, F.; Vázquez, M.; Collazo, J.; Granada, E. Applicability of infrared thermography to the study of the behaviour of stone panels as building envelopes. *Energy Build.* **2011**, *43*, 1845–1851. [[CrossRef](#)]
35. Wang, H.; Li, H.; Yuan, X.-Z. *PEM Fuel Cell Diagnostic Tools: PEM Fuel Cell Diagnostic Tools*; CRC Press: Boca Raton, FL, USA, 2011; Volume 2, ISBN 9781439839195.
36. Das, P.K.; Weber, A.Z.; Bender, G.; Manak, A.; Bittinat, D.; Herring, A.M.; Ulsh, M. Rapid detection of defects in fuel-cell electrodes using infrared reactive-flow-through technique. *J. Power Sources* **2014**, *261*, 401–411. [[CrossRef](#)]
37. Mzoughi, D.; Allagui, H.; Bouaicha, A.; Mami, A. Modeling and testing of a 1.2-kW Nexa fuel cell using bond graph methodology: Modeling and Testing of PEM Fuel Cell Using Bond Graph. *IEEJ Trans. Electr. Electron. Eng.* **2015**, *10*, 527–538. [[CrossRef](#)]
38. Allagui, H.; Mzoughi, D.; Bouaicha, A.; Mami, A. Modeling and simulation of 1.2 kW Nexa PEM fuel cell system. *Indian J. Sci. Technol.* **2016**, *9*. [[CrossRef](#)]
39. Ballard Power Systems Inc. *Nexa Power Module User's Manual, MAN5100078 (310-0027)*; Ballard Power Systems Inc.: Burnaby, BC, Canada, 2003.
40. Franc, J.; Pechanek, R.; Kindl, V.; Zavrel, M. Ventilation system with skewed rotor cooling ducts of 40-MW synchronous machine: A case study. *Electr. Eng.* **2019**, *101*, 203–211. [[CrossRef](#)]
41. Veg, L.; Skalicky, M.; Pechanek, R. Tuning of the thermal model of synchronous machine with PM by real measurement. In Proceedings of the 2020 19th International Conference on Mechatronics—Mechatronika (ME), Prague, Czech Republic, 2–4 December 2020. [[CrossRef](#)]
42. Barbir, F. Fuel Cell Operating Conditions. In *PEM Fuel Cells: Theory and Practice*; Academic Press: Cambridge, MA, USA, 2005; pp. 115–145. ISBN 9780120781423. [[CrossRef](#)]
43. Hasani, M.; Rahbar, N. Application of thermoelectric cooler as a power generator in waste heat recovery from a PEM fuel cell—An experimental study. *Int. J. Hydrog. Energy* **2015**, *40*, 15040–15051. [[CrossRef](#)]

Hypothesis

On the Nature of Electro-Osmotic Drag

Torsten Berning 

Department of Energy Technology, Aalborg University, 9220 Alborg, Denmark; tbe@et.aau.dk

Received: 14 August 2020; Accepted: 8 September 2020; Published: 10 September 2020



Abstract: Electro-osmotic drag (EOD) is usually thought of as a transport mechanism of water inside and through the polymer electrolyte membrane (PEM) in electrochemical devices. However, it has already been shown that the transport of dissolved water in the PEM occurs exclusively via diffusion, provided that the EOD coefficient n_d is constant. Consequently, EOD is not a water transport mechanism inside the electrolyte membrane, and this means that its nature is not yet understood. This work proposes a theory that suggests that the root of the EOD is located in the catalyst layers of the electrochemical device where the electric current is generated, and consequently could be linked to one or more of the elementary reaction steps. It is therefore also conceivable that EOD exists at one electrode in an electrochemical device, but not in the other. Moreover, the EOD coefficient n_d may depend on the current density as well as the oxidization level of the catalyst. The last consequence, if EOD is linked to an elementary reactions step, it could also be part of the rate-determining elementary step, and this could open pathways to increase the reaction kinetics by finding ways of enhancing the water/hydronium ion transport out of or into the polymer phase.

Keywords: electro-osmotic drag; polymer electrolyte membrane; proton exchange membrane fuel cells; proton exchange membrane electrolyzer cells; membrane water transport; elementary reactions steps; rate-determining step

1. Introduction

As we are entering the hydrogen age, proton exchange membrane fuel cells (PEMFCs) and electrolyzer cells (PEMECs) play a central role because of their high efficiencies and their noiseless and clean operation [1]. These technologies can be ideally paired with intermittent power sources such as wind energy or solar energy to create a carbon-free future energy system, using hydrogen and electricity as “energy currencies”. The synergy of electricity and hydrogen was pointed out by Scott and Häfele [1], and is illustrated along with the conversion technologies in Figure 1.

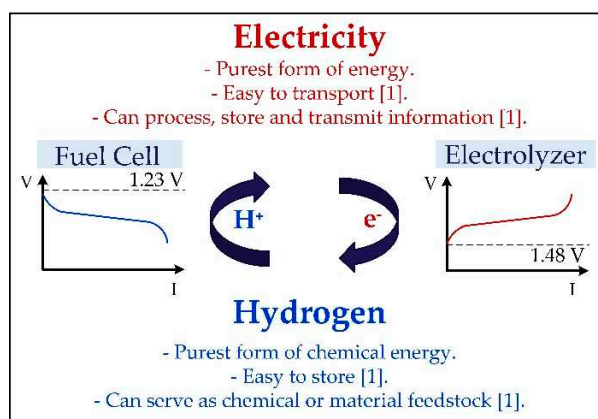
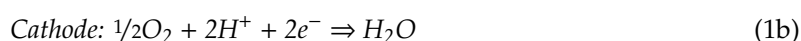


Figure 1. The “H⁺–e[−] Cycle” of polymer electrolyte membrane (PEM) fuel cells and electrolyzers.

In order to adopt a widespread use of these “neat hydrogen” technologies, however, it is imperative to make these technologies economically attractive, and this requires further improvements and fundamental understanding.

A PEMFC converts hydrogen fuel and oxygen from air into electricity. Air is fed to the cathode side of the cell while hydrogen is supplied to the anode. Oxygen and hydrogen are transported through the porous gas diffusion layers towards the catalyst layers where the electrochemical reactions occur, driven by the electromotive force of the fuel cell and local overpotentials that are the main source of waste heat (e.g., [2]). At the anode catalyst layer (ACL), hydrogen is split into protons that migrate through the polymer electrolyte membrane (PEM) towards the cathode catalyst layer (CCL) where the protons recombine with electrons and oxygen to create water. The electrons travel through the external cycle and thus provide electricity.

The half-cell reactions are therefore:



The theoretical, ideal voltage of a fuel cell can be calculated out of Gibbs free energy of the overall reaction to be 1.23 V at standard conditions [2]. In a PEM electrolyzer cell, the opposite reactions take place, and electricity must be supplied to the cells. Waste heat is usually produced here as well, and the basis for the calculation of the electrolyzer efficiency is the thermoneutral voltage, calculated out of the enthalpy of reaction, and this is 1.48 V at standard conditions [2].

For the low-temperature PEM technology, the membrane must be kept in a hydrated state while at the same time cell flooding must be avoided [3,4], which requires a careful adjustment of the operating conditions [5,6]. The water management of the fuel cell or electrolyzer cell in general and of the membrane in particular need to be fundamentally understood and the various water transport mechanisms carefully studied.

2. Water Transport Inside a Polymer Electrolyte Membrane

This section presents a brief overview of water transport mechanisms and important properties. It is, however, far from being a complete literature review, as only the most important aspects are highlighted.

A comprehensive review of the various water management issues in fuel cells, as it was state of the art at that time, was published by Dai et al. [7]. A central question in both PEMFCs and PEMECs is how the water actually crosses the membrane. The traditional view is that water crosses the membrane predominantly by the following mechanisms [3,7]:

- (1) Electro-osmotic drag (EOD), always directed from anode to cathode;
- (2) Diffusion (earlier also named “back diffusion”), typically assumed from cathode to anode in PEMFCs and from anode to cathode in PEMECs;
- (3) Hydraulic permeation from the high-pressure half-cell to the low-pressure half-cell.

Voss et al. [8] at Ballard Power Systems conducted detailed experiments and concluded that diffusion appears to be a dominant process. In that work, the authors proposed to remove excess water by the anode gas stream by imposing a concentration gradient across the membrane to counterbalance the effect of EOD, thus only considering the first two effects from above, as the pressure difference across the membrane in their work was low. The hydraulic permeation was usually considered negligible, except for the work by Bernardi and Verbrugge [9,10], who employed the Schlögl equation, which balances hydraulic permeation with a water flux driven by a potential gradient.

It is important to realize that an important transport mechanism is missing in the list above, and this is the nonequilibrium sorption (NES) of water to/from the membrane from/to the surrounding

gas/liquid phase, because any water that crosses through the membrane must first be adsorbed by the membrane. No calculation or fundamental understanding of water crossing the membrane can be complete without accounting for this effect, as was already shown in previous work [11].

The conservation equation for water inside the electrolyte phase in a fuel cell is [12]:

$$\frac{\rho^{mem}}{EW} \nabla \cdot (D_{w,mem} \nabla \lambda_w) = \nabla \cdot (n_d \frac{I}{F}) - \alpha \times k_a \times \frac{\rho^{mem}}{EW} (\lambda_{w,equl} - \lambda_w) \quad (2)$$

Diffusion = EOD - NES

This equation is the conserved form of the electrolyte water transport as it is typically employed in a computational fluid dynamics (CFD) model, and it is mathematically equivalent to a flux balance that accounts for the same phenomena. In Equation (2), the diffusion term consists of the membrane density ρ^{mem} , the membrane equivalent weight EW , and the diffusion coefficient of water inside the membrane $D_{w,mem}$. The EOD term consists of the drag coefficient n_d , the current I , and the Faraday constant $F = 96,485$ C/mole. Finally, the nonequilibrium sorption (NES) term is proportional to the area density of the electrolyte phase inside the catalyst layer α [m^2/m^3], a kinetic absorption/desorption coefficient k_a , and the membrane density ρ^{mem} divided by the equivalent weight of the membrane EW . The driving force for absorption/desorption is the deviation of the membrane water content λ_w from its equilibrium value $\lambda_{w,equl}$, and the latter depends on the relative humidity of the adjacent gas phase [3].

A similar expression was employed by Lu et al. [13] in their CFD model of a PEMFC. However, that group included the hydraulic permeation term while neglecting the NES term. This was also done in the original model by Springer et al. [14], who considered only the diffusion term and EOD. Note that the hydraulic permeation term was also included in the modeling work of our group [15], but this term was applied to undissolved, “free” water inside the membrane, and not to the water that had dissolved into the electrolyte phase. The hydraulic permeability is a strong function of the membrane water content [16,17], but it was found that the overall effect is negligible compared to the terms in Equation (2) [12]. This, however, appears to be different for electrolyzers that are sometimes operated with a high pressure gradient [18].

In their groundbreaking research, Springer et al. [14] developed a model for water transport in a PEMFC membrane where they assumed that the membrane is always in equilibrium with the neighboring gas/liquid phase, thus $\lambda_{w,equl} = \lambda_w$, and consequently the NES term would be identical to zero. This explicitly stated assumption in the model by Springer et al. [14] became for a long time an unstated, implicit assumption in many modeling attempts that followed. Even the commercial ANSYS Fluent Fuel Cell Module in its first version only accounted for EOD versus diffusion and neglected the NES term [19].

A key property in Equation (2) and for the overall understanding of membrane water transport is the EOD coefficient n_d . It was shown in a previous publication that when n_d is a constant, as it is frequently assumed (e.g., [20,21]), the picture of water transport through the electrolyte membrane can be simplified [11]. Under such conditions, the EOD term becomes identical to zero inside the membrane, and it is nonzero only inside the catalyst layers where the current is generated, and therefore the divergence of the current in Equation (2) is nonzero. A comparison between the traditional view of membrane water transport and the special case where n_d is a constant is shown in Figure 2. When neglecting hydraulic permeation, the only dissolved water transport mechanism inside the membrane is diffusion. Therefore, depending on whether n_d is a constant or not, there is a fundamental difference in the membrane water transport, and our understanding of it.

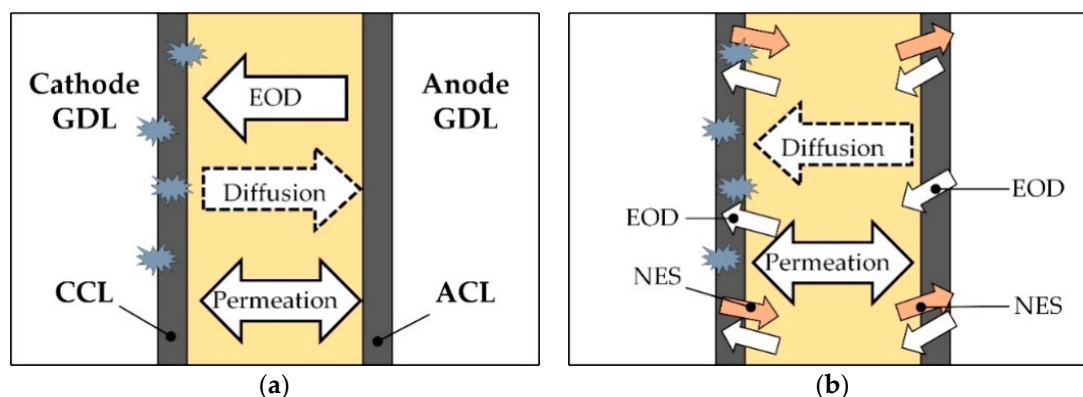


Figure 2. (a) Traditional view of membrane water transport. The stars denote water production in the cathode catalyst layer (CCL). (b) Alternative view of membrane water transport where the electro-osmotic drag (EOD) is a source/sink term of membrane water, and it is partly balanced by nonequilibrium sorption (NES). The difference between EOD and NES is the amount of water that diffuses through the membrane. Forward and backward diffusion are possible. In the alternative model, hydraulic permeation applies only to nondissolved water.

Consequently, a key task in our overall understanding of the membrane water transport is to determine the value of the EOD coefficient n_d , which is discussed in the next section.

3. The EOD Coefficient n_d

Because the value of n_d and the question whether it is constant or not is of central importance for the fundamental understanding of membrane water transport, literature on the determination of this value is briefly reviewed.

Zawodzinski et al. [3] first introduced the concept of λ as the number of water molecules per sulfuric acid group in a PEM. Depending on the water vapor activity of the adjacent gas phase, λ varies between 2 and 14, and when the membrane is equilibrated with liquid water, λ can be as high as 22. This group also found that important material properties such as the water diffusion coefficient in the membrane and the proton conductivity of the membrane exhibit a strong dependency on λ [3]. In their ensuing modeling paper, Springer et al. [14] formulated equations to describe water transport and calculate the overpotentials in a fuel cell. The applied Darken coefficient led to a spike in the water diffusion coefficient inside the membrane as function of λ , which was later on found to be a mathematical artifact owing to the fact that the curve-fit between the membrane water content and the water vapor activity in the adjacent gas phase was chosen to be cubic [22].

As for the EOD coefficient, Springer et al. [14] suggested a linear dependency between n_d and the membrane water content λ , according to

$$n_d = 2.5/22 \times \lambda. \quad (3)$$

The EOD coefficient n_d denotes the number of water molecules that are transported by each proton, i.e., an $n_d = 1$ means that each proton that crosses the membrane drags one water molecule along (it will be shown below that this picture is incorrect). An n_d value of unity thus means that twice the amount of water as is produced in the electrochemical reaction is transported through the membrane, caused by EOD.

The expression in Equation (3) was based on two measured data points: one for a membrane that was equilibrated with liquid water ($\lambda = 22$) that yielded a drag coefficient of $n_d = 2.5 + 0.3$, and one data point of $n_d = 0.9$, measured for a thermally treated, modified membrane with a water content of $\lambda = 11$ [14]. In that work, the authors were only able to obtain values for a membrane equilibrated with liquid water.

In 1992, Fuller and Newman [23] published values for the EOD coefficient based on a concentration cell experiment and analyzed their results using transport equations derived from concentration solution theory. They reported a constant value of $n_d = 1.4$ for a partially hydrated membrane. This value decreased to zero in the range $0 < \lambda < 3$. The resulting curve as was shown in reference [23] exhibits a remarkable resemblance to the shape of the diffusion coefficient as a function of the membrane water content, as proposed by our group [22].

Recognizing the advantage of the concentration cell as constructed by Fuller and Newman, i.e., that n_d values over a wide range of activity values could be obtained, Zawodzinski et al. [24] constructed a similar experimental setup. Instead of calculating the resulting EOD coefficients with equations derived from concentration theory, however, they applied a somewhat simpler but not less elegant approach, arguing that the passage of protons themselves does not lead to a change in free energy, and thus the only change in free energy is caused by water molecules crossing the membrane [24]. By correlating the change in free energy with the difference in water vapor activity between the electrodes, the EOD coefficient could be calculated out of the measured cell potential. These authors now calculated a constant n_d value of unity for all water vapor activities of a partially hydrated membrane. All experiments by Fuller and Newman [23] as well as Zawodzinski et al. [24] were conducted at room temperature.

Therefore, from the early work experiments by Fuller and Newman [23] as well as the Los Alamos group, it may be concluded that the resulting EOD coefficient was $n_d = 1$. In particular, the Los Alamos group corrected their own initial assumption made in the Springer paper [14] of having a linear dependency between n_d and the membrane water content. In that light, it is difficult to understand why the expression for the EOD coefficient according to Equation (3) is still widely employed, even in modern modeling studies as well as in commercial computational packages.

In 1999, Ise et al. [25] conducted an electrophoretic NMR and employed the laws of irreversible thermodynamics in order to isolate and determine the EOD coefficient. This method was very complex and the error bars fairly large, and the resulting drag coefficients were between 1.5 and 2.5 for Nafion at room temperature and at membrane hydration values of $\lambda = 11$ and higher, suggesting that 3–5 times the amount of product water would cross the membrane due to EOD. They also gave a very good overview of the experiments that had been done to determine n_d , and they pointed out that some results were contradictory.

Later on, a different experiment to measure the EOD coefficient was conducted by Ye and Wang [26], who used a hydrogen pumping cell and obtained constant n_d values of around 1.07 over a wide range of membrane water contents.

It is beyond the scope of this work to go into more details in all ensuing studies that attempted to measure the EOD coefficient, and a comprehensive overview of the various experimental efforts was given by Pivovar [27]. However, it should be stated that in numerous studies, authors attempted to measure the EOD coefficient by eliminating diffusion inside the membrane. For this purpose, the membrane was often equilibrated on both sides with liquid water. According to the prior reasoning of this author, it is impossible to eliminate diffusion and still have water crossing the membrane. Admittedly, in the experiments by Ye and Wang [26], the membrane was also equilibrated with water on both sides while the measured n_d coefficient was close to unity and constant.

Another critical comment is that in some studies the electro-osmotic drag coefficient appears to have been confused with the net drag coefficient of water crossing the membrane, r_d , defined as:

$$r_d = \frac{\dot{n}_{H_2O}^{an,in} - \dot{n}_{H_2O}^{an,out}}{I/F}, \quad (4)$$

where I is the total current drawn from the cell and F is Faraday's constant (96,485 C/mol). The molar fluxes are the water fluxes at the inlet and outlet of the anode side of the fuel cell.

A different experiment to isolate the EOD coefficient in an operating fuel cell was suggested in reference [11]. As argued above, inside the catalyst layers the EOD stands in competition to the NES

term, and the difference between these two terms is the water that is condensed into or evaporated out of the membrane phase. Following this argumentation, one arrives at the conclusion that if the NES term can be suppressed, then the net drag coefficient of the water that crosses the membrane (via diffusion) must be equal to the EOD coefficient, $r_d = n_d$ (see Figure 2b).

The NES term depends on the specific surface area of the electrolyte phase inside the catalyst layers and a kinetic adsorption coefficient that depends on the temperature according to the Arrhenius equation [28]. Therefore, in order to measure n_d directly in an operating fuel cell, one should build a membrane-electrode assembly with a very low electrolyte loading in the cathode catalyst and ideally conduct these experiments at a low temperature owing to the Arrhenius type of dependency. On the other hand, sufficient water has to be provided to the anode side in order to sustain an expected net drag coefficient of unity or higher. According to previous calculations, the anode side humidifier has to be operated at 85 °C and hydrogen has to be supplied at a stoichiometric flow ratio of 1.5 or higher to provide a sufficient amount of water [29]. The high temperature would make it difficult to reduce the NES term to a negligible amount, but a strong effect of the electrolyte loading in the CCL on the water balance can be expected. The overall fuel cell water balance can then be accurately measured with a hot wire anemometer [29,30].

As it was already pointed out above, the fact that n_d could be a constant has very important practical implications. Even if we limit our considerations for the moment to the membrane water content range, where n_d was found to be unity [24], then we are left with a membrane water transport picture as shown in Figure 2b. For the sake of clarity, this is now repeated:

The EOD is confined to the electrodes, and this effect is in part balanced by the nonequilibrium sorption. The difference between these two terms is the amount of water that diffuses through the membrane. Any dissolved water that crosses the membrane diffuses through it [11]. Mathematically, the EOD term becomes a source/sink term for membrane water from/to the adjacent gas or liquid phase, and this makes the EOD an interface effect, similar to the NES term. Consequently, even inside the electrodes it holds that the water transport inside the electrolyte phase is via diffusion. This is in contrast to the frequently drawn picture of an actual dragging of water by protons through the membrane. The difference between the EOD term and the NES term, i.e., the right side in Equation (2), is the amount of water that condenses into or evaporates from the electrolyte phase as this water undergoes a phase change with detectable evaporation/condensation energy.

Experiments to measure the transversal membrane water profile in a fuel cell during operation have shed some light into the question as to how the water crosses the membrane. However, it is beyond the scope of the present work to summarize the numerous different studies that were conducted in the past. It is only pointed out that as early as 1996, Mosdale et al. [31] had clear indication that even when current is crossing the membrane, the water redistributes in a diffusion-like process. Moreover, later on the same group from CEA Grenoble employed confocal Raman spectroscopy and showed that the water concentration gradient inside the membrane can also point from anode to cathode [32], thereby eliminating the concept of “back diffusion”. The measured water profile in the membrane was also near linear, which is in good agreement with CFD simulations by our group [12], but in vast contrast to early modeling results by Eikerling et al. [20].

To sum up: when the EOD coefficient n_d is constant, the only fundamental water transport mechanism inside the electrolyte phase is diffusion. This is the case for a large range of membrane water content values of up to $\lambda = 14$ [24], i.e., when the membrane is equilibrated with water vapor. Once, however, one is committed to applying a constant n_d and thereby arriving at diffusion-only water transport, it is difficult to see why this fundamental transport mechanism inside the membrane should change just because the boundary condition for the water activity may change. Either the EOD is a fundamental water transport mechanism inside the membrane, or it is not. This author claims the latter. This leads to the question concerning the nature of EOD:

If EOD is not a water transport mechanism inside the polymer electrolyte membrane, what is it instead?

In order to obtain a better view of the nature of EOD, a number of hypotheses are formulated below, which lead to a completely different understanding of EOD that is more coherent with the mathematical equations.

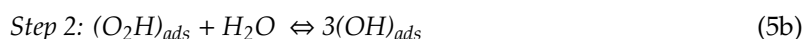
4. Hypotheses on the Nature of EOD

In the following, a picture of the EOD will be drawn that contrasts with conventional thinking. In the beginning, the only assumption is to have a constant value for n_d .

The previous argumentation arrived at the conclusion that EOD is an interface effect confined to the fuel cell (or electrolyzer) electrodes. It is similar in nature to the nonequilibrium sorption term, but different in that it is mathematically connected to the generation/consumption of electrical current. Mathematics dictate that where there is current generated or consumed, there is electro-osmotic drag.

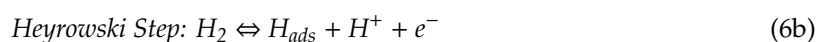
In order to better understand the nature of EOD, it is therefore instructive to investigate other phenomena that occur inside the electrodes and are connected to the generation of current. The other phenomena that occur inside the catalyst layers are the electrochemical half-cell reactions. It is known that these half-cell reactions occur in a frequency of elementary reaction steps, and in order to find the origin of EOD, it is therefore instructive to analyze these elementary reaction steps. While it is beyond the scope of this work to expand on the vast number of studies and literature on this highly complex subject, the very accessible overview and introduction to the physics of elementary reaction steps given by Koper [33] is pointed out.

For the oxygen reduction reaction that occurs in the cathode of a PEMFC, the most accepted mechanism is:



Step 1 and Step 3 were confirmed by Damjanovic and Brusic [34], and the first step was identified as the rate-controlling one. These authors also listed numerous alternative reaction mechanisms both for oxygen evolution and dissolution [34]. It is known that the reaction mechanisms may change depending on whether or not the electrode is oxide-covered, and the above mechanism was proposed for an oxide-free electrode. According to the review by Koper, it is generally believed that in electrolyzers, the steps follow in reverse order [33]. Note that in a recent paper, Reier et al. [35] stated that for the electrocatalytic oxygen evolution as it occurs in electrolyzers, none of the oxygen evolution reactions have been fully validated.

The most accepted pathway for the hydrogen oxidation reaction in acid is (e.g., [36,37]):



While many of these elementary reaction steps have been formulated with protons, it has been stated elsewhere that protons usually do not exist as free species in a solution [38], and other authors have written the reverse hydrogen evolution reaction with hydronium ions instead of protons (e.g., [39]).

The reason why these elementary reactions steps in PEMFC and PEMEC are brought up in this work that focuses on the nature of EOD, is that in fact the root cause for EOD may be found in the elementary reaction steps. It was shown above that EOD can be tracked down to the catalyst layers, and it is the next logical step to connect the EOD to the current-generating steps inside the catalyst layers as well, as it is mathematically already connected to them. Consequently, the following hypotheses are formulated:

Hypothesis 1. *EOD is not a water transport mechanism inside polymer electrolyte membranes.*

Hypothesis 2. *EOD is an interface effect and connected to the current generation in the electrodes.*

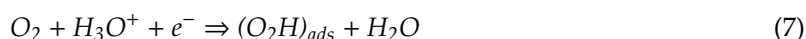
Hypothesis 3. *The EOD coefficient n_d can have a different value in the electrodes.*

Hypothesis 4. *The EOD coefficient n_d can depend on the current density and the catalytic surface.*

5. Discussion

Hypothesis 1 was already stated in previous work [11], albeit not as a hypothesis, and is only repeated here for the sake of completion. The only transport mechanism of dissolved water inside the electrolyte phase is diffusion.

Hypothesis 2 requires elaboration. The EOD coefficient may be linked to the other current-generating phenomena, i.e., the elementary reaction steps. Consequently, future research should focus on identifying the elementary reaction steps that cause EOD. It is generally difficult to see how an elementary reaction step that involves dragging a water molecule out of the electrolyte phase could be as facile as others. Damjanovic and Buric [34] have already found that the first step in the oxygen reduction reaction according to Equation (5a) is the rate-determining one. If this reaction step is written with a hydronium ion instead of a proton, it would look like:



Where the hydronium ion would be taken from the electrolyte phase, and, according to the effect of the EOD, the resulting water molecule would be located outside of the electrolyte phase. Likewise, the last step, Equation (5c), could also be written with hydronium ions to yield an additional water molecule on the right hand side of the equation. In this way, each proton/hydronium ion would bring a water molecule out of the electrolyte phase, and an EOD coefficient of unity could be explained.

Hypothesis 3 follows out of the fact that the half-cell reactions in a fuel cell or electrolyzer follow different reaction pathways. For this reason, it is also conceivable that EOD occurs in only one of the electrodes. The overall picture of membrane water transport as drawn here in Figure 2b would allow for such a scenario while the traditional view as drawn in Figure 2a would not. The “standard case” of implementing the EOD term as a source term for membrane water at the fuel cell anode side and a corresponding sink term for the cathode side was described in a previous publication [11], and it was possible to explain the observed water flow directions.

Hypothesis 4 follows out of the observation that the reaction pathways can change with current density and oxide coverage of the platinum catalysts [34].

As a final comment, it should be stated that the current view and hypotheses apply to water transport in the membrane and are therefore not in conflict with the typical view on proton transport through the membrane via two competing mechanisms, the vehicle transport mechanism and the Grotthuss “hopping” mechanism (e.g., [27]).

6. Conclusions

It can be concluded from this work that the EOD is not a transport mechanism for membrane water. Instead, it is a phenomenon that occurs only inside the catalyst layers and is (mathematically) connected to the current generation. As such, it is reasonable to propose that EOD should be linked to the elementary reaction steps. When analyzing the steps for the oxygen reduction reaction that occurs in PEMFC as proven experimentally by Damjanovic and Buric [34], it becomes obvious that when writing the first and last elementary steps with hydronium ions rather than protons, water is brought from inside the electrolyte phase to the outside. Thus, EOD is proposed to be a part of the elementary reactions steps. As it is difficult to see, how the EOD mechanisms could be as facile as other elementary reactions steps, it is also proposed that EOD is part of the rate-determining step. Because anode and

cathode follow different elementary reaction steps in PEMFC and PEMEC, it is then suggested that EOD can occur in one electrode, but not in the other. Finally, it is known that the elementary reaction steps depend on the catalyst surface treatment as well as the current density, and therefore the EOD may also vary with these conditions. This may help to explain the large variation of experimentally determined values for the EOD coefficient n_d .

Funding: This research received no external funding. The Thermo-fluids Section of the Department of Energy Technology, Aalborg University, has helped to meet the publication cost of this article.

Conflicts of Interest: The author declares no conflict of interest.

References

1. Scott, D.S.; Häfele, W. The coming hydrogen age: Preventing world climatic disruption. *Int. J. Hydrogen Energy* **1990**, *15*, 727–737. [[CrossRef](#)]
2. Barbir, F. *PEM Fuel Cells—Theory and Practice*, 2nd ed.; Academic Press: Cambridge, MA, USA, 2012.
3. Zawodzinski, T.A.; Neeman, M.; Sillerud, L.O.; Gottesfeld, S. Determination of Water Diffusion Coefficients in Perfluorosulfonate Ionomeric Membranes. *J. Phys. Chem.* **1991**, *95*, 6040–6044. [[CrossRef](#)]
4. Wilkinson, D.P.; Voss, H.H.; Prater, K. Water management and stack design for solid polymer fuel cells. *J. Power Sources* **1994**, *49*, 117–127. [[CrossRef](#)]
5. Büchi, F.N.; Srinivasan, S. Operating Proton Exchange Membrane Fuel Cells Without External Humidification of the Reactant Gases. *J. Electrochem. Soc.* **1997**, *144*, 2767–2772. [[CrossRef](#)]
6. Berning, T. The dew point temperature as a criterion for optimizing operating conditions of proton exchange membrane fuel cells. *Int. J. Hydrogen Energy* **2012**, *37*, 10265–10275. [[CrossRef](#)]
7. Dai, W.; Wang, H.; Yuan, X.Z.; Martin, J.J.; Yang, D.; Qiao, J.; Ma, J. A review on water balance in the membrane electrode assembly of proton exchange membrane fuel cells. *Int. J. Hydrogen Energy* **2009**, *34*, 9461–9478. [[CrossRef](#)]
8. Voss, H.H.; Wilkinson, D.P.; Pickup, P.G.; Johnson, M.C.; Basura, V. Anode Water Removal: A Water Management and Diagnostic Technique for Solid Polymer Fuel Cells. *Electrochim. Acta* **1995**, *40*, 321–328. [[CrossRef](#)]
9. Bernardi, D.M. Water-Balance Calculations for Solid-Polymer-Electrolyte Fuel Cells. *J. Electrochem. Soc.* **1990**, *137*, 3344–3350. [[CrossRef](#)]
10. Bernardi, D.M.; Verbrugge, M.W. A Mathematical Model of the Solid-Polymer-Electrolyte Fuel Cell. *J. Electrochem. Soc.* **1992**, *139*, 2477–2491. [[CrossRef](#)]
11. Berning, T. On water transport in polymer electrolyte membranes during the passage of current. *Int. J. Hydrogen Energy* **2011**, *36*, 9341–9344. [[CrossRef](#)]
12. Berning, T.; Odgaard, M.; Kær, S.K. Water balance simulations of a polymer-electrolyte membrane fuel cell using a two-fluid model. *J. Power Sources* **2011**, *196*, 6305–6317. [[CrossRef](#)]
13. Luo, G.; Ju, H.; Wang, C.Y. Prediction of dry-wet-dry transition in polymer electrolyte fuel cells. *J. Electrochem. Soc.* **2007**, *154*, B316–B321. [[CrossRef](#)]
14. Springer, T.E.; Zawodzinski, T.A.; Gottesfeld, S. Polymer Electrolyte Fuel Cell Model. *J. Electrochem. Soc.* **1991**, *138*, 2334–2342. [[CrossRef](#)]
15. Berning, T.; Odgaard, M.; Kær, S. Water Balance Simulations of a PEM Fuel Cell Using a Two-Fluid Model. *ECS Trans.* **2010**, *33*, 1503–1513. [[CrossRef](#)]
16. Weber, A.; Newman, J. Transport in Polymer-Electrolyte Membranes—I. Physical Model. *J. Electrochem. Soc.* **2003**, *150*, A1008–A1015. [[CrossRef](#)]
17. Weber, A.; Newman, J. Transport in Polymer-Electrolyte Membranes—II. Mathematical Model. *J. Electrochem. Soc.* **2004**, *151*, A311–A325. [[CrossRef](#)]
18. Medina, P.; Santarelli, M. Analysis of water transport in a high pressure PEM electrolyzer. *Int. J. Hydrog. Energy* **2010**, *35*, 5173–5186. [[CrossRef](#)]
19. Li, S.; Becker, U. A three dimensional CFD model for PEMFC. In *Proceedings of the ASME 2004 2nd International Conference on Fuel Cell Science, Engineering and Technology*; ASME: Rochester, NY, USA, 2004; pp. 157–164.

20. Eikerling, M.; Kharkats, Y.L.; Kornyshev, A.A.; Volkovich, Y.M. Phenomenological Theory of Electro-osmotic Effect and Water Management in Polymer Electrolyte Proton-Conducting Membranes. *J. Electrochem. Soc.* **1997**, *145*, 2684–2699. [[CrossRef](#)]
21. Büchi, F.N.; Scherer, G.G. Investigation of the Transversal Water Profile in Nafion Membranes in Polymer Electrolyte Fuel Cells. *J. Electrochem. Soc.* **2001**, *148*, A183–A188. [[CrossRef](#)]
22. Olesen, A.C.; Berning, T.; Kær, S.K. On the Diffusion Coefficient of Water in Polymer Electrolyte Membranes. *ECS Trans.* **2013**, *50*, 979–991. [[CrossRef](#)]
23. Fuller, T.F.; Newman, J. Experimental Determination of the Transport Number of Water in Nafion 117 Membrane. *J. Electrochem. Soc.* **1992**, *139*, 1332–1337. [[CrossRef](#)]
24. Zawodzinski, T.A.; Davey, J.; Valerio, J.; Gottesfeld, S. The water content dependence of electro-osmotic drag in proton-conducting polymer electrolytes. *Electrochim. Acta* **1995**, *40*, 297–302. [[CrossRef](#)]
25. Ise, M.; Kreuer, K.D.; Maier, J. Electroosmotic drag in polymer electrolyte membranes: An electrophoretic NMR study. *Solid State Ion.* **1999**, *125*, 213–223. [[CrossRef](#)]
26. Ye, X.; Wang, C. Measurement of Water Transport Properties through Membrane-Electrode Assemblies. *J. Electrochem. Soc.* **2007**, *154*, B676–B682. [[CrossRef](#)]
27. Pivovar, B.S. An overview of electro-osmosis in fuel cell polymer electrolytes. *Polymer* **2006**, *47*, 4194–4202. [[CrossRef](#)]
28. Ge, S.; Li, X.; Yi, B.; Hsing, I. Absorption, Desorption, and Transport of Water in Polymer Electrolyte Membranes for Fuel Cells. *J. Electrochem. Soc.* **2005**, *152*, A1149–A1157. [[CrossRef](#)]
29. Berning, T.; Al Shakhshir, S. Applying hot-wire anemometry to directly measure the water balance in a proton exchange membrane fuel cell for a pre-humidified hydrogen stream. *Int. J. Hydrogen Energy* **2016**, *41*, 5315–5320. [[CrossRef](#)]
30. Berning, T.; Al Shakhshir, S. Applying hot wire anemometry to directly measure the water balance in a proton exchange membrane fuel cell e Part 1: Theory. *Int. J. Hydrogen Energy* **2015**, *40*, 12400–12412. [[CrossRef](#)]
31. Mosdale, R.; Gebel, G.; Pineri, M. Water profile determination in a running proton exchange membrane fuel cell using small-angle neutron scattering. *J. Membr. Sci.* **1996**, *118*, 269–277. [[CrossRef](#)]
32. Huguet, P.; Morin, A.; Gebel, G.; Deabate, S.; Sutor, A.K.; Peng, Z. In situ analysis of water management in operating fuel cells by confocal Raman spectroscopy. *Electrochem. Commun.* **2011**, *13*, 418–422. [[CrossRef](#)]
33. Koper, M.T.M. Thermodynamic theory of multi-electron transfer reactions: Implications for electrocatalysis. *J. Electroanal. Chem.* **2011**, *660*, 254–260. [[CrossRef](#)]
34. Damjanovic, A.; Brusic, V. Electrode Kinetics of Oxygen Reduction on Oxide-Free Platinum Electrodes. *Electrochim. Acta* **1967**, *12*, 615–628. [[CrossRef](#)]
35. Reier, T.; Nong, H.N.; Teschner, D.; Schlögl, R.; Strasser, P. Electrocatalytic Oxygen Evolution Reaction in Acidic Environments—Reaction Mechanisms and Catalysts. *Adv. Energy Mater.* **2017**, *7*, 1601275. [[CrossRef](#)]
36. Marković, N.M.; Ross, P.N. Surface science studies of model fuel cell electrocatalysts. *Surf. Sci. Rep.* **2002**, *45*, 117–229. [[CrossRef](#)]
37. Durst, J.; Siebel, A.; Simon, A.; Hasche, F.; Herranz, J.; Gasteiger, H.A. New insights into the electrochemical hydrogen oxidation and evolution reaction mechanism. *Energy Environ. Sci.* **2014**, *7*, 2255–2260. [[CrossRef](#)]
38. Kreuer, K.D. Proton Conductivity: Materials and Applications. *Chem. Mater.* **1996**, *8*, 610–641. [[CrossRef](#)]
39. Dubouis, N.; Grimaud, A. The hydrogen evolution reaction: From material to interfacial descriptors. *Chem. Sci.* **2019**, *10*, 9165–9181. [[CrossRef](#)]



© 2020 by the author. Licensee MDPI, Basel, Switzerland. This article is an open access article distributed under the terms and conditions of the Creative Commons Attribution (CC BY) license (<http://creativecommons.org/licenses/by/4.0/>).

MDPI
St. Alban-Anlage 66
4052 Basel
Switzerland
Tel. +41 61 683 77 34
Fax +41 61 302 89 18
www.mdpi.com

Energies Editorial Office
E-mail: energies@mdpi.com
www.mdpi.com/journal/energies



MDPI
St. Alban-Anlage 66
4052 Basel
Switzerland

Tel: +41 61 683 77 34
Fax: +41 61 302 89 18

www.mdpi.com



ISBN 978-3-0365-1934-0